CRANFIELD UNIVERSITY

SCHOOL OF INDUSTRIAL AND MANUFACTURING SCIENCE

PhD THESIS

C FANARA

A LANGMUIR MULTI-PROBE SYSTEM FOR THE CHARACTERIZATION OF ATMOSPHERIC PRESSURE ARC PLASMAS

CRANFIELD UNIVERSITY

SCHOOL OF INDUSTRIAL AND MANUFACTURING SCIENCE

PhD THESIS

Academic Year 2002-2003

C FANARA

A LANGMUIR MULTI-PROBE SYSTEM FOR THE CHARACTERIZATION OF ATMOSPHERIC PRESSURE ARC PLASMAS

Supervisor: Prof. J NICHOLLS

April 2003

Dedicato a Francesca e Riccardo che hanno pazientemente sopportato e supportato la mia assenza fisica e mentale

Acknowledgments

I wish to thank my supervisor, Prof. John Nicholls for taking on the supervision part way through the project. I also thank him and for his patience in considering the numerous and sometimes contradictory proposed revisions and for several useful suggestions.

I feel indebted to Prof. Ian M. Richardson of Delft University for initiating me to the field of arc plasmas and for his early supervision while at Cranfield. Also I wish to thank him for the discussions on many aspects of arc physics.

Many thanks are due to Mr. Raymond Newman for his invaluable technical assistance.

Acknowledgments are due to Dr. Anthony B. Murphy of CSIRO for kindly providing data on equilibrium thermodynamical and transport properties for argon and mixtures.

I wish to thank EPSRC for its financial support through grant Nr. L8 2281

TABLE OF CONTENTS

APPENDICES

SUMMARY

The ‘high-pressure’ atmospheric (TIG) arc plasma is studied by means of a multi-Langmuir probe system. In order to determine the appropriate regime of operation, definitions of the plasma parameters for the description of the argon arc are considered and evaluations are presented. A description of the probe basic techniques is followed by an in-depth discussion of the different regimes of probe operation. The emphasis is put on atmospheric and flowing (arc) regimes. Probe sheath theories are compared and “Non-idealities” like cooling due to plasma-probe motion and probe emission mechanisms are then described.

The extensive literature review reveals that the existing probe theories are inappropriate for a use in the TIG arc, because of ‘high’ pressure (atmospheric), broad range of ionization across the arc, flowing conditions, and ultimately, to the uncertainty about onset of Local Thermodynamical Equilibrium.

The Langmuir probe system is built to operate in floating and biased conditions. The present work represents the first extensive investigation of electrostatic probes in arcs where the experimental difficulties and the primary observed quantities are presented in great detail. Analysis methodologies are introduced and experimental results are presented towards a unified picture of the resulting arc structure by comparison with data from emission spectroscopy. Results from different measurements are presented and comparison is made with data on TIG arcs present in literature. Probe obtained temperatures are lower than the values obtained from emission spectroscopy and this ‘cooling’ is attributed to electron-ion recombination. However, it is believed that probes can access temperatures regions not attainable by emission spectroscopy.

Only axial electric potential and electric field are obtained because of the equipotential-probe requirement. Estimations of the sheath voltage and extension are obtained and a qualitative picture of the ion and electron current densities within the arc is given.

1. INTRODUCTION

Among high pressure plasmas, the atmospheric (TIG) arc plasma is conventionally studied by means of optical emission spectroscopy whose main outcomes are the temperature maps.
Other useful parameters for the prediction of the arc plasma description include particle density, arc electrical structure and the determination of transport parameters.

Emission spectroscopy is limited to the core region of the arc because of the Partial Local Thermodynamical Equilibrium (PLTE) required for most of the optical methods to work. This sets a lower limit of 10,000 *K* on the temperature achievable and thus (*i*) a maximum radial distance of few millimetres from the arc axis and (*ii*) a minimum arc current of about 50 *A*. Moreover, even with up-to-date detectors (e.g. CCD) the construction of a complete thermal map by optical means requires a long measurement time. For instance, a thermal map made of ~ 1000 experimental points requires at least two hours, or double this time, if a further wavelength is required which does not fall within the monochromator spectral region employed within a single measurement. Two hours is believed to be the limiting time beyond which the arc starts showing property changes due to cathode erosion. Also, the repetition of the scans for different ('far') wavelengths implies that a *different* arc needs to be struck and the homogeneity of the data is then put into some question.

A faster technique which can also investigate wider radial distances is therefore required and the Langmuir probe method, despite its invasivity, offers appreciable benefit. Traditionally, Langmuir probes have been employed successfully in low pressure plasmas. Because the handful of published works available for probes in arcs shows paucity of theoretical justification and of relevant experimental details, it is of interest to establish the basis of the method for these kinds of plasmas. Because the latter show a range of parameters which differs considerably from the traditional 'glow-like' discharge in terms of current, voltage, ionization level, pressure and fluid flow, an extensive review is needed in order to (*i*) establish relevant arc properties and (*ii*) review probe regimes (if existing) from the literature, which is vast on probes, but scarce for probes in arcs, before any experiment can be interpreted with success.

For this reason, an extensive amount of numerical estimates on the key atmospheric pressure plasma (Chapter 2) and plasma-probe parameters (Chapters 3 to 6) has been performed in this work to pave the way for the experimental part (Chapters 7 to 15) where the measured quantities are discussed along the lines established in this 'critical assessment of the existing literature' (Chapters 2 to 6).

Outline

Chapter 2, after some definitions, reports details on cross-sections, ionization and electrical conductivity. These inter-related quantities vary considerably depending on the location within the arc and therefore on the temperature. To make homogeneous comparison among parameters, the Olsen curve for the particle density dependency on temperature has been chosen and consistently used in all the further numerical determinations, both for numerical estimations as well as in the course of the experiments. Ionization and recombination need to be addressed because of their order of magnitude influences on mechanism by which charge is maintained or lost in colder regions of the plasma. Fluid parameters become relevant in these plasmas because of the existence of magnetically generated ('pinch') flows and consequently, of the existence of boundaries at the plasma-probe interface. With the exception of Chapter 3 which outlines the probe methods 'general' terms', all the quantities derived in Chapter 2 are used throughout the work. In Chapter 4, where orders of magnitude for fluid boundary and electrical sheaths thickness are established, the different models for sheath voltages are compared numerically. Chapter 5 examines the probe regimes available in the literature, although limited to the 'high pressure' regime whose boundaries are set in Chapter 2. Despite the theoretical efforts to include 'real world' phenomena, these tend to interfere with measurements and obscure their interpretation. Therefore, in Chapter 6 evaluations of heat transfer to the probe are made and different particle emissions mechanisms from probes are examined. Also, 'chemistry' influences are evaluated in order to establish whether plasma cooling and recombination are relevant.

The aim this work is therefore: establish the degree of applicability of Langmuir probes to high ionization high pressure flowing (arc) plasmas and to explore the information obtainable concerning the arc structure.

Experimentally, the 'high-pressure' atmospheric (TIG) arc plasma is studied by means of a multi-Langmuir probe system operated both in floating and in biased conditions. Construction details are presented in Chapter 7 and 8 and an analysis methodology, mainly aimed at showing how raw data are utilized, is introduced in Chapter 9.

Because they are central to the theory, the constructed characteristic curves are discussed in Chapter 10. Here, the link between directly measured quantities and the particles dynamic parameters is established. Chapter 11 discusses the methods employed to determine the temperatures by means of probes. Also some simplified models for the charge capture are presented. Chapter 12 collects the information gained

on floating and plasma potentials and estimates of the sheath voltage are made, which are then compared with the results of Chapter 4. Chapter 13 deals with further ‘electrical’ parameters (current densities, electric field and electrical conductivity). In Chapter 14 several experimental results are presented together in order to gain a unified picture of the resulting arc structure and some observations about possible conduction structures within arcs are made.
Finally Chapter 15, after a summary of the whole work, reports the conclusions obtained and suggests further investigations.

2. THE ATMOSPHERIC PRESSURE PLASMA

2.1. Introduction

The atmospheric pressure arc is produced by an electrical discharge. Electrical discharges were studied intensively between the end of the 19th and the beginning of the 20th century. Discharges occurring at relatively low pressure and moderately high voltage, known as glow discharges were the first whose underlying principles were established. Discharges occurring at atmospheric pressure and above, give rise to different type of electric arcs [1]. Their use in technological processes varies from plasma cutting and 'gas tungsten arc welding' (GTAW) or Tungsten Inert Gas (TIG) welding to 'gas metal arc welding' (GMAW), in which the welding wire is the anode. Similar plasmas are the Constricted plasma arc, the wall stabilised arc and the atmospheric pressure Inductively Coupled Discharges (ICP) [2]. The object of this study is the Tungsten Inert Gas (TIG) arc, with the aim of determine its properties by means of electrical exploration techniques.

The TIG arc is an atmospheric pressure plasma with a wide degree of ionization, flowing with non negligible velocity. After a brief resume of its main characteristics, some basic definitions of particular interest for the atmospheric plasma are given. Descriptions of more general plasmas may be found in books by Schmidt [3] with major emphasis on kinetics [4][3]), or on the magnetohydrodynamics [5], [6] or on astrophysical plasmas [7], [8]. The books by Raizer [9] and Franklin [10] concentrate on the properties of laboratory electric discharges, while the books by Heimann [11], Manos and Flamm [12] and Lieberman [13], deal with specific technological applications. However, most of these treatments are not appropriate for the regimes pertaining to the subject of this work.

2.2. TIG Arc structure and properties

Only few notions concerning the typical TIG point-plane geometry at atmospheric pressure are reported here. Specific arc features will be given where experimental results are discussed (*cf* Chapter 14).

A TIG arc can be produced by a 'moderate' current (10 -500 A) flowing in an inert gas (argon, sometimes helium and small amounts of hydrogen may be added), under a potential difference between a tungsten pointed rod cathode (often thoriated up to 2%) and a plane surface copper anode. The electrodes are connected to a power device able to deliver high current, then brought in contact and separated. The electrodes become hot at contact and partly vaporize and produce emissions [9]; at the instant of separation the arc strikes in a 'cloud' ionized with respect to the surrounding gas and the arc starts burning.
TIG arcs are usually a few millimetres long (up to about 10) and have diameters of a few millimetres, depending on current, pressure and electrode separation. Visually, two regions are visible: the core, very bright, and a more diffused bell-shaped envelope.
The arc and the weld piece are protected from the external atmosphere by a flowing inert gas (shielding gas). The arc can be described by a Voltage-Current characteristic or by the potential as a function of the inter-electrode distance. For the argon arc, the characteristics have an ill-defined minimum at low currents ("non-thermal arc") and rise slightly at increased currents [1], [14].
The current density distribution is not well known, especially in the regions close to the electrodes. This is a feature of the vast majority of the models describing the structure of the arc, in which the current densities are generally assumed a priori and /or specified as input parameter or boundary conditions [15] or sometimes computed [16].

Three separate regions are considered [1, 14, 17, 18]:
1. the cathode zone
2. The central column
3. the anode zone.

1. *The cathode zone* extends from one Debye length (sheath, [19]) to some tens of microns (pre-sheath) from the cathode tip; the latter is usually made of pure or thoriated (1% to 2%) tungsten (in the latter case to lower the electron extraction potential thus favouring electron emission). Strong electrical field gradients, of the order of 10^7 or 10^8 Vm^{-1} and the limited size of this region make experimental investigations difficult.
The electrons are emitted from the cathode either by thermionic emission [20] or by field emission or by a combination of the two. The exact mechanism is uncertain [21]. Values of the current density at the cathode are in a range where both phenomena would be relevant. Values of 1 to $3 \cdot 10^8 Am^{-2}$ are commonly accepted for total arc currents varying from 100 to 200 A. The exact value is subject to uncertainty and it influences the correct scaling for every current density distribution investigation. Whilst the temperature of the plasma adjacent to the cathode is probably the highest of the whole arc (up to 24,000 K for a 100 A arc), the cathode tip does not reach the melting temperature (tungsten) whose erosion may be thought as due to sputtering phenomena,

in which case also secondary emission should be accounted. Temperature gradients of the order of 10^4 $K/\mu m$ are reported in this region [22].
The problem is further complicated by the existence of protrusions at the microscopic scale, both originally present and induced by erosion; this in turn depends on tip shape, angle [23] and material [24] and on the presence of contaminants, e.g. oxygen, hydrocarbons and water vapours in the surrounding gas.

2. *The arc column* extends for few millimetres (5 to 10) from the cathode zone to the anode zone. Averaged values of the electric field are typically ≈ 1000 Vm^{-1} at atmospheric pressure, while spectroscopic measurements indicate axial temperatures above 16,000 *K*, decreasing radially outwards to 10,000 *K* at few *mm* from the axis; and along the axis down to the anode zone (6,000 *K*). The 10,000 *K* limit is due to the intrinsic limitation of the spectroscopic method and possibly the edge between the plasma and the surrounding shielding gas occurs at lower temperatures (thus at greater radii). Also, the notion of isotherm should be considered with caution because it is strictly related to an underlying state of Local Thermodynamic Equilibrium which is difficult to prove (see section 2.14).
It is a purpose of this investigation to characterize the values of the radial extension, the charged particle density, the electric field and the temperatures. Very few and poorly documented attempts have been performed so far to characterize this region by means of electrical probes [see Chapter 5].

3. *The anode region* extends from the anode surface up to the arc column. Its geometrical extension varies upon conditions but in order of magnitude, it should be slightly larger than the cathode region. The electrical field is of the order of 10^7 *V/m* and the current density $10^7 Am^{-2}$. The influence of vapours from the anode surface makes the study of this region even more difficult and few attempts have been made in the past to measure the electrical and thermal transfer form the plasma to the anode ([25-27]. A dedicated project to investigate this zone is running at Cranfield [28]

2.3. Debye Length and definition of plasma

Around each charge a cloud of spatial charges of opposite sign reduces the Coulomb potential of the single charge down to zero when the ‘screening distance’ is reached. Within this distance short-range phenomena intervene, beyond, collective effects will dominate.
According to Golant [29] an ionized gas is called a plasma when the screening distance of the electric field generated by an insulated charge is small with respect to the ‘characteristic length’ of the system". The ‘characteristic length’ may be identified with the dimension of the plasma container. The screening distance is called the Debye length λ_D and it is the maximum distance over which concentrations of electrons and ions differ sensibly, causing a violation of electrical neutrality. At a global scale electric neutrality attains ("Quasi-neutrality" of the plasma).

The expression for the Debye length may be obtained by solving Poisson's equation for the potential of an isolated charge, surrounded by a large number of induced charges of opposite sign (and assumed to behave according to the Maxwellian distribution). If ion and electron concentrations are equal "at infinity" (i.e. far from the source), $n = n_i = n_e$, the generalized Debye length is

$$\lambda_D = \sqrt{\frac{\varepsilon_o k T_i T_e}{n |e|^2 (T_i + T_e)}} \tag{2.1}$$

written as

$$\lambda_D = \sqrt{\frac{\varepsilon_o k T}{n|e|^2}} \tag{2.2}$$

when an appreciable temperature difference exists between ions and electrons. In that case, T in (2.1) is the lower of the two (generally, the ion temperature $T_i << T_e$). The solution of Poisson's equation obtained away from the diverging point at the origin $r = 0$,

$$V(r) = \frac{e}{4\pi \varepsilon_o r} e^{-r/\lambda_D} \tag{2.3}$$

is the "screened potential", whose expression justifies the alternative definition of the Debye length as the distance at which the potential reduces to $1/e$ of its value at the origin.

Figure 2.1 reports the computed values of the electron density as a function of electron temperature for different Debye lengths. The higher temperature limit lies at the starting border of a fusion plasma, while its high-density values lie near the "quantum plasmas" region. Also shown are the ideal gas region limit and the Debye-Hückel limit outlined in the next section.

2.4. The Debye-Hückel theory

It is possible to represent the plasma by one or more state equations. The simplest relation of the first type is the ideal gas state equation, to be corrected for the effect of particle interactions, when the pressure approaches atmospheric values and above. A formulation of this kind is the Debye-Hückel theory for ionized gases where these corrections are taken into account. The fundamental assumption of the theory is that the interaction potential energy between neighbouring particles is obtainable from the principle of linear superposition of fields so that the potential is proportional to the electric charge [30]. This leads to a form of the Poisson's equation whose right hand side contains a factor which is the inverse of the Debye length.

The main problem with the Debye-Hückel theory lies in the relatively low charge concentration that was assumed in its original derivation. A limiting criterion for its validity is based on the argument that, at higher densities, the effect of the long-range Debye-Hückel potential has to be complemented with short-range electrostatic effects. The average distance between particles, of the order of $n^{-1/3}$ should be smaller than the Debye length, and the limiting electron density is

$$n_e^{\lim} = \frac{1}{2}\frac{1}{(4\pi)^3}\left(\frac{\varepsilon\, kT}{e^2}\right)^3 \qquad (2.4)$$

This condition implies that the Debye-Hückel theory is already inaccurate at $10^{20}\ m^{-3}$. As seen from figure 2.1 this happens well within the region of interest for the arc, the density is therefore too high for Debye-Hückel theory to apply.

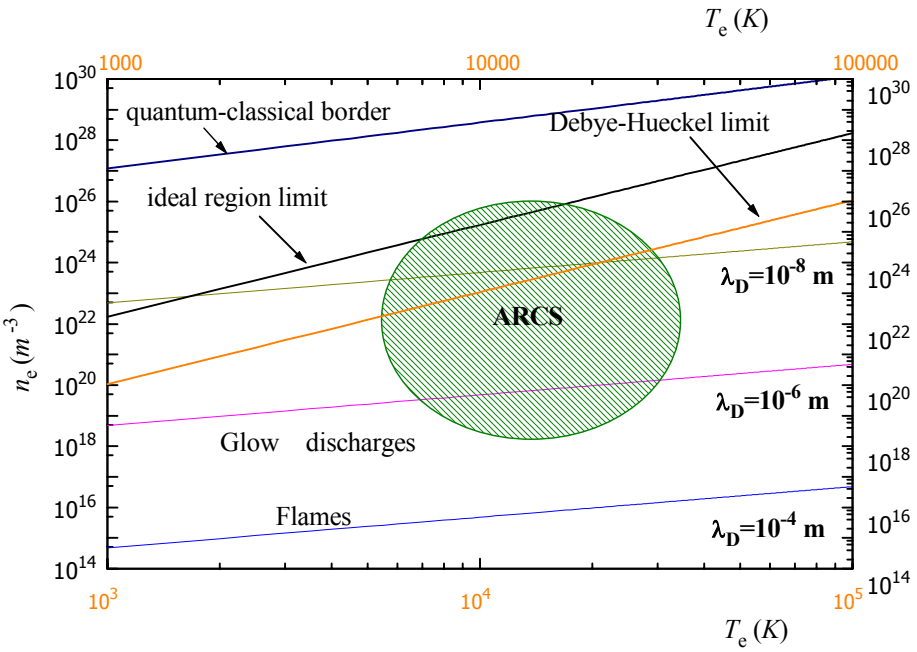

Figure 2.1. Electron density as a function of electron temperature for some laboratory gas discharges at different Debye lengths

2.5. The atmospheric arc Plasma is classical

Laboratory plasmas are classical objects. If δn is the indetermination on charged particle densities, their mean distance, that is the maximum indetermination on the coordinates for the description of the particle motion, is $\delta\, r \approx n^{-1/3}$; according to Heisenberg's principle, the corresponding momentum indetermination is

$$\delta p \approx \hbar/\delta r \approx \hbar\, n^{1/3} \tag{2.5}$$

where $\hbar \equiv h/2\pi = 1.05\cdot 10^{-34} J\cdot s$ is the reduced Planck constant. A classical description requires that the momentum indetermination must be much less than its mean value, i.e.

$$\delta p << \langle p \rangle \approx \sqrt{8 m_e k T_e} \tag{2.6}$$

Using (2.5),

$$n << \left(8 m_e k T_e\right)^{3/2} / \hbar^3 = 3.8\cdot 10^{22} \left(T_e\right)^{3/2} \tag{2.7}$$

This result is of course identical with the one obtained from the condition that the De Broglie wavelength λ_{DB} is much less than the mean inter-particle distance:

$$\lambda_{DB} \equiv \hbar / mv << n^{-1/3} \tag{2.8}$$

2.6. Quasi-neutrality and ideality

Any neutrality violation in the plasma is contrasted by the rise of intense electric fields opposing the displacement of electrons and ions (Due to the large mass ratio between ions and electrons, ion displacement can often be neglected). Neutrality in the presence of free charged particles implies equilibrium if the differences of electrostatic energy at different points are less than the thermal energies.

The electrons and ions maintain the neutrality in volumes $V \geq \lambda_D{}^3$. A perturbation of the neutrality caused by a small charge displacement (say $\approx\lambda_D$) involves the oscillation of a number of particles $n_D \approx (4/3)\pi\lambda_D{}^3 n_e$, the number of particles in the Debye sphere. The definition of quasi-neutrality, and thus of the plasma, adopted so far makes sense only if

$$n_D = \frac{4}{3}\pi n_e \lambda_D^3 >> 1$$

or, for the average inter-particle distance $\ell = n_e^{-1/3} << (4\pi/3)^{1/2}\lambda_D \approx 2\lambda_D$.

More rigorously, n_D includes also the ions,

$$n_D = \frac{4}{3}\pi(n_e + n_i)\lambda_D^3$$

neglected in the above mentioned oscillation due to their higher mass.

These conditions determine the minimum concentration of charged particles that make the plasma. From figure 2.2 it is readily seen that the system under investigation here does not fulfil the revised condition, rather $n_e^{-1/3} \approx \lambda_D$. This is a common case for atmospheric plasmas as pointed out by Goldbach *et al* [31] who noted that at

temperatures about 1 *eV* (*cf* Appendix F – Units) the number of particles within a sphere of radius λ_D is of the order of few units. The condition for an ionized gas to be called a plasma is no longer satisfied.

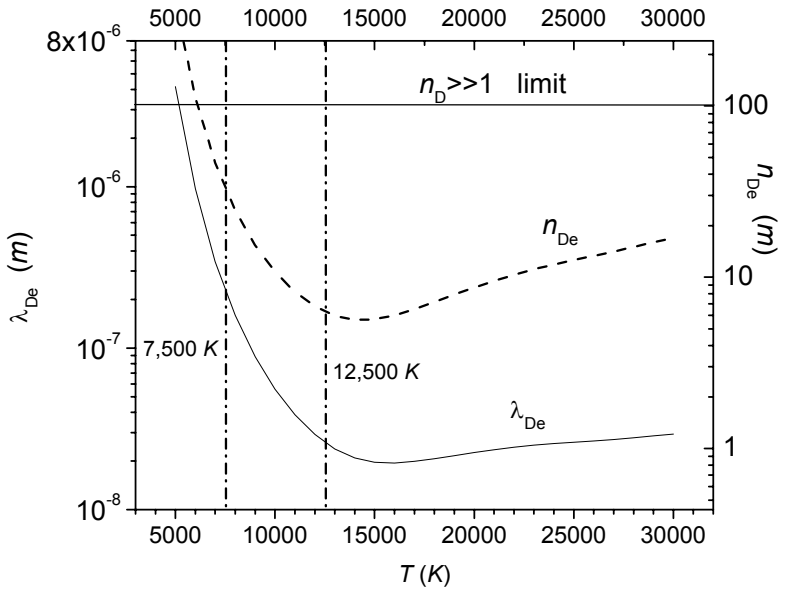

Figure 2.2. Left axis, continuous curve: electron Debye length as a function of electron temperature. Right axis, dashed curve, number of particles per Debye sphere, n_D, as a function of electron temperature T_e.

This problem is not academic though. As will be shown in the next paragraph, n_D plays an important role in the determination of the collision cross-sections.

The criterion for the plasma existence can be modified accordingly, by introducing the distance from a point charge at which the vacuum electrostatic energy equals the kinetic energy kT, the Landau length ℓ_L [29]

$$\ell_L = \frac{e^2}{4\,\pi\varepsilon_o kT} \qquad (2.9)$$

Its value is approximately $8.4\cdot10^{-10}$ *m* at $T\approx20{,}000$ *K*. The mean plasma inter-particle distance $n^{-1/3}$ must exceed this length, $n^{-1/3}>\ell_L$, to prevent recombination of ions and electrons caused by the strong electrostatic potential at short distances; differently stated, to allow for the existence of charge separation. Since the range of the electrostatic interactions in the plasma is the Debye length, the inequality $n^{-1/3} >\lambda_D$ means low recombination but also absence of "cooperative" interactions between particles, e.g. the absence of the plasma state: therefore $n^{-1/3} < \lambda_D$ is required.
The two inequalities, $n^{-1/3}\,\ell > \ell_L$ and $n^{-1/3} < \lambda_D$ merge into

$$\ell_L < n^{-1/3} < \lambda_D \qquad (2.10)$$

For the atmospheric arc, $n^{-1/3} > \ell_L$ is satisfied, while $n^{-1/3} \approx \lambda_D$ only.

Summarizing the situation up to now, it is apparent that the atmospheric arc is called a "plasma" in an improper sense, as the number of particles in the Debye sphere n_D is of the order of few units. In other words, the number of charged particles surrounding a single charge (an ion for example) is not enough to shield its potential and [31] the potential energy of the charged particles is no longer negligible with respect to their kinetic energy.

2.7. Ionization mechanisms and cross sections

1. In order to ionize a neutral atom it is necessary to provide an amount of energy called the ionization potential. The potential needed to strip the first electron, the first ionization potential, is indicated by E_I; the second by E_{II} and so on. Values for some gases of interest are reported in Table 2.1. Even though SI units are used throughout this work, the convention is followed to express the ionization potential in electron-volt ($1eV \approx 11{,}609\ K$). This applies in some cases also to the corresponding temperatures.

Gas	E_I (eV)	E_{II} (eV)	E_{III} (eV)
H	13.598	-	-
He	24.587	54.418	-
Ar	15.760	27.630	40.74

Table 2.1. Ionization potential for some gases [17]

Observing that a temperature $T = 11{,}609\ K$ is needed to give an atom a kinetic energy of 1 eV, only at extremely high temperatures does the thermal energy exceed the ionization potential. However, an ionization can be achieved even if the mean thermal energy is considerably below the ionization potential. In fact, at every temperature there are enough electrons in the high-energy tail of the electron distribution function to produce ionization.

A complete description of ionization processes should be performed in the frame of collision theories, which distinguish between elastic and inelastic collisions. For the regimes of interest of this work, the latter play a marginal role. In fact it is known [29] p.80) that the most important processes involving inelastic scattering in plasmas occur at temperatures of the order of 1 keV at least, corresponding to the thermonuclear plasma regime. In arc discharges, the average ion and atom energies do not exceed 10 eV. An exception is the case of inelastic resonances, among which is the Penning effect discovered in *He-Ne* mixtures [29].

Ion-atom and electron-atom processes can be treated in the approximate frame of short distance (essentially) binary interaction, while the charged-charged processes are intrinsically of long-range nature.

In this work the *Ar-Ar, Ar^+-Ar*, and *e-Ar* cross sections, were taken from Devoto [32]. Older data from Phelps [33] for *e-Ar* show that the total cross-sections for electron-argon are two orders of magnitude below the ones of the process Ar^+-*Ar*, and one order of magnitude below the *Ar-Ar* cross sections. For the purpose of comparison, some values for the electron-atom cross sections σ_{ea} were taken from [34]. For the charged collision cross sections σ_{ei}, the values in [32] were compared with the values computed using the approximate formula reported in [29] (p.57), actually applicable for any gas. These agree within a factor of 2 or so, enough for the present estimations, given the considerable uncertainty for the Coulomb cross-sections. Also some values read from the plots of Frost and Phelps [35] are reported.

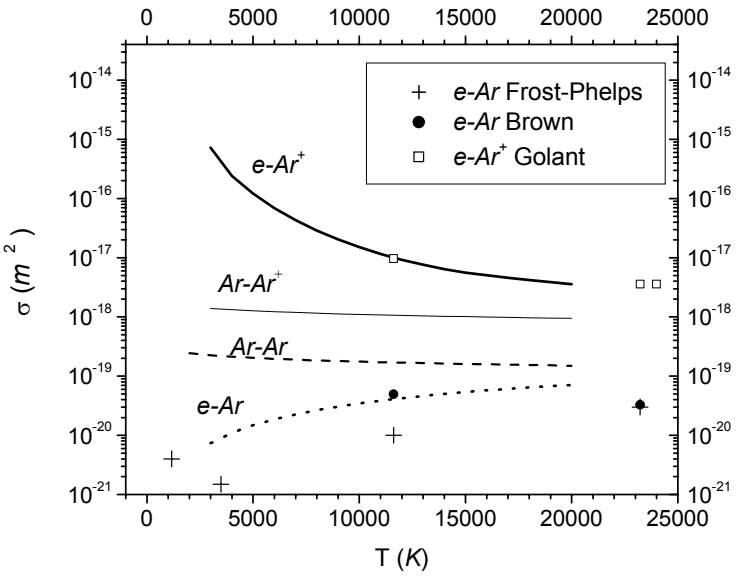

Figure 2.3. Cross-sections for *Ar-Ar, Ar-Ar*$^+$*, e-Ar, e-Ar*$^+$ collisions in argon. Continuous lines, data from Devoto [32]. Scattered points for *e-Ar* collision by Frost and Phelps [35] (crosses), Brown [34] (full-circles) and Golant [29] (open squares)

The cross sections are shown in figure 2.3 as a function of temperature. The lines refer to the determination found in [32]. In figure 2.3, crosses, circles and squares refer to [35], [34] and [29] respectively.

Among the charged particles cross-sections only *e-*Ar^+ were considered as they give the major contribution. Higher ionization states and collisions among like charged particles were neglected as these are less important energetically, although the latter can indirectly modify the electron distribution function [9].

Once estimations for the cross-sections are available, other transport quantities can be evaluated.

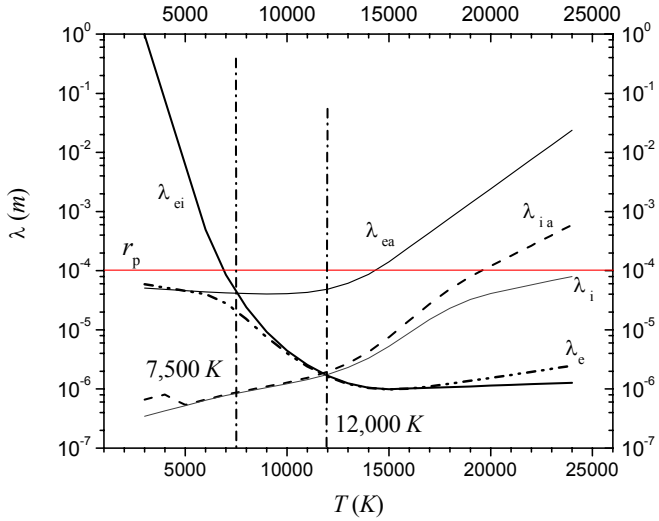

Figure 2.4. Mean free paths as a function of temperature. *ei*, electron-ion; *ea*, electron-atom; *ia*, ion-atom; *i*, ion; *e*, electron. The region between the two vertical lines identifies the intermediate ionization region. The horizontal line at 10^{-4} *m* is the typical probe radius

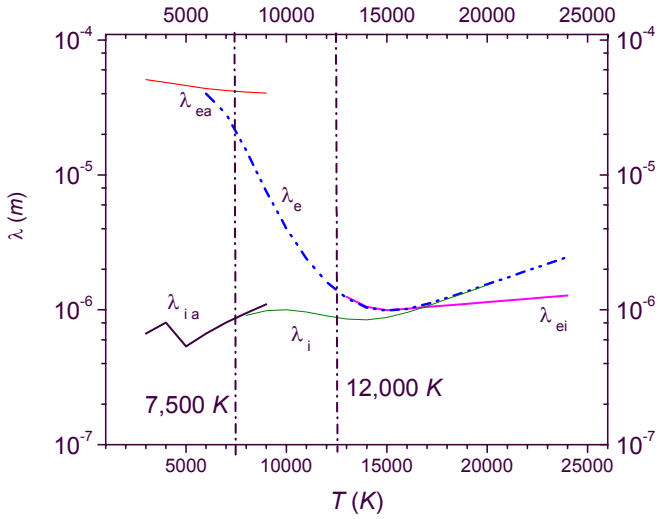

Figure 2.5. Mean free paths selected from figure 2.4. Symbols as in figure1.4

In figure 2.4 the mean free paths for the different collisions of figure 2.3 are computed as a function of temperature using the definitions from elementary kinetic theory (*a*),

with the contributions of the cross-section weighted with the corresponding number density (*b*):

$$\lambda_{ia}=\frac{1}{n_a\sigma_{ia}},\quad \lambda_{ea}=\frac{1}{n_a\sigma_{ea}},\quad \lambda_{ie}=\frac{1}{n_a\sigma_{ie}},\quad (a)$$
$$\lambda_i=\frac{1}{n_a\sigma_{ia}+\sum_k n_i^k\sigma_{i\,k}},\quad \lambda_e=\frac{1}{n_a\sigma_{ea}+n_e\sigma_{ei}}\quad (b) \qquad (2.11)$$

The curves must be read within the limitations of the different temperature regions defined by the different ionization values (see next paragraph). In figure 2.4 the two vertical dash-dotted lines represent low ionization, below 7,500 *K*; intermediate, for *T*<12,000 *K*; and high, above 12,000 *K*. In other words, λ_{ei} should be considered only for *T* >7,500 *K*, λ_{ea} and λ_{ia} should not be considered above about 12,000 *K*. In the intermediate ionization region, λ_i and λ_e should be considered (these are computed by weighting the contributions of the different cross sections).
According to these guidelines, the situation in figure 2.5 is obtained.

The degree of continuity has been obtained between the different regions in order to estimate the mean free paths for electron and ions in the broad range of arc conditions encountered by probes. In Chapters 4 and 5 it will be seen that the mean free paths, together with the Debye length shown in figure 2.2 play a central role in the classification of the probe regimes.

2. The degree of ionization ς is defined as the ratio between the charged particle density $n_e \approx n_i$ and the total particle number densities n_T: $\varsigma = n_{i,e}/(n_{i,e}+n_T)$. When ionization is 'low', among the kind of collisions considered, which are decisive for an estimation of basic kinetics (e.g. mobility, mean free path) or transport properties (conductivities, viscosity), the electron-neutral would play the most important role. Conversely, for already moderate ionization, Coulomb collisions are dominant. In effect, very low degrees of ionization are sufficient for the gas to show electromagnetic properties; the electrical conductivity of a gas is about half its maximum at ζ=0.1% and reaches its maximum at about 1% of ionization [36]. The atmospheric arc plasma shows both a state of 'low' ionization (arc fringes) and 'high' (i.e. full) ionization (arc core). The need to separate these two extremes arises when using different transport models, which depend on the collision mechanism.

It is customary to refer to 'low' ionization when $\zeta<10^{-4}$ whereas for highly ionized gases, $\zeta>10^{-4}$ [36]. A more quantitative criterion is given by Chung, Talbot and Touryan (*cf* [37], appendix, for brevity collectively named CTT in the following) based on the relative abundance of the species weighted with the appropriate cross-sections. The condition

$$\varsigma_w = \frac{n_i \sigma_{ei}}{n_a \sigma_{ea}} \leq 0.1 \qquad (2.12)$$

may be read as 'weak ionization' condition (n_a atom density, n_i ion density, σ_{ei} electron-ion cross section, σ_{ea} electron-atom cross section. The suffix 'w' stands for 'weighted'). Conversely

$$\varsigma_w = \frac{n_i \sigma_{ei}}{n_a \sigma_{ea}} >> 0.1 \qquad (2.13)$$

is the condition for "high ionization". In the latter case, the Coulomb collisions determine the plasma behaviour (*cf* Spitzer [38]).
Using formula (2.12) and the information of figure 2.3 for argon at 1 *eV*

$$\varsigma_w = \frac{5.2 \cdot 10^{22} (m^{-3}) \cdot 970 \cdot 10^{-20} (m^2)}{5.3 \cdot 10^{23} \cdot 4.9 \cdot 10^{-20} (m^2)} \approx 19 \qquad (2.14)$$

and at *2 eV*

$$\varsigma_w = \frac{2 \cdot 10^{23} (m^{-3}) \cdot 358 \cdot 10^{-20} (m^2)}{3.2 \cdot 10^{21} \cdot 3.3 \cdot 10^{-20} (m^2)} \approx 5.3 \cdot 10^3 \qquad (2.15)$$

Even with the uncertainty of a factor 2 in the Coulomb collision cross sections, 'high' ionization takes place at least from 1 *eV* upwards (1 *eV*≈11,600 *K*).
Figure 2.6 reports the ionization fraction of pure argon as a function of temperature at atmospheric pressure [39]. Similar values can be found in [40], and in [41]. With the exception of the last reference, all the references agree in the almost complete ionization for temperatures above about 20,000 *K*. [41] asserts almost full ionization in argon at 15,000 *K*. The author was not able to trace back the origin of this discrepancy.

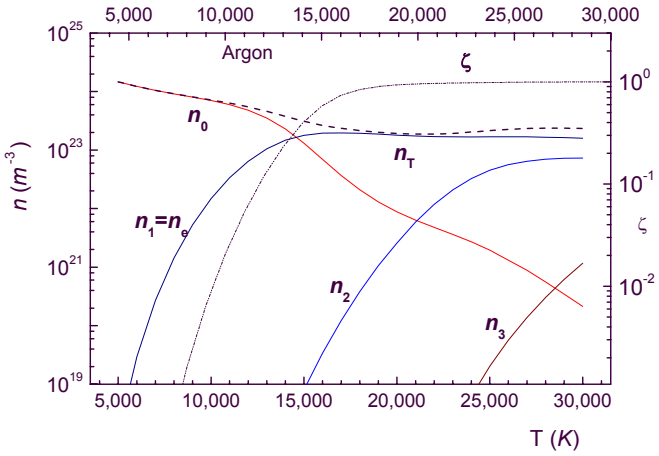

Figure 2.6. Degree of ionization for argon as a function of temperature (Data after [39]). Left axis, broken line: total number density (n_T); continuous curves, n_o=neutral density, n_i=n_e = single ion/electron density, n_i, i=2,3, multiple ion densities. Right axis, broken curve ionization fraction ζ

In figure 2.7 the weighted ionization fraction ζ_w is reported as given by the CTT criterion (left axis), together with the absolute ionization fraction $\zeta = \Sigma_i n_i / n_T = (n_1 + n_2 + n_3)/n_T$ (right axis) on logarithmic scale. The two scales are different but the 0.1 limit on the left axis gives the limiting temperature (path A), and the absolute ionization can be read on the right axis (path B).

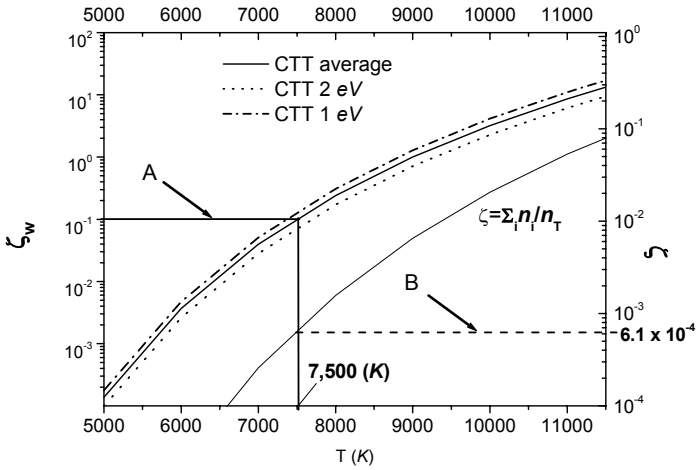

Figure 2.7. Representation of the criterion of Chung et al ('CTT') obtained comparing the weighted ionization fraction with the absolute ionization. Intersection of line A, placed at the '0.1 limit' with the average CTT curve, gives the upper temperature limit for 'low' ionization. The intersection of the vertical line with the absolute ionization fraction ζ gives the corresponding degree of ionization (line B)

Since temperature dependencies of the cross-sections were not available, three different weighted ζ_w were computed using the values for the cross sections given in figure 2.3, respectively, dashed, dotted and continuous curves, at 1 and 2 *eV*, and their averages. The criterion (2.12) gives a lower temperature limit at about 7,500 *K*, below which the plasma can be considered 'weakly ionized'. This correspond to an absolute ionization $\zeta \approx 6 \cdot 10^{-4}$. By similar reasoning, the 'strong ionization', say at $\zeta_w=10 >> 0.1$, corresponds to an absolute ionization less than 10% at 11,200 *K*. Therefore, the atmospheric arc core mentioned above can be considered always moderately to highly ionized.

2.8. Electrical conductivity

The attainment of quasi-neutrality depends on how the charges, whose motion is inhibited by collisions, respond to an electric field. This capability is called electrical conductivity. In the following discussion the symbol σ will be used for both cross-sections and conductivity, as it is standard use. The former will be always suffixed and the context should make it easy to avoid confusion between the two meanings.
Elementary kinetic theory defines the conductivity through the electric current density

$$j = en_e v_d = en_e \mu_e E = \sigma E, \quad \sigma = e\mu_e n_e = \frac{e^2 n_e}{m\nu_m} \tag{2.16}$$

valid in the weak ionization limit. Due to the high ratio μ_e/μ_i of electron to ion mobility, the only carriers considered are electrons (Here v_d is the drift velocity and *E* the electric field). Conductivity depends on the way collisions influence the motion of the charges, through the momentum transfer collision frequency ν_m (or the transport collision frequency) which in turn, depends on the corresponding cross-section. The latter depends on the degree of ionization as outlined in the preceding section.

In rigorous terms, [29], [4] use the Boltzmann kinetic equation with a Fokker-Planck collision term for electron-ion collisions and a Boltzmann collision term for the electron-neutral collisions.
The problem in the calculation of collision integrals lies in the choice of the interaction potential. references [42, 43], use a Coulomb potential truncated at a cut-off distance which has to be determined. Under such circumstances, the effective electron-ion collision frequency has the form

$$\langle \nu_{ei} \rangle = \frac{4}{3}(2\pi)^{1/2} n_e \left(\frac{e^2}{kT}\right)^2 \left(\frac{kT}{m}\right)^{1/2} \ln\Lambda, \quad \Lambda = \frac{r_s}{b_0}, \quad b_0 = Ze^2/3kT \tag{2.17}$$

where Λ is the cut-off radius and b_0 is the minimum impact parameter for ion-electron collision. The problem is therefore the determination of the cut-off distance. Complete calculations performed both by Devoto [32] and by Murphy [44] span the whole range of data in the ionization interval. These data were obtained using the same method and agree with each other, as expected, and also with the few available experimental

determinations, which however, suffer from an indetermination as much as 30% (see e.g. [32], figure 2).
Other evaluations in terms of elementary kinetic theory can only agree within an order of magnitude or so. Nevertheless, some comparisons are presented for the different ionization regimes in the following, because these illustrate the different dependencies on the charged particle densities.

The different ionization regimes are considered.
1. Weak ionization
In the weak ionization limit, formula from elementary kinetic theory

$$\sigma = \frac{e^2 n_e}{m \nu_{th}} \lambda_e = \frac{e^2 n_e}{m \nu_m} = \frac{e^2 n_e}{n_a \sigma_{ea} \sqrt{3mkT}} \tag{2.18}$$

shows a dependency on the ionization fraction though the ratio n_e/n_a. Among the electron-atom collisions the momentum transfer dominates and the corresponding cross-section can be taken from figure 2.3 above.

2. High ionization (Full ionization)
In the limit of full ionization, only Coulomb scattering contributes to the electrical conductivity through (many) small angle deflections and (few) large angle collisions. The 'geometrical' Coulomb cross section should be corrected to account for the latter circumstance leading to the formula of the resistivity η [38, 45]

$$\eta \equiv \frac{1}{\sigma} \approx \frac{\pi e^2 m^{1/2}}{\left(4\pi\varepsilon_o\right)^2 \left(kT_e\right)^{3/2}} \ln \Lambda \tag{2.19}$$

Where

$$\Lambda = \left\langle \frac{\lambda_D}{b_o} \right\rangle = 12\pi n \lambda_D^3 \tag{2.20}$$

is the maximum impact parameters in units of the minimum approach distance b_o (collision parameter) and the Debye length, because the Coulomb interaction is supposed to be smoothed out at distances larger than λ_D ("screening radius"). The average is taken over a Maxwellian distribution, therefore the notion of equilibrium is implicitly contained in (2.19). Formula (2.19) is written for convenience in terms of its inverse, the conductivity

$$\sigma \approx \frac{\left(4\pi\varepsilon_o\right)^2 \left(kT_e\right)^{3/2}}{\pi e^2 m^{1/2} \ln \Lambda} \tag{2.21}$$

With respect to formula (2.18) the dependency on n_e is only $n_e^{-1/2}$ in the logarithmic factor. This means that a current density $j=\sigma E$ through the plasma would depend only weakly on n_e. This is in contrast with the weak ionization case where the electrical

current density in (2.18) is proportional to n_e (in fact μ_e depends only on the neutral density because of the low ionization, $n_{e,i}<<n_T$).

The ln Λ terms as given by [45] seems inappropriate when there are few number of particles in the Debye sphere, in which case $n_D>>1$ is not verified; as shown in the previous section this is the case for the atmospheric arc. The consequent incomplete screening of the potential leads to a modification of the screening radius in the Coulomb logarithm by a factor $x>1$ [43], i.e. (2.21) should contain an enhanced screening radius $r_s=x\lambda_D$ [31, 46]. The failure of the Coulomb parameter as given by formula (2.21) was well known already to Devoto [32] but to the author's knowledge, this problem has not been satisfactorily overcome yet.

3. Moderate ionization

The Frost's mixing rule [47] provides the conductivity formula in terms of the weak σ_0, and the high σ_{ei}, conductivities

$$\sigma = \left(\frac{1}{\sigma_0} + \frac{1}{\sigma_{ei}} \right)^{-1} \qquad (2.22)$$

Formula (2.22), reported also in [36], has been used originally by Frost [47] who states that Spitzer's conductivity applied to his regime could be in error as much as 30%, which is not surprising, considering the maximum temperature of 4,000 *K* of his *Cs* seeded *Ar* plasma.

The method by Murphy and Arundell has been chosen here [48], based on the method of Devoto [32] i.e. on the use of cross-section determined using a (Debye length) shielded Coulomb potential. Although it must be emphasized that it relies upon local thermodynamical equilibrium (LTE), the data [44, 49], are in agreement with the few available measurements, all dating back to 1967. These are reported together with Spitzer's formula (2.21) and the Frost "mixing rule" (2.22) in figure 2.8.

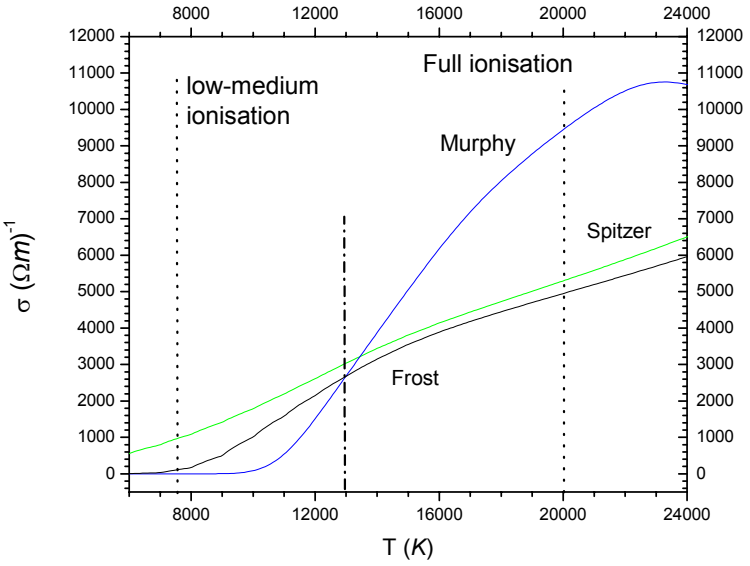

Figure 2.8. Electrical conductivity as a function of temperature for the different methods described in the text

Considering that Devoto's and Murphy's determinations lie well within 5% of each other and that the experimental determinations differ by as much as 30%, the latter limit should be considered as the uncertainty on the electrical conductivity. The uncertainty in the determination suffers also from the low number of particles in the Debye sphere, especially in the temperature range between 13,400 and 15,400 *K*, where n_D is minimum (see figure 2.2).

Spitzer's and Frost's calculated values, while in good agreement with each other, were computed using the slightly corrected elementary kinetic theory formulae and appear outside this 30% uncertainty with respect to Devoto and Murphy. All these conductivities were computed here using the same cross-section ([32]) from which the corresponding mean free-paths were consistently deduced.

2.9. Recombination

Some recombination processes are considered with the aim to evaluate an "effective" recombination coefficient.

A recombination process may be considered in many cases as the process inverse to scattering. In recombination processes, of the kind $e+A^+ \rightarrow A$, energy and momentum conservation require the presence of a third body, be it an atom, an ion, an electron or a photon. The recombination coefficient a is defined [34], [19]

$$\left(\frac{\partial n}{\partial t}\right)_r = -an^2, \quad a = \left\langle v\sigma_r(v)\right\rangle \tag{2.23}$$

Where n is the number density of charged particles, $\sigma_r(v)$ is the electron-ion recombination cross section and $\langle v\sigma_r(v)\rangle$ is a quantity averaged over the velocity distribution. In general, a depends on the electron velocity distribution and therefore on the temperature.

2.9.1. Recombination by collision

At high concentrations of charged particles the process $e+A^+ + e \rightarrow A+e$ is particularly important for electrons that find themselves in the field of an ion for a sufficiently long time.

The order of magnitude of the coefficient of recombination by collision can be found by multiplying the Coulomb cross section of scattering in a region whose dimensions correspond to the radius of the capture orbit, $\pi\, r_s^2$, by the probability that in that region a third body is present, $\pi r_s^3 n$:

$$\sigma_r = \pi^2 n r_s^5 \qquad (2.24)$$

where $r_s = e^2/(4\pi\varepsilon_o kT)$ is the orbit radius, obtained by the equality of kinetic and potential energy:

$$\sigma_r = n\left[e^2/(4\pi\varepsilon_o kT)\right]^5 \pi^2 \qquad (2.25)$$

The recombination coefficient is obtained by multiplying the recombination cross section (2.25) by the average thermal electron velocity $v_{th} = (kT_e/m_e)^{1/2}$

$$a_c = n\pi^2\left[e^2/(4\pi\varepsilon_o kT)\right]^5\left(\frac{kT_e}{m_e}\right)^{1/2} \qquad (2.26)$$

Thus a_c decreases when electron density lowers and temperature rises. Because these values are computed with formula (2.25), which does not contain any species parameter, results have to be considered with caution.

Also, there is no agreement with the values reported by Von Engel [50], $a_c=10^{-10}\ m^3 s^{-1}$.

In a paper by Sansonnes *et al* [16] a formula is reported

$$a_c^2 = 1.29\cdot 10^{-32}\left(\frac{1.353\cdot 10^5}{T}+2\right)e^{\left(\frac{4.78\cdot 10^4}{T}\right)} \quad cm^6 s^{-1}$$

valid for a local plasma temperature T>3,200 K.

A different type of ‘collisional’ recombination is the dissociative recombination reported by Brown [34] involving atoms and ions rather than electrons, according to the scheme

$$e + A_2^+ \rightarrow A + A$$

Argon molecules were observed by microwave techniques (*cf* Biondi in reference [34]). Coefficients measured for *Ar*, $a_D = 3 \cdot 10^{-14}\ m^3\ s^{-1}$ and *He*, $a_D = 1.7 \cdot 10^{-14}\ m^3 s^{-1}$, are larger than three-body recombination ($a_c \approx 6.8 \cdot 10^{-15} m^3\ s^{-1}$ for *He* and $6.8 \cdot 10^{-17}\ m^3\ s^{-1}$ for *Ar*) and in broad agreement with the values computed by using

$$a_D \approx (10^{-8} \text{ to } 10^{-10}) / (kT_e)^{3/2} \tag{2.27}$$

which is reported [29] to be applicable in the region below 1 *eV*.

2.9.2. Radiative recombination

An electron approaching an ion drops into a low lying electron orbit radiating the excess energy. Experimentally, the photon emission is detected spectroscopically as a continuum placed above the ionization potential of the atom. The probability of a transition of an electron to drop into an excited level of the atom leads to a recombination coefficients $a_R \approx 10^{-18}\ m^3 s^{-1}$ [34]. As this process is the inverse of the photoionization, the cross section can be obtained by the detailed balance principle [50] and the recombination coefficient for energies below the ionization potential is [29],

$$a_R \approx \frac{10^{-19}}{(kT)^{1/2}} \tag{2.28}$$

For energies above the ionization threshold, a_R decreases sharply for increasing temperatures. Its value remains several orders of magnitude below the collisional coefficient, but these calculations disagree with experimental determinations by orders of magnitude, although measurements are in general quite rare. Brown [34] reports $a_R = 2 \cdot 10^{-16}\ m^3 s^{-1}$ for *Ar* at T_e=3,000 *K*. If one believes the $T_e^{-1/2}$ scaling in (2.28), then at $T_e \approx 20{,}000$ *K* in argon, one would obtain

$$a_R^{20{,}000K} = a_R^{3{,}000K} \sqrt{\frac{3{,}000}{20{,}000}} \approx 8 \cdot 10^{-18}\ m^3\ s^{-1}$$

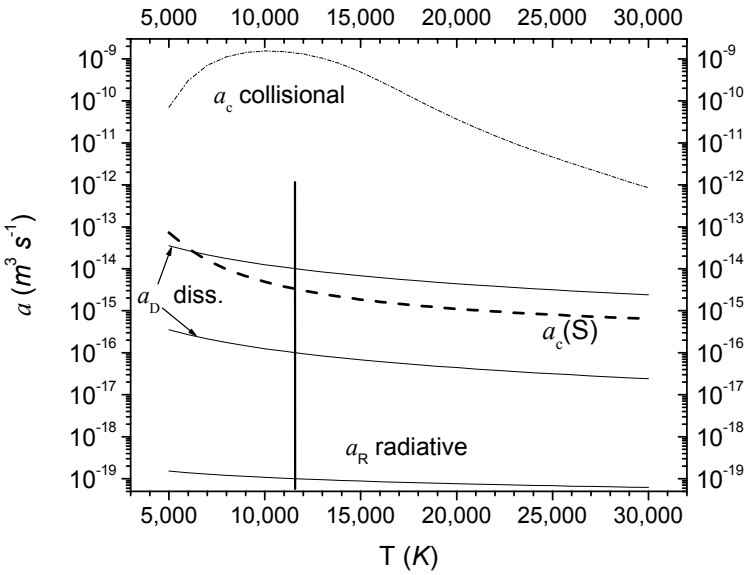

Figure 2.10. Recombination coefficients as a function of temperatures. a_c, collisional (dash-dotted line), computed using n_e=(T_e) according to preceding section. a_c(S), collisional according to Sansonnens [16] (short dashed line). Two dissociative coefficients a_D are shown (continuous curves); according to [29] the determination based on (2.28) is valid up to 1 *eV* (≈11,600 *K*, vertical line). a_R, radiative recombination coefficient (continuous curve)

Values for all three recombination coefficients are reported as a function of temperature in figure 2.10. In the computations, the collisional coefficients include explicitly the temperature dependency of the electron density. Neglecting the radiative contribution there is still an uncertainty of two orders of magnitude considering the region between the two dissociative values; however the validity of the latter is limited to the region below 1 *eV*. It is felt that the estimations of the two collisional calculations have to be chosen carefully but the uncertainty at lower *T* is even worse.

2.10. Electric field and distribution functions

The first successful attempt to deduce an electron distribution function for a gas in an electric field was performed by Druyvestein (*cf* Loeb [51]). In general, this derivation is consistent with the hypotheses that make low pressure plasma.

A higher degree of ionization influences the extent to which electric fields are felt by the charged particles in the plasma whose behaviour and in particular their distribution functions will be altered. This means that the very common assumption of isotropic and even Maxwellian distribution for the charged particles as used in most of the probe theories is not always justified. Complete computations are available in literature [29, 51, 52]. Some conditions were derived for the occurrence of the field-induced perturbation in the two

limiting cases of "high" or "low" plasma ionization for ions and electrons separately (a less qualitative meaning of "low" and "high" was given in paragraph 2 of section 2.6).
The particle distribution functions are usually derived in absence of external fields/forces. The influences of the external forces depend on the nature of the particles. Charged particles will be accelerated in an electric field with consequent variation in their energy. If, as it often occurs, the plasma particles have a 'good contact' with the outer environment (container walls or surrounding gas for the TIG arc), the average energy of neutrals is lower than the average energy of the other components and the velocity distribution might be closer to equilibrium.

1. *Weakly ionized plasma*. The conditions for an electric field to have an important influence on the velocity distributions of the charged particles in a *weakly ionized* plasma are obtained considering the action of the electric field in a time τ during which the particles are subject to an acceleration and corresponding average kinetic energy increase [29]

The energy balance makes the difference between the average charged and neutral particles (K is the kinetic energy for charged particles, K_a the kinetic energy of atoms):

$$< K - K_a > \approx e^2 E^2 / m\kappa\nu^2 \qquad (2.29)$$

therefore, the condition for a weak influence of the electric field is

$$< K - K_a > \; \square \quad < K > \; \approx kT \qquad (2.30)$$

or

$$E \; \square \; E_p = \frac{\nu}{e}\sqrt{\kappa m k T} = \sqrt{\kappa}\; kT / e\lambda \qquad (2.31)$$

where

$$\lambda \approx \frac{v_{th}}{\nu} \approx \frac{1}{\nu}\sqrt{\frac{kT}{m}}$$

is the mean free path. If condition (2.31) is not verified, the average energy of the charged particles is much higher than the average neutral particle energy.

- For *ions*, the energy transfer coefficient κ is $\sqrt{2}/2$ and (2.31) becomes
$$E(V/m) \; \square \; E_{pi} \approx 0.8\; kT_i / e\lambda_{ia} \approx 7 \cdot 10^{-5} T(K) / \lambda_{ia}\,(m) \qquad (2.32)$$

If (2.32) is not verified, the average energy and the distribution function differ noticeably from the corresponding equilibrium quantities. In that case, for the ions the

thermal velocity and the drift velocity are comparable, $v_{th} \approx v_d$ and the distribution function is essentially anisotropic (*cf* also [9])

• For *electrons* the energy transfer coefficient is much lower than one and for elastic collisions $\kappa_{ea} \approx 2m_e / m_a$. Therefore the condition for weak influence of the electric field is tighter than for ions [29, 52]

$$E(V/m) \quad E_{pe} = \sqrt{\kappa_{ea}}\, kT_e / e\lambda_{ea} \approx \sqrt{2\, m_e / m_i}\; kT_e / e\lambda_{ea} \approx 4{,}5 \cdot 10^{-7}\, T_e(K) / \lambda_{ea}(m) \qquad (2.33)$$

2. *Strongly ionized plasma*
In the electron energy balance, electron collisions with ions have to be added. In this circumstance the condition on the field influence can be written as an inequality similar to (2.31) where now the correct collision frequency is the sum of the electron-atom and electron-ion frequencies. This will affect also the ion-electron mean free path; elementary kinetic theory gives $\lambda = 1/\sigma n$; therefore, if one considers only charged encounters, equation (2.31) reads

$$E \quad E_p = \frac{v}{e}\sqrt{\kappa mkT} = \sqrt{\kappa}\; kT\sigma n / e \qquad (2.34)$$

It should be noted that the collision frequency (the inverse of the deflection time) varies with the third power of the velocity [38], therefore its variation along the particle distribution function can be very high; the collision frequency and the mean free path are therefore highly uncertain.
Using the ion-electron cross sections in table 2.1 and assuming the same κ's indicated above, one obtains:

- *ions*

$$E(V/m) \quad E_{pi} \approx 0.8\; kT_i / e\lambda_{ie} \approx 7 \cdot 10^{-5} T(K) / \lambda_{ie}(m) \qquad (2.35)$$

In the preceding equations, *K* is the (relative) collision kinetic energy and the ion density has been considered equal to the electrons and equal to a typical high ionization value (see figure 2.7).

- *electrons*

With the same notation,

$$E(V/m) \quad E_{pe} = \sqrt{\kappa_{ea}}\, kT_e / e\lambda_{ei} \approx 5.8 \cdot 10^{-7}\, T_e(K) / \lambda_{ei}(m) \qquad (2.36)$$

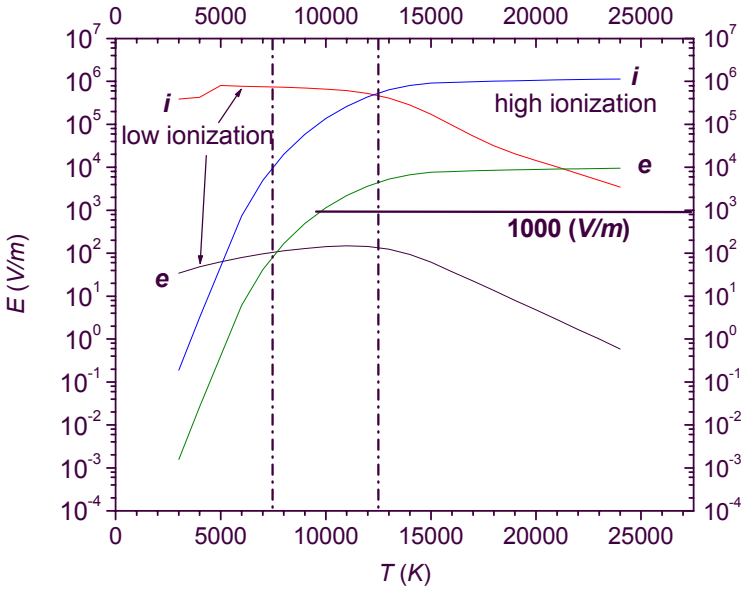

Figure 2.10. Electric fields for ions and electrons as a function of temperature in the low and high ionization limits. These were evaluated with formulae (2.35) to (2.36). The vertical lines indicate the borders between low, intermediate and high ionization. A horizontal line is drawn at the experimental limit *E*=1000 *V/m* (see text)

The conditions expressed by formulae (2.35) to (2.36) are evaluated with the aid of figure 2.10 where the corresponding limiting electric fields are reported for ions and electrons as a function of temperature, in the limiting cases of strong and weak ionization. Two regions can be identified.

High ionization, arc core. Since in a TIG arc plasma axial fields of the order of 1000 *V/m* are found at mid-height and in the cathode region respectively [14, 53]. Setting this as the 'high' experimental limit, it is seen that both ion and electron distribution functions are unaffected by the fields, at least down to arc temperatures of 10,000 *K*, figure 2.10 right hand side.

Low ionization, arc fringes. Although precise evaluations of the radial distribution of the electric field are not available, estimations of 10^2 *V/m* and below are not unrealistic. Whilst ions are still unaffected, relatively small electric fields are able to set the average electron energy, figure 2.10 left. However, in the bulk of the plasma, independently of the field intensity, the electron average velocity v_d is much less than the thermal velocity v_{th} ($v_d/v_{th} \approx \kappa^{1/2}$) and therefore the anisotropy of the *electron* distribution function caused by the field, is small. This is due to the fact that, in every collision, an electron is subject to a great change in its direction while the absolute values of the velocity and energy change very little ($\Delta K \approx \kappa K$) or, the electron takes up its energy in

many small intervals between collisions [29]. It should be mentioned that along the discussion, the electric field was computed assuming an equilibrium distribution (by using Olsen's data [39]).

2.11. The influence of the magnetic field

1. *Magnetic field*. The self-induced magnetic field is estimated with the aim to ascertain its influences on probe operation (if any) by comparing the Larmor radius with different scale lengths. The magnetic field can also cause anisotropy in the plasma and in the electrical conductivity in particular, when the cyclotron frequency is higher than the collision frequency.

Among the possible current density distributions inducing a magnetic field for the axi-symmetric arc, the Gaussian model chosen here (*cf* Appendix A) gives

$$B(r)=\frac{\mu_0 I\left(1-e^{-br^2}\right)}{2\pi r}=\frac{\mu_0 I\left(1-e^{-\pi j_0 r^2/I}\right)}{2\pi r} \qquad (2.37)$$

where j_o is related to the parameter b (z) by relationship (A.12) given in Appendix A. It is worth noting that b depends on z through j_o so one needs the dependency law $j_o=j_o(z)$ while the value very often reported in literature [54, 55] applies to the cathode, $j_o=1.0\cdot10^8$ *A/m*^{2} or $j_o=1.2\cdot10^8$ *A/m*^{2}. These values are at the limit of thermionic emission from a tungsten cathode at a temperature close to its melting point. As such, these values are taken as upper limits

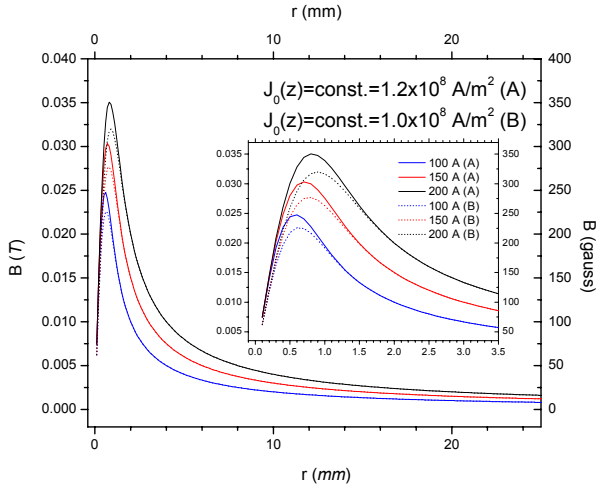

Figure 2.11. Magnetic induction evaluated for different arc total current with $j_o=1.2\cdot10^8$ *A/m*^{2} (continuous lines) and $j_o=1.0\cdot10^8$ *A/m*^{2} (broken lines)

In figure 2.11, the modulus of the induction field, B, is plotted as a function of the radial distance for these two different values of j_o and three different total arc currents. The steep decrease towards the origin is consistent with $\sim R$ behaviour for a field inside a cylindrical source generated by a uniform current distribution.
The surface section area comes into play through the arc radius. Different evaluations were made for the latter: the radius of the current conducting region (perhaps 5 *mm*, after [14]) up to the maximum radius obtainable from electrical measurements (*cf* Chapter 14).

2. *Larmor radius*. The Larmor radius is the radius of gyration of the curvilinear path of a charged particle under the action of a magnetic field

$$r_L = \frac{m v_\perp}{qB} \tag{2.38}$$

Where $v_\perp$ is the component of the particle velocity orthogonal to the magnetic induction.
Observing that

$$\frac{1}{2} m v^2 = E \rightarrow m v = \sqrt{2mE}$$

and using an ion and electron energy $kT \sim 1\ eV$, different values are obtained depending on the distance from the arc axis. The values corresponding to 2 eV can be obtained multiplying the former by $\sqrt{2}$ with respect to the values reported in Table 2.2.

Total arc current (A)	Distance from axis ($10^{-3}\ m$)	Larmor radius r_L	
		Ions ($10^{-2}\ m$)	Electrons ($10^{-6}\ m$)
100	0.6	3	136
	5	18	843
	10	37	1800
150	0.7	2	113
	5	12	566
	10	24	1160
200	0.8	2	99
	5	9	420
	10	17	800

Table 2.2. Larmor radius for ions and electrons corresponding to the values of the magnetic induction of figure 2.12. Probe diameter 200 to 250 μm (see text)

The Larmor radius for ions and electrons was estimated at three distances.

The minimum distance reported for each current (first of the three values in the second column) corresponds to the maxima of the magnetic induction extracted from figure 2.11. These vary with the current. The other two distances are the "possible" current carrying region edge (5 *mm*, see [14]) and 10 *mm*, chosen for comparison.

At increasing magnetic fields, r_L decreases and the path of the particle is disturbed with respect to the rectilinear trajectory. This can occur at different scales: the arc dimension, the probe length and radius, the mean free paths or the Debye length. Therefore the values in Table 2.2 are compared with these quantities for both ions and electrons.

• *For ions*, the Larmor radius is of the order of the *cm* or more (Table 2.2), larger than both the typical probe diameter (200 to 250 $\mu m = 2 \cdot 10^{-4}$ to $2.5 \cdot 10^{-4}$ *m*, *cf* Chapter 8) and the ion mean free path (see figure 2.5 and Table 2.2). The shortest Larmor radius, $r_L^i =$ 21 *mm*, for *I*=200 *A* at 0.8 *mm* from the arc axis, is greater than the maximum arc radius (cf Chapter 14). As this is the case also with respect to the Debye length, it can be concluded that for ions the effect of the induction field is negligible.

• *For electrons*, the Larmor radius r_L^e is of the order of magnitude of the probe diameter in the region of maximum *B*, less than 1 *mm* from the arc axis; at greater distances it is from 2.8 to 18 times the probe diameter, depending on current and distance. Also, r_L^e is smaller than the arc radius: many electron gyrations occur within the arc. The question is: do these occur within a distance r_L^e or over a much greater distance? The electron's mean free path varies broadly, depending on the arc region considered, either the weakly or the highly or fully ionized region. In fact, (*cf* figure 2.5 and 2.6), lower temperature means lower ionization and, in general, larger electron mean free path. For high ionization, using the electron number density at the two typical temperatures, 7,500 *K*, upper limit for 'low' ionization and 20,000 K, lower limit of full ionization, the electron mean free paths for collisions with ions is estimated as $\lambda_{ei} \approx 1$ to $2.8 \cdot 10^{-6}$ *m* (by means of the cross-sections reported in figure 2.3). This value is about 3% of the Larmor radius for electrons in the region where the magnetic field is maximum (See Table 2.2). Therefore, electrons collide $2\pi r_L / \lambda_{ie} \approx 200$ times along their gyration orbit; this means that the orbit itself is destroyed after each collision, i.e. a new curvilinear path forms after every collision and the effect of the field in the time between subsequent collisions is minimal. This is the 'worst case scenario': for larger distances from the arc axis, or closer to the axis (with respect to the case where *B* is maximum), the effects of the field on the electron motion are even less perceivable.

For lower ionization, the mean free path is progressively greater and is determined by collisions with neutrals. In *Ar*, $\lambda_{ea} = (n_a \sigma)^{-1}$, is now of the order of $2.5 \cdot 10^{-5}$ *m* (*cf* figure 2.5) which corresponds to region where *T* is of the order of 5,000 *K* or less, i.e. more than about 5 *mm* from the axis. There, according to figure 2.12, $B \approx 200$ gauss $r_L \approx 4$ to

$8\cdot10^{-4}$ *m* depending on the current (Table 2.2). Once again the ratio of the two, $r_L/\lambda \approx 100$ and the considerations of the preceding case apply.
The Debye length varies from 10^{-6} (low ionization) to 10^{-8} *m* (high ionization) which is of the order of or much less than the appropriate Larmor radius.

3. *Cyclotron frequency*. The electron cyclotron frequency is defined as (see e.g. [56])

$$\omega_c = \frac{eB}{m_e} \tag{2.39}$$

and in order to have a scalar electrical conductivity, i.e. an isotropic plasma, its value must be much smaller than the electron collision frequencies, related to the electron cross sections through the relationship

$$v_c = \sqrt{2} n_a \sigma_{ea} < v_{th} > \tag{2.40}$$

For weakly ionized gas, putting $n_a=10^{24}$ m^{-3} and using $\sigma_{ea}= 2\cdot10^{-20}$ m^2 at a temperature between 5,000 *K* and 7,000 *K* (see figure 2.3), $v_c\approx1.6\cdot10^{10}$ s^{-1}. From the values of figure 2.11 a maximum field of about 350 *gauss* occurs near the axis at the highest current considered, 200 *A*. However, the mentioned temperatures are likely to occur a few *mm* off the arc axis, probably beyond *r*=5 *mm*. There, $B \approx 100$ *gauss* or less and this would produce a cyclotron frequency of $\omega\approx2\cdot10^9$ s^{-1} ≈0.13 v_c at most. Therefore, while in this worst scenario $\omega/v_c<<1$ is not strictly verified (i.e. with the ratio = 0.01 as usually used throughout this work to indicate a "strong" inequality), still the anisotropy is limited. For higher ionization, the electron-ion cross section becomes dominant; since it is three orders of magnitude greater than the electron-atom value, the collision frequency will be correspondingly higher (without considering the further but weak reinforcing action of the higher temperature contained in the expression of the average thermal velocity). The inequality is therefore satisfied within the arc and the electrical conductivity can be considered scalar.

4. Relationship between magnetic self-field and electric field. A different criterion for the neglect of magnetic effects due to the induced self-field can be found in Allum [57] in form of the condition

$$E >> \frac{\mu_o I v}{2\pi R} \tag{2.41}$$

Here $\mu_o =4\pi10^{-7}$ *H/m*, v is the flow velocity and *R* is the typical arc radius. Condition (2.41) is obtained from Ohm's law

$$\mathbf{j} = \sigma\left(\mathbf{E} + \mathbf{v}\times\mathbf{B}\right) \tag{2.42}$$

and

$$\nabla\times\mathbf{B} = \mu_o\mathbf{j}\,.$$

The term $\sigma \mathrm{v} \times \mathbf{B}$ in (2.42) can be neglected if condition (2.41) applies (in other words, if the contribution to the current due to the electric field dominates the contribution by **B**). Considering the I=50 to 200 A, R_{arc}=1 to 20 mm and v=50 to 200 m/s, the two extremes values for the r.h.s of (2.50) are obtained,

$$\frac{\mu_o I \ \mathrm{v}}{2\pi R} = \begin{cases} 6.3 \cdot 10^{-3} \\ 0.2 \end{cases} \quad V/m$$

negligibly small with respect to typical arc electric field magnitudes (Allum [57]), E=100 to 700 V/m (or the 1000 V/m considered above).

2.12. Fluid parameters

As a cylindrical probe sweeps through a moving plasma it is of interest to establish the nature of the relative plasma-probe flow, i.e. 1) its degree of compressibility, 2) the possible onset of turbulence, 3) the flow separation and the influences on the plasma-probe thermal transfer and 4) the extension of the fluid "boundary layer" (BL). The latter denomination should be used only when a free-stream velocity field exists. When this is not the case, one should speak of a body induced perturbation region. However, for brevity, "boundary layer" will be used in the rest of this work in this loose sense.

In order to clarify whether compressibility, convective and turbulent effects have to be accounted for, some non-dimensional fluid parameters are examined. Attention will be limited to the sound velocity in argon and to the Reynolds number.

2.12.1 Sound velocity

The acoustic velocity plays an important role because the ratio of the flow velocity to the speed of sound, the Mach number, is an indication of the plasma compressibility. From the knowledge of the Mach number, other properties may be inferred. Here its interest lies in its influences on the onset of the sheath at a body surface, on the values of the sheath potential and on the sheath thickness (see Chapter 4).

Since the flow velocities dealt with here are sensibly lower than the acoustic velocity (see below), the flow is assumed uncompressible throughout.
This can be seen from the condition [58] $M << R^{2}$ that, using the definitions given below, translates into $v_f << c_s^2(\rho L/\eta)$, where ρ is the Argon gas density, c_s is the sound velocity defined below, M is the mach number and R the Reynolds number (defined in section 2.12.2). Here the characteristic length L is the diameter of a cylinder immersed in the plasma with his major axis perpendicular to the flow, assumed in this case to be $L=2\cdot10^{-4}$ m (typical Langmuir probe diameter). With the aid of the values reported at the end of the chapter (Table 2.3) the above condition reads $v_f << 1.4\cdot10^{5}$ m/s thus fulfilled

by the systems under study here (~2700 *m/s* has been taken as sound velocity in *Ar*, see below).

By definition the sound speed is the velocity at which small disturbances propagate through the medium adiabatically. Across a sound wave, the properties of the medium do not change appreciably. In a fluid the sound speed can be defined as

$$c_s = \sqrt{\left(\frac{\partial p}{\partial \rho}\right)_s} \tag{2.43}$$

Where the functional relationship between pressure and density has to be determined.
If one uses the isentropic relationship $p/\rho^{\gamma} = const$, the well-known acoustic velocity expression is obtained

$$c_s = \sqrt{\gamma R T_e} \tag{2.44}$$

The exponent γ is the ratio of the constant pressure to the constant volume specific heats, $\gamma = c_p / c_v$.

It is worth noting that if the ideal gas relationship is not fulfilled, the passage from (2.43) towards (2.44) is not legitimate.
The proper γ has thus to be defined. Adiabatic coefficient will refer to the traditional c_p/c_v ratio whereas other coefficients are called here 'effective' isentropic coefficients. These may be defined by means of a formula like $\gamma_i = c_s^2 \rho / p$, knowing the density to pressure ratio and where the appropriate sound velocity has to be incorporated. However Meyer's relationship allows the calculation of the sound velocity from the formula

$$c_{v_i} = \frac{R}{\gamma_i - 1} \tag{2.45}$$

if the gas behaves according to the real gas state equation $p = Z\rho RT$, where $Z=(1+\zeta)$ is the "fugacity", defined in terms of the ionization fraction ζ [36]. This has the advantage that the specific heat is readily available also for real gases. In the following however, no typographical distinction will be made among the various γ as it will be clear from context which one is used.

In [36] and more recently in Burm *et al* [59], it is stated that the Mach number of a plasma is always lower than the corresponding value for the gas. This is a consequence of the value of the isentropic exponent in plasma that, due to additional degrees of freedom with respect to the ordinary gas (e.g. ionization), is lower than the adiabatic value. In particular, as a consequence of the different behaviour of constant pressure and constant volume specific heats, it is found that their ratio is constant also for plasmas [59], provided the degree of ionization lies between 5% and 80%. For an atmospheric

plasma, whose temperatures are of the order of the *eV*, γ=1.16 instead of the γ=1.4 valid for ordinary gases.

The authors show a formula of the sound speed c_s for the non-isentropic case

$$c_s = \sqrt{\gamma R\left(T_h + \zeta T_e\right)} \qquad (2.46)$$

(*cf* the isentropic equation (2.44) written above). *R* is the mass specific gas constant, ζ the degree of ionization and *T* is the appropriate temperature. T_h refers to the ion and neutral temperatures assumed equal.

According to (2.46) the sound velocity is also function of the degree of ionization and depends on the ion temperature. However, the comparison among the different "hot" ($T_i \approx T_e$) and "cold" ($T_i << T_e$) cases, with the two limiting values for the isentropic coefficient, γ=1.16 or 1.4, non-isentropic and isentropic cases respectively, is quite complex if one adds the computed sound speed in pure *Ar* at 1 *bar* according to Murphy [49], based on a γ(*T*) not constant with temperature and only marginally approaching the value 1.16 from above. Also, if one uses the γ(*T*), from Murphy in the different formulae for the sound speed given above, still different values for the sound speed result. To try to tackle this intricacy, the first group, i.e. the sound velocity of argon is considered in the two cases of cold and hot ions (γ=1.16, continuous lines) in comparison with the isentropic case (γ=1.4), dotted lines (figure 2.12).

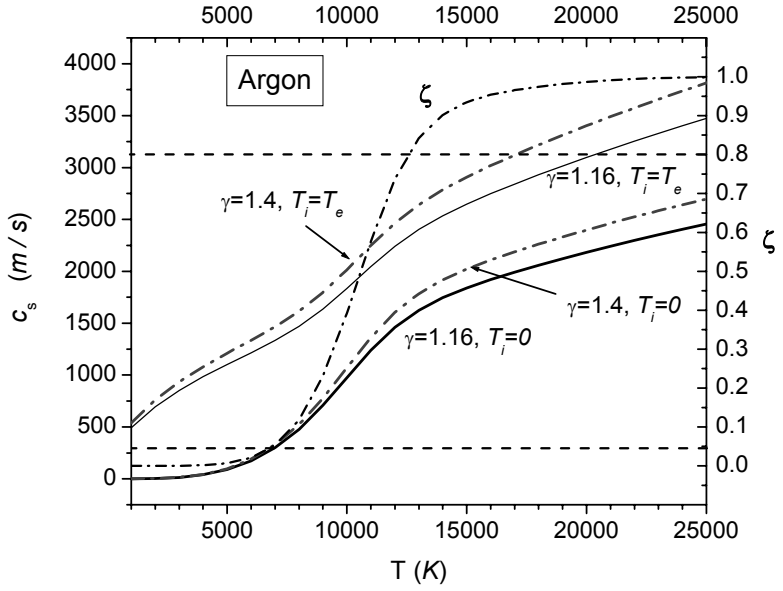

Figure 2.12. Left-axis: Isentropic (non-adiabatic, γ=1.16) and adiabatic (γ=1.4) sound velocity in *Ar* for hot (T_i=T_e) and cold (T_i=0) ion plasmas at different ionization fractions. Right axis, dot-dash curve, ionization fraction. Horizontal lines are placed at the 5% and 80% ionization limits [59]

The degree of ionization is shown (right axis) together with the 5% and 80% limits by [59] (horizontal dashed lines). It is worth noting that the major difference among the reported values is due to the hypothesis made on the ion temperature rather than the γ coefficient.

A second group of values is reported in figure 2.13; here the computed sound speed by Murphy, and the values computed for the hot and cold cases with $\gamma(T)$ as given by Murphy are reported. No surprise that the sound speed is higher in this case.

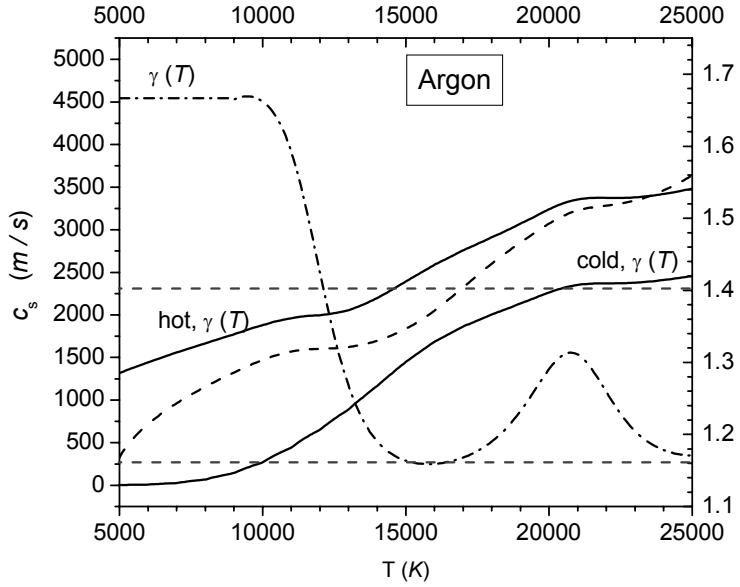

Figure 2.13. Left axis: sound speed according to Murphy [49], dashed line, compared to the two continuous curves, for cold ion and hot ion plasma cases obtained from equation (2.66) using Murphy's $\gamma(T)$. Right axis $\gamma(T)$ as given by [49]

The determination by Murphy is adopted here with the justification that it is consistent with the other plasma parameters employed.

2.12.2. Reynolds number and boundary layer thickness

The relative importance of inertia versus viscosity effects is expressed by the Reynolds number, *R* defined by the ratio [58]

$$R = \frac{\rho U L}{\eta} = \frac{\rho\, v_f r_p}{\eta} \qquad (2.47)$$

where v_f is the flow velocity and the characteristic length is the radius of the flowing probe. The viscosity η has been taken from [44]. Reynolds numbers range from R=0.2 for v_f=100 *m/s* to about R=5 for $v_f=c_s$ (sound velocity) in *Ar* (from R=0.2 to R =4.5 in *He* for the same velocities).

High values of *R* allow disturbances to develop considerable velocity gradients locally in the flow, before viscous diffusion has time to smear them out. For low *R*'s, viscosity (or viscous diffusion) would dominate. In formula (2.47) the temperature dependence for both the viscosity and the density is incorporated. Their ratio (the kinematic viscosity) for pure *Ar* has been calculated here using the same source [44] and it varies by a factor of about six in the temperature range of interest (5,000 to 25,000 *K, cf* [46]). This is the minimum degree of uncertainty that should be kept in mind in the following evaluations. In fact, as metallic (and in particular copper) probes sweep through the plasma without melting, the fluid temperature in their close neighbourhood cannot exceed about 1,357 *K* (Cu melting temperature) or 3,500 *K* (*W* melting temperature). This means that the ratio η/ρ (the kinematic viscosity) and therefore the Reynolds number given by (2.47) may be considerably lower than evaluated above. However, also η and ρ in the boundary may behave differently with respect to the situation depicted in figure 2.14. For a cylinder, the inertia terms are negligible [60], up to $R = 0.5$. In the range $R = 2$ to 30 the boundary separates at two symmetrical points and two stable counter-rotating eddies are generated in the wake. Behind them, the streamlines rejoin so that the wake has a finite extension. For Reynolds numbers greater than about 30, the eddies tend to elongate up to $R = 40$ to 70. Here the wake starts to oscillate giving rise to differential drags on the cylinder up- and down-surfaces. Considering the values for R obtained above, two situations may occur: 1) either there is no boundary layer ($R<0.2$) or, 2) if it exists it leads to a 'gentle' separation with a wake populated by a couple of stable eddies.

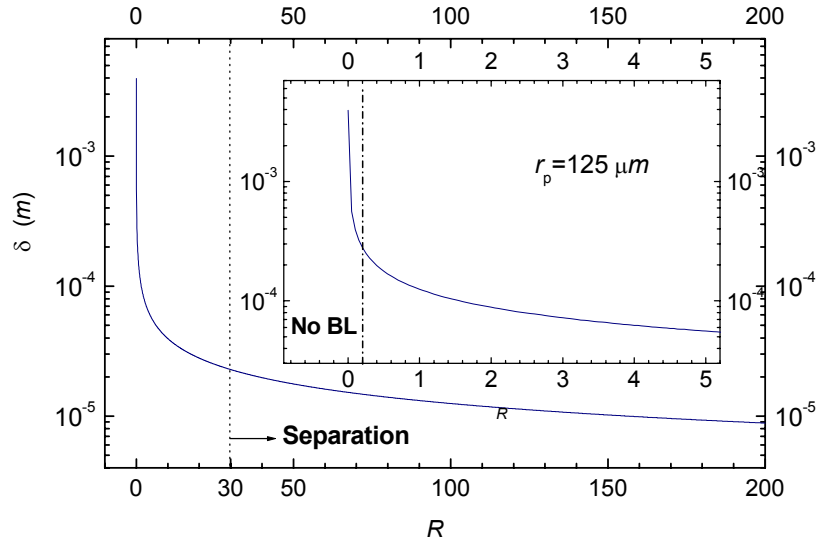

Figure 2.14. Boundary Layer thickness δ as a function of the Reynolds number. Dotted line: flow separation boundary. Inset: low Reynolds numbers region. Dash-dotted line, lower limit for the boundary formation. Probe radius 125 μ*m*.

The thickness of the boundary layer forming around the cylindrical probe is

$$\delta = r_p / \sqrt{R} = 2.2 \cdot 10^{-4} \quad \text{to} \quad 4.5 \cdot 10^{-5}\ m \tag{2.48}$$

for the two Reynolds number limits given above in *Ar* (where the probe radius has been taken as 100 μm). For *He* the two limiting values are $2.4 \cdot 10^{-4}$ *m* and $4.7 \cdot 10^{-3}$ *m* respectively.

Information about boundary layer stability against turbulence is gained by introducing the local Reynolds number [60]

$$R_x = v_f x / v \tag{2.49}$$

where v_f is the flow velocity at infinite distance, v the kinetic viscosity and the characteristic length is now x, the distance from the leading edge of the boundary layer (i.e. the point where R_x is computed). Expression (2.49) was introduced for planar geometry but with the limitations mentioned above, setting x to $\pi r_p/2$ (see below), where r_p =100 μm is the probe radius and using the same source for the viscosity [44], R_x = 11.2 to 301.6 for v_f=100 *m/s* and v_f=2690 *m/s* respectively. A criterion for the layer stability of a laminar boundary layer [60] would be $R_x \leq 10^5$ while for $R_x \geq 10^6$, a transition to turbulence would occur even for smooth surfaces and absence of turbulence in the main flow. Within the uncertainty outlined above, the two Reynolds numbers evaluated imply a 'thick' boundary layer of laminar nature that is stable with respect to the onset of turbulence.

Also, Massey [60] gives a solution for the constant flow velocity motion and an empirical expression for the boundary layer thickness as a function of the distance from the leading edge,

$$\delta' = 4.99\sqrt{vx/v_f} \tag{2.50}$$

or the ratio of the two as a function of the local Reynolds number (boundary layer Reynolds number)

$$R_\delta = \frac{\delta'}{x} = 4.99 R_x^{-1/2} \tag{2.51}$$

The latter is easily evaluated as δ'/x=1.49 (for R_x= 11.2) or δ'/x = 0.29 (for R_x = 301.6). In this case, equation (2.50) gives a boundary thickness $\delta'=4.7 \cdot 10^{-5}$ *m* or $\delta'= 2.9 \cdot 10^{-5}$ *m* (by posing $x=\pi r_p/2$), which should be compared with the $\delta= 2.2 \cdot 10^{-4}$ to $4.5 \cdot 10^{-5}$ *m* obtained above for *Ar* by the use of equation (2.47).

The macroscopic picture discussed so far holds in the limit of a continuum formulation which is established by the value of the Knudsen number [58]. The value typical in this work,

$$Kn = \lambda_{i,e}/r_p = 10^{-5}\ m\ /(100 \cdot 10^{-6}\ m) = 0.1$$

belongs to a region of transition between the purely fluid and the purely kinetic description [61] because for some cases the boundary layer thickness found above

approaches the mean free path for ions, $\delta \approx \lambda_i$. However, this latter circumstance will not invalidate the conclusions about the electrical layer thickness to be less than the boundary layer thickness (Chapter 4).

The results of this 'purely fluid description' of the probe boundary layer, can be summarized by saying that (*i*) the fluid flow is laminar in the whole range of Reynolds number considered; and (*ii*) the boundary layer extension has a minimum value of 10^{-5} *m*; it has been anticipated that this is always greater than any of the electrical sheath widths evaluated in the following (see Chapter 3). Also, it is possible to show that [46]

- A flow separation occurs at a position which is a fraction (but of the order of) one probe radius from the probe leading surface;
- Two stable eddies might form and extend in the wake for a distance of the order of one probe radius from the probe downstream surface. According to classical fluid dynamics, the majority of the heat transfer to/from the cylinder, should take place in this region;
- The flow settling time taken as the time needed for the stable structure described to develop, including the eddies, appears much shorter than the typical probe-in-arc permanence time. However, precise evaluations are not possible within this macroscopic picture.

Concerning point (*i*), observing that argon mass density varies by less than 10% between 5,000 *K* and 30,000 *K* (actually about 5% between 6,000 *K* and 30,000 *K*), the effect of compressibility can be neglected over all the range of temperatures of interest.
That a transition between fluid and kinetic regime occurs can be seen observing that on one hand one has a plasma characteristic dimension $L=2R_{arc}\approx10^{-2}$ *m* and $\lambda/L=10^{-3}$ (overall Knudsen number) which would justify a continuum treatment. On the other hand, the insertion of a small probe with characteristic length of $r_p=10^{-4}$ *m* leads to a Knudsen number of about 0.1, and for these values a purely continuum treatment breaks down.

2.13. Summary of parameters.

The physical quantities necessary to define the specific regime of interest for the arc plasma are collected in Table 2.3.

Physical parameters (*Units*)	Value/Range
1) Electron temperature T_e (K)	1 to $2 \cdot 10^4$
2) Pressure P (Pa)	10^5
3) electron number density n_e (m^{-3})	10^{21} to 10^{24}
4) Plasma flow velocity v (m/s)	100 to 150 (400)
electron mean free path λ_e low ionization high ionization (at 10^{23} m^{-3})	10^{-7} to 10^{-6}
6) ion mean free path λ_i (m) low ionization high ionization (at 10^{23} m^{-3})	$1.2 \cdot 10^{-5}$ $2.8 \cdot 10^{-6}$ (1 eV) or $1 \cdot 10^{-6}$ (2 eV)
7) electr. Mobility μ_e ($m^2 \cdot V^{-1} \cdot s^{-1}$)	$4.3 \cdot 10^{-2}$ or [$\mu_e = \mu_i$ (m_i/m_e)]
8) Ion mobility μ_i ($m^2 \cdot V^{-1} \cdot s^{-1}$)	$1.5 \cdot 10^{-4}$
9) Viscosity η ($kg\ m^{-1} s^{-1}$) (at 20,000 K)	Ar: $0.7 \cdot 10^{-4}$
10) Elec. Conductivity σ $(\Omega m)^{-1}$ for Ar, He and H	10,000; 8,500; 9,000

Table 2.3. Physical quantities for order of magnitude estimations for atmospheric arcs. Values refer to Argon. References are indicated in the text

They should be regarded as rough estimates only (hence, accuracies have not been quoted) and specifically with the arc core in mind, where they depart from the typical plasma-probe operating conditions found in literature. Some were considered explicitly in the preceding sections. A few others are commented in the following.

1) Ignoring the cathode and anode regions, for which uncertainty exists, the electron temperature in the core region is allowed to vary by a factor of roughly two. Spectroscopic measurements gave 16,000 K [22] to 23,000 K [39], while previous values from electrostatic measurements appear lower by a factor two [62]. This discrepancy forms part of the present investigation. For the present estimations, T_e is assumed to be about 20,000 K; this variability is not dramatic since T_e enters in many of the following formulae as $T_e^{1/2}$.

2) Pressure is fixed to the atmospheric value (1 bar) in the present investigation on the TIG arc.

3) The Debye length has been computed by means of formula (2.1), see also figure 2.2. Comments about the incomplete shielding of the charges within a Debye sphere, due to the low value of the plasma parameters were made in section 2.2.

4) The plasma flow velocity is considered as the value along the axis of a TIG arc. Velocity of 80 *m/s*, calculated from excess gas pressure experiments at the anode for a current value of 100 *A* [57], are in broad agreement with the calculated values of up to 150 *m/s* and 200 *m/s* respectively for the axial and radial velocities [15, 54]. Also, a value of about 400 *m/s* is considered from the work of [63] which relates to a plasma arc.

5) The sound speed in *Ar* plasma show some uncertainty (see section 2.11). However, its interest in this work is confined to the order of magnitude estimations of the boundary layer thickness compared to the electrical sheath and to the effects of compressibility.

6) The number density has been estimated with the aid of figure 2.7 (ionization as a function of temperature). This broadly agrees with the values of charged particle concentration reported in [22] but is allowed to rise up to two orders of magnitude, as in [62], i.e. to account for a higher degree of ionization. Values between 10^{22} m^{-3} and 10^{24} m^{-3} are judged reasonable. In most cases $n_e \approx n_i$ will be assumed (in the bulk) but some concerns exist about the quasi-neutrality in arc plasmas [64].

7) The mean free path for electrons in Argon has been estimated in different conditions and has been reported in figure1.4. In the low ionization region it has been considered as due mainly to electron-atom interactions, $\lambda_{ea}=1/n_a\sigma_{ea}$ (where the neutral atom density has been used). As the electron-ion collisions start to take over for increasing ionization, a value obtained by formula (2.11) was used in broad agreement with the values reported by Swift and Schwar [65] p.18) $\lambda_e \approx 1.7 \cdot 10^{-6}$ *m*, see figure 2.4 (the suffix 'a' has been dropped). For high ionization, the simplified formula $\lambda_{ei}=1/n_e\sigma_{ei}$ was employed, where now n_e has been used.

8) The mean free path for Ar^+ ions in argon, has been estimated in similar fashion (i.e. using $\lambda=1/n\sigma$) taking into account the variable degree of ionization and the corresponding cross-sections (thus λ_{ie} and λ_{ia} were computed). The curves are shown in figure 2.4 and 2.5. The data on cross sections for both the *Ar*-*Ar* and Ar^+-*Ar* collisions were taken from [32]. In the intermediate ionization case, the symbol λ_i was used.

For both electron and ion mean free paths only the first ionization stage was considered (i.e. Ar^+ only). In the calculated phase diagram for *Ar* plasmas [40], the density of Ar^{++}

ions appears non negligible (with some caution, as in the author's words), and the phase diagram reported by Boulos [66], shows an appreciable Ar^{++} density of 10^{19} m^{-3} in contrast with the 10^{23} m^{-3} of Ar^{+}, at an upper limit of 15,000 K only (but with no indications for higher temperatures). More recent values [67], indicate fractional densities for Ar^{++} (normalized to the ion species Ar^{+} taken as unity), $x = 0.001$, at about 19,700 K (1.7 eV), 0.027 at 23,230 K (2 eV) and still only 0.199 at 29,000 K (2.5 eV). For the present the choice to limit the attention to monovalent ions only appears therefore justified.

9) The data for the electron mobility μ_e are scarce and sometimes contradictory. The values of Brown [34] are chosen (since these seem to be the only measured values available). In his book a plot is reported that shows some linearity for the drift velocity as a function of E/p between 2 and 4 $V/(cm\ mmHg)$; this can be adapted (to SI Units) dividing the drift velocity by the electric field at 1 bar to give the electron mobility $\mu_e \approx 4.3 \cdot 10^{-2}\ m^2(Vs)^{-1}$ in argon; this is found to be in disagreement with what can be obtained (in absence of experimental data), multiplying the ion mobility by the ratio between electron and argon ion masses, $\mu_e = (m_i/m_e)\ \mu_i$; in this case a value of 12 $m^2(Vs)^{-1}$ is obtained.

10) The ion mobility for Ar^{+} ions in argon gas $\mu_i = 1.5 \cdot 10^{-4}\ m^2\ (Vs)^{-1}$ was found in [68] and should be compared with the older value given by Brown [34]:
$\mu_i^{+} = 1.8 \cdot 10^{-4}\ m^2\ (Vs)^{-1}$, who also gives the value for A^{++} as $\mu_i^{++} = 2.8 \cdot 10^{-4}\ m^2\ (Vs)^{-1}$ (see also below).
The available data on mobility are usually expressed as a function of reduced electric field E/N, where E is the electric field in V/cm and N is the total particle density (in cm^{-3}).
This originates from the fact that these values are measured in drift tubes and that the mobility multiplied by particle density (pressure) is a constant for a given gas (experimentally verified at least when the field is relatively weak and the drift contribution is negligible with respect to the thermal contribution [34]).

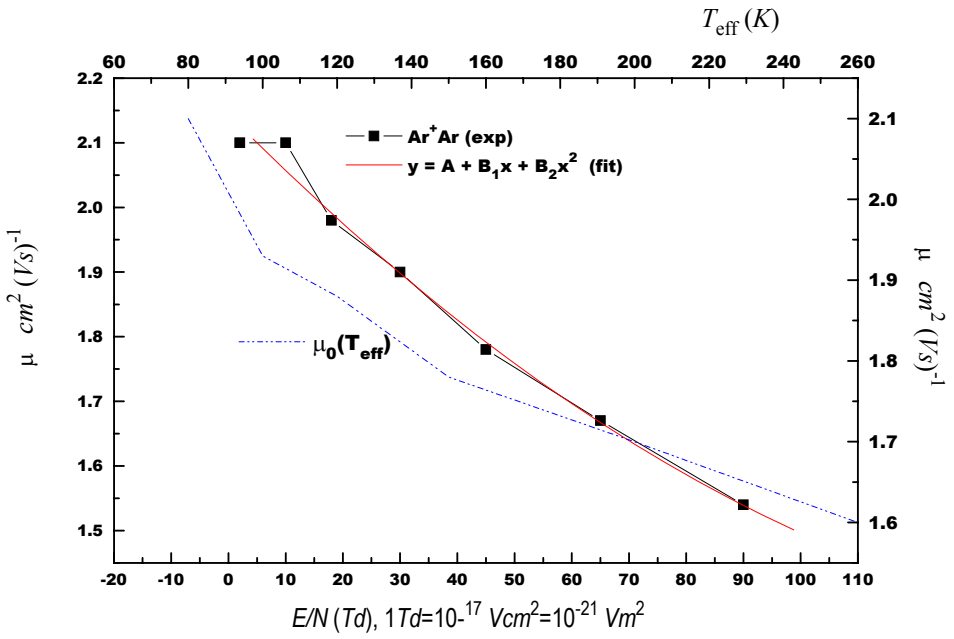

Figure 2.15. Mobility (left axis) as a function of the reduced field (bottom axis) as measured; Dash-dot line: calculated (right axis) as a function of the "effective" Temperature T_{eff} (top axis). Data based on [69]

A typical plot for Ar^+ in Ar is shown in figure 2.15 [69]. The values are expressed in standard (non-SI) units. The reduced fields and the mobility in $m^2/(Vs)$ were obtained multiplying the plotted values by 10^4. It appears that measured values (left axis continuous curves) are relatively few; a polynomial fit was made here (left axis); the calculated mobility, according to the relationship

$$\frac{3}{2}kT_{\text{eff}} \approx \frac{3}{2}kT + \frac{1}{2}m\text{v}_\text{d}^2$$

is shown on the right axis. It is based on a kinetic energy contribution arising from the field through the drift velocity (the ≈ sign was used because of the neglect of a corrective factor of the order of unity in the last term). It is of some question whether these values match with arc plasmas: the measured values are taken in an ambient gas at 77 K [69] which means that both atom and ions thermal contributions are minimized; also the calculated values, while including the effects of the field through the incorporated effective temperature, refer to values for the latter which are by far lower than any realistic arc plasma ion temperature. In effect, this is the unfortunate circumstance of the usage of swarm parameters obtained in neutral gases, to very different situations (see e.g. [70]). However, the values are of the order of μ_i =1.6 to 2.1 $\cdot 10^4$ $m^2(Vs)^{-1}$, thus not far from the values previously reported in Table 2.3 and they match to those when the field is reduced towards zero.

11) The viscosity for argon was taken from the plots produced by the numerical computations performed by Murphy [44] whose agreement with experimental results was good when a comparison was possible [48].

12) The electrical conductivity revealed the most difficult parameter to estimate. Among the different determinations found in literature and reported in figure 2.9, Murphy's, substantially equivalent to Devoto's have been chosen, with the proviso that the comparison with experimental values sets an uncertainty of the order of 30%.

2.14. Summary

A discussion on atmospheric pressure arc parameters has been conducted, with the aim of establishing a general framework for the subsequent discussion on probe theories (Chapters 2 to 4) and determine the model/s to be followed both theoretically and experimentally. More specifically:

• The criteria discussed in section 2.2 do not allow to term TIG arcs as plasmas. Strictly, this applies to the vast majority of laboratory plasmas. However, it is accepted to speak about arcs as 'plasmas' in a broad sense.

• The degree of ionization spans the whole range from the weakly ionized to the fully ionized plasma. As a consequence, the determination of crucial parameters, which depend on ionization or on temperature (through degree of ionization) proved to be a difficult task. Some were plotted along the whole range of ionization and temperatures of interest. The CTT criterion has then be used to put a somewhat arbitrary borderline between 'high' and 'low' ionization as this is needed to determine which physical scenario is appropriate in the different cases, especially for the assessment of available probe theories (see Chapter 4).

• Both the recombination coefficient and the electrical conductivity, of paramount importance for any electrical exploration, proved to be the most difficult to evaluate due to the high uncertainty in cross-section data.

• The electric field has been estimated in order to determine its influences on the particle distribution functions. With this respect it can be considered weak for both 'high' and 'low' ionization, even if for the latter case, typical of the arc fringes, the electron distribution function is likely to be 'disturbed' by a small anisotropy.

• Evaluations of the magnetic induction, the Larmor radius, the cyclotron frequency and the comparison with the electric field, has shown that the influence of the magnetic field is limited to the motion of electrons in the arc innermost region, although it is expected that the effect on probe theories is minimal.

• Although is still questionable whether a fluid rather than a kinetic description is the most appropriate, macroscopic parameter evaluations allow to depict the arc as an almost uncompressible fluid moving at speeds much lower than the speed of sound. The boundary layer around a cylindrical body was evaluated and the comparison with results from the different sheath scenarios (see Chapter 4) allows anticipating that fluid boundaries are always larger than electrical boundaries.

3. LANGMUIR PROBES

3.1. Introduction

Among the various methods of plasma diagnostics, the electrostatic probe method is perhaps one of the most commonly used since the pioneering work of Langmuir and Mott-Smith [71] from which the device takes its name. Simple in principle, the interpretation of the data it provides is rather complicated, because no simple and comprehensive underlying theory exists. Up to relatively recent years, Langmuir probes have been limited to collisionless plasmas and to ion current collection, but in more recent years they have been successfully applied to the characterization of (i) "denser" (higher pressure) plasmas where the effect of collisions become dominant [72, 73], and (ii) “higher” degree of ionization (non weakly-ionized plasmas) [74, 75] or (iii) of systems in which the plasma flow must be considered [76-78], possibly considering the cooling effects on the measured parameters [77, 79]. Also, the extension to the collection of electronic currents has been developed in the last decade [80], [81].

The physical quantities inspected depend on the application, but typically they are the electron temperature and the electron number density, although some works exist for the determination of the electrical conductivity (see for example [82]). While it is quite difficult to exhaust the tremendous amount of literature existing on the subject as taken in general terms, a very limited selection of published works is available on the use of this technique for arc plasma diagnostics and TIG arcs in particular [63], [62].

The apparent simplicity of a typical probe operation necessary to obtain the "characteristic curve" is outlined, starting with the simple model pertaining to low-pressure (i.e. rarefied) plasmas. Langmuir’s work [71] is based on assumptions that are used as a starting point in Chapter 4 where the discussion about their validity and the consequences of their failures on probe operation in arcs is addressed. There, orders of magnitude estimates are developed for atmospheric arc plasma parameters in order to determine the appropriate regime of probe operation. Some of the values are taken from Chapter 2. Once the regime is established, a discussion of the currents obtained follows. A comprehensive inspection of the plasma regimes involved, requires a careful analysis of the results from sheath theories in order to correctly relate the electron or ion densities n_e, n_i or, in general, the electron or ionic distribution functions, and the

temperature(s), to the directly measured quantities (currents). This is considered in Chapter 3.
A discussion of the non-idealities that "real-life" systems introduce is included in Chapter 5. There, the main difficulties are explained with particular emphasis on emission mechanisms and probe cooling effects.

For most of the present discussion the plasma will be assumed to be in a single component "frozen chemistry" state [83], i.e. in absence of chemical reactions, although effects of ionization and recombination, covered in Chapter 2 are discussed in connection with the classification of the regimes [84] in Chapter 3. In some cases, data are compared for different gases of interest, argon, helium and hydrogen.

3.2. Principles of operation

An electrostatic probe consist of one (single probe) or more (double and triple probe) conductors, biased positive or negative to some potential with respect to the medium in which these are immersed, either at rest or in motion. The current recorded when varying the applied probe potential V_p, defines the "Probe Characteristic Curve" (or simply "characteristic"), whose qualitative features for the single probe, depicted in figure 3.1, are common to all geometries, and explained as follows.

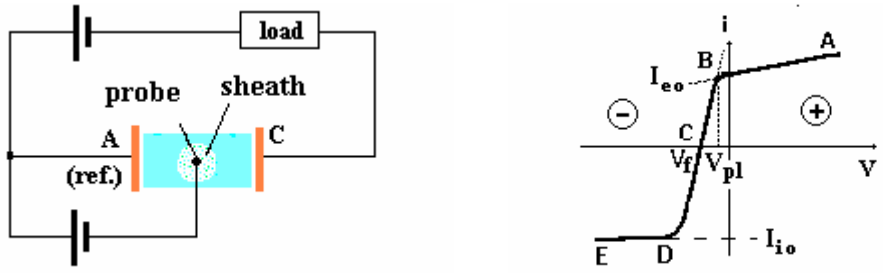

Figure 3.1 Left: basic single probe circuit (shaded area: plasma). A, anode (reference); C, cathode. Right: typical current-voltage characteristic. V_f, floating potential; V_{pl}, plasma potential (see text)

Following Cobine [85], Swift and Schwar [65] Manos *et al* [12], Raizer [9] and Schott [86] the physics of the device is based on the simplifying assumptions that:

1) electron and ion concentrations are equal;

2) electron and ion mean free paths are much greater than the probe radius;

3) electron temperature is much higher than the ion temperature ("Cold plasma");

4) the probe radius is much larger than the Debye length;

5) electron and ion velocities have a Maxwellian distribution.

These conditions define the "low pressure plasma regime". In addition, it is often assumed that a small probe causes negligible disturbances to the carrier concentration and that the distortion due to the probe potential is limited within a region thinner than the probe size.
Assumption 1 seems well justified as long as "frozen chemistry" is assumed (no charge disequilibrium exists due to the introduction of electronegative gases for example, but by considering ionization and recombination this hypothesis will be somewhat relaxed in the following), or only one gas component is present. Assumption 2 is at least questionable for the present study with respect to the regimes discussed below (see Section 3.1), where in fact, the opposite occurs. Conditions 3 and 5 deal with the more general problem of the appropriate distribution of the charge carriers, whether in equilibrium or not. Condition 4 can be easily fulfilled with a "suitable" probe radius.

With these limitations it is possible to proceed from the simplest case towards the more complicated by removing ‘unsound’ assumptions. In the following the principles of the method are outlined.

Referring to figure 3.1 above, the following quantities are defined:
V_{AP} = potential between the probe surface (p) and reference electrode (A); this is made up of the potential drop V_{AS} between the reference A and the sheath boundary plus the potential V_{PS} of the probe surface with respect to the sheath edge, thus $V_{AP} = V_{AS} + V_{PS}$.
In the following V_p will always indicate the probe potential with respect to the reference electrode (thus V_{AP}), V_{pl} the plasma potential with respect to the same electrode, and V_{sh} the voltage drop between electrode and plasma respectively and the floating potential V_f (see below). The current to the probe is I_p and the partial contribution due to electrons and ions are I_e and I_i respectively; a suffix ‘o’ is added when referring to saturation conditions.

If an insulated probe is allowed to "float" in the plasma, in absence of an applied potential difference between probe and plasma, it will attain a negative potential, called the *floating potential* V_f. The floating potential is the potential measured by an insulated probe and it is the potential at which no current flows in the external circuit. It should be noted that it cannot be the potential assumed by the plasma at the same point before the insertion of the probe (the *plasma potential* V_{pl}). Since charges reach the electrode essentially by thermal motion, the probe will charge negatively due to the higher mobility of electrons; the potential will decrease until an equal number of negative and positive charges per unit time reach the probe (equalization of the carrier fluxes). A positive charge sheath forms in front of the probe and grows until an equilibrium between ions and electrons currents is achieved, a situation corresponding to zero net

current to the probe. If the ion and electron temperatures correspond to an energy of (say) 1 eV, then the probe potential cannot exceed -1 V, otherwise the probe would continue to collect ions (no more electrons could reach it) until the recovery of the original potential. Since the electron mobility is higher than the ion mobility, the potential of the insulated probe cannot be equal to the plasma potential.

For "cold" ions (i.e. when $T_e >> T_i$) and in absence of secondary emission from the probe surface, V_f is given by

$$V_f = \frac{k\,T_e}{2\,e} \ln\left(\frac{m_i}{2\,K\,m_e}\right) \qquad (3.1)$$

where e and m_e are electron charge and mass, m_i is the ion mass and K a constant discussed below. From equation (3.1) the electron temperature could be obtained.
Under these circumstances, the probe finds itself in the conditions:

$$V_p = V_f, \quad I_e = I_i \quad \text{and} \quad I_p = 0 \qquad (3.2)$$

A probe biased negatively with respect to one of the discharge electrodes will collect less and less electrons as its voltage V_p is driven negatively enough ($-eV_p >> kT_e$). The ions will instead continue to flow towards the probe until a positive space-charge forms adjacent to its surface; the resulting random current density or ion saturation current I_{io} will be almost constant as V_p is made more negative (region "E" in figure 3.1(b)) the only effect being the change in the thickness of this sheath. Its outer part "reflects" further ions, and the plasma is not affected by the probe voltage that is confined within the sheath. This *ion saturation region* (ED in figure 3.1b) can be used to compute either the electron temperature or the electron density n_e.
In effect, a further branch is possible in principle, when the potential is highly negative, region EF in figure 3.1b; here the ions have such a high impact energy to cause electron emissions from the surface [56].

When the voltage is increased (i.e. driven less negative), the fastest electrons begin to penetrate the sheath and reach the probe, increasing in number the greater the voltage, decreasing the net current. The net current is zero when the floating potential V_f is reached. Continuing to increase V_p, an exponential increase in electronic current is observed (region DB in figure 3.1). When V rises further, the probe reaches the plasma potential V_{pl}, represented by the knee of the characteristic curve. The knee fixes the space (plasma) potential corresponding to a net probe potential near to zero (Sheath potential close to zero). In principle, this allows the determination of the plasma potential V_{pl} provided the knee is sharp enough. Here the probe receives the entire

random currents due to electrons and ions, the plasma is unperturbed by the probe and the sheath region disappears. When this potential equals exactly zero, the probe current is equal to the difference between the random ion and random electron currents. The steep part of the characteristic (DB, see figure 3.1b), referred to as *ion retarding region* or *electron accelerating region,* is used to determine the electron temperature T_e.

The general expression for the net current density j, the *characteristic*, that accounts for the ion saturation (first term, j_i region ED) and the steep electron retarding part of the curve (second term, j_e, region DB), is

$$j = j_i + j_e = n_e\, e \left[k \left(\frac{T_e + T_i}{m_i} \right) \right]^{1/2} - \frac{1}{4} n_e\, e \left(\frac{8kT_e}{m_e} \right)^{1/2} \exp\left(- \frac{eV}{kT} \right) \qquad (3.3)$$

where $V = V_{pl}$-V_p is the difference between the plasma (V_{pl}) and the probe potentials, $T_{e,i}$ the electron or ion temperature, n_e the electron density, $m_{e,i}$ the electron and ion mass and e the electric charge.

When V_{pc} increases above V_{pl}, there is only a slow dependence of j on the applied voltage, due to the "drift" of the pre-sheath further into the plasma. This region is the *electronic saturation* regime and is depicted in the part BA of figure 3.1, where its slope has been exaggerated (but see below for a discussion of the attainability of electron saturation). This region is rarely considered in the literature for the purpose of the electron temperature determination, although some work has been published in the frame of Orbital Motion Limit theories [87]. Also, in [80, 81] this region is used because it provides high currents in their relatively low pressure (and low ionization) regimes.
Beyond this region, in a similar fashion as to region EF, the electrons accelerated to the probe are in such a high number that the curve does not show saturation (steep part past point A in figure 3.1 *cf* Fuhs [56]).
The *ion saturation* and the *retarding* regions of the characteristic curve are outlined in some more detail below.

3.2.1. Ion saturation region: positive ion collection

In the theory of Langmuir-Mott-Smith [71] the region surrounding the probe is made of a positive sheath impermeable to electrons and a unperturbed region in which $n_i \approx n_e$, impermeable to the field generated by the potential applied to the probe. Between these two regions, a quasi-neutral region forms, the "pre-sheath" where $n_i \approx n_e$ is still satisfied, but in which the plasma conditions, due to the withdrawal of ions to the probe, have been modified; although the potential drop in this region is much smaller than in the inner sheath region (i.e. towards the probe), because the mean ion energy is smaller than

the electron mean energy. A small field penetrating the quasi-neutral region is able to distort the ion energy distribution at the boundary, causing a directed ion motion to the probe. This situation is illustrated in figure 3.2. (A quantitative analysis of the sheath is given in Chapter 3).

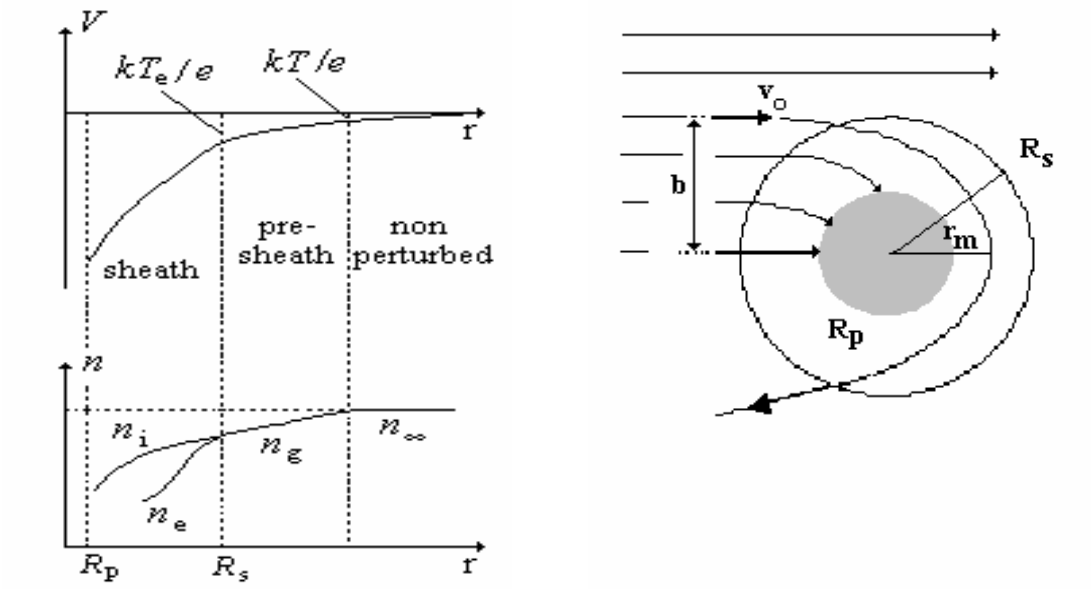

Figure 3.2. Left: qualitative behaviour of Potential and particle distribution from the probe surface (radius r_p) outwards for a negatively biased probe. The figure refers to the low-pressure 'orbital theory'. r_s s the sheath radius (see text), while n_i, n_e, n_g, n_∞ are the ion, electron, gas, and equilibrium particle densities. Right: (orbital model) behaviour of charged particles towards an attracting spherical or cylindrical probe (section); v_o initial particle velocity, b impact parameter, r_m distance of minimum approach

This means that the ions are affected in that they are collected not by the sheath boundary, but by a surface of larger radius, lying in this quasi-neutral region. Considering the sheath boundary as the distance at which the electron concentration n_e starts to decrease appreciably, the potential difference V_s between the sheath-edge and the undisturbed plasma, must be sufficient to prevent the electrons from entering the sheath:

$$-e\,V_s \approx k\,T_e/2 \approx m v_r^2/2, \qquad V_s < 0 \tag{3.4}$$

This gives the radial velocity of the ions arriving at the sheath

$$v_r(s) = \sqrt{\frac{-2\, e\, V_s}{m_i}} \tag{3.5}$$

At the sheath edge $n_i \approx n_e = n_{e\infty} \exp\,(eV_s / k\,T_e)$, $V_s < 0$, and the ion current, $i_i = j_i A_s$, with density $j_i = n_i\, e\, v_r(s)$, is

$$i_i = e\, n_{e\infty}\, \exp\left(\frac{eV_s}{k\,T_e}\right) \sqrt{\frac{-2\, e\, V_s}{m_i}}\, A_s \tag{3.6}$$

where $n_{e\infty}$ represents the concentration in the undisturbed plasma and A_s is the area of the sheath surface. It can be shown that using (3.4), and the adsorption radius r_s [65] the ion current becomes:

$$i_i = \kappa\, n_{e\infty}\, e \sqrt{\frac{k\,T_e}{m_i}} A_s \tag{3.7}$$

where the proportionality coefficient $\kappa \approx 0.6$ [65] is related to the ratio reduction of density at the sheath edge. From an estimation of i_1, together with the thickness of the sheath (and therefore the area A_s), the number density $n_{e\infty}$ of the undisturbed plasma can be deduced.

The usefulness of (3.7) relies upon the fact that the adsorbing and probe radii are practically equal and that the current shows saturation.

3.2.2. Retarding region: electron collection

In the region DB of the curve, some electrons overcome the potential V_p. For Maxwellian distributed electrons and pressure low enough to neglect loss of electrons by collisions with gas atoms when crossing the sheath edge, the electron current is

$$i_e = i_o \exp\left(\frac{e\, V_p}{k\, T_e}\right) \qquad V_p < 0 \tag{3.8}$$

where the i_o is the electron current reaching the probe when at plasma potential V_{pl}:

$$i_o = -\frac{1}{4}\, n_\infty < v_e >\, e\, A_p = -n_\infty\, e\, A_p \sqrt{\frac{k\, T_e}{2\,\pi\, m_e}} \tag{3.9}$$

A_p is the area of the probe surface and $<v_e>$ the mean thermal electron velocity within the discharge.

From the last two equations

$$\ln(-i_e) = \ln(-i_o) + \frac{e\, V_p}{k\, T_e} \tag{3.10}$$

so that a graph of $\ln(i_e)$ versus V is linear with slope e/kT_e and allows the determination of the electronic temperature.

3.3. Determination of plasma properties

The different regions of the characteristic curve ("V-I curve" in the following) are reported for convenience from figure 3.1 in figure 3.3 left. This is the traditional way the curve is presented in literature. In the following it will be shown that the 'interesting part', D toE in figure 3.3 left, corresponds to the region D to E displayed in figure 3.3 right. These figures differ for the opposite choice of the reference electrode, taken as the anode in this work (*cf* Chapter 7).

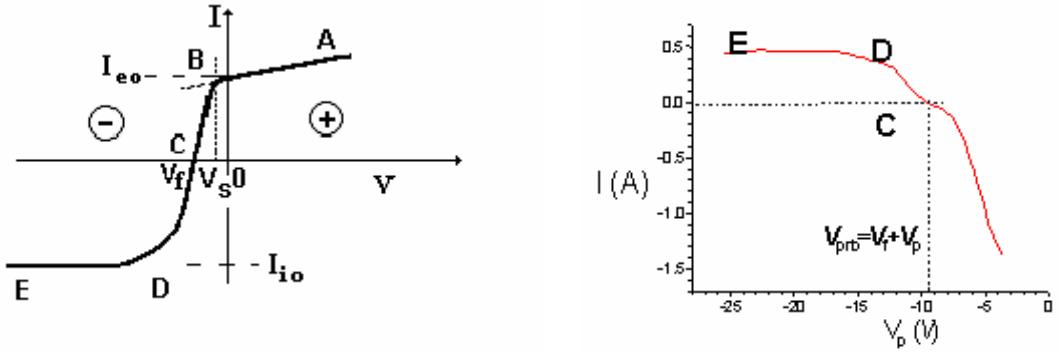

Figure 3.3 Left: single probe characteristic curve. Right: portion of V-I curve as appearing in the present work. The Labels correspond to the traditional picture shown on the left.

As mentioned in Chapter 2, the different regions available are:

- The ion saturation region, FE
- The steep (ion retarding) region, ED(B)
- The electron saturation region, BA.

It has been mentioned that the latter is of no use in atmospheric pressure plasmas because currents of several amperes flow through the probe as a result of a positive bias and the perturbation induced in the arc cannot be neglected. The other two regions are considered in the following.

Kagan and Perel [88] consider single cylindrical probes, in both the retarding part and the ion saturation region of the characteristic, where the probe potential is negative. For the first, the electron velocity distribution function (EVDF) is assumed isotropic and homogeneous, and with the aid of energy and momentum conservation, is shown to be dependent only on the potential at the probe surface, V_{prb}. An *electron* current density is then obtained independent of the probe shape provided it is convex,

$$j_e = \frac{2\pi e n_e}{m^2} \int_{eV}^{\infty} (\varepsilon - eV) f_o(\varepsilon) d\varepsilon \qquad (3.11)$$

that can be double differentiated to give the EVDF as a function of the measured electron current density (Druyvestein)

$$\frac{d^2 j_e}{dV^2} = \frac{2\pi e^3}{m^2} n_o f_o(eV) \qquad (3.12)$$

If f_o is Maxwellian, (3.12) leads to formula (3.3), a part of a geometrical factor. If, conversely, the region DB of the *V-I* curve is rectilinear on a semi-logarithmic plot, then the EVDF is Maxwellian, and the slope of its linear part gives the electron temperature T_e.

Also, the abscissa where the linearity breaks is the location of the space (plasma) potential.
Moreover, the current corresponding to $V=V_{pl}$ allows to find the electron number density

$$n_o = \frac{4 i_o}{e \langle v_e \rangle S} \qquad (3.13)$$

(S is here the probe surface and $\langle v_e \rangle$ the thermal electron velocity). However, due to possible reflections from the probe surface, whose surface conditions are poorly known, the value obtained from (3.13) may be overestimated. Langmuir [89] proposed to locate the plasma potential where the branch AB intersect DB (see figure 3.1), the "intersection method".
The influence of ions sets in where the ion and electron current become comparable (break of the characteristic curve, see figure 3.3 right). According to Kagan and Perel [88], the use of the first derivative of the probe current versus the probe potential di_p/dV_p, is more accurate than the widely used extrapolation of the ion part ED (e.g. the accuracy of the "law" on which the latter is based is hard to determine). The approximate equality $di_p/dV_p \approx - di_e/dV$ allows the determination of the electron temperature when electron are Maxwellian distributed because in this case a plot of ln (di_e/dV) versus V is a straight line whose inclination on the V axis is T_e. This method is especially important when the region DB is distorted or cannot be obtained.

In the ion part of the characteristic curve where the potential is negative, ED in figure 3.3 right, $i_{tot}=i_i$ and a theory of the probe attracting ion is necessary. This point is also

considered by Schott [86]. A simplified theory is presented which gives the saturation current in terms of

$$i_{\mathrm{i}} = cn_{\mathrm{o}}e\sqrt{\frac{2kT_{\mathrm{e}}}{m_{\mathrm{i}}}}A_{\mathrm{s}} \tag{3.14}$$

(which a part of the constant c coincides with the first term of equation (3.3), except that here T_{i} is neglected). The cylindrical case is obtainable from the spherical geometry by projecting the electron velocity v_o onto the plane orthogonal to the probe axis, see figure 3.4.

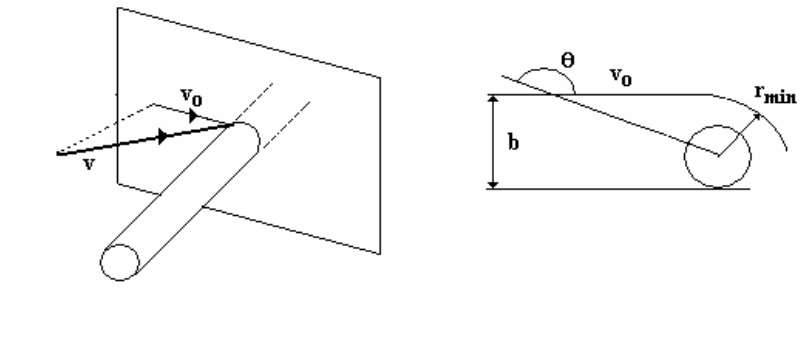

Figure 3.4 Left: projection of the quantities used for spherical probes onto the plane orthogonal to probe axis, used for cylindrical probes. Right: particle deflection by probe potential

The method is as follows. At large negative potential, $i=i_{\mathrm{i}}$; from i_{i} and V use Kagan and Perel's formula for i_{i} the ion current per unit length [88]

$$i_{\mathrm{i}} = 2\pi e r_{\mathrm{p}} n_{\mathrm{o}}\sqrt{\frac{2kT_{\mathrm{e}}}{m_i}}\alpha'(\gamma), \qquad \alpha'(\gamma) = f(\gamma), \quad \gamma = \frac{T_{\mathrm{i}}}{T_{\mathrm{e}}} \tag{3.15}$$

and the electron density is obtained as

$$n_{\mathrm{o}} = \frac{i_{\mathrm{l}}}{2\pi e r_{\mathrm{p}}}\sqrt{\frac{m_{\mathrm{i}}}{2kT_{\mathrm{e}}}} \tag{3.16}$$

T_{i} is unknown and the factor γ is difficult to evaluate but the situation $\gamma \equiv T_{\mathrm{i}}/T_{\mathrm{e}} \approx 0.1$ is relatively common and in this case $\alpha_{\max} \approx$ 0.8 to 0.6, whereas for $\gamma \equiv T_{\mathrm{i}}/T_{\mathrm{e}} \approx 1$, $\alpha_{\max} \approx$ 0.43 to 0.5 (thermal plasma, *cf* [88] figure 13). Both the minimum and maximum values of α vary slowly with γ, by less than 0.15 in the range γ=0 to 1 ($T_{\mathrm{i}}=T_{\mathrm{e}}$), therefore the error of the procedure lies mainly in this approximation.

Determine T_e using the steep part of the V-I curve if this portion is available (formula 3.10), where the effects of the ions are negligible; otherwise use the differentiation of the characteristic curve. Therefore, the part DC, close to the floating potential is usable.

Summarizing the procedures for the V-I curve,
1) The saturation part gives either the electron density or the electron (or plasma) temperature;
2) The steep part gives
the electron temperature from the couple (ln i ,V);
the plasma potential V_p from the knee of the *V-I* curve (intersection method) or from the maximum of the derivative *di/dV*, see section 3.4.

This procedure, (3.15) to (3.16), is therefore feasible if the electron temperature from the V-I curve, (3.10), is attainable. If this is not the case, a 'direct' method can be employed, based on the use of formulae (3.15) or analogous formulae where some known relationship between the density and temperature is employed in order to construct a $I(T)$ relationship (See Chapter 4).

The determination of the plasma parameters according to 1) is discussed in the next section (3.4) whereas the second point implies the existence of a more or less complete characteristic curve, which is not available for atmospheric pressure arcs.

3.4. Floating and plasma potential relationships

a. Floating potential
Several formulae express the floating potential in terms of temperatures and/or particle density. Some are assessed directly with data in Chapter 12. Their importance lies in the determination of the plasma potential and the consequent calculation of the electric field.

1) Formula (3.1) for the 'low-pressure' regime which however contains an empirical "constant" K difficult to evaluate (perhaps 0.6 [65])

$$V_f = \frac{kT_e}{2e} \ln\left(\frac{m_i}{2Km_e}\right) \qquad (3.17)$$

2) Das et al [90] formula which takes into account pre-sheath effects and removes the cold plasma approximation

$$V_f = \frac{kT_e}{e} \ln\sqrt{\frac{T_e m_i}{T_i m_e}} \qquad (3.18)$$

but requires the knowledge of the electron to ion temperature ratio, unless used in the 'thermal plasma' assumption of equal ion and electron temperatures.

These two formulae coincide for T_e/T_i =0.83 (factor 1/(2*K*) in (3.17)) Also, by inserting all the constants in the thermal case (T_e/T_i =1), the two formulae differ by less than 1%. Moreover, these relationships are substantially equivalent to Raizer's 'low-pressure' formula a part of an uncertain numerical factor ([9] p 115).

4) Raizer's 'high pressure regime' formula [9]

$$\frac{eV_f}{kT_e} = \ln\left(\frac{2}{\pi}\left(\frac{m_i}{m_e}\right)^{1/2}\left(\frac{T_i}{T_e}\right)^{1/2}\frac{r_p}{\lambda_i}\frac{1}{\gamma}\right) \tag{3.19}$$

obtained using the equality of ion saturation current at 'high pressure'

$$I_{i\,sat} = S\left(\frac{\pi}{8}\right)^{1/2} en_e\left(\frac{kT_e}{m_i}\right)^{1/2}\left(\frac{T_e}{T_i}\right)^{1/2}\frac{\lambda_i}{r_p} \tag{3.20}$$

and the classical Maxwellian electron current (3.8). In (3.19) the factor γ is given

$$\gamma = 1+\left(\frac{1}{2}\frac{\lambda_D}{\lambda_e}\frac{kT_e}{eV_p}\right) \tag{3.21}$$

Formula (3.19) suffers from uncertainties in the various numerical factors and on the hypothesis of Maxwellian distributed electrons; furthermore it requires the knowledge of the ion mean free path and of the temperatures ratio.

b. plasma potential

A part of the interception method indicated in section 3.3, other methods for the determination of the plasma potential can be adopted that can be used when the (lower) inflection point of the characteristic curve is not well defined, namely,

1) By plotting di_p/dV_p against V_p and defining the plasma potential where the first (or the second [88]) derivative is maximum;

2) Using the dependency of the ion saturation current on the probe potential $I \propto V^{1/2}$ [86, 91]; a plot of I^2 against V is a straight line if the electrons are Maxwellian. Only in

this case the linear extrapolation of the straight line to the V axis intercepts the latter at the probe potential

$$V_{prb} = V_{pl} + kT_e/e \quad \Rightarrow V_{pl} = V_{prb} - kT_e/e \tag{3.22}$$

determining the plasma potential from the measured electron temperature T_e and the probe potential V_{prb}, or, alternatively, allowing the determination of T_e if V_{pl} is given independently.

In practice one can also measure the probe potential with respect to the reference electrode and subtract (algebraically) the value of the floating potential as determined by the electron temperature if the latter is known.

3) If the "knee" of the V-I curve is not identifiable, then where $i = i_i$ (point C, with probe floating, e.g. at the probe potential corresponding to zero net current) the relationship could be used [88]

$$\frac{eV_1}{kT_e} = \ln\left[0.3\sqrt{\frac{m_i}{m_e}}\frac{r_p}{r_{pl}}\frac{1}{\alpha(\gamma)}\right] \tag{3.23}$$

Where r_{p1} is the radius of the sheath layer when the probe is at floating potential. If $r_{p1} \approx r_p$ then V_1 is the potential of the plasma *relative* to point *C*, point where the probe is at the floating potential (figure 3.3) and V_1 is thus the plasma potential.

3.5. Discussion

The assumptions made at the beginning of this chapter are not fulfilled in the high pressure regime; in particular, assumption 2, that electron and ion mean free paths are much greater than the probe radius is incorrect for the regimes considered in this work, given the fixed probe radius of about 10^{-4} *m* (see Chapter 2).
The assumption 3 of "Cold plasma" is easily fulfilled in low pressure regimes. In the atmospheric pressure regime the effectiveness of collisions for thermalization of the plasma is by no means obvious. Atmospheric arcs are often believed to be in an equilibrium state [9] but the opposite might occur (*cf* Chapter 14) so that also condition 5 (that electron and ion velocities have a Maxwellian distribution and more generally that an equilibrium distribution exists) can fail. This assumption is often made for the sake of simplicity, but should be regarded with care as other steady state distributions are equally possible [51]. This also implies that the $T_e >> T_i$ assumption on which 'Cold plasma' probe theories are based is doubtful, whereas the uncertainty on the attainment of LTE leaves the question open as whether the 'thermal assumption is justified (T_i=T_e).

The modification to the above mentioned hypothesis needed to extract particle densities and temperatures from the currents will be reported in Chapter 5.

4. ARC - PROBE D.C. SHEATHS

4.1. Introduction

A sheath is a spatial region forming in the neighbourhood of a body immersed in a plasma, in which quasi-neutrality breaks down as a consequence of the perturbations induced. Electric fields of considerable amplitude can develop leading to a "medium" whose properties can be quite different from the bulk, i.e. collisionless, fully collisional or more often in between these two extremes. The sheath thickness plays a crucial role in the definition of both the sheath regime and the probe regime. A reliable evaluation of the sheath thickness and voltage distribution is a basic step towards the understanding of the Langmuir probe operation.

Some remarks [10, 92-94] are reported to illustrate the mathematical difficulties that arise in nearly every theoretical attempt to characterize the sheath, but also because they give a general idea about the sheath structure, clarifying the role of the Bohm criterion for sheath formation (section 4.2). The requirement of a monotonically decreasing potential (from the body outwards) means that a cut-off energy (or velocity) exists below which the ion distribution function vanishes. For the case of monoenergetic ions, this corresponds to the Bohm criterion [92] which imposes the lower limit for the formation of the sheath: the ions must approach the sheath edge at the (acoustic) sound velocity.

A summary is presented on the widely discussed planar geometry [65] in section 4.3. For this group of works, computations are made to evaluate sheath thickness and potential distributions. Collisionless models are evaluated (section 4.3.1) following the works of Mott-Smith and Langmuir's [71], the first starting in the 60's (and collected in [65, 95]). Collisional models were developed up to these days [92-94, 96] both in the frame of hydrodynamical (Two-fluids, [90, 92, 96, 97]) or kinetic models [92]. In section 4.3.2 these are briefly illustrated and computations of voltages and thickness following Sheridan [97] and Mukherjee [98, 99] are performed. Few experimental measurements are considered [84, 91, 98] and attention is paid also to floating conditions, when no external bias is applied to the immersed body.

For large electric potentials, that is, highly biased probe or walls the potential distribution is given by Child's law [95] originally developed for a vacuum diode [100]. Several enhanced versions of this potential law have been developed [90, 101, 102] often as “by-products high-potential limiting cases” in works that include however less restrictive hypotheses with respect to the original Child’s treatment.
It is not possible to account for all these works. Also a complete analysis would require quite involved formalism leading to treatments that are far beyond the phenomenological scope of this work. Furthermore, there is still considerable debate about the conditions for sheath formation.
The basic question addressed here is the character of the sheath (when existing): collisional, collisionless or intermediate between the two.

4.2. Sheath formation: The Bohm criterion

The sheath existence can be predicted from the argument that the electrons have a much higher mean velocity with respect to the ions. This is because of the limited fractional energy loss for the electron during a collision with the ion. In the elastic case this can reach the maximum value $4m_e/m_i$, so that the efficiency of energy transfer for electrons is much less than for ions. Since the mean electron velocity of the electrons is much higher than the ion’s, the random current densities of the two species satisfy the inequality

$$j_e = n_e < v_e > /4 \quad >> \quad n_i < v_i > /4 = j_i$$

The electronic current to an insulated body brought to contact with the plasma is initially higher than the ionic current and the body will charge negatively until its potential is lowered to the point at which the fluxes of ions and electrons equalize. This sheath region must repel some of the electrons from the bulk plasma and attract the ions that enter it. Consequently, the electron density in the sheath is lowered with respect to the bulk plasma and can be considerably lower than the ion density, leading to the breakdown of quasi-neutrality.

The basic difficulty of any sheath treatment consists in understanding how/if the sheath solutions extend into the plasma.

1. According to Schott [86] the fact that in low pressure plasmas the expressions for both ion and electron currents are similar is due to the assumption that for both type of charges a well defined edge for space charge effects exists, out of which the potential is constant. This is not true when a species has a mean energy substantially lower than that of the other species. This case occurs for example when $T_i << T_e$. The discrepancy between measured currents values, higher than the theoretically predicted ones, is due to the fact that the ions entering the sheath carry an energy $kT_e/2$, not the thermal one ($\approx kT_e$). For a probe charged at a negative potential with respect to the undisturbed

plasma, until the inequality $|eV_{sh}| < kT_e/2$ holds, some electrons are able to overcome the retarding field of the probes due to their thermal velocity (V_{sh} is the plasma to probe negative potential). The plasma at the probe remains quasi-neutral. Consequently, in the range of the negative potentials

$$0 < -V_{sh} < \frac{1}{2} kT_e / e$$

no space charge is formed in front of the probe. The formation of the space charge sheath starts when the probe is made more negative than $-kT_e/2e$ when all electrons are repelled. At probe potentials $V_{sh} > kT_e/2e$ only the part $|V_{sh}| - kT_e/2e$ is due to the charge sheath. Therefore, between unperturbed plasma and sheath a quasi-neutral intermediate region (pre-sheath) develops in which the probe potential penetrates and where ions gain directional energy corresponding to the voltage drop $kT_e/2e$, which in the pre-sheath is virtually independent of the probe voltage. These considerations lead to the criterion of minimum ion energy necessary for the set-up of the sheath, which is the Bohm criterion (See Appendix B).

2. More formally [92], the mathematical discontinuity which arises when trying to match the solutions of the plasma and the sheath can be overcome *only* by the requirement of the limit $\lambda_D \to 0$ which introduces two scales in the problem: a collision-free sheath and a quasi-neutral pre-sheath. It is the singularity that arises because of the boundary conditions that forces the introduction of an additional "transitional" layer between sheath and plasma.
The screening of the sheath ends at the edge that does not coincide with the unperturbed plasma; since $T_e >> T_i$, a field in the region preceding the sheath is necessary to overcome the ion inertia and set the velocity values needed to satisfy the Bohm criterion. This is the origin of the pre-sheath. The main argument leading to such an additional region is constructed using a model consisting of an infinite plane wall [92]. The electronic repulsion gives rise to a positive space-charge region that shields the neutral plasma from the negative wall. A condition like $\lambda \approx \lambda_D << L$, where L is the characteristic dimension of the system, implies a collision free sheath. However, wall losses distort the ion distribution causing the shielding to be impossible unless the Bohm criterion is fulfilled: the ions have to enter the sheath with a high velocity that cannot be generated by the thermal motion alone; they have to be accelerated by a field penetrating a pre-sheath region. The boundary layer is then split into two parts: a collision free sheath of the order of the Debye length and a quasi-neutral pre-sheath of the order of the mean free paths. The singularity arises at the sheath edge where the two regions are required to merge, when $\lambda_D/\lambda_i \to 0$. According to [92] it is the location of this singularity which defines the sheath edge and the result of his paper refers to the fulfilment of the limit $\varepsilon = \lambda_D/\lambda_i$ small but finite (in a paper of 1997 [103] the order of this scale and the conditions are given).

This outcome is not universally accepted. According to Godyak *et al* [87] the correct choice of the boundary condition would be a sheath edge occurring at the position where the electric field is strong enough to break down the quasi-neutrality of the plasma. In this case it appears that the Bohm criterion would not be necessary. It has been pointed out that in the intermediate region (pre-sheath), collisions need to be accounted for and that in a truly collisional case, the Bohm criterion cannot be fulfilled simply because collisions would prevent ions to reach the critical velocity [94].

Formally, by considering "high" and equal carrier densities, the boundary conditions assumed at the wall, $n_e(0) \approx n_i(0) = 0$, imply that the potential, electric field and charge density diverge because the equality of the fluxes implies instead $n_{i,e} \neq 0$. As a consequence, a transition sheath from the high-energy plasma to the low energy wall arises (the aforementioned pre-sheath) in which considerable field potential differences exist and a large charge separation occurs.

The Bohm condition (for a derivation, *cf* Appendix B) requires $v_{oz}^2 \geq v_B^2 = kT_e / m_i$, where v_{oz} is the minimum velocity of the ions impinging the wall. Physically it is the slower decrease of n_i with respect to n_e due to the increasing potential that renders the formation of a positive space charge shielding possible. The Bohm criterion describes a condition to be satisfied near the sheath edge but does not say anything about the global sheath structure. The reason is that it is derived in the small scale λ_D/λ_i and therefore it would be inappropriate to extend its conclusions on a wider scale [92].

The following conclusion can be drawn from the preceding discussion: either the field extends beyond the sheath edge into the pre-sheath in order for the Bohm criterion to be satisfied. In essence it means that the field is able to impart the necessary velocity to the ions in the pre-sheath, which in the opinions of some authors suggests a collisionless sheath. Alternatively, the field ends its influence at the sheath edge (the field is shielded) and the Bohm criterion is not necessary for the collisional sheaths. In these cases, it can be thought that the mechanism that drives the ions towards the sheath is of diffusive nature rather than mobility driven.
However, the main question whether the Bohm criterion is *always* a necessary condition for the sheath formation remains.

3. For *Ar* ions, the parameters of Table 2.3, give a Bohm velocity of the order of the sound velocity in the medium (~2700 *m/s* for *Ar* in thermal plasma at 16,000 *K*).
A modified Bohm criterion can be obtained by removing the cold ion assumption [90], i.e. accounting for the finite ratio $\gamma = T_i/T_e$ of ion to electron temperature as follows:

$$M > \sqrt{1 + 3\gamma} \qquad (4.1)$$

Where $M = v_i / v_B^0$ is the Mach number, v_B^0 is the "cold" ion Bohm velocity and $\gamma = T_i/T_e$ is the temperature ratio. The enhanced Bohm velocity is shown in figure 4.1 together with the 'cold' case for different γ.

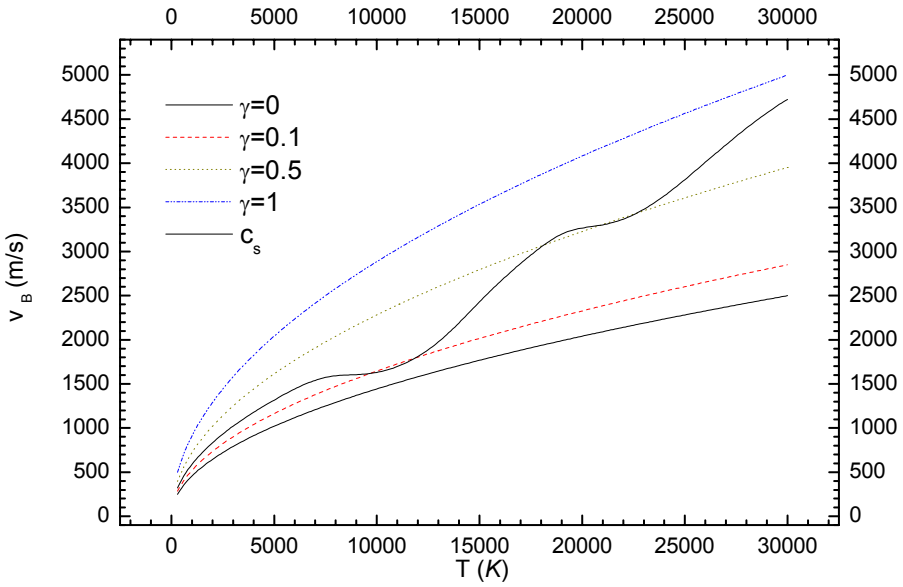

Figure 4.1 Bohm velocity as a function of electron temperatures for different $\gamma = T_i/T_e$ using formula (4.1) in [90]. The cold case corresponding to $\gamma=0$ ('cold ions', $T_i=0$) is shown for comparison (lowest continuous curve). Also shown is the sound speed c_s determined from thermodynamical quantities (non-monotonic continuous curve, after [44]

It is clear that at the temperatures of interest, the ratio between the thermal ($\gamma=1$) and the cold ($\gamma=0$) case is of the order of two.

As a consequence, also the expression for the floating potential V_W is modified with respect to the one given by the 'cold' formula (*cf* formulae 4.11 below and 3.1)

$$V_W = \frac{kT_e}{e} \ln \sqrt{\frac{T_e m_i}{T_i m_e}} \qquad (4.2)$$

(ion flux conservation is assumed within the sheath, i.e. ionization and recombination within the sheath are neglected). The effect of the finite ion temperature ratio is to reduce the sheath thickness. In fact, since the ions move at a velocity greater than v_B, they have a larger kinetic energy: more ions hit the boundary and this lowers the negative wall potential. The ions recombine with the wall electrons. The reduction of

the wall potential means that the ion attraction reduces and so does the charge separation n_i-n_e, with the effect of a sheath thickness reduction.

4.3. Sheath classification

Whether or not there is an applied voltage, the study of the planar geometry has its "in-principle" usefulness even for different geometry. The condition to consider the curvature of the surface immaterial is that the boundary layer should be much thinner than the probe: $\delta << r_p$. For a radius of 125 μm the ratio of the two is just about three (a thickness of 2 to $4 \cdot 10^{-5}$ *m* has been considered in Chapter 2 [see (2.51) or comments after (2.54)], thus the mentioned condition is not fulfilled and the curvature *must* be considered. For the electrical sheath the thickness is much smaller than the probe radius ($\delta_s << r_p$) and the planar assumption is more justified. Some 'plane plate models' are considered to illustrate the general mathematical difficulties associated with the different regions between bulk plasma and body.
A classification of d.c. sheaths is given which broadly divides sheaths in collisionless and collisional [104].

4.3.1. Collisionless sheaths

Some common features for the collisionless case are considered. The hypotheses common to the models are:

1. Maxwellian distributed electrons at a temperature T_e;
2. Cold plasma, i.e. T_i=0;
3. Quasi-neutrality in the bulk and at the origin of the coordinate, which is the plasma sheath edge (x=0);
4. The potential is zero in the origin.

The equation of motion is [104]

$$\frac{d^2V}{d\,x^2} = \frac{en_s}{\varepsilon_o}\left[e^{eV/kT_e} - \left(1 - \frac{V}{K_s}\right)^{-1/2} \right] \tag{4.3}$$

Where n_s is the charged density at the sheath edge, $K_s = m_i v_s^2 / 2$ is the ion kinetic energy and v_s^2 is the initial ion velocity (at the edge) satisfying the Bohm criterion, $v_s \geq v_B$. Equation (4.3) is non linear. Its first integral, obtainable numerically, is known to exist only if the ion velocity exceeds the ion sound speed (Bohm velocity, see Appendix B).
The potential in the pre-sheath, which gives the final ion velocity as the Bohm velocity, is

$$eV_p = kT_e/2 \tag{4.4}$$

and the electron density at the sheath edge is then

$$n_s = n_b e^{-eV_p/kT_e} \approx 0.61 n_b \tag{4.5}$$

where n_b is the bulk plasma electron density.
The wall potential with respect to the sheath is obtained by the equality between ion and electron fluxes

$$\Gamma_i = n_s v_B = \frac{1}{4} n_s \langle v_e \rangle e^{eV_w/kT_e} = \Gamma_e \tag{4.6}$$

And using the expression for the mean speed for electrons (thermal speed)

$$\langle v_e \rangle = \sqrt{\frac{8kT_e}{\pi m}} \tag{4.7}$$

The potential of the wall with respect to the sheath-pre sheath edge (therefore, under the hypothesis of zero field and potential at the edge, with respect to the plasma) is

$$eV_w = -kT_e \ln \sqrt{\frac{m_i}{2\pi m_e}} \tag{4.8}$$

Remarkably, this depends only on the electron temperature. For *Ar* ions with thermal energy $kT_e \approx 1\ eV$ at the edge, the kinetic energy of the impact at the wall would be $K_w \approx 4.7 kT_e = 4.7\ eV$. This can be compared with the result given by formula (4.2), which is $K_w \sim 5.6\ eV$.

In principle, a measurement of the probe potential and the knowledge of the computed potential (4.8) would give the plasma potential, which in turn would give the electric field, but the latter is supposed known in the derivation of (4.8). Moreover, the plasma potential is not always necessary if the field has to be found. In the following, few models of collisionless planar sheath are considered. It will be seen that their range of validity is severely limited by the necessity of high-biased wall, i.e. high wall potentials. Figure 4.2 shoes the choice of the coordinate system used.

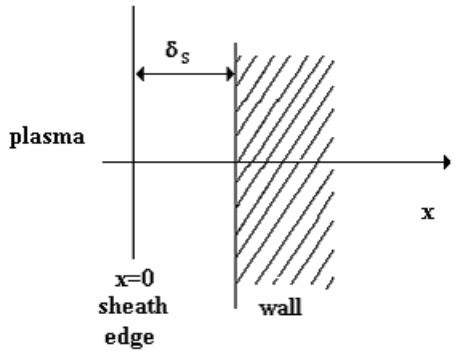

Figure 4.2

For the boundary conditions in planar geometry. Pre-sheath is omitted and the origin of the abscissa is taken at the sheath edge.

1. A 'matrix' sheath forms in the case of a highly biased wall or probe substantially free of electrons (thus $n_e \approx n_s e^{eV/kT} \to 0$) and has uniform ion density: integrating twice Maxwell equation

$$\nabla \cdot E = \frac{\rho}{\varepsilon_o}, \text{ or } \frac{dE}{dx} = \frac{en_s}{\varepsilon_o} \tag{4.9}$$

with the conditions $x = 0,\ V = 0,\ E = 0$, the field and the potential are

$$E = \frac{en_s}{\varepsilon_o} x \text{ and } V = -\frac{en_s}{\varepsilon_o}\frac{x^2}{2} \tag{4.10}$$

And the sheath thickness is obtained in terms of the potential at the sheath edge V_o, by posing $x=\delta_s$

$$\delta_s = \left(2\varepsilon_0 V_0 / en_s\right) = \lambda_D^s \left(2V_o / kT_e\right)^{1/2} \tag{4.11}$$

Where $\lambda_D^s = \sqrt{\dfrac{\varepsilon_o kT_e}{n_s e^2}}$ is the Debye length at the sheath edge.

2. In the Child-Langmuir law sheath model, assuming the initial ion kinetic energy at the sheath edge smaller than the potential

$$K_s = \frac{1}{2} m_i v_s^2 << eV_s$$

the current density is constant, and the ion density is $n_i(x) = j_0 / ev_i$ so that and using Poisson equation, both the field and the potential are obtained [104]

$$V = -V_o\left(\frac{x}{\delta_s}\right)^{4/3}, \quad E = \frac{4}{3}\frac{V_o}{\delta_s}\left(\frac{x}{\delta_s}\right)^{1/3} \tag{4.12}$$

and the sheath thickness can be written as

$$\delta_s = \frac{2}{3}\sqrt{\frac{\varepsilon_o}{en_s v_B}}\left(\frac{2e}{m_i}\right)^{1/4} V_0^{3/4} \tag{4.13}$$

Using again Poisson's equation with the electric field in (4.11) gives the ion density within the sheath as a function of the position within the sheath

$$n = \frac{4}{9}\frac{\varepsilon_o}{e}\frac{V_o}{\delta_s}\left(\frac{x}{\delta_s}\right)^{-2/3} \tag{4.14}$$

Whereas in [62] Brown's Child-Langmuir formula [95] is quoted as

$$\delta_s{}^2 = \frac{4\pi}{9}\left(\frac{V}{T}\right)^{3/2}\lambda_D{}^2 \tag{4.15}$$

This expression was used in atmospheric TIG arcs and it is based on the hypothesis of Local Thermodynamic Equilibrium (LTE), with equal ion and electron temperatures T and a thin (i.e. collisionless) sheath.

3. Swift [65] considers Poisson's equation for the particles distributions at equilibrium in the origin n_{eo}, n_{io} (which is now chosen at the wall)

$$n_{eo} = n_{e\infty}\, e^{-\frac{|e|V(x)}{k\,T_e}}, \qquad n_{io} = n_{i\infty} e^{-\frac{|e|Z_i\,V(x)}{k\,T_i}} \tag{4.16}$$

or explicitly,

$$\frac{d^2V}{d\,x^2} = -\frac{e}{\varepsilon_0}\left(Z_i n_{i\infty}\, e^{-\frac{|e|\,Z_i\,V(x)}{kT_i}} - n_{e\infty}\, e^{\frac{|e|\,V(x)}{kT_e}}\right) \tag{4.17}$$

where $n_{i\infty}$ and $n_{e\infty}$ are the bulk ion and electron densities. The solution of equation (4.17) gives the variation of the potential within the sheath. In principle, solving this equation will yield the values of the number densities. However, its non-linearity forces the approximation of the exponential to the first order, i.e.

$$\frac{d^2V}{dx^2} = \left(\frac{Z_i^{\,2} \left|e\right|^2 \, n_{i\infty}}{\varepsilon_o k \, T_i} + \frac{\left|e\right|^2 \, n_{e\infty}}{\varepsilon_o \, k \, T_e} \right) V \tag{4.18}$$

provided the two conditions

$$Z_i e \, V_p < k \, T_i, \qquad \left|e\right| \, V_p < k \, T_e \tag{4.19}$$

are fulfilled. This gives the potential

$$V(x) = V_p \, e^{-x/\delta_s} \tag{4.20}$$

where δ_S is the sheath width

$$\delta_s = \frac{1}{(Z_i \, \left|e\right|^2 \, n_{i\infty} / \varepsilon_o \, k \, T_i + \left|e\right|^2 \, n_{e\infty} / \varepsilon_o \, k \, T_e)^{1/2}} \tag{4.21}$$

Simplifying in the two limiting cases:

a) T_i=T_e = T (“Thermal” plasma)

$$\delta_s \approx \sqrt{\frac{\varepsilon_o \, k \, T}{n_{e\infty} \, \left|e\right|^2 \, \left(Z_i + 1\right)}} = \lambda_D \frac{1}{\sqrt{Z_i + 1}} \tag{4.22}$$

so the greater the n's the shorter δ_s (it has been assumed $n_{i\infty} = n_{e\infty}$).
b) T_e>>T_i a situation referred to as "cold ion plasma"

$$\delta_s \approx \sqrt{\frac{\varepsilon_o \, k \, T_i}{n_{i\infty} \, \left|e\right|^2 \, Z_i}} \tag{4.23}$$

In order to verify the conditions under which the approximation (4.19) was made, namely $Z_i e \, V_p < k \, T_i$ and $\left|e\right| \, V_p < k \, T_e$, the potential in the origin, V_p can be calculated

assuming the equality for the temperatures, i.e $T_i \approx T_e \approx T$. At equilibrium, the net current fluxes must be zero:

$$n_{io}\ Z_i\ |e|\ < v_{io} >\ = n_{eo}\ |e| < v_{eo} > \tag{4.24}$$

$$< v_{i,e\,o} >= \sqrt{\frac{8\ k\ T}{\pi\ m_{i,e}}} \tag{4.25}$$

so that, using (4.16) in (4.24), putting $n_{e\infty} = n_{i\infty}$ and resolving for V gives

$$V_p = \frac{k\ T}{2\ |e|\ (Z_i + 1)}\ \ln\ \sqrt{\frac{m_i}{m_e}} \tag{4.26}$$

Since $m_i >> m_e$ and $2(Z_i + 1) > 1$, at best $|e|\ V_o \approx kT$ and the conditions (4.19) are not valid. However, Swift states that from a practical point of view, a "physical" assumption $eV < kT$ could be assumed everywhere, except for $x \to 0$. But in fact, it is just in this limit that the condition becomes questionable; if in the pre-sheath the effect of the field is to drive the ions towards the sheath [92, 93] this condition has no real "physical" significance: the pre-sheath edge may be well beyond the $x \to 0$ limit.

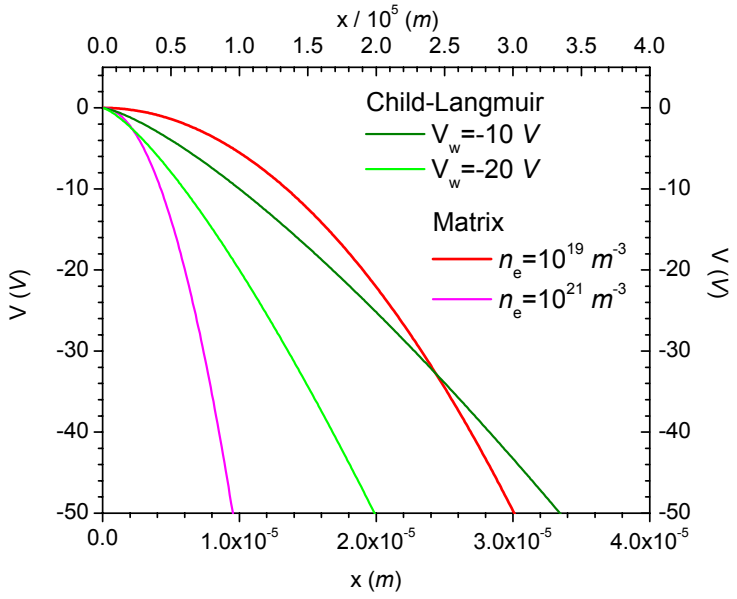

Figure 4.3 a, sheath potential distribution according to Matrix model (abscissa is bottom axis), for two number densities; and Child-Langmuir for two wall potential (abscissa is top axis) [formulae (4.10) and (4.12)].

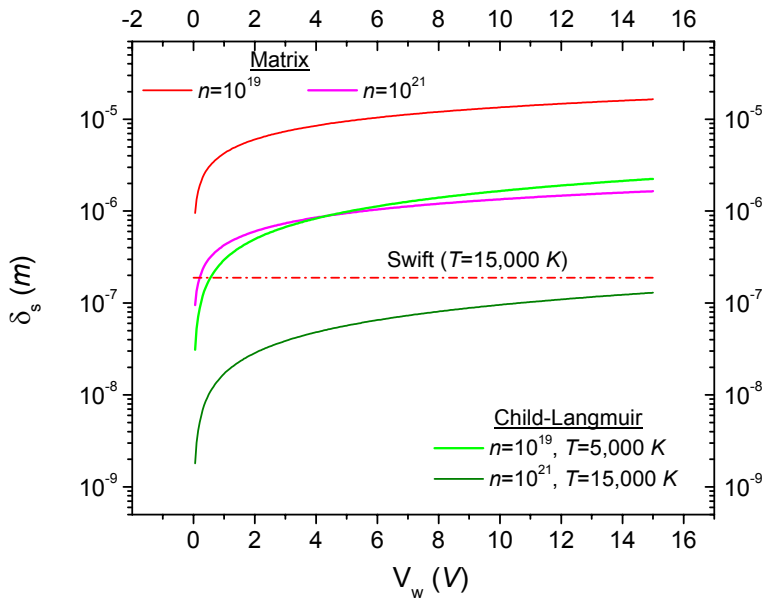

Figure 4.3 b, sheath thickness: "Thermal" (4.22) (Swift), Matrix for different sheath number densities and Brown's C-L (4.29) formulae for different number densities and temperatures.

In figure 4.3 left the potentials for the matrix and the Child-Langmuir models are shown. The Child-Langmuir model depends on the wall potential which has been chosen V_w= –10 and –20 *V*; also, the *x* dependency (4.12) is expressed in terms of the x/δ_s ratio (upper abscissa). An arbitrary factor 10^5 has been chosen for the scaling. *If* the sheath is 10^{-5} *m* then when the ratio reaches unity, the edge has been reached. For lower values of the ratio the sheath extends beyond 1.

For the matrix model, two different densities have been chosen, generally 100 to 1,000 times less than the core bulk density (sheath depletion, see figure 5.13 in Chapter 5).

Figure 4.3 rights, shows the thickness computed for the two potentials of figure 4.3 left. Since Child-Langmuir's depends on electron temperature, a relatively "high", 15,000 *K* and a "low" 5,000 *K* value were chosen. Also shown is the value after Swift (formula (4.22)).

Except in the latter case, where it is equal to the Debye length, the thickness varies considerably in the other cases. A temporary upper limit of about 10^{-5} *m* is taken as result of the Matrix model for $n=10^{19}m^{-3}$, although in this case, it can be expected that a correspondingly higher neutral density would be present within the sheath. But the collisionless nature of the latter would not break down. This can be seen by comparison of this value with the mean free paths evaluated in Chapter 2 (figure 2.5).

By using the formulae of this section, it is possible to evaluate and plot the number density within the sheath; however, a part of the limitations indicated at the beginning of the section, it should be mentioned that both Matrix and Child-Langmuir models were developed for highly biased walls. In particular, Child-Langmuir's was originally developed for vacuum tubes and large sheath potentials with respect to the electron temperature; therefore, it is only valid for the case of a highly biased wall or probe in rarefied plasma. In atmospheric arcs, the wall potential (i.e. the probe) can rarely be biased at values above 30 *V*. Among these collisionless model, Swift's is the closest to the experimental conditions of interest within this work, namely a somewhat 'lower' wall potential, possibly a floating wall (this also explains the choice of the wall potential at 10 and 20 *V* made above). As mentioned earlier in this section, the validity of the assumption used in its derivation turns to be incorrect (condition (4.19) and comments thereafter), however it provides an order of magnitude for the sheath thickness.

4.3.2. Collisional sheaths

1. Collisions alter the ion distribution of velocities when entering the sheath [98] but it is difficult to account for the different collision mechanisms (rates, cross sections).
The fact that according to literature, the sheath extends for some Debye lengths gives some hints about the degree of collisionality under he circumstances of this work.

1. The Debye length ($\lambda_D \approx 10^{-8}$ *m*) is of the order of the mean inter-particle distance, $n^{1/3}$ (see Chapter 2)

2. The number of particles per Debye sphere, $n_D = 4\pi\lambda_D^{4/3}/3$, amounts less than 10 (*cf* [31] and figure 2.2)

3. The mean free path of ions, depending on ion collisions, is one to three orders of magnitude greater than λ_D (*cf* figures 2.2 and 2.4), while for electrons it is always at least two orders of magnitude greater than the Debye length.

Therefore, the number of particle encounters within the sheath must be limited. The ratio between the ion and neutral number densities within the sheath is important as from this number depends the rate of ion-atom collisions and in particular the rate of charge exchange reactions. It is of interest to assess the collisional models within the parameter range of this work. It will be seen that their limit converges to the collisionless conditions.
In the collisional case the ion mean free path is less than the sheath thickness. Both the mobility and mean free path of ions depend on ion velocity, however two extreme cases can be considered depending on pressure and ion velocity: either $\lambda_i \approx const$ or $\mu_i \approx const$.

1) In the first case, $\lambda_i \approx const$, the ion density, the electric field, the potential ("improved" version of Child-law) and the current density are reported as [104]:

$$n_i = \frac{n_s v_s}{\left(2e\lambda_i E/\pi m\right)^{1/2}}, \quad E = \left[\frac{n_s v_s}{2\varepsilon_o \left(2e\lambda_i E/\pi m\right)^{1/2}}\right]^{1/2} x^{2/3} \tag{4.27}$$

with $E(0)\approx 0$ at the sheath edge, and

$$V = -\frac{3}{5}\left(\frac{3}{2\varepsilon_o}\right)^{2/3} \frac{\left(en_s v_s\right)^{2/3}}{\left(2e\lambda_i/\pi m\right)^{1/3}} x^{5/3} \tag{4.28}$$

where $V(0)=0$. Since $en_s v_s = j_o$, putting $V=-V_o$ at the probe position $x=\ell_s$, the constant current density is

$$j_o = \frac{2}{3}\left(\frac{5}{3}\right)^{3/2} \varepsilon_o \left(\frac{2e\lambda_i}{\pi m}\right)^{1/2} \frac{V_o^{3/2}}{\delta_s^{5/2}} \tag{4.29}$$

which is the collisional form of the Child-Langmuir law at constant mean free path that is independent of ion velocity (note that the origin $x=0$ was chosen at the plasma-sheath edge).

2) At higher pressure, the ion collision frequency and therefore the ion mobility μ_i is independent of velocity ('constant') and an expression for the ion current density is given

$$j_o = \frac{9}{8}\varepsilon_o \mu_i \frac{V_o^2}{\delta_s^3} \tag{4.30}$$

For very high collisionality the ion velocity at the sheath is different from the Bohm velocity and their ratio can be written as [87]

$$\frac{v_s}{v_B} \approx \frac{1}{\left(1+\pi\lambda_{De}/\lambda_i\right)^{1/2}} \approx \left(2\lambda_i/\pi\lambda_{De}\right) \tag{4.31}$$

(where in the last equality a first order expansion was used for $\lambda_i << \lambda_{De}$)

2. The span from collisionless to fully collisional treatment has been covered in [97] who identify a distinguishing criterion in the average number of collisions within the sheath (collision parameter) [97, 98] by the product of $\beta=\lambda_D/\lambda$ and $d = \delta_S/\lambda_D$

$$\beta\, d = \frac{\lambda_D}{\lambda_i}\frac{\delta_s}{\lambda_D}.$$

Thus for $\beta d>3$ the solutions obtained by solving the exact sheath equations match the ones obtained from a collisional solution [97]. These equations are obtained by balancing the forces due to the electrical field with the mobility driven resistance contribution (mobility drag). This can be also seen as the neglecting of the convective term in the ion momentum equations, which means that the collisional drag term dominates the convective term in the momentum equation pertaining to the sheath.
In the opposite case both terms play a role. In the extreme case of βd very small, the convective terms dominate, resulting in the fully collisionless case.
In [98] attention is drawn on the full range of collisionality in order to determine the potential distribution that has to supersede the one given by Child's law ('Generalized Child-Langmuir'). A power law is determined and the ion distribution function within the sheath is determined. These results are obtained under conditions of planar geometry and cold ions following mono-dimensional trajectories. Further, since a static sheath is considered, the electrons are considered in equilibrium; this means also that the dynamical aspects of the model can be accepted as long as the time scales of interest are larger than the ion plasma period.
This can be checked comparing the ion plasma frequency ω_i with the electron-atom collision frequency $2\pi\nu_{ea}$. The first can be taken as $\omega_i = 10^{11}$ to 10^{12} *rad/s* for the ions of interest here (*Ar*, *He*, see Chapter 2); the second can be estimated using the electron-atom collision cross section, $\sigma_{ea} = 0.15\cdot10^{-20}\ m^2$ (for *H)* or $\sigma_{ea}=5\cdot10^{-20}\ m^2$ (for *Ar*); using $\nu_{ea} = \sqrt{2}n\sigma_{ea} < v >_e$ where $< v >_e = \sqrt{8kT/\pi m_e} = 1.56\cdot10^6\, m/s$ (atoms considered at rest with respect to electrons), the collision frequency is $2\pi\nu_{ea} = 2\cdot10^9$ to $6.9\cdot10^{10}$ *rad/s* (for *H* and *Ar* respectively) so that $2\pi\nu_{ea} < \omega_i$ and the hypothesis of a static medium is 'just' satisfied for *Ar.*
The authors consider only electron neutral collisions, which is justified only when the degree of ionization is 'low'. Therefore, for the varying conditions found in the present study, these conditions *could* be of interest far from the arc core if the sheath were collisional. On the other hand, the latter circumstance implies a low temperature and therefore [98], the neutral density within the sheath is much larger than the charged density, a condition that would be always fulfilled in collisional cases. Among the different ion neutral interactions, the charge transfer seems to play a predominant role [98] and thus is the only collision considered. Other hypotheses are that the electrode is perfectly adsorbing and secondary emission arising from ion bombardment is neglected. Finally, the pre-sheath existence is not considered as its potential drop is assumed

'small'. This is reflected in the choice of the boundary conditions, with potential and electric field vanishing at the interface, although the ion impinging velocity is not small. The authors solve the ion equation exactly by numerical methods and compare the results with approximate analytic solutions. The latter match the numerical outcomes better when the electronic contributions are considered. The potential distribution in the sheath and the ion velocity distribution at impact on the electrode are determined. In particular, the ion energy distribution from the power-law potential distribution is obtained by taking into account the electron contribution. It is found that ions cannot acquire the whole energy from the field so that as the parameter $\beta=\lambda_D/\lambda_i$ increases, the impact velocity at the electrode decreases.
Similar is the work of [97] where the sheath thickness was computed using the three 'dimensioned' equations for the collisionless and collisional sheath regimes:

A) Collisionless regime: Child-Langmuir formula

$$\delta_s = \frac{2^{5/4}}{3}\left(\frac{v_o}{c_s}\right)^{-1/2}\left(-\frac{eV_s}{kT}\right)^{3/4}\lambda_D \qquad (4.32)$$

where c_s is the sound speed.

B) Collisional, specialising the general case given by the author and taking for the ions upstream of the wall the sound speed $v_i=c_s\approx 2{,}700\ m/s$ (Chapter 2, [59]), i.e. $M=1$ to see the effect (if any) of the Bohm criterion; in the two extreme cases

B1) constant ion mean free path λ_i, numerically,

$$\delta_s = 4.47\cdot 10^3\left(\frac{\lambda_D}{\lambda_i}\right)^{-1/5}\left(-\frac{V}{T}\right)^{3/5}\lambda_D \qquad (4.33)$$

B2) constant mobility

$$\delta_s = 2.8\cdot 10^4\left(\frac{\lambda_D}{\lambda_i}\right)^{-1/3}\left(-\frac{V}{T}\right)^{2/3}\lambda_D \qquad (4.34)$$

Formula (4.33) gives the plots in figure 4.4. Unfortunately, case B2 gives unrealistically low sheath thickness (10^{-11} and $10^{-12}\ m$) and is neglected.

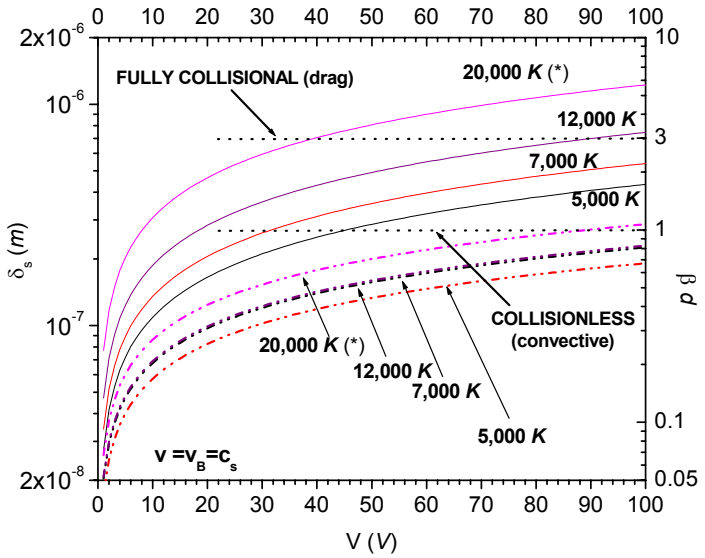

Figure 4.4 a continuous curves, sheath thickness (left axis); broken curves, collision parameter (right axis) within the sheath as functions of the probe potential for different electron temperatures. The collisional case for constant mean free path is shown [97]. Ion speed taken as the Bohm velocity at the corresponding temperature. The region below βd=1 is collisionless, above βd=3, is fully collisional. (*) The 20,000 *K* computed using ion-electron collision mean free path.

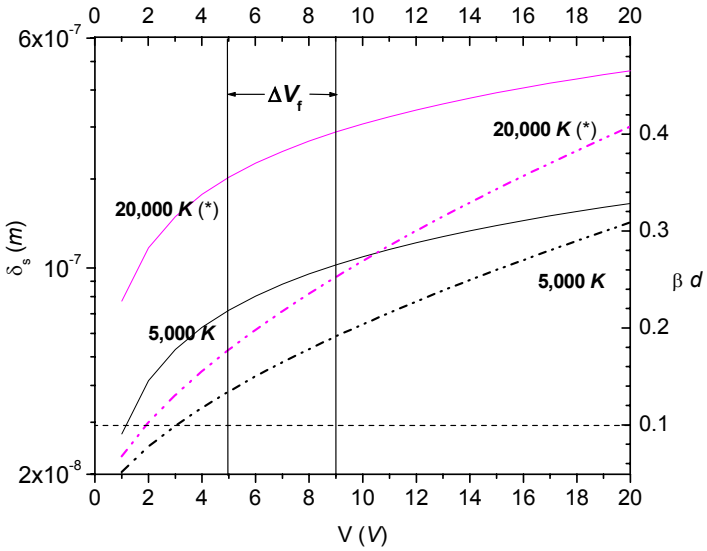

Figure 4.4 b, Particular of figure 4.4 left. Horizontal broken line at 0.1 is the upper limit for convection. The potential for floating probes under atmospheric arc conditions is believed to vary between 5 and 9 *V* (*cf* Chapter 9).

The regions in figure 4.4 right are subdivided using the criteria given in [99]; for number of collisions below 1 (strictly speaking 0.1 in the original paper) the sheath is collisionless. In this region the convective term in the ion momentum equation dominates. The region above βd=3 (number of collisions) is fully collisional; here the drag term (i.e. ion mobility) dominates in the mentioned equation. In between the two regions both convective and drag terms play a role.
However, the highest number of collisions (right axis) reaches unity only for very high wall potential (~100 V) and temperature of 20,000 *K*. At the same temperature, it is about 0.6 at 40 *V*. In contrast with the other temperature cases reported in figure 4.4, the sheath thickness at 20,000 *K* was evaluated as a limiting case using the mean free path for ion-electron collision, because ion-atom collisions are negligibly small. Correspondingly, the electron density was used. This is difficult to assess because at negative probe potential, the electron density is likely to drop within the sheath. Also, it is unknown whether substantial cooling would occur within the sheath, driving the composition towards lower temperatures and charged particle densities. In these cases the thickness curve would lower towards the 12,000 *K* case. The other cases were computed using the *neutral* density and the ion-atom mean free path, both computed at the appropriate temperature (consistently with the parameters of Chapter 2).
Therefore, it may be concluded that the sheath can be considered collisionless with respect to ion-atom interactions; this holds as long as a low ionization ratio is assumed which occurs in the edges of the arc. When electron-ion collisions become important, the sheath can be considered weakly collisional.

4.4. Varying Sheath

The "varying" sheath corresponds to the experimental situation of a moving probe entering the atmospheric pressure arc from the cooler and less dense outer regions towards the hot and dense core. It is likely that the potential and the thickness of the sheath will vary with time as the probe varies its position in time during the motion. Given probe permanence times between 1 and 10 *ms* (*cf* Chapter 9), a true sheath variation 'time scale' can be introduced by considering the plasma changes in the time necessary for the slowest components, namely the ions, to redistribute during the probe transit time. This can be considered as the sheath "formation time".
The time for the ions to rearrange following a variation in the electric field could be estimated as the ratio between the Debye length and the ion thermal velocity [84]

$$\tau = \lambda_D \big/ v_{th}^i \qquad (4.35)$$

or slightly higher when using $\delta_{sh} \geq \lambda_D$. Using the values reported in Chapter 2, for *Ar* at 20,000 *K* this gives $\tau \approx 8 \cdot 10^{-11}$ *s*, whereas, at 5,000 *K*, $\tau \approx 6 \cdot 10^{-12}$ *s*. Debye length and thermal velocity were computed using the temperature dependency of the charged particle density (Chapter 2). If one takes as characteristic length the (longer) mean free

path, $\lambda_i \approx 10^{-6}$ *m*, the longest characteristic time would still be only ≈ 2 or $4 \cdot 10^{-10}$ *s*. Alternatively, one could argue [76] that the time for the plasma (perturbed by the probe) to relax back, is the time needed for the flow to move a 'probe diameter away', $\tau = 2r_p/v_f$, where flow speed is now considered. Under the circumstances of this work, this would mean $\tau \approx 1.3$ μ*s* (v_f =200 *m/s*) to 5μ*s* (v_f =50 m/s). This argument was used by Thomas [76] to infer the time needed for the sheath to form within a flame, in his case of the order of a *ms*. It is perhaps worth mentioning that in [105] Thomas's statement is applied uncritically, of a "few *ms*" formation time in conditions which are widely different from Thomas' and in fact closer to those dealt with here. For the conditions reported in [105], this time results $\tau \approx 0.5$ μ*s*, thus much shorter than the reported '1 *ms*'. According to this picture, 5 μs is the maximum sheath formation time considered here. Within the time resolution of the system under study the sheath can be considered approximately 'static'. The latter is obtained as $\tau_R \sim 20$ μs by taking the minimum spatial resolution *a*=100.4 μ*m* and the probe speed v=5.02 *m/s* from the experiment (*cf* Chapter 8). Therefore, considering the longest among the formations times, 5 μs, as many as 4 sheaths of the estimated thickness can be formed during the minimum resolved time.

4.5. Summary

1. From the previous discussion, the following conclusion can be drawn on the validity of the Bohm criterion: either the field extends far beyond the sheath edge into the pre-sheath in order for the Bohm criterion to be satisfied, suggesting a collisionless sheath; or, the field ends its influence at the sheath edge, and the Bohm criterion is of no use for the collisional sheaths. However, this conclusion holds only with respect to the charged-atom collisions, which dominate where low-ionization levels are attained. In this case, it can be thought that the mechanism that drives the ions towards the sheath is of diffusive nature rather than mobility driven. When the ionization ratio is higher, higher cross-sections for charged encounters (see Chapter 2) imply that electron-ion mean free paths must be used, the field 'leakage' out of the sheath is greater and the validity of the presented models breaks down.

2. The hydrodynamic boundary layer is generally of the order of or thicker than the sheath thickness evaluated above. At Reynolds number *R*=40 (100 *m/s*) the boundary layer is $\delta = 3 \cdot 10^{-5}$ *m* in argon (*cf* figure 2.14). In the collisionless case, the sheath thickness varies from $\delta_s = 10^{-5} m$ in the 'Matrix' model, down to less than $\delta = 10^{-6} m$ in the Child-Langmuir case. For the collisional regime, $\delta_s = 2 \cdot 10^{-6}$ *m* (see figure 4.4) [97] only for relatively high potentials and at high temperature (20,000 *K*). The upper limit was reported at 100 *V* although in atmospheric arcs *V*=-40 *V* is close enough to the probe-to-anode breakdown conditions [62]. For lower voltages, at values close to the floating potential, say between 5 and 10 *V*, the sheath thickness is $\delta_s = 7 \cdot 10^{-8}$ *m* at 5,000 *K* and $\delta_s = 2 \cdot 10^{-7}$ *m* at 20,000 *K* (this voltage is "averaged" because it is an overall estimate of conditions where the currents drop to zero).

3. The validity of the sheath models presented is largely limited by highly biased walls in low ionization plasmas. It is felt that alternative models are needed, which should suit the present cylindrical geometry and the lower field, at least for the floating operating conditions.

4. It is also clear that some theoretical and experimental evidence is needed towards the understanding of the sheath structure and the kind of motion governing the charged particle approach to the probe. In the following chapter, a review of the probe operating regimes will attempt to clarify whether diffusion, convection or electric field effects are the driving mechanism, and then compared with the experimental findings in subsequent chapters.

5. PROBE OPERATING REGIMES AND CURRENTS

5.1. Introduction

Although considerable works on ion (and some on) electron current collection exists, the only publications dealing with current amplitudes appropriate for the present work, are the paper by Gick *et al* [62] some technical reports [106], [63] and, to some extent [107, 108]. The paper by Schott [86] covers a review of the basic works of Lam [109], Cohen [110] and others, but the experimental agreement with the theory is limited to relatively low pressures (some *mTorr*). The book by Swift and Schwar [65] underlines the difficulties when dealing with "high" pressure plasmas, where the effect of collisions makes the interpretation of the characteristic curve rather involved if not impossible [86]. Furthermore, the impressive number of publications by Clements and Smy [78, 79, 82, 91, 111-117] while apparently covering a broad range of experimental conditions, are mostly limited to the study of flame plasmas. These are characterized by electron temperatures varying from 1,500 *K* to 3,000 *K*, and in which the electron density does not exceed 10^{18} m^{-3}, some four orders of magnitude below the regimes dealt with in this work, although Smy [84, 118], and Smy and Noor [118], mention charge density up to 10^{20}-10^{23} m^{-3}. To the author's knowledge, the works dealing with these high values are only Clements and Smy's paper of 1972 [113] and Holmes *et al* [105]. Also, Dawe *et al* [81], while stating the validity of the "sheath convection mode" (attributed to Smy [84] for regimes from 10^{20} m^{-3} up to 10^{29} m^{-3} (evidently a print error!), limits his experimental analysis to flames similar to those discussed by Clements and Smy [79, 91, 111, 114, 115].

Another major difficulty scarcely accounted for in literature on atmospheric plasmas is the limited ionization degree. The aforementioned works refer to ionization levels always less than 10^{-4} thus classified as "low" (see Chapter 2). In only one case is the question addressed in literature for ionization levels up to 10% [74] but in this case the treatment is limited to stationary and homogeneous plasmas.

This lack of coverage poses serious difficulties for the dramatic scaling up needed for the use of the different current formulas derived by these authors (a factor ≈10 for the electronic temperature and up to seven orders of magnitude for the electronic density).

Notwithstanding the plausibility of the classifying criteria fulfilled by the atmospheric arc, considerable limitations due to the specific hypothesis arise when treating the current collection modes. With variations of one or two orders of magnitude, the total currents obtained experimentally by all but [107, 108], [62, 106] and [62, 63], are always below 0.1 *A*. Gick [62] presents ion current values of the order of 1 *A,* even if the plasma parameters derived may be subject to some criticism as will be discussed later in this analysis [115]. Due to the distinguishing physical similarity to the experimental conditions dealt with here, the works of Gick [62, 106] and to a limited extent, Allum [63] will be taken as test cases within this review.

In the following, a list of the works of interest in this review is presented together with the either measured (when available) or calculated currents corresponding to the present experimental conditions, i.e. by using the parameters reported in Chapter 2, provided the appropriate regime applies. It should be observed, that the use of the equilibrium $n(T)$ dependency as given by Olsen [39] is questionable; however, the use of this hypothesis is limited to the search for applicability criteria for one or another probe theory. The values obtained for the currents are therefore given as order of magnitude estimates.
Mention is made of works with some correspondence with the results of the regime classification outlined in section 5.2 "Regime classification". All these values refer to cylindrical geometry.

Table 5.1 summarizes the parameter values used for the current computations reported below. Some are taken from Chapter 2. The probe length has been considered approximately equal to the arc diameter, i.e. from about 10 *mm* to 15 *mm* even when longer; this means that only the 'active' part is considered, i.e. that the probe is fully immersed in the plasma and its edges might emerge from it (but see also Chapter 6). The flow velocity has been assumed to be 100 *m/s*, a value characteristic for the TIG arc [57].

Parameter	Value
Probe radius r_p	10^{-4} *m*
Probe length L	$5 \cdot 10^{-3}$ *m*
Ion mobility μ_i	$1.2 \cdot 10^{-5}$ *m*
Electron mobility μ_e	$4.3 \cdot 10^{-2}$ *m*
Plasma flow Velocity v_f	100 *m/s*

Table 5.1. Quantities used for the calculation of the currents

The comparison will be made as follows

1) From each model, the expressions for the current (and sometimes for other interesting parameters) are reported

2) These are evaluated using the parameters listed in Tables 2.5 and 5.1

3) The plasma parameters that are left free in the above formulas, namely temperatures and charge densities, are compared with experimental findings. In some cases however, both the charge density and the temperatures are unknown. When no formula is given for the derivative of the characteristic curve the density must be determined by different means

4) A comparison is made with experimental conditions similar to those of interest here (when available). In particular, the currents for the appropriate regimes will be compared.

5.2. Some orders of magnitude

One source of complication in the interpretation of probe signals stems from the fact that the electrostatic probe is an intrinsically perturbing device. Its invasive nature is reflected by the birth of boundaries in which the plasma equations fall down. Around the conductor, the quasi-neutrality condition of the plasma is not fulfilled and a layer forms in which the electron and ion densities differ. This layer, called the *Debye sheath* (or simply *sheath*, see Chapter 4) can develop and sustain high electric fields. The sheath existence, geometrical extension, charge and regime depend on the values of the plasma parameters (see Chapter 4). The analysis may be further complicated 1) by the occurrence of thermionic emission, when the probe temperature is high enough, or 2) by the cooling of the electrons when the plasma flow is not negligible. Both effects will be discussed in Chapter 6.

To the physical quantities that defined the arc regime in Chapter 2, some are added to define the plasma-probe interaction; others are calculated and reported in Table 5.1.

1) The probe radius has upper dimensions limited by an "acceptable" spatial resolution, considering the arc length of 3 to 5 *mm* and an inner radius of the arc column of about 5 *mm*, while its lower limit is fixed by simplicity of construction. In most cases in the present discussion it will be considered fixed at r_p=100 μm.

2) The parameter $\alpha=\lambda_D/r_p$ ranges from $3\cdot10^{-4}$ for charge density $n_e= 10^{23}\ m^{-3}$, to 10^{-3} for density of $10^{22}\ m^{-3}$ at a temperature of 20,000 *K* and a probe radius of 100 μm. Its

reciprocal, the Debye Number D_λ, interpreted as the number of Debye lengths within a probe radius, is shown in figure 5.1.

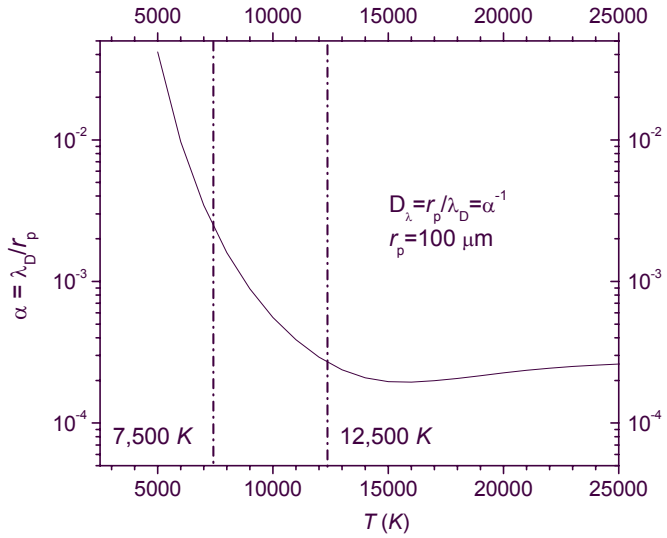

Figure 5.1 ratio of the Debye length to the probe radius (Inverse of the Debye number) as a function of temperature.

3) The ratio $\beta_{i,e}=\lambda_D/\lambda_{i,e}$ interpretable as the number of ion or electron collisions within a Debye length ("i" and "e" stand for ions and electrons respectively), is shown in figure 5.2.

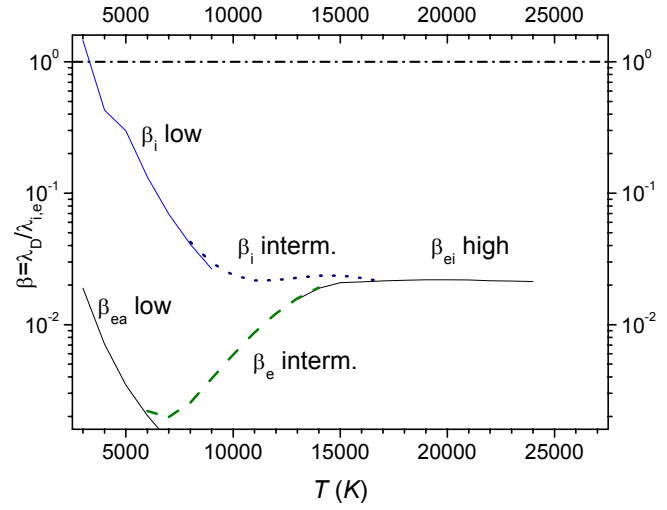

Figure 5.2. Ratio of Debye length to mean free paths as a function of temperature. The Debye length was taken from figure 2.2 and the mean free paths were chosen according to figure 2.5 (i.e. selecting the appropriate temperature range)

It ranges from $2\cdot10^{-3}$ for ions (λ_i=1.2 10^{-5} *m*) to 0.1 or 0.32 for electrons ($\lambda_e=10^{-6}$ *m* or $\lambda_e=3\cdot10^{-7}$ *m*) in the case of charged-neutral collisions (low-ionization). For high ionization $\lambda_i=10^{-6}$ *m* or $\lambda_i=2.8\cdot10^{-6}$ *m* and β_i=0.1 to 0.28.

A possible combination of the last two parameters, β/α can be interpreted as the number of collisions occurring in a region extending for a probe radius r_p. It is the inverse is the Knudsen number described below.

4) The Knudsen numbers, $Kn=\lambda_{i,e}/r_p$, for electron are $Kn_e\approx$ 0.02 (for $\lambda_e= 1\cdot10^{-6}$ *m*), or $Kn_e\approx$ 0.008 (for $\lambda_e= 3\cdot10^{-7}$ *m*); for ions and low ionization $Kn_i\approx$ 0.1 (for $\lambda_i= 1.2\cdot10^{-5}$ *m*); for high ionization ($\lambda_i= 1\cdot10^{-6}$ *m*), $Kn_i\approx$ 0.02; typical probe radius $r_p = 1.25\cdot10^{-4}$. Knudsen numbers are shown for some electron and ion mean free paths in figure 5.3.

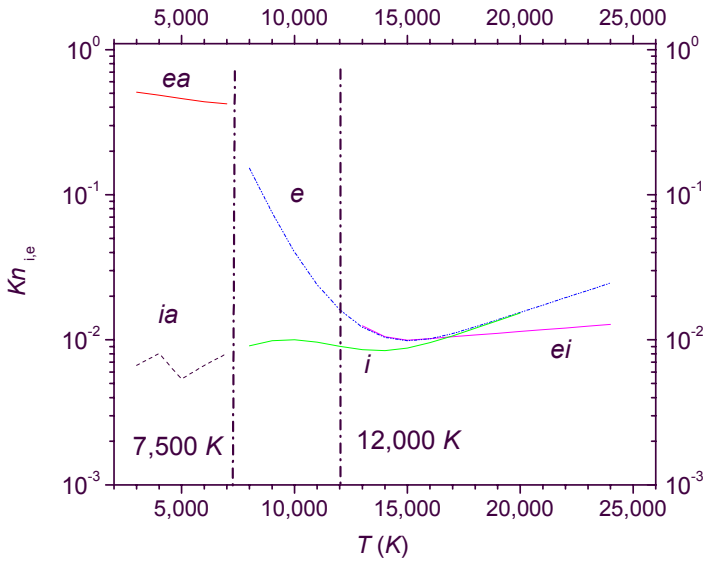

Figure 5.3. Knudsen numbers $Kn_{i,e}= \lambda_{i,e}/r_p$ as a function of temperature for some electrons and ion mean free paths. The relevant mean free paths are indicated. Probe radius fixed at 10^{-4} *m*.

The ratio β/α (the inverse of the Knudsen number), has values 8.3, 99.9 and 333 for ions and electrons respectively and for a probe radius of 100 μm.

5) The hydrodynamical Reynolds Number *R* was defined in Chapter 2

$$R = \frac{\rho U L}{\eta} = \frac{\rho\, v_f r_p}{\eta}$$

where also the thickness of the 'fluid' boundary layer forming around the cylindrical probe was reported in figure 2.15.
The hydrodynamic boundary layer is thicker than the sheath thickness evaluated in Chapter 4. In particular (see figure 4.3) δ_s=2 or $3\cdot10^{-5}$ *m* in the collisionless Child-Langmuir regime [97] or δ_s=2 or $3\cdot10^{-7}$ $m \approx \lambda_D$ in the collisional case (see figure 4.4), while at Reynolds number *R*=40 (100 *m/s*), $\delta=3\cdot10^{-5}$ *m*.
Of course when $\delta >> \delta_s$ it is immaterial whether the sheath thickness is evaluated in non flowing conditions because the plasma flow velocity within δ drops rapidly towards zero at the surface (non slip condition) and can be assumed negligibly small at distances of 10^{-5} to 10^{-7} *m* from the surface.

6) The Electrical Reynolds number, defined as the product of the hydrodynamic Reynolds Number and the Schmidt Number [112]:

$$Re = \frac{v_f \; r_p \; e}{\mu_i \; k \; T_e}$$

where μ_i is the ion mobility. *Re* can vary from 40 to about 10^4, in the range of the flow velocity, v_f = 100 to 2,700 *m/s* (*Ar* sound speed) and an electron temperature T_e = 10,000 or T_e = 20,000 *K* (probe radius r_p, =100 μ*m*). *Re* is plotted in figure 5.4 as a function of temperature (left-bottom axes) or flow velocity (top-right axes).

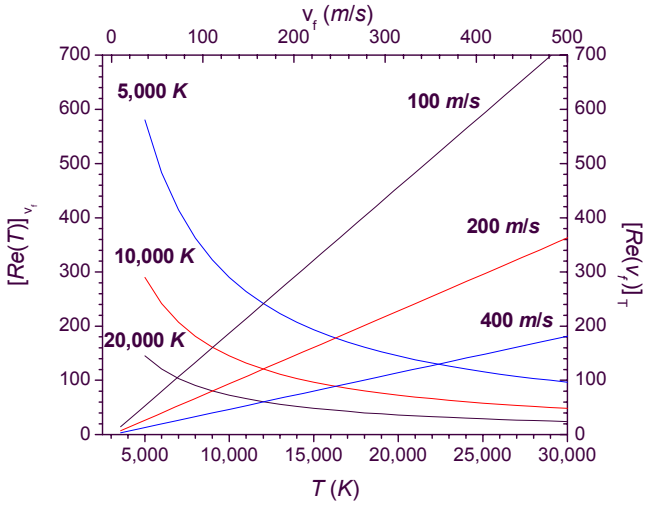

Figure 5.4. Electrical Reynolds number *Re* in *Ar* as a function of temperature (left-bottom axes) and of flow velocity (top-right axes). Probe radius $r_p=10^{-4}$ *m*.

7) The reduced potential is a non-dimensional parameter defined as the ratio of the electric potential energy eV_p supplied to the probe (either through the bias or the floating voltage V_p, no distinction between the symbols is made here) and the thermal energy of the electrons, kT_e. Previous experimental conditions very similar to the ones discussed here [62], suggest voltages up to about V_p=40 *V* before the occurrence of breakdown. Numerically, $eV_p/kT_e \approx 11{,}600\ V_p/T_e$ (*V*/*K*) and the two limiting temperatures considered 7,500 and 12,000 *K*, see Chapter 2, give 1.5 V_p and 0.9 V_p, while at 20,000 *K*, $eV_p/kT_e \approx$ 0.6 V_p. The maximum voltage would occur at 7,500 *K*, and would be 60 *V*.
The parameters discussed above are listed in Table 5.2.

Physical parameter (Units)	Range
1) Debye length λ_D (*m*)	$7 \cdot 10^{-8}$ to $10^{-7} m$
2) Debye number $D_\lambda=\alpha^{-1}=r_p/\lambda_D$	10^3 to 10^4
3) $\beta_{i,e}=\lambda_D/\lambda_{i,e}$ (LI) $\beta_i=\lambda_D/\lambda_i$ (HI)	$2\cdot10^{-1}$ (*i*) $2\cdot10^{-3}$ (*e*) 2 to $4\cdot10^{-2}$ (*i*,*e*) (*cf* fig. 5.1)
4) Knudsen numbers $Kn_{i,e} = \lambda_{i,e} / r_p$	0.01 (*i*); 0.01 to 0.5 (*e*) (LI) 0.01 (*i*,*e*) (HI) (*cf* fig. 5.2)
5) Hydrodynamic Reynolds number *R*	0.2 to 5 (*Ar*); 0.2 to 4.5 (*He*)
6) Electrical Reynolds number *Re*	40 to $1.2\cdot10^4$
7) Reduced potential $\chi = eV_p/kT_e$:	0.6 to 1.5 V_p

Table 5.2. Physical quantities calculated from the parameters of Table 2.3. (LI=Low Ionization, HI=High Ionization).

Many computed parameters depend explicitly on the mean free path; the latter depends on the collision cross-sections, specific of the particles species and interactions, which in turn, depend critically on the ionization fraction (see Chapter 2).
It is worth noting that the probe theories under assessment here were developed for 'low' ionization ratio. The consideration of higher ionization ratios is one of the aims of this study.

5.3. Remarks and Classification

In the published literature, the authors that appear to provide a comprehensive review of the probe operation theories, are (I) Swift and Schwar [65], (II) Chung, Talbot and

Touryan ('CTT' [37, 119]), (III) Smy [84], Clements and Smy (collectively 'CS' in the following, [78, 79, 82, 91, 111-117]), (IV) Tichy *et al* [120-122] and V) Benilov [123].
The choice of these works is somewhat arbitrary, however, in the frame provided by these groups of publications, mention is made of specific works (like the classical papers by Kagan and Perel [88], Su and Lam [73], Su and Kiel [72], Lam [109], Kiel [75], Cohen [110], Carrer and Fendell [124], Schott [86] among the others). The choice reflects the different points of view that these references provide. In particular a balance was deemed necessary between the rigorous theoretical presentations in (I) and (II) against the more experimental and practical considerations found in (III). Also, these works originate from different fields of research and /or different regimes (Low-pressure laboratory plasmas (I), re-entry problems of vehicles through atmosphere (II) and flame plasmas (III). Although none of these fields resembles very closely the medium under investigation in this work, it is a purpose of this review to try to match the different limiting cases from opposite directions. The tempting methodology to follow a 'selection by exclusion' procedure saving the 'right tools' for the case under study here was found unfeasible. Moreover, a comprehensive and in-depth state of the art review on probe operation in "high" pressure regimes was felt necessary (at cost of some lengthiness) because very often, special cases are only treated in a sparse fashion.

Four groups of parameters were chosen according to the works found in the literature. The first is based on the Debye length and the probe radius (section 5.2.1); the second deals with ion and electron mean free path and probe radius (i.e. Knudsen numbers, section 5.2.2). The third, takes into account the plasma probe relative motion by means of the electrical Reynolds number (section 5.2.3). The fourth analyzes the plasma-probe relative motion using a hydrodynamic model and partly incorporates the third.
Following an identification procedure, the explanation of the terminology is reported. For each group this will be done according to the following steps:

- List of the classification criteria;
- Description of the different regimes proposed together with the origin of the classification criteria;
- Evaluation of their key parameters and justification of the choices made.

After the regimes are identified, a review is made of the available experimental methods to extract plasma parameters (section 5.7).
Open questions and problems related to plasma cooling, thermo- and field-emissions and the relaxation of the "frozen-chemistry" condition remain and are reported in Chapter 6.

5.3.1. Classification based on Debye length and probe radius

The book [65] deals extensively with the basic theory of probe operation dedicating a chapter on "Probes in high-pressure plasma"; it also provides a final table summarizing the different regimes for high pressure plasma probe operation, based on the ratio of Debye length and probe radius and on limits on the probe potential; the references however, dated up to the mid 1960s, are limited to low degree of ionization and mostly to spherical geometries. The probe current depends on the probe potential also at high pressures. The effects of the electrical field in the sheath near the probe are considered although evaluations are problematic since the sheath thickness can extend from a few to a few hundred mean free paths.

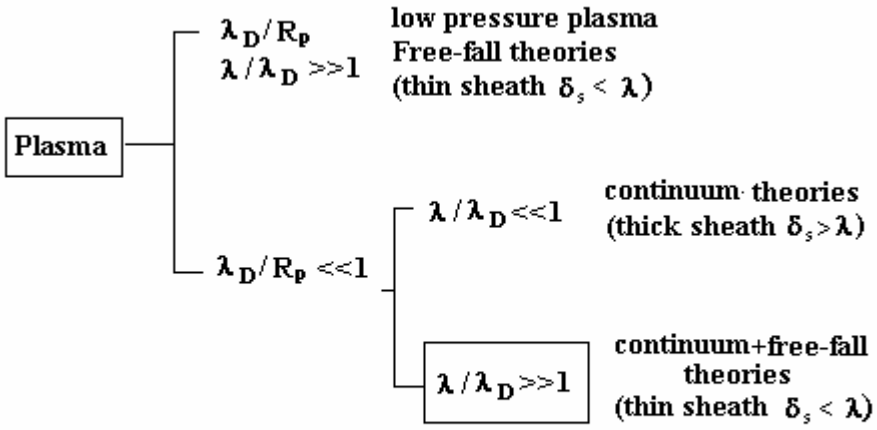

Figure 5.5. Probe operating regimes according to Swift and Schwar [65]. The regime chosen in the present work is indicated by a box

The condition $\alpha = \lambda_D / r_p << 1$ is assumed here as prerequisite; the different theories in the frame of high pressure plasmas, "continuum" and "continuum plus free-fall" theories, are reported according to the sub-criteria depicted in figure 5.5. They are explained as follows.

(i) The "Continuum theories" ([110], [73], [72]) in which $Kn<<1$, in addition require $(r_p/\lambda_i)^{1/3}(\lambda_D/\lambda_i)^{2/3}>>1$. These theories consider mobility and diffusion-based flux equations in the whole plasma; the sheath thickness δ_s can extend for many collision paths ("thick" sheath).

(ii) The "Continuum plus Free-fall" theories ([125]), that require $r_p / \lambda_D >>1$, and a "thin" and collisionless sheath around the probe,. $\delta_S << \lambda$. In the adjacent transition

region and in the rest of the plasma, charge carrier motion is considered mobility and diffusion-driven.
It can be demonstrated [65] that the “Continuum” and the “Continuum plus free fall” theories are special cases of the “General theories” from which they can be derived.
The “General Theories” of Wasserstrom, Su and Probstein [126] use flux equations (transport equations) for the ion and electronic current based on the Maxwell-Boltzmann transfer equation, without assuming an explicit type of flow for the charge carriers. When $\lambda << r_p$ (i.e. $Kn << 1$) the flow equations describe the collision dominated plasma and for highly negative biased probes ($V_p << 0$) these theories give expressions for the currents in the ion-saturation region of the characteristic curve. The case $\lambda >> r_p$ (i.e. $Kn >> 1$) belongs to the flow of carriers under the “Free-fall theory” of ‘Orbital’ type, in which the particles ‘fall’ towards the probe without suffering interactions. These are adequate for low-pressure regimes not dealt with here. Conversely the "Continuum theories” are obtained requiring $\lambda_{i,e} << r_p$ and $\lambda_D >> \lambda_{i,e}$, . The "Continuum plus free-fall" are obtained when $\lambda_{i,e} >> \lambda_D$ (or $\beta_{i,e} << 1$). The espression “Continuum plus Free-fall” stems from the fact that the plasma is considered collisional in the undisturbed region while the sheath is considered thin and collisionless.
These two regimes are described below.

5.3.1.1. Continuum theory

Conditions: $\alpha = \lambda_D / r_p << 1$ and $\lambda/\lambda_D << 1$ therefore, $\lambda << \lambda_D << r_p$.
The theory belongs to Su and Lam [73] and Cohen [110] for the case of spherical geometry, and Su and Kiel [72] for cylindrical probes. Results are reported here only for the cylindrical geometry. Su and Kiel [72] find the potential in four different regions that, starting from the probe and moving radially outwards, are (I) the Diffusion layer, (II) the sheath, (III) the transitional region (often called pre-sheath) and (IV) the quasi-neutral (undisturbed) region. From the knowledge of the potential, the probe current is determined, allowing for the construction of the characteristic curve. The assumptions are:

- The plasma is only slightly ionized so that collisions between charged particles are negligible compared to charge-neutral ones; also, the diffusion coefficients are independent of the ionization levels.

- the equality of the carriers both at the probe and in the bulk of the plasma, $n_i = n_e = 0$ at the probe, where $V = V_p$, and $n_i = n_e = n_\infty$ in the undisturbed region, where $V = 0$. This means also that $n_e = \exp(eV/kT_e) \rightarrow 0$ at the probe. The potential is considered to be made of three contributions $V_p = V_{sheath} + V_{tran} + V_{Qn}$, of the sheath, of the transition and of the quasi neutral regions respectively.

- Crucial in these works is the assumption of a plasma at rest, formally translated as the absence of convection terms so that the continuity equations for the charged species are governing diffusion within the plasma,

- It is assumed that the sheath thickness is of the order of several mean free paths.

Within this frame, in steady state conditions the charge motion is described by the equations

$$\begin{aligned} &\nabla\cdot\Gamma_i = 0, \qquad \Gamma_{\mathrm{i}} = n_i \mathrm{v}_i = -D_i\left[\nabla n_i + \left(\frac{n_i e}{kT_i}\right)\nabla V\right] \\ &\nabla\cdot\Gamma_e = 0, \qquad \Gamma_{\mathrm{e}} = n_e \mathrm{v}_e = -D_e\left[\nabla n_e - \left(\frac{n_e e}{kT_e}\right)\nabla V\right] \end{aligned} \tag{5.1}$$

while the potential distribution is determined by Poisson's equation. [$\Gamma_{i,e}$ are the ion and electron fluxes]. After a change to ellipsoidal coordinates (allowing treatments of generic probe shapes) and some rearrangements, Su and Kiel [72] obtain a coupled system of equations in the potential for the quasi-neutral region, in which the requirement of charge equalities gives the densities and the potential. A modification of the equations for the region near the probe surface is based on the assumption of $\lambda_D << r_p$, in which case, *assuming* a thin sheath, the sheath edge is taken at the probe surface. This leads to an approximate form of Poisson's equation and for the consequent system of coupled equations identical to the one of Su and Lam [73], and resolved numerically. Ion and electron currents in the saturation regions are

$$\begin{aligned} I_{\mathrm{i\,sat}} &= n_\infty\left[2\pi Lk\left(T_{\mathrm{e}}+T_{\mathrm{i}}\right)\mu_{\mathrm{i}}/\ln(\pi L/4r_{\mathrm{p}})\right] \\ I_{\mathrm{e\,sat}} &= n_\infty\left[2\pi Lk\left(T_{\mathrm{e}}+T_{\mathrm{i}}\right)\mu_{\mathrm{e}}/\ln(\pi L/4r_{\mathrm{p}})\right] \end{aligned} \tag{5.2}$$

where L is the cylinder length, assumed much greater than the sheath radius,

$$\begin{aligned} \mu_{\mathrm{i}} &= eZ_{\mathrm{i}}D_{\mathrm{i}}/kT_{\mathrm{i}} \\ \mu_{\mathrm{e}} &= eD_{\mathrm{e}}/kT_{\mathrm{e}} \end{aligned} \tag{5.3}$$

are the mobilities and

$$\sigma = n_\infty e^2\left(\frac{ZD_{\mathrm{i}}}{kT_{\mathrm{i}}}+\frac{D_{\mathrm{e}}}{kT_{\mathrm{e}}}\right) \tag{5.4}$$

the electrical conductivity. The slope of the characteristic curve in the electron accelerating region is

$$\frac{dI}{dV_p} = \frac{3L\,\pi\,\sigma}{\ln\frac{\pi L}{4r_p}\ln\frac{r_p}{\lambda_D}} \qquad (5.5)$$

This is appropriate for a thin sheath at whose edge, the density is reduced by a factor of the order $\approx\left(\lambda_D / r_p\right)^{2/3}$ □ 1.

With the aid of Table 5.2 above, the currents (5.2) and (5.3) are numerically

$$I_{i\,sat} = n_\infty \left(T_e + T_i\right) \cdot 2.921\cdot 10^{-31}\ A \qquad (5.2a)$$

$$I_{e\ sat} = n_\infty \left(T_e + T_i\right) \cdot 1.047\cdot 10^{-27}\ A \qquad (5.3a)$$

$$\sigma = n_\infty \cdot 6.887\cdot 10^{-21}\ \ \left(\Omega m\right)^{-1}$$

is the electrical conductivity and

$$\alpha^{2/3} = \left(\lambda_D / R_p\right)^{2/3} \approx 7.884\cdot 10^{-3} \text{ to } 10^{-2}$$

is the charge density reduction factor at the sheath edge with respect to the bulk plasma.
Formulae (5.4) and (5.5) show that once the bulk density n_∞ is known, the temperature can be derived from the two saturation currents. Alternatively, if the temperature is determined by some other mean, the density can be deduced. The electrical conductivity can be deduced once the diffusion coefficients are known.
The two saturation currents are shown as a function of temperatures for the cold plasma approximation ($T_i << T_e$) in figure 5.8 (section 5.3.1.2). The values corresponding to thermal plasma are a factor two larger.

It should be emphasized that these currents were evaluated using the (implicit) dependency of the electron density on temperature as given in Chapter 2, where equilibrium distributions were assumed.
In principle, the use of both formulae within one experimental run, i.e. the determination of the complete characteristic curve, allows both the density and (one of the) temperatures to be determined. However, a serious limit is the lack of saturation expected when the limit $\alpha = r_p/\lambda_D >> 1$ is not verified. This is due to the fact that the electric field extends beyond the sheath. When the probe collects current the voltage is predicted to decay as r_p/λ_D whereas for a complete Debye shielding $V \sim \exp(-r/\lambda_D)/(r/\lambda_D)$ is needed [110].
Moreover, in practical terms, a part of the ability to obtain the complete characteristic curve for atmospheric pressure arc plasma, problems might occur at electronic

saturation because the electronic current appears too high for a non-perturbative probe (several percent for a TIG arc at 100 A).

5.3.1.2. Effects of moderate ionization

To the author's knowledge, the only published work dealing with non-negligible ionization is Su and Sonin's work [74]. These authors extend the work of Su and Lam [73] and Cohen [110] in the continuum by adding to the fluxes equations two terms

$$\beta_{i,e} J_{i,e}, \quad \beta_{i,e} = \frac{D_{i,e,g}}{D_{i,e}} \frac{n_{e\infty}}{n_T}, \quad J_{i,e} = \frac{j_{i,e} r_p}{e n_{e\infty} D_{i,e,g}} \tag{5.6}$$

[$D_{e,i,g}$ binary electron-gas and ion-gas diffusion coefficients, j the current density] which account for the contributions of collisions. The asymptotic solutions sought in the limit $\alpha=r_p/\lambda_D >>1$, show that these 'corrective terms' disappear both in the quasi-neutral and in the thin sheath. The difference survives in the probe potential terms that incorporate the combination (5.6). In the quasi-neutral region the charge unbalance $\left(n_e - n_i\right)/n_{e\infty} \sim \left(\lambda_D/r_p\right)^2$ ~10^{-4} to 10^{-6} for our range of parameters and the terms (5.6) scale as $\beta_{i,e}/\alpha^2$ and as $\beta_{i,e}/\alpha^{2/3}$ in the thin sheath. Thus these two scale converge to [73, 110].

For large negative potential the electron current density is zero whereas the ion current density is

$$j_{isat} = 2 e n_{e\infty} D_{ig} / r_p \quad \text{and} \quad i_{isat} = 4\pi e l n_{e\infty} D_{ig} \tag{5.7}$$

which can be compared to (5.2). Here the D is a binary diffusion coefficient and can be related with the mobility through the Einstein relationship provided ion-gas collision is the dominant mechanism (thus, the saturation current is not affected by ionization).

When V_p is less negative a transition to a linear *V-I* portion occurs and in this region

$$\frac{dj_e}{dV_p} = \frac{\sigma}{r_p}\left(1+\beta_e\right) / \left[\ln \alpha^{2/3} + \left(\beta_i + \beta_e\right)\right] \tag{5.8}$$

which can be compared with (5.5) and where

$$\sigma = \frac{n_{e\infty} e^2 D_{eg}}{\left(1+\beta_e\right) kT} \tag{5.9}$$

is the conductivity (*cf* (5.4))

It appears that the major influence of non-weak ionization (up to 10% in fact) is limited to the linear region of the *V-I* curve while the saturation currents should not be affected. As such, in common with the continuum, it shows lack of saturation when the limit $\alpha=r_p/\lambda_D >>1$ is not verified [110].

5.3.1.3. Continuum plus Free Fall theory

1. Here $\lambda << r_p$ and $\lambda/\lambda_D >> 1$ therefore, $\lambda_D << \lambda << r_p$.
Chang and Bienkowksi [125] assume

$$\lambda/\delta_s >> 1 \text{ but } \frac{\lambda}{\delta_s}\left(\frac{\lambda_D}{R_p}\right)^{2/3} << 1 .$$

These imply some assumptions about the sheath extension. The inequality $\lambda_D << \lambda << r_p$ is consistent with Wasserstrom, Su and Probstein treatment ("dense case") [126], whereas Swift considers this case as "Special" [65] and presents the approximated treatment of Waymouth [127] and Little and Waymouth [128] whose results are substantially identical with those of [126]. These authors match the ambipolar flux at the sheath edge to the free-fall flux crossing the sheath region, unlike Cohen [110] who considers diffusion of ions and electrons up to the probe surface. The assumptions for a continuum plus free-fall theory to hold are:

Electrons and ions have a Maxwell distribution, with temperatures independent of the position and unchanged by the probe;
The probe radius is small with respect to the plasma container, but greater than both the mean free paths and much greater than the sheath thickness (or alternatively the sheath thickness is smaller than the mean free paths);
The ion mobility is small with respect to electron mobility and ions may be considered at rest.

The particle number density is sought in the different regions:

A. Sheath edge
Under the assumptions

- of thin sheath, $r_s \cong r_p$, ($\delta_s << r_p$ for a sheath thickness δ_s measured from the probe surface, while sheath and probe radii, r_s and r_p, are measured from the centre);
- $n_e = n_i$ at the edge;
- $n_{is} = n_{es} = n_s$, (the subscript '*s*' stands for sheath edge)

The carrier concentration at a radius *r* in the quasi neutral region is found assuming $\lambda_i << r_p$:

$$n_{edge} = \frac{2}{3}\frac{n_\infty \lambda_e}{r_p}\frac{\left(1+T_i/T_e\right)}{\varepsilon_e + \frac{\lambda_e T_i}{\lambda_i T_e}\varepsilon_i} \qquad (5.10)$$

where

$$\varepsilon_e = \left(\frac{r_p}{\delta_s}\right)^2 \exp\left(\frac{V_s}{V_e}\right), \quad \varepsilon_i = 1, \quad V_s < 0 \tag{5.11}$$

$$\varepsilon_e = 1, \quad \varepsilon_i = \left(\frac{r_p}{r_s}\right)^2 \exp\left(-\frac{V_s}{V_i}\right), \quad V_s > 0 \tag{5.12}$$

and V_s is the potential drop at the sheath edge.

The carrier concentration at the sheath edge is evaluated for both the "cold" ($T_i << T_e$) and the "thermal" conditions considering the sheath voltage to be positive or negative and taking into account two different electron mean free paths (see Table 5.3).

Particle density at sheath edge n_{edge} (m^{-3})				
Plasma	**Cold ($T_i << T_e$)**		**Thermal ($T_i \cong T_e$)**	
m.f.p. λ_e (m)	$3\cdot10^{-7}$	10^{-6}	$3\cdot10^{-7}$	10^{-6}
$V_s > 0$	$2\cdot10^{19}$	$7\cdot10^{19}$	$4\cdot10^{19}/[1+2.5\cdot10^{-2}e^{-V_s/V_i}]$	$1.4\cdot10^{20}/[1+8\cdot10^{-2}e^{-V_s/V_i}]$
$V_s < 0$	$2\cdot10^{19}e^{V_s/V_e}$	$7\cdot10^{19}e^{-V_s/V_e}$	$2\cdot10^{19}/[e^{V_s/V_e}+2.5\cdot10^{-2}]$	$7\cdot10^{19}/[e^{V_s/V_e}+8\cdot10^{-2}]$

Table 5.3 CFF: Particle density at the sheath edge for the cold and thermal plasma models and different electron mean free paths (m.f.p.) and sheath voltages

In this limit ($\lambda_i << r_p$) these values depend on the ratio between the probe potential $V_{e,i}$ and the sheath voltage drop V_{sh} in the two saturation regions. A value of the sheath potential is thus needed. However, assuming a strong ion attracting probe potential (ion saturation region of the *V-I* curve) and a thermal plasma (because equation (5.8) shows that in the cold plasma case, n_{edge} diverges), one has $\varepsilon_e \to 0$, $\varepsilon_i \to 1$, $n_{edge} \approx 1.6\cdot10^{21}$ m^{-3}. In the opposite case of strong electron attracting probe (electron saturation region) one obtains $\varepsilon_i \to 0$, $\varepsilon_e \to 1$, $n_{edge} \approx 4\cdot10^{19}$ to $1.3\cdot10^{20}$ m^{-3} within a multiplicative factor 2 that depends on the "cold" or "thermal" plasma assumption.

B. Saturation currents

Under the conditions $\lambda << r_p$ and $\lambda_D/\lambda << 1$ the saturation currents both for ions and electrons under strongly accelerating potentials can be found.

1. For the positive ion attracting probe, ($V_p << 0$), $\varepsilon_e = 0$ and $\varepsilon_i = 1$ and the carrier concentration at the sheath edge is

$$n_s = \frac{n_\infty}{r_p}\frac{2\lambda_i}{3}\frac{T_e}{T_i}\left(1+T_i/T_e\right) \tag{5.13}$$

$$I_{i\,sat} = 4\pi r_p n_\infty \mu_i k T_e\left(1+\frac{T_i}{T_e}\right) \tag{5.14}$$

For the strongly electron attracting probe (V_p>>0),

$$n_s = n_\infty \frac{2}{3}\frac{\lambda_e}{r_p}\left(1+T_i/T_e\right) \tag{5.15}$$

$$I_{e\,sat} = -4\pi r_p n_\infty \mu_e k T_e\left(1+T_i/T_e\right) \tag{5.16}$$

Formula 5.13 can be estimated in the thermal case to give

$$n_s = \frac{n_\infty}{r_p}\frac{4\lambda_i}{3} \sim 10^{21}\ m^{-3} \text{ for } \lambda \sim 10^{-6}\ m \text{ and } n \sim 10^{23}\ m^{-3}$$

C. Quasi neutral region

The probe potential is made of the contributions of the sheath and of the quasi-neutral region:

$$V_p = V_s + V_{qn} \tag{5.17}$$

The first determines the flux of carriers crossing the sheath and, if V_{qn} denotes the drop across the quasi neutral region $V_s = V_p - V_{qn}$ relating V_{qn} to V_s, V_s to V_p then the theoretical probe *VI* characteristic can be plotted.

It is found that when r_p / λ_D >>1, the probe induced disturbance to the plasma can be confined to a region adjacent the probe whose thickness is of the order of

$$\delta_s = r_p\left(\frac{T_i}{T_e}\right)^{1/3} \Bigg/ \left[\left(\frac{r_p}{\lambda_D}\right)\left(1+\frac{T_i}{T_e}\right)^{2/3}\right]^{2/3} \tag{5.18}$$

so that a “continuum assumption” is valid when

$$r_p\left(\frac{T_i}{T_e}\right)^{1/3}\Bigg/\left[\left(\frac{r_p}{\lambda_D}\right)\left(1+\frac{T_i}{T_e}\right)^{2/3}\right]^{2/3} >> \lambda \qquad (5.19)$$

or

$$\frac{r_p}{\lambda}\left(\frac{\lambda_{D_i}}{r_p}\right)^{-2/3}\left(\frac{T_i}{T_e}\right)^{1/3}\left(1+\frac{T_i}{T_e}\right)^{-4/9} >> 1 \qquad (5.20)$$

Where

$$\lambda_{D_i} = \sqrt{\frac{kT_i}{4\pi n_o e^2 Z_i}} \qquad (5.21)$$

is the ion Debye length and Z_i is the charge of the ion (assumed "+1" in (5.21)). It turns out that provided the characteristic mean free path of the charged particles is small with respect to the characteristic length of the problem, the continuum assumptions reported above apply (weak ionization and plasma at rest):

- The plasma is only slightly ionized so that the predominant collision mechanism is between charged and neutral particles; this also implies that the diffusion coefficients D_i and D_e do not depend on the local ionization levels. The plasma is considered as quiescent because the neutral particles are not influenced by the presence of the probe.

- The appropriate characteristic length of the problem is taken as the distance from the probe surface towards the point where the quasi-neutral region increases in importance.

The following results are then deduced: for highly negative potential, the disturbance (current) induced by/flowing to the probe is proportional to the square root of the potential; for intermediate and 'near-plasma' potential, I is a function of $(\lambda_i/ r_p)^{1/3}$ (in the latter case with a corrective factor accounting for the ion to electron temperature ratio).

2. A more recent treatment of 'high pressure regime' dealt with by Schott [86], fits into the CFF classification because of the conditions $r_p >> \lambda_{i,e}$ and $\lambda_D << \lambda_{i,e}$ and, provided the electric field can be considered weak over a mean free path, $e\lambda_{i,e}\left|\nabla V\right| < kT_e/2$, no dependency of the mobility upon $\left|E\right| = \left|\nabla V\right|$ exists and the orbital motion is "destroyed" [86] so that the relevant motion equation are of the diffusive type (thus equal to (5.1) of the continuum case, *cf* also [9])

$$\Gamma_e = -D_e \nabla n_e \mp n_e \mu_e \nabla V \tag{5.22}$$

If in addition, Bohm's point of view is taken [129] that for probes operated close to plasma potential (i.e. limiting the bias voltage) the mobility term can be neglected, the preceding equations become

$$\Gamma_e = -D_e \nabla n_e \tag{5.23}$$

and using the continuity equation with the requirement of negligible volume recombination

$$\nabla \cdot \Gamma_e = n_e \beta$$

and negligible carrier production (β is the ionization rate), and Poisson's equation

$$\Delta V = \nabla \cdot (\nabla V) = -4\pi e(n_i - n_e)$$

Laplace equation would result, under the hypotheses of constant diffusion coefficient

$$\Delta V = 0, \quad n_e \approx n_i \tag{5.24}$$

which has non trivial solutions only for *finite length* probes. Similarly to Bohm, by making use of a formal analogy, after some manipulations, Schott [86] arrives at

$$\int_A \frac{\Gamma_e}{D_e} \cdot \mathrm{d}\mathbf{A} = i_e / eD_e = -\int_A \nabla n \cdot \mathrm{d}\mathbf{A} = -4\pi C(n_o - n_A) \tag{5.25}$$

where the lower integration limit has to be chosen one mean free path away from probe surface A placed at $(r_p+\lambda_i)$ because the diffusion model holds "sufficiently far" from the probe. The current to this surface is then

$$i_e = -4\pi C_{r_p+\lambda} eD_e (n_o - n_{r_p+\lambda}) \tag{5.26}$$

But the current to the probe surface is the random current

$$i_e = -\frac{1}{4} n_{r_p+\lambda} e \langle v_e \rangle \alpha A \tag{5.27}$$

where α is a factor accounting for possible reflections (α=1 for perfectly adsorbing probe). Therefore, eliminating $n_{r_p+\lambda}$, the general formula is obtained

$$i_e = -\frac{1}{4} n_o e \langle v_e \rangle \alpha A \left(1 + \frac{\langle v_e \rangle \alpha A}{16\pi C_{r_p+\lambda} D_e} \right)^{-1} \tag{5.28}$$

Which can be specialized to cylindrical geometry, $A = 2\pi\left(r_p + \lambda\right)l$, perfect adsorbing probe (α=1). Using the classical diffusion coefficient D_e= (λ<v_e>)/3 and the fact that in cgs units $C_{r_p+\lambda} = r_p + \lambda$, the result is

$$i_e = \frac{n_o e r_p \pi (r_p + \lambda)\langle v_e \rangle}{2}\left(1 + \frac{3l}{8\lambda}\right)^{-1} \tag{5.29}$$

which for the "very high pressure" case r_p>>λ reduces to

$$i_e = -\frac{\pi n_o e r_p \langle v_e \rangle l}{2}\left(\frac{8\lambda}{8\lambda+3l}\right) \tag{5.30}$$

finally, observing that

$$i_{cgs} \rightarrow (i/\sqrt{4\pi\varepsilon_o})_{SI}$$

$$i_e = -\sqrt{4\pi\varepsilon_o}\,\frac{\pi n_o e r_p \langle v_e \rangle l}{2}\left(\frac{8\lambda}{8\lambda+3l}\right)$$

or, because in present conditions l>>λ,

$$i_e = -\left(4\pi\right)^{3/2}\sqrt{\varepsilon_o}\,\frac{n_o e r_p \langle v_e \rangle \lambda}{3} \tag{5.31}$$

Also (5.31) requires the knowledge of both the mean free path and of the thermal electron velocity <v_e>, which can be estimated both once the electron temperature is known. This can be avoided using the approach of Gick *et al* [62] (see section 5.3) remembering though that (5.31) refers to conditions close to plasma potential.
It should be emphasized that in Bohm's [129] treatment, which pertains to ions, the random model, arising from elementary kinetic theory, which provides a relationship for ions equivalent to (5.27), is substantially equivalent to the purely diffusive model, provided the ratio of the mean free path to the probe radius is <<1, which is the circumstance of this work. Therefore, in the following it is immaterial whether to name a current as 'diffusive' or 'random' because under the present circumstances, the two yield the same flux of particles.

Evaluation of the criteria
The parameters mentioned above are shown in figure 5.1 and 5.2 for the atmospheric arc. The first is the ratio $\alpha=\lambda_D / r_p \approx 10^{-4}$ to 10^{-3} <<1 (figure 5.1). It is seen that its value is well below 0.01 (right axis) consistent with the condition α<<1 for both the Continuum and the Continuum plus Free-Fall theories to apply.

However, $\beta = \lambda_D/\lambda_{i,e}$ is $\beta_e \approx 2\cdot10^{-3}$ to 10^{-2} for electrons, but $\beta_i \approx 1$ down to $2\cdot10^{-2}$ for ions, thus β is almost less than 1 (*cf* figure 5.2). These last values are appropriate for the "General Theories" in the limit of Free-fall case and thus set the system outside the domain of the purely continuum theories.

For the other condition that Swift [65] sets for the validity of the CFF theory, namely $\delta_s << \lambda_i$, it is seen from figure 4.4 (Chapter 4) that $\delta_s \approx \lambda_i$ for a sheath thickness evaluated following the collisional cases of Sheridan [97] although $\delta_s << \lambda_i$ for the collisionless Child-Langmuir case: in effect, a theory built to account for collisions [97] cannot be valid for collisionless cases. In addition, the theory requires δ_s as a prerequisite rather than giving it as a result.

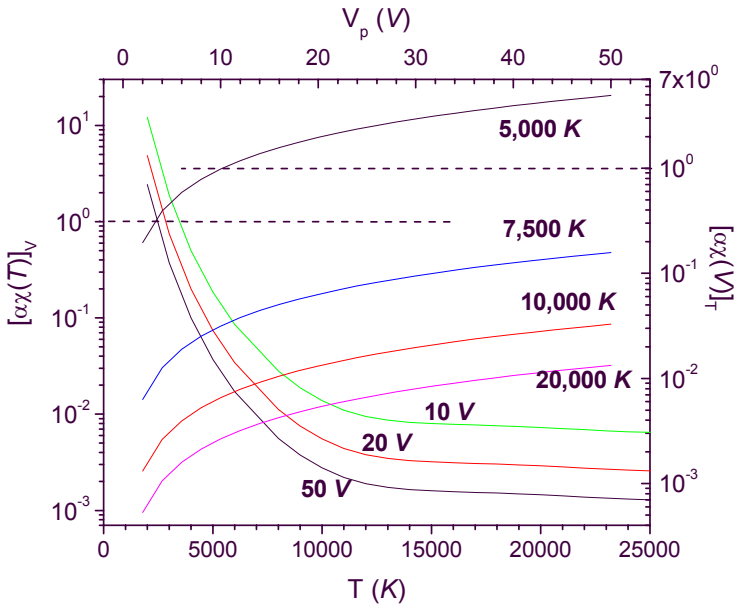

Figure 5.6. $\alpha\chi$ as function of temperature for some selected probe potentials (Left-bottom axes) and as function of probe potential for some selected temperatures (Right top axes) Probe radius 100 μm. Both "1" limits are shown (see text).

A way to qualitatively check the sheath thickness is to test whether the non dimensional parameter [73]

$$\alpha\chi \equiv \frac{\lambda_D}{r_p}\frac{eV}{kT}$$

significantly exceeds one. In this case it would be appropriate to talk about "thick" sheath. It is in fact believed that the effect of the field is to expand the sheath thickness

as the potential increases. This circumstance however is almost never achieved by the system under study as can be seen from figure 5.6. Here a family of $\alpha\chi$ curves as a function of temperature for different probe voltages is shown on the left-bottom axes. The same parameter is also shown on the top-right axis as a function of probe voltage for some selected temperatures. The probe radius is fixed at 100 μm. It should be noted that the left axis family was computed taking into account the Debye length variation with temperature, based on the $n(T)$ dependency as given by Olsen [39] and shown in Chapter 2. This applies also to the right axis family (in particular taking Olsen's values for the selected temperatures). The probe voltage range has been chosen considering the limited values achievable in arc plasmas. In all cases, except for the 'low' 5,000 *K* case (arc fringes), values of $\alpha\chi$ well below 0.1 were found. Following to the mentioned criterion, a thin sheath is thought to develop.

According to the CFF theory the sheath thickness can be evaluated by means of formula (5.14), for a 'thermal' plasma ($T_i \approx T_e$), the result is shown in figure 5.7 (right axis), where also its ratio to the ion and electron mean free paths is shown (left axis). A horizontal line at value one for these ratios is shown, and the two borderlines indicating 'low' or 'high' ionization are also displayed at T=7,500 and 12,500 *K* respectively (see Chapter 2). The sheath thickness appears always less than the mean free paths except in the colder and less ionized regions. Correspondingly, condition (5.16) is fulfilled marginally for ions. Therefore, the assumption of a purely continuum regime fails.

Summarizing the above considerations it is apparent that:

- The condition $\alpha \equiv \lambda_D / r_p << 1$ is fulfilled, setting the system in the realm of 'high' pressure regimes in contrast with the 'low' pressure regime defined by the opposite condition. Therefore a "continuum" treatment might appear to be appropriate. However:

- Condition (5.16) on the sheath thickness is not fulfilled for the continuum model to apply;

- The condition on β for the 'pure' continuum theory to apply, namely $\beta_{i,e} >> 1$ is not respected as $\beta_i << 1$ for ions, and $\beta_e \leq 1$ (only) for electrons.

- The CFF regime is thus more appropriate (with the proviso for electrons).

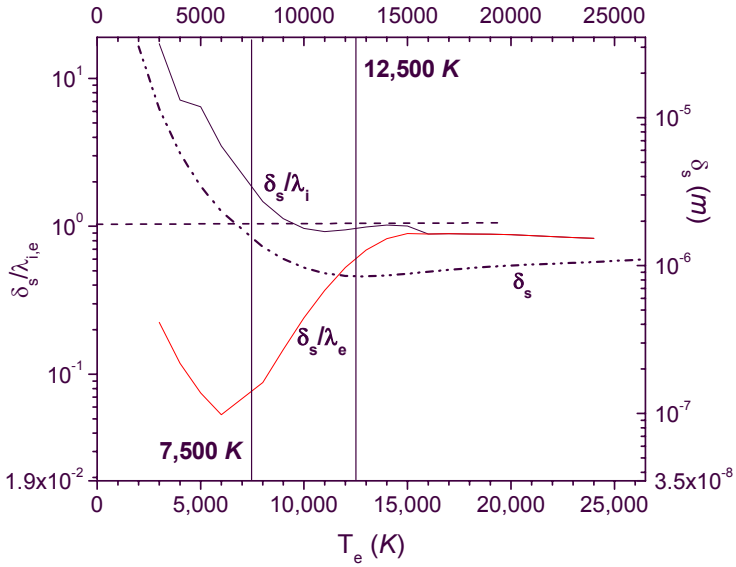

Figure 5.7 Ratio of the sheath thickness (left axis) to the ion and electron mean free paths. Right axis: sheath thickness.

Also, from the reconsideration of the condition $\delta_s << \lambda_i$ pertaining to the Child-Langmuir collisionless case, $\delta_s \leq \lambda_i$ (Sheridan collisional case [97], see Chapter 4) and it is expected that 'some' ion collisions could take place within the sheath.

Furthermore, the consideration of the combination $\alpha\chi$ leads to a 'thin' sheath, in agreement with the evaluation of equation (5.15) where the sheath thickness (10^{-6} to 10^{-7} *m*) remains well below the probe radii considered in this work (10^{-4} *m*). Also Sheridan's sheath thickness [97, 130], visible in figure 4.4, is at least one order of magnitude less than the probe radius. Therefore a CFF model can be assumed for a 'thin' sheath, mostly collisionless (perhaps with some ionic collisions) due to the "$2^{-1/3}(r_p/\lambda_i)^{1/3}(\lambda_D/\lambda_i)^{2/3}$ criterion".

In the following sections, other discriminating criteria will be considered, which include plasma motion.

Although it was stated that only the CFF appears relevant for the case under study, a comparison is made with continuum theory as the values of the current obtained in the two cases are equal within a factor of ≈3 (see below), which is reasonable, considering the limited accuracy attainable in the measurements.

The formulae reported by Swift [65] are given for positive strongly ion attracting probe, (ε_e=0 and ε_i=1, see section 5.2.1)

$$I_{i,\,sat} = 4\,\pi\, r_p n_\infty \mu_i k T_e \left(1 + T_i / T_e\right) \qquad V_p << 0 \qquad (5.32)$$

and for the strongly electron attracting probe

$$I_{\text{e sat}} = -4\,\pi\, r_{\text{p}} n_{\infty} \mu_{\text{e}} k T_e \left(1 + T_{\text{i}} / T_{\text{e}}\right) \qquad V_{\text{p}} >> 0 \qquad (5.33)$$

Numerically:

$$I_{\text{i,sat}} = 2.081 \cdot 10^{-31}\; n_{\infty} \left(T_{\text{e}} + T_{\text{i}}\right) \qquad V_{\text{p}} << 0 \qquad (5.28a)$$

$$I_{\text{e,sat}} = 7.489 \cdot 10^{-28}\; n_{\infty} \left(T_{\text{e}} + T_{\text{i}}\right) \qquad V_{\text{p}} >> 0 \qquad (5.29a)$$

These currents are plotted together with the continuum case in figure 5.8.

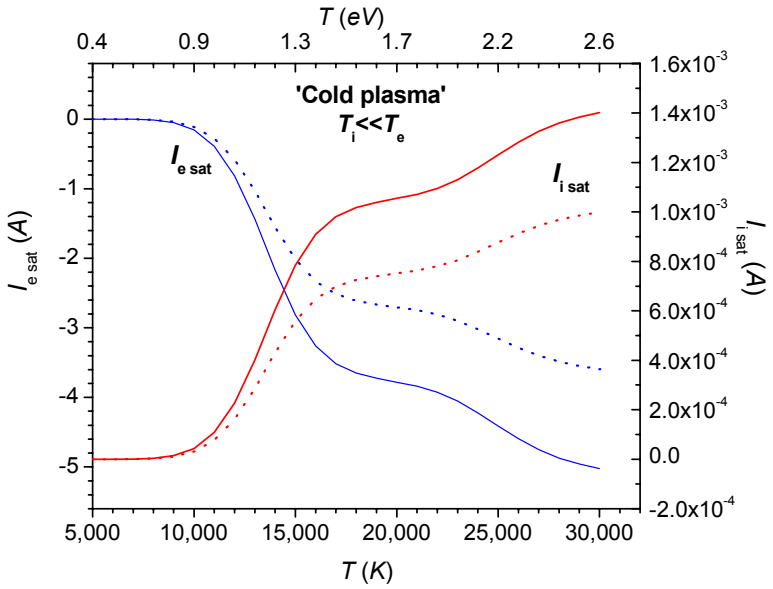

Figure 5.8. Continuum (—) and CFF (…) theory electron (left) and ion (right) saturation currents as a function of the electron temperature (cold ion approximation). The 'thermal plasma' currents are obtained by multiplying by a factor 2.

These curves were computed for temperatures up to 30,000 *K*, well above the 'moderate' ionization level (below 12,000 *K,* see Chapter 2) which is the regime for which these models were developed. A comparison of the two models is appropriate only in the intermediate region between the two, where $\lambda \approx \lambda_D$ and thus, according to figure 2.5 in Chapter 2, to temperature below 7,500 *K* for electrons (and *never* for ions). Under these circumstances the two currents are indistinguishable. A difference of 10% would arise at 12,000 *K*.

5.3.2. Classification based on Knudsen numbers

Chung, Talbot and Touryan [37, 119] “CTT” in the following) set the domains in which the probe can operate as determined by two families of parameters. The first is composed of $\alpha=\lambda_D/ r_p$ and the Knudsen number $Kn=\lambda/ r_p$, where λ_D is the Debye length, λ is the appropriate mean free path for collisions and r_p is the probe radius. The second family of parameters comprises the reduced potential $\chi_p=eV/kT$, the temperature ratio $\varepsilon=T_i/T_e$, and the two Damkohler numbers 1) $D_e = k_r L^2 N_{eo}^2 / D_{io}$ (the degree of thermal equilibrium in the plasma between electrons and heavy particles) and 2) D, that represent the degree of chemical equilibrium in the plasma by verifying "frozen chemistry" conditions (i.e. absence of recombination and ionization). Since the interpretation of the regimes by means of this last group is less straightforward, its use will be deferred in Chapter 5.

The characterizing criteria are actually somewhat different when looking at the two most important literature sources. According to Chung, Talbot and Touryan's book [37] the Knudsen number appears as the ‘first level’ discriminating parameter. Then, in the frame of continuum models two different criteria follow; the first is based on the relative magnitude of probe radius, mean free paths and Debye length. In the paper [119], it is the electrical Reynolds number that plays a major role. The following figure 5.9 reports these two points of view.

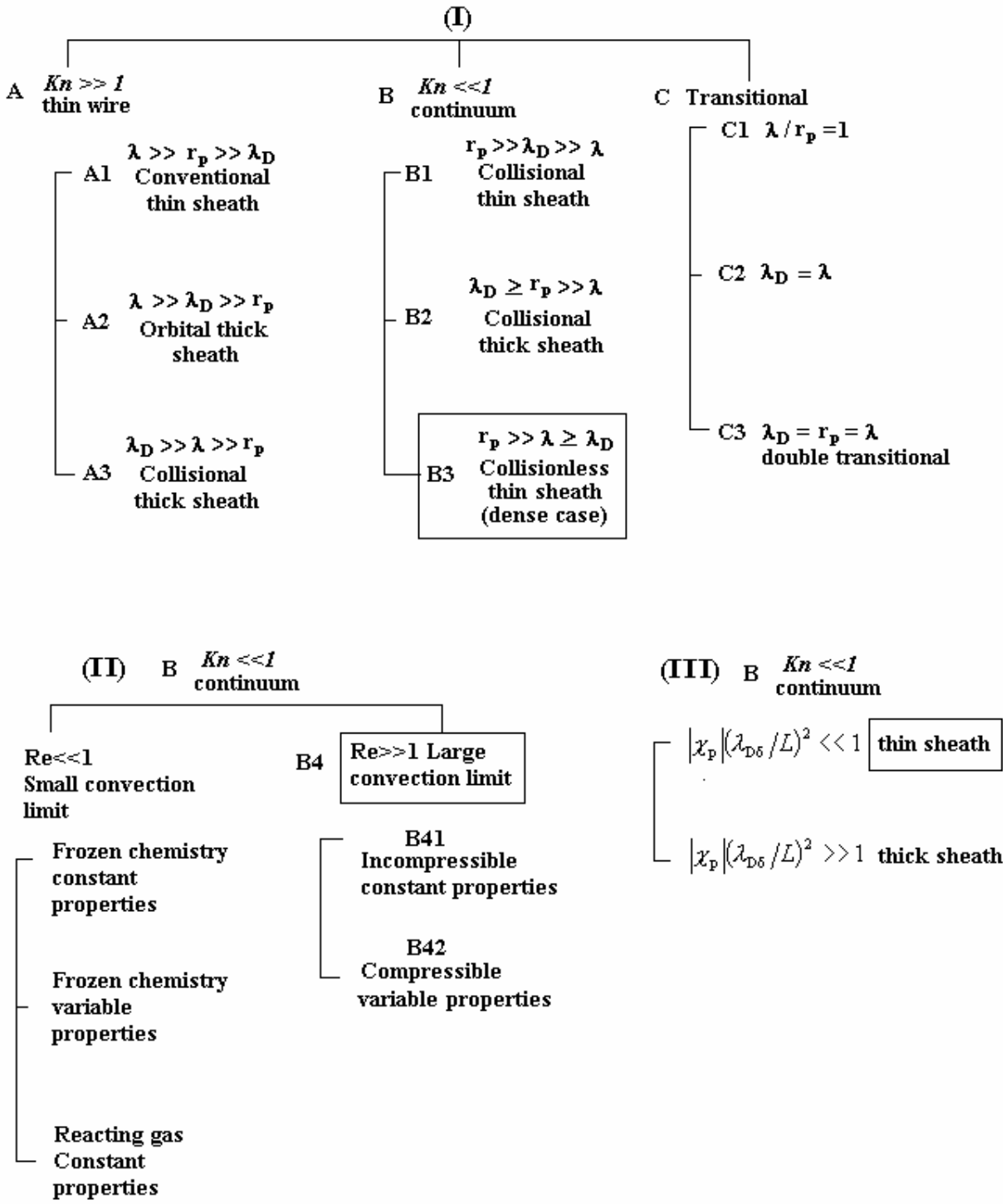

Figure 5.9. The regime classification according to Chung, Talbot and Touryan; the upper part refers to Chung *et al* [119], the lower to Chung *et al* [37]. A box surrounds the regime chosen in the present study (see text). [CTT=Chung, Talbot and Touryan]

In the following, the first group, relating to the stationary probe is analyzed first.

The first group of parameters defines six regimes of probe operation under two domains (A and B in figure 5.9, upper part) and three transitional cases (C, figure 5.9, upper part):

Domain A) Kn >>1, "Classical" thin wire Langmuir probe subdivided in the regimes:
A1) $\lambda >> r_p >> \lambda_D$, conventional thin sheath;
A2) $\lambda >> \lambda_D >> r_p$, orbital limit, thick sheath;
A3) $\lambda_D >> \lambda >> r_p$, collisional thick sheath.

Domain B) Kn <<1, Continuum electric probe split in the regimes:
B1) $r_p >> \lambda_D >> \lambda$, collisional thin sheath;
B2) $\lambda_D \geq r_p >> \lambda$, collisional thick sheath;
B3) $r_p >> \lambda \geq \lambda_D$, collisionless thin sheath (dense case).

In between the preceding regimes, the following transitional regions are identified:
C1) $Kn \approx 1$,
C2 $\lambda_D \approx \lambda$,
C3) $r_p \approx \lambda \approx \lambda_D$ (double transitional case).

5.3.2.1. Domains and origin of the criteria

The nomenclature reported by the authors is briefly summarized from their work as follows. The (kinetic theory) Boltzmann equation is applied employing higher order expansions in the BBGKY hierarchy (from Bogoljubov, Born, Green, Kirkwood, Yvon, see [4]) of the Liouville equation for the particle distribution function in order to overcome the problems related to the long-range intermolecular forces occurring in partially ionized gases, in contrast to ordinary neutral gases, where the two-body (short-range) interactions suffice in most cases [29]. The set of equations is made of the Boltzmann equations and is closed by the Liouville equation [4, 131]. Ad-hoc physical assumptions are needed to solve the system that, even for the case of two equations is rather complicated; the first member of the system of k possible permutations of the N particles, is expressed as a function of the k+1 permutations on the right hand side (thus 'hierarchy'), so that some truncation rule must be found; moreover, the right hand side of the equation that represents the effects of particle interactions ('collision integrals'), is not necessarily an explicit function of the particle distribution function.

The problem is thus governed by the Boltzmann and Poisson's equations for a certain distribution function. First, the equations are normalized using appropriate characteristic quantities; the first three of which are characteristic lengths, namely (i) the length of the "flow system" L; (ii) a length that represents the range of intermolecular forces,

assumed as the square root of the collision cross section in the undisturbed plasma; (iii) the range of the electrostatic force, i.e. the "shielding" or Debye length λ_D. As long as charged-charged collisions are concerned, the latter two lengths are equal. The (molecular) velocities are normalized to the equilibrium Maxwellian factor $\sim(kT/m)^{1/2}$. The equations are then solved with boundary conditions describing probe configuration and plasma flow conditions. The importance of the different terms is determined by the Knudsen number, $Kn = \lambda/L$ and by the ratio $\alpha=\lambda_D/L$ (where L is often but not always identified with r_p, see below).

Domain A

The first parameter appears as $1/Kn$ in the collision terms of the equations, so that as $Kn \rightarrow \infty$ means $\lambda \rightarrow \infty$, there is absence of collisions and the system is found in the classical domain (A) investigated by Mott-Smith and Langmuir [71] whose results and following developments are reported among the others by [65, 86]. This condition deals with non flowing (i.e. stationary) collisionless plasma in which all the mean free paths are much larger than the probe dimensions. From the condition $Kn \rightarrow \infty$ the only characteristic length that survives is L that may be then identified with the probe radius r_p. The Boltzmann equations without collisional terms are referred to as Boltzmann-Vlasov equations.

For the second parameter, α, the case $r_p >> \lambda_D$ (regime A1) means that no charge separation can be sustained so that the sheath is necessarily thin [In the opposite case $r_p << \lambda_D$ a thick sheath may develop (regime A2)]. Here, Langmuir's Orbital Motion Theory, can be applied both to monoenergetic or to Maxwellian distributed charged particles, for which the (two body) central force problem is solved, showing that none of the charges can be prevented from reaching the probe provided that they have sufficient energy to do so (thus implying the absence of potential barriers able to reflect the particle impinging the probe). This corresponds to the limit of a thick sheath (in effect formally infinite, because $r_p / \lambda_D \rightarrow 0$). This theory is able to give upper limits for the probe current under collisionless conditions because the occurrence of potential barriers at finite r_p / λ_D ratios can only reduce the number of particles reaching the probe.

A theory due to Allen, Bernstein and Rabinowitz, known as "ABR" or "radial" [132] assumes a cold plasma, in which the condition $\varepsilon=0$, implies an inward radial path for the ions attracted to the probe. Ion velocity is shown to arise only from the probe potential. Their fundamental equation was found to be the correct basis for subsequent treatments by Laframboise [133] and Chen [134] for situations in which ion-ion collisions start to become important ("ABR-Chen"), or further, to ion finite temperature by Fernandez Palop *et al* [135].

The effect of collisions between charged and neutral particles (case A3), still for stationary plasmas, but far from the continuum limit, is discussed by Chou, Talbot and Willis [136] who obtain an analytical formulation by taking sufficient number of moments of the Boltzmann equation in order to determine the unknown parameters of a previously assumed particle distribution. The effect of the electric field in the plasma is explained by observing that the field necessary to clear all the electrons out of the space within one Debye length from the probe is $E' = en_{e\infty}\lambda_D/4\pi\varepsilon_o$ (where $n_{e\infty}$ is the electron density outside the sheath) and this is thus the maximum value of the electric field that can exist locally in the absence of surface emission or breakdown. This can be understood as follows. At a time t=0 with zero bias applied to the probe, the electron density near the probe surface is $n_{e\infty}$ (neglecting the fact that the probe will attain a floating potential V_f). At a certain time t>0 a field at the probe surface is switched on. After a relaxation time (unimportant here) the electrons will settle at a distance λ_D from the probe surface; the field necessary to do this is $E'=en_{e\infty}\lambda_D/(4\pi\varepsilon_o)$. For the parameters in Table 5.1 and 5.2 $E'\cong 1.4\cdot 10^6$ *V/m*. To clear the electrons further away, a field $E>E'$ must be applied. Note that $V'=E'\lambda_D \cong 0.1$ *V*, so even a relatively "small" potential can give rise to a noticeable field.
A field $E=V\lambda_D$ larger than E' applied to the surface will penetrate beyond λ_D clearing the electrons and causing a thickening of the sheath until the potential accommodates, because
E is constant. So when the ion-neutral Knudsen number lowers, the sheath extends further
into the plasma. The region out of the sheath where $n_i \approx n_e$, is the "ambipolar" or quasi-neutral region.

Domain B
It is by no means possible to report the whole work of the authors also because the physical picture is similar to Swift's [65] reported "continuum and continuum plus free-fall theories" considered above. A brief summary is as follows.
The domain B is obtained in the limit of small Knudsen numbers (the smaller of the two, i.e. the electron *Kn*). In the quasi-neutral region the predominance of collisions establishes the continuum, while in the sheath the regime depends on the value of $\beta^{-1}=\lambda_e/\lambda_D$: either $\lambda_e/\lambda_D << 1$ (thin B1 and thick B2 sheaths) or $\lambda_e/\lambda_D \approx 1$ (dense collisionless case B3). In the latter case the charged particle motion is described by a continuum theory in the bulk (with diffusion and mobility phenomena) while in the sheath adjacent to the probe the motion is collision-free, the sheath thickness being small with respect to the collision mean free path.

The authors [37] present a treatment allowing the determination of the ion current and the particle density at the sheath edge that is valuable for a flush-mounted probe (major axis parallel to flow) in compressible flow with 'variable chemistry' (i.e. unfrozen)

plasmas. In particular an expression for the determination of the ion density is given that is equivalent to the Bohm criterion for the sheath formation ([37], Chapter 4). Formally, this case is complicated by the occurrence of two singularities in the mentioned expression (Bohm criterion); in the first, the collision term is of the order of β, so the limit $\beta \to 0$ implies a collisionless sheath, while the other term, related to the quasi neutral region accounts for the predominance of collisions. The solutions of the equations must then be found separately for the two regions and matched thereafter.

5.3.2.2. Evaluations

Considering the values in Table 5.1 and the diagram CTT II in figure 5.9 above, it is seen that, with $Kn_{i,e} << 1$ (*cf* figure 5.2 above), and $\lambda \geq \lambda_D$ (*cf* figure 5.6 above), $r_p >> \lambda \geq \lambda_D$ and regime B3 applies.

The way the two inequalities are fulfilled by electrons suggests that some consideration could be given to the double transitional case C3 when the temperature is 'very low', i.e. probably at the arc outer edges when the electron mean free path reaches perhaps 50% of the probe radius. However, under these circumstances, the ion mean free path is still a factor of 50 or more lower.

It is then seen that the following correspondences between Swift's and present regimes hold:
The Swift continuum is here identified exactly by regime B1; the continuum plus free-fall case of Swift requires $\lambda >> \lambda_D$ while here, the closest possible CTT's regime, B3, requires only $\lambda \geq \lambda_D$. In any case it is felt that the "continuum" part of the CTT diagram (I) should be chosen.

5.3.2.3. Effects of plasma-probe relative motion

Considering the second part [CTT(II)] of the diagram in figure 5.9, the electrical Reynolds number, plotted in figure 5.4 is safely greater than one even at the relatively low velocity of 100 *m/s*, therefore convection effects are important (sub-regime B4 in figure 5.9). Considering that in the system under investigation the flow velocity is believed to stay below some hundreds of meters per second, the flow can be considered laminar and incompressible. Actually, Allum [57] measured v_f=80 *m/s* so that with a sound speed of c_s~2,700 *m/s* (*cf* Chapter 2), the Mach number is M=0.03 to 0.1 and the effects of compressibility can be neglected in most cases.

5.3.2.4. Continuum (III)

Before investigating the values of the parameters reported in the frame of the continuum (CTT (III) in figure 5.9), a clarification about some of the symbols is needed. From figure 5.9 it is seen that some combinations are given in terms of "thin" versus "thick"

sheath, “high” and “low” convection limits and of “constant” or “variable” plasma properties. Nevertheless an attempt is made here to evaluate these parameters, starting from the ‘thin/thick’ criterion, figure 5.9 part (III).

The microscopic characteristic length λ_{D_δ} is the Debye length at the edge of a hydrodynamic boundary layer of thickness δ due to the relative plasma-probe motion (Re>>1). The boundary layers thickness has been shown in Chapter 2. Its evaluation depends critically on the knowledge of the ion density within the boundary layer. Following Smy [84], as a consequence of the inequality $\lambda_{i,e} << r_p$, the ionization density in the sheath could be depleted down to $n_i' = n_i \lambda_i / r_p$. [In effect this can be discussed in a slightly different although equivalent manner (see the following section)]. To put this quantity in numbers, for the time being ignoring secondary effects of the flow (like cooling) a limiting value of $\lambda_{D\delta}$ can be obtained using

$$\lambda_{D\delta} = \sqrt{\frac{\varepsilon_o k T_i T_e}{n_i \frac{\lambda_i}{r_p}\left(T_i + T_e\right)}} \tag{5.34}$$

(*cf* formula 2.3) for ions and electrons and is shown in figure 5.10. Also shown are the values of the charged number density at the sheath edge (broken line) with respect to the bulk of the plasma. The decisive parameter that remains to be evaluated in order to choose between “thick” and “thin” sheath [figure 5.9, CTT(III)] is the normalized potential $\chi = eV/kT_e$. For the latter a ratio corresponding to a potential less or equal to 40-45 V can be set as a limit (before occurrence of breakdown at atmospheric pressure [62]. So 0.6 $V_p \leq 45$ V means that $V_p \leq 75$ V for the CTT(III) inequality to be satisfied to better than 1%, i.e. a “thin” sheath develops around the probe.

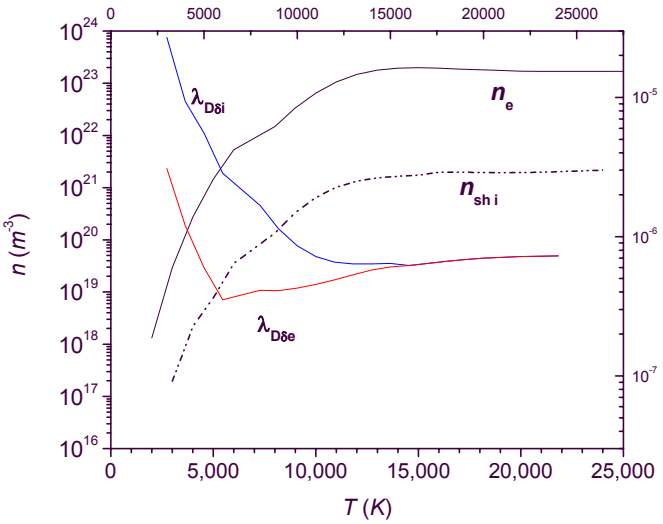

Figure 5.10 (Left axis) charged particle density for bulk (—) and edge (…) as a function of temperature according to Smy [84]. Right axis, Ion and electron Debye length in the sheath (*cf* 5.21)

In summary, the criteria of CTT for the system under study suggest a continuum i.e. fully collisional plasma in the bulk with a collisionless thin sheath (termed "dense") which is incompressible as the bulk; in this regime convection plays an important role.
For the case of sheath depletion down to a factor 10^3 with respect to the bulk (see also section 5.3.3), the double transitional regime C3 could into play, although, interestingly (and unfortunately), the authors do not extensively cover this case.
From the practical point of view, the current expressions reported by CTT, are relevant for almost planar and "flush-mounted probes", i.e. for probes whose detecting surface is parallel to the flow, whereas in the case under study here, cylindrical probes with main axis perpendicular to the flow are considered.

5.3.3. Classification based on Electrical Reynolds number

A somewhat different approach can be found in the works of Clements and Smy, who covered many aspects of probe theory and operation over the last 30 years. Mention is made in particular to the work of Smy [84] and to the papers of Clements and Smy [78, 79, 91, 111, 114], for brevity collectively referred as "CS" in the following. An outline of their criteria is reported in figure 5.11; it is not complete, but it contains the criteria that were found more "stable" in analyzing their works.

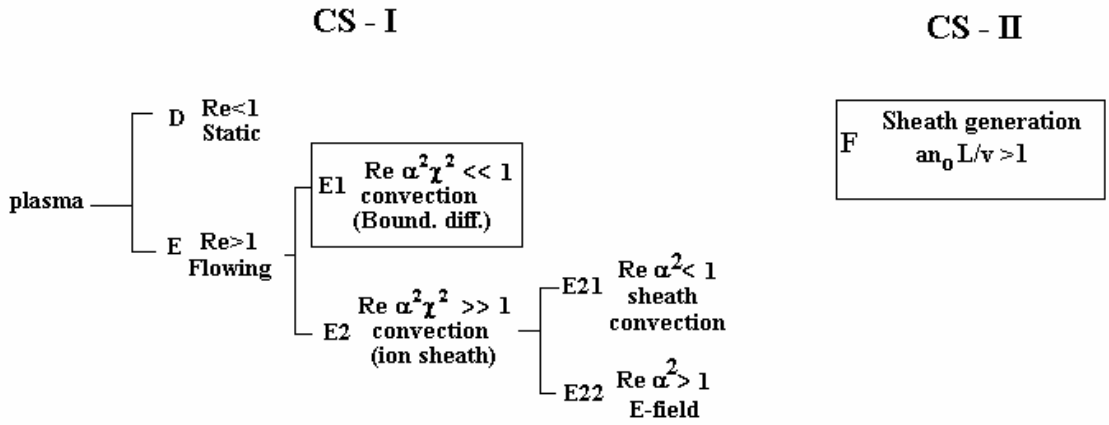

Figure 5.11. Clements and Smy's classification criteria (CS = Clements and Smy). Symbols defined in Table 5.1 and 5.2 above.

Clements and Smy [82, 114] deal with the question about the effects of plasma flow velocity. Therefore, their discriminating criteria are based in the first instance on the values assumed by the electrical Reynolds number *Re*. The other parameters are $\alpha=\lambda_D$

/*L*, where *L* is a characteristic length of the probe (again identified for our purpose with the probe radius), and the "reduced" potential $\chi = eV_p/kT_e$, where V_p is the probe bias, or by different combinations of them. The domains are:

D) *Re* <1, plasma at rest, for which reference is made to [110] and [72, 73], whose works are referred to as "conventional diffusion relations" or "Continuum theories", and

E) *Re* > 1 ion convection to the probe that they treat in detail, considering the sub-regimes:

*E*1) *Re* $\alpha^2\chi^2$ □ 1 ion convection via diffusion boundary layer, or

*E*2) *Re* $\alpha^2\chi^2$ □ 1, convection supported ion sheath, provided that the sheath is wider than the boundary diffusion layer. This takes into account the "high" plasma flow velocity in that charges are transported by convection due to the plasma flow rather than by diffusion due to charge concentration gradients. It is further subdivided into the two cases *E*21 (sheath convection), when *Re*α<1, and *E*22 (E-field) for *Re*α>1.

What is more, in a subsequent publication [78] the influence of thermal charged species generation (ionization) and recombination was considered introducing a "sheath generation regime" whose occurrence depends on the values assumed by a "recombination coefficient" *a* or by the Damkohler number D as the overall charge density is increased. This regime is labelled here as "*F*" (CS (II) in figure 5.11 above) and it will be analyzed further in Chapter 6.

5.3.3.1. Domains and origin of the criteria

The domain *D* is essentially the one described by the static theories [72, 73, 110] for the plasma at rest. This is then what Swift calls the "Continuum regime". The ion and electron equations for the current, together with Poisson's equation, all in spherical geometry, are solved for the two adjacent regions of bulk and sheath; the matching of the two solutions in the so-called transition region, for moderate negative probe potential, gave the currents in the saturation region and the particle number density in exponential form (*cf* equation (7), sec. 2.4.2), which is appropriate for a thin sheath. When the probe potential is highly negative, the sheath expands, with the consequence that the probe ion current will no longer saturate but will instead continue its increase with the sheath thickness.

Domain E, Re>1

Here, the flow effects cannot be neglected. The effects of plasma velocity are considered by Smy [84] and also by Thomas [76, 77] and Freeston and Kelk [107]. Thomas considers the transient behaviour of the probe current in a flowing plasma (v_f ≈3 *m*/*s*). The interesting argument for a moving probe is that the plasma in which the probe moves is different at different time intervals and the plasma is newly perturbed;

this implies that the ions in the 'new' region are more numerous than the ions in the 'old' (i.e. the just swept region) and progressively decay in number while collected by the probe. Of interest is the time formation of the sheath, that for its experimental conditions is of the order of the millisecond (but see Chapter 5). Moreover, in this view the relative motion seems to cause an increase in the sheath dimensions.

Lam [109] by considering the electron and ion flow equations in which convective terms arise from the flow velocity, obtains an equation made of three terms: a diffusive term, a convective one and an ion current driven by the sheath electric field; the latter is shown to be negligible when $Re\,\alpha^2\chi^2 \ll 1$ (see below). In this case, the current is governed by diffusive and convective terms. This regime is called the "diffusion convection" regime *E*1. The opposite case occurs when the diffusive term, can be neglected from his equation. There, in domain *E*2, convection and sheath effects are important; which of the two will dominate depends on the value of the product $Re\,\alpha^2$, so that ions convected to the probe are driven to the probe by the sheath electric field when $Re\,\alpha^2 <1$ (sheath-convection regime). Conversely the sheath field is able to drain only a fraction of the ions convected to the sheath, when $Re\,\alpha^2 >1$ is fulfilled (called, perhaps misleadingly, the '*E*-field' convection regime, after Sonin [75]). It can be noted that in Clements and Smy's [114] the transition cases are studied, where the inequalities leading to subregimes E1 or E2 are considered as less stringent (i.e. the strong inequalities, '<<' , are replaced by weaker ones, '<').

Origin of the criteria

1) The discrimination between stationary and flowing plasma is based upon the value of the electrical Reynolds number; this is seen by recalling that the plasma surrounding the probe may be considered stationary if the ambipolar diffusion velocity is greater than the flow velocity. In fact, since the mean free paths of ions and electrons are much less than the probe diameter, the ionization near the probe is depleted to a level $n' = n\lambda / r_p$. This case has been show already in the previous section (figure 5.10). Moreover, the ion drift velocity is $v_d \approx v_i\, \lambda / r_p$; these two relationships imply that the sheath thickness is increased by a factor $(\lambda / r_p)^{-1}$ with respect to the stationary plasma and that the relative probe-plasma velocity must be lower than $v_d \approx v_i\, \lambda / r_p$ for the plasma to be considered stationary. This means that the ion (ambipolar) diffusion velocity is of the order of the product of the ambipolar electric field, $kT_o / 2r_p e$ and the ionic mobility μ_i the condition for this diffusion velocity to dominate the flow velocity v_f is

$$v_f < \mu_i \frac{kT_o}{2r_p e} \tag{5.35}$$

that is equivalent to the condition *Re*<1 (*Re* is defined in section 5.1).

2) The $Re\alpha^2\chi^2 \ll 1$ criterion is obtained from Lam's work [109] by considering the electron and ion flow equations in which convective terms arise from the flow velocity. For an equilibrium plasma with equal ion and electron temperatures and large Reynolds numbers, the equation mentioned above is obtained that is made of three terms: a diffusive term, a convective term and an ion current driven by the sheath electric field:

$$2\frac{\partial^2 N_i}{\partial \eta^2} - \left(u\frac{\partial N_i}{\partial x} + \mathrm{v}Re^{1/2}\frac{\partial N_\mathrm{i}}{\partial \eta_\mathrm{i}} \right) = Re\alpha^2 \frac{\partial}{\partial \eta}\left(\frac{\partial \chi}{\partial \eta}\frac{\partial^2 \chi}{\partial \eta^2} + \frac{\partial^3 \chi}{\partial \eta^3} \right) \qquad (5.36)$$

This equation is written for the normalised charge concentration $N_\mathrm{i}=n_\mathrm{i}/n$, ($n_\mathrm{o}$ is the bulk plasma density) the y coordinate in the non-dimensional form $\eta=yRe^{1/2}$, $\alpha=\lambda_\mathrm{D}/\ r_\mathrm{p}$ and the normalized potential $\chi=eV/kT$. This equation originates from the flux equations that take into account convection in the ion and electron flows, through the convective velocity $\mathbf{v} = (u,\mathrm{v})$ whose component are parallel to x and y coordinates respectively. These are the boundary layer coordinates with x parallel and y normal to the probe surface. The flux equations are considered together with Poisson's equation.

The three terms to be considered in equation (5.32), from left to right are: a diffusion current (related in fact to the Laplacian of a concentration), of the order $O(\eta^{-2})$; a convective term between parenthesis (left hand side of equation 5.32) in terms of the components of **v**, of the order of 1, and the third, at the right hand side, is the ion current driven by the field. It is of the order of $Re\alpha^2\chi^2/\eta^4$. Therefore, $Re\alpha^2\chi^2 \ll 1$ implies that the last term can be ignored and explains the term 'diffusion/convection' regime. Conversely, if $Re\alpha^2\chi^2 \gg 1$, the term to be neglected in (5.32) is the first, and the current is governed by convective (second term of (5.33)) and sheath effect (right hand side).

The condition on $Re\alpha^2$ derives from the consideration of the $Re\alpha^2\chi^2$ irrespective of the bias potential (in the non-dimensional form χ) that, as seen from the previous evaluations can be the 'transition' parameter from one regime to the other. More precisely, the ions that enter the sheath reach the probe only if the field-induced velocity of an ion in the sheath is larger than the flow velocity. This is discussed by Smy [84] also in connection to plasma cooling effects (see Chapter 5). For a flat plate of length L enclosed in a sheath of thickness δ_s the ions entering the sheath will reach the probe before being swept away downstream only if $\mu_\mathrm{i}E\mathrm{v}_\mathrm{f} > \delta_\mathrm{s}/L$ [84]. If $E \approx V_\mathrm{p}/\delta_\mathrm{s}$ and $\delta_\mathrm{s} \approx L(\alpha^2\chi^2/Re)^{1/2}$, this condition is satisfied only if $Re\alpha^2 < 1$. This is the sheath convection regime (E2.1 in figure 5.11) although in the analysis by Smy and Noor [118] the limit to sheath convection regimes is expressed including χ. For $Re\alpha^2 > 1$, the field is able to attract to the probe only a fraction of the ions convected to the sheath (*E-field* convection regime, E2.2 in figure 5.11). The physical picture however is the same [84]: as the ionization decreases, α increases and the average electric field in the expanding sheath decreases until most of the ions convected to the sheath are convected out of the sheath and do not reach the probe.

5.2.3.2. Evaluations

Static versus flowing plasma

In the present case $Re \approx 40$ to 10,000, thus regime E 'flowing plasma' applies. Following Smy [84], the criterion of a small electrical Reynolds number proves to be a severe one, because with the values reported in table 2.3 and 5.1, a flow velocity of less than 1.6 *m/s* is required to consider the plasma at rest; in practice therefore, considering the reported value of 100 *m/s* or more typical for atmospheric arcs, the system considered within this work is a flowing system. This result is equivalent to the one obtained by CTT in the preceding section.

Boundary diffusion versus convection

The combination $Re\alpha^2\chi^2$ depends on flow velocity, probe radius, ion mobility, electron temperature and therefore number density, and probe voltage. In figure 5.12 the first three were held constant (v_f=100 *m/s*, r_p= 100 μm, μ_i=1.6 $m^2V^{-1}s^{-1}$ see figure 2.15). T_e (and n_e consistently) were varied keeping V_p as parameter (figure 5.12 left); or V_p was varied taking the temperature as parameter (figure 5.12 right). In both cases, all the dependencies with T (implicit or explicit) were accounted for. The horizontal line drawn at 0.01 corresponds to the strict borderline (within 1%) of the diffusion-convection regime condition. The line at 1 sets a broader limit. The picture shows that in almost all cases Regime $E1$ applies here.

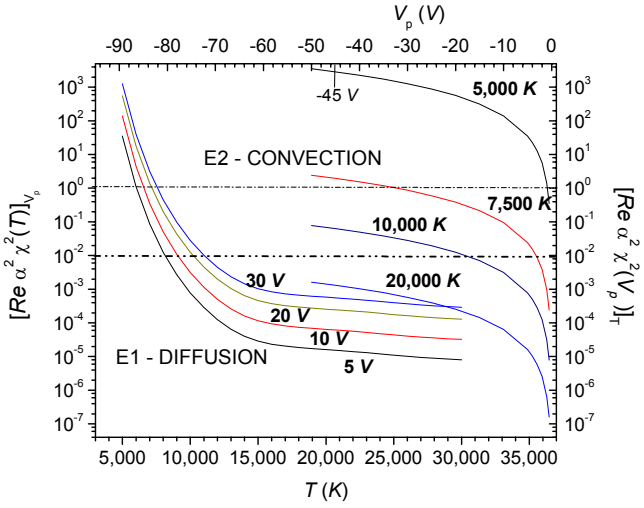

Figure 5.12. $Re\alpha^2\chi^2$ as a function of temperature (left-bottom axes) for different probe voltages; and of probe potential (right-top axes) for different electron temperatures. Plasma flow velocity v_f = 100 *m/s*, probe radius r_p =10^{-4} *m*. Horizontal line at $Re\alpha^2\chi^2$ = 0.01 (dashed) and 1 (continuous) represent $Re\alpha^2\chi^2$ <<1 (i.e. 1%) and $Re\alpha^2\chi^2$=1 (maximum limit) for the diffusion regimes to apply (see text). Also shown is the breakdown limit at –45 *V*. The two ordinates have a common scale.

More precisely, the condition $Re\alpha^2\chi^2 \ll 1$ applies strictly (1% limit):

- for electron temperature from 7,500 *K* (at 5 *V* and below) to 12,500 *K* (at 30 *V* and below), see left hand side;
- probe voltages of about 18 *V* or less and $T_e \geq 10{,}000$ *K*, see right hand side;

These limits are shifted towards convection for higher flow velocities. Also, the colder the plasma, the less effective is the action of the probe potential in keeping diffusion as the dominant mechanism. Or, stated differently, the higher the probe potential, the less diffusive the regime will be. Experimentally, some freedom appears to exist in the choice of the regime, for instance varying the probe radius. However, the latter is kept constant within a factor 2 or so, only the probe voltage and, to some extent, the plasma flow velocity can be varied. For the first, mention should be made to the case reported by Gick [62] in which in the ion saturation region a probe bias V_p of -45 *V* gives rise to gas breakdown, for conditions very close to those dealt with in the present work (atmospheric arcs). For the flow velocity, this is not a common option in TIG arcs because this would require an increase of the electric current (flow velocity scales as $v \propto I^{1/2}$ [57]) which is one of the properties of the arc inducing variations in the parameters under investigation.
When $Re\alpha^2\chi^2 > 1$, regime *E*2 applies. Therefore, it appears that with respect to probe operation, the arc manifests itself as a two-regime environment: diffusive in the hot core and convective in the outer cooler regions.

Sheath convection versus 'E-field' regime
In the latter case, the quantity

$$Re\alpha^2 = \frac{v_f r_p e}{\mu_i k T_e}\left(\frac{\lambda_D}{r_p}\right)^2 = \frac{\varepsilon_o v_f}{e\mu_i r_p n_e} \qquad (5.37)$$

has to be evaluated in order to decide whether $Re\alpha^2 \ll 1$ and *E*21 ("Sheath convection") or $Re\alpha^2 \gg 1$ and *E*22 ("E-field convection") sub-regimes apply. It turns out that even keeping the temperature (and therefore the electron density) within the lower region of figure 5.13, namely at temperatures less than or equal to 12,000 *K*, this parameter is negligibly small even at velocities close to the sound speed.

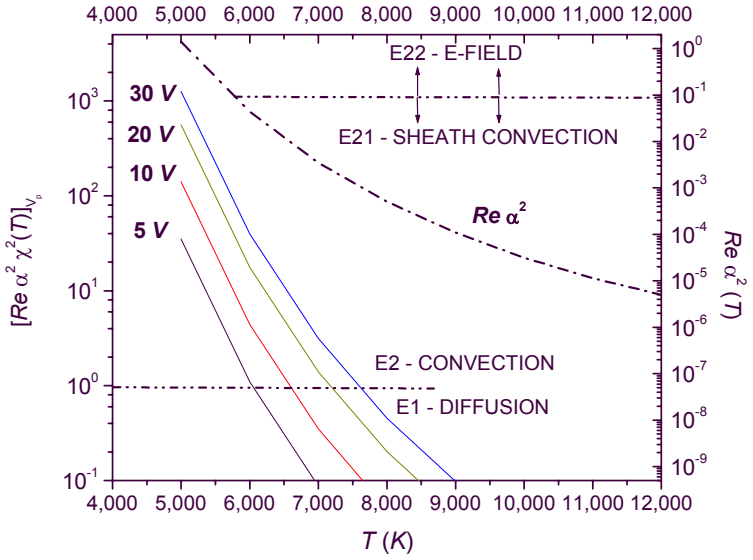

Figure 5.13. $Re\alpha^2\chi^2$ as a function of temperature (left-bottom axes) for different probe voltages in the $Re\alpha^2\chi^2$ high value region of figure 5.12; it is compared to $Re\alpha^2$ (right-top axes) for different electron temperatures.

Therefore, even if $Re\alpha^2\chi^2 >> 1$, still $Re\alpha^2 << 1$ and regime *E*21 "Sheath convection" applies down to 6,000 *K* (or 6,000 *K* for the weaker inequality). This is true even if the sheath charge density is depleted down to 10^{18} m^{-3} and if flow velocities are increased (figures 5.14 and 5.15 were obtained for v_f=100 *m/s* but clearly, they could scale only of factor of the order of unity).

Transition between Boundary diffusion and convection regimes

The results of the preceding subsections indicate that the range of parameters of interest for the arc plasma spans both diffusion and convection regimes. The transition region between the two has been investigated in [79, 116] with increasing accuracy. In [116] the effects of adiabatic compression are taken into account; when the sheath thickness increases either because of the increased probe potential or of the decreasing ionization density, the contribution to the probe current arise from both diffusion and convection of ions to the probe. The current would therefore be greater than the one given by the two mechanisms separately, but less than the sum of the two separate currents [116]. This convection-diffusion current is shown in broad agreement with measurements obtained in a MHD generator ($n_e \approx 10^{18}$ m^{-3}), systematically higher than either of the two currents. The corresponding expression will be given in the next section.

Sheath depletion

A parameter similar to $Re\alpha^2$, is $Re\alpha$, obtained considering the maximum space-charge electric field attainable as a consequence of inequality of ion and electron densities

across a Debye length distance [84]. $E \approx kT_e/e\lambda_D \approx 1.7\cdot10^8$ *V/m*. The corresponding ion maximum drift velocity is $v_d=(kT_e/e\lambda_D)\mu_i \approx 10^3$ *m/s*, where μ_i is the ion mobility. Since upstream of the probe the ion velocity is of the order of the flow velocity v_f, the continuity of ion flux implies that, at the sheath edge, the ionization is much smaller than the bulk value (*sheath depletion*) if $v_d>v_f$ or $(kT_e/e\lambda_D)\mu_i>v_f$, that is equivalent to the condition $Re\alpha<1$. If the drift velocity is high enough across a distance of the order of the Debye length, sheath depletion would take place.

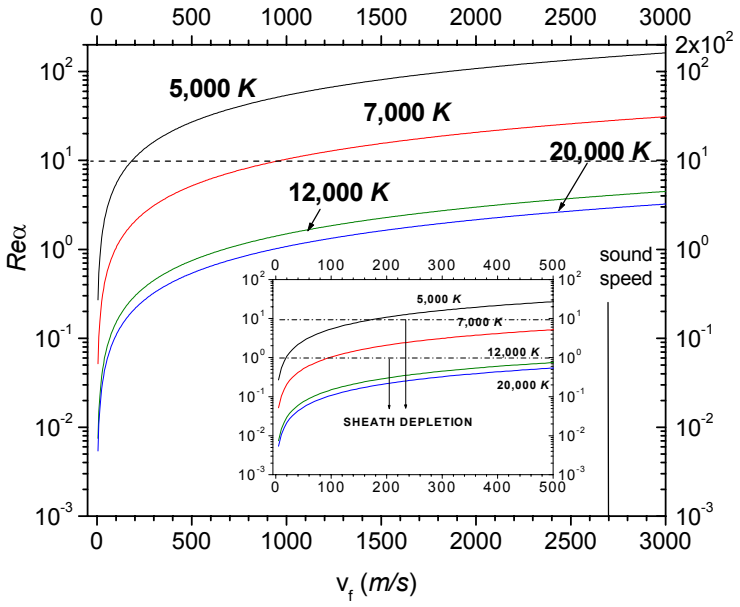

Figure 5.14. The $Re\alpha$ combination as a function of the flow velocity at different electron temperatures (Sound speed: 2700 *m/s*). Inset: the region 0 to 500 m/s. The region where depletion in the ion sheath is expected is limited from above by the horizontal line at $Re\alpha$ =1 or 0.1 (see text).

An equivalent argument based on a distance *comparable to the sheath edge* gives values of $Re\alpha$ about 10 times higher (see Chapter 4). The situation is depicted in figure 5.14 where a mobility $1.6\cdot10^{-4}$ $m^2/(Vs)$ has been taken (and the high electric field reported by Smy [84] has been corrected for the lack a of factor 4π (*cf* section 5.3.2.1, Domain *A*). The values at the different temperatures have been computed with the relevant (n_e, T_e) from Olsen (see Chapter 2). It appears that the effect of depletion become less important at higher flow velocity or, for higher flow velocity, it is progressively less probable that the ion drift velocity can reach and overcome the average flow velocity v_f. For the "Debye length formulation" all the curves lay below the limit imposed by criterion $Re\alpha<1$ and the sheath is depleted in all cases. For the "sheath thickness formulation", one may shift the horizontal limit down by a factor 10. In this case, for temperatures above 7,000 *K*, and typical flow of 100 *m/s*, the sheath is depleted whereas, for lower

temperatures, the depletion would be much smaller or negligible (at 5,000 *K*). In this second case, with regard to sheath depletion, the arc appears as a multi-regime object. In general however, both the results of this paragraph appear in contradiction with respect to the previous sections where a *diffusive* regime was found applicable. This circumstance requires some clarification. A high drift velocity could be thought to cause sheath depletion *only* for sheath larger than the fluid boundary layer. In this case the strong electric field (supposing weak shielding due to the neutrality of the surrounding particles) would rapidly attract the ions towards the negatively biased probe and repel electrons, thus 'depleting' the sheath of ions and electrons with respect to the 'undisturbed fluid' boundary layer.
This question is re-addressed in the next section.

Summary
Summarizing the results of the criteria reported in this section, the following conclusions can be drawn. From the experimental point of view, apart from the probe bias voltage, the occurrence of a mixed regime for the system under study in this work, is due to the sweeping of the probe through a plasma that is of variable temperature and density. It can be concluded that at fixed (low) plasma flow velocity (say a few hundreds *m/s*) and for bias low enough (well below breakdown) the system is in a diffusion-convection regime in the central region of the arc plasma. Electrical field driven effects of the sheath should appear a) at higher voltages and b) plasma velocities c) in the periphery of the arc column where both temperature and charge densities are lower (less dense plasma). But as the outer regions are characterized by lower velocity, it appears that the electrical field driven effects can be neglected.

5.3.4. Hydrodynamic models

According to Benilov [123] a hydrodynamic treatment of the problem is possible under absence of thermal and pressure diffusion and of flow velocity limited to weak ionization (e.g. absence of electrohydrodynamic effects). For ions, the condition for a hydrodynamic treatment to be valid is $\lambda_i < r_p$ (e.g. a small Knudsen number). In case of weak electric field the ion mobility and therefore the ion flux μn depends only on temperature. In case of high electric field, $eE\lambda \geq kT$, the diffusion flow is $\sim\lambda_i/r_p$ of the drift flux and therefore negligible; this explains why the Einstein relationship $\mu_i = eD/kT$ is valid even in strong fields. However, $\mu_i n = f(T, E/n)$.

For electrons at least one of the two conditions has to be satisfied

$$\lambda_u = \lambda_e / \sqrt{\kappa} \qquad (5.38)$$

where $\kappa = 2m_e / m_i$ is the elastic energy transfer coefficient. For the regimes considered in this work (see also Chapter 2) $\lambda_u \sim 5\cdot10^{-5}$ to 10^{-6} $m << r_p = 1.25\cdot10^{-4}$ m. In this case the

dominant term in the electron distribution function will depend on *T*, *E/n* and the coordinate. In case of weak field it will depend on *T* only.
The other condition is

$$\lambda_e \left(\nu_{ei}/\nu_{ee}\right)^{1/2} \ll r_p \qquad (5.39)$$

in which case the first term of the electron distribution function is a function of the electron temperature only, and $p_e = nkT_e$.
Under the assumptions of perfectly absorbing probe with zero potential at infinity and zero density at the surface (boundary conditions justifiable on the basis of estimations of the various boundaries, see below), the solution of the hydrodynamic equations are sought in form of asymptotic expansions in the following cases:
1. Large Reynolds number, small Mach number with $\lambda_D \ll \Delta \le d$ where $\Delta = r_p/\sqrt{\mathrm{Re}}$ is the scale thickness of the gas dynamic boundary layer and *d* is the scale of reaction length (e.g. recombination);
2. Probe and plasma at rest with $\lambda_D \ll d \ll r_p$, that, by taking *d* as the mean free path, coincides with the Continuum plus Free-Fall regime.

Limiting attention to the first case (the second was considered in section 5.3.1.2), the following regions are identified starting from the bulk of the plasma:

- the fluid Non Viscous region (NV) where charged concentrations are equal and equal to their value at infinite distance from the probe. The electric field is $E \sim kT/e\Delta$ and drift dominates diffusion;
- a quasi-neutral Gas Boundary layer (GB) where the particles equality is only approximate, whose scale is Δ. Also here $E \sim kT/e\Delta$ but drift and diffusion are of comparable magnitude;
- a Debye Layer (DL) whose scale y_D is discussed below.

For all the three scales, diffusion is possible and its magnitude $J_{i,e} \ll D_{i,e} n_{i,e}/\Delta$ is determined by the scale of the gas boundary layer.
The DL can be uniform with diffusion equalizing drift $\sim D_{i,e} n_{i,e,\infty}/\Delta$ and the estimates $n_{i,e} \ll n_{i,e,\infty} y_D/\Delta$ and $E \ll kT/ey_D$, inserted in Poisson's equation allow the evaluation of the thickness $y_D \ll \left(\lambda_D^2 \Delta\right)^{1/3} << \Delta$.
Two situations may arise:

- $y_D \ll \left(\lambda_D^2 \Delta\right)^{1/3}$ but $y_D \ge \Delta$; the layer is non uniform and one recovers Su and Lam's structured sheath including 1) a transitional region that incorporates the major part of the GB and where almost all particles are attracted to the probe with motion driven by drift; and 2) a diffusion drop region of scale $<<y_D$ where diffusion and drift are comparable.

- $y_D << \Delta$ and a thin DL ('thin sheath' in the terminology used so far). In absence of particle generation (ionization) the current to the probe is determined by the fluxes from the GB to the outer part of the DL (the potential of the probe affects the GB region) and is bounded between $I_i \approx eD_i n_{e\infty} r_p^2 / \Delta$ and $I_e \approx eD_e n_{e\infty} r_p^2 / \Delta$.

The Plasma potential (written here as the difference between the probe floating potential and the plasma potential, e.g. with respect to the anode as reference electrode) can be expressed by

$$V_f - V_{pl} \approx \frac{kT_p}{e} \ln\left[\left(\frac{\lambda_D}{\Delta}\right)^{2/3} \beta\right] = \frac{kT_p}{e} \ln\left[\left(\sqrt{\frac{\lambda_D}{r_p / \mathrm{Re}}}\right)^{2/3} \frac{D_i}{D_e}\right] \quad (5.40)$$

which requires prior knowledge of the probe temperature, flow velocity and of the diffusion coefficients.

The analysis of the *V-I* curve is performed according to three guidelines:
1. $I_i < I < I_e$ the DL is uniform and the non viscous region dominates the fluxes; the *V-I* is linear;

2. $I>I_e$, y~Δ, the NV and the DL contribute to the probe-plasma potential difference with

$$\frac{kT_e}{e}\frac{r_p}{\Delta} \quad \text{and} \quad \frac{kT_e}{e}\frac{\Delta}{\lambda_D}$$

and their ratio is

$$\frac{r_p \lambda_D}{\Delta^2} \; \square \; \frac{\mathrm{Re}\,\lambda_D}{r_p}$$

2a. If $\frac{r_p \lambda_D}{\Delta^2} >> 1$

then the DL dominates and

$$\frac{dI}{dV_p} \approx \sigma_{¥} r_p \frac{\lambda_D}{\Delta^2} << \left.\frac{dI}{dV_p}\right|_{I_i<I<I_e} = \sigma_\infty$$

the *V-I* saturates at $I=I_e$

2b. $\frac{r_p \lambda_D}{\Delta^2} \; \square \; 1$ implies the two region contributions are comparable and no clear electron saturation occurs.

3. $I<I_i$, y~Δ, and the ratio of the NV and DL contributions, $\beta\frac{kT_e}{e}\frac{r_p}{\Delta}$, where $\beta=\frac{D_i}{D_e}$, $\frac{kT_e}{e}\frac{\Delta}{\lambda_D}\beta\frac{r_p\lambda_D}{\Delta}$, determines whether the ion current saturates (ratio ≈1) or increases linearly (ratio >>1).

However, the two saturation approaches (1. and 3.) are not applicable when

$$\frac{r_p\lambda_D}{\Delta^2}\not\ll 1 \quad \text{and} \quad \beta\frac{r_p\lambda_D}{\Delta^2}\not\ll 1$$

although it is not clear whether this is because the problem ceases to be one dimensional (each individual region of the probe contributes in a different manner) or saturation would not occur at all under these circumstances [123]. With the values recalled in Chapter 2 and in table 5.1, the first of the two conditions can be evaluated

$$\frac{r_p\lambda_D}{\Delta^2}=10^{-6}\text{ to }10^{-3}\not\ll 1$$

so the saturation currents given by the author do not seem of any use under these circumstances.

The linear part of the *V-I* curve can be employed to determine the plasma conductivity through the probe capacitance. The method should not suffer from the limitations of the characteristic curve methods outlined above and is valid provided (a) the hypothesis of weak field is verified (in addition to the conditions mentioned at the beginning of the paragraph). Under these conditions, the plasma bulk electrical conductivity in the region of non-viscous and incompressible flow ($M<<1$) satisfies $\nabla\cdot\left(\sigma\nabla V\right)=0$, with $\sigma_\infty=\sigma$ that can be determined from the slope of the characteristic curve (in SI units):

$$\frac{i}{V_p}=C\sigma_\infty/\varepsilon_o,\quad C=2\pi\varepsilon_o l_p/\ln(l_p/r_p) \tag{5.41}$$

where the cylindrical capacitance for a probe of length l_p and radius r_p was taken. Inverting for the conductivity

$$\sigma=\frac{i}{V_p}\frac{\ln(l_p/r_p)}{2\pi l_p} \tag{5.42}$$

which requires the measurement of the net electron current in the linear part of the characteristic curve and the corresponding probe potential.

5.3.5. Currents in flowing plasmas

The current examined in the following pertains to the ion saturation of the characteristic curve. As such, it can be used to determine the electron (or plasma) temperatures. Four different expressions are reported in [111], depending on the regime chosen.

1) To assess the effects of plasma motion on ion saturation currents the first is the stationary plasma ion saturation current, typical of diffusion regimes, i.e. independent of probe bias, given by Su and Kiel [72],

$$I_{\mathrm{i}} = \frac{4\pi n_{\mathrm{e}} k T_{\mathrm{e}} \mu_{\mathrm{i}} l}{\ln\left(\pi l / 4 r_{\mathrm{p}}\right)} \tag{5.43}$$

This is the current given by the continuum equation (5.2) with $T_{\mathrm{e}}=T_{\mathrm{i}}$.

2) The second is Kagan and Perel's ion saturation current as given by (3.15).

3) The Continuum plus Free Fall (CFF) expression reported here for ions in saturation conditions

$$I_{\mathrm{iCFF}} = 4\pi r_{\mathrm{p}} n_{\infty} \mu_{\mathrm{i}} k T_{\mathrm{e}} \left(1 + \frac{T_{\mathrm{i}}}{T_{\mathrm{e}}}\right) \tag{5.44}$$

4) The formula of Lam [109] (also reported in [114]) valid in the diffusive and flowing regime:

$$I_{\mathrm{i}}^{sat} = 4\left(e\ \mu r_{\mathrm{p}} \mathrm{v}_{\mathrm{f}} k T_{\mathrm{e}}\right)^{1/2} n_{\mathrm{e}} \tag{5.45}$$

5) Clements and Smy [111] compare these currents with two formulae they obtain for the sheath convection regime, defined by the occurrence of the condition $\mathrm{Re}\alpha^2\chi^2>1$ (see previous section), where the ion motion within the sheath is mobility dominated These currents are

$$I_{\mathrm{i}} = 5.3\ \left(n_{\mathrm{e}} e \mathrm{v}_{\mathrm{f}}\right)^{3/4} \left(\mu_{\mathrm{i}} \varepsilon_{\mathrm{o}} r_{\mathrm{p}}\right)^{1/4} l V_{\mathrm{p}}^{1/2} \tag{5.46}$$

$$I_{\mathrm{i}}' = \left(2 n_{\mathrm{e}} e \mathrm{v}_{\mathrm{f}}\right)^{3/4} \left(9\pi \mu_{\mathrm{i}} \varepsilon_{\mathrm{o}} r_{\mathrm{p}}\right)^{1/4} l\ V_{\mathrm{p}}^{1/2} \tag{5.47}$$

These differ by a numerical factor of the order of 30% (the ratio of (5.46) to (5.47) is about 1.37). Equation (5.46) corresponds to the assumption that the component of the flow velocity parallel to the electrode surface is constant and approximately equal to the flow velocity v_{f} whereas in (5.47) this assumption is removed.

6) In addition, the value of the current in the transition between diffusion and convection regimes (*cf* 5.2.3.2) is reported [116]

$$I = I_{\mathrm{d}}\left[1+1.3(\mathrm{Re}\,\alpha^2\chi^2)^{1/4}\right] = I_{\mathrm{d}}\left[1+1.3\left(\frac{\varepsilon_{\mathrm{o}}\mathrm{v}_{\mathrm{f}}e}{\mu_{\mathrm{i}}r_{\mathrm{p}}n_{\mathrm{e}}}\right)^{1/4}\left(\frac{V_{\mathrm{p}}}{kT_{\mathrm{e}}}\right)^{1/2}\right] \qquad (5.48)$$

where $I_{\mathrm{d}} = I_{\mathrm{i}}$ is given by Lam's equation (5.2) and where the Debye length contained in α has been explicitly expressed in terms of the electron temperature. Differently from the purely diffusion case, in (5.48) a dependency on the probe voltage appears.

Comparisons are made between the two diffusive currents of [72] and [109] and the improved convection formula (5.27) of [111] and the transitional formula (5.48). Since the CFF case, considered in the thermal version (T_{e}=T_{i}) differs from Su and Kiel's expression only by the geometrical factor

$$\frac{I_{\mathrm{CFF}}}{I_{\mathrm{SK}}} = \frac{2r_{\mathrm{p}}}{l}\ln\left(\frac{\pi l}{4r_{\mathrm{p}}}\right) \approx 1.15 \qquad (5.49)$$

These currents are reported in figure 5.15 (except CFF which was shown in figure 5.8).

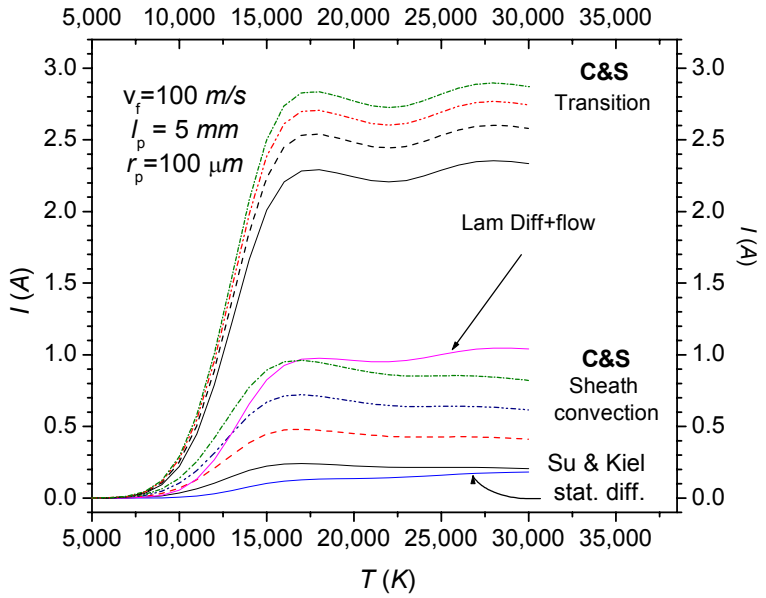

Figure 5.15 Ion saturation currents. From bottom, diffusive regime of Su and Kiel [72] (stationary), sheath convection regime currents of Clements and Smy [111] for different probe voltages (continuous 10 V, short dash 20 *V*, dash-dot 30 *V*, dot 40 *V*; Lam diffusive for flowing plasma [109]. Clements and Smy [116] transitional for different probe voltages (continuous 10 *V*, short dash 20 *V*, dash-dot 30 *V*, dot 40 *V*). The CFF case can be obtained by multiplying Su and Kiel's value by 1.15 (see text)

In figure 5.15, the flow velocity is v_f=100 *m/s*, the mobility is $\mu_i=1.6\cdot10^{-4}$ $m^2/(Vs)$, the probe radius is r_p=100 μm and the length l = 5 *mm*. The diffusive stationary plasma ion saturation current of Su and Kiel [72], the flowing diffusive regime of Lam [109] are compared with the sheath convection regime of Clements and Smy's [111] and the diffusion-convection transitional currents of Clements and Smy [116]. In contrast to what would be "expected" from a sheath convection regime, the currents of the latter just reach Lam's diffusion value (instead of exceeding it) and this occurs only at the highest bias voltages achievable in arcs. In effect, the regime where these currents are believed to be applicable differs somewhat from the circumstances of this work (see also [116]). This was recognized by the authors during experimental verification of the transition between the two main regimes, diffusion or sheath convection. The authors [113, 116] found qualitative agreement between expected and measured transition from the saturation characteristic of diffusion regimes to the $V^{1/2}$ behaviour of sheath convection, however, the transition occurred at values of electron density higher than expected, leading to an $Re\alpha^2\chi^2\approx10^{-3}$ instead of the expected ~1. Also, the saturation currents of the diffusive case were found lower by one order of magnitude with respect to the values predicted by (5.45), and very close to the values obtainable by convective

equation (5.46, 5.47). Also, the transitional case described in [116] with the parameters dealt within this work, significantly overcomes both the diffusion and the convection cases and, contrary to the results in [116], the current is greater than the sum of the two cases taken separately.

In [111] the comparison is carried further taking as "measure of inadequacy" of the alternative models the Reynolds number or, more precisely, the quantity $Re\alpha^2\chi^2$. However, for the sheath convection regime, critical is the assumption of the rough equality between the electric and the viscous boundary layer, whereas the sheath is supposed larger than the viscous boundary layer. This is in contrast with the evaluations performed above (*cf* Chapter 2 and Chapter 4) where it has been shown that under the present circumstances (TIG arc) the opposite does in fact occur.
Up to this point, the comparisons in figure 5.15 shows that the different regimes of diffusion, for steady or flowing plasma, convection, or even better the transitional case, should be easily distinguishable from the experimental point of view.

5.4. Comparison and summary

Different groups of criteria have been considered in an attempt to:

- fix the operating regime for a probe sweeping through an atmospheric arc with experimental conditions similar to the ones dealt with in this work;

- see whether the different schemes converge to a unique description.

The results of the criteria given by the three groups of works considered in this review can be summarized as follows:

- The results given by the criteria of Swift and Schwar [65], $\alpha<<1$ and $\beta<<1$ as well as $2^{-1/3}(r_p/\lambda_i)^{1/3}(\lambda_D/\lambda_i)^{2/3}>>1$, put the system in the domain of "Continuum plus free-fall theories" characterized by a thin and collisionless sheath. However, no mention is made about plasma motion.

- Chung, Talbot and Touryan (CTT [37, 119]), using the small Knudsen numbers criterion $Kn_{i,e}<<1$, and by the high electrical Reynolds number criterion $Re>>1$, classify the system as a flowing plasma (B4) with a dense sheath (B3). The criterion $|\chi|(\lambda_{D\delta}/L)^2<1$ specifies the sheath as thin. Some consideration should be given to the double transitional case C3.

- Clements and Smy (CS, [79, 91, 111, 114], [84]), by $Re>>1$ set the system in the flowing plasma regime and, by the $Re\alpha^2\chi^2<<1$ criterion, in the 'diffusion via boundary layer convection' although, when flow velocities, probe bias and/or

sheath charged particle depletion are high enough, consideration must be given to ion convection regime, either in the sheath convection or in the *E*-field sub-domains. This might be particularly true in the periphery region of the electric arc, where temperatures and densities are lower than in the bulk of the column. Sheath generation effects are difficult to evaluate until a reliable estimation for the recombination coefficient *a* is known, but should become significant only when the flow velocity is sufficiently small (This point is specifically addressed in Chapter 6).

In summary, the discriminating conditions are reported in Table 5.4, where the regimes of probe operation are indicated following the nomenclature described above.

Classification following:	Chosen regime / applicable theory/Notes
1) Swift and Schwar [65]	Continuum plus Free-Fall theory. No mention of plasma motion.
2) Chung, Talbot, Touryan [37, 119]	*B*3/ flowing Continuum plasma with "dense" collisionless sheath. *C*3 Double transitional.
3) Clements and Smy [78, 79, 91, 111, 113, 114], Smy [84]	*E*1 Diffusion-mobility regime. When T_e, v_f are low enough, sheath electric field are effective (*E*21 and *E*22).

Table 5.4. Summary of the classification regimes. Models: C= Continuum theory, CFF = Continuum plus Free Fall, DD = Diffusion dominated, CD = Convection Dominated

A comparison of the domain described in the three cases reveals a common "Continuum" background. After this has been established, both collisionality and thickness of the sheath surrounding the probe has been addressed. For the latter, the result in all cases is of a thin sheath. In particular, in the work reported by Swift and Schwar [65] the Continuum plus Free-Fall theory has been seen as appropriate to establish a collisionless sheath. Although in the static case, this is in agreement with the collisionless thin sheath ("dense" case) of CTT.

These results are consistent with the various estimated sheath thickness, always of the order or below one ion mean free path. However, since Swift [65] does not account for the general problem of plasma flow, only the works of CTT and CS were reported. Results from both rely upon the consideration of the high electrical Reynolds number leading to a "flowing regime". CTT's "Large convection" and CS's "flowing plasma" are thus equivalent. In the frame of CTT's classification it was possible to re-define a "thin" sheath by evaluating the relative depths of the boundary layer and the electric sheath.

The next step was obtained by considering the effects of plasma properties and geometrical and field effects altogether. This was done in the frame of CS's classification. Here the emphasis was on the investigation about the way the ions reach the probe: it has been found that for 1) relatively low probe potentials, 2) low flow velocity and 3) high temperatures, ion diffusion via boundary layer convection is the dominant process. However, flow velocities and probe potentials high enough lead to the opposite case of convection through ion sheath, where the effects of the electric field are not negligible. It has been shown that both the "sheath convection" and "*E*-field" sub-regimes can apply for a probe moving through a variable characteristic plasma column with lower temperatures and densities in the peripheral regions of the arc.
Several expressions for ion saturation current have been reported, some belonging to the 'Continuum' and 'CFF', deliberately ignoring plasma flow effects. The first mainly for

comparison purposes; the second, i.e. CFF currents, also because they can be considered as starting points for the regimes encountered in this work: after all, they represent well-established results for the non flowing case.
Also, a current expression valid in stationary plasma for probes close to plasma potential [86] was reported and will be checked against experiment.

It can be expected that in circumstances where flow velocity is not too high, sheath depletion (i.e. occurrence of the condition $Re\alpha^2<1$, see figure 5.13) will occur and therefore the measured current values could lie close to the values predicted by the CFF theory, at least for the ion saturation region of the characteristic curve (figure 5.8). On the other hand these current values are considerably lower (down to some *mA* in the arc core region) than any experimental value ever obtained in an atmospheric pressure arc (about 1 *A*). A full verification of the values given by these theories will be possible only after further experimental measurements.

The values for the electrical current reported for plasma flowing conditions contain several of Clements and Smy's results. Not all of them appear appropriate for the regime studied. To the result of Lam [109], see figure 5.15, essentially limited to the flowing plasma in a diffusive regime, showing saturation, Clements and Smy add the 'convective' regime by the two slightly different equations (5.46) and (5.47). The latter values are considerably lower than the diffusive values (shown in figure 5.7). In particular the 'convective' currents should be comparable with experimental reported values [63] only at 'high' electron density, i.e. above $n_e=10^{24}\ m^{-3}$. Therefore, in agreement with what emerges from Chapter 4, it appears that Clements and Smy's diffusive regime is appropriate for the conditions dealt with in this work. However, as stated earlier, high ionization is not contemplated. Moreover, from the experimental point of view, the impression is that some of their results are applicable to a range that appears contiguous but not superimposed to the experimental conditions of interest in this work. The fact that these authors contest the ion current values as *measured* [62], which show to saturate contrary to their $V^{1/2}$ prediction, if not their interpretation, reinforces this impression.

Of interest is the way they present the current lack of understanding in charge generation and recombination within the sheath. In particular, the order of magnitude comparison with the current values quoted by [62, 106] and Allum [63], defines a range for the "recombination-electron density" combination. It is then possible that measurements of the electron density could indicate orders of magnitude estimation for the recombination coefficient within the sheath.

The last work considered is due to Benilov [123] in the frame of a hydrodynamic plasma with low degree of ionization. Given that the applicability of his theory was

ruled out, of some interest is the possibility to obtain the electrical conductivity by measurement of current and voltage to be performed in the steep part of the characteristic curve. Whether this method is fully exploitable will be left to the experiment.

6. NON-IDEALITIES

6.1. Introduction

The interpretation of experimentally determined parameters, particularly the electric current, by means of the theories sketched in the preceding chapters, was based on simplifying ("ideal") assumptions on plasma and probes. Some of these have to be removed in order to gain a realistic picture but the greatest difficulty is that in literature "non-idealities" are never addressed *at the same time*.
These are:

1. The plasma-probe thermal interaction has been ignored except in [63] (*cf* Chapter 4). Probes 'survive' into a medium whose temperature is much higher than probe melting temperature and plasma cooling by probes could be substantial [137]. Heat transfer is treated in section 6.2 and whereas criteria for cooling effects of the plasma by the probe are illustrated.

2. The probe is a perfect charge collector. However, it has already been mentioned that probes withstand high temperature fields and steep potential distribution in proximity of probe surfaces. These two circumstances could lead to thermionic and field emissions; they are considered for the two probe constitutive materials (*Cu* and *W*) in section 6.3. Also, the surface bombardment by the incident ions could cause secondary emissions which alter the current sensed with respect to the case where these phenomena were absent.

3. Ionization and recombination effects in the region occupied by the probe have been almost ignored ("Frozen Chemistry" assumption). For the main bulk of this work a one-component (*Ar*) plasma is considered. Therefore, the "chemistry" lies in the contribution of ionization and recombination to the charged species both in the bulk and in the sheath. The "frozen chemistry" assumption in all but [83] and [78], neglects these effects that contribute typically with different rate laws. Evaluations of these hypotheses are considered in section 6.4.

4. Several effects of geometrical nature, combined with the ambient pressure determine disturbances which distort the electronic portion of the characteristic curve. These are discussed in section 6.5.

6.2. Heat transfer to probes: mechanisms

The fact that both copper and tungsten probes survive many runs without vaporizing and actually degrading their behaviour (*cf* Chapter 8), indicates that the mechanisms of direct energy transfer are inhibited by the existence of a thermally insulating layer [137]. Moreover, the fact that probes remain much colder than the surrounding plasma raises the question about their thermal influence on the plasma and in particular on the value of the information extracted ("Plasma Cooling", [79, 84, 91]).
In general, the heat transferred to a cylindrical probe sweeping through the hot plasma and the probe energy loss may be ascribed to one or more of the following processes:

1. Heat conduction from the plasma to the immersed body and heat losses towards the colder gas out of the arc;

2. Radiation from the plasma to the probes and their re-irradiation at different wavelength.

1. Heat conducted from the plasma to the body
A "cold" probe at ambient temperature (300 *K*) moves across an arc with temperature varying from about 5,000 *K* (edges) to 20,000 *K* (core). It is assumed that the heat transfer is mainly convective across a boundary layer. This *thermal* boundary layer may differ from the viscous boundary layer discussed in Chapter 2. However, based on the assumption that the Prandtl number [58, 60] is close to one [46, 138] it is possible to conclude that the two boundaries are of the same order of magnitude.
Also it is possible to estimate the heat transfer coefficients [46] by assuming the fluid ideal and obtain, for tungsten $h \approx 8 \cdot 10^5$ to $4 \cdot 10^6$ $Wm^{-2}K^{-1}$ or 0.8 to 0.4 $Wmm^{-2}K^{-1}$ (in the range of Prandtl number corresponding to argon temperatures between ambient and 5,000 *K*). These heat transfer coefficients can be compared to the values measured by Petrie and Pfender [137]. These authors used a tungsten probe in an 'hot wire anemometer' configuration and inferred both the temperature difference between plasma and wire and the heat transfer coefficients *h* (*W*/*mm* °C), by measuring the electrical resistance of a wire swept through a 10 *mm* 200 *A* arc plasma. The agreement between measured and theoretical heat transfer coefficients was stated to vary from 5 to 15%. It was further assumed that the small current drawn by the wire (1 *mA*) did not alter the heat exchange. Petrie and Pfender's heat transfer coefficients are of the order of the estimation made above.
One could try to determine the plasma temperature from these coefficients and the measured probe temperature, by using a linear law like Newton's law (a steady

conduction law) applied to two coaxial cylinders with the thermal conductivity replaced by a 'global' transfer coefficients h (conduction and convection) [46]. Moreover, the maximum temperature difference between plasma and probe can be estimated, as if it were due to conduction and convection only [46]. The heat necessary to melt typical probes (L=50 *mm*, r_p=10^{-4}*m*) is q=2.88 *J* for copper, q=5.80 *J* for tungsten. Since the probe-in-arc permanence time τ is of the order of 5 *ms*, this gives the heat flux needed per unit time to melt the probe *within* that time: q_{Cu}= 576 *W* to q_W = 1160 *W*. From this steady state 'cooling' law, one could infer the maximum plasma-probe temperature difference of the order of 500 to 2,000 *K*. Taking for the probe length 15 *mm* instead of the 50 *mm* (i.e. only the 'active' part of the probe) would increase this differences by a factor 3.3 and thus the maximum difference could be about 6,600 *K,* which added to the probe temperature, say 3,000 *K* for tungsten, would lead to 10,000 *K* (closer to but still lower than accepted values). These temperature differences are lower than commonly accepted arc temperatures. The fact that they would rise considerably by considering a limited portion of the probe only shows that the knowledge of the *radial* dependency of the heat transfer is mandatory.

2. Radiative transfer

It is possible to use the radiative transfer equation [8, 139] to compute the heat produced in the plasma and transferred to the probe immersed into it. The radiant energy density is negligibly small in comparison to the energy of the fluid provided the gas density is not too "low" and the temperature not too "high". The equilibrium radiant energy density and the thermal energy density for monoatomic gas, equalize at a density n=$2.67\cdot10^{25}$ m^{-3} (standard air density) and at T=900,000 *K* (and beyond when considering heating with subsequent ionization, [139]). Below these densities the effect of the radiant energy density on the fluid motion is negligible. However, effects of radiation on fluid motion exist in that the radiant energy lost by the fluid and the radiant heat transfer may be appreciable even at lower temperatures. This is due to the low ratio of fluid velocity v to the speed of light c, v<< c: the energy flux in the fluid Ev, and the radiant energy flux in the fluid *Uc can be comparable* even if the corresponding densities are appreciably different ($Uc \approx E$v even if $U << E$ because $c >>$ v [139].

The amount of the radiated heat depends on the optical thickness of the medium [46].
An optically thick body looses its radiation from the surface while an optically thin body looses it from the whole of the body. Therefore, the radiation spectrum of the thick body is closer to the Planck spectrum corresponding to the surface temperature whereas the thin body distribution can be very different from the Planck spectrum corresponding to the temperature of the body, especially if the absorption coefficient is a strong function of the frequency. The energy losses of two bodies at the same average temperature, one with large dimensions and optically thick; the other smaller and optically thin, are both less than σT^4.
The upper limit of global emission from a homogeneous arc at 20,000 *K* is

$$\sigma T^4 = 5.67\cdot10^{-8}\ W/m\text{-}^2K^{-4}\cdot(20{,}000\ K)^4 = 9\cdot10^9\ Wm^{-2} \qquad (6.1)$$

where $\sigma = 5.67\cdot10^{-8}\ W/m\text{-}^2K^{-4}$ is the Stefan constant. The fraction impinging on the probe surface can be obtained multiplying by the probe surface $2\pi r_p l$, and the energy deposited is obtained by using the probe in arc permanence time (~*ms*). This gives about 1 *kJ*, well above the melting heat of the probe (*cf* above, q=2.88 *J* for copper, q=5.80 *J* for tungsten).
A better estimate is obtained using the data taken from Menart *et al* [140] and reported in Table 6.1 for the heat radiated by a TIG arc.

Region (z,r)	Radial flux S_{rad} (W/m^2)	Axial flux S_{ax} (W/m^2)	Source term (W/m^3)	T (K)	Em. Coeff. ε (W/m^3sr)
8.5,0.3	$9\cdot10^6$	$1.2\cdot10^7$	$2\cdot10^{10}$	20,000	$6\cdot10^{10}$
0,6	$\leq2\cdot10^6$	$-5\cdot10^5$ (*)	0	8,000	$<10^7$

Table 6.1. For the estimation of arc radiated power. Data points extracted from the arc maps shown in [140]. Arc length 10 *mm*. (*) See text

These authors compare 'uncoupled' and 'coupled' system, the coupling occurring among radiative, flow and thermal fields. Some observations are possible.

1. The temperature gradients are 'high' and therefore the estimations performed in the following are coarse

2. The radial and axial fluxes are off-axis, which is understandable when one accepts that these quantities are both transported values which therefore depend not just on *local* properties but on the global temperature

3. In the anode arc region radiation adsorption prevails on emission (negative value for the axial flux reported in table 6.1). The first rows correspond to two extreme cases of core region (1.5 *mm* down the cathode near the axis) and to the anode region (6 *mm* off the axis) of a 10 *mm* argon arc.

Using these values for axial and radial fluxes (W/m^2) in the form $< J >= (J_{ax} + J_{rad})/2$ at the two locations; and assuming a distributed source of the order of the probe surface $2\pi r_p l$, the radiant heat flux impinging on the probe surface per probe length l would be

$$W/l = 2\pi r_p \cdot < J >= \begin{cases} 6.6 & kW/m \\ 471 & W/m \end{cases} \qquad (6.2)$$

corresponding to 99 *W* and 7.1 *W* for the 15 *mm* active region of the probe. Multiplying by the ratio of the permanence time (1 to 10 *ms*) to 1 second, a maximum of Q=0.1 *J* or a minimum of Q=7.1 *mJ* energy would be released to the probe. These values are both much lower than the heat of fusion.

A summary of the order of magnitude evaluations is reported in Table 6.2.

Mechanism	Heat per unit surface (W/m^2)
Conduction/convection	$1.8 \cdot 10^8$, $7.6 \cdot 10^{10}$, $9.1 \cdot 10^{11}$
Radiation	$4.5 \cdot 10^9$ (blackbody), $1 \cdot 10^7$ ([140])

Table 6.2 Comparison of heat transfer mechanisms.

It can be observed that radiative effects were not considered. At these arc regimes the effects of radiation would amount to perhaps a few % of the conductive/convective heat transfer to probes.

6.2.1 Plasma-probe motion

The problem of the 'low' probe temperature was considered by Smy [84] and is related to probe-plasma relative speed.

(i) stationary plasma
The effect of cooling is treated by Thomas [76] that extends Su and Lam [73] and Su and Kiel [72] theories for probes that are cooler than the gas. Using Fourier equation the temperature distribution is determined and taken as the gas temperature around the probe; the diffusion-mobility equations are modified and the characteristic curve obtained shows that Su and Lam's [73] and Su and Kiel's [72] results are still applicable. However, these works pertain to low temperature and low ionization media. Smy considers flames for which the temperature around the probe is of the order of the gas temperature and it is not reduced. This means also that radiation effects are completely negligible.

(ii) Moving plasma
In general, the probe must be at a different temperature with respect to the plasma or it will melt or, perhaps emit electrons ([78, 117], *cf* section 6.3). This heat and mass transports appear as an increase in pressure of the order of 0.1 per cent near the probe for atmospheric plasmas ("cooling effect") [78, 84, 117]. These authors state that the ion saturation current is not altered from the "uncooled value" by a "cold" probe.

The physical picture consists of electrons supposed frozen at the bulk plasma temperature. In case of electronic cooling, a useful measurement of electron temperature is still possible, provided the ionization fraction is below a critical value (10^{-6}). The effects of the heat conduction from the hot species to the probe on the characteristic curve would be twofold: the neutral density near the probe could increase, because the pressure has to remain constant ($p=nkT$ is assumed). Therefore, the ionic mobility decreases according to the kinetic $T^{1/2}$ law. In second place, the electrons are cooled by collisions with the colder neutrals depressing the electron temperature near the probe.
A criterion for these phenomena to occur can be found studying the relationship between the ratio r_p/v_∞ of the probe radius and the probe sweep velocity in the unperturbed plasma as a function of the non-perturbed electron density $n_{e\infty}$; the relative plasma-probe motion could be effective in preventing cooling, provided that [84]

$$r_p / v_\infty < 10^{-4}\ s \qquad (6.3)$$

This should ensure a reliable estimate of the electron temperature T_e. The condition is fulfilled within one order of magnitude for the values reported in Table 5.2 (Chapter 5), since the ratio is now of the order of about 20 μs. The following observations for formula (6.3) can be made:

1. The actual regime considered by the authors is quite far from arc conditions since the reported electron temperature is $T_e \approx 1{,}800\ K$ and the electron density does not exceed $10^{15}\ m^{-3}$

2. The criterion was derived in [91] from an energy balance equation in which collisions between charged particles were neglected; this is justified as long as either the ionization rate is very low (of the order of 10^{-6}) as in typical flames, or a thin collisionless sheath is considered

3. In the original formulation [84] the 'plasma motion' is due by the relative motion of a steady plasma and a sweeping probe; in the present work the plasma flow velocity largely exceeds the probe sweeping speed. In this case, a flow velocity of 40 to 200 *m/s* is much greater than the probe velocity (1 to 5 *m/s*) and the criterion would be fulfilled *a fortiori*.

Therefore, cooling due to electron energy loss for collisions with neutrals is excluded in the region around the probe for 'low' temperatures.

In [84] the characteristic cooling time is taken [91] as a balance between electronic heat conduction and collisional losses

$$\tau_c = \frac{m_i}{m_e}\frac{\lambda}{v_i} \tag{6.4}$$

where m_i is the ionic and m_e the electronic mass and in which electron and ion–neutral mean free paths were considered equal. If the flow time τ_f (time needed to cover a distance X at the velocity v_f) is greater than this value, there will be substantial cooling and electron and gas temperatures will be in equilibrium. In the opposite case the electron temperature will remain 'frozen' at T_e (e.g. 'uncooled').
In summary, the condition for the depression of the electron temperature would be

$$\tau_f \equiv \frac{X}{v_f} > \frac{m_i}{m_e}\frac{\lambda}{v_i} \tag{6.5}$$

The left hand side is

$$\frac{X}{v_f} = \begin{cases} r_p / v_f = 10^{-4}/100 = 10^{-6}\,s \\ l / v_f = 50\times10^{-3}/100 \approx 5\times10^{-4}\,s \end{cases} \tag{6.6}$$

depending on the chosen characteristic length (the probe radius, $X = r_p = 100\ m\mu$ or the probe length $X = l = 50\ mm$). For the right hand side of (6.5)

$$\frac{m_i}{m_e}\frac{\lambda}{v_i} \approx \frac{679}{T_i} = \begin{cases} 2.3 & (300\ K) \\ 2.7\times10^{-2} & (25{,}000\ K) \end{cases} \tag{6.7}$$

where ion diffusion velocity was reported in Chapter 5 (where it was shown that the flow velocity dominates the ion velocity because $Re>1$)

$$v_i = \mu_i \frac{kT_i}{2r_p e}$$

The ion mean free path and mobility has been taken from Chapter 2 ($\lambda_i = 1.2\cdot10^{-6}\ m$, $\mu_i = 1.5\cdot10^{-4}\ m^2\cdot V^{-1}\cdot s^{-1}$ *cf* also Table 5.1). The ion temperature can be considered in between the two extremes of a 'cold' plasma (i.e. gas ambient temperature, $T_i = 300\ K$) or the "thermal plasma limit" ($T_i = T_e = 25{,}000\ K$ in the core). In both cases ($X = r_p$ or l) condition (6.5) is never fulfilled and electron cooling would not occur.

6.3. Probe Emissions

For a probe to be considered non-perturbing, the current drained must be negligible with respect to the current flowing through the arc plasma. The current carried by

atmospheric arc plasmas varies from tens to some hundreds of amperes and within an arc column, far from the electrodes, it produces a field 10^2-10^3 *V/m* [14]. If the electrical conductivity is of the order of 10^4 $(\Omega m)^{-1}$, the current density within the arc column varies from $j = \sigma E = 10^6$ to 10^7 A/m^2.
Given the typical current estimated in Chapter 5, the question arises whether electron emissions occurring as a result of probe temperature (heat transferred, see previous section), electric field or impinging particles can produce currents *from* the probe comparable with the probe current in absence of those effects. The result would be a modification of the effective amount of charge seen by the probe.

Probe electron emission may be caused by the onset of a critical temperature of the emitter that allows the electron to overcome the potential barrier existing at the material surface (*work function*) and escape out of the metal (*thermionic emission*). Also, a probe to plasma potential, giving rise to a sufficiently "strong field" across the sheath can cause *field emission* (or *cold emission* see below). *Secondary emission* may occur as a result of scattering of electrons or ions that, impinging on a surface could release one or more electrons.
From the experimental point of view it is difficult to discriminate the different emission phenomena ("perturbing" effects) with respect to ion-surface recombination that leads to the formation of the "true" probe electric signal (current).

The (integrated) emitted current is the product of the emitted current density and of the probe surface $S_p = 2\pi r_p l = 6.28 \cdot 10^{-4}\ l\ (m)$. For a probe residence time of 1 to 10 *ms* in the arc column, the number of emitted electrons can be compared with the ion flux expected at the probe surface in absence of emissions.

6.3.1 Thermionic, Field and Thermionic-Field (TF) emissions

Thermionic emission from a metal surface at temperature T obeys the Richardson-Dushman equation [141]

$$j = AT^2 \exp(-\varphi / kT) \tag{6.8}$$

where T is the metal temperature and the "constant" A is calculated [142]

$$A = \frac{emk^2}{2\,\pi\,\hbar^3} = 1.2 \cdot 10^6 \tag{6.9}$$

or measured, $A = 7.2 \cdot 10^5\ A\ m^{-2}\ K^{-2}$ or $10^6 A\ m^{-2}\ K^{-2}$ [141, 143].

The exponent φ is the metal work function, i.e. the energy needed to release an electron from the metal and bring it at rest at infinite (sometimes written as the difference between a "potential" φ and the maximum kinetic energy of the escaping electron). It varies among metals from 1 to a few *eV*. Work functions for tungsten and copper are φ=4.54 *eV* and 4.65 *eV* respectively [144]. Oxide layers may lower the value down to 2 *eV* for many metals.

If the emitting body is set at a potential much lower than 10^8 *V/m*, the electronic current as a function of temperature saturates. 'Long-life' tungsten at 2,500-2,600 *K* has a saturation emission variable from j_{sat}=3,000 to 5,000 A/m^2 [143].
Relationship (6.8) has no dependency on the electric field. Its modification is then necessary due to the following effect.
When the field is "high" enough, ~ 10^8 *V/m*, the probability of an escape from the metal surface by means of "Tunnel effect" is not negligible provided the distance of application of the field is of the order of 1 *nm*. One speaks then of "High-Field" emission from a *Cold cathode*, since thermal effects are now of minor importance. Since the electrons do not have to overcome a potential barrier, their energy is of the order of the Fermi energy E_F.

Therefore, in the following equation (6.10) the "external" potential energy φ' must be evaluated as a function of the distance from the surface and in the case under consideration can be identified with the sheath potential (energy).
Formula (6.8) is modified to

$$j = AT^2 \exp\left[-\left(\varphi - \varphi'(x)\right)/kT\right] \qquad (6.10)$$

where the term φ'(*x*) is the external field (potential) energy subtracted from the work function and evaluated at a distance *x* from the surface.
The use of Richardson-Dushman equation for tungsten is not legitimate [145] and an alternative formula is shown where the current depends on the transmission coefficient *D*. The emitted current density is shown to vary as a function of the electric field, between 10^{-2} (for 1,500 *K*) to $2\cdot10^5$ A/m^2 (3,000 *K*) for virtually zero field, to about 10^5 to 10^8 A/m^2 for $E= 3\cdot10^9$ *V/m* at the same temperatures.
The Nordheim-Fowler formula for field emission [18] is

$$\begin{aligned} j_F &= CE^2 \exp(-D/E) \qquad (A/m^2), \\ C &= \frac{e^2\varphi_m^{1/2}}{2\pi h\varphi_b\varphi^{1/2}} = 6.2\cdot10^{-6}\frac{1}{\varphi_b}\sqrt{\frac{\varphi_m}{\varphi}} \qquad (A/V^2), \quad [\varphi] = eV \\ D &= \frac{8\pi}{3h}(2me)^{1/2}\varphi^{3/2} = 6.83\cdot10^9\varphi^{3/2} \quad V/m \end{aligned} \qquad (6.11)$$

where

$$\varphi_b = \varphi + \varphi_m \tag{6.12}$$

φ is the work function and φ_m is the band potential, i.e. the depth of the electron energy band in the metal, estimated by

$$\varphi_m = \frac{h^2}{2me}\left(\frac{3n}{8\pi}\right)^{2/3} = 3.65\cdot 10^{-19} n^{2/3} \quad eV \tag{6.13}$$

where n is the metal electron number density (~ 1 electron per metal atom). Estimations for *Cu* and *W* are reported in Table 6.3.

	$n\ (m^{-3})$	$\varphi_b=\varphi+\varphi_m\ (eV)$	$C\ (A/V^2)$	$D\ (V/m)$
Cu	$8.46\cdot 10^{28}$	11.68 = 4.65 + 7.03	$6.61\cdot 10^{-7}$	$6.65\cdot 10^{10}$
W	$6.30\cdot 10^{28}$	10.32 = 4.54 + 5.78	$6.73\cdot 10^{-7}$	$6.41\cdot 10^{10}$

Table 6.3. For the determination of the terms of Nordheim-Fowler relationship (6.14) in copper and tungsten.

(Incidentally, the value of φ_m=9.0 *eV* for tungsten reported in [18] is incorrect. In the table the correct φ_m= 5.78 *eV* computed here is reported). From these values, the emission current can be estimated and are reported in figure 6.1.

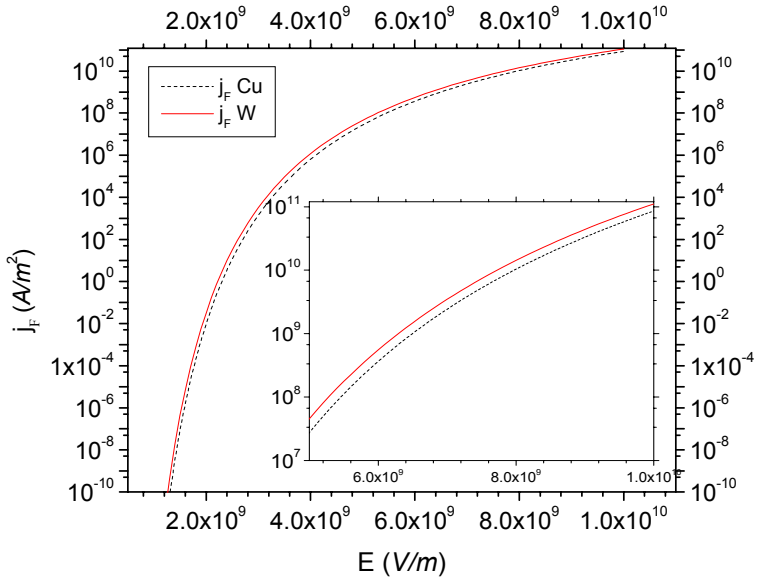

Figure 6.1 Field-emitted current density j_F according to Nordheim-Fowler relationship (6.11) in tungsten (solid line) and copper (dash-dot line).

It can be observed that the current starts to be appreciable when the field overcomes the value $E=3\cdot10^9$ *V/m*. Also, the differences between copper and tungsten are minimal. Raizer [9] compares the three phenomena of thermionic, field and TF emission as a function of the electric field. The values reported in his Table 4.8 [9] for the field emission agree with those computed here.

The purely thermionic and the uniform field emissions are now compared. For field emission we use the sheath thickness given in Chapter 4, Swift's (4.21) and (4.22) for the thermal and cold plasma; improved Child-Langmuir (4.28); Mukherjee 'collisional' (figure 4.4) can be used to calculate the voltage at the sheath edge. It is assumed for simplicity that in (6.11),

$$j = AT^2 \exp\left[-\left(\varphi - \varphi'(x)\right)/kT\right]$$

the 'corrective' potential energy φ' is uniform, $\varphi'(x) \approx const = 4\ eV$ (corresponding to $x=\delta_s=10^{-7}\ m$ where the potential is V= –4*V*, see figure 6.2). It should be mentioned that the choice of the Child-Langmuir solution (fig. 6.2) implies an electric field of the order of $5\cdot10^7$ *V/m*, corresponding to the potential variation from V_f =–9 *V* at the probe location, to the –4 V of the sheath edge over the distance $\delta_s=10^{-7}\ m$ [The Child-Langmuir case was just one of the cases dismissed because of its high voltage applicability]. The condition $eV/kT<<1$ is satisfied within present regimes and in floating conditions a weaker probe-plasma voltage, perhaps 0.5 *V* is attained. The resulting saturation current densities are shown in figure 6.2 for these extremes.

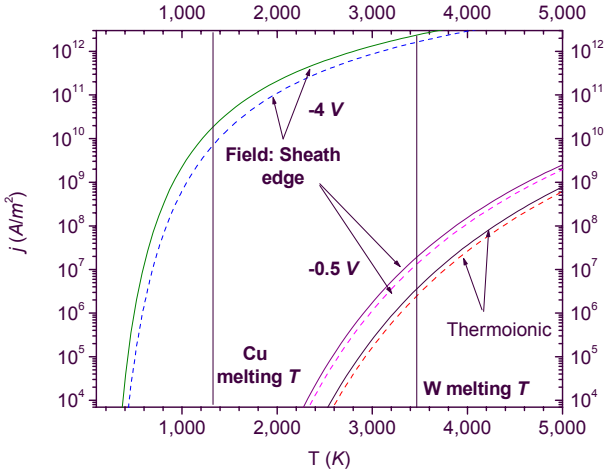

Figure 6.2 Thermionic and field emission current densities as a function of temperature for electric field corresponding to sheath potential V=- 4 *V* or –0.5 *V* at the sheath edge. Tungsten, full lines, copper, dashed lines. The vertical lines at 1,358 *K* and 3,695 *K* indicate copper and tungsten melting temperatures.

From figure 6.2 several total emitted current can be extracted [46] in a range varying from the *nA* to the tens of *A*, depending on the probe temperature. In any case:

- The *purely thermionic* current densities are much lower than field enhanced emissions.

- Although precise evaluations are impossible given the steep (exponential) dependency on temperature, thermionic emission for tungsten seem difficult to be ruled out from these data, whereas for copper figure 6.2 shows negligible currents below its melting temperature.

- For *field enhanced* emission, the current density is of the order of $j=10^{10}\ Am^{-2}$ and $j=10^{12}\ Am^{-2}$ at copper and tungsten melting temperatures and sheath potential V=–4 *V*; these are by far larger than the values at V=–0.5 *V*.

It is worth to mention the results computed by Testé *et al* [145] for tungsten at $E=4\cdot10^{8}$ *V/m*: $j=6\cdot10^{6}\ A/m^2$ at 3,000 *K*, $j=8\cdot10^{5}\ A/m^2$ at 2,500 *K*, $j=6\cdot10^{2}\ A/m^2$ at 2,000 *K* and $j=3\cdot10^{-1}\ A/m^2$ at 1,500 *K*. These would correspond to the probe currents

$$I = jS = j2\pi r_p l = \begin{cases} 56.5\ A\ (3{,}000K) \\ 7.53\ A\ (2{,}500K) \\ 5.65\ mA\ (2{,}000K) \\ 2.82\ \mu A\ (1{,}500\ K) \end{cases} \tag{6.14}$$

A qualitative picture for pure Thermionic, Thermionic plus Schottky, Thermo-field (TF) and Field plus Schottky can be obtained by a numerical model ([9], p70) that gives emission current densities from which the following conclusions can be drawn:

1. At temperature of 3,000 *K* and fields $E> 8\cdot10^{9}\ V/m$ pure field emission dominates;

2. At $E< 5\cdot10^{8}\ V/m$ Thermionic plus Schottky dominate;

3. At lower field purely thermionic should occur.

6.3.2. Secondary emissions

S*econdary electron emission* from a metal surface occurs when an electron impinging on a surface has energy high enough to overcome the elastic contribution to the scattering. The elastic reflection coefficient is about 0.1 – 0.4 for energy range 3-20 *eV*

of the colliding electrons and decreases at higher energies [29]. For the plasma the inelastic contribution is a particle loss, given by an inelastic reflection coefficient always less than 0.5 for every material. Other phenomena include the energy loss of electrons due to Coulomb scattering with the material.

Secondary emission can also be due to *ion* impingement on the surface. As such, it is also called *Auger* emission [9, 13]. Ions impinging to the metal surface can lead to elastic, inelastic collision, or adsorption, possibly accompanied by electron-ionic emission. The electron emission due to ion bombardment can occur for two main reasons: if the ion impinging energy is about twice the potential needed for the electron to leave the metal, an electron *potential-pickup* occurs. The state "ion on the metal surface" can be considered as an excited state leading to a de-excitation via electron capture from the metal surface. The energy released can be transferred to another electron (*Auger effect*). The yield coefficient for monovalent *He* ions in this process is of the order of $\gamma_i \approx 0.3$ to 0.5, being much lower for other species. However, in case of multiply ionized atoms, it can reach values greater than one. Ions ordinarily do not posses the high kinetic energy to directly knock out electrons [9]. The ions build a thin and low potential barrier at the surface (the sheath). The electrons then tunnel neutralizing the ion. If the energy release exceeds the extraction potential, $I - e\varphi > e\varphi$ a further electron is emitted.
The electron yield on a clean tungsten surface for Ar^+ and He^+ impinging ions is reported in Table 6.4. For *He* this is a reference value only as a non-monotonic curve is instead necessary ([34] p. 230).

Ar^+	0.09 to 0.11	e^-/ion	0-1000 *V* ion energy [34]
	0.09	e^-/ion	≤1 *keV* ion energy [9]
	0.096– 0.095	e^-/ion	10 *eV*-100 *eV* (L94)
He^+	0.30 to 0.25	e^-/ion	0-1000 V ion energy [34]
			100 *eV*, [13]
	0.21	e^-/ion	≤1 *keV* ion energy [9]

Table 6.4 Ion secondary emission yields (e^-/ion) at different ion energies for *Ar* and *He* on tungsten. Data after [9, 34] , [13] and references therein.

The total yield (due both to electrons and ions), can be altered by 'impurity' layers on the target surface. It is perhaps worth mentioning the 1/3 reduction of yield for *Ar* on tungsten in presence of a layer of nitrogen (e.g. air impurities [29]).

In general the effectiveness of ion neutralization by a metal surface is relatively high; in the region 10 to 1,000 *V* ion energy almost all positive ions are neutralized at the surface [13]. For inert gas ions, the *reflection* coefficient without neutralization is of the order of about 10^{-1}-10^{-2} % [29]. From the probe operation point of view, this means that ions are almost completely 'collected' by the probe surface.

Evaluations

For a probe at a negative potential (biased or floating), electron emission is due to positive ions only. The emission coefficient is taken as $\gamma_i \approx 0.1$ electrons/ion (*cf* table 6.4) in *Ar* and $\gamma_i \approx 0.3$ electrons/ion in *He*. In order to evaluate the number of electron emitted per unit time by the probe surface an estimate of the flux of the impinging ions is necessary. In effect, it would be appropriate to consider all the phenomena occurring at the surface as consequence of ion striking the probe, i.e. "true absorption", corresponding to ion neutralization at the surface; and "true" secondary emission of electrons due to ion impingement, e.g. the surplus electron emitted *in addition* to neutralization. $\gamma_i \approx 0.1$ in argon means that 10% of the impinging ions free one electron from the surface. Experimentally, the measured (e.g. electron) current would consist of a 90% due to adsorption, e.g. recombination at the surface, and 10% to electron ejection. There is no way to distinguish between an electron that left the surface to recombine with the impinging ion (giving rise to the detection of a charge *e*), and the electron ejected from the surface as a result of ion scattering, which may leave either a charge *e* or 2*e*.

6.3.3. Discussion

Table 6.5 summarizes the different emission mechanism described in the previous sections. The average electron current densities emitted from the probe are compared.

Mechanism	Current density A/m^2	Formula/e Note
Thermionic	$j=6\cdot10^6\ Am^{-2}$ $j = 7.3\cdot10^3\ Am^{-2}$	(6.8) *W* melting *T;* *T*=2560 *K* (*W*)
T-F	$j= 6\cdot10^6\ A/m^2$ at 3,000 *K*, $j= 8\cdot10^5\ A/m^2$ at 2500 *K*, $j= 6\cdot10^2\ A/m^2$ at 2000 *K*, $j= 3\cdot10^{-1}\ A/m^2$ at 1500 *K*.	(6.17), [145] $E=4\cdot10^8\ V/m$
Field	$j_F = CE^2 \exp(-D/E) \approx 10^4\ A/m^2$	Nordheim-Fowler (6.11) $E=3\cdot10^9\ V/m$
Secondary	10% (*Ar*) –30% (*He*)	?

Table 6.5 Comparison of different emission currents on a probe

Within the great uncertainties outlined above, and taking into account the current densities impinging on the probe at 20-25,000 *K* (i.e. the currents reported in Chapter 5, divided by the probe surface) that vary from $j \approx 3 \cdot 10^2$ A/m^2 in the CFF model, see figure 5.8, to the flowing plasma $j \approx 10^5$ A/m^2 (Lam) or $j \approx 10^4$ A/m^2 (Su and Kiel), see figure 5.15, it appears that:

- *Thermionic emission* seems effective only for tungsten: too low current densities, $j \approx 10^{-4}$ A/m^2 are predicted for copper at melting temperature (*cf* figure 6.2)

- At comparable temperatures *T-F emission* dominates thermionic emission at all temperatures in both cases of 'low' (e.g. 0.5 *V*) or 'high' (-4 *V*) probe to sheath voltage (*cf* figure 6.2). In particular for the 'low' case, copper seems immune from T-F emission

- Purely *Field emission* seems negligible given the fields considered in this work, always lower than 10^9 *V/m* (at this fields, $j \approx 10^{-4}$ A/m^2)

- Thermionic and T-F emission currents given above at the tungsten melting temperature or slightly below, are always greater than any of the ion saturation current densities obtained in Chapter 5 (*cf* Table 6.5)

- *Secondary emission* is sensibly independent of temperature but dependent on surface and environmental conditions that may be much less than ideal (therefore reducing the yield γ) as outlined above. The values of the emitted current may be as high as 10% to 30% of the impinging ions, but is not distinguishable from the 'true' current. The effect would be a comparable overestimation of the collected charge as a consequence of surface electron depletion.

The 'worst scenario' is therefore the one dominated by T-F emission in the region of 'high' tungsten temperatures, 2,500 to 3,500 K, or the tungsten melting temperature in the thermionic scenario, where the current densities are close to $j \approx 10^6$ A/m^2, greater than any of the probe current densities values reported in Chapter 5: the current to the probe would then be mostly determined by emissions and the Langmuir probe would be of no use.

From the characteristic curve point of view, the analysis of thermionic and or field emissions was performed by Chang and Bienkowski [125] who studied the influence of emissions of half-Maxwellian electrons from the probe surface. They found that electron emission was both space-charge and diffusion limited. In their scheme, the

distribution of the potential from the (spherical) probe surface outwards, is characterized by the appearance of a maximum between the probe surface and the bulk plasma, in correspondence of an electron sheath, followed by a decrease towards the ion sheath edge and the transitional region to the quasi-neutral region ("double sheath"). According to CTT [37, 119], the consequences on the interpretation of the probe characteristic curve would be that the space-charge limitation phenomenon at low to moderate probe potentials, would invalidate both the ion and the steep electron attracting part of the curve, leaving the electron saturation region unaltered. The ion saturation current would be increased by the emission. The electron temperature could be determined provided a correction to discriminate the electron contribution from the apparent ion current existed.
This picture however, is relevant for tungsten, a material which is an emitter. The results shown above indicate that copper is immune to these problems.

6.4. Chemistry

In the bulk of the arc, a steady (if not equilibrium) density distribution n_o is attained, perhaps solely by ionization and recombination balance (i.e. neglecting external contribution from the power supply). In the vicinity of the probe, this 'equilibrium' is perturbed by the sheath; the electrical neutrality no longer holds and mass and charge diffusion, and heat conduction take place. When recombination and ionization rates are high enough, the "frozen-chemistry" may no longer hold (In *frozen* conditions the chemical reactions occur on a time scale much longer than the observer's time scale). This is true when the ionization density is significantly depleted near the probe and/or when the ionization rate an_i^2 and recombination rate an_o^2 differ substantially (a [volume/time] is the recombination coefficient, supposed equal to the ionization coefficient at equilibrium). The problem was analyzed by Carrer and Fendell [83] who considered both the cases of frozen and reacting gas ions, electrons and neutral species. The influence of recombination is expressed by the Damkohler number,

$$\mathrm{D} = n_i a r_p^2 / D_i \qquad (6.15)$$

where a is the recombination coefficient, dependent on temperature and the number density is named 'ambient' in [36] therefore presumably in the bulk of the plasma. The value of the Damkohler number can be seen as a suitable criterion for the departure from the frozen-chemistry conditions. According to CTT [37] the condition $\mathrm{D}<<1$ stands for frozen chemistry condition; conversely, $\mathrm{D}>>1$ would imply equilibrium (or *relaxed* conditions, in which the variations are so quick that on the time scale of interest an average stationary situation can be envisaged). Using a characteristic length L_D through the relationship [37]

$$\mathsf{D} = 2r_p^2 / L_D^2$$
$$L_D^2 = \frac{D_i}{an_{eo}} = \frac{\mu_i kT_i}{ean_{eo}} \qquad (6.16)$$

(Note that here with respect to (6.15) a factor 2 appears). A criterion for limited spatial extension of the 'chemical disturbance' would read

$$\lambda_D / L_D << 1 \qquad (6.17)$$

implying the occurrence of reactions limited to the ambipolar region of the plasma-probe region, which for the present circumstances would mean to the pre-sheath (as discussed in Chapter 5, the diffusional behaviour dominates outside the collisionless sheath) If instead $\lambda_D / L_D \geq 1$, chemical reactions should be accounted for in the sheath. According to definitions (6.15) or (6.16), the evaluation of the Damkohler value requires the knowledge of the particle densities, the recombination coefficient and the ion diffusivity within the sheath. These are evaluated in the following.

Sheath particle densities

Of the charged particle densities estimated in Chapter 4 the collisionless case expressed by equation (4.5) delivered the density at the *sheath edge* $n_s = n_b e^{-V_p/kT_e} = 0.61\, n_b$. A sheath depletion (a factor 100 to 1,000, figure 5.10) was given in the "matrix model", whereas, on the basis of condition $Re\alpha<1$, a qualitative conclusion of almost certain depletion was made (*cf* figure 5.14). In the continuum plus free-fall theories a charged density of the order of $10^{19} \cdot e^{|Vs/V|}\ m^{-3}$ can be estimated; provided the sheath edge to probe potential V_s is not far from the floating value (say, a few volts; for example, for $V_s = -4\ V$ and $V_f = -9\ V$, $V_s / V_f = 0.4$ and $e^{Vs/Vf} \approx 1.55$; in this case $n_i \approx 10^{19\div 20}\ m^{-3}$). Alternatively, at the sheath edge, evaluation of (4.17) gave $n_i \approx 10^{21}\ m^{-3}$.

Recombination

The major sources of recombination *within the plasma* were considered in section 2.9. An average of collisional and radiative recombination will be considered in the following for the two assumed (depleted) sheath densities, $a = 6 \cdot 10^{-20}\ m^3/s$ if $n_i = 10^{19}\ m^{-3}$ or $a = 2.6 \cdot 10^{-20}\ m^3/s$ for $n_i = 10^{20}\ m^{-3}$. Noticeably, in the bulk plasma the situation is rather different: the charged density may be higher by a factor 10^3, making the radiative contribution less important. In this case $a \approx a_c = 4.4 \cdot 10^{-11}\ m^3/s$, for $n_e = 10^{22}\ m^{-3}$ or $a_c = 4.4 \cdot 10^{-10}\ m^3/s$, for $n_e = 10^{23}\ m^{-3}$.

Ion Diffusivity

The ion diffusion coefficient can be obtained from Nernst-Einstein relationship

$$\mu_i = \frac{eD_i}{kT_i}, \quad D_i = \mu_i kT_i / e \qquad (6.18)$$

From the three estimated quantities, the Damkohler number (6.16) can be evaluated

$$\mathrm{D} = n_i a 2 r_p^2 / D_i = \frac{n_i e a 2 r_p{}^2}{\mu_i k T_i} \approx 2 \frac{n_i a}{T_i} \qquad (6.19)$$

Considering the two opposite situation:

a. sheath, with depleted density, $n_i \approx 10^{19 \div 20}\ m^{-3}$ and $\mu_i = 1.6 \cdot 10^{-4}\ m^2\ (Vs)^{-1}$. For a cold plasma with $T_i = 300\ K$, $\mathrm{D} \approx 0.03 << 1$ and it appears that the recombination effects in the sheath would be negligible. Of course, the use of a thermal temperature $T_i = 20{,}000\ K$, would make the contribution even smaller.

b. plasma bulk, $n_i \approx 10^{23}\ m^{-3}$ and $\mu_i = 1.6 \cdot 10^{-4}\ m^2\ (Vs)^{-1}$ and $T_i = 15{,}000\ K$, $\mathrm{D} \approx 5 \cdot 10^8 >> 1$ and the bulk would be subject to recombination.
Clearly, the magnitude of the recombination coefficient(s) and the degree of sheath depletion are decisive in establishing which of the two circumstances would occur.

CTT's criterion (6.17) would give, for the recombination coefficients pertaining to the bulk of the plasma (because obtained from an expression containing the bulk density n_∞) in the "thermal plasma" case (say $T_e = T_i = 20{,}000\ K$)

$$\frac{\lambda_D}{L_D} \approx \sqrt{\frac{\varepsilon_o a}{\mu_i e} \frac{T_e}{T_i}} \approx 3.8 \div 17 \qquad (6.20)$$

and also criterion (6.20) leads to recombination effects important in the bulk of the plasma.

Flowing plasma
In Smy's work [84] account is taken of the flowing plasma comparing the creation/recombination rates for ions (within the ion flux to the probe) occurring within a recombination time $\tau = 1/(a n_o)$, with respect to the flow time $\tau_f = r_p / v_f$. In this terms, recombination effects are significant if the time for recombination is greater than the time needed for the ion flux to cover a distance comparable to the probe dimensions:

$$\frac{\tau}{\tau_f} = \frac{1}{a\ n_o} \frac{v_f}{r_p} = \frac{\mathrm{D}}{\mathrm{Re}} > 1 \qquad (6.21)$$

According to the value of D found above and using the electrical Reynolds number 0.4 to 40 evaluated in Chapter 4, it is seen that condition (6.21) is never fulfilled within the depleted sheath; whereas recombination effects must be considered in the bulk.

6.5 Limitations due to perturbing action of the probe

Several perturbing effects on the *V-I* curve are reported in literature [65, 86, 88]:

1) Influence of the perturbing region with respect to ionization; the assumption that the probe current due to ionization is much less than the current drawn by the probe from the unperturbed plasma, requires the limitation (at high pressure and $T_e >> T_i$), $\lambda_{i,e} << R_{arc}$,

$$\delta_s << 0.2 \frac{R_{arc}}{\lambda_{i,e}} \left(\frac{T_i}{T_e} \right)^{3/2} R_{arc} \tag{6.22}$$

Assuming a 'worst scenario' sheath thickness $\delta_s \approx 10^{-5}$ *m* (*cf* figures 4.3 and 4.4) and using the values for the mean free paths reported in Chapter 2, $\lambda_{ie} \approx 10^{-6}$ *m*, this condition is fulfilled for an arc radius $R_{arc} \approx 10$ *mm* (say), in cylindrical geometry.

2) Influence of neglect of ion-electron collisions in the unperturbed region: for the ion part of the *V-I* curve and $T_e >> T_i$, if the scattering parameter $b << \lambda_{i,e}$, it is required that

$$\delta_s << \lambda_{i,e} \left(\frac{T}{T_e} \right)^{1/2} \tag{6.23}$$

For the electron part

$$\delta_s << \lambda_e \left(\frac{T}{T_e} \right)^{1/2} \tag{6.24}$$

(6.23) is 'just' verified if $\delta_s \approx 10^{-6}$ *m* whereas for smaller values there should be no appreciable influence of electron-ion collisions in the unperturbed region on the ion current. For thicker sheath or, if the perturbation region is of the order of the 'boundary layer', then (6.23) is never fulfilled and it is expected that ion-electron collisions alter the magnitude of the ion current.
Instead (6.24) is never achieved under the present circumstances because the electron mean free path is now $\lambda_e \approx 10^{-5}$ *m*. This is the origin of the statement that the characteristic curve method is not exploitable at "high" pressures (*cf* also Tichy [122]): at high pressure collisions destroy the electron part of the characteristic curve.

3) Electron Energy Distribution Function (EEDF). In general, it is disturbed both by probe and holder; the particles that recombine at the probe must be replaced by collisional ionization within the plasma. These two quantities can be compared as follows [86]. At the floating potential (i.e. at current equilibrium) the number of particles reaching the probe of length l and radius r_p per unit time is

$$\frac{2i_i}{e} \approx 2\pi r_p l \frac{n_o < v_e >}{2} \sqrt{\frac{\pi m_e}{m_i}} \tag{6.25}$$

On the other hand, denoting by R_d the extent of the probe disturbance, the charge production (ionization) within the (hollow) cylinder of length l and thickness R_d- r_p is

$$2n_o < v_e > \pi(R_d^2 - r_p^2) l / \lambda_i \tag{6.26}$$

so that the extension of the disturbance must be lower than the smallest mean free path for collisions with neutrals ($\lambda_m < R_{arc}$ here)

$$R_d^2 = r_p^2 + r_p \frac{\lambda_i}{2} \sqrt{\frac{\pi m_e}{m_i}} << \lambda_m^2 \tag{6.27}$$

With respect to the parameters of this work, the l.h.s. of (6.27) ~$4.9 \cdot 10^{-8}$ to $8.86 \cdot 10^{-7}$ whereas the r.h.s is ~ 10^{-8} to 10^{-12} i.e. (6.27) is never satisfied. Therefore, the extension of the perturbation induced by the probe cannot be neglected. This is not surprising as in (6.27) the main source of disturbance is the probe radius that, in low-pressure theories, is always smaller than any mean free path. This indicates that the electron part of the characteristic curve is not usable under the regimes of interest. The ion part of the characteristic curve can be used with perhaps acceptable approximation also in the worst case, i.e. in the fringes of the arc or, say, for $T_e \leq 7{,}500\ K$ (see Chapter 2).

According to Tichy [122] the "intersection" method for the determination of the plasma potential is more accurate than both the tangent method and the determination of the maximum of the second derivative of the current. A condition is set for the rounding effect of the knee of the characteristic curve to be negligible for the cylindrical probe

$$Kn_e(Kn_e + 1)\left(Kn_e + \ln\left(\frac{l_p}{r_p} \right) \right)^{-1} > 1 \tag{6.28}$$

where Kn_e is the electron Knudsen number and $l_p \approx 20\ mm$ ('active portion') and $r_p \approx 200\ \mu m$, the probe length and radius. The l.h.s of (6.28) is at most 0.4 when $\lambda_e=10^{-4}\ m$, but it is generally lower, down to 0.02 and 0.002 for shorter electron mean free paths ($\lambda_e=10^{-5}\ m$ and $\lambda_e=10^{-6}\ m$). Therefore, according to this author, the high-pressure regime implies that both the characteristic curve distortion and the rounding of its knee always take place. The last consideration, together with the failure of all the conditions 1) to 3) under the regime of interest in this work reinforces the conclusions about the low pressure theories as inadequate.
In addition, a part of the obvious requirement of attaining ion saturation, the reason why usually 'high and negative' probe potentials are used lies in the condition

$$\frac{r_p}{R_{arc}} << \frac{\lambda_i}{\lambda_e}$$

for the charge drained by the probe to be considered 'small' [65]. It can be noted that this condition is somewhat difficult to meet in the range $\lambda_i/\lambda_e=1$ to 10^{-2} (see Chapter 2) and $r_p/R_{arc}=5\cdot10^{-3}$ for $T_i=T_e$. In fact, one would obtain (*cf* figure 2.4)

$0.12 << 1, \quad T_i = T_e = 12,000K,$ moderate to high ionization
$0.12 << 0.01, \ T_i = T_e = 7,500K,$ low ionization

For non thermal plasma ($T_i<<T_e$) the ratio of the radii can be multiplied by the ion to electron temperature ratio, and the condition is easier to fulfil [65]. But it is questionable whether $T_i<<T_e$ can be used in conjunction with the reported mean free paths, computed for *thermal* plasma.

6.6 Summary

The following conclusions can be drawn from the analysis performed.

1) Ionization
Ionization plays a crucial role in determining the regimes for probe operation through important kinetic parameters described in Chapter 2. Almost none of the theories of probe operations account for degree of ionization higher than about 10^{-4}. These are typical of flames or low pressure plasmas. The only work dealing with relatively high ionized plasmas is the one by Su and Sonin [74]. The term 'moderately ionized' used by Su and Sonin is certainly appropriate as they treat ionization ratios up to about 10%, which imply for instance a Coulombic electrical conductivity (section 2.6). However, this is probably the only work that could be used if the *flow effects* were accounted for (which is not the case). In addition, it was shown that the effects of 'high' ionization were limited to the steep part of the characteristic curve.

2) *Heat transfer and cooling*

The heat balance between arc and probes proves to be a very difficult task. The evaluations made suffer from severe assumptions concerning the linearity of heat transfer for both the conductive and convective cases. These were found inadequate to describe situations in which the temperature gradients are not 'small' (section 6.4.1). It has been shown that the latter circumstance is not verified. This is the likely reason why unsatisfactory estimates were obtained when comparing conductive and convective values with the (few) experimental findings (section 6.4.2).

An upper limit for radiative transfer was evaluated in section 6.4.1 using published data (max 10^7 W/m^2 [140]), preferred to the 'unlikely' blackbody (10^9 W/m^2).
The comparison among the different heat transfer mechanisms cannot be made reliably until the conduction and convection contributions can be firmly established. A hint can be based on the generally agreed 'low' contribution of radiative heat transfer (perhaps few %) with respect to conduction, for arc currents limited to 100 A.

Within the uncertainties two different criteria were adopted to establish whether cooling is effective in depressing electron temperature (section 6.4.3) and in general, to what extent cooling could influence the interpretation of the characteristic curve. It has been found that both these criteria indicate that plasma cooling due to probes is not substantial, if not absent.

3) Probe emissions

Among the probe electron emission mechanisms, thermionic and field emission seem to play a role mainly for tungsten. Copper seems immune to thermionic effects. Problematic is the estimation of the emitted currents due to the steep temperature dependency. Also, the use of some information gained from the analysis performed on sheaths (Chapter 4) did not shed much light as the use of sheath thickness evaluated there to infer sheath electric potential gave values which are presumably too high and correspondingly, relatively high values of the current were obtained. Some values computed by different authors were reported. It appears that T-F emission dominates thermionic emission and for this reason, copper should be immune once more. Secondary emission was difficult to estimate as no theory which includes evaluations of 'true' current plus 'apparent' or emitted current was found. The use of the empirical reduction factor 0.1 to 0.3 only means that *if secondary emission occurs* then it is of the given order of magnitude. The problem lies in the difficulty in discriminating the extent of each contribution in the course of measurements.

4) Chemistry

In inert gas arcs, the chemistry lies in the existence and influence of the ionization and recombination processes both in the bulk and in the probe region (the influence of metastable states were not considered). While in the former case, some kind of

ionization equilibrium can be inferred, of which the ionization curve of figure 2.7 is an example (within the restrictions of LTE), the sheath poses its difficulty in the evaluation of the charged particle densities and the values for both ionization and recombination coefficients.
Conditions on the Damkohler coefficient based on density in the bulk plasma showed that chemistry is not important in the depleted sheath. In the bulk of the plasma, incorporating the probe boundary layer, the opposite is true and a charge reduction must be expected. A phenomenological version of the Damkohler criterion due to Smy agrees with the other criteria.

5) Perturbing action of the probes
The criteria based on geometrical quantities seem to show that in the limit of their applicability (questionable in the thermal case), a certain degree of disturbance translates into a non negligible ion-electron collisions when these take place in a region wider than the estimated sheath thickness. In this respect, alterations of the ion part of the V-I curve can be expected. However, the most important 'disturbing' factor is related to the electron part of the characteristic curve.

From the above discussion, it is concluded that no comprehensive probe theory exists for the highly ionized atmospheric pressure flowing plasma (the TIG arc), which is able to describe the effects of high ionization, heat transfer, emissions and recombination on the probe signals *at the same time*. Even if some of the non-idealities can be avoided (e.g. emissions by the choice of copper as probe material) the use of the characteristic curve in the terms described in Chapter 3 is not justifiable because it emerges that the retarding region and the electron saturation region are those which suffer most. For the ion part, the conclusions seem to indicate fewer problems. After all, the very few experimental works available on arcs show that ion saturation does occur; whether the interpretation currently accepted is applicable or not is left to the experiment.

7. INTRODUCTION TO THE EXPERIMENTAL INVESTIGATION

7.1. General observations on arcs

The TIG arcs studied in this work have currents limited within the range 50 to 200 *A*. Lower currents give rise to unstable and asymmetric arcs. Runs performed in the range 10 to 40 *A* showed unstable arc roots at both the electrodes where spots wandered about the cathode tip and across the anode plane. Current fluctuations of the order of 1 *A* were observed, whereas the voltage changed as much as 0.2 *V* to 0.3 *V*. These general features are independent of the shielding gas flow rate (changed by as much as 50% from the 10 *slm* used for Ar arcs throughout this work).

At currents from 45 *A* upwards, the spots at the electrodes tend to locate on the axis and the arc stabilizes; current and voltage fluctuations disappear and the common axy-symmetric bell shape is restored. It comprises a luminous spot in the *core*, extending from the cathode down to half-length and perhaps 1 *mm* wide. This region is enveloped by a less (but still) luminous region extending radially outwards for some millimetres depending on the arc current.

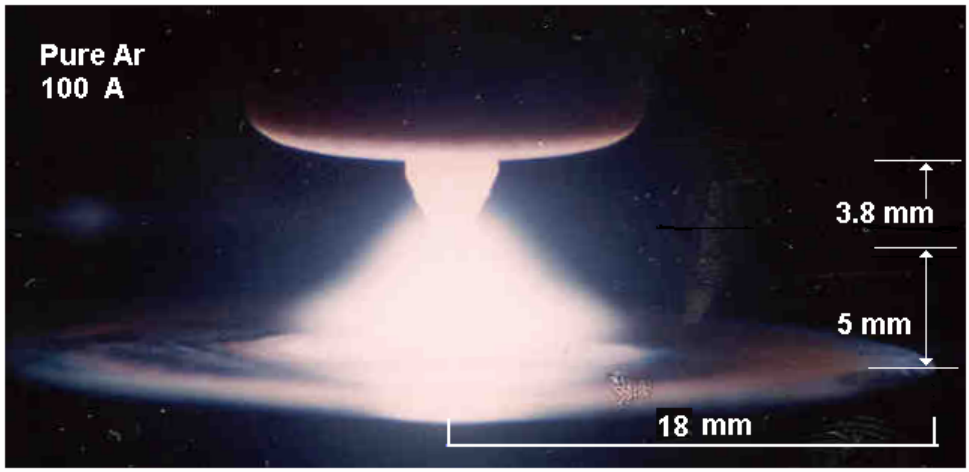

Figure 7.1 A 100 A argon TIG arc, with typical dimensions

The photograph of figure 7.1 shows a 100 A TIG arc in argon. Typical dimensions are also shown.

The variation of the arc voltage with the current, the *arc characteristic curve*, has the shape shown in figure 7.2 for the typical 5 *mm* long arc. The addition of helium and the increase of the electrode distance both have the effect of shifting the curve towards higher voltages.

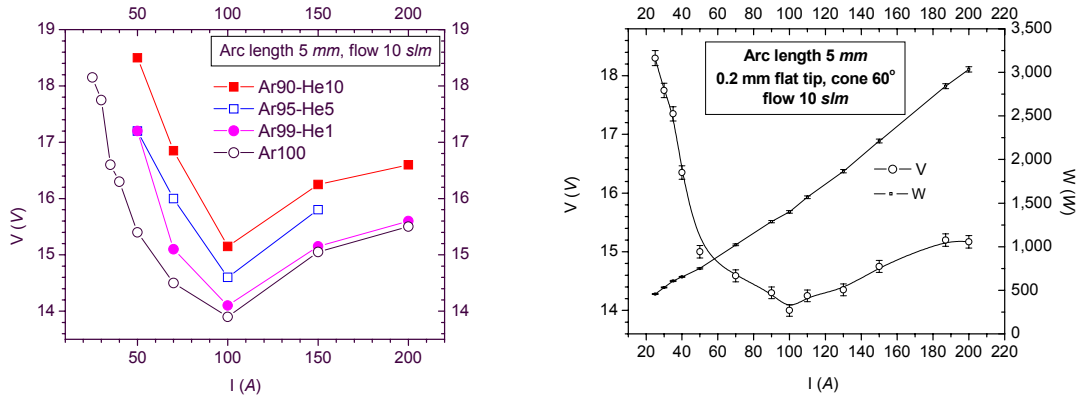

Figure 7.2 Left, some arc characteristic curves for argon and argon-helium mixtures. Right, measured characteristic arc and power curve for pure argon. Arc length 5 *mm*.

7.2 Range of parameters accessible to probes

The present investigation aims at the determination of the arc temperatures, the charged particle density, the electron and ion current densities, the electric field and the potential distribution within the TIG arc. Also, the onset of a sheath around the probes is investigated (sheath thickness and voltage fall). The techniques described in Chapter 3 will be assessed against experiment. In particular, the use of the characteristic curve requires an interpretation of the measured currents, both the ion saturation curve, from which the particle number density may be determined, and the steep part of the characteristic curve (when available) which could deliver the electron temperature or, in more general cases (e.g. non-Maxwellian), the electron energy distribution function (EEDF). The measured ion saturation currents will be compared with the predictions of the Continuum plus Free Fall theory (*cf* section 5.3.1.1, figure 5.8), with the diffusive regime currents of Lam and Clements and Smy for the arc core (figure 5.14). The current-temperature relationship with the "direct method" of Gick and Allum (*cf* sections 5.5 and 5.7.5) will be extended to these cases.

A sufficiently extended steep part of the *V-I* curve would allow the determination of the plasma potential although the latter can be estimated from the knowledge of the floating potential.
Attempts will be made to assess the existing methods of determining the plasma conductivity as given in section 5.7.4, and to verify whether a direct measurement, based on the use of current and voltage measurements is feasible.
Unbiased conditions and particularly floating conditions, are virtually absent from the literature on Langmuir probes in arcs with respect to plasma parameter determination. These methods will be described in the appropriate sections; a choice will be attempted between the different formulae for the floating potential; this choice can be assessed once the electron temperature is known. In general though, unbiased methods will be used to infer the *electric map* of the arc, with some caution with regard to the definition of the "electrical arc radius". The latter will be used for the determination of the local arc cross section at a given arc height. As the signals observed in biased conditions differ from the floating condition signals, both in extent and shape, a comparison of the biased electrical radius can be employed to reconstruct the arc current carrying region.
More complete schemes of the interrelations among the parameters investigated are reported in Chapter 9.

Because the characteristic curve method does not always give straightforward responses, an alternative path will be explored, which is based on simple kinetic considerations applied to the directly measured flux of particles impinging the probe, and to the independent measurement of the power per unit length sensed by the probe whilst immersed in the arc. Under a few simplifying hypotheses, these simple relationships allow the derivation of the energy per particle when striking the probe surface, the local particle density at the edge and the voltage fall across the sheath edge. These quantities can in turn be compared with the results obtained from the characteristic curve method. Also, to overcome some difficulties in the selection of the correct hypotheses, a comparison with independently determined temperatures and charged particle densities is made. The latter are determined from emission spectroscopy. The ultimate aim is to assess whether electrostatic probes can be successfully employed within atmospheric pressure flowing plasmas. Optical measurements, being in substantial agreement with other published work on the subject for identical experimental conditions, will constitute a framework for the assessment of the results obtained from probes.

7.3 Structure of the experimental Part

In Chapter 8, the experimental set up is described including design and construction details for the probe system. The characterisation from the electrical point of view is split into unbiased (and floating) and biased operating conditions because the electronic signal acquisition, although simple, differs in the two cases. The acquisition program is

briefly described leaving the code listings to the appendices. Biased and floating modes of operation, mutually exclusive with the present arrangement, are described together with the complete experimental procedure.
General analysis procedures are described in Chapter 9. The analysis of the electric signal is strictly related to a correct interpretation of the charge-capture mechanism in the plasma. Depending on the model assumed the latter might differ. A discussion of the possible line-inversion techniques employed has been performed even if a thorough comparison has been made elsewhere [1]. The procedural steps for the data analysis are outlined leaving some software implementation details to the appendices. The measurements, performed under different arc conditions are then described and a complete synopsis is reported of the experimental studies performed. In order to follow the complete procedure, this chapter contains some general consideration about the way the data are structured, extracted and aggregated. The aim is to single out details at this stage whereas the subsequent determination of the physical parameters of interest follows a case-by-case strategy in individual chapters. Chapter 10 contains the description of the way the different possible characteristic curves are built and how these are then used in the following. Also it contains simple kinetic relationships used to re-determine some of the physical parameters.

Chapter 11 explores thoroughly the possible method to determine the temperature, both by means of the V-I curve method or by the alternative (kinetic) methods outlined in the second part of Chapter 10.

In Chapter 12 methods for the determination of the plasma and floating potentials are described. Several attempts are presented to obtain these quantities from direct measurements as well as ways to derive these from primary measured parameters.
Attempts are made to evaluate sheath properties in terms of voltage fall and thickness according to the results of Chapter 3.

In Chapter 13 ion and electron current densities impinging on probes are shown and their relationship with the ‘true’ arc current densities is outlined. Also, requirements for a complete determination of electrical conductivity and electrical field are presented. The former can be determined directly from the measured current and voltage, or indirectly through the knowledge of the temperature. In either case, the use of the current density presented in Chapter 13 allows the determination of the field. Alternatively, the axial plasma potential can be used to obtain the corresponding electric field.

In Chapter 14 some of the results obtained in the previous chapters, are presented together in order to obtain a unified view of the TIG arc structure and properties that these parameters allow. In particular electric current densities and temperatures are

presented in two-dimensional maps and the notion of the current carrying region is explored.

Chapter 15 provides a summary and the conclusions of the whole work, following the order of the previous chapters, highlighting the main issues addressed and indicating possibilities of further work.

The experimental uncertainties arising in probe measurements are often substantially higher with respect to the relatively well established optical methods. This issue will be addressed during the discussion but the details of the uncertainty determinations will be left to the appendices.

8. EXPERIMENTAL DESIGN AND PROCEDURES

8.1 The Chamber

The system considered works either in open atmosphere, with the arc surrounded by air, or in closed vessel, ensuring control of the composition of both the 'environmental' and shielding gas. Arcs with mixed shielding gas were operated both in closed and open chamber.

The Chamber (sometimes 'vessel' in the following) has an outer diameter of 48 *cm*, an inner diameter of 43 *cm*, height of 56 *cm* up to dome; dome to top about 10 *cm*, approximate volume 85 *l*, volume of internal set up 12 *l* (Uncertainties about 10%). A Vyton® *O*-ring seals the chamber to the horizontal base plate; this hosts several feedthroughs for the electrical signals, the gas inlets and for the cooling liquid. A dual stage vacuum pump (Leybold TRIVAC-D16B, 16 $m^3/h \approx 4.4$ *l*/*s*) is connected to the chamber bottom plate and ensures an ultimate vacuum of 10^{-3} *mbar*. The pressure inside the chamber is controlled by an atmospheric gauge (Druck PMP100, 0-5 *bar* absolute) and a vacuum Pirani gauge (Leybold TR-211 tungsten filament gauge with a gas selectable Thermovac® TM20 controller).

Of the two gas lines, one is dedicated to the filling of the chamber (usually with Argon), the other leads to the cathode nozzle. The mass flow of the gases is controlled up to 1% by means of a Mass Flow Controller (Unit Instrument PRC-3000) capable of delivering up to 40 *slm* (full scale) on the *Ar* and *He* channels (see figure 7. 2).

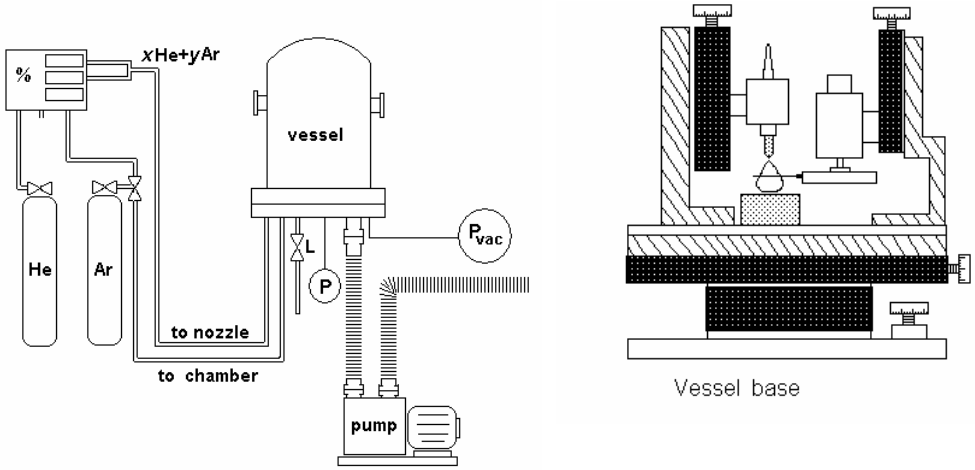

Figure 8.1 Left, the vessel hosting the experimental setup with gas and vacuum feedthroughs, and the gas system. Right, overview of the experimental basement contained in the chamber ("vessel").

Although unfortunate in its denomination, the *mass* flow is usually expressed in *standard litre per minute*. The standard litre is defined as the mass of specified gas occupying a volume of 1 litre at STP, 1 $slm = 2.97 \cdot 10^{-5}\ Kg\ s^{-1}$ of argon.

8.2 The arc system

The chamber contains a three degree of freedom manipulator supporting the electrode assembly and the multi-probe set up (figure 8.1, right). The whole arrangement can be moved vertically and horizontally by means of two stepper motors (Time and Precision Unislide). A third stepper motor allows the torch vertical motion to ensure arc ignition by electrical contact between the anode and cathode.

The TIG arc source is a water-cooled copper block torch. A threaded copper feedthrough keeps the cathode tip in place. The gas is fed laterally from a hose entering the cathode block (figure 8.2 right). After joining the hollow threaded feedthrough, the gas finds its way towards the lower end of the block through several holes oriented radially; it is then forced towards the cathode tip by the curved surface of the ceramic nozzle. The 3.2 *mm* tungsten 2% thoriated electrode is ground to a 60° included angle and truncated to a 0.2 *mm* flat top (figure 8.2, right) to prevent erosion, facilitate arcing operation and allow reproducibility. Although relatively complex in geometry, it is believed that the gas flow at the nozzle exit is laminar on the basis of an estimated Reynolds number below 10^{-4}.
The 37 *mm* copper anode disk is held in a water-cooled anode block and can be substituted after each run.

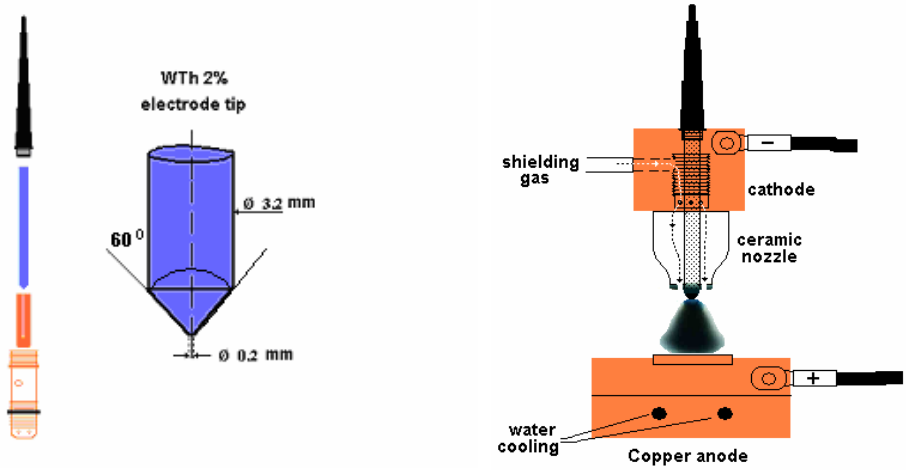

Figure 8.2 Left, particular of the cathode electrode set up and specification of the cathode tip. Right, complete arc torch set up. The anode is also visible.

8.3 The Power supply

The arc power supply consists of a series-regulated power supply (AWP H350SR by GEC Industrial Controls) capable of 350 *A*, 110 *V* and specifically built for the uniform and stable output of arc currents (output ripple less than 0.1 *A*). This system was originally built to control underwater welding stations and as such, it is made of a "Down" station computer which effectively controls the power supply and a "Top station" computer where the operator can choose the welding parameters. The two computers communicate through a serial link. Current and voltage rising time and slopes can be entered and current values can be input either to operate continuously with one setting or stepwise with several current values (for a duration of up to 3000 seconds each). The arc is struck by contacting the cathode tip and the anode; once the spark produced ignites the gas, the cathode is lifted in steps of 0.1 until the desired electrode spacing is met. The initial open circuit voltage is 85 *V* whereas touchdown current and voltage are selectable and are kept at 10 *A* and 1 *V* respectively throughout this work.

8.4 The multi-probe system

The multi-probe disk is placed inside the chamber on the 'arc assembly' (*cf* figure 8.1 right) and its individual components are described in the following sections.

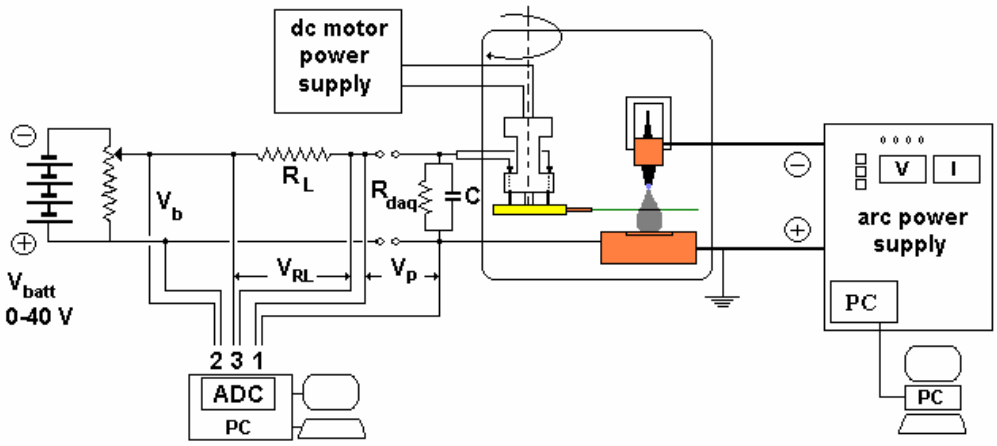

Figure 8.3 Overview of the experimental apparatus including the acquisition system with conditioning circuit. Probe disk assembly and arc power supply. Disk and electrodes set up are enclosed within the chamber shown in figure 8.2

8.5 Probe Materials

Thermal properties

Langmuir probes are traditionally made of refractory metals like tungsten or molybdenum. In this work, copper and tungsten wires where tested against factors including workability, and ultimately the choice of copper was made primarily because of the ease of fabrication. Also, as mentioned in section 6.3, this rules out emissions, possible for tungsten. Some thermal properties of both metals are reported in Table 8.1.

Metal / property	Copper	Tungsten
Density $\rho(kgm^{-3})$	8,960	19,300
Melting point ($°C$)	1,084.62	3,422
Boiling point ($°C$)	2,562	5,555
Fusion enthalpy H (kJ/mol)	13.0	35.2
Atomic weight μ (g/mol)	63.55	183.85

Table 8.1 Thermal properties of Copper and Tungsten [2]

The heat necessary to melt the probes $q=nH$ is a quasistatic quantity. H is the molar fusion enthalpy and n the number of moles of the metal sample. One can use the probe-

in-arc permanence time τ (of the order of some *ms*) to infer the heat flux that would be needed per unit time to melt the probe *within* that time. This power would be the upper limit of the heat flux to the probes. It should be noticed that the possibility of direct vaporization and therefore the use of sublimation heats have been neglected. Taking the enthalpy of fusion from Table 8.1, using typical probe geometry (L=50 *mm*, r_p=10^{-4}*m*), q=2.88 *J* for copper, q=5.80 *J* for tungsten, an average power q_{Cu}= 576 *W* or q_W = 1160 *W* is necessary in the two cases to melt the probes within (say) 5 *ms*.

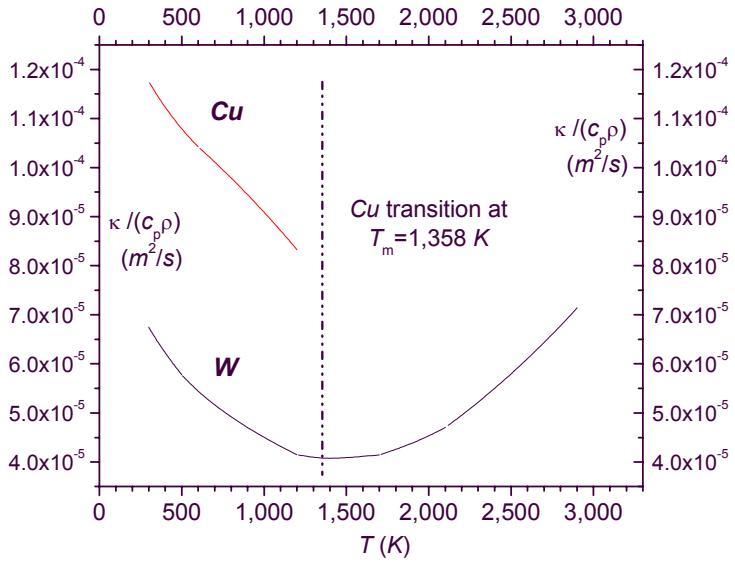

Figure 8.4 Thermal diffusivity of tungsten and copper as a function of temperature

From the melting temperature alone, copper should be ruled out as a suitable material. However, the thermal diffusivity of the two materials [ratio of thermal conductivity to density and specific heat]

$$D_T = \frac{\kappa}{\rho c_p}$$

shown in figure 8.4 as a function of temperature, differs by only a factor of about 2 over the interesting range of temperatures (i.e. below the melting temperature of copper) indicating that copper may be used.

Electrical properties

Figure 8.5 shows the electrical resistivity (left) and the resistance per unit length (right) for both copper and tungsten wires. The probe diameters shown are the typical values chosen within this work.

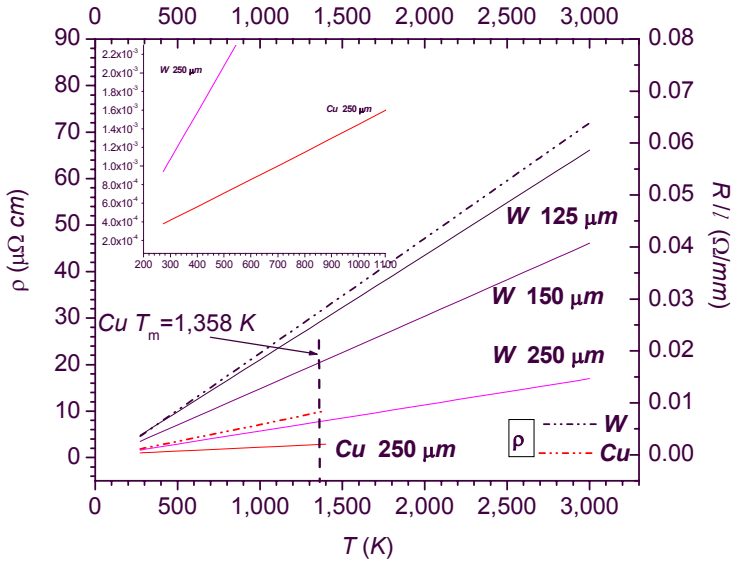

Figure 8.5 Left, electrical resistivity of copper and tungsten as a function of temperature. Right, electrical resistance per unit length for some probe diameters (see text). Inset: particular for copper wire resistance.

It is worth noting that an "equivalent plasma–wire" of comparable size has a resistance per unit length varying from 2 to 20 Ω/mm depending on the chosen plasma conductivity, taken here between 10^3 and 10^4 $/(\Omega m)$, see Chapter 2. Thus it is a factor 1,000 or higher than *Cu* wires and a factor 500 or more than *W* probes. This issue will be discussed later in connection with probe signal.

Other properties

Concerning oxide formation due to varying thermal conditions, comparatively low temperatures are needed to form *Cu* and *W* oxides (below 300 ^oC for *W*) while the copper and tungsten oxides melt just above 1200 and 1500 ^oC respectively; WO_2 boils and Cu_2O decomposes at about 1800 ^oC, which is 'low' even when compared with the arc fringe temperatures. Oxide formation is not an issue when working in controlled atmosphere (closed vessel) as oxides possibly present on surfaces are destroyed in arc conditions and cannot reform during cooling outside the arc in an oxygen-free atmosphere. However, oxidation might be a disturbing phenomenon when operating in open chamber conditions, especially for tungsten probes.

8.6 Probes system constructive details

Probes

Cylindrical probes (wires) of copper and tungsten with diameter varying from 50μ*m* to 250 μ*m* have been constructed. The choice of the cylindrical geometry is determined by simplicity of construction; the choice of the diameter aims at a "good" spatial resolution. The alternative spherical form had to be ruled out because of the need to construct holders of insulating material sufficiently small to avoid significant arc alterations and 'spurious' charge collection.

With an arc of radius 5 *mm*, characterized by steep variations of physical parameters within distances of few microns (temperature for instance, *cf* section 2.9), attempts were made to keep the wires as thin as possible. However, the harsh thermal environment at the highest values of the currents (150 *A* and 200 *A*) prevented use of copper wires with diameter lower than 250 μ*m*; for example, copper probes of 150 μ*m* are destroyed when the current reaches 150 *A* in *5 mm* long arcs. These limitations were found by considering the compromise between arc current and minimum probe velocity to avoid melting. Tests were performed at various probe velocities (0.5 to 5 *m/s*) to ascertain the optimum probe-in-arc permanence time with respect to the characteristics of the signal. The chosen diameter corresponds to a lower limit for the spatial resolution of about four probes/*mm* e.g. 40 probe diameters would cover the whole arc section, also implying that accuracies less than a probe diameter are meaningless. For tungsten probes, the corresponding lower limit for the diameter is 125 μ*m*, doubling the spatial resolution. The axial resolution is worse as a limited number of probes was employed (12, but more often 11) to scan the electrode spacing along the arc axis. Several types of probes were constructed.

1) Tungsten wires (Advent W557512) 0.125 *mm* diameter, overall length of 40 to 60 *mm* 2) Copper wires (Advent code CU510515) 0.250 *mm* diameter); 3) some commercial wire (e.g. copper alloy), diameter 0.125 *mm*. All the probes were straightened manually and individually crimped into copper-nickel sleeves.
Wires are usually delivered wound on reels of some centimetres in diameter so that when freed from the reel these showed a residual curvature which had to be eliminated. From the construction point of view, it was much easier to construct straight copper wires than straight tungsten wires, especially for diameters greater than 100 μ*m*. Copper can be easily straightened by hand using flat pliers and a vice.

Defining a measure of straightness *s* as the ratio of the average $<\delta>$ of the end displacements from a straight line passing through the probe mid length, δ_1 and δ_2, to the probe length *l*, (all lengths in *mm*), a value less than $s = <\delta>/l = 0.5/50 = 0.01$ was obtained for copper probes, making their shape practically indistinguishable from a straight line with the naked eye.

A procedure similar to the one used for copper wires was adopted for tungsten but the resulting straightness as defined above, $s \approx 0.05$, was poor with respect to copper probes and the wires presented additional irregularities along the length.

Disk and motor assembly

The probe holder consists of a brass disk, 80 *mm* in diameter, rotating in the horizontal plane orthogonal to the arc axis. Its vertical edge surface is drilled with 12 holes where the probes can be plugged in. The holes are spaced by 30° on the horizontal plane and graded vertically in 0.5 *mm* steps, starting from 0.1 *mm* from the lower surface.

When the disk is kept at the proper distance from the arc centre (from 85 to100 *mm*, as high as possible to minimize the non-parallelism error) the horizontal distance between two probes is larger than the arc diameter and only one probe at a time can be within the arc. On the disk top surface small holes accommodate precision screws that are used to lock the probes in place.

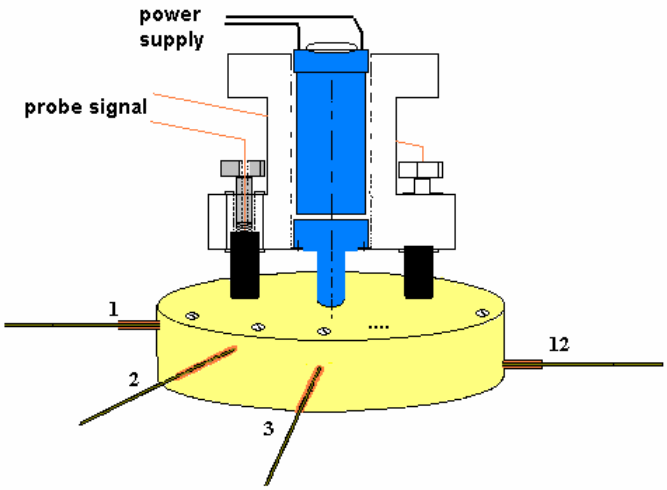

Figure 8.6 Motor and probe disk assembly. Probes mounted at different heights.

In almost all the tests conducted, one hole is left empty ("gap") to facilitate probe identification (see Chapter 9). In principle it is possible to mount a few more probes instead of the chosen 12, but if only one probe at a time is required in the arc, this would make the probes impractically long (beyond about 70 *mm*). With maximum probe lengths of 60 *mm*, it is believed that the bending induced by drag with the atmospheric pressure gas is negligibly small. This was qualitatively assessed by rotating the disk in air up to 5 *m/s* and observing the probe shape using a stroboscopic light system. In any

case, permanent (e.g. non elastic) probe deformation after runs in the arc were not found.

Two squared section carbon brushes mounted vertically 180 degrees apart collect the charge from the disk upper surface towards the acquisition circuit. The choice of two instead of one brush placed at symmetric position with respect to the disk axis was made in order to balance the mechanical action of the brush and its wear by friction against the brass surface.

The disk was rotated by means of a dc motor (Maxon, 0-25 *V*) able to deliver a rotating speed of 700 *rpm* under disk load (e.g. with the disk mounted) and equipped with a special gearbox. The central speed of a probe mounted on the disk is variable from 'zero' (in practice a few *mm*/s due to friction), to about 5 *m*/*s* by means of a dc voltage power supply (Farnell Ltd, 0-30 *V* d.c.). In order to correct for oscillations of the motor axis, a system made of conical ball-bearings was mounted between motor and gearbox, thus decoupling the disk from the axis oscillation. This resulted in a final oscillation of the disk about the horizontal plane not perceivable by the naked eye, but quantifiable in few microns at the disk edge, as measured by means of a clock (Dial gauge or Dial Test Indicator) placed on the disk surface whilst in rotation.

A certain degree of fluctuation in the angular velocity is unavoidable. This is due to the intrinsic fluctuations in the supply voltage, the intrinsic non-uniformity mechanical response of the motor and to the friction of the carbon brushes on the disk surface. The fluctuation was quantified initially by using a stroboscopic light source, with frequency set to follow the motion of the stroboscopic image of a probe holder. To evaluate both the rotation speed and its fluctuation, a *He-Ne* laser beam illuminated the disk lateral surface. Attempts were made to keep the probe holder image on the laser spot or, at least, at a fixed distance from it, but the image slightly drifted either forward or backward with respect to the spot. A crude measurement of the time needed by an image to reach the position of the spot back and forth, covering the distance between two subsequent holder images, was performed and repeated with the image both drifting forward and backward with respect to the spot, and finally averaging the results. The angular velocity as a function of voltage imparted to the motor was very irregular at all voltages, indicating either a highly fluctuating rotation speed or the inadequacy of the stroboscopic instrument used.
Repeating the measurement with a tachometer put in contact with the disk edge (the contact was held 'as light as possible'), several sets of measurements were recorded at each motor voltage and repeated reversing the motor rotation. Results for the angular velocity as a function of the motor voltages are reported in figure 8.7 (The error bars correspond to an error of less than about 3%).

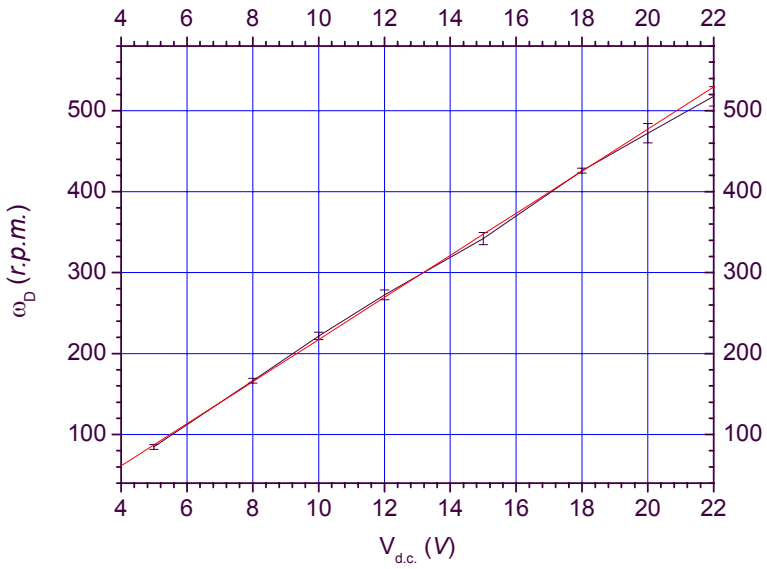

Figure 8.7 Probe disk velocity as measured with a wheel meter system. Error: 2 to 3%.

The absolute value of the angular velocity was checked against the value obtainable using the analysis of the readings (probe signals). Knowing the radial path of the probe R_{path} and the time T needed to obtain the same peak (period), the linear probe velocity at the corresponding radius is determined, $\omega = v/R_{path}$, $v = 2\pi R_{path}/T$. This was found in good agreement with the values reported in figure 8.7. In later measurements, this 'electronic' method was preferred for its superior accuracy and because it intrinsically incorporates possible speed drifts variations caused by the frictional wear due to carbon deposits on the brass disk surface (i.e. the speed is measured as a by-product during *each* probe dataset).

Probe assembling and mounting

Each probe was obtained by crimping the straightened wire into a holder made of a standard electronic "socket /pin" (made of commercial copper alloy) cut at mid-length and freed from the external steel layer. Probe lengths varied between 58 and 60 *mm*.

Figure 8.8 Probe mounting. Left, bending at holder edge.

The manual insertion of the probe in the holes of the disk does not preserve the straightness of the probe and holder assembly; an angle is likely to form at the probe close to the socket edge (figure 8.8) and sometimes also the holder is deformed. Therefore, after the probes were in place on the disk their straightness was re-checked and, when necessary, adjusted manually. It should be noted that this complex series of operations results in non equi-spaced probes along the vertical direction in the majority of the cases. In some cases also the 'grading' along the vertical direction is not preserved. For example, measuring probe heights from the anode plane, a probe inserted in hole number j might end up at a height h_j *lower* than h_{j-1}. In contrast to conventions used in the literature on arcs, the anode disk plane is taken as reference. The *vertical* position of the probes and their straightness was measured with the aid of an ocular with micrometric vernier, allowing a maximum precision of up to 0.01 *mm* (figure 8.9, left).
The *radial* alignment was checked with the aid of a common low power *He-Ne* laser mounted on a support with adjustable height: the probes were considered reasonably straight when their entire length fell within the laser beam width (Practically when a relatively uniform sheath of light enveloped the probe length). The laser was aligned with the disk axis and the probe screw; the disk was then adjusted vertically to match the beam. The laser beam *was made visible* with the aid of some smoke.

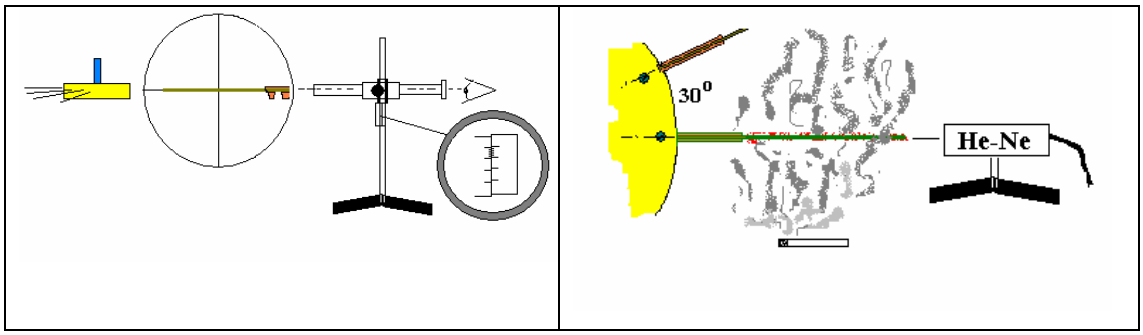

Figure 8.9 Probe vertical positioning with ocular and vernier. Right: laser beam enveloping the probe surface (made visible with some smoke) to check for horizontal straightness

Probe biasing system
The probes are biased with the aid of a power supply (see figure 8.3). In the first version of the system a bench-top power supply (TTI, 0-35 *V*, 0-10 *A*) was connected with the negative output to the probe and the positive lead to the anode of the chamber through a series resistor. However, this arrangement was unsatisfactory for reasons clarified in section 8.7.2. A set of three to four batteries (~12 *V*, 7 *Ah* each, *Pb*-acid type) were therefore connected to a manual rheostat (Berco, R=0 to 10.8 Ω, I_{max}= 8 *A*). The voltage was selectable in the range 0 to ±38 *V*.

Data Acquisition System

The acquisition consisted of a simple conditioning circuit which is detailed in section 8.7 and a commercial acquisition board. The first measurements were performed with an Amplicon PC30AT ADC board, (0 to 10 *V* analog input, 12 bit resolution, ±1 *LSB*=4.88 *mV*) operated at its maximum rate of 30 *kHz* (software sampling) on a single channel in floating conditions. In subsequent measurements a four-channels board (National Instrument PCI 6110E, 0 to 42 *V* analog input, 12 bit resolution, max. sampling 2 *MS/s* on each channel, equipped with a signal box SCB-68), was employed at up to 70 *kHz* on each of the three channels used.

To ensure repeatability, in the early measurements the acquisition program stored up to 10 data files (150 to 300 *ms*) per arc current condition.

The performance of the circuit was tested with respect to the response to an input signal with the aid of a signal generator (TTI TG2001) and an oscilloscope. Both sinusoidal and square wave form signals were fed at the input terminals, with frequencies varying from 10 *Hz* to 100 *kHz*. As a result, a small capacitor, *C*=20 *nF* was placed in parallel to the read-out resistor R_{DAQ} when operating in unbiased (or floating) condition, for resistors up to 1 *k*Ω (but not for the highest used, 211 *k*Ω). The "load" resistor R_L was kept to a few ohms (4 Ω in the course of the measurements presented in the following chapters). Some circuit details and the choice of the resistor values are discussed in the next section. The signal generator was also used to check the timing of the signals when operating with the first acquisition board.

8.7. Probe circuits

The basic requirement in both floating and biased conditions is to draw the least possible current from the plasma to avoid perturbations induced by the probe.

Several unsuccessful attempts were made in order to construct a single circuit suitable for the two operating conditions at the same time. To keep the structure simple, it was decided to use two alternative set ups, interchangeable during operation. These correspond to the two parts separated by the empty circles shown in figure 8.3 and are described as follows.

8.7.1. Unbiased and floating conditions

The circuit shown in figure 8.10 was used for unbiased or floating operation, the two conditions being distinguished only by the value of the resistor R_{daq} used. The probe resistance, sum of the combination probe-tips + disk + carbon brushes + leads was considered negligibly small with respect to all other impedances except the arc resistance (an actual four-wires measurement supported this statement).

Referring to figure 8.11, the read-out resistance R_{daq} was chosen after a set of preliminary runs in order to:

- keep the current drawn from the arc to a minimum by ensuring $R_{daq} >> R_{pl}$. For the purpose, an average value for the plasma "resistance" R_{pl}, can be estimated from the slope of the arc characteristic curve. From figure 8.1, at 50 A, $R_{pl} \approx 0.3\ \Omega$, whereas at 200 A, $R_{pl} \leq 0.1\ \Omega$.

- keep the voltage drop across the resistor (probe potential) within the typical 0-10 V limits of commercial DAQ boards. This was the case for tests performed with the earlier board; with a National Instruments board this was not an issue.

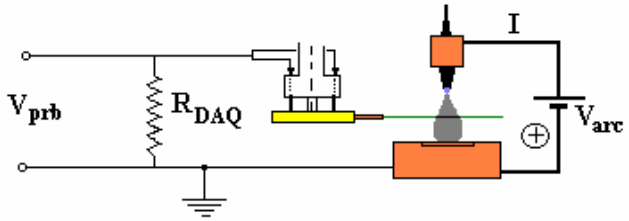

Figure 8.10 Circuit for floating operation

In the first case, a voltage divider was used to keep the read-out voltage low, but the multiplication of the read value by the voltage divider ratio $(R_2+R_1)/R_1$ added a corresponding noise level to the signal. The final choice was made of a $R_{daq} = R_1 = R_2 = 10\ k\Omega$ with the voltage read across R_2. The value of the capacitor in parallel with R_{daq} was felt satisfactory in noise reduction at $C=20\ nF$ up to about 1 $k\Omega$.
In the second case, a single resistor was chosen in the range 149.5 Ω to 219.0 $k\Omega$, to perform both unbiased and floating measurements (see section 8.7).

Choice of the read-out resistor
A range of resistors was tested in order to:

1. Achieve floating conditions by increasing the resistor value from its unbiased value.
2. Operate in unbiased conditions, with the (initial) aim of studying the variation of the signal due to resistor changes and possibly of determining the plasma conductivity (*cf* Chapter 13).

1. Even if a 'high' R_{daq} is chosen, rigorous floating conditions are never achieved as a small current $i_{prb}=V_{prb}/ R_{daq}$ will always be collected by the electrode. Voltage and current signals are of the kind shown in figure 8.11 (for arc current $I=90\ A$).

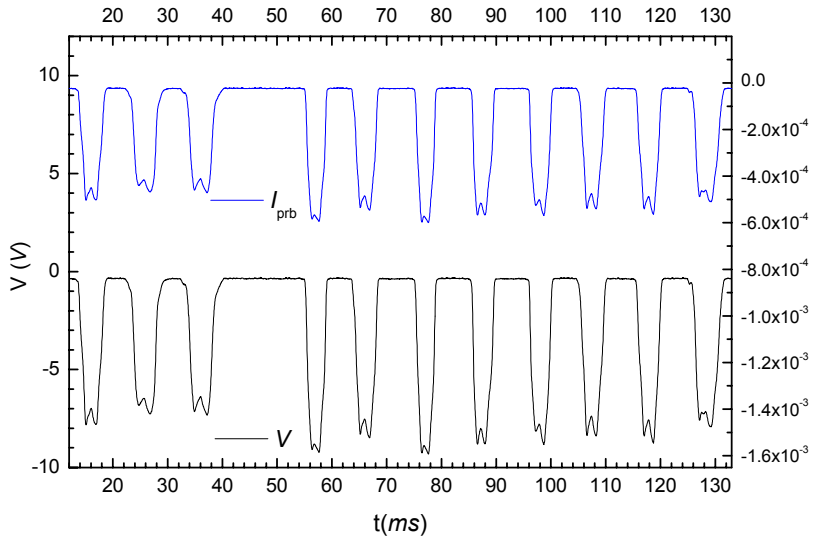

Figure 8.11 Probe current (upper signals) and voltage (lower signals) for I_{arc}=90 *A*. Read-out resistor R_{daq} ≈15.54 *k*Ω (see text)

In practice however, true floating conditions can be obtained using a sequence of increasing resistors.

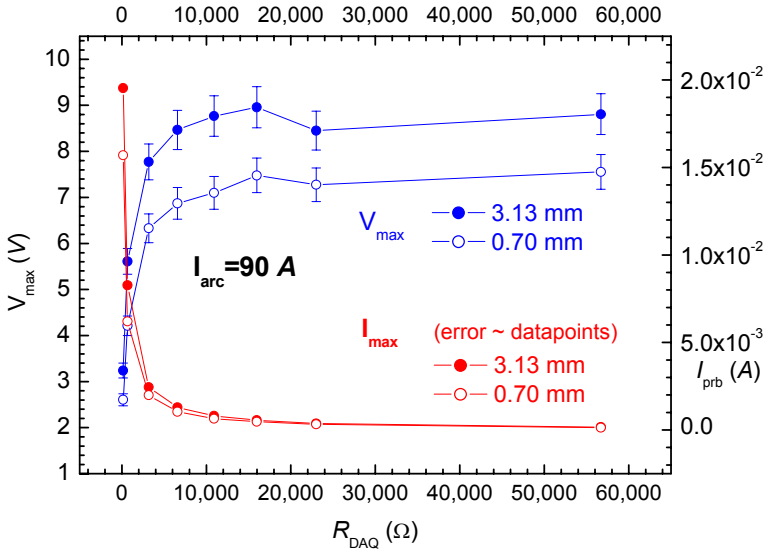

Figure 8.12 Variation of central voltage and probe current for two different probes as a function of read-out resistor R_{daq} for I_{arc}=90 *A*.

It is observed that the increase in probe voltage fall upon R_{daq} shows tendency to saturation. In the present circumstances, the threshold value of R_{daq} for saturation was observable just above 15 $k\Omega$, see figure 8.12).

Figure 8.12 refers to the signals shown in figure 8.11. The current is shown on a linear scale to emphasize its rapid convergence to small values (I_{prb}= $5.6\cdot10^{-4}$ A and $4.6\cdot10^{-4}$ A for the highest and lowest probes respectively, at $R_{daq.}$= 15.98 $k\Omega$). Two curves are shown for two different probes (e.g. heights within the arc). Results for other arc current conditions and different probes are very similar.

The justification for identifying the onset of voltage saturation as 'floating conditions' (corresponding to zero probe current in biased conditions) is given below. It is anticipated that the difference between these two measured probe potentials, is always below the experimental uncertainty.

2. For the purpose of checking whether the plasma conductivity is accessible to measurement in unbiased conditions, a series of resistors ranging from a few ohms to a few $k\Omega$ was employed. It is intuitive that the order of magnitude of the read-out resistor must not be too far from the resistance of the plasma resistance, less than 1 Ω. From general arguments (see e.g. [3]) it follows that in floating conditions a sheath voltage of the order 0.5 kT_e is not unreasonable. For $kT_e \approx 1$ eV, $V_{pl} \approx 0.5$ V and therefore the resistor must be lower than the one used in floating conditions (for the case considered above less than 15.98 $k\Omega$).
More quantitative observations suggest that one should measure the plasma conductivity in the region of (or below) the plasma potential. The latter however is not known *a priori*. If it were, the current corresponding to the condition $|V_{fl}| < |V_{pl}|$ could be estimated and matched against the current shown in figure 8.12 (right axis, I vs R_{daq}), to read the corresponding resistor. However, the mentioned current has to be determined from biased measurements, e.g. from the characteristic curve (see section 8.7.2). It is anticipated that depending on arc current and on probe heights the probe voltage interval –8 to –3 V should be used. Since the V curve shown in figure 8.13 is rather steep, the corresponding resistor interval is relatively broad (from 100 Ω to 3 $k\Omega$).

8.7.2. Biased conditions

The circuit used fro biased measurements is shown in figure 8.13. A load resistor R_L is placed in series with the probe, and the current through the probe $I_{prb} = V_{RL} / R_L$ can be read upon variation of the battery voltage. The voltage across R_L is read as a floating signal. The bias voltage V_b is read upon variation of the setting of the rheostat, manually operated, whereas the battery voltage is fixed. The probe voltage V_{prb} is read in this

configuration. This redundancy can be used for checking purposes and to determine the additional series resistance corresponding to the rheostat setting if needed.

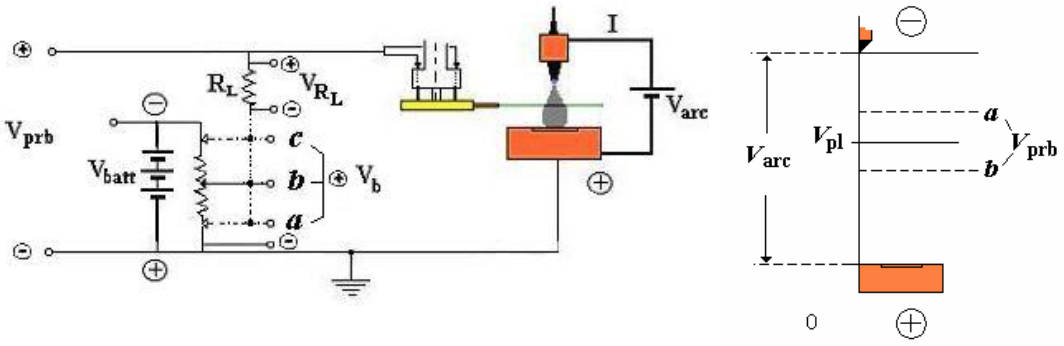

Figure 8.13 Circuit used in biased conditions. Legend: V_{prb} probe potential; V_{batt}, constant total battery voltage; R_L, load resistor; V_{RL} fall across load resistor; V_b, applied voltage (bias), measured from *a*, *b* or *c* and earth. Polarity at battery corresponds to 'negative' bias (see text). Polarities indicated by 'small' circles refer to the sign of the voltages as seen at the acquisition channel. Right, some voltage references (see text)

The polarity of the batteries shown in figure 8.13 refers to a nominal 'negative bias', when V_b has negative value with respect to the anode (thus 'nominal'). The polarities shown by the *smaller* circles at the individual voltages points refer to the way the signals are connected to the (differential) channels of the acquisition board. For example, V_{R_L} is positive if the point labelled '⊕' is at a higher potential than the point labelled '-'. Similarly, V_b will be negative whenever its '⊕' (either *a*, *b* or *c*) is at a lower potential than the ground (anode), which, from the point of view of the single channel acquisition, is 'negative', thus labelled '-'.

The value of R_L was chosen to be large enough to limit the current drawn by the probe (thus higher than the 1Ω used by Gick *et al*) but low enough to provide sufficient sensitivity (see below). The probe biased by regulating the rheostat between the positions labelled *a* to *c* in figure 8.13. The effective bias will be the value of V_b diminished by the voltage fall across the load resistor R_L. In what follows it is assumed that the plasma potential is not greatly altered by the insertion of the probe in a 'sufficiently restricted' region in the probe surrounding (this questionable assumption is made here for simplicity and is discussed further and justified in Chapter 10).

A probe outside the arc is biased at $V_{prb} = V_b$, it enters the arc and the effective voltage, V_{prb}, will now differ from the baseline value V_b, e.g. $V_{prb} = V_b - V_{RL}$ because of the probe current flowing through R_L. Taking the polarity as shown in figure 8.13, the following

scenarios, represented in figure 8.14 and 8.15 (examples of voltage signals), are considered.

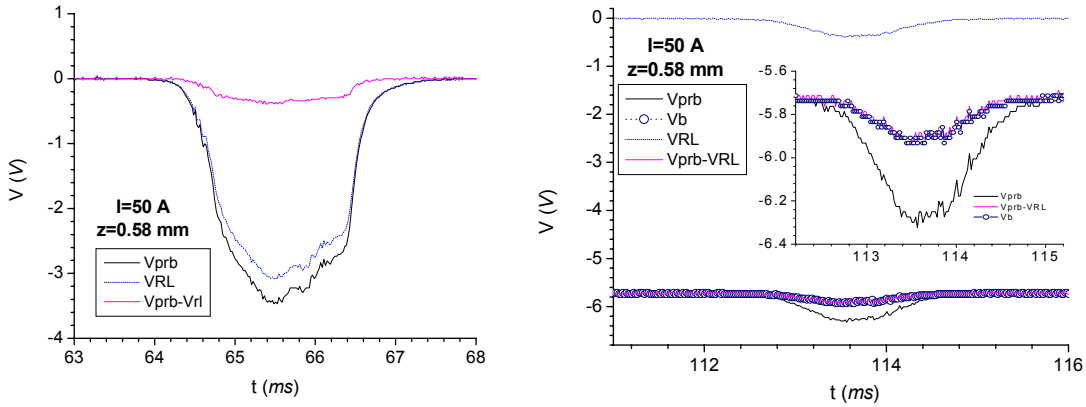

Figure 8.14 *I*=50 *A*, probe N.12, z=0.58 *mm*.
Left, voltages in biased configuration at zero bias. This correspond to rheostat set at position *a* in figure 8.14. Black line, V_{prb}. Dash-dotted, V_{RL}; continuous grey, difference of the two. Reference to case 1 in main text.
Right, the same quantities (with inset showing V_{prb} difference to V_{RL} and V_b in open circles, almost indistinguishable from the latter) at a nominal bias V_b=-5.7 *V*. Rheostat at 'some' position *b* in figure 8.13. Reference to case 2 in main text below

Case 1. Rheostat shorted, e.g. V_b=0 (figure 8.13, point labelled *a*). The probe is in unbiased (however non-floating) conditions and it will attain a negative potential, whose value depends on the resistor R_L chosen. The current drawn by the probe, of the order of 0.1 to 0.5 *A* depending on arc conditions and location within the arc, is "negative" implying a net draw of electrons from the plasma. The voltages are shown in figure 8.14 left.

Case 2. A 'small' negative bias is applied to the probe. (Rheostat is at a position *b* in between *a* and *c* in figure 8.13). The probe will attain a potential $|V_{prb}| < |V_{pl}|$, *cf* dotted line *b* in figure 8.13 right. Both current and voltage signals are negative. The current drawn is now lower than in the previous case (in absolute value) and will decrease further upon increase of bias (e.g. V_b more negative) until it reaches 0. The corresponding probe potential V_{prb} is then the probe reading when the probe is at floating potential $V_{prb} = V_{R_L} + V_b$. Tests performed in all the experiments presented in this work have shown that this value of the probe potential coincides with the potential measured in floating conditions of section 8.7.1 within the limits of the experimental error. As in the previous case, down to $V_{prb} = V_{pl,}$ probes are positively biased with respect to the plasma. Figure 8.14 right, shows the voltages for a bias still 'positive' with respect to plasma (the current is negative). It can be seen that the difference

between the probe potential and the fall on the load resistor, is indistinguishable from the bias.

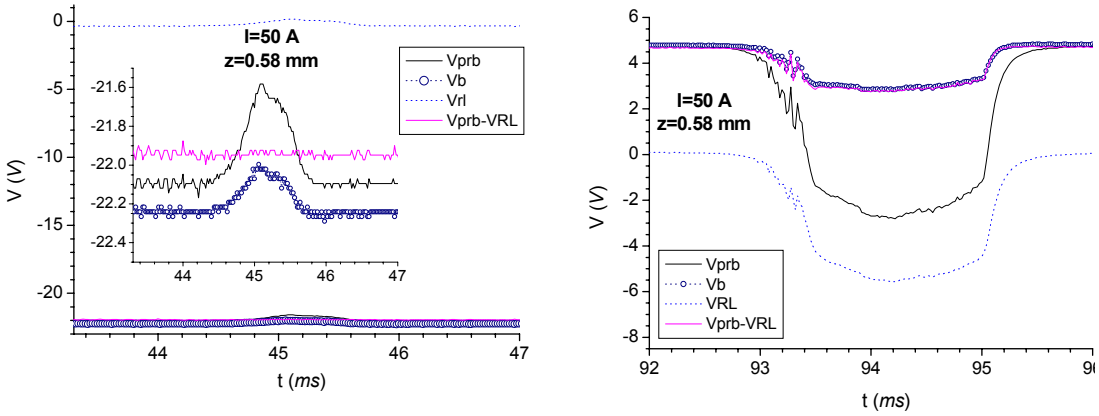

Figure 8.15 I=50 A, probe N.12, z=0.58 mm.
Left, voltages at bias corresponding to ion saturation, $V_b \cong$-22.2 V. Rheostat set at *b* (close to *c*) in figure 8.13. Black line, V_{prb}; dash-dotted, V_{RL}; continuous grey, difference of the two; open circles, bias V_b. Reference to case 3 in main text. In the main of the figure the positive V_{RL} is visible corresponding to a positive current.
Right, the same voltages at a nominal 'positive' bias V_b=+4.80V. Rheostat at 'some' position *b* (close to *a*) in figure 8.13 but with inverted polarities. Reference to case 4 in main text

Case 3. Decreasing the bias further sets the probe at a negative potential with respect to the plasma and the recorded peaks progressively appear more and more positive with respect to the baseline (dotted line *a*, figure 8.13 right). The net current is now positive. Also, depending on probe position and on arc current, it can show saturation (ion saturation of the *V-I* curve, *cf* Chapter 10). An example of voltage signals is shown in figure 8.16 left, for a nominal bias V_b = - 22.2 *V*.

Case 4. Reversing polarity implies that with respect to the case described in Case 1, the probe attains a potential more and more positive with respect to the floating potential. Relatively modest positive biasing leads to high electron currents whose magnitude is comparable with the ion saturation current. Examples of the different voltages are shown in figure 8.15 right, for a nominal bias V_b = + 4.80 *V* ('nominal positive bias'). Whether this is also positive with respect to the plasma potential remains to be seen and it is discussed further in Chapter 12.

Choice of load resistor

Currents of the order of 1 *A* and above are very easily drawn from the arc; a part of any consequence on the validity of the *V-I* method, discussed later. This implies that considerable power may be drawn into the acquisition circuit. In order to limit the power and keep the design as simple as possible, a high power load resistor was chosen. The (contrasting) requirements for a 'good' load resistor value are:

1. R_L should be kept as small as possible to succeed in biasing the probe; in fact the location of the resistor (*cf* figure 8.13) implies that a voltage fall will occur before the probe;

2. R_L should be kept high enough to prevent a large current being drawn from the arc.

The voltage that enters the equation for the power, $W=\Delta VI$, is the difference between the effective probe voltage and the bias voltage imposed; the latter constitutes a baseline set and maintained until the probe is out of the arc and from which the probe voltage peak amplitudes depart. Once in the arc, probes sense the local potential and try to compensate by drawing a net current.

In previous tests a dc generator (TTI, 0-35 *V*) was used as biasing system but it was abandoned in subsequent measurements. In fact, due to an *RC* stage at the output of the unit, a distortion in baseline and peaks was observed: when the power supply was set at zero, and the probe entered the arc sensing a local potential of (say) 5 *V* the capacitor started to discharge with a delay dependent on the $\tau=RC$ of the system, see figure 8.16.

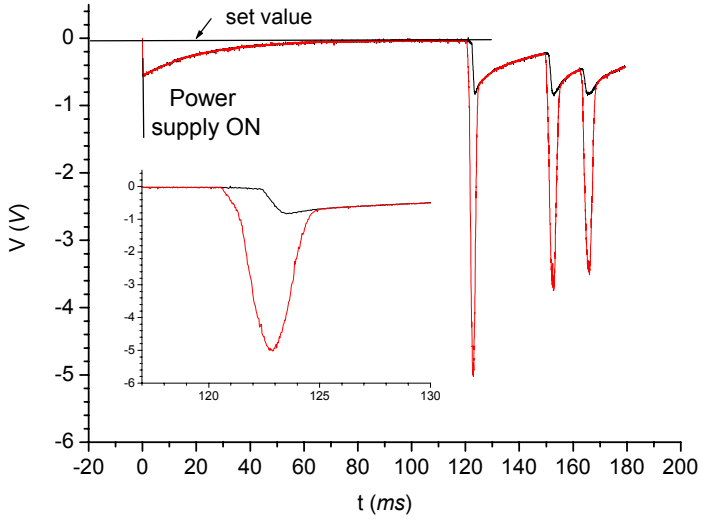

Figure 8.16 RC-like behaviour with power supply. Few voltage peaks (first enlarged) are shown together with the bias voltage ("set value")

A set value of zero bias resulted in a 0.35 to 0.5 V voltage displacement, gradually 'compensated' in a time $\tau \approx 120$ *ms*. When the peak started its "natural" decrease, the power supply tried to follow the probe starting a discharge. The effect was observed also at biases from –1 to –4 *V*. In addition, a reversal of polarity revealed a constant offset of 0.35 to 0.45 *V* between the two configurations at nominal zero voltage. Both effects disappeared when using batteries.

An observation about the general features of signals reported so far is necessary. The preceding discussion implicitly assumed a uniform potential. In fact, every probe exhibits a *peaked* signal each point corresponding to a specific region of the arc at a given time. "Plasma potential" and "floating potential" may differ in neighbouring points within the plasma and are intended above as a guidance for the discussion. In other words, a probe may sense (and a single probe signal may be at) floating potential at a specific point and time instant, being above or below this value when in a neighbouring point. This will be discussed in connection with the interpretation of the data.

Uncertainties
The overall *V* read and acquired across R_{daq} is subject to uncertainties determined by:

- class of the resistor
- resistance variations with time
- uncertainty of the voltage readings

All the resistors chosen had 1% tolerance. The time variations of the resistances were monitored during operation and it was found that during a typical set of measurements, a variation of less than 0.5% was normal. This is lower than the error determined by the tolerance class. The uncertainty on the voltage depends on the 12 bit resolution of the acquisition board which corresponds to 1 *LSB*=4.88 *mV* in bipolar mode. The source of error on *V* is determined by the statistical fluctuation of the signal, which is assumed to follow a Gaussian distribution. A statistical analysis revealed that it would be consistent to take the total uncertainty of the voltage measurement as the standard error of the mean, e.g. the standard deviation divided by the number of readings (every dataset, corresponding to a complete family of probe signals, is made of 7,500 points).

8.8. Experimental procedure and conditions

8.8.1 Procedure

The complete set of operations performed to run the probe system is summarized in the following steps and discussed below:

1) closure of the bell chamber and pumping down to about $4 \cdot 10^{-5}$ *mbar*;
2) argon admission at atmospheric pressure followed by new pumping (i.e. 'flushing' of the chamber);
3) argon admission and filling of the chamber at a pressure slightly exceeding the atmospheric pressure (1.1 *bar*) to impede impurity entrance from the external environment;
4) preparation of the arc shielding gas mixture either pure *Ar* or *Ar-He* ("processing gas" in the following) and admission through the arc nozzle (cathode);
5) regulation of a spill valve in order to compensate for the shielding gas flow entering the chamber through the nozzle (e.g. to maintain constant chamber pressure);
6) arc ignition upon short circuit at controlled current (10 *A*);
7) separation of the electrodes with onset of the selected current; the arc voltage varies accordingly;
8) multiprobe motor put in rotation at the selected speed;
9) start of probe data acquisition program in unbiased and floating conditions by changing the acquisition resistor in the specified range during the measurement;
10) in biased conditions, variation of the probe voltage bias in order to construct the *V-I* curve, by manually regulating the rheostat

Steps 1 to 5 are performed when operating in closed vessel. When operating in open vessel condition the sequence starts with step 4 (when dealing with mixtures) or 6 (for pure argon arcs). In order to ensure that the arc surroundings are not contaminated with ambient moisture the vessel was evacuated in about half an hour to the limiting pressure allowed by the pump and the chamber set up. The chamber was then filled with argon up to a pressure of 1.1 *bar* and then flushed through the vacuum pump; this operation should reduce residual contaminants. For the same reason the chamber was kept slightly overpressure with respect to the external atmosphere. In step 4 the flow controller sets a pure *Ar* or if required, a *Ar-He* mass flow (mixture within 1%). The use of a manually operated spill valve, step 5, is necessary to hold the chamber pressure constant as a gas mass flow of 6 to 10 *slm* would significantly increase the chamber pressure and therefore alter the arcing conditions. These steps are necessary when running with gas mixtures.
Step 9 and 10 constitute the measurements of the arc properties by changing the read-out 'on the fly' according to the requirement discussed in section 2.6.

8.8.2 Experimental conditions

The distance between the electrodes has been kept constant at 5 *mm* to adhere to the conventional TIG arc length conditions prevailing in the literature. The same applies to the choice of the shielding gas mass flow range, always between 8 and 10 *slm*.

The rotation speed of the multi-probe disk has was chosen after a careful analysis of the signals obtainable. Several factors were considered. In the first place, depending on the acquisition speed of the board it was felt that each probe signal could be satisfactorily characterised by some hundreds of points; in almost all cases a value of 100 to 300 points was chosen. Moreover, the inversion procedure needed to extract local information is very sensitive to 'fidelity' to the original data (*cf* Chapter 9). This restrains the maximum speed. Also, for probe speeds comparable to the plasma flow (100 to150 *m/s*, see Chapter 2), a vectorial composition of probe and plasma flow velocity would be needed. To avoid this complication, a value of few m/s was chosen accordingly (5.02 m/s for the results presented). Secondly, to avoid probe destruction, especially at the higher power, a lower limit for the probe speed had to be set. The compromise was in the range 2.5 to 5.1 *m/s*. Some checks performed within this restricted range, did exclude alterations of the signal characteristics (*cf* Chapter 9).
The full immersion of each probe within the arc, with the emergence of a portion of a comparable (if not equal) length at the opposite side has some advantages. First, assuming a cylindrical symmetry of the arc, the probe is homogeneously subject to the same electrical conditions when moving from the probe edges towards its centre.
Moreover, small bodies are especially subject to the well-known "point effect" when immersed in a region where a significant electric field exists. As a consequence, the increase of the local electric field at the probe end when the latter is immersed in the plasma, could cause the drawing of a considerable current by the probe, greatly altering the properties of the arc, which is undesirable.

8.8.3 Type of measurements

It is important to note that a set of measurements is always completed within a few minutes ensuring that the experimental conditions (arc, state of the probes and electrodes, temperature of the electronics) are reasonably constant. In addition, when operating in single component gas, steps 9 and 10 are repeated for all the programmed probe biases voltages along a complete sequence of pre-determined arc currents, e.g. without interrupting the arc. This was not always possible because of 'incidents'. With the exception of the arc power supply and of the acquisition program, everything else was operated manually.
In the earlier measurements, performed only in floating conditions, the whole range of arc currents (50, 70, 100, 150 and 200 *A*) could be completed in 15 to 20 minutes depending on the number of multiple acquisitions per experimental point. In the later measurements, 20 minutes were necessary to scan a single arc current (floating, unbiased and biased measurement). The *whole range* of arc currents (50, 70, 100, 150 and 200 *A*) could be completed in about 100-110 minutes. It is worth noting that this duration is of the order of magnitude of the duration needed for an emission spectroscopy experiment to collect data for a *single* arc current [4].

9. DATA ANALYSIS PROCEDURES AND VALIDATION

9.1 Introduction

The analysis techniques employed in this work aim at the understanding of the operation of the Langmuir probe instrument and at its applicability in the arc environment in order to obtain information on arc structure and properties. These two purposes cannot be distinguished easily.

In this chapter attention will be limited to the general procedures required for parameter extraction from the measured data irrespective of their physical basis. The present chapter has the role to 'filter' out the procedures which are then employed in the following chapters where the discussion will be concentrated on the physical information gained.
In section 9.2 the general methods for the determination of the plasma parameters in biased and floating conditions are summarized. General features of the peaks and their variations upon bias are reported in section 9.3 whereas an illustration of the use of the peaks is presented in section 9.4. A brief discussion on the Abel inversion technique, extensively used in this study, is made in section 9.5.

9.2 Procedures description

9.2.1 Summary

Figure 9.1 shows a schematic of the links between the measured parameters and the possible derived quantities. These are the methods selected on the basis of the review performed in part I and believed to be applicable to the present experimental conditions. Some correlations, which were assumed at the beginning of the analysis stage (e.g. prior to assessment with real data), were dropped because inadequate or unpractical or inaccurate for the present conditions.

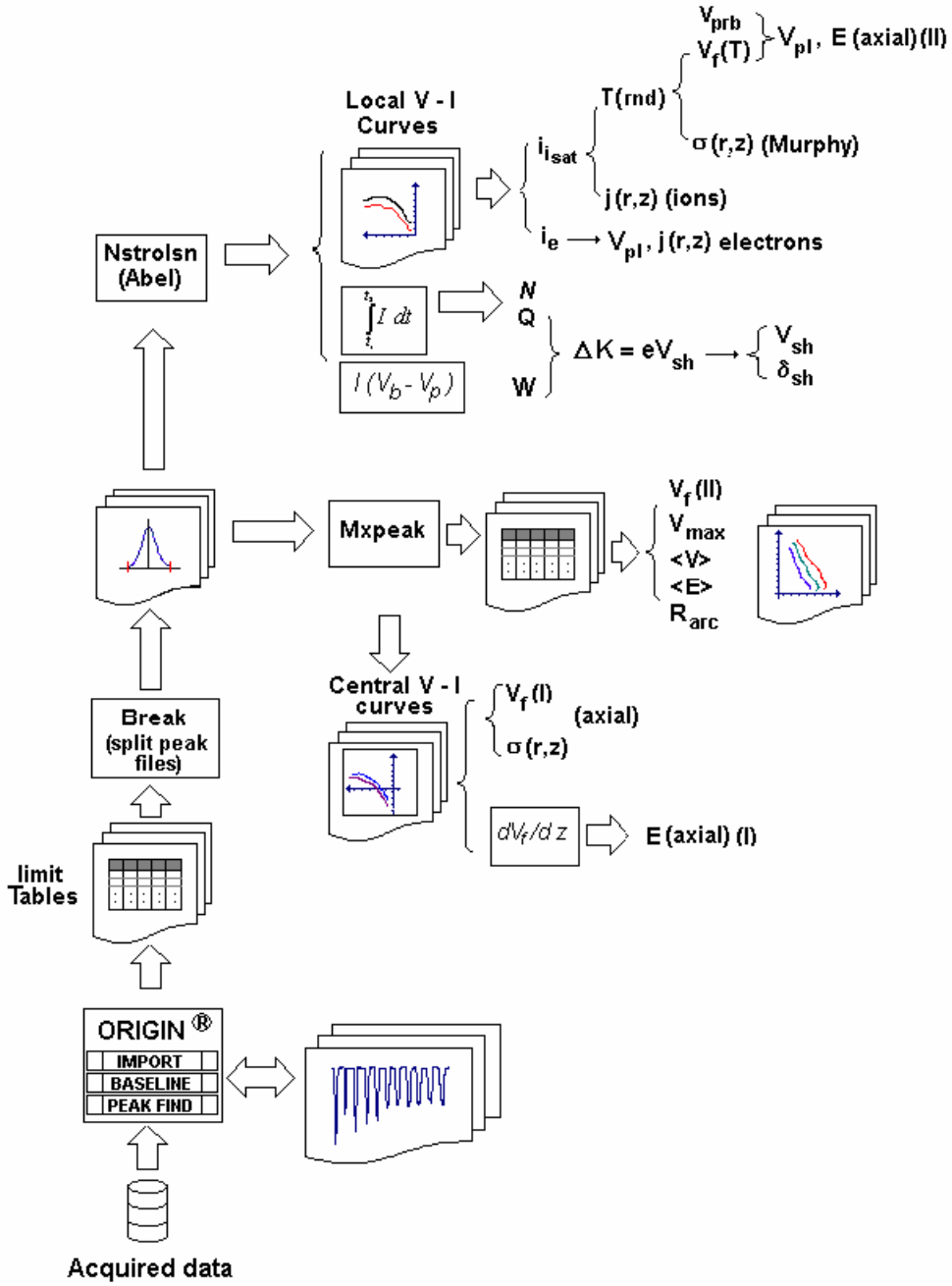

Figure 9.1 Analysis procedures: possible paths for data treatment (see text). Symbols as in Notation (*pp* ii onwards)

Using figure 9.1, read from the bottom upwards, a summarized description of the various steps follows.

9.2.2. Analysis steps

Raw data are pre-treated using a commercial package, with the purpose of extracting single peaks feature from each dataset. These are stored into separate tables, one for each dataset and subsequently accessed by independent programs and routines.
The creation of these tables is the longest and most delicate step. Due to variability of probe signals (probes in different position), different biasing conditions, sometimes data-set dependent background, this phase of the analysis had to be performed 'by hand'. There are two reasons for this.

- In the acquisition system no trigger is available; therefore when the measurement starts, it is not known which probe will be acquired first in the dataset. Due to harsh environment no easy technical solution has been found (e.g. photodiode to mark the passage of a certain probe). There is obviously the need to assign to each probe signal ("peak" in the following) a probe name and therefore a height within the arc. For this purpose, as indicated in Chapter 7, a probe position is left empty; from the knowledge of the gap angle and duration, the whole probe sequence can be reconstructed. A criterion (e.g. a program), based on probe signal to background comparison, could be used only in floating mode (because in biased mode the reference is the variable biased voltage, different for each dataset) and on the condition that all probes are placed at consecutive increasing heights (which is not always the case, *cf* Chapter 7). Therefore, it was abandoned.

- Even if some software tools are available to search and characterize peaks in a 'spectrum' (as in specialized spectroscopic software) there is always a chance of failure in both finding a peak and in determine properly its edges. Sometimes within the same spectrum, very similar peaks are treated differently. Similarly, a purposely written program, based on a clear-cut background criterion also showed variable behaviour ('good' for one dataset, bad for the following experimental conditions) and was therefore abandoned.

The manual procedure is then as follows. The Origin® Baseline Tool was used to construct a baseline and the "Find Peak" tool to locate peak heights and edges. The spectrum was inspected to correct by hand the location of the peak edges and the central peak value, if necessary. This procedure is certainly not rigorous and to some extent depends on the observer's judgment. However, tests performed by selecting a point rather than the two neighboring ones, at the maximum graphic resolution, showed that the error of 'judgment' was certainly much smaller than the error on the read quantities. The situation is worse for current peaks close to the floating potential (where the current approaches zero) because the judgment of width and height is more uncertain. The

alternative (e.g. automated procedure) would be to discard these peaks. It was decided to keep these as the situation close to floating conditions is particularly important.
The central value of the peak instead of the maximum was chosen in this phase; the two may differ because of the occurrence of multi-peaked signals. This information was used to construct averaged V-I curves (cf Chapter 10). The data subset made of probe number-arc height was used throughout the analysis for both averages and local values.
This procedure was followed for voltage datasets (in floating conditions measurements), or for voltage and currents for datasets originated from biased conditions. The resulting 'peak feature tables' ("PF tables"), containing peak center coordinate, voltage or current value and peak edges, are central for the subsequent analysis for both biased and floating conditions.
With respect to the first, these tables can be used to determine radially averaged, chordal averaged and local *V-I* curves (*cf* Chapter 10).
With respect to unbiased and floating conditions these tables can be used to determine:

- The floating and plasma potential (with consequent estimation of the electron temperature;

- The conductivity from direct measurement or as a derived quantity;

- The charge unbalance in unbiased conditions and electron current estimation in floating conditions.

The same PF tables were accessed by a subsequent routine to calculate the electrical radius as seen by the probes using the known probe speed and the duration of the signal both in floating and biased conditions.

A program ("Break") used the information in the PF tables to split the original dataset into individual peak files. These files were then accessed by different programs depending on the action needed. Following the flow-chart in figure 9.1

- The local energy, e.g. the integrated power collected by the probe, given by the I_p (V_p - V_b) was compared with the charge obtained above to infer an average energy deposited per ion.

- The potential curves (floating potential variations in the axial direction) were obtained, which allowed the calculation of the *axial* electric field by differentiation).

- Local values of plasma parameters were obtained after performing an Abel inversion (NstrOlsn routine, central upper part of the diagram in figure 9.1). Of

the very high number of possible *local* V-I curves obtainable, only a few are selected (see discussion in Chapter 10).

Starting from the initial dataset ("ASCII" in figure 9.1), the procedure was as follows.

9.2.3 Background subtraction and Peak individuation

A typical complete dataset peak is illustrated in figure 9.2 left. It refers to the biased configuration, but with zero applied voltage.
Background subtraction was performed using inter-peak intervals and/or initial/final part of the signal "spectrum". The background differs depending on the experimental conditions. In most cases, biased voltages presented a contribution with respect to the ideal zero baseline of about 25 *mV*, see figure 9.2 right.

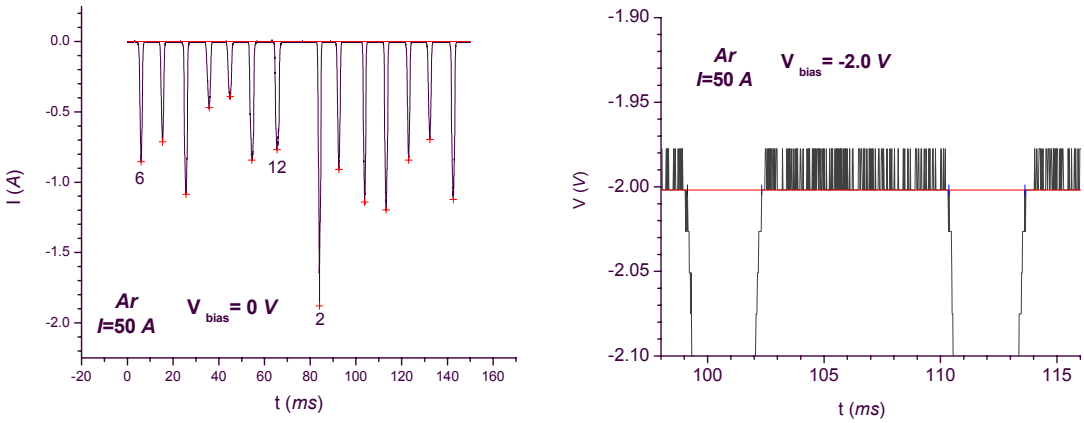

Figure 9.2 Left, typical peak family at zero bias in biased operating conditions. The data markers (crosses) refer to the 'maxima' of the peaks (see text). Right, background band of ~25 *mV* for a nominal bias V_b=–2*V* case.

For the biased case situation of currents close to zero (e.g. closer to floating conditions) the contribution was typically 50 *mA* (see figure 9.3 left).
Using Origin® (Baseline Tool) it was possible to enter a specific type of baseline and, upon request, subtract it from the signal. This was done in the floating case (with respect to zero) and for the currents in the biased case. The voltage signal in the biased case is referenced to the applied biased voltage, which is the probe voltage prior to entrance into the arc.

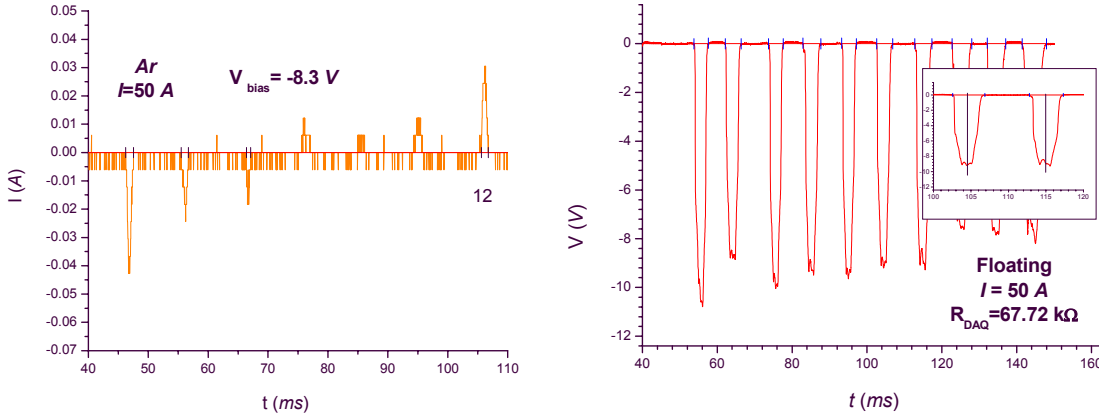

Figure 9.3 Left, portion of peak family in biased conditions V_b=–2V close to plasma potential; some peaks are negative others are positive. Right, central peak values taken in place of the 'maxima' for the floating condition dataset (see text)

Upon different biases this reference varied and therefore a subtraction *was not* performed. The other reason why it was not performed is that the peaks present in different orientation with respect to this line, either 'below' it up to the floating potential, or 'above' it for increased negative bias (figure 9.3 left). Despite this asymmetry, it is worth noticing that the contribution of the background to the relative error on the measured *voltages* is of a few percent therefore totally negligible.

Subtracted or not, the baseline level was used by a subsequent Origin® (Find Peaks) routine to find peaks maxima and edges. Especially in floating conditions no unique peak maximum can be established due to the more complex peak structure, and the central coordinate and height are determined by hand (voltage or current, depending on the dataset, see figure 9.3, right). This applies also to peak edge positions, sometimes shifted considerably with respect to the criterion of 'intersection' with the baseline. This lengthy procedure was performed by hand on each of the dataset of both biased conditions, 21 to 25 files per current condition, plus 4 'unbiased' files (of which one floating). Each contains 11 peaks (actually more were recorded for consistency check purposes, typically 14 to 15); thus over 300 peaks for each experimental condition. This resulted in a set of 21 to 25 "PF tables" (one for each dataset) per experimental condition. Since each experimental condition corresponds to one arc current case and because the latter are I=50, 70, 100, 150 and 200 *A*, about 125 of these tables were built by hand examining individually over 1,700 peaks.

9.3 Some signal features

9.3.1 Peak shapes

Although the analysis of the data performed in this work pertains to peaks obtained in exactly equal experimental conditions it is of interest to establish whether a dependency of the peak shapes on probe velocity exists. This has been checked in two ways:
1) by comparing peak shapes obtained at different probe velocities;
2) by looking at the differences between the leading and trailing edges in the peak shape.

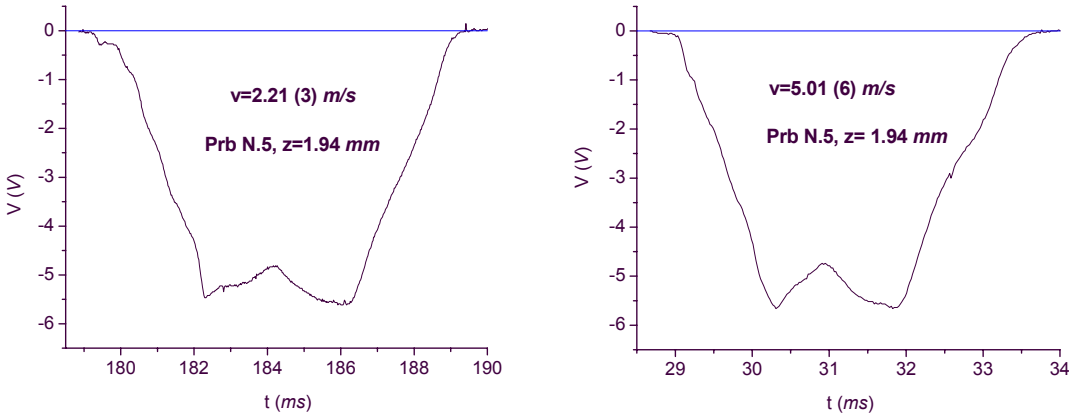

Figure 9.4a. Two peaks chosen for signal structure comparison upon probe velocity variation.

As an example, figure 9.4a shows two peaks obtained in floating conditions from the same probe (in the same arc), by varying the probe velocity from 2.21 to 5.01 *m/s*. Figure 9.4b shows the two superimposed (time normalization with respect to the shortest peak) with area, width and height.

Figure 9.4b

The two peaks of previous figure 9.4a superimposed and comparison between corresponding features

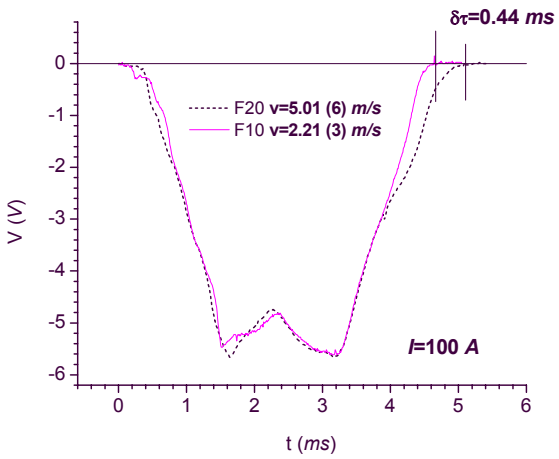

In figure 9.4c, the leading and trailing edges of the two peaks were compared with respect to time delays/differences between comparable peak features.

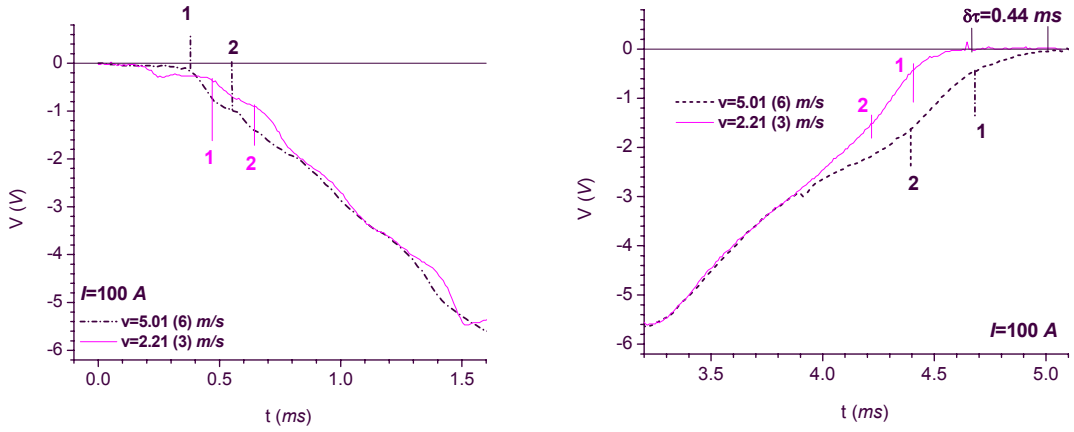

Figure 9.4c Leading and trailing edges for the two peaks in 9.4a and 9.4b. "1-2" label the time intervals compared at the two sides of the peaks

It is quite difficult to establish precisely the equivalent points, but the comparison between the different peak features shows:

- The fastest peak leading edge anticipates the slowest by about 0.30 *ms* whereas the trailing edge delays by 0.44 *ms*; this implies a mismatch of about 0.14 *ms* corresponding to 2.7% of the total peak duration. The latter can be compared with the actual probe velocity fluctuation (*cf* Chapter 7) which was established to be between 2 and 3%;

- The leading edge interval "1-2" are ~ equal for the two, whereas the trailing edges of the fastest is slightly longer;

- The area of the two peaks differ by up to 5% (here the worst case of the two most different peak has been considered, to give an upper limit). As the integral of the peaks represents the total charge collected by the probe during the time interval, this can be taken as the error on the charge captured;

- The FWHM (Full Width half Maximum) of the two peaks differ by 2% whereas the heights differ by 0.8%.

Within the limitations of the experimental accuracy (See Appendix E on Error Analysis) it can be said that there is no appreciable difference between peaks upon variation of the velocity in the interval from 2 to 5 *m/s*.

9.3.2 Peak behaviour upon bias

Before proceeding with the analysis of the characteristic curves in Chapter 10, it is worth starting from the directly measured quantities to look at their evolution upon variation of the applied bias voltage V_b. The purpose is to show the general features of the probe potential V_{prb} in comparison with the probe current I_{RL}, measured by the voltage V_{RL}, and demonstrate their evolution with respect to the position of the probe both in height (z from anode) and in radial distance (or along the coordinate x, position of the probe in the arc). Two probes are analyzed in detail, at an arc current Iarc=50 A: probe N.2, at z=4.03 *mm* and probe N.12, at z=0.58 *mm* from the anode surface.

1. For probe 2 (z=4.03 *mm*) the sequence of current peaks reveals an inversion of the current peak in correspondence of a bias voltage between -9.39 and -10.0 V. Looking at figure 9.5 where the two peaks are reported, the scenario is as follows.

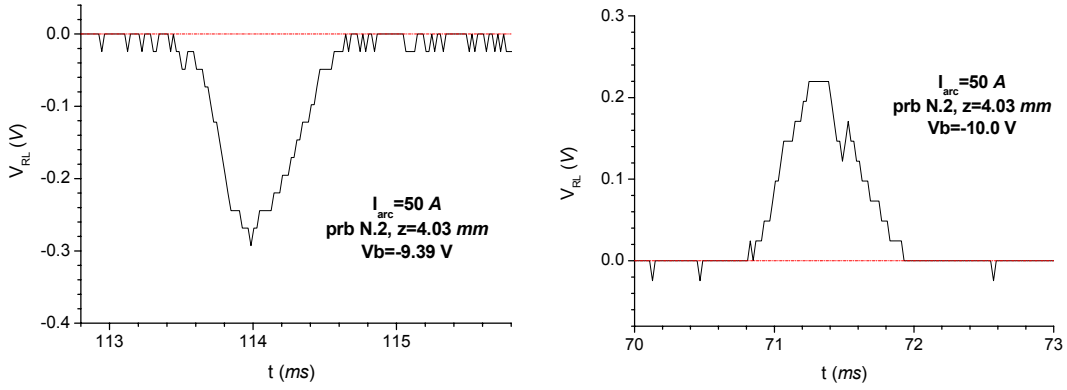

Figure 9.5. I=50 A, prb N.2 z=4.03 *mm* from anode. Left, Vb=-9.39 V. Right, Vb=-10.0 V

Referring to figure 9.5 Left, V_b=-9.39 V, as the probe enters the arc (left to right), a negative current is felt across the load resistor which increases in amplitude approaching the arc centre: in these conditions more electrons are sensed (the probe current I=V/R_L, R_L=4 Ω is negative) and the more so towards the arc centre. On the right of figure 9.5, at V_b=-10.0 V, the peak is positive, the bias has the effect of repelling an increasing number of electrons (e.g. more ions are collected at the centre of the arc). It can be observed that the inversion of the peak occurs in a quite narrow range of applied bias: the variation of bias voltage is ΔV_b=-0.61 V and corresponds to the difference (in sign) between the peaks of the two V_{RL} signals shown in the figure. Also, the inversion is accompanied by a variation of probe voltage greater in the periphery with respect to the centre: the central values shown in figure 9.6 for the two peaks differ by ~0.2 V and the current between 0.15 and 0.19 A.

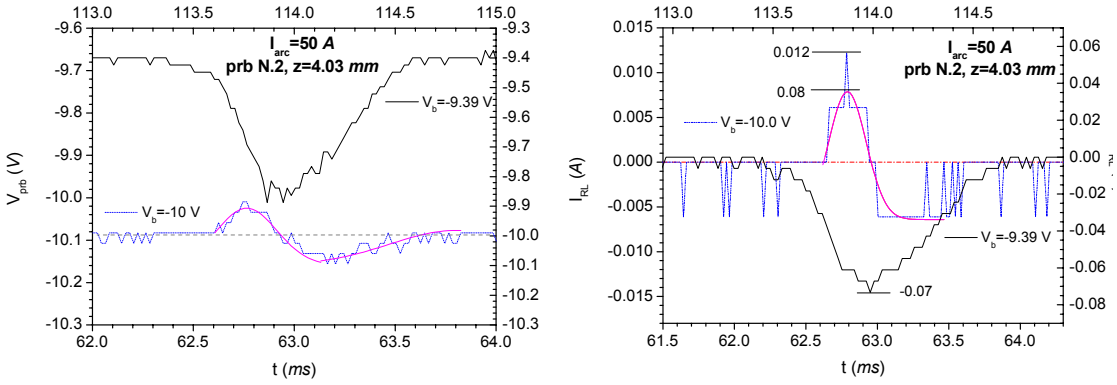

Figure 9.6. *I*=50 A, probe 2, z=4.03 *mm* from anode. The two cases close to peak transition (see text). Left, comparison of probe voltages (V_b=-10 *V* left axis, V_b =-9.39 *V* right axis). Right, comparison of currents (same axes)

The probe voltage shown in figure 9.6 above (left) is enlarged in figure 9.7 left and it is compared with the peak obtained in floating conditions (figure 9.7 right)

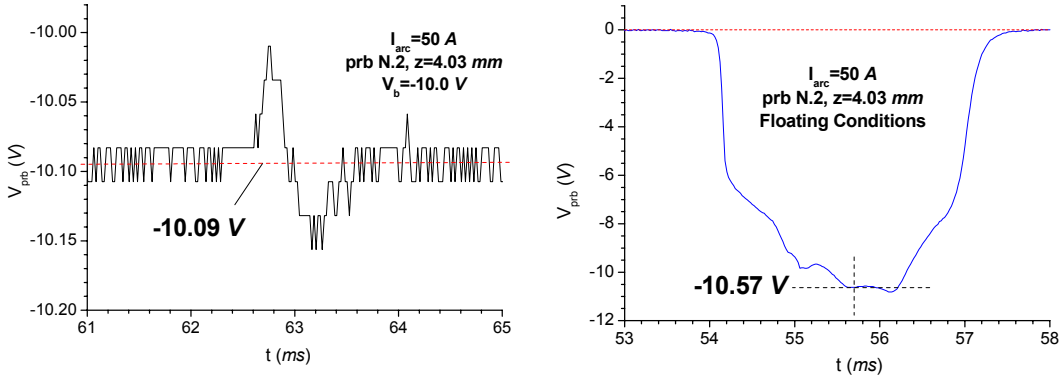

Figure 9.7 Probe potential in biased conditions at Vb=-10.0 V compared with the floating conditions probe voltage

Assuming the dashed line at about -10.09 V as the baseline for this peak, this is the value for the probe voltage corresponding to floating conditions. It differs by 0.48 *V* from the voltage measured in floating conditions shown on the right.
Unfortunately, the bias spacing (e.g. the number of cases in this voltage range) is too coarse to identify the exact location of the transition. It is by comparison of the characteristic curve and the voltages measured in floating conditions that the consistency of the evolution can be found (this is discussed in Chapter 10).

2. A similar analysis is performed on probe 12 (z=0.58 *mm*). With respect to the previous case, the transition between negative and positive peaks occurs in a narrower bias range (here the acquired data points happen to be very close to the transition), as can be seen in figure 9.8. Correspondingly, the current peak is very small, at the limit of detection capability of the system.

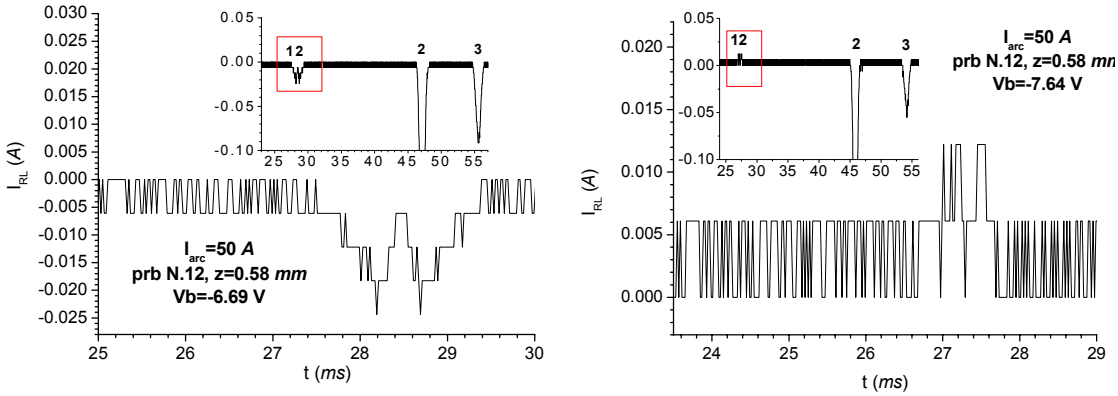

Figure 9.8 I=50 A, probe 12, z=0.58 mm from anode. Probe currents at V_b=-6.69 *V* (left) and V_b =-7.64 *V*(right)

In this case, for a probe closer to the anode, a characteristic bi-peaked signal is observed, especially visible in figure 9.8 left. For the case shown on the right, the limited sensitivity does not provide any meaningful information, although the corresponding *probe* potential of figure 9.9 does show this character. The latter is observed for probes at low height within the arc when measuring in floating conditions (when the peaks are oriented 'negatively' as in figure 9.9 left).

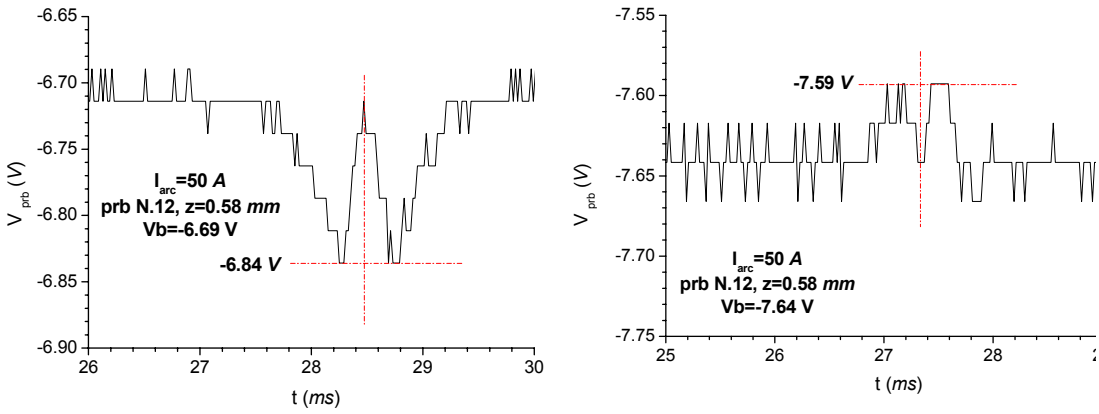

Figure 9.9 I=50 A, probe 12, z=0.58 mm from anode at V_b=-6.69 *V* (left) and V_b =-7.64 *V*(right). Possible maxima are indicated

Re-applying the reasoning of the previous higher probe, in figure 9.9 left, the negative current increases when the probe is deeper in the arc but, approaching the arc centre it drops to values close to zero. Then it increases again to the second maximum and disappears when the probe is out of the arc. Therefore, the dominance of the electron current lowers at the arc centre, where the contribution of the ions is increased. When increasing the bias to the value shown in figure 9.9 right, ions are more numerous in the centre of the arc. The probe potentials measured in these two cases are compared with the measured probe potential in floating conditions in figure 9.10.

The value of the probe voltage found when measuring in *floating conditions* is consistently in between the extremes measured in these two *biased* cases.

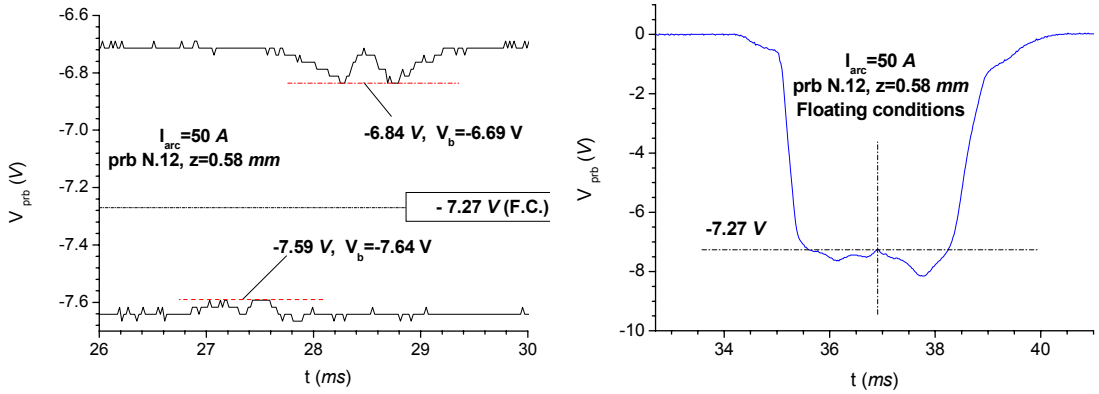

Figure 9.10 I=50 A, probe 12, z=0.58 mm from anode at V_b=-6.69 *V* and V_b =-7.64 *V* shown together (left). The value obtained from the peak in floating conditions (right) is also indicated

9.4 Use of the individual peaks

Once the peak features are fixed (especially the coordinates of the peaks edges), a dedicated program splits each dataset into individual peak files. Also, several other programs access the tables either to directly read information on a specific peak (width, central value) or to use the built in probe-peak-height relationship as a primary key for data selection and extraction, and the build up of different relationships.

For example, the peak width (expressed in *mm*) can be used to determine the arc electrical radius as a function of height from anode. This 'electrical radius' is discussed more thoroughly in Chapter 13.

The data contained in the tables are used to generate additional information for both biased and unbiased and floating conditions. In particular, it is possible to obtain a range of "radially averaged" (r.a.) parameters. These are "radially averaged" in that the value

used are the convolutions of all the contributions arising from the different lengths of the probe within the arc with the probe at the centre, with its longitudinal axis collinear to the arc radius (see section 9.3 on Abel inversion). Similarly, 'chordal averages' are accessible, by considering the contributions of the portions of the probe when the latter is off arc center and taking only the contributions that make the signal value at the corresponding instant of time. This has the purpose of indicating parameter variations along the *probe* length (*cf* Chapter 14). Furthermore, to determine *arc* properties, local quantities are obtained by Abel inversion of the signals read.

9.5. Abel inversion

The use of Abel inversion techniques in plasma physics is well known but almost limited to the inversion of optical line intensity obtained from emission spectroscopy measurements of axi-symmetric plasmas. The total line intensity, either line peak height or area, is obtained for different regions of the arc and plotted as a function of the coordinate whose direction is orthogonal to the line of sight. An Abel inversion procedure converts this function into a 'source' function (the emission coefficient) which depends on the radial coordinate [1]. Gick [5] applied the technique to Langmuir probes but the method is different with respect to the optical case. For Langmuir probes moving in arc plasmas, the analogue of the intensity function is the height of the probe peak read at a given coordinate from the peak centre. This is the integral of the 'source' function, performed along the probe length (parallel to the observer's line of sight) which determines the particular value of the 'peak'. The situation is depicted in figure C.1 in Appendix C.

It is not possible to cover the vast literature on Abel inversion techniques because this has been partly accomplished in previous works [1] where several techniques were reviewed and tested with spectroscopic data. In the present work, a choice is made and justified in the following section.

9.5.1. Method performance and uncertainty

The schematics of the techniques together with the basic relationships are reported in Appendix C. The earlier methods, compared in [1] and [6], collectively indicated by Anderssen [7] as 'finite difference' methods, suffer from the error propagation that the use of equation (9.3) below induces in the results. The 'typical case' is the Nestor Olsen method [8] used here in the form Nestor Olsen B" (Appendix C) in order to avoid uncertainty propagation due to subtraction between adjacent data points.
According to Anderssen [7], all these methods generate functions whose errors on the inverted datum may be amplified with respect to the original datum (supposed subject to a single datum perturbation). Using Nestor Olsen notation (see Appendix C), a single inverted value from the relationship

$$F_{\mathrm{i}} = \frac{2}{\pi a}\sum_{\mathrm{j=1}}^{N} B_{\mathrm{ij}} Q_{\mathrm{j}} \tag{9.1}$$

is subject to an uncertainty

$$\delta F_{\mathrm{k}} = \frac{2}{\pi a}\frac{1}{\sqrt{2k+1}}\delta Q_{\mathrm{k}} \tag{9.2}$$

when the original datum is subject to a 'perturbation' δQ_{k} and is therefore amplified by the factor

$$A = \frac{2}{\pi}\frac{1}{\sqrt{a(2k+a)}} \tag{9.3}$$

With the choice made in this work, of a "natural" step a=100.4 μm, where k ranges from 1, close to the center of the peak to, say, 150, at the peak edge in floating conditions, this would lead to an amplification by a factor of 22.5 for the first inverted point, the closest to the peak center (worst case), or of 3.7 close to the peak edge. Therefore, the error of the inverted datum is very sensitive on the magnitude of the initial error (on the read quantity) and on the position of the datum to be inverted. However, the argument ([7], formula (2.4) page 331) is based on the computation of a single perturbation which would affect only the terms which are multiplied by the matrix elements immediately below the diagonal (the matrix B is lower triangular). Because it is difficult to assess the procedure solely on this basis, tests were performed using 'true' experimental data (and not data with artificially generated noise). Moreover, no interpolation in the original function (peak) was employed.

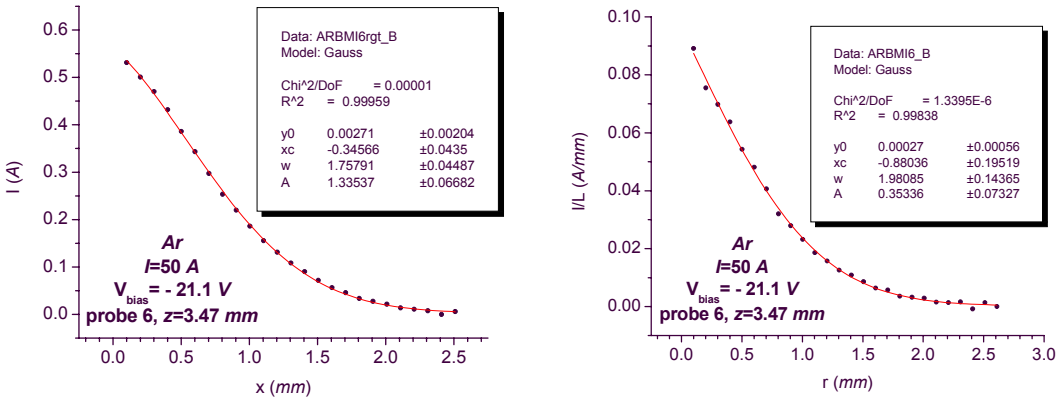

Figure 9.11 Measured (left) and Abel inverted signal (right) obtained using Nestor Olsen for biased conditions (see text)

As an example, in figure 9.11 a plot is reported of the original measured signal in biased conditions, together with its Gaussian fit (left). The corresponding inverted function determined from the Nestor Olsen B is shown on the right, together with its Gaussian fit.
Besides the comparable smoothness of the inverted signal in this specific case, a few observations can be made.
The signal in figure 9.11 left was filtered before inversion using a 4-points adjacent average algorithm. There is obviously a certain degree of arbitrariness in any smoothing procedure, but the effects on the features of the signal, whose original (e.g. unsmoothed form) is visible in figure 9.12, are negligible, whereas the filtering helps towards the inversion procedure.

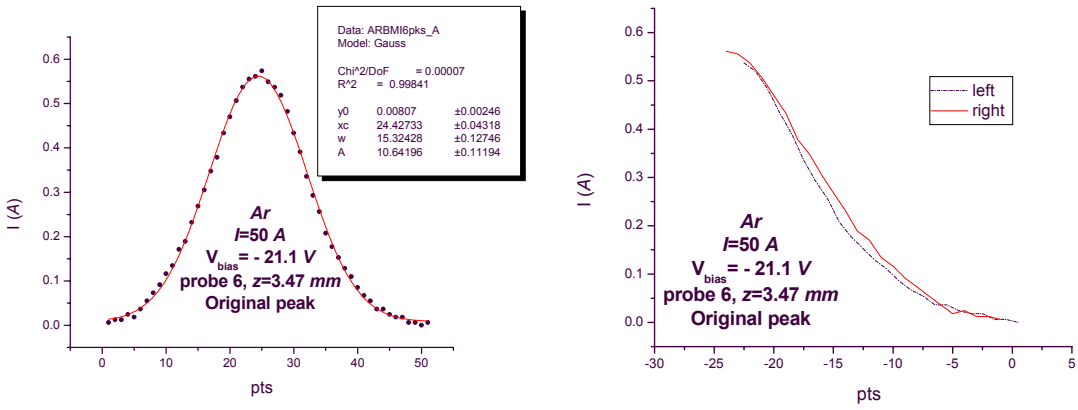

Figure 9.12 Original peak corresponding to the case of figure 9.11. Continuous curve, Gaussian fit of the four-point adjacent average of the experimental points. Right, superposition of the two peak halves

This specific case, while relatively common in biased conditions, in a situation relatively far from the (local) floating potential, is not the general case. Close to the floating potential the current peak tends to disappear (*cf* figure 9.3 above) and in floating conditions, the voltage peak structure is more complex.

10. CHARACTERISTIC CURVES AND PARTICLE ENERGY

10.1 Introduction

Central to the use of Langmuir probes is the notion of characteristic curve (*cf* Chapter 3). The V-I curve method requires establishing the relationship between the current drawn by the probe as a function of its voltage. It is by no means obvious what this means. In fact, characteristic curves can be constructed for probes in the axially symmetric arc in four ways:

1.Take the maximum of the read-out probe current peak and plot it as a function of the corresponding maximum of the voltage peak; this gives rise to the "averaged" V-I curve (in the sense clarified below).

2.Take all values of the current peak as a function of the corresponding values of the probe voltage peak, e.g. at the same abscissa along the peak signal (time or *x* axis); this also gives rise to an 'averaged' V-I curve, although more 'local' than case 1.

3.Take the Abel inverted values of the currents as a function of the Abel inverted values of the peak voltage for equal radial distances; this gives rise to the 'most local' V-I curves;

4.Take the Abel inverted values of the current peaks as a function the non-inverted values of the voltage peak.

The purpose of the procedure/s is to establish *local* physical parameters for the arc. Case 1) is the 'diameter average' of the current as a function of the instantaneous central (or maximum) probe voltage, which can be an average if the probe senses local variations of the plasma potential (along its length), or the common probe potential if the probe is equi-potential. Case 2) constitutes 'chordal' averages where each chord corresponds to the probe length within the arc at the time *t* or position *x* (and whose length is assumed to be half the peak width).

At first sight, case 3) seems the best choice in terms of local parameters, except that the meaning of the inverted voltage (whose dimensions are of a voltage per unit length, *V/l*) is obscure, given that the potential is an intensive and not extensive quantity. Finally, case 4) would stand on the assumption that the voltage is the same all along the probe length, whereas the current is not. A preliminary discussion of the probe voltage is therefore necessary.

10.2 Equipotential probe

It is clear that to obtain plasma parameters, it is important to establish whether the probe is *always equipotential* when traversing different regions of the arc, or whether it is able to sense local values of the potential (along its length), which certainly exist in the plasma in both axial and radial directions. In other words: how can the probe signal be representative of a local voltage distribution given that the surface of a conductor immersed in an electric field is set ‘instantaneously’ to an equipotential value? The charged particle flux (ion flux) will hit the conductor surface and neutralize there; an electron pulse will appear at the read-out end of the circuit. The pulse is made up of a certain number of conduction electrons on the surface of the probe. If the impinging flux is continuous in time, a certain number of electrons will be continuously generated and reach the read out circuit as a 'positive current'. The problem of maintaining a structured signal at the probe surface can then be formulated as follows; as long as the number of impinging ions is ‘high enough’ to replenish the electrons which ‘instantaneously’ reach the read out circuit, a stable signal will be maintained. Conversely, if the impinging flux is low, then the conduction electrons will ‘short’ the probe surface and no '*V* structure' can be revealed.

The importance of the question lies in the fact that:

- if the probe is always equipotential then the characteristic curve should be built by coupling the Abel inverted value of the current with the corresponding equipotential value of the probe voltage, which is read at the same time (and thus at the same arc transverse position); this would mean that of the four methods outlined above, method 4 would be the most appropriate.
- Conversely, if the probe senses local variations of the potential, thereby its signal being made of different contributions along its length, then the V-I curve should be built by coupling the local (Abel inverted) value of the potential to the local (Abel inverted) current, and method 3 would be valid.

To resolve this issue, consider an equipotential conductor (probe outside the arc) set at a potential determined by the bias circuit, and let this potential be much less negative than any value of the plasma potential so that when the probe enters the arc, ion saturation occurs.

When the probe is within the arc, it experiences a flow of ion charges given by the local distribution *j(r)*. Different portions of the probe will sense different values of this distribution. The impinging ions will neutralize at the probe surface thanks to a corresponding number of electrons drawn from the bias circuit. Therefore, the negative potential the probe had before entering the arc will be reduced in magnitude. The question is then whether different portions of the probe will respond with different amount of charges depending on the impinging flux, which means that the electron arriving from the circuit neutralize the ions 'locally'. This implies onset and maintenance of a 'V structure' where different points of the probe surface are at different voltages.

From the circuit point of view, the electrons are sent to the probe because of a mismatch between the externally imposed bias potential and the instantaneous value sensed between probe and reference electrode. It is immaterial whether this unbalance is 'distributed' along the probe or whether it is an integrated quantity (along the probe length). This charge flow is measured as a probe current, and being at saturation, is identified with the ion saturation current.

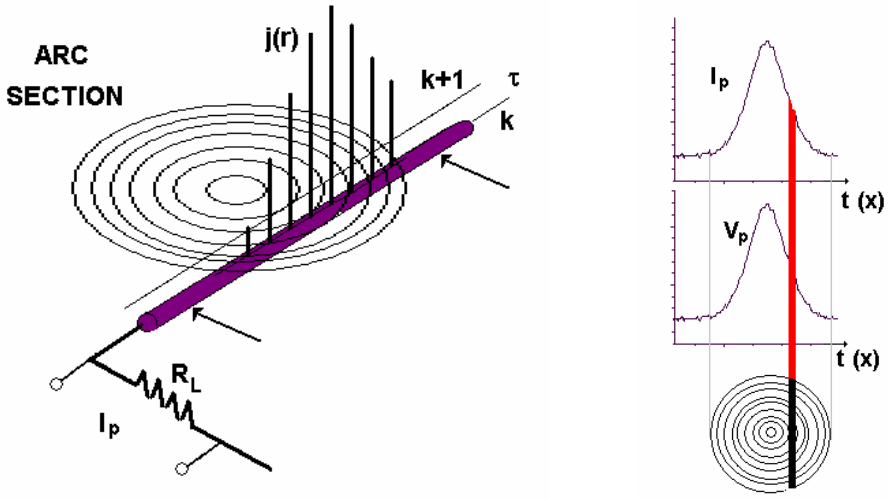

Figure 10.1 for the construction of the V-I curves Left, probe in arc, current distribution on the probe at location *k* (see text). Right, method 2 ('chordal' averages)

Assuming a discrete space/time structure, if the probe is at the position x_k, it will stay there for a time of approximately $\tau \sim (250 \cdot 10^{-6}\ m)/(5\ m/s) \sim 50\ \mu s$ for a probe velocity of 5 *m/s* and a probe radius of $125 \cdot 10^{-6}\ m$. After, it will be 'one probe position away', e.g. at x_{k+1}. This time has to be compared with the time needed for an amount of charge *q* collected at a given location along the probe length to redistribute over the probe surface (onset of an equipotential state). However, this *relaxation time* cannot be easily computed in the frame of classical theory (see e.g. E.M. Purcell in [9]). As an example, one can use the relationship for the conductivity,

$$\sigma = \frac{ne^2\tau}{m_e}$$

taking $n \sim 10^{29}\ m^{-3}$ in copper, inserting the constants and inverting for the relaxation time $\tau = 2.1 \cdot 10^{-15}\ s \sim 0.002\ ps$. This number is suspiciously low and, more importantly it is independent of any length scale (e.g. the length scale could be set to obtain an electron velocity higher than the speed of light!).
Alternatively, one can take the number of impinging charges form the current density (either measured, *cf* Chapter 13, or a fixed value $j_o = 10^7 A/m^2$, typical for the column of an I=200 A arc [10]) and compare it with the amount of charge available for conduction in the probe in the same time interval. If the two quantities are comparable, a potential 'structure' may persist on the probe surface; otherwise, the latter is the classical 'electrostatic' equipotential surface of a conductor. First note that the whole of the probe volume participates in the conduction because the skin effect is negligible even for typical pulse frequency of 300 *Hz*, which corresponds to the inverse of the pulse duration (probe signal about 3 *ms*). In this case the skin depth would be above $\delta \sim 3.5\ mm$ thus greater than the probe radius (r_p=0.125 *mm*) [The skin depth would become important only for frequencies~300 *kHz*].
The chosen volume is the probe 'elementary volume' taken as the sectional area multiplied by the probe radius (close to the step length of 100.4 μm set as the spatial resolution, see Chapter 8),

$$V = \pi r_p^2 \cdot r_p \approx 6.14 \cdot 10^{-12}\ m^3$$

The number of available electrons in this volume, N_e, is obtained multiplying by the average number density of particles in copper, $n_e = 8.45 \cdot 10^{28}\ m^{-3}$ (see e.g. [11], neglecting temperature dependency in first approximation and assuming one conduction electron per atom): $N_e = n_e V = 5.18 \cdot 10^{17}$.
The chosen plasma current density, $j_o = 10^7 A/m^2$ corresponds to a particle flux $j_o = 10^7\ A/m^2 = 10^7 \cdot 10^{19} / 1.602\ m^{-2}s^{-1}$
impinging on the surface $S_p = 2\pi r_p \cdot r_p = 9.82 \cdot 10^{-8} m^2$, e.g. $N/\tau = 6.13 \cdot 10^{18}\ s^{-1}$, and a normalization to the probe-in-arc permanence time is needed. Taking the latter τ=3 *ms*, $N = 1.84 \cdot 10^{16}$ particles impinge on the chosen surface during the whole probe-in-arc permanence time. Even considering half of the probe surface as the collecting surface (*cf* Chapter 11), $N' = 9.2 \cdot 10^{15}$, two out of hundred of the available electrons would be used to neutralize the impinging ion (if the ion branch of the V-I curve is considered).

If one considers instead the number of available plasma charges per unit volume as if all participated in the conduction, e.g. by using the plasma charged density (normalized to the probe volume) say $n_e = 10^{23}\ m^{-3}$ (*cf* Chapter 2), then the particles contained in an elementary 'probe volume' would be $N = 1.2 \cdot 10^{12}$. This is a much more realistic number

for the majority of the arc column: only one out of ~10^5 of the N_e copper electrons would be used to neutralize the impinging charged particle. In other words, the effect of the impinging charges on the population of the charges locally available at the surface is negligible. Hence, a localized voltage structure cannot be maintained with these flux values. This conclusion is supported in Chapter 11 where it will be shown that the order of magnitude of the measured number of ions on the elementary probe portion is N~10^{11}.

Having established that the probe is an equipotential surface, the construction of the V-I curves according to method 3 is incorrect. The local characteristic curves therefore, have to be built according to method 4. The *V-I*'s determined according to methods 1 or 2 are averaged characteristic curves. The first gives points corresponding to the central current and voltage values (maxima of the peaks). The second gives chordal averages.

In the following, method 1 will be used to determine the *central* values of the plasma parameters, whereas method 4 has will be employed to extract all the *local* parameters.

10.3. Use of the V-I curves

The use of the characteristic curve according to the methods described in Chapter 2 requires the fulfilment of a number of features, namely:

- The occurrence of an electron saturation region and
- of a steep or linear part;
- the identification of the location for the plasma potential;
- the existence of an ion saturation region.

A selection of characteristic curves for method 1 is presented in figure 10.2 a to e for arc currents 50, 70, 100, 150 and 200 A.

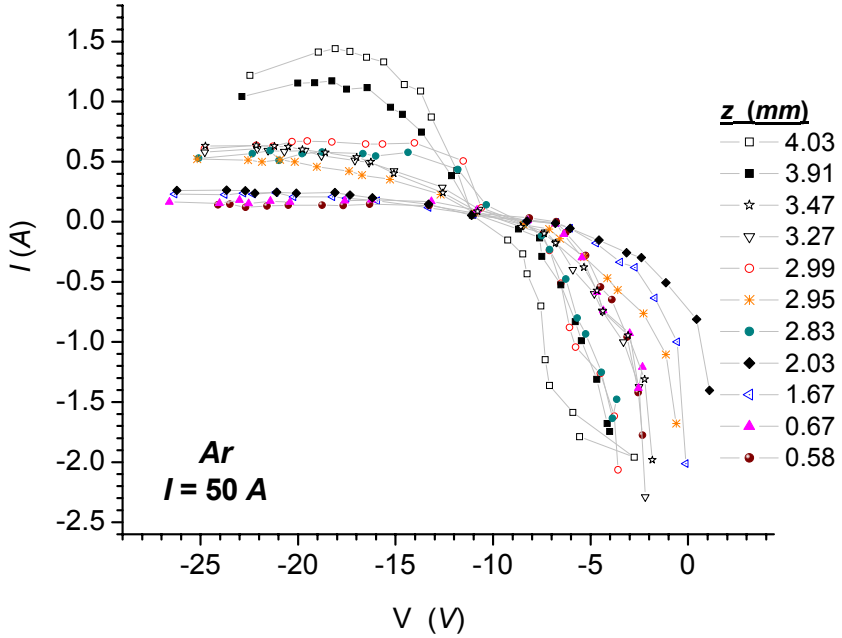

Figure 10.2 a V-I curves according to method 1 (see text). Arc current 50 A

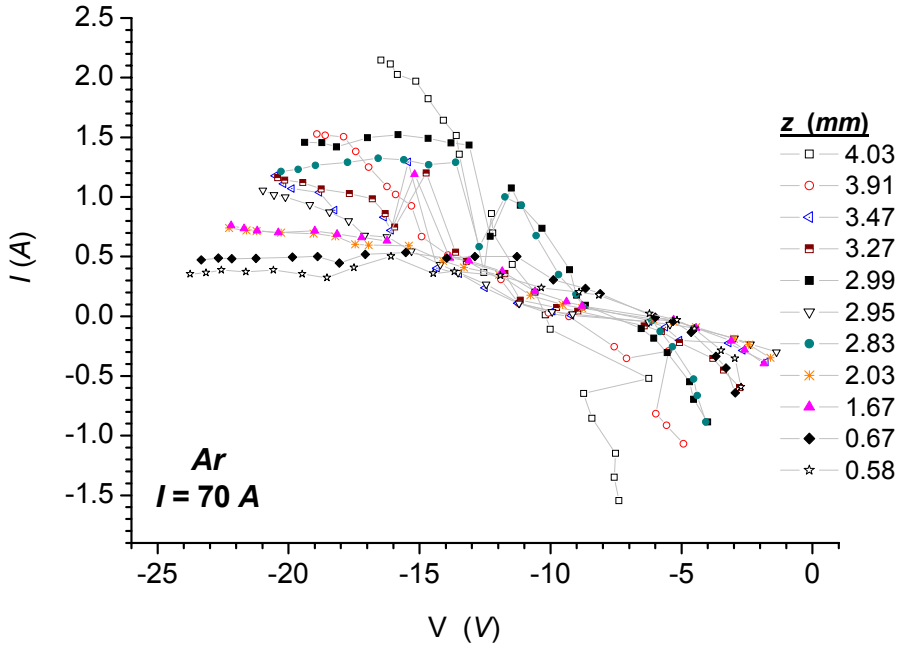

Figure 10.2 b V-I curves according to method 1 (see text). Arc current 70 A

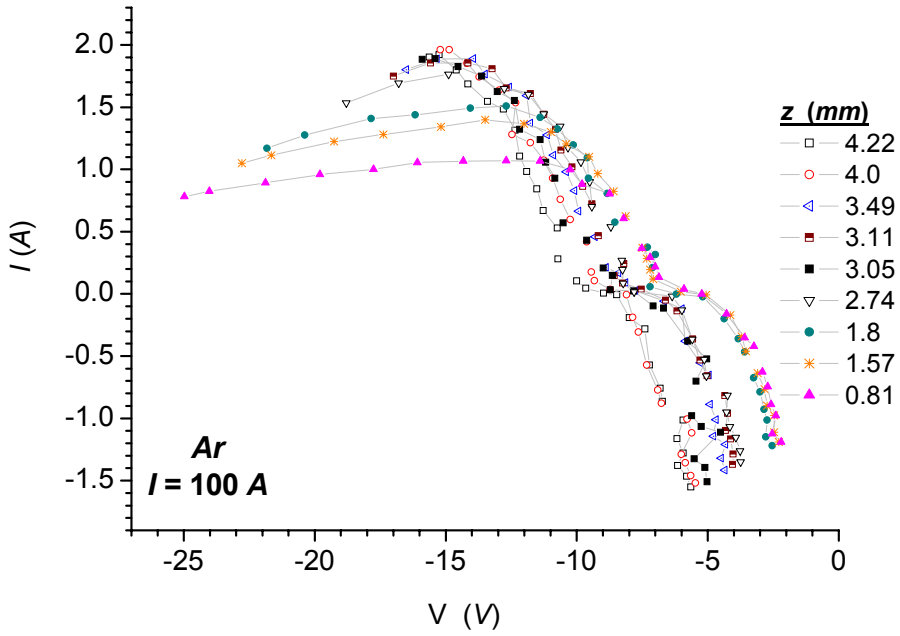

Figure 10.2 c V-I curves according to method 1 (see text). Arc current 100 A

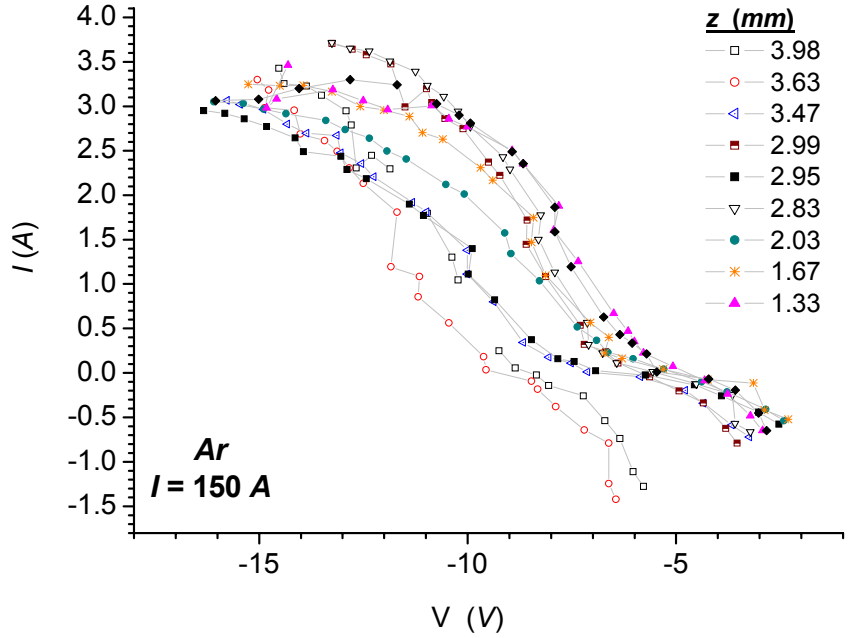

Figure 10.2 d V-I curves according to method 1 (see text). Arc current 150 A

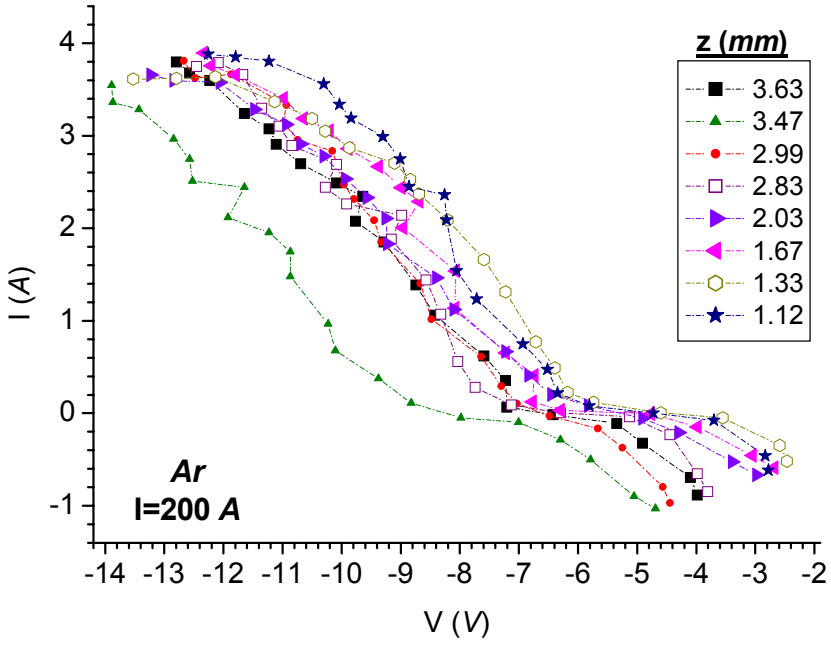

Figure 10.2 e V-I curves according to method 1 (see text). Arc current 200 A

Examination of the curves reveals that electron saturation is not achievable because of the high electron current that would result from moderate positive bias voltage (with respect to the plasma potential). The steep linear part is only partly visible and its extension is ill-defined because of the difficulties in identifying the plasma potential (see Chapter 12, potentials). The only clearly identifiable part is the ion saturation region. For this reason this is the region investigated more closely and as a consequence, only a handful of the various V-I methods presented can be used. This is the reason why the temperature determination from the V-I curve relies only on ion saturation (see Chapter10).

Looking at the curves for the different arc current cases (figure 10.2), some conclusions can be drawn.

The highest probes (further from anode) do not show clear saturation at the highest arc currents (150 and 200 *A*). This clear saturation should manifest as a constancy of the current upon bias increase, although, saturation with *V* dependency has been described and considered in Chapter 4 (*cf* formulae (4.13) for the CFF theory or Lam's (4.45), independent of the potential, in contrast to (4.46)-(4.48) for sheath convection regime, where the current shows a $V^{1/2}$ dependency). This implies that for the highest probes the currents are underestimated. As a consequence, the corresponding temperatures could

be also underestimated (See Chapter 11). An examination of these V-I's shows that any attempt to extrapolate the missing current values would fail, as no clear tendency to a 'close saturation' (e.g. for neighbouring values of the probe potential) exists. Moreover, the question remains open as to whether these probes would reach saturation at all and / or whether the value of the current would be 'high' with respect to the requirement of a 'negligible' current drawing from the arc.

By looking at the variability of saturation along the radial coordinate, it is possible to identify some specific regions within the arc possibly characterized by different physical conditions. This may be related to the selection of the probe theory most appropriate to the local arc structure. This means that it is of interest to find the geometrical locus in the plane (*r,z*) where a transition occurs from saturation (and thus random/diffusional behaviour) to a voltage dependency of probe current. Since the number of experimental points for all the 5 arc currents is limited, and because a clear indication of saturation may be established only 'by eye' using as few as 2 or 3 points, this curve will be approximate. Finally, there may be circumstances in which saturation occurs but not with a flat curve, but a convex saturation curve revealing some $I \propto V^n$ dependency.
As an example, figure 10.3 reports the case of three probe V-I's at I_{arc}=200 *A* and z=3.63 (a) *mm*, z=2.95 *mm* (b) and z=1.12 (c) *mm* from the anode. For the first, saturation sets in perhaps at *r*=0.6 *mm*; for both second and third, *r*= 0.5 to 0.6 *mm*.

The curve built by examining all the characteristic curves as a function of the radial distance for all the probes of the 200 A case, is shown in figure 10.3 d. This curve divides the (*r,z*) plane into a non-saturating (points to the left of the curve) and a saturating region (points to the right of the curve).

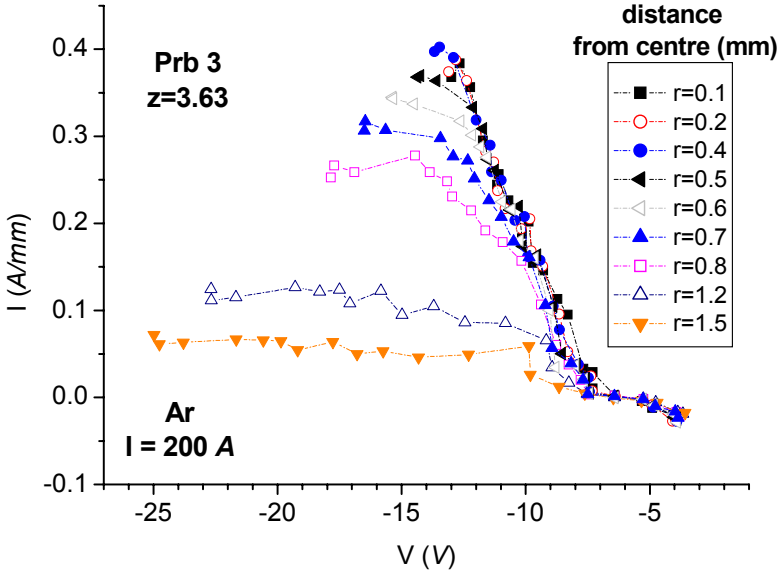

Figure 10.3 a Characteristic curves according to method 4; *z*=3.63 *mm*, for the 200 A case.

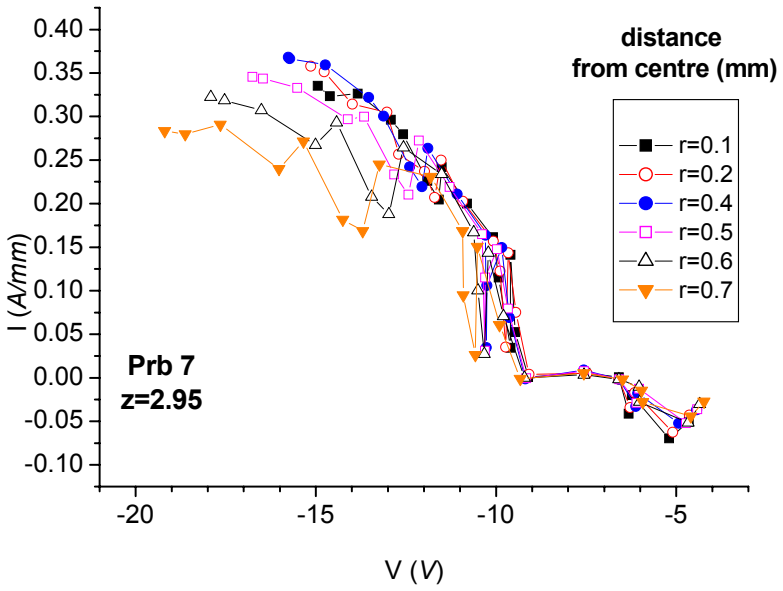

Figure 10.3 b Characteristic curves according to method 4; z= 2.95 *mm* for the 200 A case.

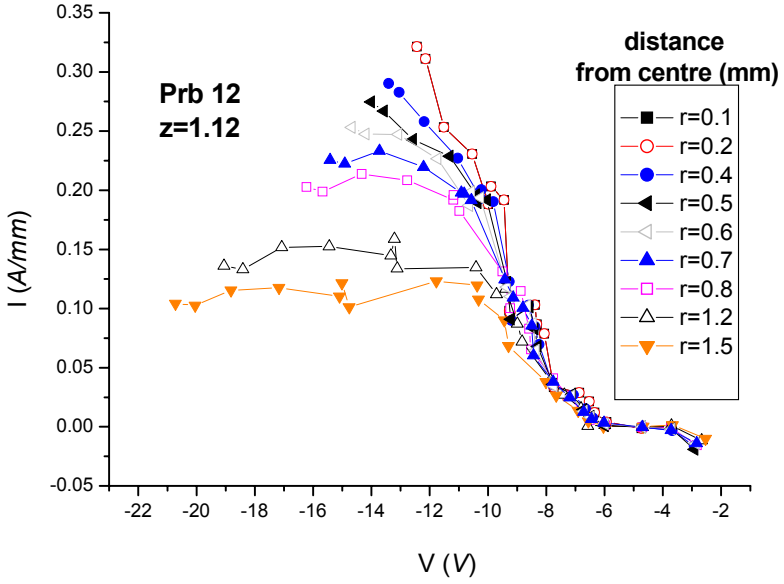

Figure 10.3 c Characteristic curves according to method 4; *z*= 1.12 *mm* for the 200 A case.

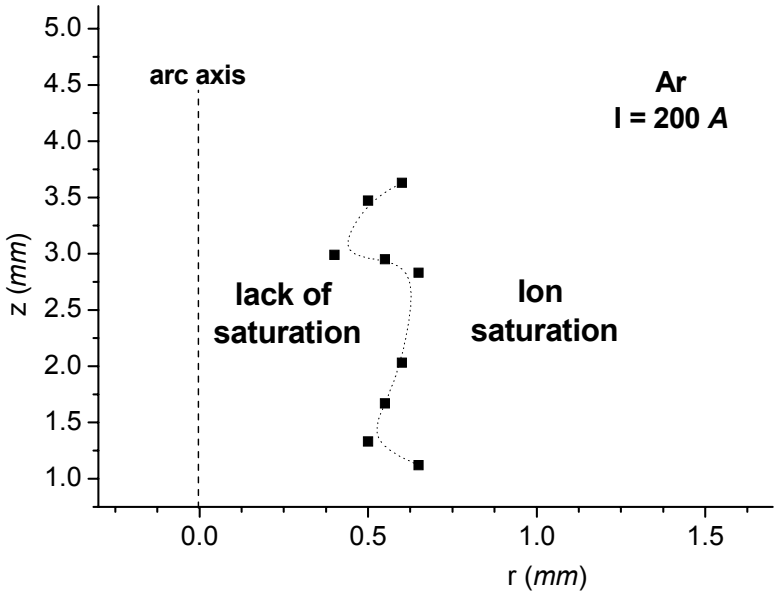

Figure 10.3 d. The transition to ion saturation defined by a radial coordinate exceeding the experimental points, $r>r_{sat}$. I =200 A

This operation can be repeated for all the currents. The corresponding curves (full symbols) are shown in figure 10.4 a – e, for the arc currents 50, 70, 100, 150 and 200 A. For comparison, the current conducting region, defined by the empty circles, is also shown (and discussed in Chapter 13).

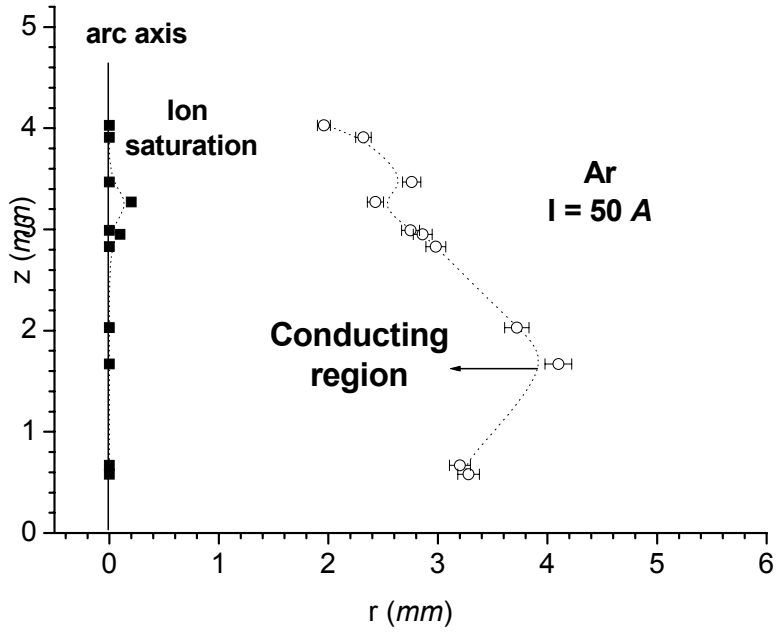

Figure 10.4 a Saturation transition curves for I=50 *A* (see text). Full squares: transition between ion non-saturating (left of curve) and saturating (right of curve) characteristic curves. Empty circles: current carrying region shown for comparison (*cf* Chapter 13)

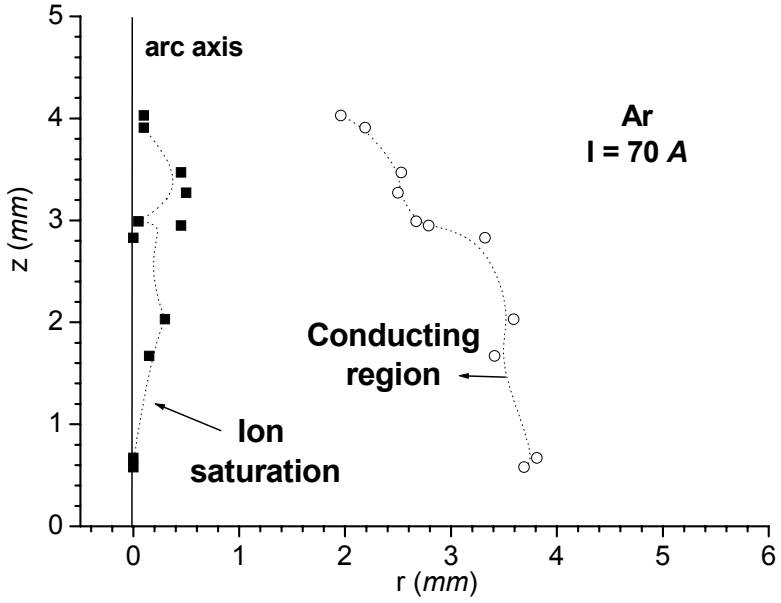

Figure 10.4 b Saturation transition curves for I=70 *A* (see text). Full squares: transition between ion non-saturating (left of curve) and saturating (right of curve) characteristic curves. Empty circles: current carrying region shown for comparison (*cf* Chapter 13)

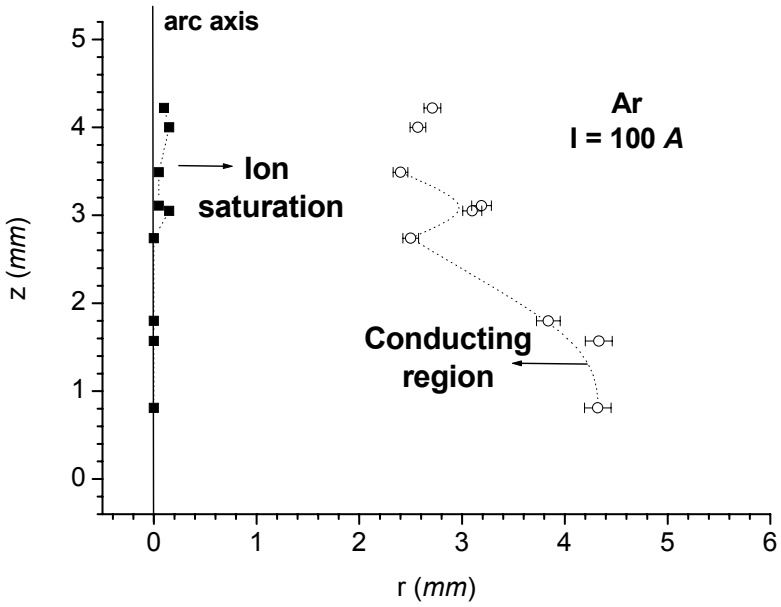

Figure 10.4 c Saturation transition curves for I=100 *A* (see text). Full squares: transition between ion non-saturating (left of curve) and saturating (right of curve) characteristic curves. Empty circles: current carrying region shown for comparison (*cf* Chapter 13)

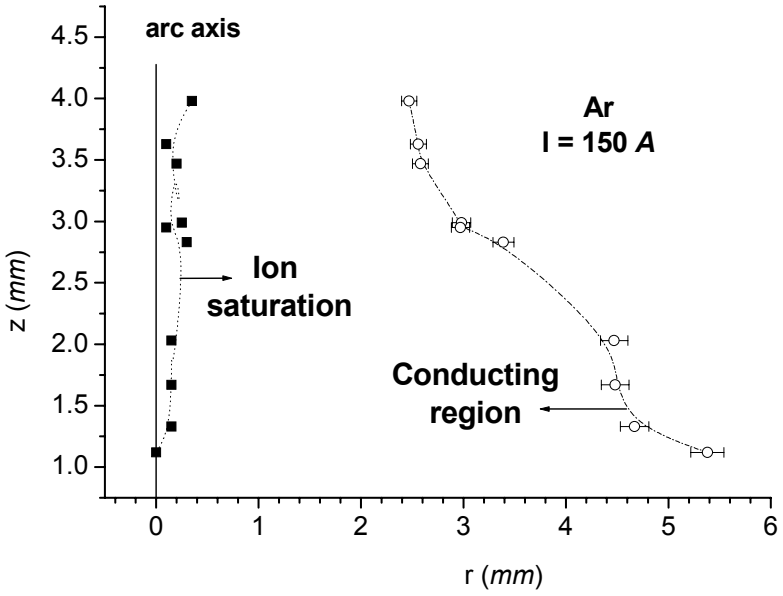

Figure 10.4 d Saturation transition curves for I=150 *A* (see text). Full squares: transition between ion non-saturating (left of curve) and saturating (right of curve) characteristic curves. Empty circles: current carrying region shown for comparison (*cf* Chapter 13)

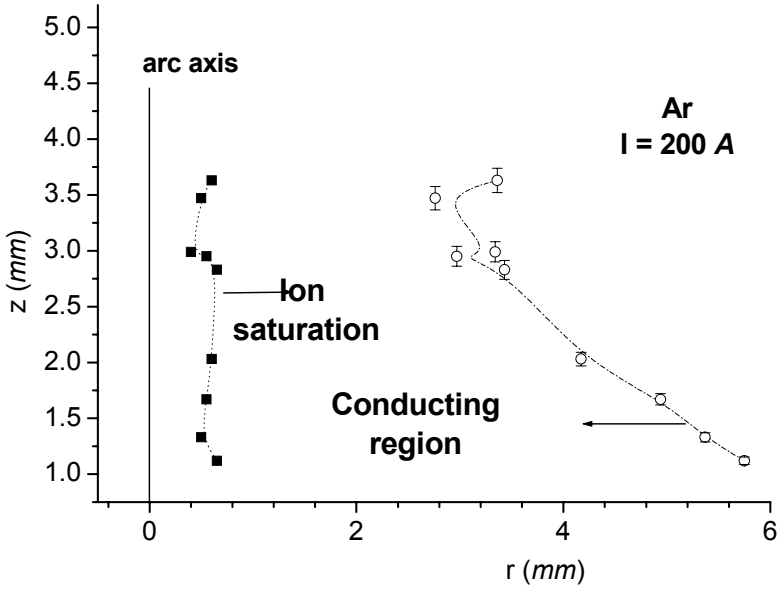

Figure 10.4 e Saturation transition curves for I=200 *A* (see text). Full squares: transition between ion non-saturating (left of curve) and saturating (right of curve) characteristic curves. Empty circles: current carrying region shown for comparison (*cf* Chapter 13)

The observations on axial and radial behaviour of the V-I curves can be summarized in Table 10.1 (*cf* figure 10.2 to 10.4)

Arc current (*A*)	**Saturation (Complete/Partial)**	Up to z (*mm*)/from *r* (*mm*)
50	**C**	Whole arc height, z=4.22 *r*=0(>0.3 1 point)
70	**P**	Whole arc height, z=4.22 *r*≥0.5
100	**P**	Whole arc height, z=4.22 'just' (2 points), *r*≥0.2
150	**P**	2.99, *r*≥0.3
200	**P**	2.95, *r*≥0.4 to 0.7

Table 10.1 Ion saturation for different arc currents for central (method 1) and 'hybrid' (method 4) V-I curves. Vertical distances measured from anode, radial distances from axis. 'Whole arc' means up to the highest probe available (see text) and across the arc radius. Shielding gas, *Ar*, mass flow 10 *slm*=0.297 *g/s,* length 5 *mm*

The general trend is that saturation occurs almost completely for the lowest current arc, I=50 *A* and less and less completely with increasing arc current, and increasing probe height within the arc. Saturation at the highest current almost never occurs in the central region (e.g. below 0.5-0.8 *mm* at 200 *A*) whereas moving radially outwards, saturation occurs again.

10.4 Energy and particle number densities

Physical parameters are obtainable by considering the probe as an instrument measuring the number of impinging particles, and the power released whilst immersed in a particle flux (the arc). It is the purpose of this section to investigate the dynamic parameters from measured voltages and currents and in particular, the ion flux to the probe, the velocity of ions at the probe, their kinetic energy and the charge released. The interest lies in the initial values of the kinetic energy and temperature which characterize the ion particles in the bulk and pre-sheath.

Moreover, it is useful to reinterpret the general shape of the V-I curve in terms of the variation of the current *due to displacement of electrons*, which have higher mobility and diffusion coefficient. According to this view, the part of the characteristic curve which shows ion saturation 'unveils' an almost exclusive ion current because the effect of the bias is to remove an increasing number of electrons from the probe region. When 'ion saturation' takes place, there are no electrons left to be removed in the probe

vicinity. At lower probe bias, e.g. closer to floating conditions, the electrons are comparable in numbers to ions (in fact in sufficient number to maintain the probe negative with respect to the plasma and the two currents equalize at the floating potential). At plasma potential the electron population dominates and in fact maintains the negative plasma potential at the probe surface. The advantage of this point of view is that the ion current appears as a 'background' present in all the bias conditions. Therefore, the expressions for the ion flux and the ion velocity are the same under different bias conditions.

We start with the energetics available from the data acquired corresponding to a given bias value. The kinetic energy of the impinging particles can be determined from the measurement of the probe voltage and current. This can be accomplished in ion saturation conditions when a fully developed positive sheath surrounds the probe However, the principle is valid at any point of the characteristic curve (provided the correct interpretation of the currents in terms of charge components is available) and in particular also in the region of the V-I curve where the probe voltage is close to the floating and/or plasma potential.

10.4.1 Particle energy and power to the probe

Any point in the plasma before the insertion of the probe is characterized by the plasma potential V_{pl}. Assuming not too brusque variations of the latter in the undisturbed plasma region (which is reasonable), the insertion of the probe is supposed to maintain this value of the potential within a short-range distance, of the order of a sheath radius (obviously the insertion of the probe at the *exact* location will greatly alter the plasma, now replaced by a portion of copper rod). According to the results of Chapter 4, we assume a thin sheath so that the above assumption is justified. The voltage difference between plasma and probe is therefore

$$V_{\mathrm{sh}} = V_{\mathrm{pl}} - V_{\mathrm{prb}} \tag{10.1}$$

We assume that at the sheath edge, the ion, at potential energy $\sim eV_{\mathrm{pl}}$, experiences the effects of a 'leaking' field that will drive it towards the probe, i.e. a pre-sheath. In effect, this 'small leakage', required to attract the particles to the probe contrasts with the requirement that the ion is at the exact local plasma potential (*cf* Chapter 4 and see discussion below). The ion's initial kinetic energy

$$K_{\mathrm{io}} = \frac{1}{2} m_{\mathrm{i}} \mathrm{v}_{\mathrm{i}}^2$$

will vary along the sheath by the amount eV_{sh} before hitting the probe. The final kinetic energy K_{if} just before impact is

$$K_{\mathrm{if}} = \frac{1}{2} m_{\mathrm{i}} \mathrm{v}_{\mathrm{f}}^2 = \frac{1}{2} m_{\mathrm{i}} \mathrm{v}_{\mathrm{i}}^2 + eV_{\mathrm{sh}} = \frac{1}{2} m_{\mathrm{i}} \mathrm{v}_{\mathrm{i}}^2 + e\left(V_{\mathrm{pl}} - V_{\mathrm{prb}}\right) \tag{10.2}$$

[Suffix 'i' refers to ions, 'o' to initial and 'f'' to final value]. Because the probe is negative with respect to the plasma, V_{sh} is positive and ions are accelerated.

The exact value of K_{if} will depend on the hypothesis made for the ion velocity. The latter can in fact be the (Maxwellian) thermal velocity

$$\mathrm{v}_{\mathrm{i}} = \sqrt{\frac{8kT_{\mathrm{e}}}{\pi m_{\mathrm{i}}}} \tag{10.3}$$

or, satisfy the Bohm criterion, the sound speed in the medium (also called 'thermal velocity' [3])

$$\mathrm{v}_{\mathrm{B}} = \sqrt{\frac{kT_{\mathrm{e}}}{m_{\mathrm{i}}}} \tag{10.4}$$

or the (Maxwellian) most probable value

$$<\mathrm{v}> = \sqrt{\frac{2kT_{\mathrm{e}}}{m_{\mathrm{i}}}} \tag{10.5}$$

10.4.2 Choice of velocity and flux expression

1. Velocity

In general, in the pre-sheath both a thermal and a drift term should be considered for the charge fluxes. Because the velocity expressions enter the formulae for the fluxes at the sheath edge (e.g. not within the sheath), the velocity to be chosen is the velocity in the pre-sheath ('initial' velocity). Depending on the bias conditions (fully developed sheath in ion saturation or small sheath in floating conditions or absence of sheath when the probe is at the plasma potential) and the particle type (ions or electrons) the expression for the velocity is different. If one assumes an equilibrium (thermal) plasma in the pre-sheath, the speed of the ions is given by (10.3). This is justified only if the field leakage from the sheath into the pre-sheath is negligible. However, to accelerate the ions towards the probe region, an 'initial kick' is necessary, given by a potential (even if relatively weak). The random motion of the ions (far from the probe) is destroyed by the leakage of the electric field that extends into the plasma beyond the sheath edge and directs the ions towards the probe.

If the ions are directed towards the probe already in the pre-sheath, one has to assume a non thermal velocity as in equation (10.5): in ion saturation conditions the sheath is fully developed, its potential is a maximum and the choice of a purely thermal velocity would seem unjustified. The choice made by Gick [5] was the 'most probable value', formula (10.5). The correct expression of the ion velocity at the sheath edge is dependent of the field. If the field is weak (*cf* section 2.10 and [12]), the ion kinetic energy is $E_i = kT$ per degree of freedom, with an electron or an ion temperature (depending on the plasma being at equilibrium or 'cold'). For almost mono-directional ions, one degree of freedom implies $v_i = \sqrt{2E_i / m}$ and use of (10.5).

Moreover, both (10.3) and (10.5) overcome the Bohm value (10.4), so it is of question whether the latter is at all appropriate. In fact, if a field leaks in the pre-sheath and its final effect is to *accelerate* the ions towards the sheath edge, the initial values of the velocity cannot be higher than the Bohm velocity (velocity at the sheath edge). This is the reason why the expression (10.4) is abandoned.
The expression for the kinetic energy variation for the chosen most probable value (10.5) is therefore

$$e\left(V_{pl} - V_{prb}\right) = \frac{1}{2} m_i v_f^2 - kT_e \qquad (10.6)$$

where v_f is the final impact ion velocity at the probe. Formula (10.6) relates the sheath voltage fall (and thus a difference between the measured probe voltage and the plasma potential) to the electronic temperature at the sheath edge and to the ion final velocity at the probe surface.

2. Fluxes
Similar considerations arise for the particle fluxes whose expressions lie in between the mono-directional and mono-energetic $\Gamma = nv$; or the flux $\Gamma = nv/4$ where only half of the particles move towards (a plane) probe surface and where the average is taken of the cosine of the angle between the direction of the velocity and the normal to the area element [3, 13]. This multiplicative factor (1/4) is subject to uncertainty in view of the possible directionality of the charge capture mechanism: if (say) only one-half of the probe surface is involved in charge capture, a corresponding factor has to appear in the expression for the current. The latter circumstance could also depend on the plasma motion characteristics in the vicinity of the probe at a particular bias.
As seen in the introduction to this section, the expression of the ion current is the same under all bias circumstances. The most employed expression inherited from the low-pressure theory (*cf* Chapter 2) is the random flux $\Gamma = nv/4$ which assumes a directed motion perpendicular to a plane surface with a selection of only 'half' of the particles. The results of Chapter 4 concerning the sheath thickness, showed that in the worst case

(thickest sheath) $\delta_{sh}\sim10^{-5}$ *m* whereas the probe radius is 12.5 times larger. This would make it possible as a first approximation to assume the planar form of the flux, because the majority of the alternative sheath thicknesses are at least one order of magnitude smaller.

10.4.3. Power to the probe

Voltage and current measurement can be used to determine the total and local power released on the probe at a given position within the plasma. In fact, the probe is biased to a potential V_b with respect to anode before entering the arc; at this stage, the probe and bias potential coincide. When entering the arc the probe potential will change. The instantaneous difference between the imposed (fixed) bias and the actual probe voltage, gives the potential variation; multiplying by the corresponding current collected per unit length (e.g. the Abel inverted current) gives the power per unit length released on the probe at the given location. Multiplying by the time interval corresponding to the minimum spatial resolution, and by the latter as well (the elementary step in the Abel inversion procedure), the total energy collected by the probe in the portion considered is

$$\mathrm{E_n} = \left(\frac{W}{a}\right)\tau a = \left(V_b - V_{prb}\right)\left(\frac{I}{a}\right)\tau a \qquad (10.7)$$

To obtain the energy carried by a single ion it is necessary to divide the latter expression by the corresponding number *N* of particles striking the probe portion at the same time and location. This is given by the charge collected, e.g. the integral of the measured current over the time elementary time step τ (this translates to a simple multiplication), divided by the elementary charge, and multiplied by the elementary (probe) length *a*

$$N(r,z) = \frac{q_N(r,z)}{e} = \left(\frac{I}{a}\right)_{(r,z)} \tau a / e \qquad (10.8)$$

Dividing (10.7) by (10.8), the single particle (ion) energy released to the probe is

$$\mathrm{E_i}(r,z) = e\left(V_b - V_{prb}\right)_z \qquad (10.9)$$

10.4.4. Comparison and identification of the energies

It is important to look for a relationship between the latter energy and the dynamical parameters of the particles (ions). The argument can be outlined as follows. If there were no sheath, i.e. when $V_{prb}=V_{pl}$, the power released to the probe would be $W' = V_{pl} I_{prb} > W$, where *W* refers to ions in saturation conditions.

In fact, if one follows the argument [14] that the ion current is always present from ion saturation conditions until the point where the probe is in *floating conditions*, where the ion and electron fluxes equalize, then the power released to the probe would consist of an additional energy flux due to the electrons, thus greater than the value due to ions alone. Moreover, if the probe were at the *plasma potential*, where the electrons are overwhelming, because of the higher electron mobility, the number of impinging electrons and therefore the power deposited to the probe would also be larger than at ion saturation. Experimentally, this corresponds to the 'high' electron current situation, where the power released to the probes causes their melting.
The introduction of probes in ion saturation conditions implies the formation of a sheath thus a potential difference which has the result of accelerating the ions and of removing the electrons. The question is which voltage should enter the general expression of the electrical power transferred, $W = VI_{\mathrm{prb}}$, where I_{prb} is the probe current. Because the probe is at a negative potential V_{prb} with respect to the plasma, one would be tempted to assume this voltage as the candidate. However,

1.the fluxes in floating conditions must be equal;

2.the power in floating conditions must be higher than at ion saturation and

3.the ion flux is fixed.

Hence, the voltage chosen must be numerically less than the plasma potential, whereas here $\left|V_{\mathrm{prb}}\right| > \left|V_{\mathrm{pl}}\right|$. For the same reason, V_{b} has to be discarded because when biasing negatively, always $\left|V\right|_{\mathrm{b}} \geq \left|V_{\mathrm{prb}}\right|$ where the equality holds only when in floating conditions or when the probe is outside the arc. Therefore, *it is proposed* that the voltage contribution to the expression of the power is $V_{\mathrm{b}} - V_{\mathrm{prb}}$, e.g. the difference between the nominal bias and the actual probe potential. The two coincide out of the arc and it is their difference which causes the ion acceleration. In other words, the identification of (10.2) and (10.6) is made in the following and the final kinetic energy at the end of the ion travel is

$$\mathrm{E_i} \equiv K_{\mathrm{if}} = e\left(V_{\mathrm{b}} - V_{\mathrm{prb}}\right) \tag{10.10}$$

As a consequence, the value of the ion final velocity prior to impact with the probe surface is

$$\mathrm{v_f^2} = \frac{2K_{\mathrm{if}}}{m_{\mathrm{i}}} = \frac{2e}{m_{\mathrm{i}}}\left(V_{\mathrm{b}} - V_{\mathrm{prb}}\right) \tag{10.11}$$

The latter can be inserted in (10.6) to obtain

$$e\left(V_{\mathrm{pl}}-V_{\mathrm{prb}}\right)=e\left(V_{\mathrm{b}}-V_{\mathrm{prb}}\right)-kT_{\mathrm{e}} \tag{10.12}$$

From this set of relationships, one could obtain:

A. the plasma potential, by inversion of (10.14) to (10.16) if the temperature is known

$$V_{\mathrm{pl}}=V_{\mathrm{b}}-\frac{kT_{\mathrm{e}}}{e} \tag{10.13}$$

B. the temperature, if an independent method to determine the plasma potential is available:

$$T_{\mathrm{e}}=-\frac{e}{k}\left(V_{\mathrm{pl}}+V_{\mathrm{prb}}\right) \tag{10.14}$$

The latter can be compared with the results obtained from the use of the characteristic curve.

C. The sheath voltage fall from the variation of the kinetic energy of the particle if the temperature is known (either from B or other methods, *cf* Chapter 11)

$$V_{\mathrm{sh}}=\left(V_{\mathrm{b}}-V_{\mathrm{prb}}\right)-\frac{kT_{\mathrm{e}}}{e} \tag{10.15}$$

and compared with the order of magnitudes estimations made in Chapter 4. This is done in Chapter 12.

D. Since the voltage sheath fall is the difference between the unknown plasma potential and the measured probe voltage, the plasma potential can be estimated

$$V_{\mathrm{pl}}=\left|V_{\mathrm{sh}}-V_{\mathrm{prb}}\right| \tag{10.16}$$

E. Finally, because of the existing relationships between sheath voltage and thickness (*cf* Chapter 4), an attempt can be made to estimate the latter in one of the collisionless models available, namely the Swift ‘thermal case’ or the CL (Child-Langmuir) approximation. This is investigated further in Chapter 12.

11. TEMPERATURES

11.1 Introduction

The Plasma temperature can be determined by using the only available portion of the V-I curve, which under the present experimental circumstances, is the ion saturation region. In particular, a method employed by Gick [5] can be generalized to several current models and the resulting methods are named 'direct methods' in the following. These are discussed along with the result these provide in the first part of this chapter. It is anticipated that these methods provide temperature values lower than expected (e.g. than determined from optical means). Reasons for this 'apparent cooling' are investigated in view of the flowing nature of arc plasmas.

11.2 Direct methods

1. Principles of the method

With "direct methods" it is meant that relationships like

$$i_{sat} = f[n(T), T] \tag{11.1}$$

can be employed to extract the plasma temperature if the relationship between current (per unit length), charged particle density and temperature is known. The various formulae for the ion saturation current described in the following depend on the direct $n(T)$ relationship data available after Olsen [15] and are based on the read current supposed in the form of a flux of the type $j_i = ne\mathrm{v}_i / 4$, or a continuum plus free-fall type, which includes the mobility $j_i = k\mu_i ne\mathrm{v}_i / 4$. Diffusive and random flux differ only by the choice of the 'factor' multiplying n [16].

As shown in section 9.4, the nature of the constants has to be determined according on the model assumed for the charge collection. For example, Benilov [17], states that only the upstream portion of the probe surface is effective in collecting ions. This would lead to a halving of the theoretical current for the simplest diffusive model. If following Tsuij [18], the collecting surface consisted of the upstream 240°/360° of the cylinder cross section, and a factor 2/3 would be necessary.

The direct models are examined critically, including the Continuum plus Free-Fall and the Su and Kiel models (*cf* Chapter 5). These all pertain to steady plasmas, but the

absence of direct experimental evidence on flow velocity distribution within arcs, impedes the use of the formulae where this velocity dependency of the current is explicit.
Comparison with data from emission spectroscopy could deliver an 'empirical' correction method, to be used for reconstructing the probe-determined temperatures, in cases where information on flow velocity is missing.

The current read in the diffusive case is $I_i = ne\mathrm{v}_i S/4$, where S is the probe surface $S = 2\pi r_p l = 2\pi r_p a,$ and $a = 100.39\mu m$ is the elementary spatial step (spatial resolution) corresponding to the time (resolution) interval $\tau = 2\cdot 10^{-5}\ s$. Accordingly, the current per unit length obtained after Abel inversion of the ion saturation current is

$$\frac{I}{a} = 2\pi r_p n(T) e\mathrm{v}(T)/4 = \frac{\pi r_p}{2} n(T) e\mathrm{v}(T) = \theta n(T)\mathrm{v}(T) \qquad (11.2)$$

where the temperature dependency of the ion density at the sheath edge (either n_∞ or n_s) is given according to Chapter 2 (Olsen [15]). In low-pressure probe theory the ion density at the edge is n_s=0.6 n_∞. The constant θ in (11.2) includes the geometry and the factors that depend on the choice of the ion velocity.

If a continuum plus free fall model (CFF) is chosen according to formula (4.13), then an additional dependency on ion velocity and temperature enters in the expression of the current via the mobility, because by using $\mu_i = eD/kT_e$ and $D_i = \lambda_i \mathrm{v}_i/3$,

$$\mu_i = \frac{eD_i}{kT_i} = \frac{e\lambda_i \mathrm{v}_i}{3kT_i} \qquad (11.3)$$

It should be noted that here the 'thermal assumption' T_e=T_i must be made, unless an independent means of determining the ion temperature is found. Moreover, the ion mean free path was used according to the determination given in Chapter 2 for the different temperature ranges, again under the thermal assumption. As in the random case also in the CFF model, the different forms of the ion velocity have to be considered (depending on whether a pre-sheath is assumed or not) as well as the collecting surface variations.

To facilitate the identification of these different possibilities, Table 11.1 reports the corresponding constants needed in the calculation of the ion current density per unit length at ion saturation. These constants were used to build the property table referred to in the next section. On the right hand side, the expression of the current per unit length is shown with the possible combinations of constants. The first factor is common to all formulae; the others may be present or not (pre-sheath factor) in different combinations (probe surface and ion velocity). Note that the temperature is the electron value.

Ion velocity	Probe surface	
$\mathrm{v} = \sqrt{2kT_\mathrm{e}/m_\mathrm{i}}$	$S/a = 2\pi r_\mathrm{p}$	$I_\mathrm{n} = \underbrace{\frac{e\pi r_\mathrm{p}}{2}}_{\text{constant}} \cdot \underbrace{(0.61)}_{\text{pre-sheah}} \cdot \underbrace{\begin{cases} 1 \\ 1/2 \\ 2/3 \end{cases}}_{\substack{\text{probe} \\ \text{surface}}} \cdot \underbrace{\sqrt{2k/m_\mathrm{i}}}_{\text{v, most probable}} \cdot n(T_\mathrm{e}) \cdot \sqrt{T_\mathrm{e}}$
	$S/a = \pi r_\mathrm{p}$	
	$S/a = 4\pi r_\mathrm{p}/3$	

Table 11.1 For the determination of the ion current expressions at ion saturation. Left, ion velocity, centre surface: whole, half and two-thirds. Right, combinations of the constants in the expression for the current (see text)

2. Extraction of the information from data

Due to the high number of *V-I* curves, radial averaged, chordal-averaged, and the 'local' curves (*cf* Chapter 9), it is necessary to automate the information extraction procedure. This has been done using the tables of the characteristic curves, and a table containing the physical properties as a function of temperature. To clarify the method, the structure of these tables is reported in figure 11.1.

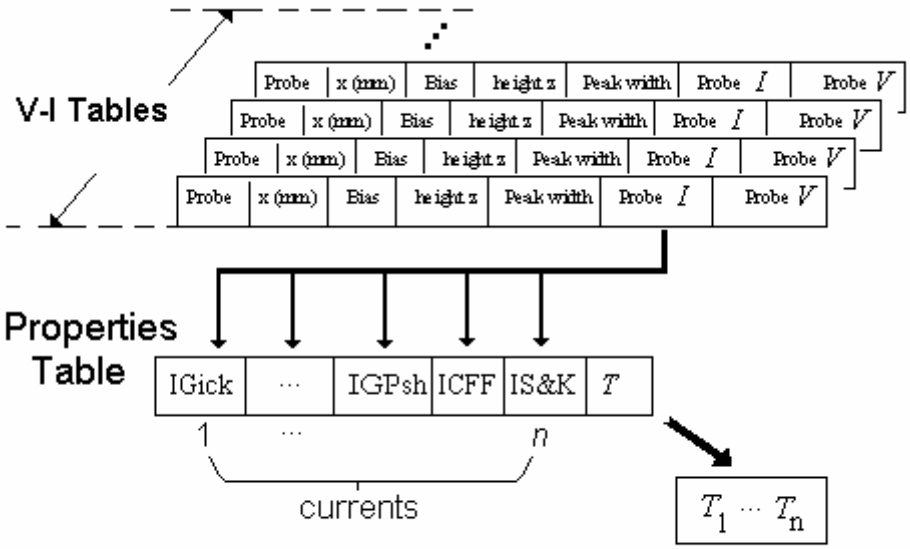

Figure 11.1. The *V-I* Tables values for the currents (per unit length) are searched for in the "Properties" Table (see text). Legend: Gick, random; IGPsh, Gick model with pre-sheath, CFF, Continuum plus Free-Fall; S&K, Su and Kiel; *T* electron temperature/s

Each of the V-I tables available is accessed with the measured currents (normalized to the contributing length for the averaged case or to the minimum step size for the Abel inverted ones) in order to:

- determine the maximum values (three) of the current and average those (after verification that the difference within each couple is of the order of the experimental error, and thus belong to saturation);

- extract the corresponding probe potential and coordinates (r and z);

- Search for the saturation currents individually within each of the columns in the 'properties' table in order to read, after interpolation, the corresponding temperatures.

As can be seen from the different values of the constants, the results differ quite widely one from the other. Also, three major problems occur for this method.

- CFF's currents rely on the mobility, computed through the ion mean free path, which in turn, depends on temperature; this may add additional uncertainty to the obtained temperature.

- Olsen's dependency is based on *LTE*, therefore all the temperatures obtained are equilibrium temperatures, T_e=T_i.

- For the random cases, the current-temperature relationship is not monotonic above ~17,800 *K* as can be seen from figure 11.2 (left). In this case, ambiguities arise in the choice of the correct temperature.

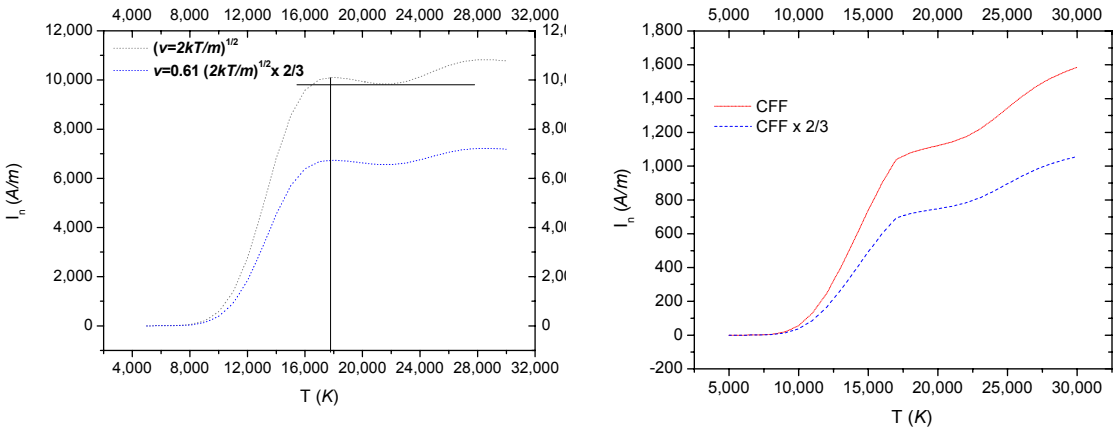

Figure 11.2 Probe (ion) currents per unit length (*A*/*m*) as a function of temperature. Left, Random/diffusion currents for different θ coefficients (see text). The non-monotonicity is indicated by the two lines are drawn at 17,800 *K* and 18,900 A/m. Right, Continuum plus Free Fall (CFF) for whole and partial (2/3) collecting surface

Owing to the additional mobility factor and to the different current-temperature relationships (*cf* Table 11.1), this problem is not present for the CFF-type currents shown in figure 11.2 right.

The non monotonicity of the I/*l* versus *T* curve is due to the corresponding character of the *n*(*T*) curve shown for clarity in its inverse form in figure 11.3 left. Beyond $n \sim 1.6 \cdot 10^{23}\ m^{-3}$ the temperature is not unique (This influences any attempt to determine the temperature from the knowledge of the ion density). Figure 11.3 right shows the result on the current computed according to the random model with a pre-sheath and a 2/3 collecting surface. Any current per unit length in excess 6,558 *A*/*m* would lead to temperature ambiguity. This could be a limitation because the algorithm used in this work limits the search only to the first of the possible *I*-*T* correspondences.

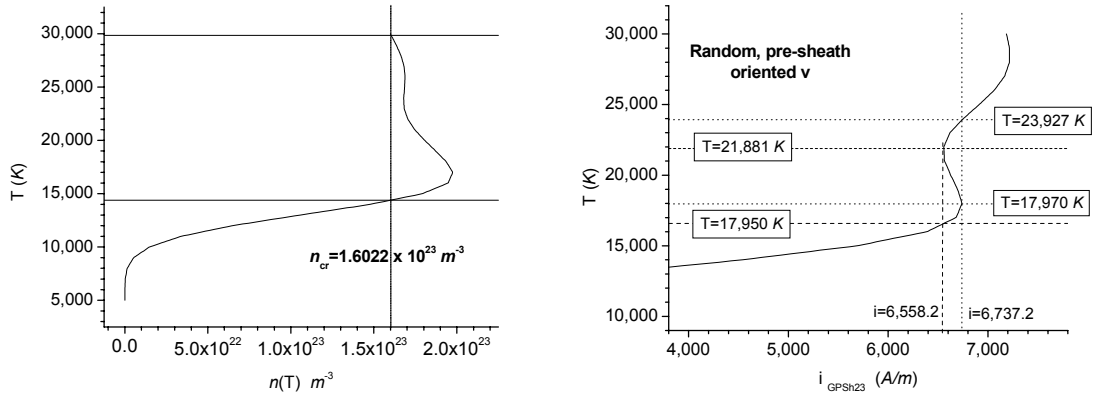

Figure 11.3 Left, non monotonicity of the *n*(*T*) function (*cf* [15] and Chapter 2). Right, consequences on the current per unit length as a function of temperature.

However, it will be seen that none of the temperatures belonging to this group ever reaches the critical value beyond which the curves are not monotonic or more appropriately for this experiment, the current per unit length does not reach the critical value indicated in figure 11.2 and 11.3 right, in any of the experimental cases considered within this work.

11.3 Temperature computations

The temperatures computed for the different coefficients are shown for each arc current, in figure 11.4 a to e for the five arc currents. The series is obtained according to the guidelines indicated in Table 11.1 and refers to axial temperatures. For the cases where optical measurements were available, the corresponding optical temperatures are also shown.

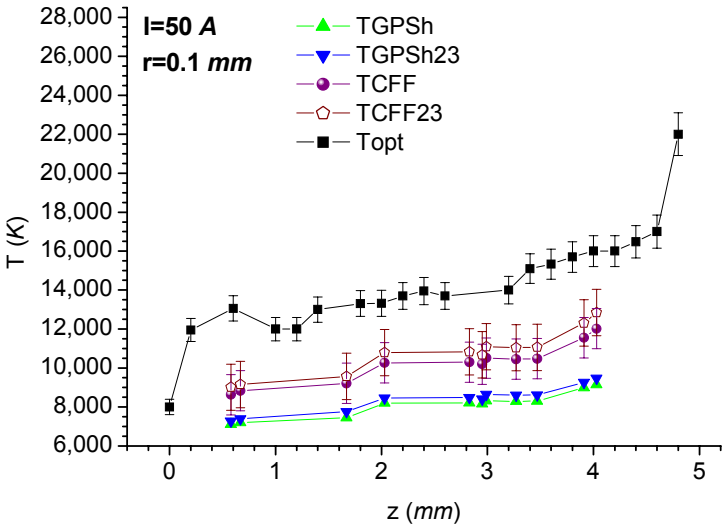

Figure 11.4 a I=50 *A*. Temperatures obtained form probes, compared with optical spectroscopic values (available at 50, 100 and 200 *A*).

LEGEND (see text for definitions): TGPSh/TGPSh23, Gick's random current temperature with pre-sheath / and 2/3 collecting surface; TCFF /TCFF23, Temperature from Continuum plus Free-Fall / with 2/3 collecting surface; Topt**,** Optical (Emission Spectroscopy determined) Temperature

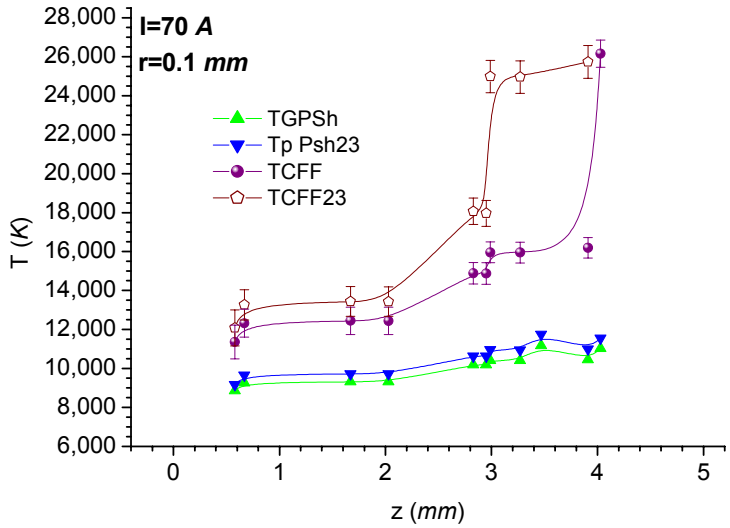

Figure 11.4 b I=70 *A*. Temperatures obtained form probes, compared with optical spectroscopic values (available at 50, 100 and 200 *A*).

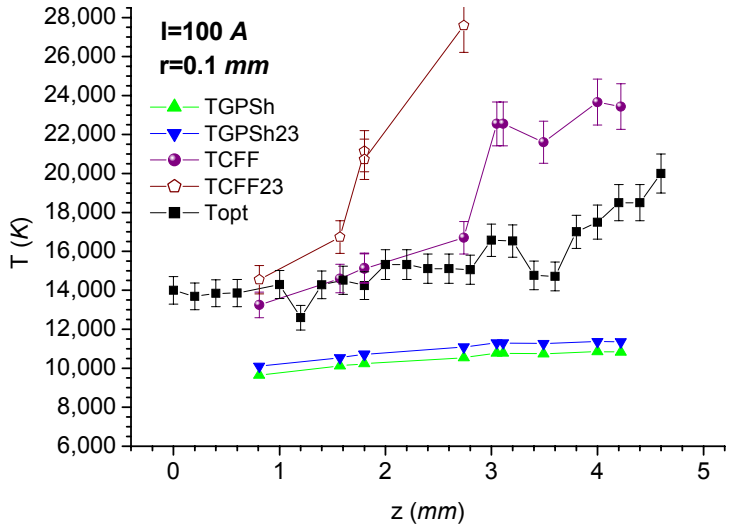

Figure 11.4 c I=100 *A*. Temperatures obtained form probes, compared with optical spectroscopic values (available at 50, 100 and 200 *A*).

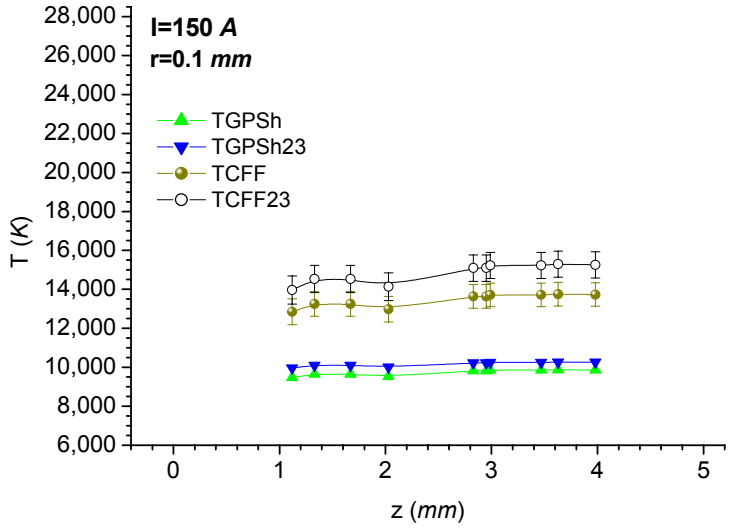

Figure 11.4 d I=150 *A*. Temperatures obtained form probes, compared with optical spectroscopic values (available at 50, 100 and 200 *A*).

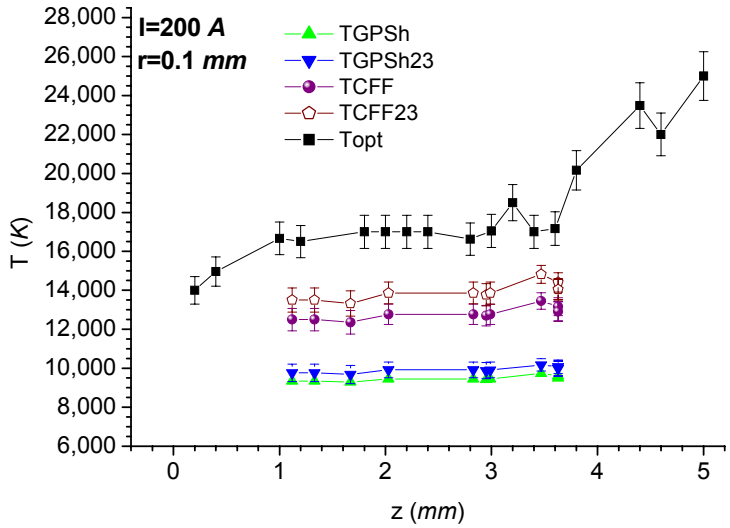

Figure 11.4 e I=200 *A*. Temperatures obtained form probes, compared with optical spectroscopic values (available at 50, 100 and 200 *A*).

Looking at the graphs for the temperatures in figures 11.4 some observations are possible:

1. The probe temperatures appear to be grouped in two classes, a higher, defined by the CFF model, and the lower of the random type;

2. the temperatures of the random group are lower by a factor 0.58 to 0.62 with respect to spectroscopic determinations;

3. The CFF group temperatures reach 0.7 to 0.8 of the optical values (when available); in the 100 A case it exceeds the optical values.

4. Langmuir probe temperature variations are limited to a range between 1,000 *K* and 2,000 *K*, similar to the values from emission spectroscopy in the comparable arc height range (*z*).

6. All the probe temperatures increase from 50 to 100 *A* and thereafter decrease at 150 and 200 *A*. The decrease from 150 to 200 *A* is perhaps within the experimental error. In contrast, the optical determinations increase monotonically with the arc current.

These trends extend to off-axis positions. It should be noted that each of the ion saturation currents has been computed under the assumption of a thermal plasma (T_e=T_i) because it is under this assumption that relationships are available which relate particle density and temperature; and because independent ways of determining the particle

number densities do not exist or present very poor accuracy. Whilst the existence of LTE is in serious doubt for the lower current cases, *I*=50 and 70 *A*, and even if uncertainty exists about the onset of LTE even for high current arcs, the 200 *A* case is believed to show a good degree of LTE at least in the core region.
The selection of the proper temperature can be aided by the use of Table 11.2 where the observations are grouped per arc current.

Iarc (*A*)	Highest T's (among probe T's) in decreasing order	Probe T closest to Optical	Notes
50	**TCFF23** **TCFF**	**(TCFF23)**	-
70	**TCFF23** **TCFF**	**-**	TCFF23 some points out of range
100	**TCFF23** **TCFF** **TGPSh23**	**TCFF** **TGPSh23**	TCFF up to *z*=2.5 *mm* TCFF23 overcomes optical
150	**TCFF23** **TCFF**	**-**	
200	**TCFF23**	**TCFF23**	-

Table 11.2. Summary of observations on temperatures for the different arc currents. Nomenclature as in figure 11.4

The table allows the following selection considerations.

- Among the probe determined temperatures there is the dominance of the CFF model with a prevalence of the reduced collection surface (TCFF23). However, for the latter, there is no clear uniformity of behaviour with increasing arc current. At 100 *A*, the model overcomes the optical values and is actually beyond the possible tabulated values for the given temperature, at arc heights above z=2.8 *mm*. Since there are no optical data available at 70 *A* it is not possible to determine whether this occurs already at 70 *A* although, CFF probe temperatures at this current, if correct, would be comparable with optical determinations at 200 A.

- The probe temperatures most closely approaching the optical values is the TCFF23 at the extreme current values (50 and 200 *A*) whereas at 100 *A*, the closest temperature is the simple TCFF which, however, exceeds the optical at z=2.6 *mm* (*cf* figure 11.4).

11.4 Temperature selection

Of the several temperature candidates a selection is made based both on the proximity with the optical values and on considerations on the experimental error. In all cases the error on the optical values has been estimated to within 5%. The probe temperature errors vary due to the variable error on the read current (see Appendix E) and a preliminary conclusion can be made that the discrimination of the correct value among the 'random group' (lowest in all the plots) is extremely difficult.
With the purpose to search for a model valid under all the arc current circumstances, the temperatures in the CFF group appear to provide values closer to the optical. The CFF23 is the closest to the optical values but it tends to increase steeply with increasing arc current. In contrast, CFF seems the most stable [obtained using the whole collecting surface, even if not perfectly monotonic (because of the 100 *A* case) but common to the other determinations]. However, because (i) there is the possibility of an unknown factor that drops temperatures of the random type and (ii) it is difficult to discriminate the best value among the random group, an empirical procedure of selection will be followed.

The choice of a temperature based on its proximity with an independent measurement must be justified on a physical basis. In the first place, the chain of hypotheses that led to the various formulae for these temperatures, imply a choice for the constants that can compensate for other more physical phenomena which cannot be excluded, like cooling. In other words, the partial agreement between one of the selected probe temperatures (the TCFF up to about mid-arc at 100 *A*, figure 11.4) with the optical temperatures may be incidental.
The CFF temperature determination is based on the collisionless sheath that breaks the homogeneity of the continuum plasma; the motion of the ions past the sheath is mobility dominated and in fact this is the quantity entering the corresponding relationship (5.14). Also, by using the thermal assumption the pre-sheath is assumed to be absent. In practical terms, a further 'simplification' has been introduced by the use of the Einstein relationship to express the mobility in terms of the diffusion coefficient (which requires thermal equilibrium). The diffusion coefficient has been expressed in terms of the ion mean free path and thermal velocity. The mean free path dependency on temperature has been used according to the curves given in Chapter 2. All these steps imply a degree of a Maxwellian PLTE at least, because on this assumption are based the calculation of $n(T_e)$, $\mu_i(T)$, $\lambda_i(T)$, $v_i(T)$ and furthermore $T_e=T_i$ was implied as a starting point of formula (11.2).

The Random representative, TGPSh23 arises from a thermal motion up to a pre-sheath, where the effects of the field start to become important; the field accelerates the ion towards the probe thereby modifying the ion velocity which, at the sheath entrance is

the velocity of a quasi-monoenergetic flux of particles. This velocity is higher than the Bohm velocity required for the sheath formation.
A provisional choice is made of two temperatures: the CFF model and the highest among the closest to the optical in all cases, e.g the TGPSh23 which is the random model with most probable velocity v, existence of a pre-sheath factor (~0.61) and partial collection surface (2/3).
Since these two temperatures are both lower than the spectroscopically obtained electron temperatures, a method to identify and correct the discrepancy is needed. This will be discussed in section 11.5
Since none of the current models employed contain a dependency on the flow velocity, there is some question concerning the use of stationary plasma formulae to describe a flowing system. Some attempts to include the flow dependencies into the determination of the temperatures are discussed in sections 11.6 and 11.7.

11.5. Correlation between ion saturation temperatures and optical temperatures

The emission spectroscopy electron temperatures are obtained with the Fowler-Milne method [1], which assumes PLTE. These temperatures are in good agreement with published data on electron temperatures obtained by this method, at least for currents greater or equal than 100 *A* (doubts persist about the attainment of LTE in lower current arcs, e.g. I=50 *A* [19], especially at low arc heights and in the in the fringes [20]).

As an example, figure 11.5 shows typical temperature maps obtained using the 696.54 *nm* Ar line with the Fowler-Milne method, for arcs operating at 50 and 200 *A*.

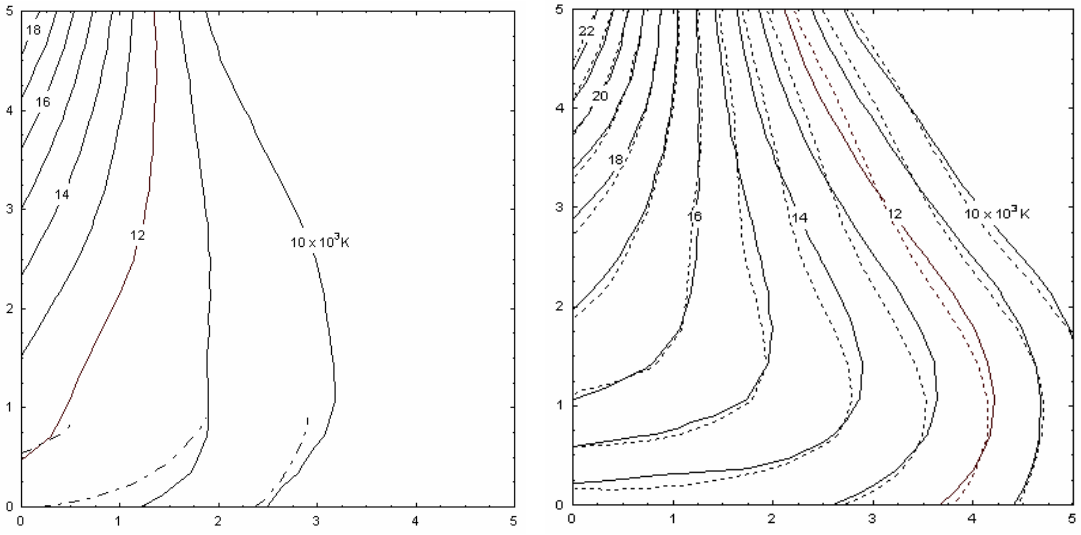

Figure 11.5 Temperature maps from emission spectroscopy (Fowler-Milne method) in Ar. Left, 50 A from 696,54 Argon line, right Ar, 200 A (Fowler-Milne from 696,54 nm Ar line (solid lines) and 706.2 nm (dashed lines).

If the arc is in LTE, these optical temperatures should agree with temperatures obtained by the probe method. In contrast, a plasma which is not in LTE nor in PLTE may still be characterized by these electron temperature which then describe the electron population ("kinetic temperatures"). Probe temperatures are systematically lower. This may be due to the plasma cooling by the probe, which would therefore measure a boundary layer temperature at the sheath edge of the undisturbed bulk plasma, perhaps in LTE, or it may be due to an LTE violation irrespective of the probe cooling.
If the plasma is in LTE then the probes *could* measure a comparable electron temperature, even taking into account the cooling, which means that even if the absolute values of the electron temperatures obtained by probes were substantially lower, these could be reconstructed towards the 'correct' values, provided some correlation between the two families of temperatures were available.

The correlation can be looked at by comparing the optical temperatures against the probe temperatures obtained from the ion saturation current. The sets of graphs in figure 11.6 a to f, show a selection of the radial temperatures for arc currents I = 50, 100 and 200 *A*. Subsequently, the same probe temperatures are shown as a function of the corresponding optical temperature for probes at comparable arc heights in figure 11.7.

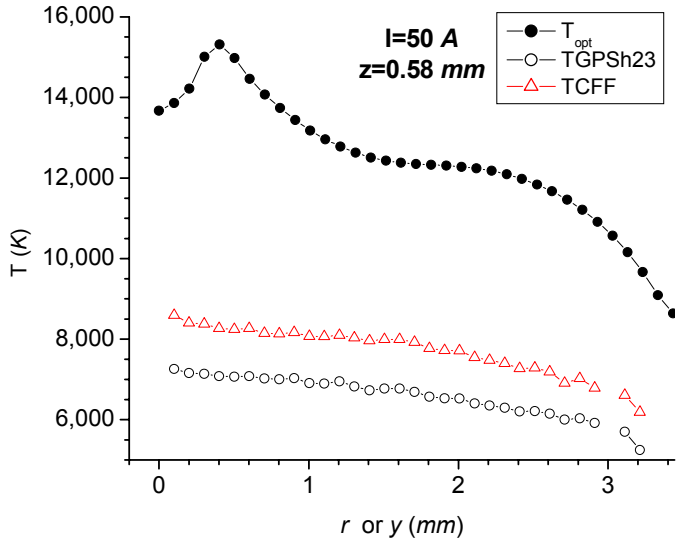

Figure 11.6 a Selection of temperatures for I=50 *A*. Optical temperatures (full circles) and probe temperatures (empty symbols) at z=0.58 mm

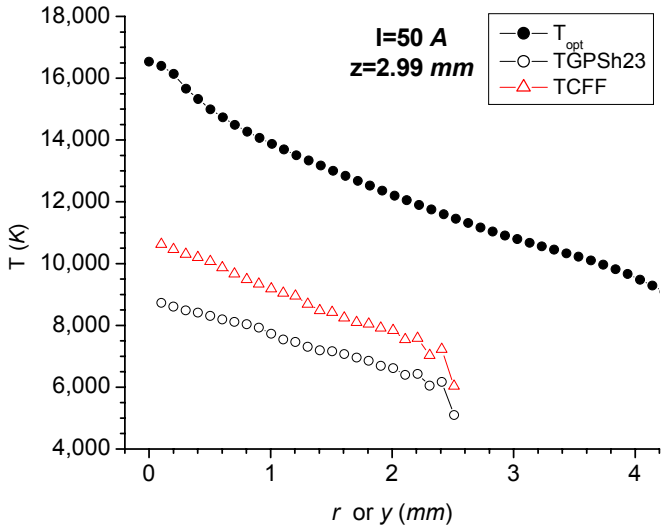

Figure 11.6 b Selection of temperatures for I=50 *A*. Optical temperatures (full circles) and probe temperatures (empty symbols) at z=2.99 mm

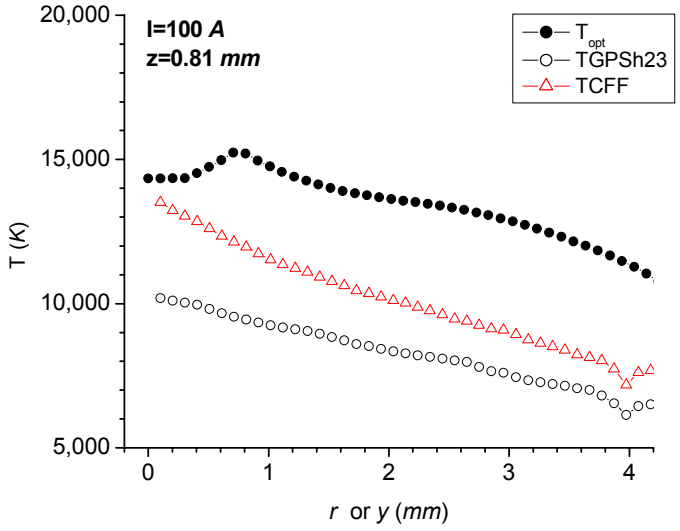

Figure 11.6 c Selection of temperatures for I=100 *A*. Optical temperatures (full circles) and probe temperatures (empty symbols) at z=0.81 mm

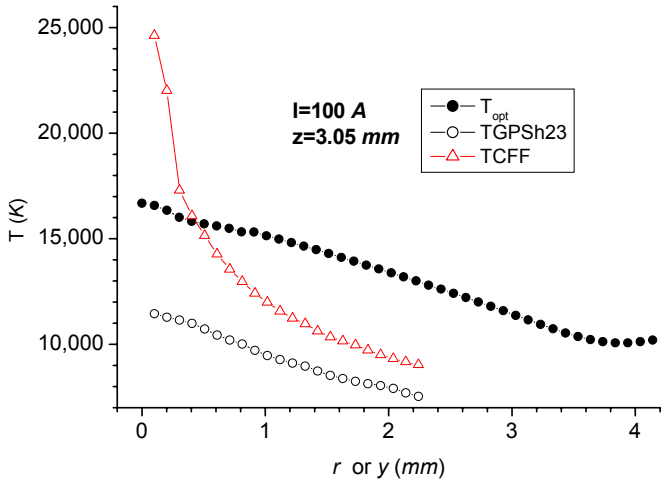

Figure 11.6 d Selection of temperatures for I=100 *A*. Optical temperatures (full circles) and probe temperatures (empty symbols) at z=3.05 mm

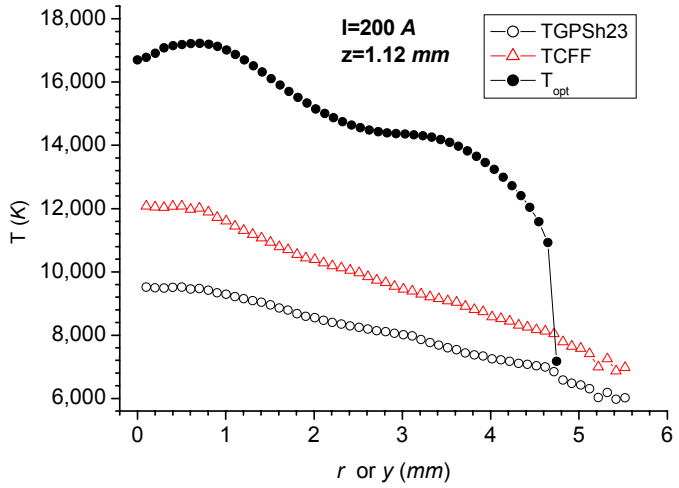

Figure 11.6 e Selection of temperatures for I=200 *A*. Optical temperatures (full circles) and probe temperatures (empty symbols) at z=1.12 mm

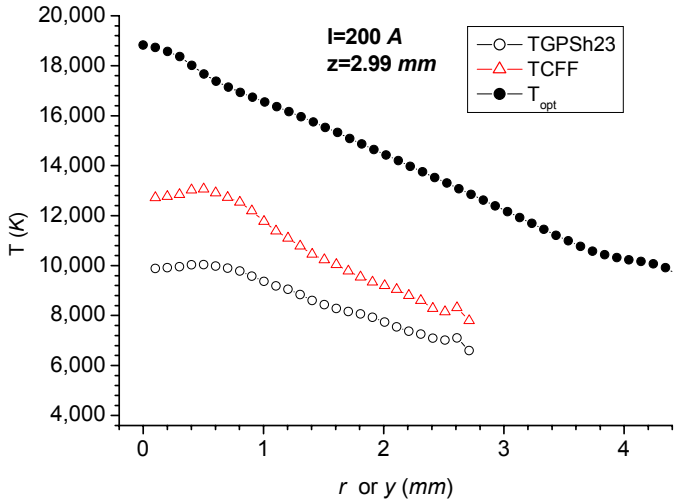

Figure 11.6 f Selection of temperatures for I=200 *A*. Optical temperatures (full circles) and probe temperatures (empty symbols) at z=2.99 mm

From figure 11.6, the following observations can be made:

1. The trends of the probe and spectroscopic curves as a function of arc height are the same across the range of currents examined.

2. The gradients of the probe temperatures are less than the corresponding optical measurements but they are determined mainly by the points closer to electrodes, not accessible to probes. If one limits to the common region (in the *z* coordinate), within 1 *mm* from the arc centre, this gradient is an increasing function of the arc current, e.g. the higher the *I*, the higher *gradT*.

3. In the 50 *A* and in the 200 *A* case, the probe temperatures are lower than the optical temperatures;

The correlation of the two pre-selected probe temperatures with the optical is shown in figure 11.7 a to f.

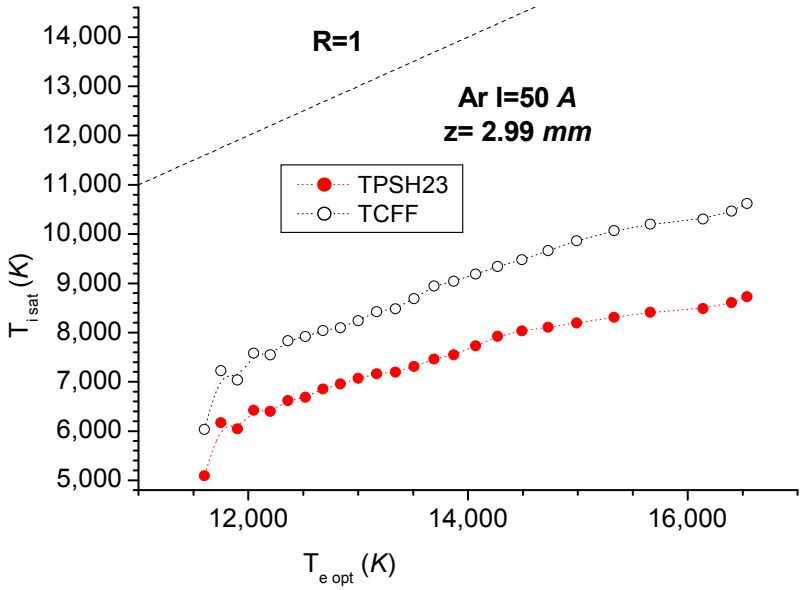

Figure 11.7 a. Selection of temperature correlations for I=50 *A* for the case shown in figure 11.6 a

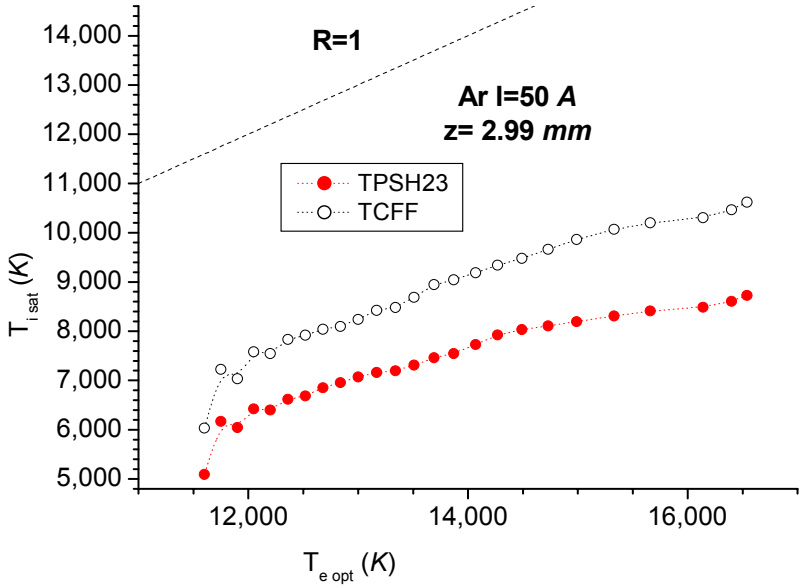

Figure 11.7 b. Selection of temperature correlations for I=50 *A* for the case shown in figure 11.6 b

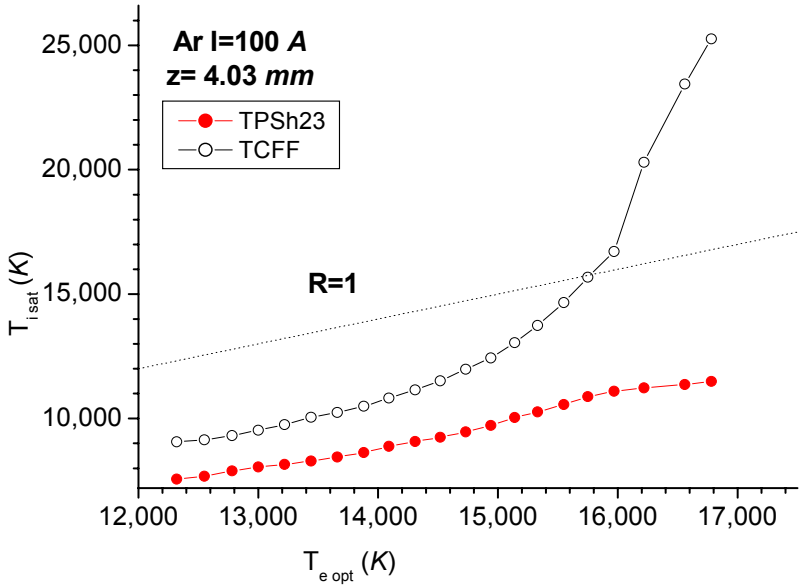

Figure 11.7 c. Selection of temperature correlations for I=100 *A* for the case shown in figure 11.6 c

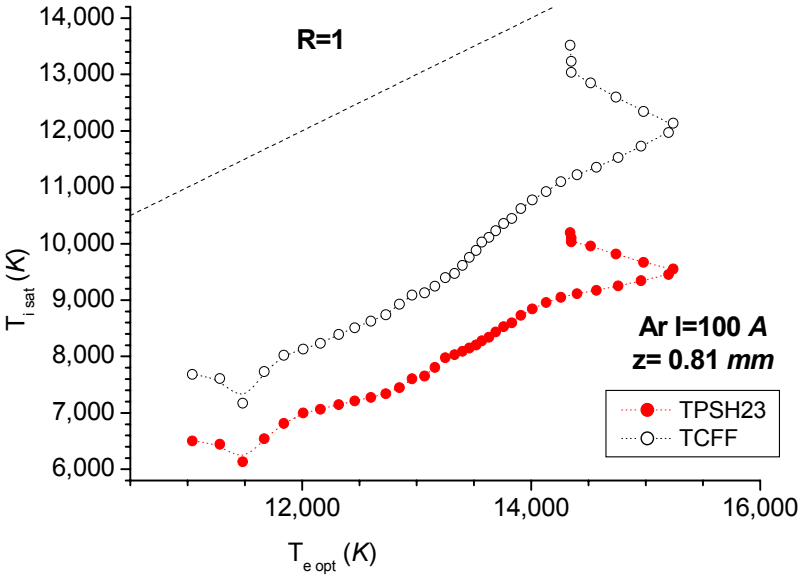

Figure 11.7 d. Selection of temperature correlations for I=100 *A* for the case shown in figure 11.6 d

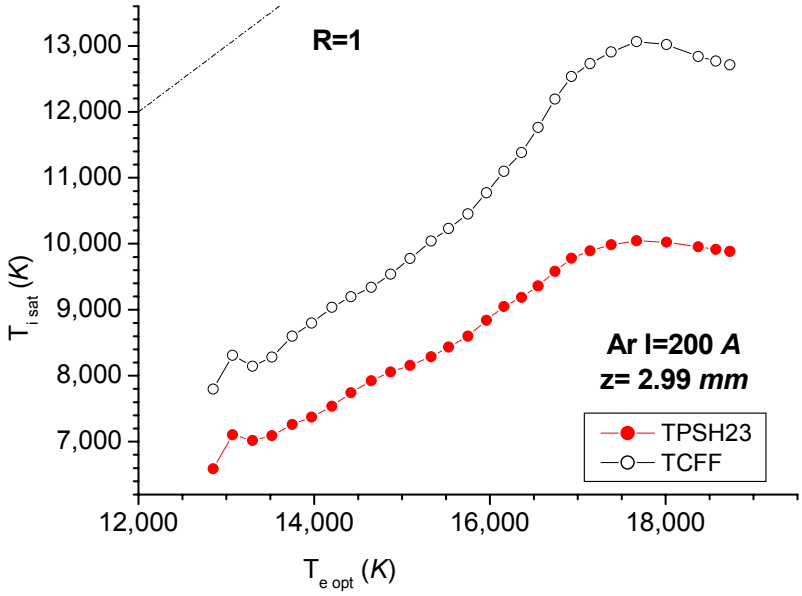

Figure 11.7 e. Selection of temperature correlations for I=200 *A* for the case shown in figure 11.6 e

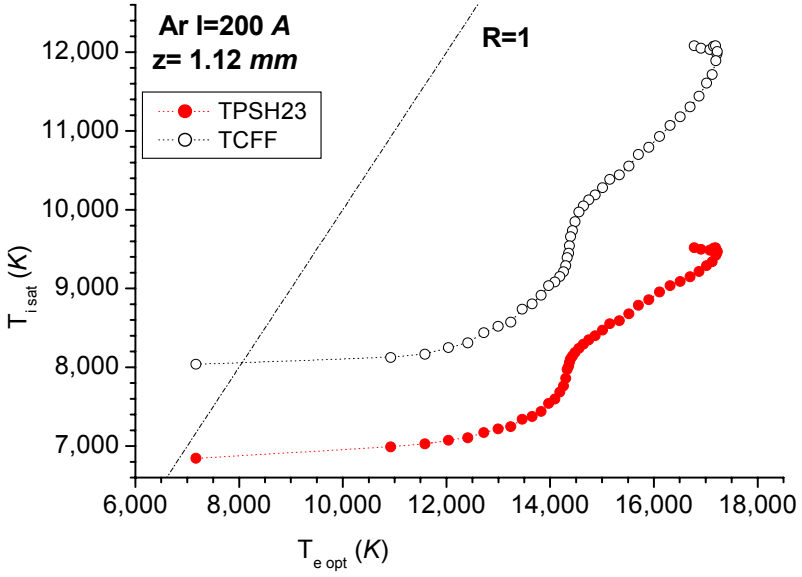

Figure 11.7 f. Selection of temperature correlations for I=200 *A* for the case shown in figure 11.6 f

The two probe temperatures for purely random ion current (labelled "TPSH23", *cf* Table 11.2) and of continuum plus Free-Fall ion current model (TCFF) are shown as a

function of the optical determined temperature. The ideal correlation is shown by the straight line labelled *R*=1.

The correlation between the optical and probe temperature can be also looked at by plotting the ratio of probe to optical temperatures as a function of the radial distance in view of an identification of a possible correction factor. The graphs corresponding to the temperatures of figures 11.6 and 11.7 are shown in figure 11.8 a - f.

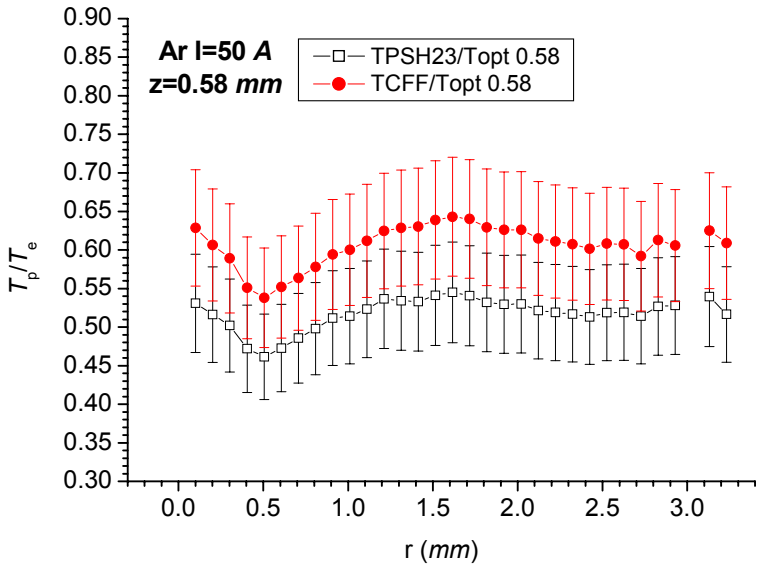

Figure 11.8 a. I=50 *A*, probe to optical temperature ratios for the case of figure 11.6 a

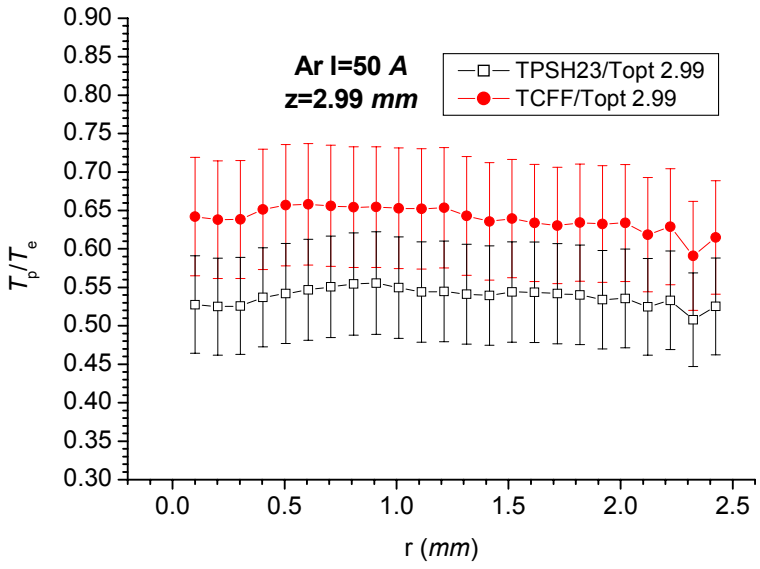

Figure 11.8 b. I=50 *A*, probe to optical temperature ratios for the case of figure 11.6 b

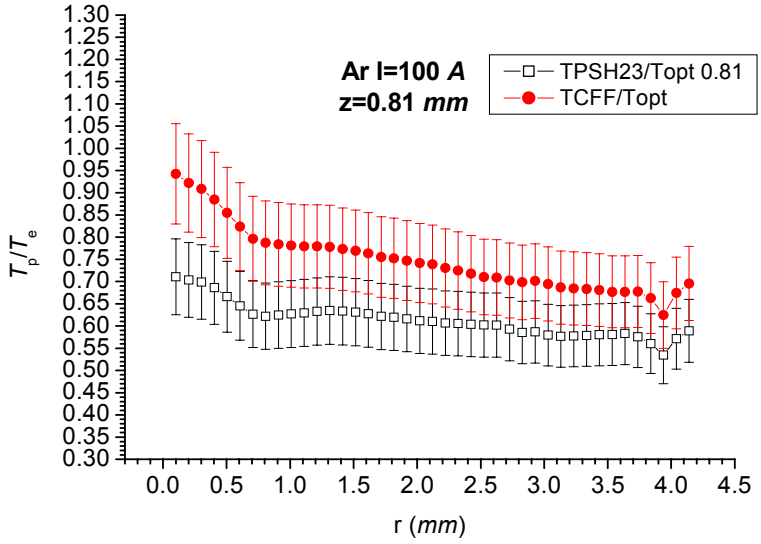

Figure 11.8 c. I=100 *A*, probe to optical temperature ratios for the case of figure 11.6 c

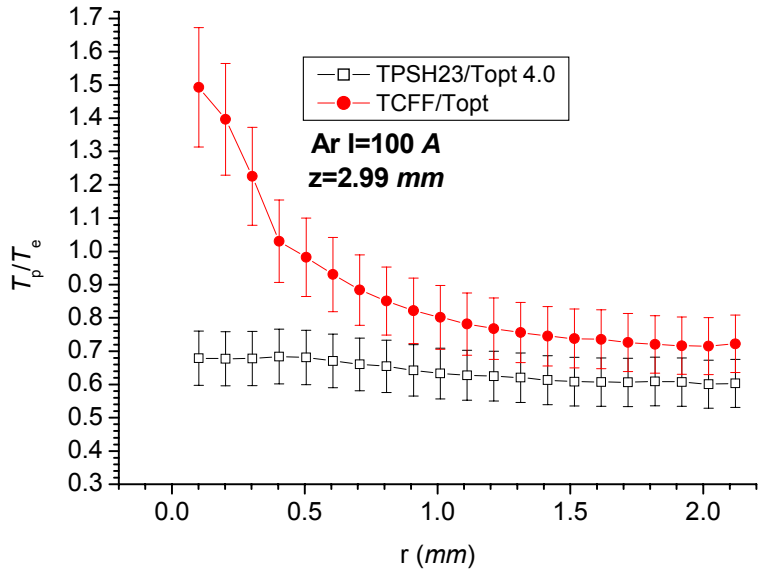

Figure 11.8 d. I=100 *A*, probe to optical temperature ratios for the case of figure 11.6 d

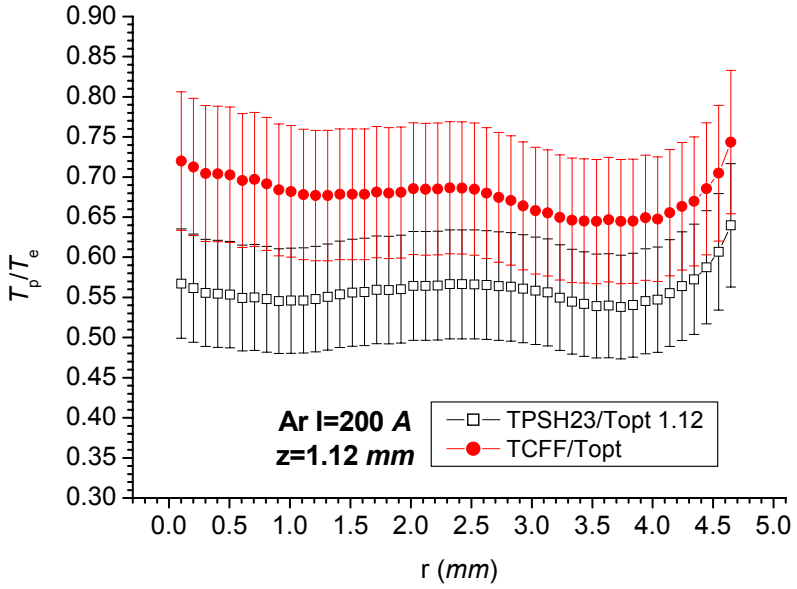

Figure 11.8 e. I=100 *A*, probe to optical temperature ratios for the case of figure 11.6 e

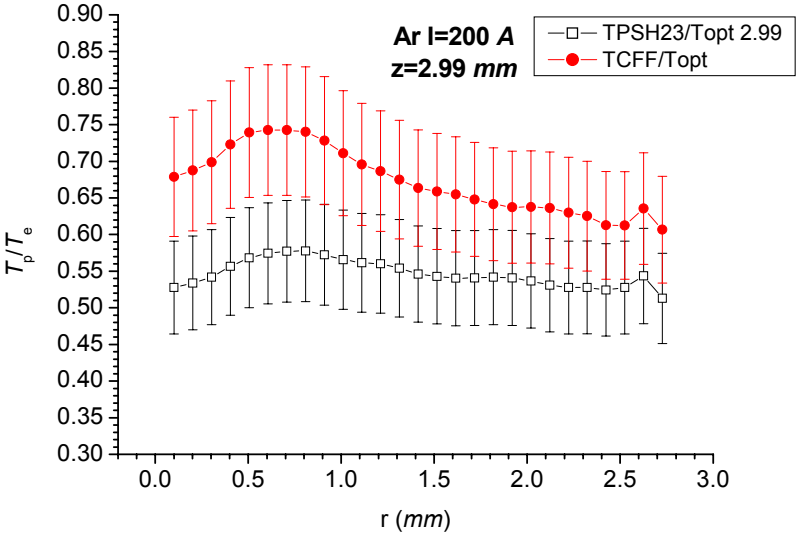

Figure 11.8 f. I=100 *A*, probe to optical temperature ratios for the case of figure 11.6 f

Even considering 1) the restricted selection shown here and 2) the relatively high uncertainty on the ratios (up to about 12% due to the error on the probe measurements, see Appendix E), it is shown that the trends in the three cases are different. The ratios for I=50 *A* and I=200 *A* can be considered constant to a first approximation (*cf* figure

11.8). This is somewhat confirmed in the ratios shown in figure 11.5. The I=100 *A* is less clear because the probe temperature exceeds the optical one for the CFF case and shows a slight tendency to increase for the other case, as the radial distance is reduced. So a lack of monotonicity makes the use of the ratio in the intermediate case I=70 *A* and I=150 *A* difficult (at the two sides of the I=100 *A* case).

Up to this point, it has been shown that:

- Of the many possible temperature from random-like expressions at saturation, two can be chosen due to their proximity with optical temperatures, the TCFF or because of the simple model they suggest, TPSH23 (which does not include mobility dependency);

- All probe temperatures, except in one case are lower than the optical values;

- There is no complete monotonic behaviour of the possible corrective factor T_{prb}/T_{opt} in passing from the lowest to the highest arc current although, two out of three cases in the CFF case (e.g. 100 A case is an exception) and all of three in the random case, show relative constancy of the probe to optical ratio. This is discussed further in section 11.9.

Without judging on the validity of the spectroscopic determination (due to excellent agreement with previously published data [21]), a few possible explanations for the lower temperatures are discussed in the following sections. These include:

- Use of relationships which do not account for plasma motion (*cf* 11.6 and 11.7)

- The currents measured at saturation are too high, perhaps perturbing the arc (11.8)

- Cooling of the plasma (11.9)

11.6 Inclusion of flow velocity in the expressions for the currents

In order to evaluate the currents in flowing conditions, in addition to the probe potential corresponding to 'saturation' (with the exception of Lam's (4.13) diffusive current), the flow velocity is required. This quantity is unknown experimentally, therefore some evaluations are attempted in the following by taking this quantity as a free parameter in the range believed to apply to the TIG arc, for the case, I=50 *A*, between 50 and 100 *m/s* (*cf* Chapter 2); for the 200 *A* up to 400 *m/s*. In section 11.7 a different approach based on the search for a velocity-arc current relationship is followed.
Some columns of the “properties” table in figure 11.1 were substituted by the flowing currents of Lam (4.13) and by Clements and Smy's convection regime (4.46 and 4.47).

The last two were computed for comparison, although in the present I=50 *A* case, ion saturation is always observed in contrast to Clements and Smy's convection model (although this is not necessarily be the case for higher arc currents, *cf* Table 9.2).

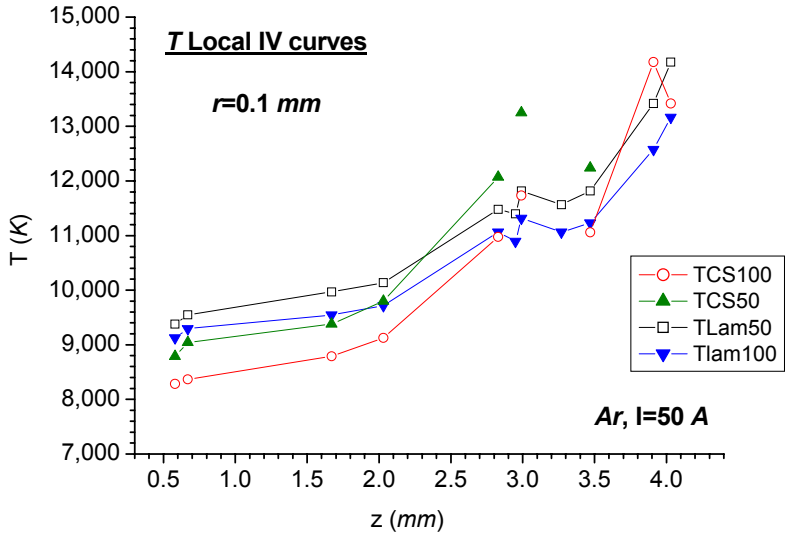

Figure 11.9 a Temperatures obtained from the ion saturation currents parametrized with different but uniform flow velocity and radial distance. r=0.1, *mm* from centre.

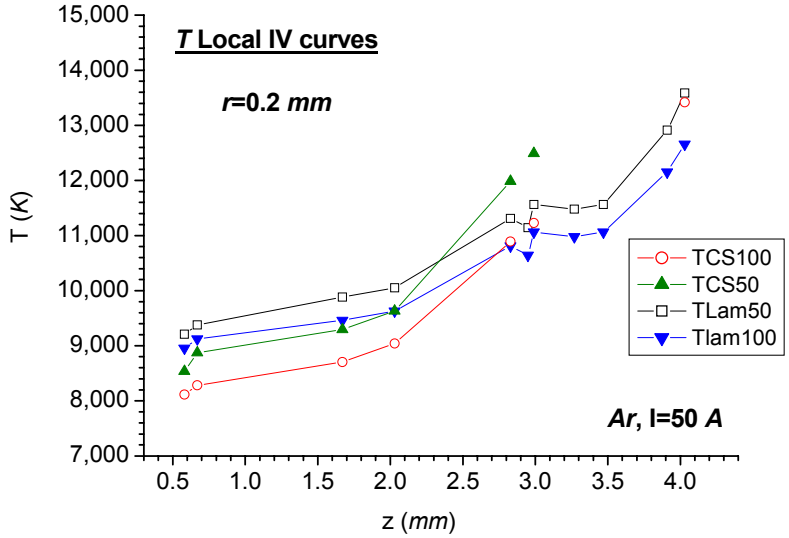

Figure 11.9 b Temperatures obtained from the ion saturation currents parametrized with different but uniform flow velocity and radial distance. r=0.2 *mm* from centre.

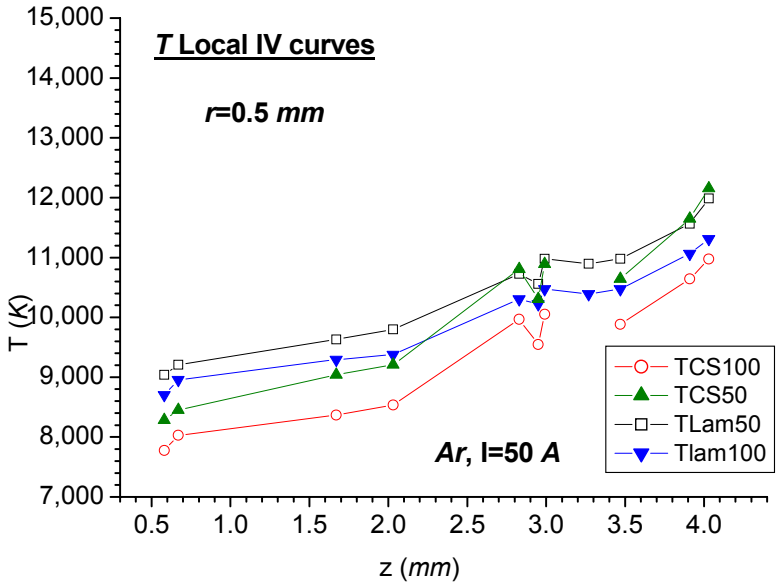

Figure 11.9 c Temperatures obtained from the ion saturation currents parametrized with different but uniform flow velocity and radial distance. r=0.5 *mm* from centre.

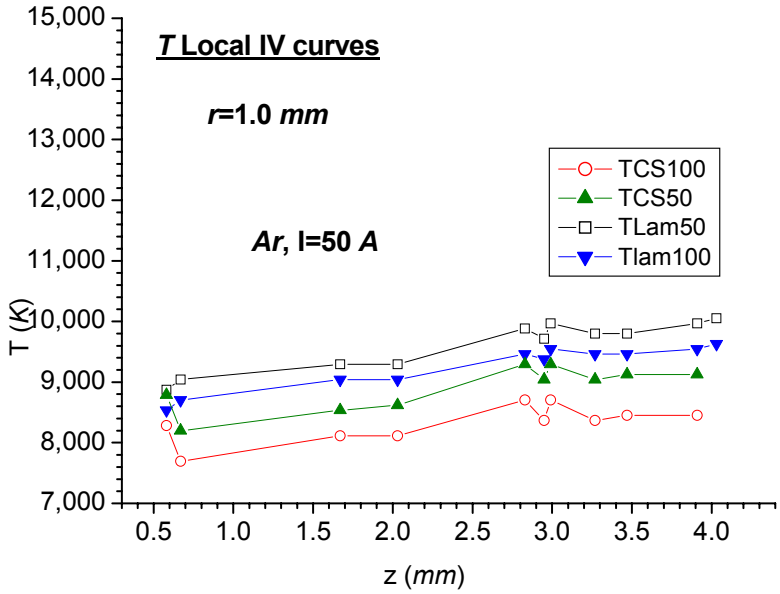

Figure 11.9 d Temperatures obtained from the ion saturation currents parametrized with different but uniform flow velocity and radial distance. r=1.0 *mm* from centre.

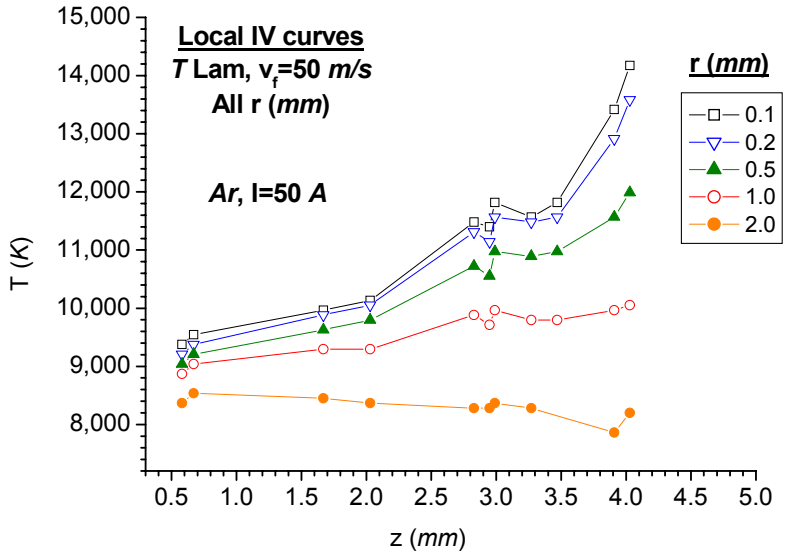

Figure 11.9 e Lam's diffusive temperature at v_f=50

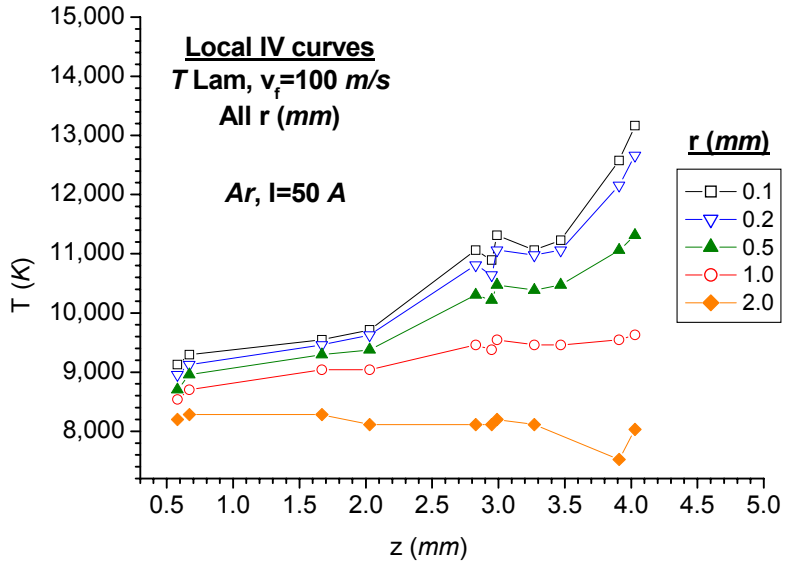

Figure 11.9 f Lam's diffusive temperature at v_f=100 *m/s*

The results for the currents at v_f=50 and v_f=100 *m/s* for each of the two cases at I=50 *A*, are shown in the first two graphs of figure 11.9. The last two graphs report Lam's temperatures for all the radial distances at the two velocities (left v_f=50 *m/s*) and right (v_f=100 *m/s*), because this model predicts (correctly) ion saturation (The discontinuity at z~3.0 mm has been observed in several temperature determinations but has been left unexplained).

At first sight, the fact that these temperature values are higher than the values obtained for stationary plasmas is encouraging. However, the use of temperatures parametrized by the flow velocity is somewhat misleading because the latter could vary with position within the arc both radially and axially. In the first case therefore, especially at the fringes, the values of the temperatures may be seriously in error (overestimated because the velocity is assumed higher than real) with respect to the core of the plasma for which those parameters were chosen. Correspondingly, core the temperatures may be underestimated. Conversely, because the velocity decreases along the vertical axis the temperatures would be underestimated in the anode region.
Furthermore, with respect to the small temperature gradient along the axis, if flowing plasma cooling effects are of relevance, then it can be expected that approaching the anode the flow velocity eventually reduces to zero (stagnation point). This would mean that errors due to probe cooling decrease approaching the anode. As can be seen from figure 11.8, because the ratio of probe to optical temperature is actually constant with reducing z, this is not the case. A further comparison is made in section 11.7 where the effects of a different flow velocity are addressed.

11.7 Arc current - velocity relationships

If the cooling of the plasma is due to arc flow velocity, and since some indications of monotonic dependency (proportionality) of flow velocity on arc current exist [22], one would expect to have greater cooling where the arc current is higher.
Figure 11.10 left, shows the average axial velocity for two hypotheses of cathode exit flow velocities, normalized to the free-stream flow velocity v(∞) [22].
On the right, arc flow velocity as a function of arc temperature has been computed for different arc currents by means of the Reynolds number [22] calculated with the density and viscosity temperature dependencies from Murphy [23] (and shown in Chapter 2).
These two pictures are used in conjunction. For a given current chosen on the left plot, say 100 *A* on the lower curve, the corresponding velocity can be read as ~100 *m/s* and could be sought in the picture on the right. Here, the curve labeled 100 reaches the velocity axis value of 100 *m/s* at a temperature of 15,000 *K*. In the first figure, the lower value of the normalized velocity is chosen (according to Allum [22] and [24] values), thus the lowest of the two curves. This is somewhat in disagreement with the picture shown on the right where for instance, a higher value of the temperature would be expected for *I*=200*A*. A different choice, however, would lead to temperatures which are higher than accepted value for the corresponding current (for instance a choice of the upper curve on the left graph, would imply an axial temperature close to 30,000 *K* for the 200 *A* case).

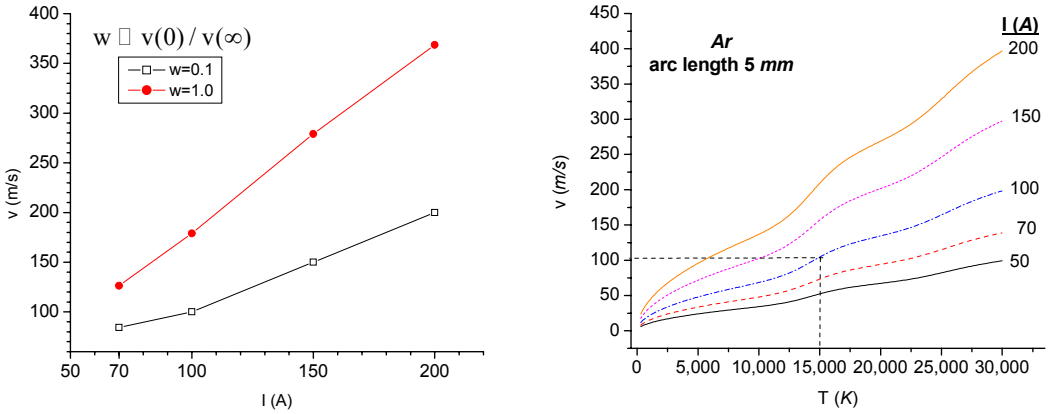

Figure 11.10 Left, axial flow velocity as a function of arc current for different hypotheses concerning normalized cathode exit flow velocity (a parabolic flow velocity profile was assumed; points were taken from figure 2 in [22]). Right, arc flow velocity as a function of temperature for different arc currents, evaluated from the Reynolds number [22].

This seems to indicate that the temperature values reported in figure 11.10 right may be overestimated by as much as 20%.

Also by noting that such a dependency can be employed only on the axis of the arc, a method can be devised for the determination of the axial arc velocity by using optical temperatures with the relationship suggested by figure 11.10 right. The temperature gives the velocity for the corresponding arc current. This velocity is then used at the same coordinate (z, r=0) in the formulae to give the ion current as a function of temperature including the flow velocity contribution (*cf* [22] p.1050)

$$\mathrm{Re} = \frac{I}{\pi\eta}\left(\frac{2\mu_o \ln 2 \cdot \ln 20}{0.95}\right)^{1/2}$$

where the computed Reynolds number is inserted in the definition (1.65) inverted for the velocity. The hope is to have an approximation of the probe temperatures by means of current formulae that *account* for the velocity, which is better than the one given in figure 11.14 where the velocity was assumed uniform throughout the arc.

The method is then as follows:

- take the optical temperature at the given coordinate and access the temperature velocity table based on figure 11.1

- divide the measured probe current by the read flow velocity (according to Lam's formula 4.13 its square root) and use the result to access the current-temperature table to obtain the temperature.

[Of the available currents in the flowing case only Lam's provides values typical of this work, Clements and Smy's similar tables fail here because they provide too low currents]. The results are shown in figure 11.11a and b for I=50 and 200 *A*, and where also the axial flow velocity is indicated.

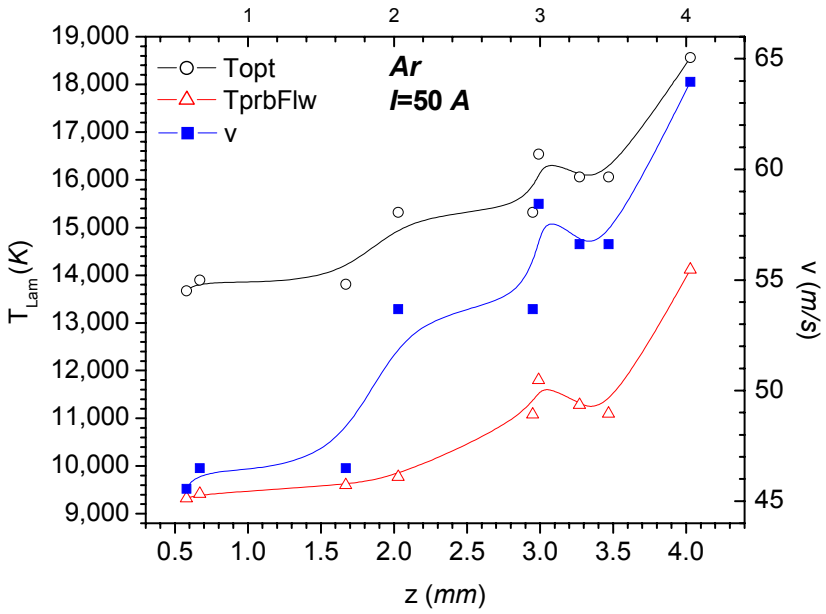

Figure 11.11 a Left axes, probe and optical axial temperatures at I=50 *A*. Probe temperatures include variable axial flow velocity (shown on the right axes).

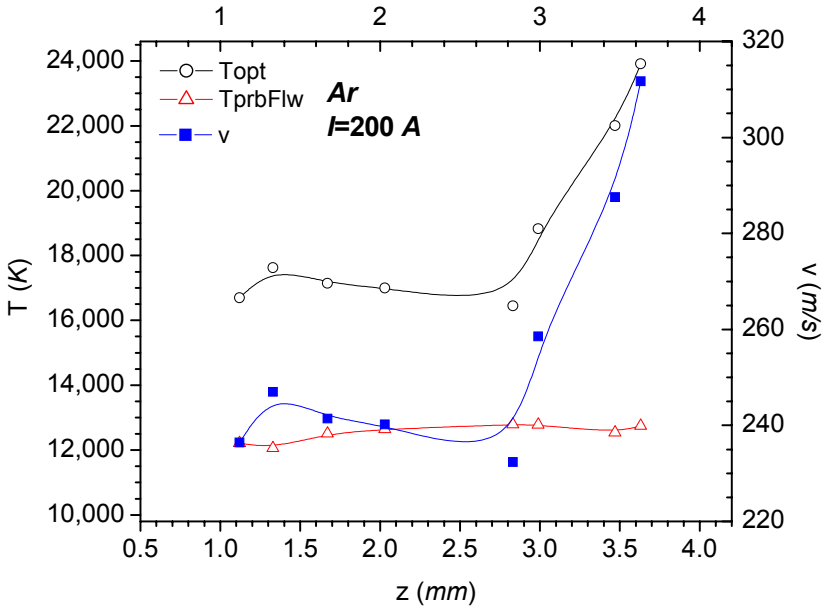

Figure 11.11 b Left axes, probe and optical axial temperatures at I=200 *A*. Probe temperatures include variable axial flow velocity (shown on the right axes).

The I=100 *A* case is not shown because the computed currents resulted in too high values (e.g. beyond any of the possible values in the tables, greater than 30,000 *K*).
It should be emphasized that the non-monotonicity mentioned for the diffusion models (*cf* figures 11.2 and 11.3) and present also in Lam's case, is not an issue because all the current measured fall below the region where the problem occurs.

These results can be compared with the results for the two provisory temperatures obtained in the steady state plasma shown in figure 11.4, without inclusion of velocity. This is done in figure 11.12.

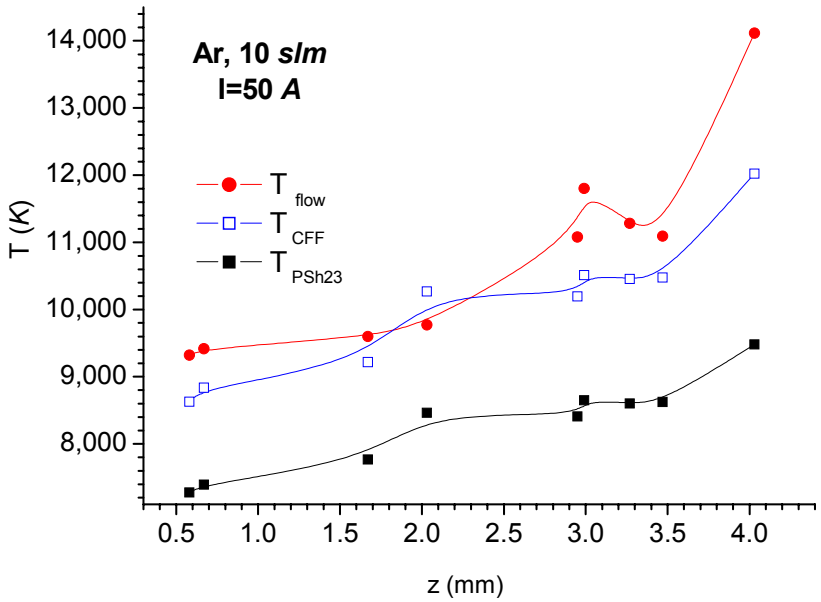

Figure 11.12 a Comparison of steady state (no inclusion of velocity, T_{CFF}, T_{PSh23}) and variable axial velocity determined temperatures (T_{flow}) for I=50 *A*

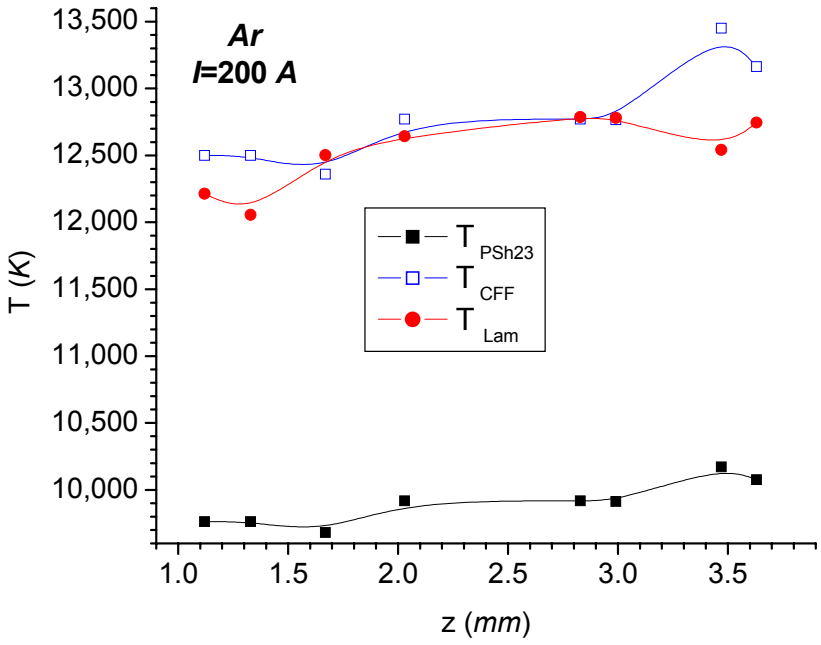

Figure 11.12 b Comparison of steady state (no inclusion of velocity, T_{CFF}, T_{PSh23}) and variable axial velocity determined temperatures (T_{flow}) for I=200 *A*

Also, a comparison with the uniform (constant) velocity case presented in figure 11.9 is now shown in figure 11.13 a and b.

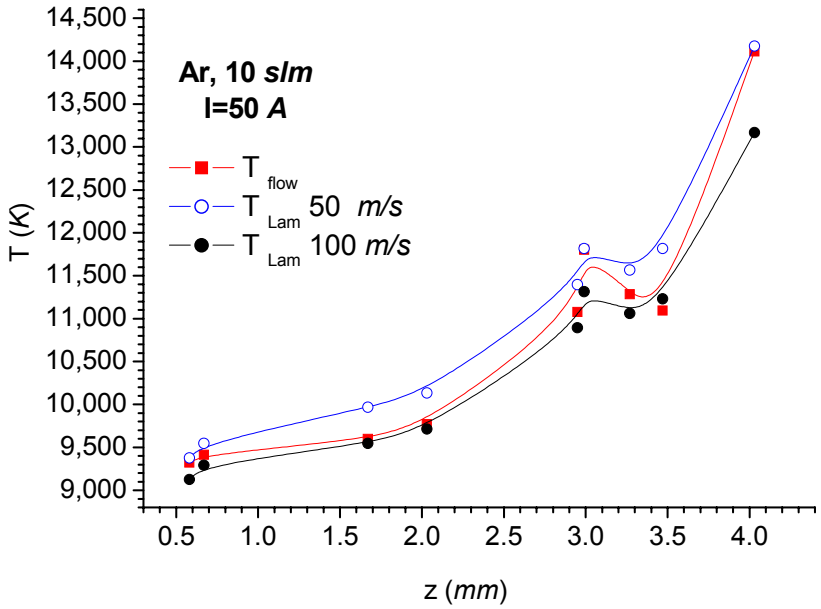

Figure 11.13 a Comparison of optical and variable velocity temperatures for the arc current case I=50 *A* (velocity v=50 and 100 *m/s*)

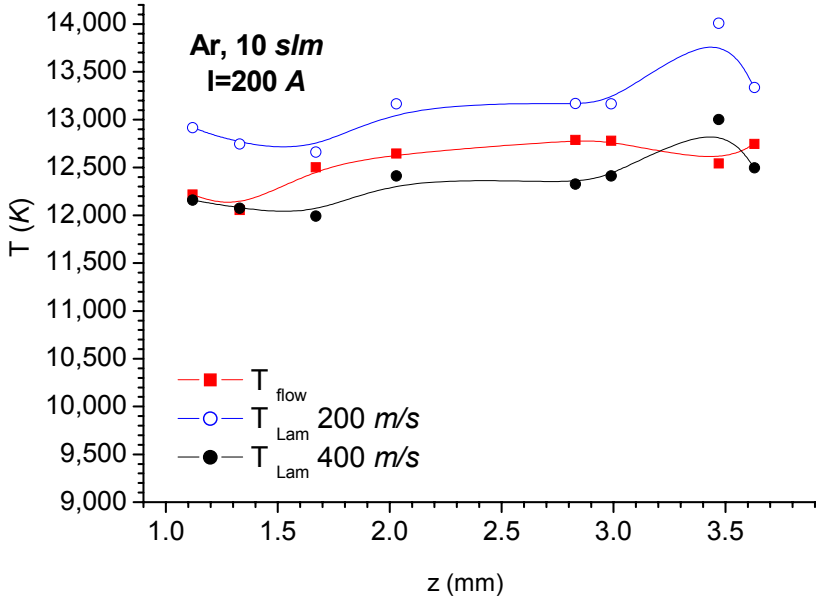

Figure 11.13 b Comparison of optical and variable velocity temperatures for the arc current case I=200 *A* (right, v=200 and 400 *m/s*)

Bearing in mind the errors on the steady temperatures and the approximations involved in the flow velocity (perhaps up to 20% see section 11.7), figures 11.9 to 11.13 suggest the following observations:

- For both the 50 and 200 *A* cases the random with pre-sheath predictions (T_{PSh23}) seem to be exceeded by all the other cases, leaving the CFF model in between the steady state and the constant velocity cases.

- In general it appears that at 50 *A*, the inclusion of the variable velocity flow does not change the temperature gradient (substantially equivalent to the optical case) although, the inclusion of the flow enhances the temperature with respect to the steady-state (figure 11.13 left). This is probably due to the fact that the velocity appears as a $1/\sqrt{v}$ multiplicative factor. Also, the variable velocity spans the range 45 to 63 *m/s*, intermediate between the two extremes given (50 and 100 *m/s*) and the flowing values do not differ substantially (figure 11.13 left). The CFF case therefore appears the closest with respect to inclusion of the flow be it of constant or variable flow velocity.

- At 200 *A* the situation is different in that the flowing case 'flattens' the temperature gradient considerably with respect to the optical case in the region closer to the cathode (figure 11.11, 12, 13 right). Even here the CFF model seems the more appropriate, matching in fact the flowing cases in the central region but 'killing' the CFF gradient close to the cathode (figure 11.12 right). In the 200 *A* case, the variability in the flow velocity along the axis does not affect greatly the result in that the steady state temperature (T_{flow}) lies in between the two extremes. Note also that the temperature gradient is low in a more limited variability band (~2,000 *K* for all three the temperatures) than the 50 *A* case (~3,000 *K*) if the common region between z = 1.1 and 3.6 *mm* in arc height is considered.

11.8 Current drawn in ion saturation and arc perturbation

1. All the models considered are based on a random (or modified random or diffusion) current with different multiplying factors (*cf* formula (11.2) and Table 11.2). The question is whether a modification in the expression of the current, for example a multiplication by a factor accounting for the geometry, will increase or decrease the temperature. This is related to the form of the function (11.2)

$$i\left(\frac{I}{a}\right) = Cn(T)\sqrt{T}$$

for the currents. Any factor less than one multiplying the right hand side of (11.2) will give rise to a reduction of the current and an increase of the temperature upon enquiry of the current-temperature conversion table. A decrease of the constant C by (say) multiplying by 2/3 (e.g. collecting surface reduction) given the same n and T, leads to a lower i, or, a lower i is now required to get the same (n, T). So, due to the functional dependency on T, analyzed further in section 11.9.1), any *reduction* in the expression of the current (not the current itself, which is *measured*) implies that the read current will correspond to a *higher* temperature. Conversely, any increasing factor will shift the same current (measured) to a *lower* temperature. Therefore, it is useful to consider whether a low temperature may be the result of a 'too high' current.

2. The argument can be looked at from a different point of view. The charged particle density obtained from the current density measured by probes could exceed the density obtained by use of the optical temperature. In this case the probes would draw a current corresponding to a density greater than the available density at the edge. Under these circumstances, the probe would greatly perturbing the arc. As a consequence any temperature determined from this density would overestimate the value at the sheath edge. From the measured current density it appears that this is the case for I=100 A at ion saturation. Is it possible to find a condition such that 'just' the right number of particles is drawn? Starting from the known (correct) optical n's there is a need to account for cooling from the boundary layer edge down to the sheath edge.

In Chapter 9 it has been emphasized that the probe is a detector sensing a flux of impinging particle. If those relationships are correct, this ‘too high’ temperature corresponds to a particle density which is in fact *higher than the density obtained by using the same n(T) relationship from optical temperatures*. In other words, by using the ion saturation part of the characteristic curve, in the CFF case at 100 A, the current drawn is higher than the available number of particles in the probe vicinity. This is more the case considering that a cooler boundary layer surrounds the probe so that the density inferred from optical temperatures is overestimating the real (boundary layer) number density even at LTE.

As an example, the particle number densities obtained from optical measurements and probe measurements (measured current) in ion saturation conditions are shown in figure 11.14 for the highest probe, z=4.22 *mm* from anode.

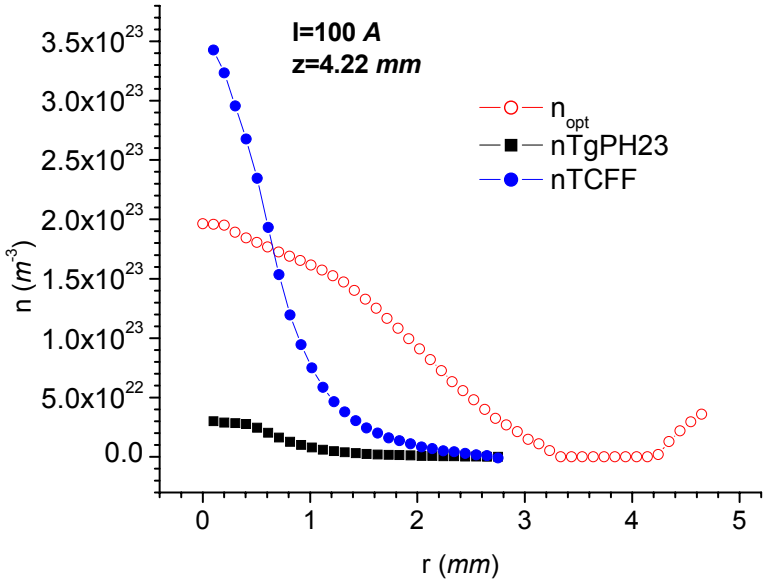

Figure 11.14 I=100 *A*, particle (ion) density obtained in ion saturation conditions compared with the optical densities at probe height z=4.22 *mm*.

It is observed that this probe experiences a particle density exceeding the n_{LTE} density, so that the current drawn is certainly too high, e.g. perturbing. This is true if the CFF model is followed, whereas for the random pus pre-sheath case, the density is greatly reduced even at the highest probe height (figure 11.14). In this case the optical number density can be used as an upper limit for the point on the V-I curve that has to be considered for the collected ions. In other words, it is necessary to limit the number density obtained by probes by using the optical density. This way, a different point on the V-I curve needs to be selected which corresponds to a lower current. Because ion saturation occurs this implies the choice of a point where saturation does not occur. As a consequence, the method of the V-I curve would fail for this arc current case. Because the 'violation' occurs only when using the CFF temperature-computed density, and not when using the random model (TGPSh23) one may conclude that CFF is incorrect.
In addition, as indicated in section 5.4, the CFF model predicted ion saturation currents of the order of the *mA* for typical arcing conditions, whereas values of the order of the ampere are found here. This explains why an 'artificially' higher temperature is delivered by this method, given the temperature dependency of the ion current per unit length.

11.9 Corrections for the temperature

A comparison among some of the optical and the corresponding probe temperature was shown at the beginning of the chapter. It is the purpose of this section to obtain some quantitative information about the temperature ratio along the radial direction as a

function of the height in the arc for the three currents for which the optical measurements are available in order to reconstruct 'computed-optical' temperatures, possibly close to a 'true' temperature for the two cases where optical data are not available.

The ratio for the probes to optical temperatures for the case of random with pre-sheath probe temperatures are shown for I=50 *A* In figure 11.15 a (full region) and 11.15 b (inner region).

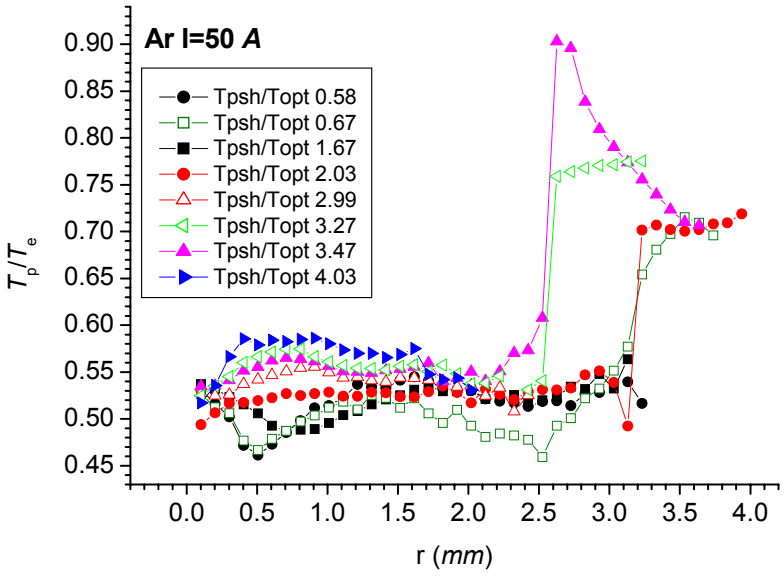

Figure 11.15 a, I=50 *A* Probe to optical temperature ratios as a function of the radial distance, full curves. The numbers in the legend indicate probe height from anode (in mm).

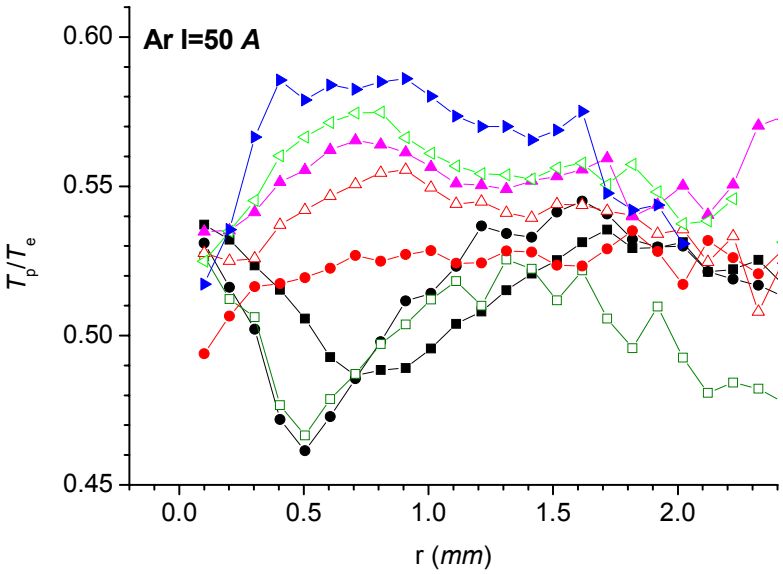

Figure 11.15 b, I=50 *A* Probe to optical temperature ratios as a function of the radial distance, region from 0 to 2.4 mm (inner region). The numbers in the legend indicate probe height from anode (in mm).

Despite the considerable uncertainty, these ratios show the following tendencies for higher to lower probes:

1. a minimum of the ratio close to the axis is followed almost monotonically in z by an increasing ratio moving radially outwards, up to a point where the ratio stabilizes or perhaps drops again; the outer regions are regions where the probe to optical ratio increases again;

2. Probe at z=2.03 *mm*, not far from arc centre, seems more uniform across the radial direction;

3. A decrease of the ratio moving radially outwards up to 0.5 *mm* (z= 0.58 and 0.67 *mm*) to 1 *mm* (at z=1.67 *mm*). Thereafter, the probe temperatures regain importance.

In terms of interpretation of cooling due to flowing conditions one could easily identify the central minima of the highest probes with the region of the arc where the flow velocity is the highest. This region extends probably out to 0.5 *mm* and down to about 2 *mm* from the anode.
The dramatic increase of the ratios at higher radii could be explained by the absence of substantial flow in the periphery of the arc: here the probes sense a more realistic temperature. However, the 50 *A* case is a limit with respect to the correctness of the

temperatures, because it is the case furthest from LTE and moreover the optical temperatures closer to the anode were obtained with increasing difficulties because of larger uncertainties in the intensity maxima.

In figure 11.16a the ratio for the probes to optical temperatures for the case of random with pre-sheath probe temperatures are shown for I=100 *A*; the inner region is shown in figure 11.16 b.

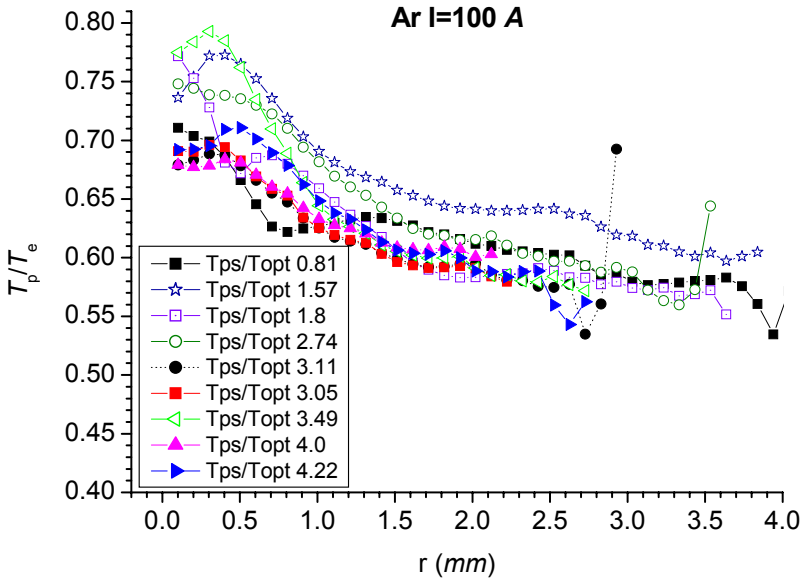

Figure 11.16 a, I=100 *A* Probe to optical temperature ratios as a function of the radial distance, full curves. Right, region 0 to 2 mm

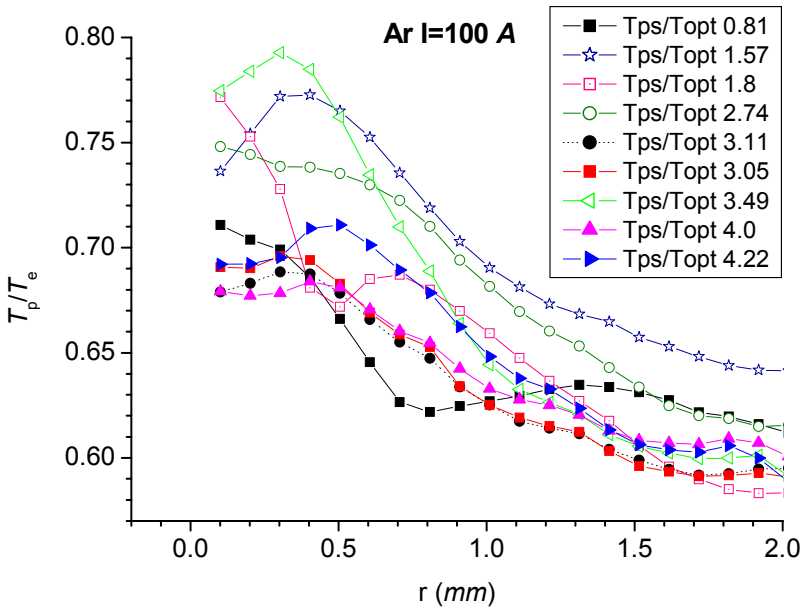

Figure 11.16 b, I=100 *A* Probe to optical temperature ratios as a function of the radial distance, region 0 to 2 mm

The trend for the 100 *A* case is less clear. In general, the ratios of probe to optical temperatures are higher than for the 50 *A* case, as if the cooling due to the flow were less effective, especially in the core region where in contrast, the flow velocity is expected to be higher. Also the ratios seem to decrease outwards across the arc as if the effects of the flow were dominant in the outer edges.

In figure 11.17 the ratio for the probes to optical temperatures for the case of random with pre-sheath probe temperatures are shown at I=200 *A*.

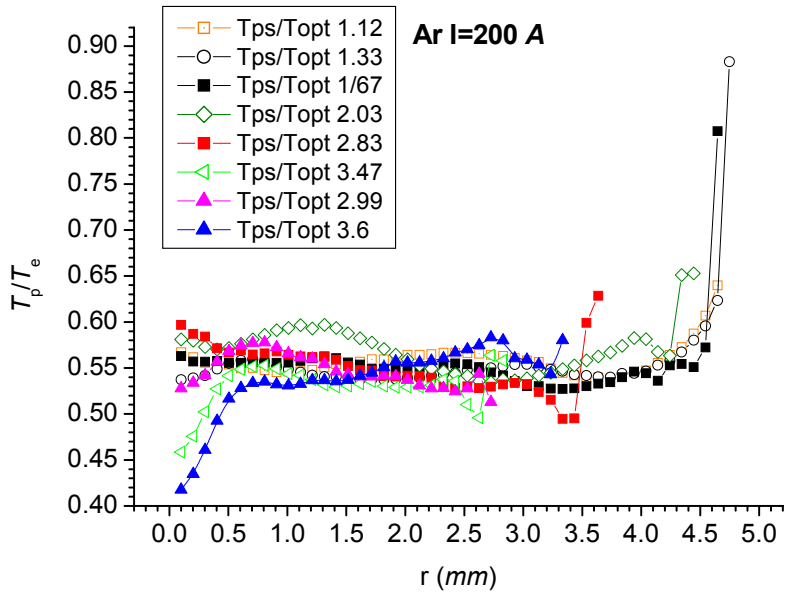

Figure 11.17 a, I=200 *A* Probe to optical temperature ratios as a function of the radial distance, full curves. Right, inner region

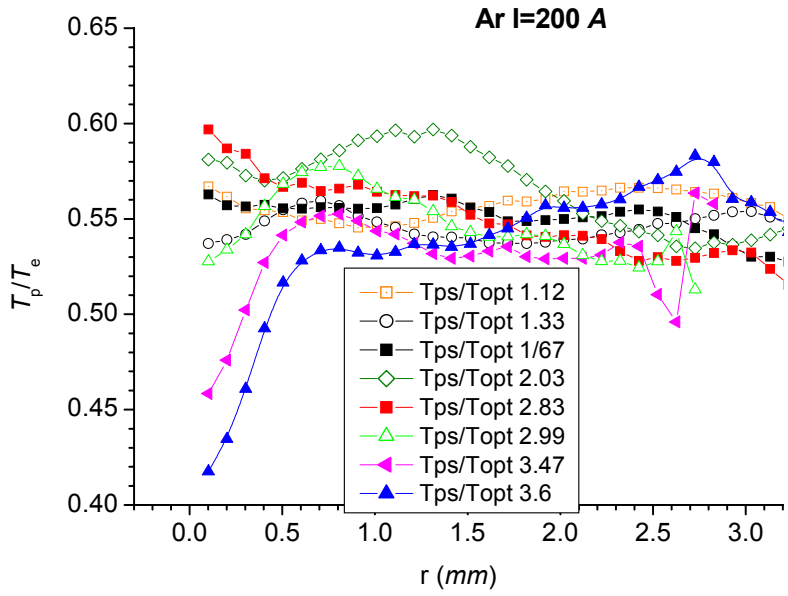

Figure 11.17 b, I=200 *A* Probe to optical temperature ratios as a function of the radial distance, inner region

The behaviour of the ratios are similar to the 50 *A* case in that an inner depression is visible, probably due to the greater central velocity. A region of about 2 mm follows and the outer edges indicate a progression towards more realistic probe temperatures

(less cooled), although the outer regions are limited in validity by the requirement for the optical temperatures to be at or close to LTE.

The trend for these temperature ratios are grouped per radial distance and subsequently interpolated along the axial distance; in this way the corresponding values for the missing heights are generated. A subsequent interpolation between the 50 and 100 *A* and between the 100 and 200 *A* case is performed in order to generate the corrective factors that need to be applied to obtain 'missing optical' temperatures. These are computed for the cases I=70 and 150 *A*.

As an example, figure 11.18 shows some computed optical temperatures as a function of arc height for selected radial distances and I=70 *A*, whereas the case I=150 *A* is shown in figure 11.19 a to d.
By construction, these preserve some of the features of the probe temperatures (also shown in figure 11.12) from which they were partly generated. In particular, the points corresponding to the anode and cathode zones are missing as no probe data are available in these regions.

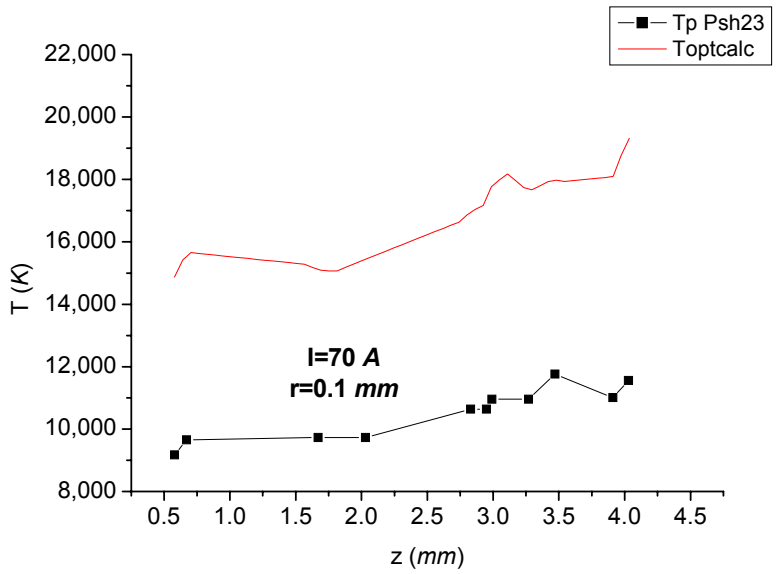

Figure 11.18 a, I=70 *A*, optical generated temperatures (Toptcalc) and the corresponding probe temperatures that these correct for radial distances *r*=0.1 *mm* from the arc centre.

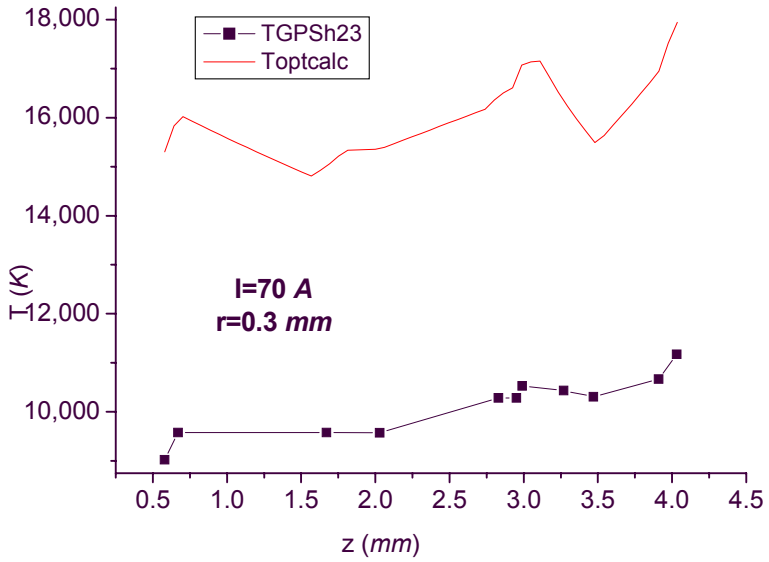

Figure 11.18 b, I=70 *A*, optical generated temperatures (Toptcalc) and the corresponding probe temperatures that these correct for radial distances *r*=0.3 *mm* from the arc centre.

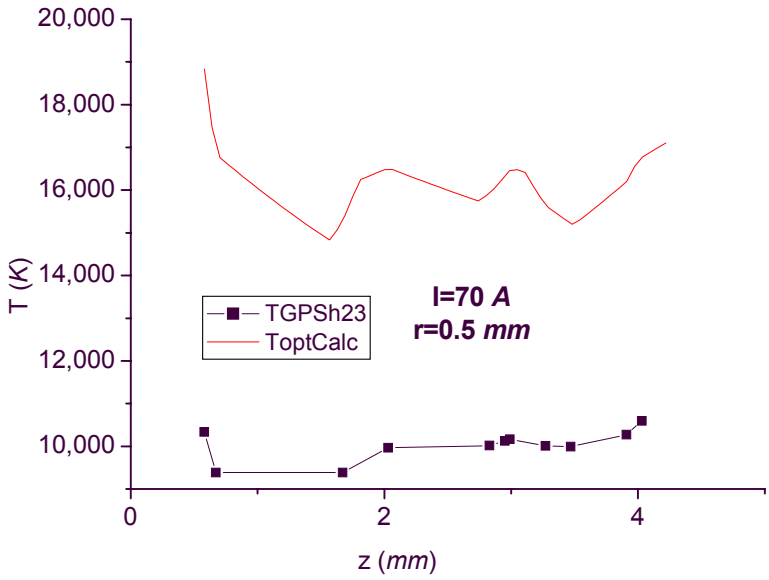

Figure 11.18 c, I=70 *A*, optical generated temperatures (Toptcalc) and the corresponding probe temperatures that these correct for radial distances *r*=0.5 *mm* from the arc centre.

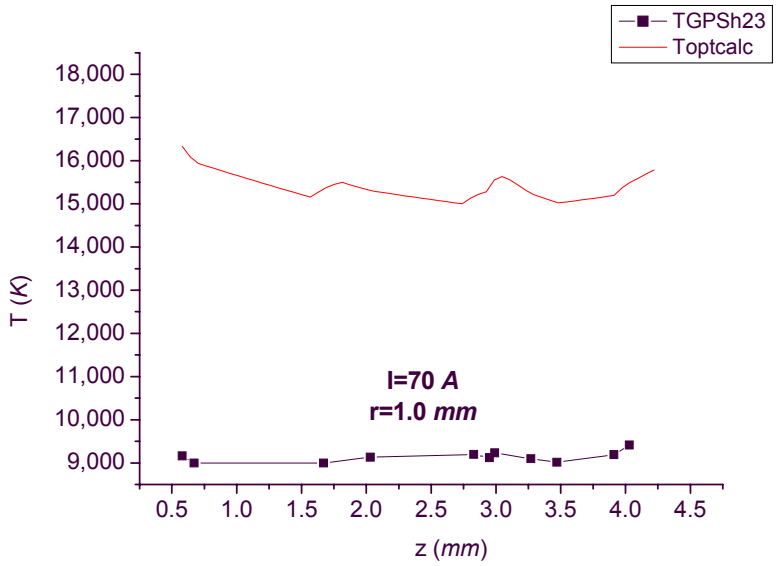

Figure 11.18 d, I=70 *A*, optical generated temperatures (Toptcalc) and the corresponding probe temperatures that these correct for radial distances *r*=1.0 *mm* from the arc centre.

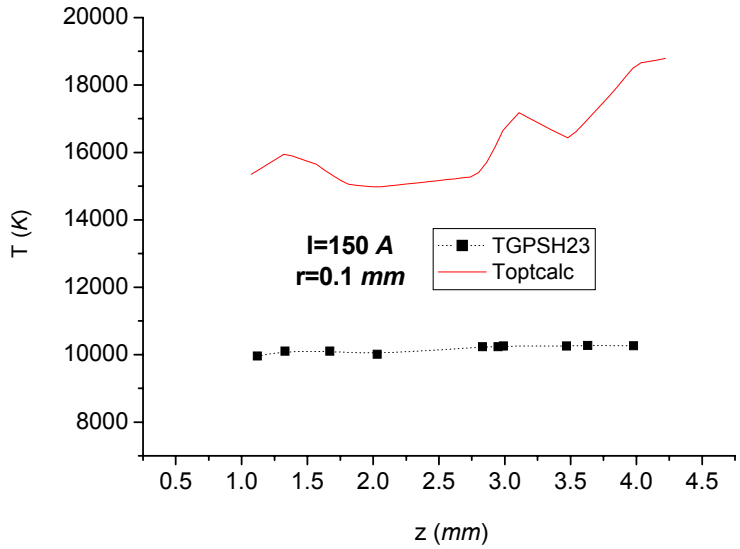

Figure 11.19 a, I=150 *A*, optical generated temperatures ($T_{optcalc}$) and the corresponding probe temperatures that these correct for radial distance *r*=0.1 *mm* from the arc centre.

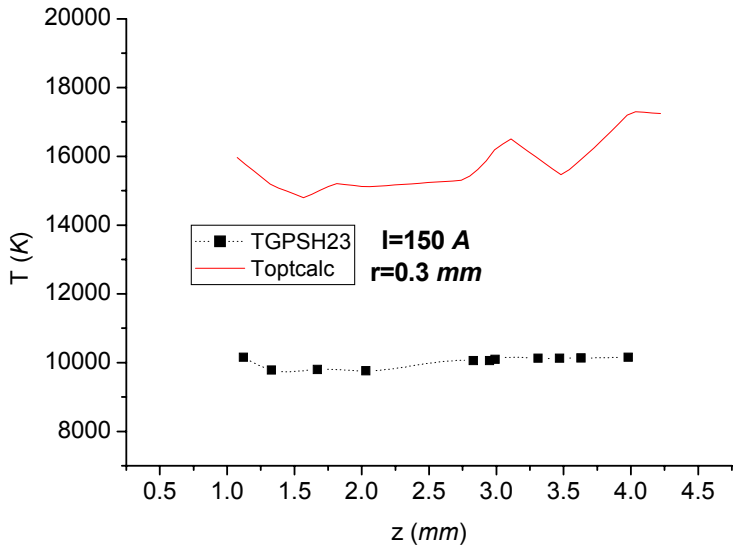

Figure 11.19 b, I=150 *A*, optical generated temperatures ($T_{optcalc}$) and the corresponding probe temperatures that these correct for radial distance *r*=0.3 *mm* from the arc centre.

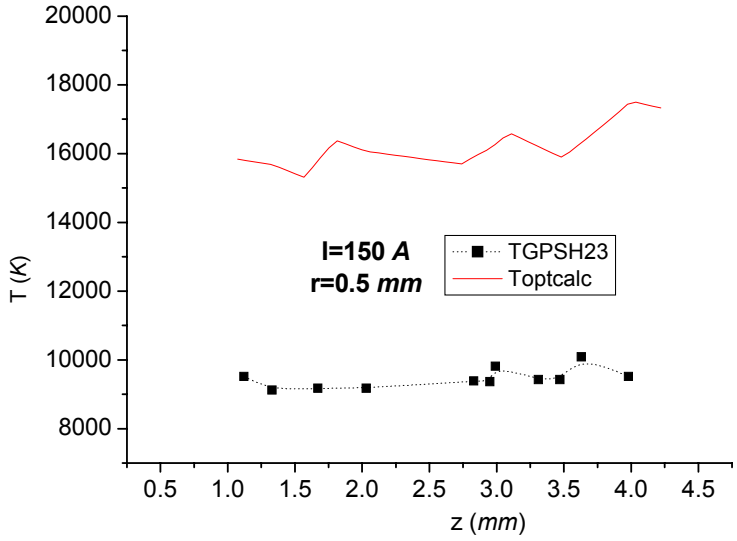

Figure 11.19 c, I=150 *A*, optical generated temperatures ($T_{optcalc}$) and the corresponding probe temperatures that these correct for radial distance *r*=0.5 and 1.0 *mm* from the arc centre.

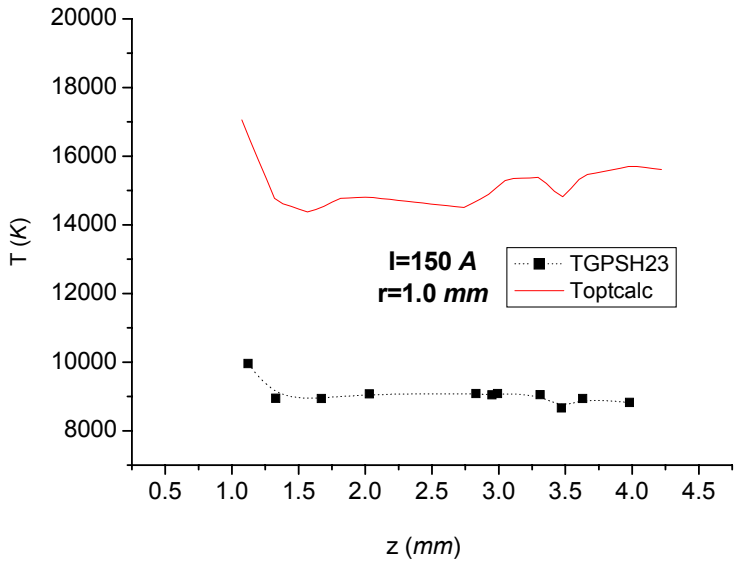

Figure 11.19 d, I=150 *A*, optical generated temperatures ($T_{optcalc}$) and the corresponding probe temperatures that these correct for radial distance *r*= 1.0 *mm* from the arc centre.

A cross-check based on the optical temperatures for the neighbouring I=50 *A* and I=100 *A* case and on the number density corresponding to these generated temperatures shows these are consistent and of the right order of magnitude. For the latter, the check is performed to ensure that none of the measured particle densities based on the electrical current and the probe determined temperature exceed the LTE particle density (determined by these computed temperatures). For example, the density obtained from the probe temperature shown at z=4.03 *mm* for r=0.1 *mm*, T_{PSh23} = 11,600 *K* is n= $5.4 \cdot 10^{22}$ $m^{-3}$and for the computed optical, T_{opt}=19,300 *K*, n_e= $1.8 \cdot 10^{23}$ m^{-3}.
Obviously, the approximations involved impede any claim to a high degree of accuracy; even assuming a negligible error in the construction procedure, the initial error on the ratios of the temperatures, in turn largely determined by the uncertainties on the probe temperatures, renders it very difficult to state accuracies better than 20-25%.
Furthermore, the acceptance of this method is subject to the assessment of the underlying physical model. This is discussed in section 11.11.

11.10 Reasons for "Cooling"

Further possible causes for “cooling” (“depressed probe determined temperatures”) are:

1. *Charge depletion by fluid convection*

2. *Charge depletion by recombination*

3. Ions energy loss

4. Temperature obtained is a modified ion temperature

Each of these causes is outlined in the following. A more detailed treatment follows in separate sections thereafter (except for point 1 below).

1. Charge depletion by fluid convection
Ions directed to the probe with a velocity forming a non zero angle with the flow will be 'deflected' by the arc flow. The amount of deflection will depend on the ratio of the relevant ion velocity to the arc flow velocity and /or to the relative arc-probe velocity.
The relative probe to arc velocity ratio is of the order of 10% at maximum, as the probe velocity is of the order of 5 *m/s*, whereas the arc flow velocity varies from some tens to a few hundreds of *m/s* depending on the arc current, thus relative arc flow-probe motion can be neglected. The ion individual velocity, depending on the arc regime, either purely random (thermal) or electric-field driven (drift), is at least a factor of 10 higher than the flow velocity. Therefore, in the worst case of ion velocity vector orthogonal to the arc flow velocity vector, still the latter can be neglected and in first approximation fluid convection appears at least not the major cause of charge flux depletion, if it is a cause at all.

2. Ion energy loss
The ions directed to the probe loose energy by collision with the colder neutrals in the boundary layer. The energy loss by collision with neutrals of the same species can be very effective in greatly reducing the initial ion kinetic energy after very few collisions.
The kinetic energy of the ions is now defined by the value of the local temperature. If the system persists in an LTE status, this is also the electron temperature. In this case, it must also be assumed that the energy transfer mechanism from the field to electrons and from these to ions, keeps its effectiveness in maintaining the temperature equality. However, irrespective of the LTE onset in the boundary layer, the average of the ion kinetic energy does change because of collisions. In fact, although for energies below ~1 *keV*, dominant collisions are elastic and the only non elastic collisions are of the resonant charge-exchange type, collisions of ions with neutrals do change the momentum of the ions considerably. The motion of ions is altered in that ions loose their original identity: a fast ion impinging a neutral will be deflected at a small angle thus loosing a small fraction of energy. However, after the scattering it may capture an electron and become a neutral atom. In contrast, the atom, which is initially considerably slower, acquires a charge during the scattering and sensing the effects of the field it is accelerated. On the average a slowing mechanism is in place and the averaged velocity over the ion population is reduced.

3. Charge depletion by recombination
The assumption of conservation of the number of ions in the boundary layer is not justifiable because of recombination. Differently to the previous case, if ions carry a kinetic energy reminiscent of the electron temperature, e.g. v is not greatly altered during the travel across the boundary layer, the product $ne\mathrm{v} = n(T_\mathrm{e})\mathrm{v}(T_\mathrm{e})$ transforms to $n'e\mathrm{v} = n'(T_\mathrm{e})\mathrm{v}(T_\mathrm{e})$ where $n'<n$ and T_e is the original value of the electron temperature outside the boundary. The effectiveness of recombination is determined by the local value of the temperature. In Chapter 2 the three-body collisional recombination coefficient was computed as a function of temperature although it was not explicitly stated *which* temperature was employed. In the absence of further information it is assumed that it is an LTE *plasma* temperature.

The temperature at the boundary layer edge is generally higher than the temperature at which the recombination coefficient shows its maximum (*cf* figure 2.10). The ions are progressively reduced in number following the a_c curve from the high tail (high T) 'back to its maximum (the T is decreasing towards the probe, so there will be a 'band' in the boundary layer where recombination is the most effective). However, as the ions approach the probe less and less electrons will be available to recombine due to the lower temperature (ionization is progressively less effective and so will be recombination).

4. *Temperature is ion temperature*
Following Bohm ([16] see also section 4.3.1.3), the collection of ions is independent of the ion temperature provided $T_\mathrm{i}<T_\mathrm{e}$. In fact it is shown [16] that in the range where $T_\mathrm{i} \leq 0.5\ T_\mathrm{e}$ the ion current density increase that would occur by including the ion temperature in the expression of the flux, is confined within a 20% value, which is the typical order of accuracy in probe determined temperatures. In other words, the ion density in the expressions for the ion saturation currents depends mainly on electron temperature. However, if the plasma is thermal, $T_\mathrm{e}=T_\mathrm{i}$ this is not necessarily true.

If the ions were in LTE before meeting the cooler layer, thus at a temperature equal to the electron temperature, the (kinetic) energy decrease would translate into a 'loss of information' about the initial electron temperature; the probe temperature could no longer represent the electron temperature of the undisturbed plasma. If the number of ions did not change during the motion across the boundary layer, the factor $ne\mathrm{v} = n(T_\mathrm{e})\mathrm{v}(T_\mathrm{e})$ in the current density would be reduced to $ne\mathrm{v}' = n(T_\mathrm{e})\mathrm{v}'(T_\mathrm{i})$ when impinging the boundary layer edge. Thus it would be determined by the instantaneous value of the ion velocity v'<v after the collision(s) and therefore by a lowered value of the kinetic energy, e.g. perhaps by a (local) *ion* temperature.

The collisions reduce the ion kinetic energy and after very few collisions, the relationship to the electron temperature is lost, unless a mechanism is found to restore it.

If the plasma is not in LTE (as is presumably the case of the boundary layer, assuming a *practical* limit for LTE at T=10,000 K in the spectroscopic measurements) and is characterized by 'cold' ions (e.g. by a two-population two-temperatures system) the probe determined temperature based on the random ion flux *can* be an electron temperature according to Bohm. In other words, dealing with a cooled plasma as implied by the existence of a boundary layer, impedes assessment of whether the plasma was originally in LTE before probe insertion. In any case the plasma is 'cooled' and the probe obtained temperatures, of the order of 10-12,000 K for the random model, are close to the limit where onset of LTE is dubious. These must be electron temperatures according to Bohm.

11.10.1 Ion energy loss versus recombination

Assuming the conclusion of the previous paragraph is correct, the cause of the cooling has to be ion energy loss or recombination. It is possible to estimate the relative effects of energy loss and recombination going back to the functional form of the current-temperature relationship reported in figure 11.20 Left. The analytical determination of the dominant factor within the expression $J = Cn(T)ev(T)$, shown in figure 11.20 left, is not achievable.

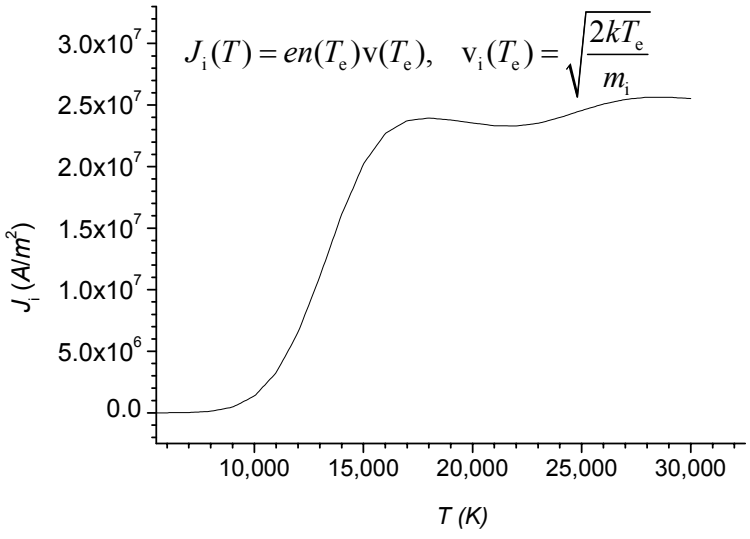

Figure 11.20 a, the function $J(T)$ versus temperature.

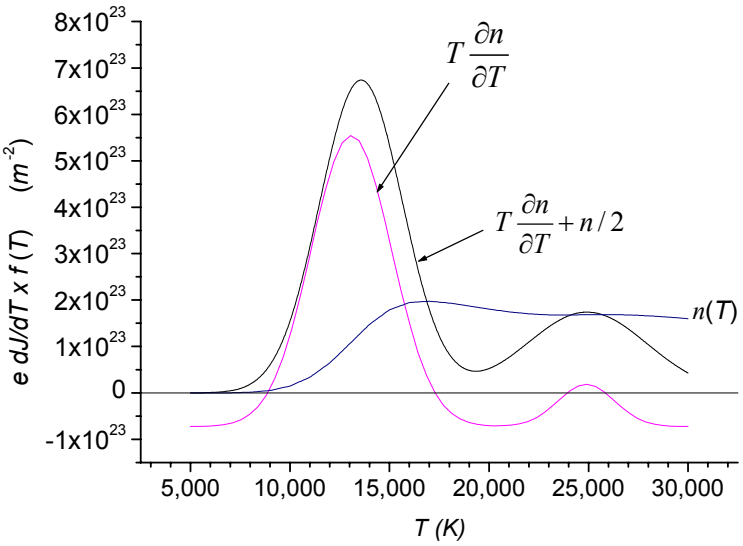

Figure 11.20 b, total derivative of the function $J(T)$ as a function of temperature. Both the density $n(T)$ and the contributions of the partial derivatives of J are shown

The ion energy loss, represented by a reduced particle density n, and the cooling represented by a reduced velocity (thus temperature) are not separable in factors depending on one variable alone.
The total derivative

$$\frac{dJ}{dT} = \frac{\partial J}{\partial n}\frac{\partial n}{\partial T} + \frac{\partial J}{\partial \mathrm{v}}\frac{\partial \mathrm{v}}{\partial T} \tag{11.4}$$

contains the variations of the current density with temperature and particle density (derivative of the current density with respect to the velocity, which depends on the temperature through $\mathrm{v} = B\sqrt{T}$; and with respect to the number density). (11.6) can be written in modified form

$$\frac{\sqrt{T}}{eB}\frac{dJ}{dT} = T\frac{\partial n}{\partial T} + n/2 \tag{11.5}$$

and is shown in figure 11.20 right. A remarkable decrease in the current due to the reduction of the number density with increasing temperature (first derivative) causes a drop of a factor 5 in the current density in the region between 15,000 K and 20,000 K. A further negative contribution takes place above 26,000 K. The latter contribution, where n is almost constant above about 15,000 K has little influence.

Because we are interested to the relative contributions of cooling (lowering of kinetic energy, thus v) and recombination (lowering of n) these two contributions can be compared, as the corresponding partial derivatives:

$$\frac{\partial J}{\partial n} = e\mathrm{v}(T), \quad \mathrm{v} = \sqrt{\frac{2kT}{m_\mathrm{i}}} = C\sqrt{T}$$
$$\frac{\partial J}{\partial \mathrm{v}} = en(T) \tag{11.6}$$

Now n increases perhaps exponentially (faster than T^4) whereas v goes as $T^{1/2}$ so at least below 15-16,000 K the dominant mechanism with lowering T is the reduction of number of particles (*cf* figure 11.21). This conclusion is supported by the fact that the recombination coefficient is a maximum in this range (*cf* figure 2.10).

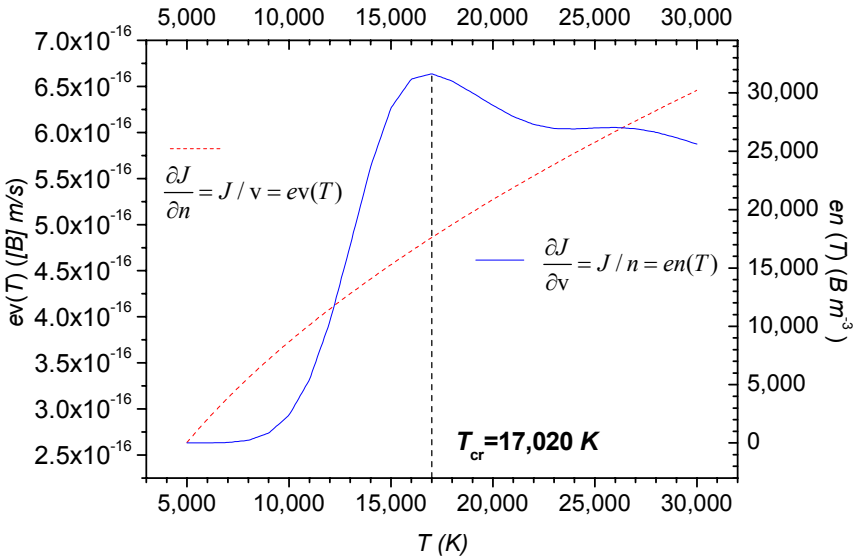

Figure 11.21 Separate contributions of the partial derivatives of the current density function as a function of temperature

Conversely, for temperatures higher than about 17,000 K, a reduction of the current is due to the reduction of the kinetic energy of the ions, although in this range, the effect is partly masked by an increase of the particle density.

The general result of this section can therefore be stated as follows. While there is no easy way to compute the relative variation of the current density $\Delta J / J$ for a single variation of n or v because of the functional form of J, still two temperature regions can be identified where either of the two effects dominates. Furthermore, because the probe temperatures, accurate or not, are the sign of a intrinsically reduced temperature in the 'cool' boundary layer, the region beyond 17,000 K is never attained for the chosen random model. For this reason, in first approximation the dominant mechanism for the apparent 'cooling' in the boundary layer is the reduction of the particle density.

11.11 Models

The effect of cooling would be to lower the plasma temperature in a region whose extension is identified with the boundary layer. In other words the probe would sense a fluid boundary temperature (Chapter 2 and 4) and not to the plasma bulk temperature. The situation may be depicted in figure 11.22 as follows. For a floating probe in motion the sheath is fully embedded in the fluid boundary layer. When a negative bias is applied, the electrical sheath expands and progressively more and more ions reach the surface of the probe. When the probe is in saturation conditions, either of the two extreme cases depicted in figure 11.22 occurs: the sheath, even at its maximum spatial extension, is still fully contained within the boundary layer; or it overcomes the boundary layer. If the sheath were extending beyond the boundary layer, (figure 11.22 d) the effect of the field would be dominant and the sheath depletion, by lowering the thermal conductivity, would impede substantial cooling; this is the situation common in low pressure discharges. In this case the ion saturation current, made up of all the particles reaching the uncooled sheath would be representative of the bulk of the plasma as would be the obtained temperature. In this case, the temperature given by ions would be the electron temperature. In the opposite case of fully developed (but embedded) sheath, the particles reaching the sheath edge and therefore the probe are the particles arriving from a boundary layer substantially cooler than the plasma bulk (figure 11.22 c).

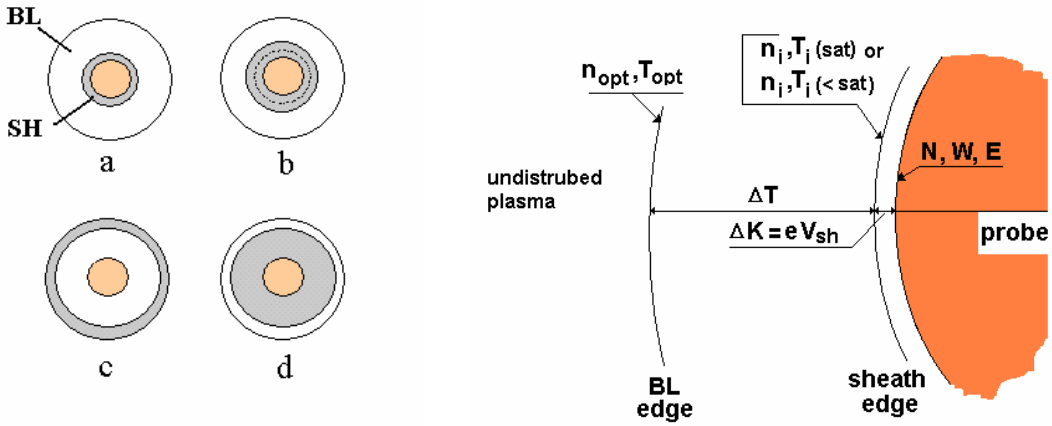

Figure 11.22 Left, qualitative relationship between fluid boundary layer and electrical sheath (includes pre-sheath for simplicity). a) in floating conditions b) 'slightly' biased c) high bias, ion saturation with sheath edge approaching boundary layer edge; d) sheath overcoming the boundary layer. BL=Boundary Layer (in white), SH=Sheath (in dark grey). Right, Schematics of the different layers surrounding the probe for sheath fully embedded in BL, e,g. b) or c) on the left. N=collected particles, W, power released, E, energy per particle at the probe

Thus, referring to figure 11.22 ions travel towards the probe crossing different regions present as a consequence of the probe insertion within the plasma. These regions are the bulk of the plasma, a boundary layer induced by the relative plasma-probe motion, a pre-sheath (possibly embedded within the boundary layer) and the sheath. The existence of the pre-sheath seems well established and the choice made of the ion velocity at the sheath edge (when considering negatively biased probes) has to reflect this. Hence, the most probable value of the velocity is required due to an accelerating potential, originating at the probe surface, but leaking outside the sheath edge into the pre-sheath (This a second reason for selecting the temperature from the random model). The fate of the ions from the bulk of the plasma is now followed towards the probe.

The physical scenario depicted in figure 11.22 right would be as follows. In absence of probe, the couple $(n,T)_{\mathrm{LTE}}$ defines density and temperature at the probe location (r,z). When the probe is inserted at (r,z) a boundary layer and an embedded sheath arise. The original density is depressed by 'cooling' and a number n' lower than n will be present in the boundary layer. Of this number, a fraction $n''<n'<n$ will reach the probe. If $n''>n'$ then there would be charge formation by ionization which is excluded. If $n''>n$ the sheath would be overpopulated with respect to the boundary layer which is also excluded. The assumption made here is that the number density obtainable from the number of charges impinging the probe is representative of the sheath edge population, embedded in the boundary layer. The density drop across the boundary layer (excluding

the sheath) is computable as the difference between the optical (LTE) density and this measured quantity.

The temperature drop can be obtained as the difference of the optical (LTE) temperature and the temperature computed from *n*" assuming LTE. This has been shown in section 11.9 where from these corrections, 'computed-optical' temperatures were presented. Figures 11.23 to 11.25 report some radial densities (left) and probe to optical density ratios (right), computed for arcs at *I*=50, 100 and 200 *A*.

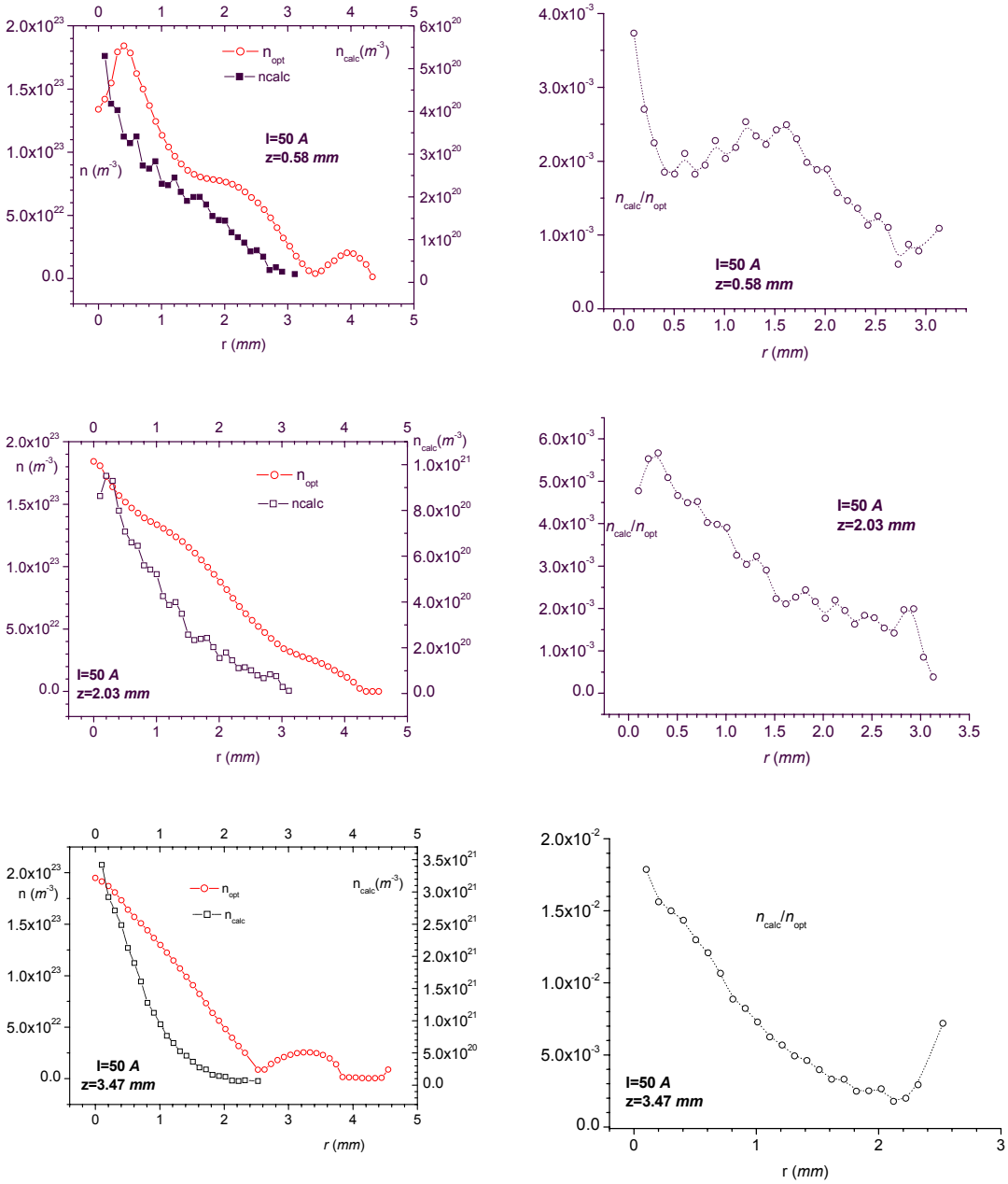

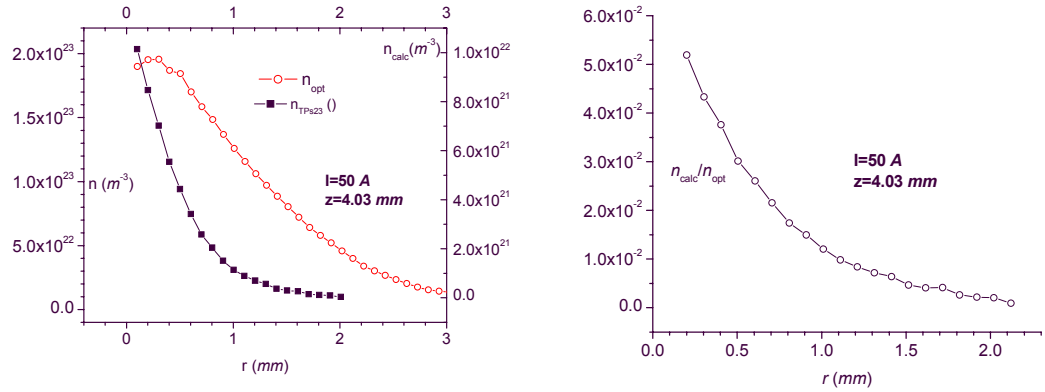

Figure 11.23, I=50 *A*. Left, charged particle densities obtained from optical temperature under LTE assumption (n_{opt}) and probe obtained density from the current and the corresponding probe temperature measured at saturation (n_{calc}). Right, computed to optical density ratio. Values shown from top, z= 0.58 2.03, 3.47 and 4.03 *mm*

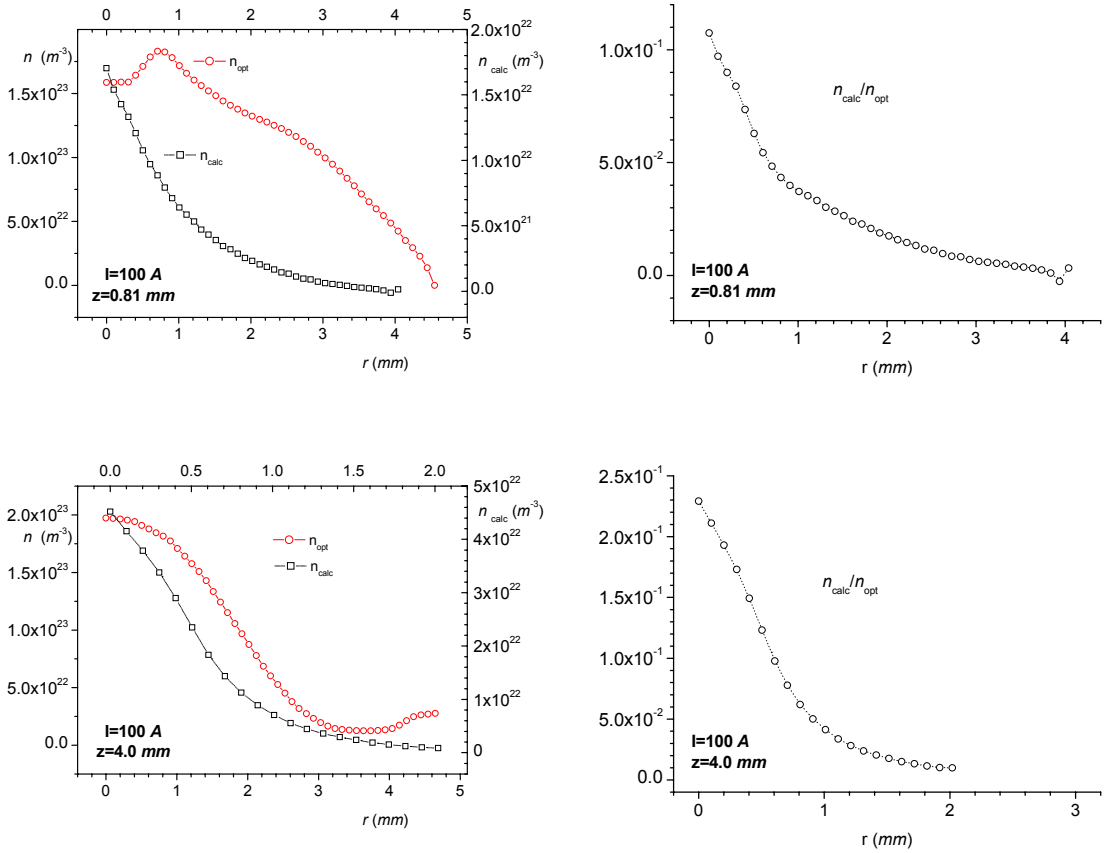

Figure 11.24, I=100 *A*. Left, charged particle densities obtained from optical temperature under LTE assumption (n_{opt}) and probe obtained density from the current

and the corresponding probe temperature measured at saturation (n_{calc}). Right, computed to optical density ratio. Values shown from top, z= 0.81 and 4.0 *mm*

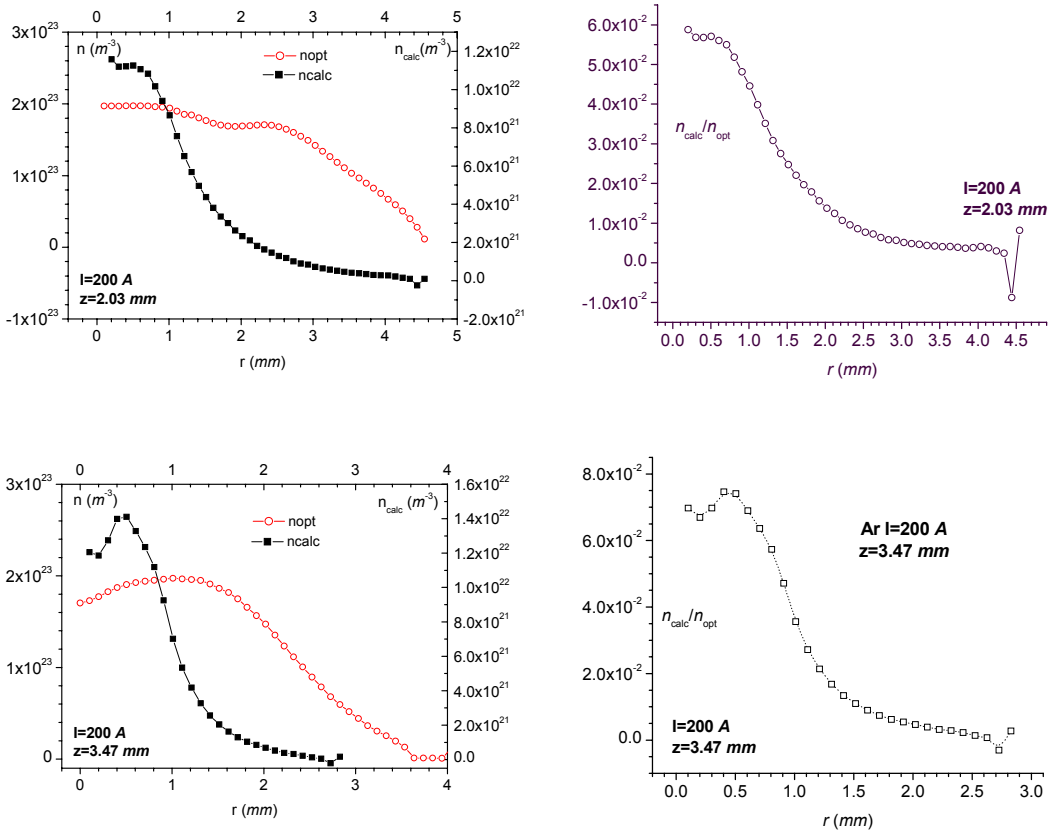

Figure 11.25, I=200 *A*. Left, charged particle densities obtained from optical temperature under LTE assumption (n_{opt}) and probe obtained density from the current and the corresponding probe temperature measured at saturation (n_{calc}). Right, computed to optical density ratio. Values shown from top, z= 2.03 *mm* z= 3.47 *mm*

The values shown for these density reductions in figures 11.23 and 11.25 span the 2 to 10% range, e.g. the probe computed density is of the order of few % of the optical value. This is the order of magnitude of the particle reduction in passing from the bulk plasma to the (sheath edge and thus making the flux to the) probe surface.

It is interesting to compare the last result with the recombination coefficient normalized to the volume spanned by the probe in the time needed to cover a distance of the order of the boundary layer thickness estimated in Chapter 2 ($\delta \approx 0.2$ *mm* = $2 \cdot 10^{-4}$ *m*, in broad agreement with some computational results, 3 to 4 probe radii, $\delta \approx 0.5$ *mm* = $5 \cdot 10^{-4}$ *m* [25]).

The probe velocity is ~5 *m/s* thus the time needed to cover this thickness is $\tau \approx 0.4$ to 1 *ms*. Multiplying by the recombination coefficient shown in Chapter 2 (figure 2.10), assuming cylindrical symmetry for the spanned region and ignoring the temperature

drop law across the boundary layer (which is around 50 to 70%), the reduced recombination coefficient is of the order of $a_{cNorm}=5\cdot10^{7}$ so that it varies from 1 to 7% in the temperature region of interest, as shown in figure 11.26.

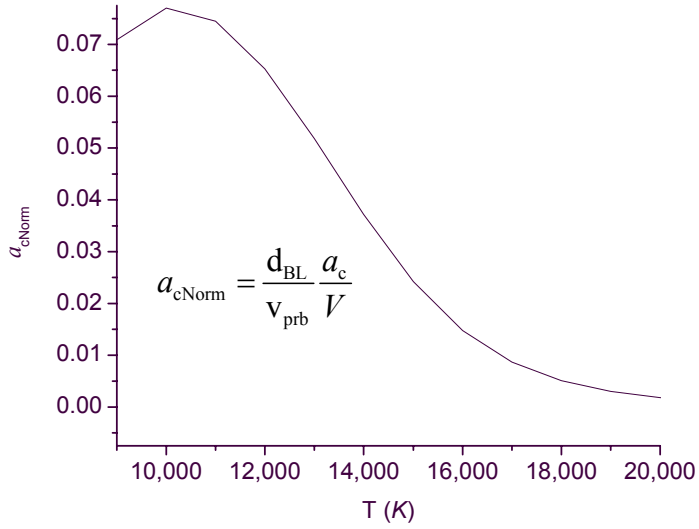

Figure 11.26 Estimates of the (normalized) three-body collisional recombination coefficient in the temperature range of interest. v_{prb}, probe velocity, δ_{BL}, boundary layer thickness, V spanned boundary layer volume

This is the reduction factor to be applied to the particle density per unit volume. Even if the approximation used is very coarse, this result substantiates the notion of recombination as the 'cooling' prevailing mechanism in lowering the temperatures with respect to the optical values.

The boundary layer has a lower temperature with respect to the plasma so that thermal and concentration diffusion takes places. Ions move from the bulk region towards a cooler boundary layer because of diffusion. In this region, electron and ion densities are lower than the equilibrium bulk values as recombination takes place reducing the charged particle density (depending on temperature, *cf* Chapter 2). This reduction causes further diffusion. The charge density, assuming for now LTE, is characterized by the density $n_{BL}<n_{\infty}$.

Ions that happen to be just within the pre-sheath start sensing the field. Since it is assumed that the pre-sheath is fully embedded within the boundary layer. Hence, of the n_{BL} density, only a fraction n_{PS} will be subject to the effect of the field. Because the pre-sheath is collisional, a further reduction of density takes places via recombination. Of this population, variable with distance from the probe surface, a fraction n_{SE} will fulfill the Bohm criterion and actually enter the sheath. In fact, the pre-sheath development

ensures that the ion motion is directed and determined by the most probable velocity so that the latter condition is automatically satisfied.
For a developed pre-sheath, low pressure Langmuir probe theory prescribes this density as $n_s \approx 0.61 n_b$ (*cf* Chapter 3); here n_b *must* be the boundary layer concentration n_{BL}.
Because the sheath is collisionless, the density providing the amount of particles reaching the probe surface out of the sheath edge population is n_{SE} which is a function of the measured current. According to this scenario, the most important mechanisms that vary the ion current is recombination which progressively reduces the number of ions.

11.12 Summary

An attempt has been made to obtain plasma temperatures using the direct method of Gick *et al* [5] extended to different current models, on the basis that several mechanisms should be taken into account, including incomplete collection surface, possible oversimplification of the purely random models, existence of a pre-sheath, and above all, the existence of a boundary layer. The fact that in Gick *et al* [5, 26] (and in the 'ameliorated version of Allum *et al* [27]) the obtained temperatures were low but nevertheless surprisingly of the 'correct order of magnitude' is considered to be incidental. In fact, in Gick *et al* [5, 26] completely neglect cooling effects, but an analysis of the perturbing action in terms of collected current was not made. From the analysis performed in this work it is evident that the perturbing action of the probe manifests in several ways: 'apparent cooling' (e.g. temperature reduction) due to boundary layer, and perturbation of the arc by collection of a current which is too high if use has to be made of the characteristic curve method. The latter circumstance, limited to the TCFF model in the 100 *A* case led to the selection of the random model of Gick, modified to include pre-sheath and orientation effect in the collecting surface, taken as 2/3 of the probe surface.
The inclusion of flow velocity dependency, both uniform, figure 11.14, and variable (only axially, figures 11.15 to 11.18) has shown temperature variations which are relatively minor with respect to the discrepancies with optical values. This is possibly due to some missing factor in those formulae or perhaps in the approximations implied in these. Qualitatively, one could conclude that a smaller lowering at the fringes is not unreasonable.
From the practical point of view, it has been possible to reconstruct 'optical-computed' temperatures from probe data by interpolating the values obtained from the optical values at different currents, by the use of the 'corrective factors' (section 11.9)
The mechanisms which may account for the temperature reduction, i.e. 'cooling' are ion energy loss and recombination. To a first order of approximation it has been found that recombination seems to be dominant. This is substantiated by a semi-quantitative analysis of the current density function in terms of its derivatives and by the fact that density reduction factors in crossing the boundary are similar to the reduced collisional

recombination coefficient estimated from simplified considerations. This result confirms the estimations made in Chapter 6 based on the criteria (6.23) and (6.27), predicting ‘reactions’ in the pre-sheath, which according to the model depicted in section 11.11 is embedded in the boundary layer.

12. POTENTIALS

12.1 Plasma and Floating potential

It was one of the purposes of this work to ascertain whether floating methods can be used in conjunction with more conventional characteristic curve methods in order to characterize the electric arc.
Also, because as shown above, the characteristic curve methods cannot be fully exploited for the present circumstances, information gained from the measurements of charge and energy indicated in section 9.4 will be employed to obtain further information on plasma and sheath potentials.
As mentioned in Chapter 3, a probe free to float within a plasma attains a (negative) potential with respect to the plasma potential. Whilst an order of magnitude for this difference can be easily estimated as "a few electronvolts" [12, 28], the exact determination is difficult with a purely floating method (see the determinations in Chapter 4). The literature available on probes in arc plasmas is very poor if compared with the literature dealing with the more general plasmas and it is almost exclusively devoted to the "characteristic curve methods". Despite these difficulties, the floating methods can be used to infer electrical information on the arc.
When a Langmuir probe is at the floating potential, the measured probe potential, with reference to the anode of the arc discharge, is given by the voltage drop on the read out resistor (cf Chapter 7)

$$V_{\mathrm{prb}} = iR = V_{\mathrm{pl}} + V_{\mathrm{f}} \qquad (12.1)$$

Where both V_{pl} and V_f are unknown. The floating potential is the particular probe to sheath edge voltage drop corresponding to zero net current.

The following floating potential formulae will be assessed against experiment:

- Das equation (3.18) because it is the only formula which accounts for collisional pre-sheaths in the probe 'vicinity'. However, due to the lack of knowledge of the ion temperature it has to be employed in the 'thermal' limit T_e=T_i;

- Kagan and Perel formula (3.27)

$$\frac{eV_{FC}}{kT_e} = \ln\left[0.3\sqrt{\frac{m_i}{m_e}}\frac{r_p}{r_{pl}}\frac{1}{\alpha(\gamma)}\right]$$

for the probe potential in the vicinity of the floating potential, is the only relationship that allows a direct computation of the plasma potential (for the insulated probe) if the electron temperature is known. In this formula, r_{pl} is the radius of minimum approach of the ions. In the thin sheath approximation ($r_p = r_{pl}$) it gives

$$V_p = \frac{kT_e}{e}\ln\left[0.3\sqrt{\frac{m_i}{m_e}}\frac{1}{0.426}\right] \qquad (12.2)$$

where the constant 0.426 has been used for the thermal assumption [29] to apply.

For the latter potential, the procedure would then be as follows.
1) Determine the plasma potential with (12.2) using the temperature determined in Chapter 11;

2) Since the probe potential is measured, use (12.2) in (12.1) for the floating potential

$$V_f = V_{prb} - V_{pl} = V_{prb} - \frac{kT_e}{e}\ln\left[0.3\left(\frac{m_i}{m_e}\right)\frac{1}{\alpha(\gamma)}\right] \qquad (12.3)$$

The latter can be compared with determination (3.18). Moreover the plasma potential from (12.2) can be compared with the values determined indirectly through (12.1) from the knowledge of the floating potential.

The differences between probe voltages adjacent in height can be used to compute the electric field in the hypothesis that a) the radial component of the electric field is zero and b) that the variation of the floating potential between adjacent points along the arc axis is minimal (ideally zero). This is discussed further in section 12.5 and in Chapter 12.
The importance of the plasma potential determination from probes lies in two further circumstances:

- The plasma potential allows the characterization of the sheath, both in terms of voltage and thickness, using the arguments presented in Chapter 4 and 9.4. This point is discussed in section 12.6

- For a probe at the plasma potential, the absence of the sheath implies that the measured current, purely electron, is of the random type and can be taken as representative of the electron current distribution within the arc plasma. This is discussed in Chapter 12.

12.2 Observables

Probe potentials are the directly measured quantities either in floating conditions, using a 'high' resistor, or in biased conditions using a 'low' load resistor (*cf* Chapter 7). For the latter, the variability together with the probe current has been illustrated in the characteristic curves of Chapter 10.

In floating conditions the probe voltages correspond to the voltages measured in biased conditions at zero current as shown in Chapter 7. Probe potential general behaviour is shown in figure 12.1 where the potentials for all the probes are displayed as a function of the arc current; the arc characteristic curves are also inserted for comparison. From this picture it is clear that the probes follow the general trend of the total arc characteristic curve. In particular, increasing arc currents imply lower overall potentials in the lower arc current regime and a slight increase past the minimum at higher arc currents.

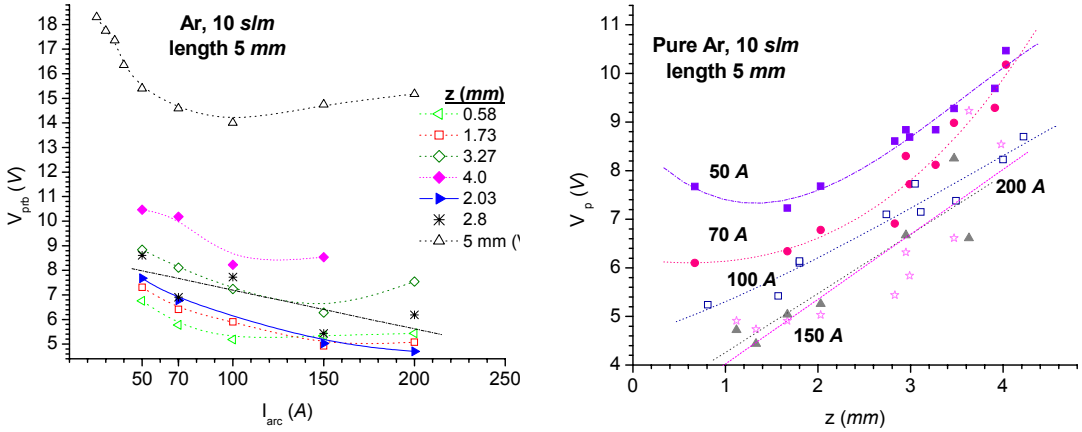

Figure 12.1 Left, probe voltages as a function of arc current (only points at common height are shown). A portion of the arc characteristic curve of figure 7.1 is also shown for comparison. Right, probe voltages as a function of probe heights for various arc currents

The voltages are also shown as a function of the probe height in the arc for the different arc currents in figure 12.1 right. Despite some scattered data at the highest currents, there is a degree of monotonic behaviour: the greater the arc current the lower is the probe potential at a given location.

12.3 Potential measurements

The purpose of this section is to illustrate the attempts to obtain plasma and floating potential independently from each other using the measured probe potential and a simplified description of the measuring circuit. The measurements referred to are in floating conditions (*cf* section 7.11, figure 7.7.1). The measured potentials are assumed to be valid for true floating conditions on the basis that (*i*) they show saturation when the read out resistor R_{DAQ} is taken sufficiently 'high' (see figure 7.13; R_{DAQ} = 67.72 kΩ has been used throughout) and (*ii*) differences with the value obtained form the zero current point (on the *V-I* curve) in biased conditions are below the level of experimental error.

Because R_{DAQ} is not truly infinite, a non-zero current is drawn by the probe in the course of the measurements. Depending on arc current, values range typically from 10^{-5} to 10^{-4} *A*. This could alter the sheath impedance and an error in the subsequent floating and plasma potential arises if the presumption is made that the measured potential is the probe potential taken in exactly floating conditions.

1. A simplified model of the circuit in floating operation is shown in figure 12.2, where all impedances have been considered purely resistive. The plasma and the anode sheath have been represented by two resistors to anode.

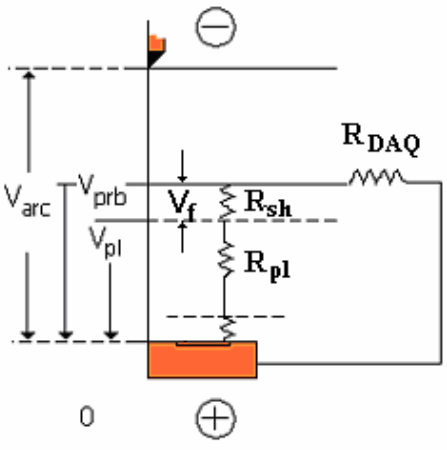

Figure 12.2

Simplified model for probe in arc in floating conditions. From above, cathode, probe with acquisition resistance, probe sheath, plasma and anode sheath. Nomenclature (see text):

V_f=floating potential

V_{pl}=plasma potential

V_{prb}= measured probe potential

V_p=probe potential in exactly floating conditions

If V_p is the probe potential in the *perfectly floating conditions*, then

$$V_p = V_{pl} + V_f \qquad (12.4)$$

The sheath contributes with a current that lowers the level V_{p}, to the *measured* probe potential V_{prb}, by an amount $R_{\mathrm{sh}} i_{\mathrm{prb}}$ and

$$V_{\mathrm{prb}} = V_{\mathrm{p}} + R_{\mathrm{sh}} i_{\mathrm{prb}} = V_{\mathrm{f}} + V_{\mathrm{pl}} + R_{\mathrm{sh}} i_{\mathrm{prb}} \tag{12.5}$$

The model can be described as follows. The measured voltage divided by the read-out resistor is the probe current; it is assumed that this is equal to the ratio of floating voltage to sheath 'resistance', i.e.

$$\begin{cases} i_{\mathrm{prb}} = \dfrac{V_{\mathrm{prb}}}{R_{\mathrm{DAQ}}} \\ i_{\mathrm{prb}} = \dfrac{V_{\mathrm{f}}}{R_{\mathrm{sh}}} \end{cases} \tag{12.6}$$

so that eliminating i_{prb} and solving for the resistances ratio

$$\frac{R_{\mathrm{sh}}}{R_{\mathrm{DAQ}}} = \frac{V_{\mathrm{p}} - V_{\mathrm{pl}}}{V_{\mathrm{prb}}} \tag{12.7}$$

This relationship involves three unknowns, the correct probe potential (e.g. in 'true' floating conditions), V_{p}, the plasma potential V_{pl} and the sheath resistance R_{sh}. Measuring the probe potential V_{prb} using two different resistors ("R_{DAQ}") relationship (12.7) can be used twice. Under the assumption of constant plasma potential one could write in simplified notation

$$\begin{aligned} &\frac{R_{\mathrm{sh1}}}{R_1} = \frac{V_{\mathrm{p1}} - V_{\mathrm{pl}}}{V_1} \\ &\frac{R_{\mathrm{sh2}}}{R_2} = \frac{V_{\mathrm{p2}} - V_{\mathrm{pl}}}{V_1} \\ &R_{\mathrm{k}} \equiv (R_{\mathrm{DAQ}})_{\mathrm{k}}, \quad V_{\mathrm{k}} \equiv V_{\mathrm{prb\,k}}, \quad k = 1, 2 \end{aligned} \tag{12.8}$$

The question is whether the sheath voltage fall remains the same for different resistors; if it did, then, because of (12.4), $V_{\mathrm{f}} = V_{\mathrm{p}} - V_{\mathrm{pl}}$ and one would obtain $R_1/V_1 = R_2/V_2$, contrary to the observation that the currents measured across two neighbouring resistors in floating conditions, differ by a factor of three. Therefore, the two equations in (12.8) cannot be equalized to eliminate R_{sh}.

It follows that hopes This is only possible under the assumption of negligible sheath voltage fall, e.g. neglecting $R_{\mathrm{sh}} i$ in (12.5), which turns out to be incorrect.

2. Alternatively, the problem can be attacked by constructing graphs of the measured probe potential either as a function of the read-out resistor, along the lines of figure 7.11, or as a function of its inverse and performing extrapolations to the voltage or (voltages)$^{-1}$ axes. In other words, from the study of the limits

$$V_{\text{ext}}(1) = \lim_{1/R_{\text{DAQ}} \to 0} V_{\text{prb}} = V_{\text{p}}$$
$$V_{\text{ext}}(2) = \lim_{R_{\text{DAQ}} \to 0} V_{\text{prb}} = V_{\text{pl}} \qquad (12.9)$$

the value $V_{\text{ext}}(1)$ obtained from the (extrapolated) intercept of the measured potential with the V axis when $R_{\text{DAQ}} \to \infty$ would be the true potential corrected for the sheath impedance; whereas the second extrapolation, $V_{\text{ext}}(2)$ would be the plasma potential.
As a consequence, the extrapolated probe potential gives the floating potential if the plasma potential is known.
In figure 12.3 the probe voltage as a function of read-out resistor shows the mentioned voltage saturation (used in Chapter 7 to assess the occurrence of floating conditions).

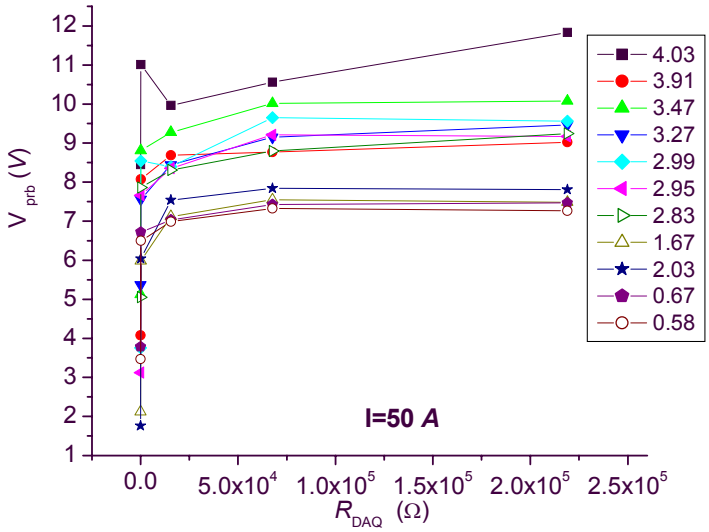

Figure 12.3 a, 50 *A*. Measured potential as a function of read out resistors (R_{DAQ}) for all probes (height in arc).

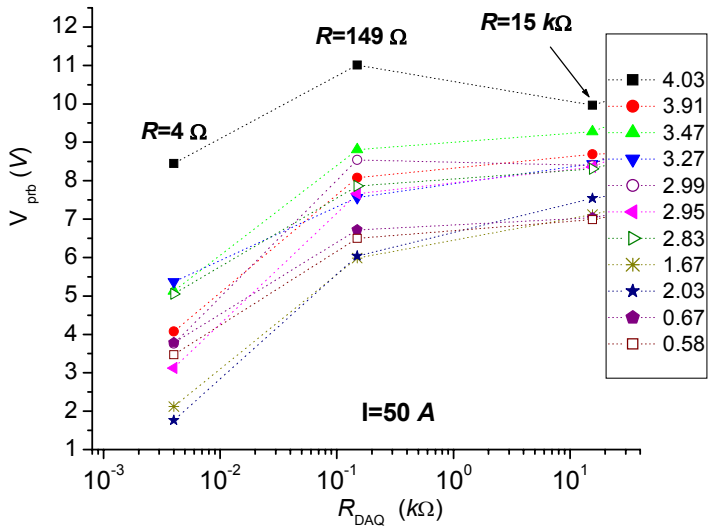

Figure 12.3 b, 50 *A*. Particular for the three lowest resistor values of figure 12.3 a

However, the extrapolated potentials obtained in the limits (12.10), suffer from the following drawback: a whole range of possible values would then result as shown in figure 12.3 b and in figure 12.4.

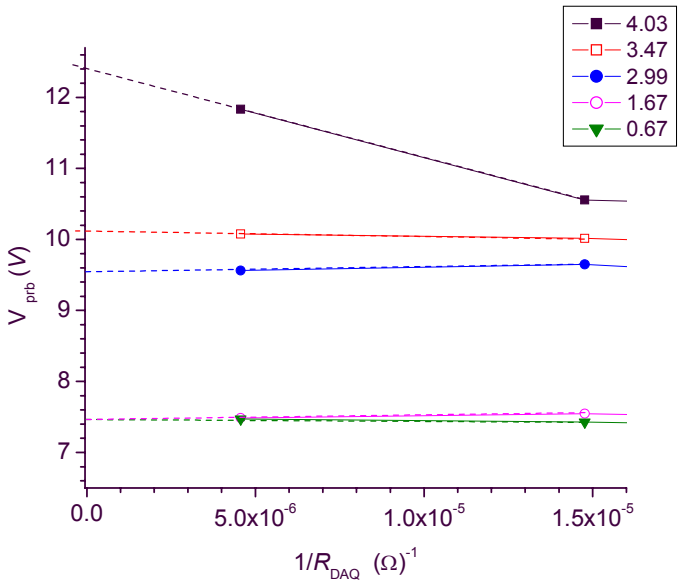

Figure 12.4 a, 50 *A*, detail of figure 12.3 in the region $R_{DAQ} \rightarrow \infty$. For reasons of visibility, the data points have been split in two sets, five probes here and six probes in figure 12.4 b. The linear extrapolation towards the *V* axis is also shown for each case

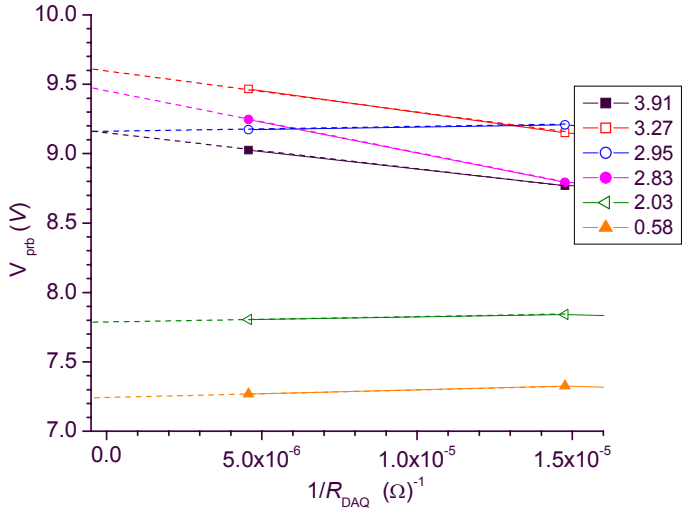

Figure 12.4 b, 50 *A*, detail of figure 12.3 in the region $R_{DAQ} \rightarrow \infty$. Six probes of the 11 of figure 12.3

In fact, it is clear that any attempts to obtain the axis intercept (thus the required *V*) from the intercept with the *V* axis is destined to failure because the necessary extrapolation can be greatly in error. There is no clear functional trend of the curves and the situation is complicated by the fact that not all the 'curves' are monotonic with respect to the last point-to-point line (towards the axis). This may be due either to scatter intrinsic in the measured data or it may indicate a true non monotonic trend.

The choice as which is the correct extrapolation and the consequent axis intercept is open to question even if the initial model can be ameliorated (perhaps considering different factors entering the voltage expressions). It is therefore unprofitable to pursue this line further.

By contrast, there is some merit to progressively lowering the read out resistor, which will induce a greater and greater current flow towards the probe increasing its negative potential towards the plasma value. Therefore, this latter evaluation can be taken as a first order estimate of the region where the true plasma potential should lie. However, because of the unpredictable way the data approaches the potential axis there is no way to establish whether this is a lower or an upper limit. The limitations of this method lie almost entirely with the need to perform extrapolations using a very limited (coarse) set of points in the axial direction.

12.4 Plasma potential from the *V-I* curve

This type of determination of the plasma potential is complicated, considering that the arc characteristic curves do not show a clearly defined ‘knee’ in the electron saturation region. The technique based on the differentiation of the *V-I* curve in the ‘linear part’ suffers similarly because the steep part is either not linear or not complete in all cases.

The use of numeric differentiation on data that are not smooth enough leads to inaccuracies. As an example, a determination of the plasma potential by means of the derivative method from the V-I curve is shown in figure 12.7. It can be seen from the derivative curve and the original V-I curve, limited somewhat arbitrarily to the interval V= -12 to –4 V, that a local maximum of dI/dV is hard to define.

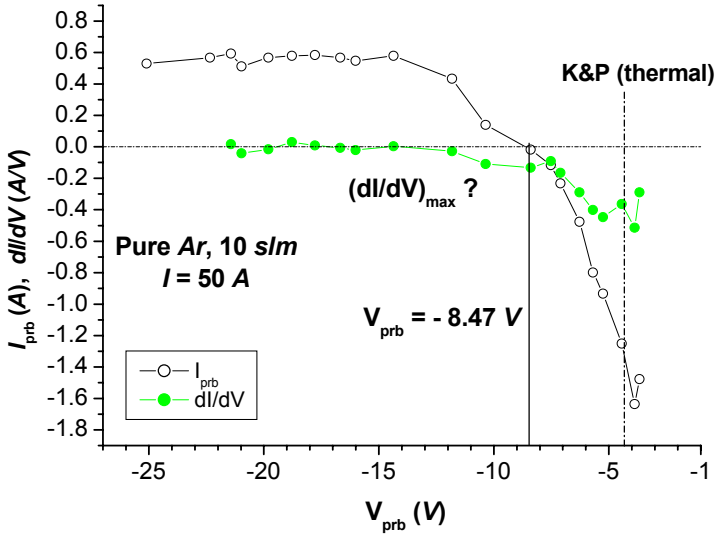

Figure 12.7 I=50 *A*, central characteristic curve for probe N. 8, *z*=2.83 *mm* from anode (empty circles). The vertical line shows the probe potential corresponding to floating conditions. For the first derivative of the of the V-I curve (full circles), even limiting to the 'linear' portion starting at ~ -12 V, the maximum is difficult to define.

The policy for the choice was that if the intercept method and the derivative method gave greatly different value (well beyond the experimental error on the measured voltages) then no plasma potential can be assigned. This procedure is far from error-free. As an example, at I=150 A, all the values of the plasma potential obtained from the V-I curve methods are greater (in absolute value) than the measured probe potential. This means that the plasma potential would be negative with respect to the probe potential where floating conditions are attained, contrary to the expectation that the floating potential location should correspond to a probe *negative* with respect to the plasma. For these reasons it is felt that the determination of the plasma potential directly from the V-I curve is not justifiable.

12.5 Floating potential from probe temperature

1. In the last two sections it has been shown that any attempt to determine either of the two relevant potentials independently from each other or from other quantities is

destined to failure. The remaining choice is to compute either the floating potential or the plasma potential using the temperatures obtained in Chapter 11.
The choice is made to compute the floating potential from the probe temperature obtained under ion saturation conditions. The plasma potential will be subsequently computed form relationship (12.1) and compared with literature in section 12.5.1.
The relationships employed for the determination of the floating potentials are those presented in section 12.1.

Figure 12.8 shows the axial floating potential computed according to the temperatures which were obtained from the random model formula with partial collecting surface and pre-sheath existence employed in Chapter 11. The formula employed for the potential is the relationship of Das *et al* equation (2.28) [30] which accounts for the existence of the pre-sheath, and evaluated in the thermal hypothesis (T_e=T_i), in line with the probe temperature choice. The cases I=50 to 200 *A* are shown in sequence. Note that the absolute value is shown [The correct values are negative].

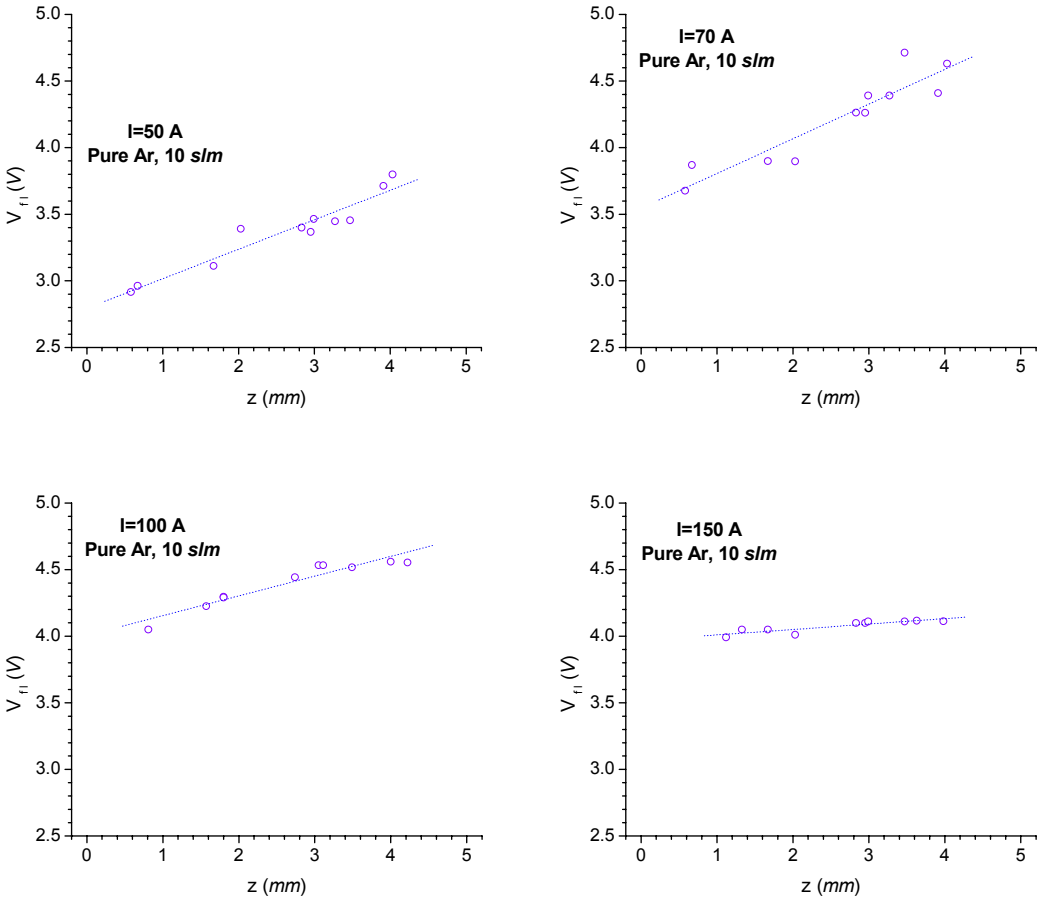

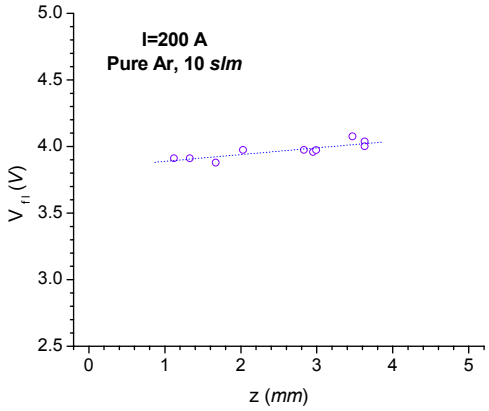

Figure 12.8

Floating potential computed from the axial temperatures in the T_{GPSh23} case at ion saturation according to the formula of Das et al [30]. From above, left to right: arc current I_{arc}=50, 70, 100, 150 and 200 *A*

The floating potential variation along the arc height decreases by increasing the arc current. At 50 *A* this is of the order of 1 *V* whereas at the highest current the floating potential is practically constant. This constancy of the 'contact potential' along the arc height is a key hypothesis for the estimation of the axial electric field (*cf* Chapter 12).

12.5.1 Plasma potential: corrections and comparison with literature

The plasma potential can be determined using the computed floating potential of figure 12.8 as the algebraic difference between the measured probe V_p and the computed floating potential. Figure 12.9 shows the results obtained.

Figure 12.9

Plasma potential computed from the difference of the measured probe voltage and the computed floating potential of figure 12.8. In each case a fit is shown, linear (full curve) and /or 2nd degree polynomial (P2, dotted line). In the 200 A case a spline through the experimental points is also shown

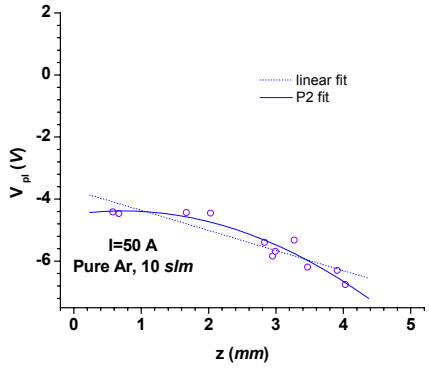

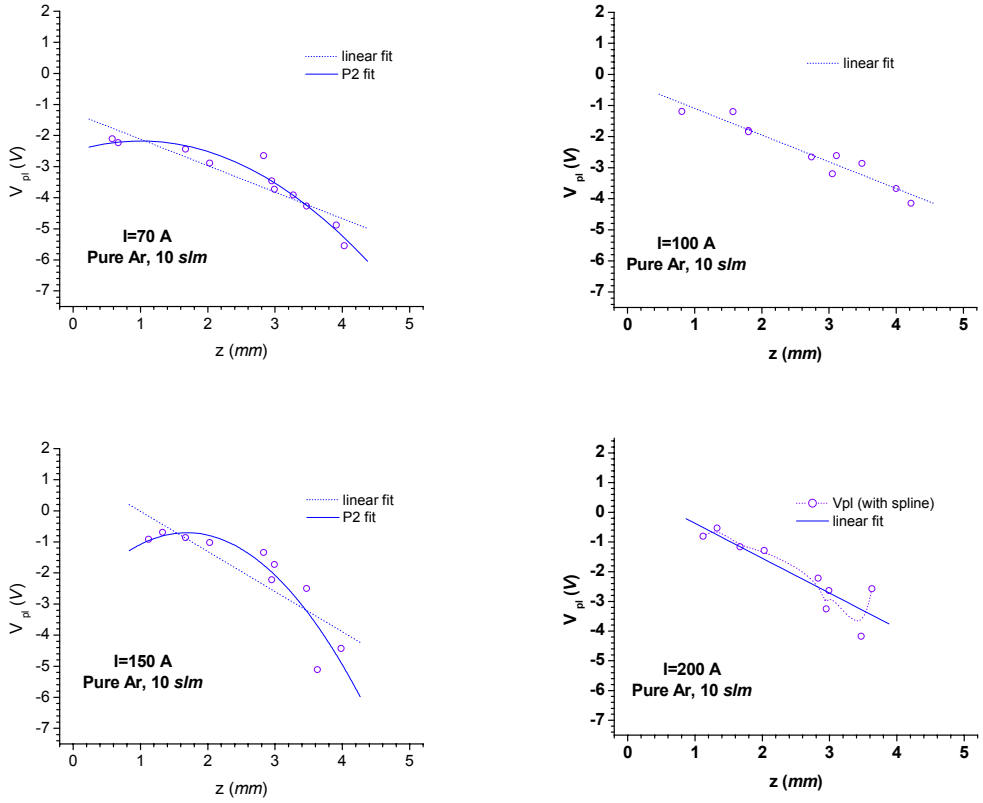

It should be observed that while the floating potential is a characteristic of a conductor immersed in the plasma, the plasma potential is an intrinsic plasma feature. In other words, because the temperatures used in the calculation of V_{fl} were depressed values, the true corrected electron temperature should be used according to Chapter 11. By applying this correction, e.g. multiplying the probe temperatures (or, which is the same the floating potentials) by a factor which is the ratio of optical to probe temperature (variable with z), the plasma potentials shown in figure 12.10 are obtained. It should be emphasized that whereas the 'corrected' floating potential has no physical meaning (because as consequence of probe insertion the *true* floating potential is the "uncorrected" one shown in figure 12.8), the plasma potential is actually fixed by the correct temperature. Because the optical temperature is available only for I=50, 100 and 200 A, it is for these that the correction was applied.

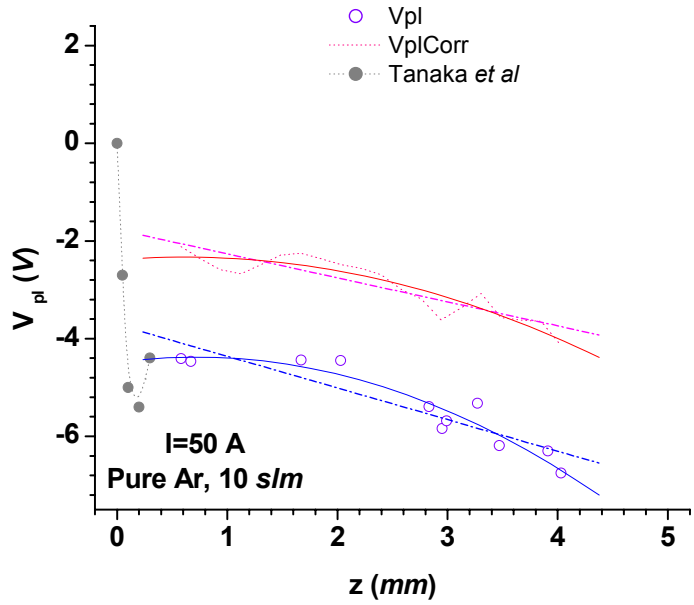

Figure 12.10 a Corrected axial plasma potential for I=50 (uncorrected data empty circles, corrected values dotted line, both shown with the fits of figure 12.9). Comparison is made with measured values of Tanaka *et al* [31] obtained in the anode region (full circles).

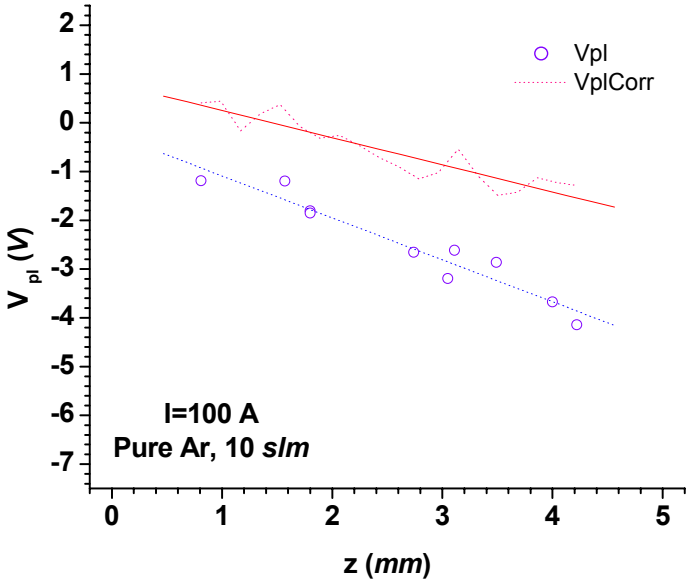

Figure 12.10 b Corrected axial plasma potential for I=100 *A*.

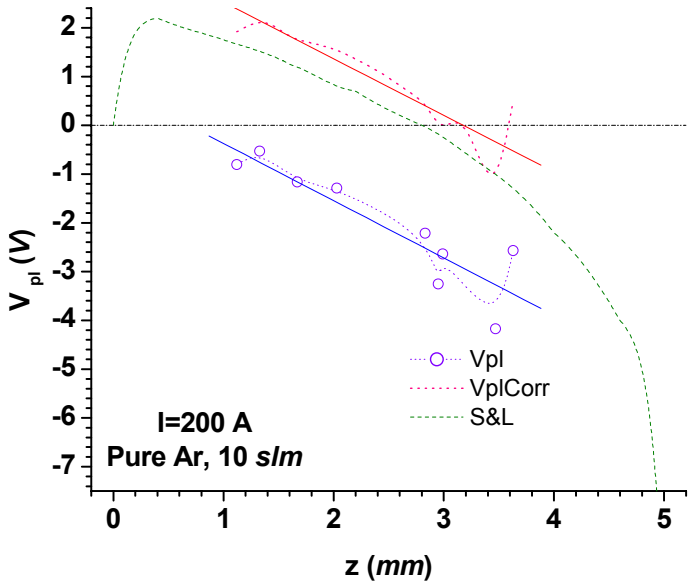

Figure 12.10 c Corrected axial plasma potential for I= 200 *A*. Comparison is made with the model of Sansonnes and Lowke (S&L [32])

Perhaps excluding the first value at 50 *A*, the curves show a common trend of a partially negative potential, e.g. of the existence of an inversion point along the axis where the potential changes sign. This location in height increases with the arc current.

It can be observed that in all cases the resultant plasma potential is made more positive by the use of the higher (optical temperature). In the 50 *A* case the correction appears 'detrimental' in that the original uncorrected points (empty circles) are closer to the measurements of Tanaka *et al* (full circles,) obtained in the anode region (up to about 300 μm), than to the corrected value.

The 200 *A* case shows some agreement with the numerical model of Sansonnes *et al* [32]. In the present determination the tendency seems the opposite when moving closer to the cathode However, other experimental points at higher z are not available to confirm this trend. Moreover, there are differences between the present over-all arc voltage, 15 *V* here, and the lower 13.2 *V* of [32] but the behaviour in the column, where the two potentials differ by about 30% is similar; both the determinations show an inversion of the potential around mid height.

12.5.2 Computation according to Kagan and Perel [29]

The values for the plasma potential computed with (3.27) have been obtained using both the optical and the probe determined temperature. In figure 12.11 a-c, a comparison is made with the values determined in the previous section.

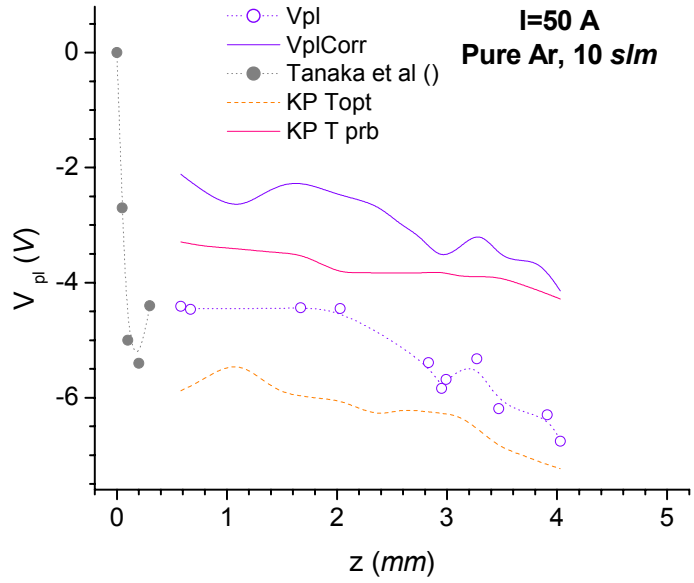

Figure 12.11 a. I=50 A, Plasma potential according to Kagan and Perel formula (3.27) shown for probe temperature (continuous) and optical temperature (dash) together with the curves plotted in figure 12.9 and 12.10 for the plasma potentials obtained from the floating potential in the uncorrected (empty circles) and corrected case (dotted line)

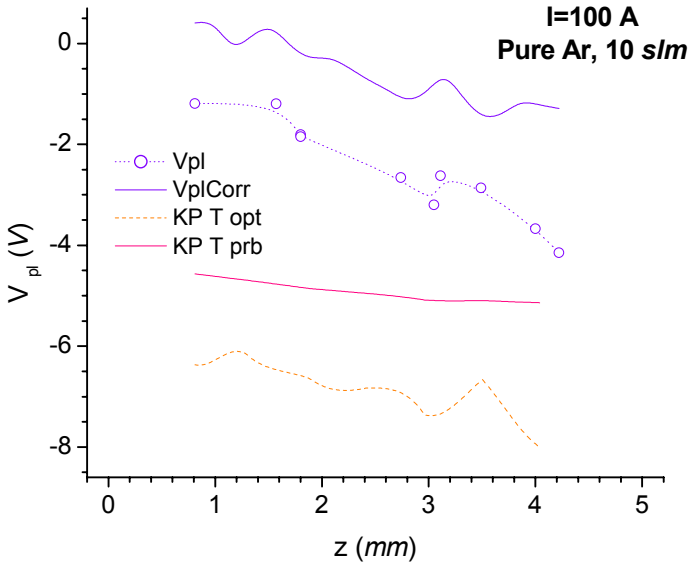

Figure 12.11 b. I=100 A. Plasma potential according to Kagan and Perel formula (3.27) are shown for probe temperature (continuous) and optical temperature (dash) together with the curves plotted in figure 12.9 and 12.10 for the plasma potentials obtained from the floating potential in the uncorrected (empty circles) and corrected case (dotted line)

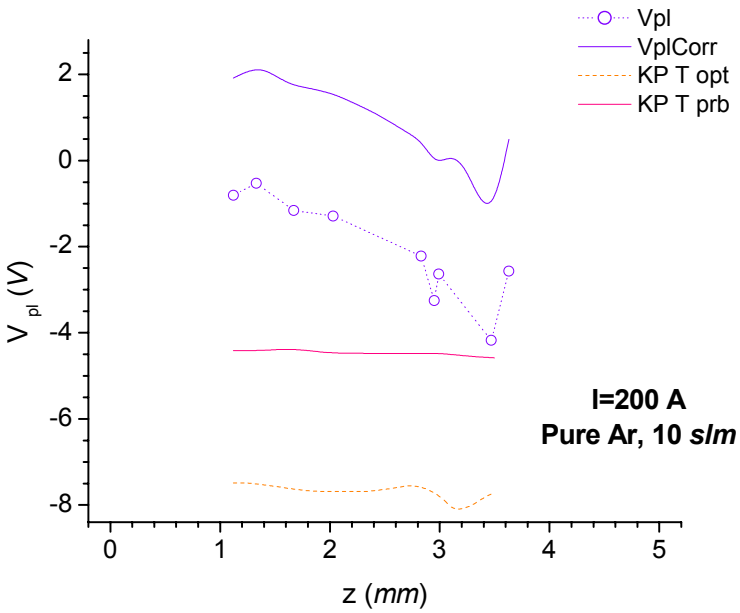

Figure 12.11 c. I= 200 A. Plasma potential according to Kagan and Perel formula (3.27) are shown for probe temperature (continuous) and optical temperature (dash) together with the curves plotted in figure 12.9 and 12.10 for the plasma potentials obtained from the floating potential in the uncorrected (empty circles) and corrected case (dotted line)

With respect to the values obtained from the floating potential in the previous section, Kagan and Perel's plasma potentials are more negative. Also, the correction performed using the optical against the probe temperature shows an opposite trend with respect to the determinations of section 12.5.1. In fact, an increase of the temperature from probe to optical, shifts the potential towards lower values (e.g. greater in absolute value). This is the opposite of what is expected on the basis of a lowering of the potential at greater heights within the arc and fixed arc current. Also, the indication that appears from measured probe voltages (cf section 12.2) and from the arc characteristic curve (cf figure 7.) is that below the voltage minimum, located around 100 A, an increase of the arc current decreases the potential. Therefore, a decrease in voltage is accompanied by an increase in temperature (when passing from 50 to 100 A). This is not shown by the determinations based on Kagan and Perel where the use of a higher temperature (optical) corresponds instead to a higher potential (and thus a lower current). Moreover, for currents greater than the voltage minimum of the arc characteristic curve, an increase in voltage is accompanied by higher current and thus higher temperatures (from 100 to 200 A). This is shown in Kagan and Perel determination, but the transition from these two behaviours is not shown. Rather, the case 100 and 200 A do not differ very much one from the other. In contrast, the values of the difference between uncorrected and corrected plasma potential for the determinations obtained from the floating

potentials of section 12.5.1 do decrease or increase as expected (cf figure 12.11). For these reasons, the determinations based on Kagan and Perel are assumed not correct for the present circumstances.

12.6 Sheath voltage and thickness

If the plasma potential is known across and along the arc, the voltage fall between plasma and probe surface, the sheath voltage, can be obtained. The plasma potential however, has been determined only along the axis of the arc. The major difficulty in obtaining localized values for the latter is associated with the requirement made in Chapter 10 that the probe is equipotential. As a consequence it is doubtful that the difference between the probe voltage, constant along its whole length and the plasma potential, which is presumed to vary along the same coordinate (one sheath thickness away from the probe), can be obtained as a local quantity.
The sheath voltage fall and the sheath thickness along the probe length can be computed by the use of the kinetic energy variation of the ions (measured), and in particular by the use of the temperature determined in Chapter 11. Within the validity region of the latter (as seen above, determined by the matching of the particle densities) it is possible to give a qualitative picture of the sheath structure.
Therefore, some estimates are made using the information gained form the measured energy and particle densities. The sheath thickness is computed using the formulae given in Chapter 4, Child-Langmuir's (4.12) and (4.13), representative of a fully collisionless sheath (vacuum diode in fact) and Swift's determination (4.20) and (4.22) for the thermal plasma.

The sheath voltage is obtained by use of relationships (10.15) having chosen the random with pre-sheath and partial collection surface temperature of Chapter 11. This is an independent way with respect to the procedure used for the floating potential; the latter cannot be used here, because it holds only in floating conditions. It is worth emphasizing that acceptance of the assumption implied in relationship (10.9) that the quantity E_i is the final energy per impinged particle is critical. Also, the selection of the data has to account for the geometry which now implies variability along the probe y direction instead of radial direction. Certainly, when comparing the sheath voltage corresponding to biased conditions leading to floating probe, the central value of the sheath voltage should coincide with the (central) value of the floating potential because the two sheaths must be equivalent.

The voltage is computed irrespective of the model, so its value can be compared with the values of Chapter 4 with same parameter in order to see which approaches the experiment better. Because the ion sheath develops upon increase in (negative) bias, it is interesting to follow its evolution for different probe voltages and probe height.

1. Sheath voltage and thickness for different probes

In figure 12.12 left a set of sheath voltages is compared for three different arc heights. On the right the sheath thickness corresponding to thermal Swift case (formula 4.22) and the Child-Langmuir case (formula 4.13) are shown. The probe radius is inserted for comparison (r=1.25·10^{-4} m).

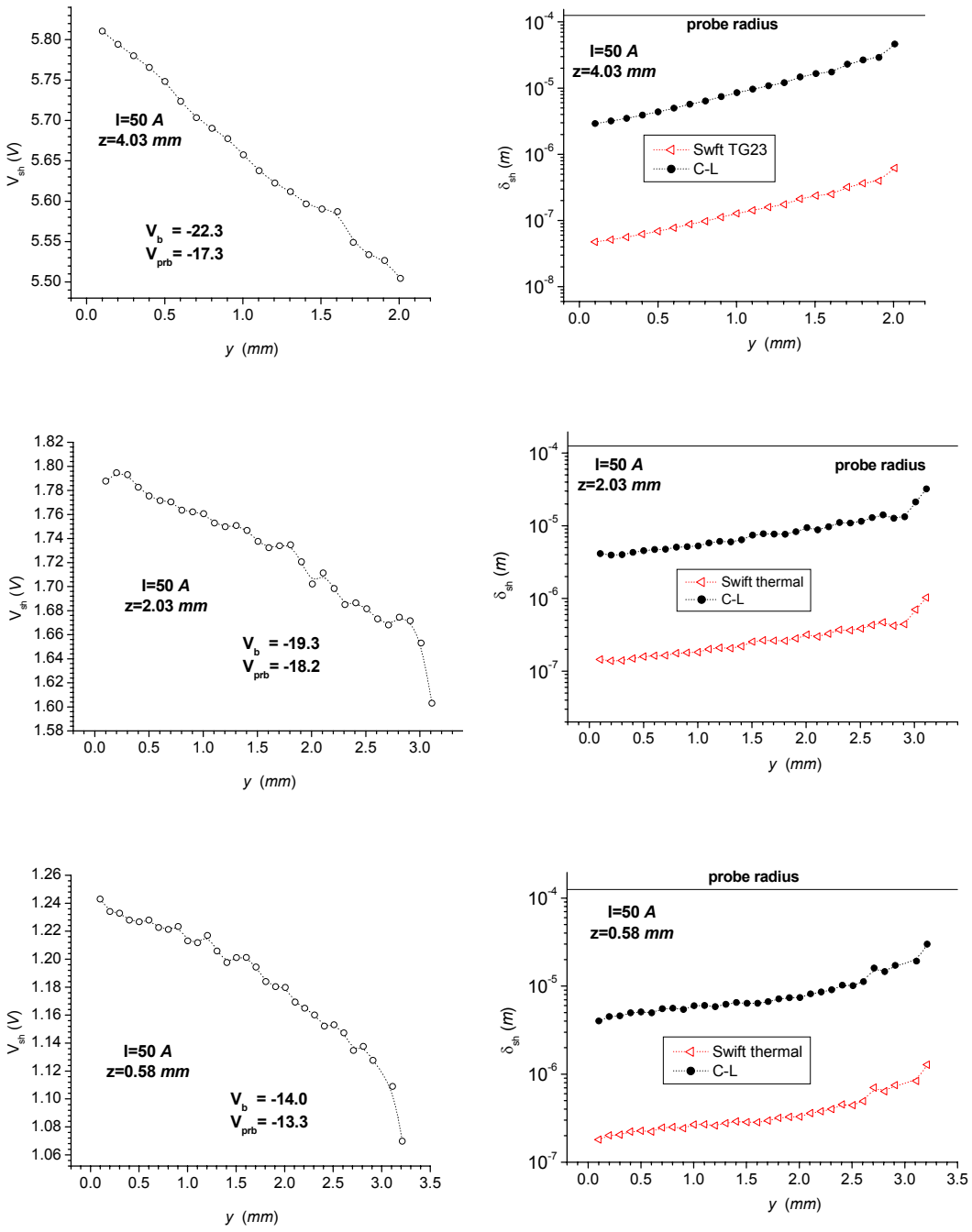

Figure 12.12. I=50 *A*. Left, Sheath voltage computed from temperature and particle energy to the probe. The nominal bias V_b and the effective probe voltage V_{prb} are also

shown. Right, corresponding sheath thickness according to Swift's thermal model (4.22), (C-L) Child Langmuir's (4.13). The probe radius is also shown for comparison.

It can be observed that Swift's case is by construction the 'thermal' Debye length for equal ion and electron temperature, which differs from the electron Debye length by a factor $\sqrt{2}$ (*cf* formula 2.3).

The voltage fall across the sheath decreases at lower arc heights as well as its range of variability. The sheath thickness of the thermal model is always lower than the Child-Langmuir model (C-L). These values can be compared with the predictions shown in figure 4.3 for the C-L model and 4.4 for Swift's thermal model. The 'wall' potentials of Chapter 4 are here the probe voltages V_{prb} indicated in figure 12.12

- For the C-L model, figure 4.3 says that, for the probe at z=4.03 *mm* (top of figure 12.12), taking the central sheath voltage at 5.81 *V* and searching for a 'wall' of V_{prb} ~ -17 *V* in figure 4.3, a thickness of the order of $\sim 6 \cdot 10^{-6}$ *m* is found, close to the $\sim 7 \cdot 10^{-6}$ *m* given in figure 12.12 right. Similar agreement can be found comparing the values of figure 12.12 for the other two probes with the constructed values of figure 4.3.

- Swift's model is independent of the probe voltage and the values shown in figure 4.4 were computed at fixed temperature. Because for probe 2 at *z*=4.03 *mm* the temperature is 9,980~10,000 K, thus half way between two values given in figure 4.4, $\delta_{sh} \sim 7 \cdot 10^{-6}$ *m* is obtained, close to the $3 \cdot 10^{-6}$ *m* read from figure 12.12.

This 'agreement', is only taken as a measure of likelihood for the correctness of the whole chain of computations. The observations made above do not make it possible to choose between the two models, as the experimental results were obtained precisely because the corresponding C-L or Swift hypotheses were employed. However, the representation of figure 12.13 is correct at least qualitatively. Furthermore, by comparing the value of the sheath voltage at the centre (*y*=0) with some values of the floating potential from figure 12.8 it is seen that the sheath voltage drop is higher than the floating potential as it should be.

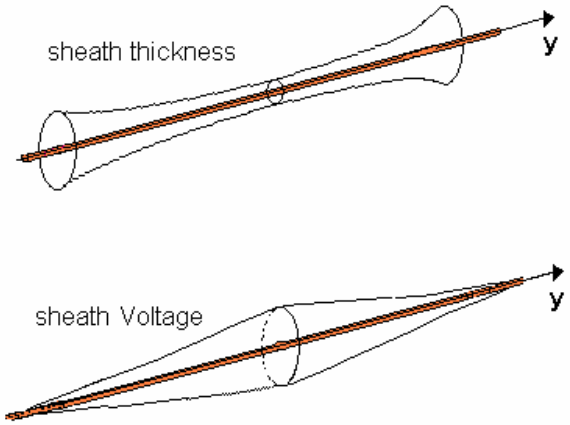

Figure 12.13 upper, qualitative shape of the sheath thickness along the probe length; lower, the amplitude of the voltage fall across the sheath along the probe.

2. Sheath voltage and thickness for different bias

In general, it is expected that both the sheath voltage and the corresponding layer thickness are reduced when moving towards less negative biases. In order to perform a more quantitative assessment of the results shown, there are two arguments against which the sheath voltage and thickness need to be confronted.

The first relates to the verification of the voltage interval corresponding to the sheath existence criterion according to section 4.2.
The second is related to equation (10.15) which follows from the assumption (10.12).
These two arguments are tested with the experimental data of figure 12.14 which shows different sheath voltages compared with the temperature (expressed in *eV*) in order to (*i*) study the variation of the sheath voltage with bias and (*ii*) to determined the limiting region for the existence of the sheath according to (12.10).

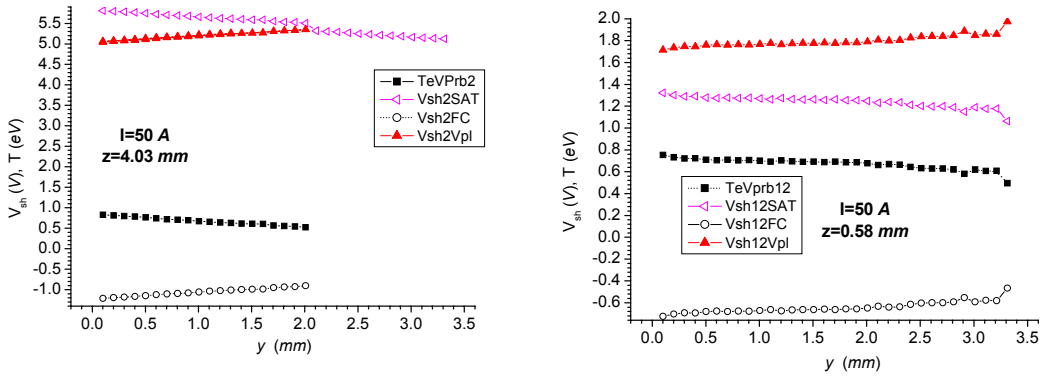

12.14. I=50 *A*. Selection of sheath voltages for probe at z=2.03 *mm* (left) and at z=0.58 *mm* (right). The temperature obtained according to the methods of Chapter 11 is shown compared with sheath voltages obtained under different bias conditions.

1. Sheath existence

In section 4.2 a limiting criterion for the existence of the sheath was formulated by means of the inequality

$$\left|eV_{\mathrm{sh}}\right| > kT_{\mathrm{e}}/2 \qquad (12.10)$$

requiring the sheath fall to exceed half the temperature for the sheath to exist. (This led to the Bohm criterion).

A computation of the voltage sheath and thickness by means of relationship (10.15), shown for two probes at I=50 *A* in figure 12.14, under varying bias conditions shows that:

1. In *ion saturation conditions*, the sheath fall exceeds the temperature (and half its value) and condition (12.10) is verified as it should;

2. The sheath voltage in *floating conditions* is now negative, and the condition for the existence of the sheath is not fulfilled. The negative value implies also that the effect of the sheath would be to reduce the ion energy with respect to the value at the sheath edge, which is determined by the temperature, thus it would suggest a negative sheath, in contrast to what expected in floating conditions. Moreover, the absolute value of this voltage at y=0 (centre probe) is lower than the central value of the floating potential computed for the same case and shown in figure 12.8.

3. When the probe is at *plasma potential* (assumed the latter is available) the sheath voltage should be zero whereas here it is close to the maximum sheath voltage (at ion saturation) and it even overcomes the latter for the z=0.58 *mm* case.

2. The use of energy relationship and assumption (10.12)

Relationship (10.12) implies that:

$$0 = V_{\mathrm{b}} - V_{\mathrm{prb}} - kT_{\mathrm{e}}/e$$

e.g., that the plasma temperature is determined by the difference between applied bias and read probe voltage. Under the circumstances of this work (equipotential probe) this would mean a uniform plasma temperature along the probe length, contrary to the expectation that the temperature should decrease in the peripheral regions of the arc (and, with the appropriate geometrical transformation, also along the probe). Moreover, at any potential (e.g. at any bias), the sum of plasma potential and temperature would be determined by the applied bias

$$V_{\mathrm{pl}} - V_{\mathrm{b}} = -kT_{\mathrm{e}} / e$$

This is unacceptable in view of the requirement of a ‘non perturbing probe’. Therefore, considering the hypothesis that led to relationship (10.6), it is felt that the equation for the final kinetic energy (10.2) and the average ion energy (10.9) are plausible as taken separately. However, the identification carried forward by (10.10) is incorrect.

The two groups of arguments lead to the conclusion that:

1. The plausibility of relationship (12.10) for the existence of a sheath does not seem unreasonable even if the effect of the pre-sheath required in the present formulation were not included (these are required because of the choice of the temperature, *cf* Chapter 11) and therefore the analysis conducted is only semi-quantitative.

2. The serious difficulty lies in the energy identification implied by (10.6) and following relationships. The fact that the energy gained by the ions exceeds the energy at the edge is not sufficient *per se* in attributing to the difference between the probe and bias voltages the excess of kinetic energy gained by the ions.

It is the latter problem that makes it impossible to obtain local features of the sheath.

13. CURRENT DENSITIES, ELECTRIC FIELD AND CONDUCTIVITY

13.1. Introduction

It is the purpose of this chapter to present values of electrical parameters which should complete the picture of the information that probes in arc can provide. The discussion is focused here on individual parameters leaving the 'integrated picture' to the next chapter (Chapter 14). Data are presented for ion and electron current densities and for the electric field. The implications of a comparison between the two are discussed.
Some attempts made to measure the electrical conductivity directly are presented. These would provide an independent mean of determining the electron temperature. Unfortunately, this aim was not attained, and the conductivity is therefore obtained using the temperature previously determined in Chapter 11.
The *axial* electric field can be determined indirectly from the knowledge of the plasma potential or directly by using the measured probe voltages, provided the assumption of uniformity of the floating potential can be proved. In Chapter 12 it was shown that, whereas this hypothesis is fulfilled in the columns of 150 and 200 *A* arcs, for the lower 50, 70 and perhaps 100 *A*, the gradient of the floating potential is not negligible.

13.2. Ion Current densities

1. Ion current densities measured by probes are representative of the true ion currents within the arc provided the current drawn by the probe is not perturbing the arc. As shown in Chapter 11, a necessary but not sufficient criterion is that the particle density reconstructed from the current measured in ion saturation conditions, should not exceed the local equilibrium density determined by the undisturbed (optical) electron temperatures. As seen in Chapter 11, with the choice of the correct temperature model, this condition is respected. However, because of boundary layer cooling, this limiting density is probably shifted to a lower value difficult to evaluate independently. In Chapter 11 an order of magnitude estimate for the *electron* density reduction within the boundary layer was given (ratio of optical to probe density ~ 50 to 70, *cf* figure 11.11) and as a similar value is to be expected for the ion densities (because of the dominant role of recombination as a cooling mechanism), this factor could be taken as an

ameliorated condition for non-perturbation, e.g. $n_p \leq 50$ to 70 n_{LTE} where n_p is the number density computed from the current read by the probe.

2. A further condition for 'representiveness' lies in the form of the current. The use of a random model for the current at ion saturation and the hypothesis of non complete collecting surface imply some kind of directionality of the current. This would mean that the probe could be thought as of being immersed in a macroscopic flow *containing* charged particles, thus ions directed from the cathode to the anode, contrary to the direction of the field that a simple cathode to anode structure suggests. Considering that in section 12.4 plasma potential values were presented which suggest inversion along the cathode to anode distance the latter statement is not completely unsound.

3. The ion current densities were obtained by taking the points of the characteristic curve where the ion current shows saturation. Since the currents obtained from the local characteristic curve (Abel inverted) are currents per unit length, a normalization using the minimum step of 100.4 μm was used (the minimum spatial resolution corresponding to the minimum time resolution).

a. Ion saturation radial current densities for different heights in arc

A comparison between all the ion saturation current densities measured at I= 50, 70, 100, 150 and 200 *A*, is shown in figure 13.1 a to e.

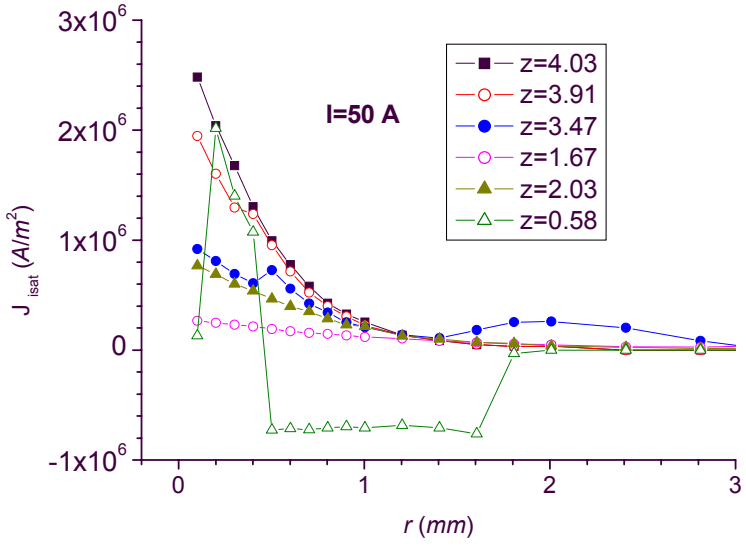

Figure 13.1 a Arc current I= 50 *A*, Ion saturation current densities as a function of radius at fixed arc heights

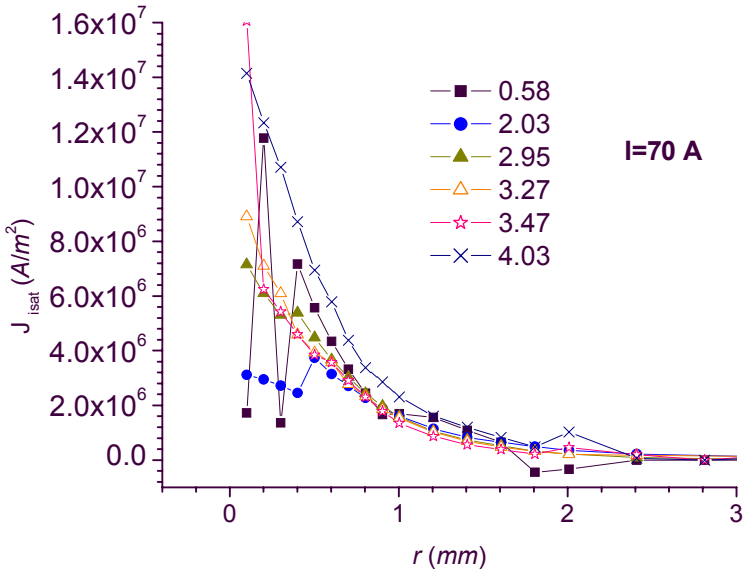

Figure 13.1 b Arc current I= 70 *A*, Ion saturation current densities as a function of radius at fixed arc heights

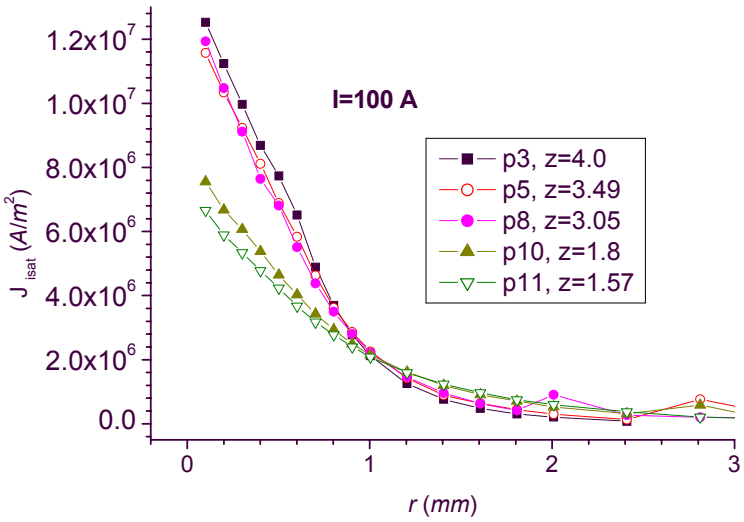

Figure 13.1 c Arc current I= 100 *A*, Ion saturation current densities as a function of radius at fixed arc heights

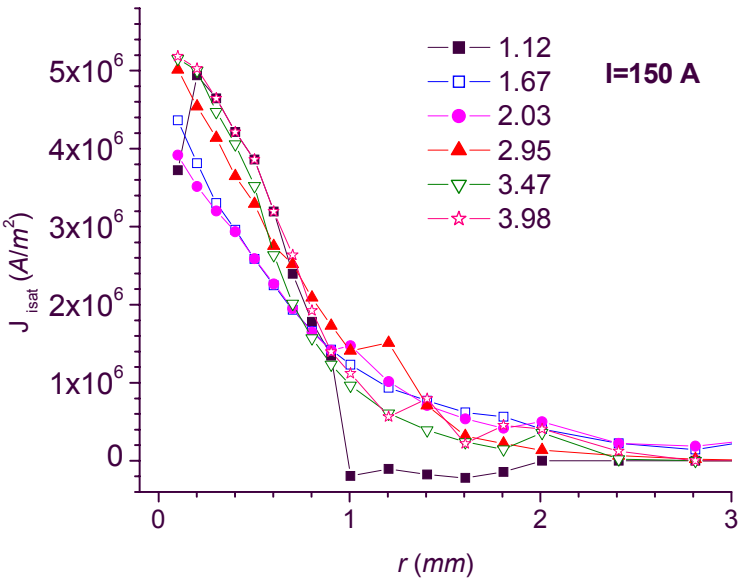

Figure 13.1 d Arc current I= 150 *A*, Ion saturation current densities as a function of radius at fixed arc heights

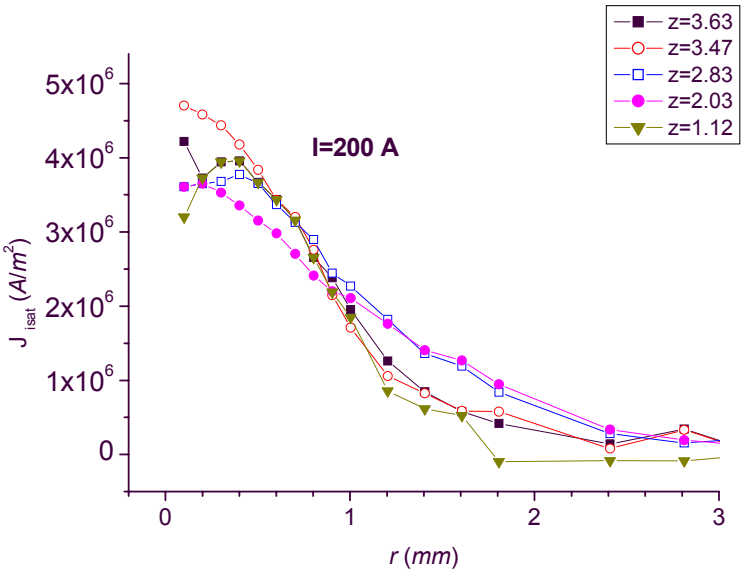

Figure 13.1 e Arc current I= 200 *A*, Ion saturation current densities as a function of radius at fixed arc heights

b. Selection of some ion current densities

There seem to be a dependency of the radial distribution for each height and the total arc current. This can be seen from figure 13.2 where a selection of ion current densities from the different arc current cases is presented.

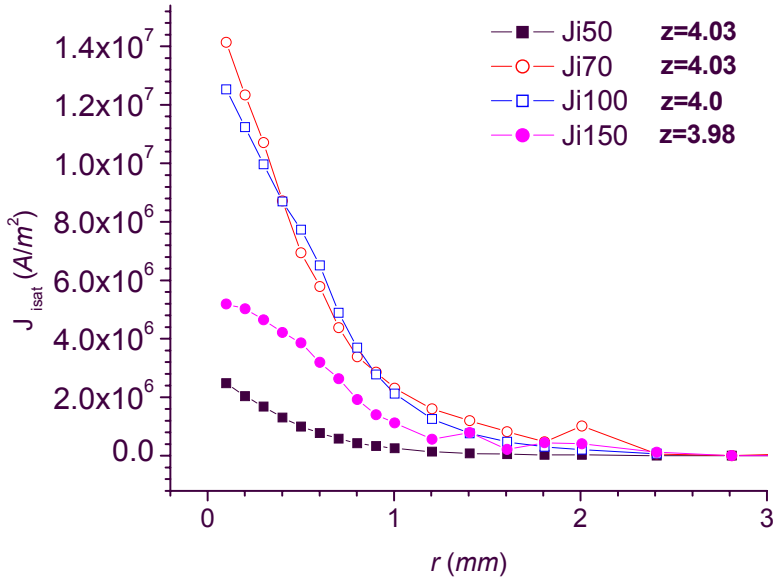

Figure 13.2 a Selected current densities grouped for comparable arc height at different arc currents

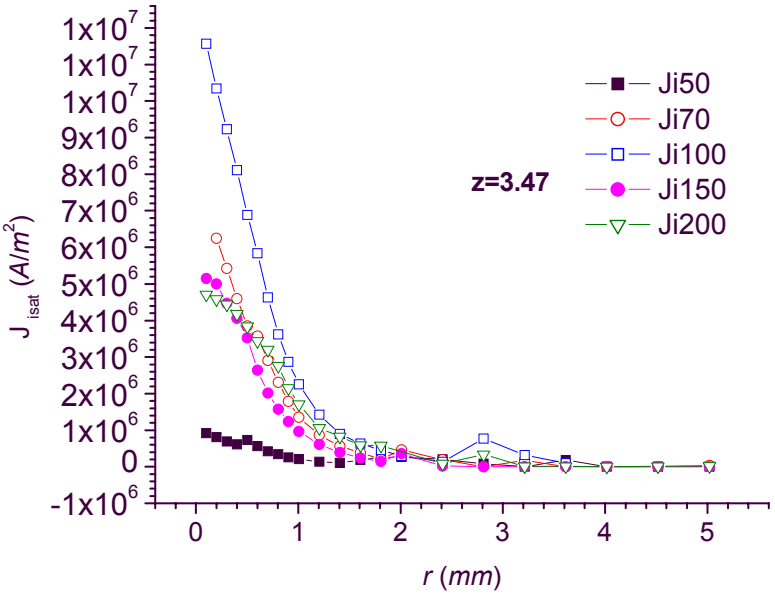

Figure 13.2 b Selected current densities grouped for comparable arc height at different arc currents

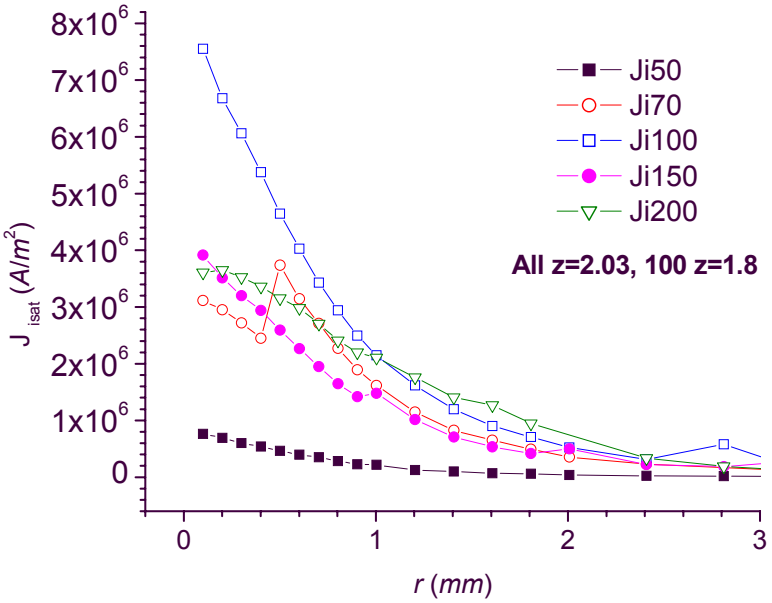

Figure 13.2 c Selected current densities grouped for comparable arc height at different arc currents. Plot limited to the available data.

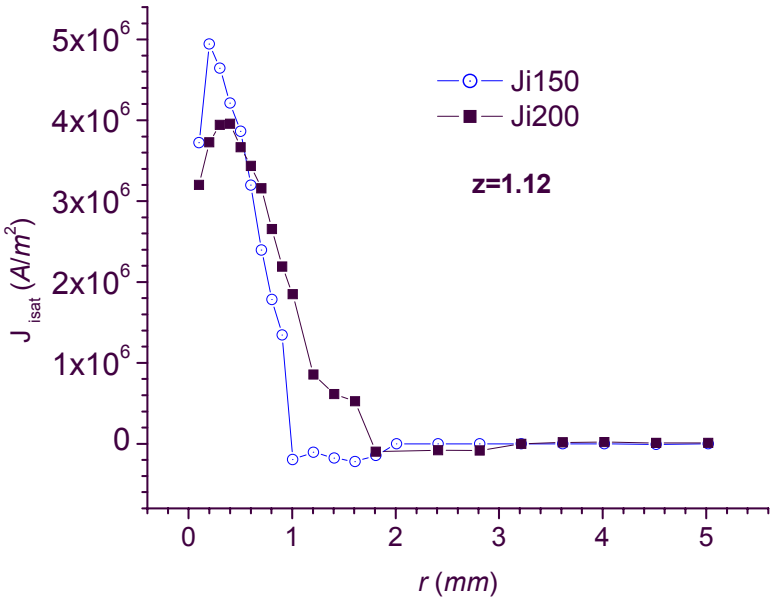

Figure 13.2 d Selected current densities grouped for comparable arc height at different arc currents. Plot limited to the available data.

Since the data were not taken with exactly the same probes for all the arc current cases (e.g. some probes were substituted in between the runs), only four groups have been taken broadly corresponding to a height of 4, 3.5 and 2 *mm* from the anode and by values closer to the anode, about 1.1 *mm*, available only for two currents.
Each plot in figure 13.2 can be read in ascending order of arc current suggesting an increase of J for arc current from 50 to 100 A, followed by a decrease for higher arc currents. The increase seems verified in the region close to the anode (see 0.58 *mm* case where J70 is higher than J50); the decrease beyond 100 A seems confirmed by the 1.12 *mm* case, where J150>J200. At grater arc heights, above 4 *mm*, unfortunately no further data are available to confirm the trend.

13.3. Electron current densities

The measured electron current density can be obtained when the probe is at plasma potential. The determination of the plasma potential was discussed in Chapter 11. The peak files (current peaks) corresponding to the point where $V=V_{\mathrm{pl}}$ are extracted and the radial distribution of the current density per unit length (as obtained from the Abel inversion) divided by the probe radius gives the current per unit surface.
It must be observed that because the goal is the measured electron current density, the uncorrected plasma potential obtained from the floating potential (corresponding to the probe determined 'cooled' temperature) must be used.
However, difficulties in the exact location of the plasma potential make the electron current density determination complicated. The results shown in Chapter 11 imply that the current density for the highest arc currents is not accessible because it should be computed from datasets, which actually *do not exist*. These data are missing because it is not possible to draw a high electron current without damaging the probe. As a consequence, the values shown in figure 13.4 and 13.5 are limited to the 50 and 70 A cases where those datasets were available.

The current densities for the missing 100, 150 and 200 A cases could be determined using the following argument. At the plasma potential the current can be considered to be entirely carried by electrons as can be seen from the behaviour of the electron density as a function of the plasma potential. Supposing that the temperature at two locations (1) and (2) on the V-I curve is the same, and using the fact that on the linear part of the curve, $j_{\mathrm{e}} \propto e^{-eV/kT}$ (*cf* Chapter 3), the ratio of the electron current at the two locations with probe potentials V_1 and V_2 can be written

$$\frac{j_{\mathrm{e}}(1)}{j_{\mathrm{e}}(2)} \approx e^{-\mathrm{e}(V_2-V_1)/kT} \tag{13.1}$$

The 'correction' of the electron current density would then work as follows

- take the (Abel) inverted current files which show voltage V_2 closest to the plasma potential, V_1 and read the corresponding current density $j_e(2)$

- use equation (13.1) to obtain the 'corrected' electron current density $j_e(1)$.

In formula (13.1) the temperature used is the probe determined temperature of Chapter 11. There are a few problems with this correction:

1. A clear linear ("steep") part of the V-I curve does not exist or is incomplete. However, because the value of the probe voltage used is always more negative than the plasma potential there would be some justification in using this correction (one is still in the region where a linear part would be expected if existing).

2. The voltage difference in (13.1) needs to incorporate a radial dependency, not available in neither of the two voltage components:

- The probe potential V_{prb} in zero bias condition (the 'closest available voltage'); one could use the hypothesis made in Chapter 11 for the determination of the plasma potential, that the corresponding current density belongs to the *same dataset* where the probe is subject to the same external conditions (bias). However, probes at different position may reach the local plasma potential under different bias conditions. This agrees with the general trend of the plasma potential with arc height. In the present method, by choosing the *same* external bias file (the 'closest') any dependency on probe height is in fact negated

- Because the plasma potential is the difference of floating and measured probe potential, despite the availability of a radial dependency for the temperature, included in the floating potential, the measured probe potential is not radial dependent. In Chapter 10 it was concluded that the local Abel inverted probe potential has no physical meaning; because of this, any radial dependency of the voltage is not accessible to probes (*cf* section 10.2).

For these reasons the choice is made to present the electron current density for the two cases where the current data corresponding to plasma potential are directly available. This is done in figure 13.2.

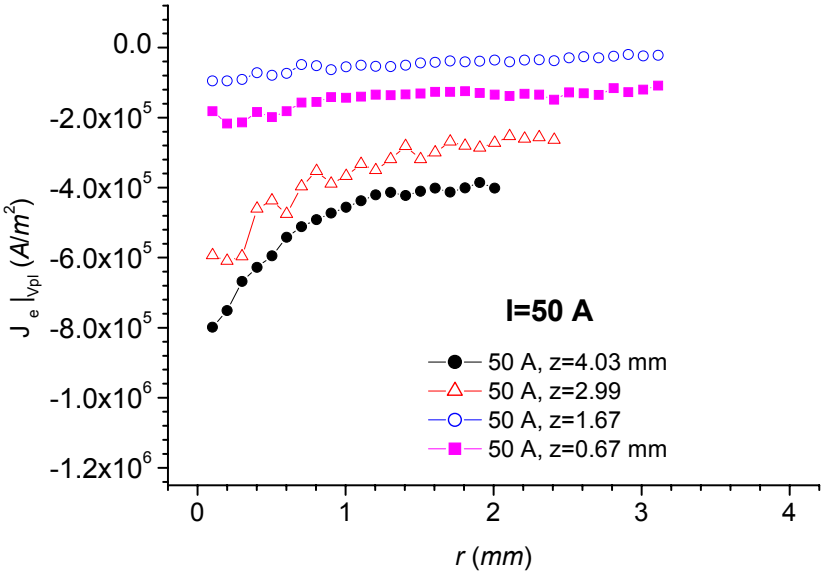

Figure 13.3 a, Comparison between selected electron current densities measured for probes at plasma potential. Arc current 50 A

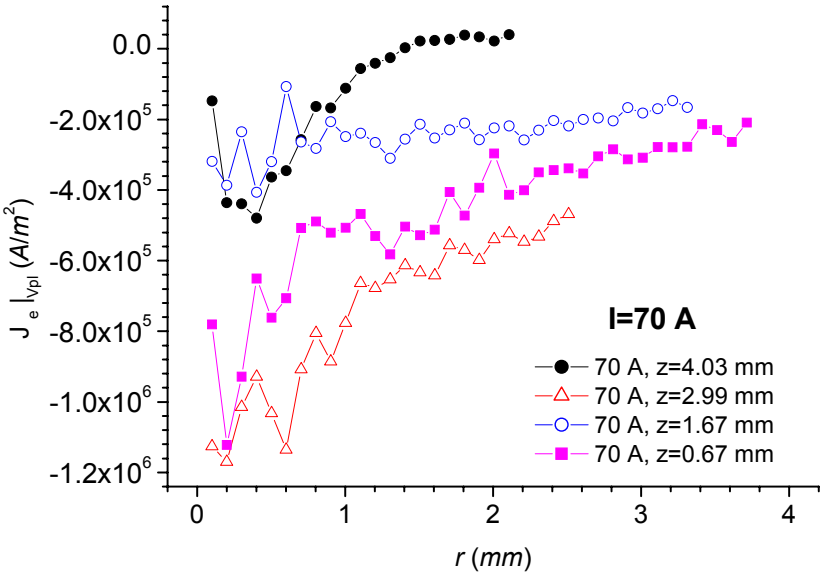

Figure 13.3 b, Comparison between selected electron current densities measured for probes at plasma potential. Arc current 70 A

It can be observed that at 50 A, the current density increases with probe height except at the lower heights where an inversion is found (figure 13.3 left). The 70 A case shows non monotonicity with respect to probe height: a higher probe does not necessarily

mean greater electron current density (*cf* figure 13.3 right). A more thorough analysis with comparison with ion current densities is presented in section 13.6 whereas a method to assess the values obtained so far is presented in the next section.

13.4. Assessment of the current densities

A way to assess the correctness of the current densities is to invoke conservation laws. The integration of the ion and electron current density distributions corresponding to different probes should give total currents in agreement with the actual total arc currents. In addition, it is necessary to evaluate the magnitude of the error in the determination of both the current densities. Whereas the latter, reported in Appendix E, shows relative errors of the order of some percents for both ion and electron current densities, the first method is used in the following. Integration of the densities gives

$$I_{\text{arc}} = \int_S j dS = 2\pi \int_0^{R(z)} rj(r)dr \qquad (13.2)$$

where an integration around the axis has been performed and the upper limit, the radius at the given height, $R(z)$, has to be determined. It can be observed that (13.3) can be employed directly with the original data, determining an apparent total arc current as seen from a probe which 'cools' the plasma; or the corrected values of the particle densities shown in figures 10.23 to 10.25, sensing the 'true' total arc current. Also, it was decided to use the raw data instead of the (often Gaussian) fit because the upper radial limit between fitting function and data may differ considerably. An additional check is that current continuity along the arc implies that two determinations obtained at different heights must deliver the same total arc current.

The procedure is then as follows. Use the $j(r)$ data multiplied by the local radial coordinate and integrate the product from the axial position to the intersection of the curve with the abscissa, if any (otherwise use an estimated current carrying radius, *cf* Chapter 14). It is clear that the degree of uncertainty lies in (*i*) the experimental error on the density distribution and in (*ii*) the width of each individual peak (the radial upper integration limit $R(z)$ in equation (13.3)). The computations were performed for both the current densities and the results are shown in Table 13.1

I_{arc}	*rJ* correction used in formula (13.2)	j_i integral (A)		j_e integral (A)		Matching total arc current (j_i, j_e) *Y, N*
		hi	*lo*	*hi*	*lo*	
50	*none*	3.14	4.7	5.6	4.1	*N, N*
	$n_{\text{prb}}/n_{\text{opt}}$	283	534	1,005	2,000	*N, N*
	norm. recombination	45.1	24	79.9	58.3	*Y, Y*
70	*none*	31.4	22	16.9	15.6	*Y,Y*
	norm. recombination	452	320	16.9	222	*N, (Y,N)*
100	*none*	24.4	27.7	*N.A.*	*N.A.*	*N*

	n_{prb}/n_{opt} *norm. recombination*	572 349	585 394			*N* *N*
200	*none* n_{prb}/n_{opt} *norm. recombination*	21 613 225	32.7 2,000 484	*N.A.*	*N.A.*	*N* *N* *Y*
50 low z=0.67, high *mm, z* =4.03 *mm*; 100 low z = 1.18 *mm*, high z =4.0 *mm*, 200 low z =1.12 *mm*, high z =3,47 *mm*						

Table 13.1 For the comparison of the integrated current densities (*cf* (13.3)) with the total arc current using: no correction ('none', cooled data), n_{prb}/n_{opt} (particle density reduction) and normalized recombination coefficient of section 11.11. Two probes per each case are used, '*hi*' highest probe in arc and '*lo*', lowest probe in arc. Matches assumed 'positive' ('*Y*') when within a factor of 2 to 3 from the true total arc current. *N.A.* = Not Applicable, refers to the missing electron current densities. The 70 *A* case lacks the *n* ratio corrections as no optical data are available for this case

It must be emphasized that the result is extremely sensitive to the radial uncertainty. Moreover, the indicated error on the densities propagates on the total arc current determinations and therefore, additional uncertainties on the latter arise. Despite these severe limitations, from the examination of table 13.1, some qualitative observations are possible.

- The integration of the ion current density gives internally consistent values in that the obtained integrals differ by no more than a factor of the order one.

- The ion current density corrections according to the particle density reduction factor of Chapter 11 are systematically higher than the true total arc current by a factor which varies with the current, but which is often of the order of 10 or more.

- The correction based on the normalized recombination coefficient of Chapter 11 gives results closer to the total arc current but the method uses a constant value close to the maximum of the function (*cf* figure 10.26). However, even if in this determination no account was taken for the temperature reduction (up to 50%, *cf* Chapter 11), the accuracy of this latter reconstruction, of the order of one is not worse than the preceding one.

- Similar remarks apply to the electron current density, as the requirement of the quasi-neutrality in the bulk and the consequent identical reduced recombination coefficient imply the same order of magnitude of the reconstructed currents. It can be observed that the almost identical values obtained for the integrals contrast somewhat with the central value of the difference $j_i - j_e$, always positive, as shown in the next section (*cf* figure 13.3). However, (*i*) the opposite

occurs for the outermost radial values of the electron current density and (*ii*) at 50 *A* the electron current density systematically exceeds the ions' j_i

13.5. Comparison of the current densities

The conclusion of Chapter 11 about the perturbing action of the probe limited to recombination in the probe boundary layer makes it possible to assume that the *ion* current density obtained in the ion saturation condition is representative of the ion current density within the arc. The directly measured values refer to the 'cooled' boundary layer and the reduction factor estimated in Chapter 11 permit the determination of the ion density in the bulk of the undisturbed plasma. Because the latter is assumed to be in thermal equilibrium (LTE) the corresponding electron particle density in the bulk must be the same.

The *electron* current density presented in section 13.3 has been obtained using the plasma potential of Chapter 12. To determine to what extent these values represent the 'true' electron current density within the arc, these could be compared with the electron current density in floating conditions. The latter is not directly available, because in floating conditions the total current density to the probe is zero. In Chapter 11 it was stated that only the electrons are displaced by increasing negative biases and that the ion flux, always the same would be 'unveiled' by making the bias value more and more negative. If this is correct, the ion current density obtained at ion saturation and the electron current density in floating conditions must be equal

$$j_e\big|_{FC} = j_{isat} \tag{13.3}$$

As a consequence:

1. The ion current density at saturation, now playing the role of the electron current density in floating conditions, must be lower than the current density at plasma potential, given that the plasma potential is less negative than the floating potential. The opposite, $j_e\big|_{FC} = j_{isat} > j_e\big|_{V_{pl}}$ would imply a plasma potential negative with respect to the floating potential which is incorrect. In fact, when the probe is more positive than the plasma potential, the electron current density should be higher than that of the ions.

2. The ion and electron current densities shown were determined from the cooled temperature of Chapter 11, in which the cause of cooling has been found to be recombination. The reduction factor applicable to the two *current densities* should be the same for the *number densities* on this basis of LTE (and consequent quasi-neutrality). In any case, it will increase the absolute values of both by a factor ~12 to ~160 depending on the arc radial location (*cf* section 11.11)

These points are addressed in the following.
1. A comparison between ion and electron current densities is presented in figure 13.4 a-d for I_{arc}= 50 *A* and in figure 13.5 a-d for the I_{arc}=70 *A*.

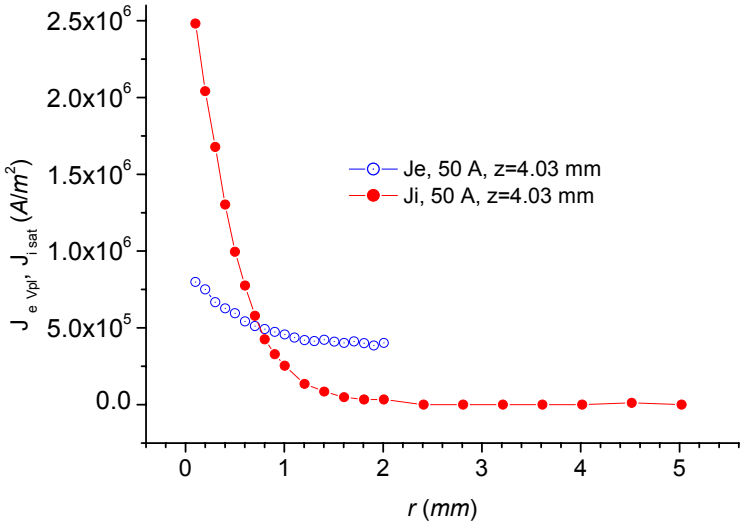

Figure 13.4 a, Arc current 50 A. Comparison between selected ion (full circles) and electron (empty circles) current densities for the same probes of figure 13.3. To facilitate comparison, the vertical scales of the last two values differ by a factor 5 with respect to the first two values. z=4.03 mm from anode

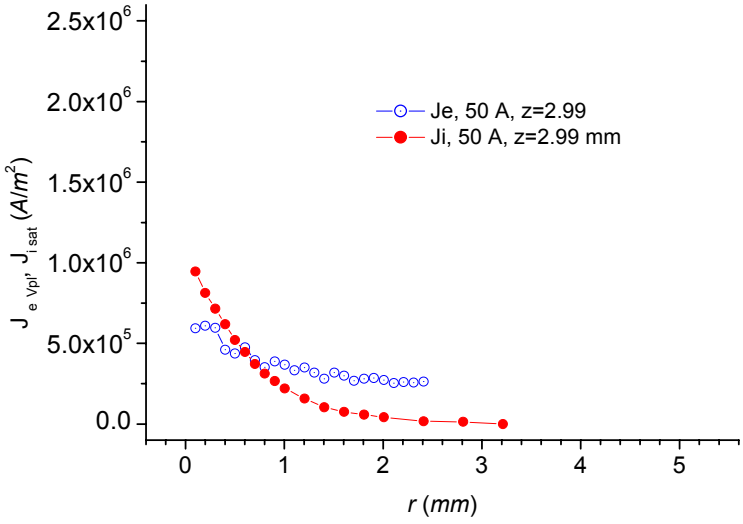

Figure 13.4 b, Arc current 50 A, same as before, z=2.99 mm from anode

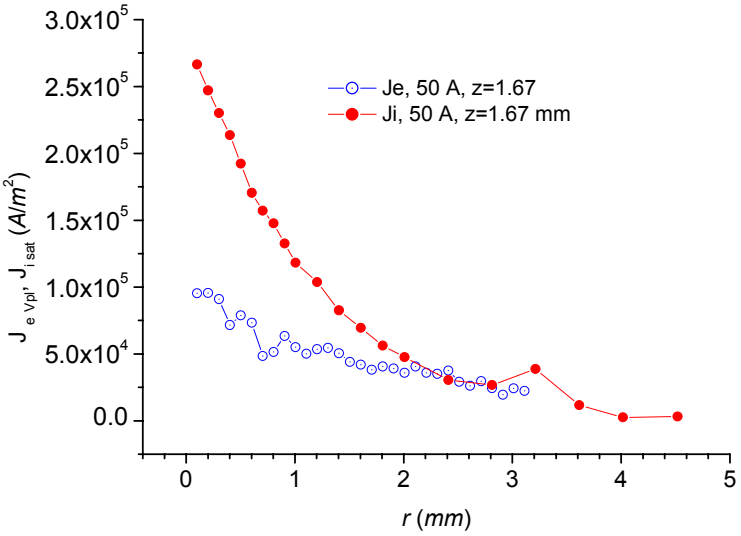

Figure 13.4 c, Arc current 50 A, same as before, z=1.67 mm from anode

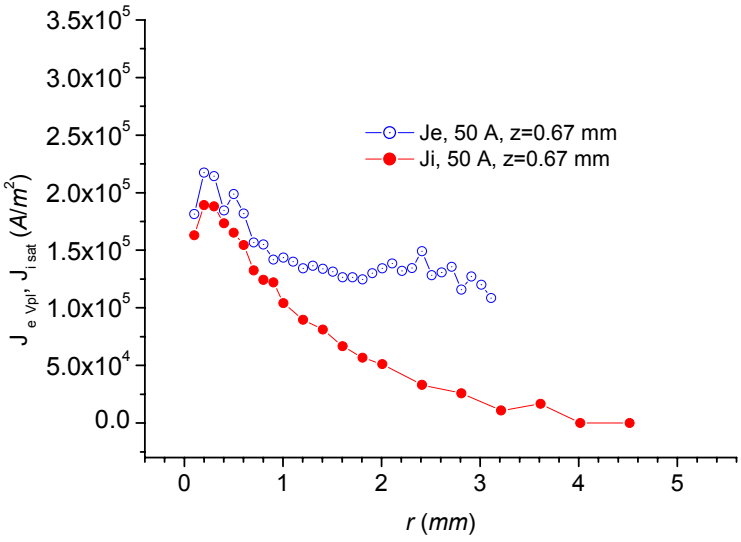

Figure 13.4 d, Arc current 50 A, same as before, z=0.67 mm from anode

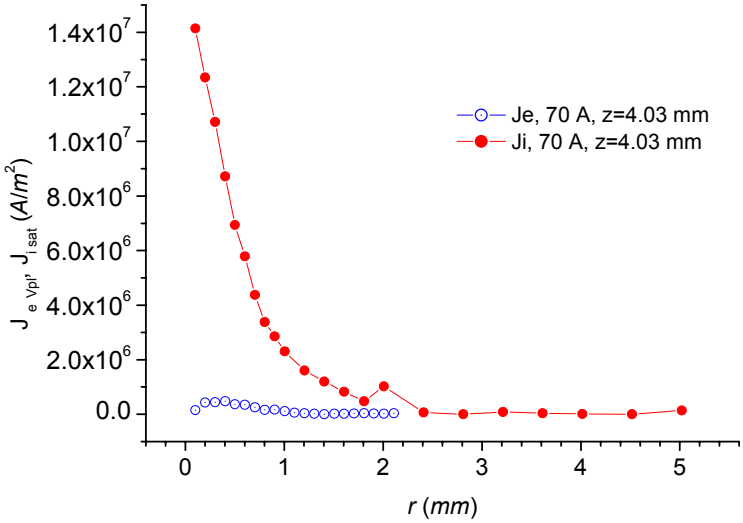

Figure 13.5 a, Arc current 70 A. Comparison between selected ion (full circles) and electron (empty circles) current densities for the same probes of figure 13.3. To facilitate comparison, the vertical scales of the last two values differ by a factor 4 with respect to the first two values. z=4.03 mm from anode

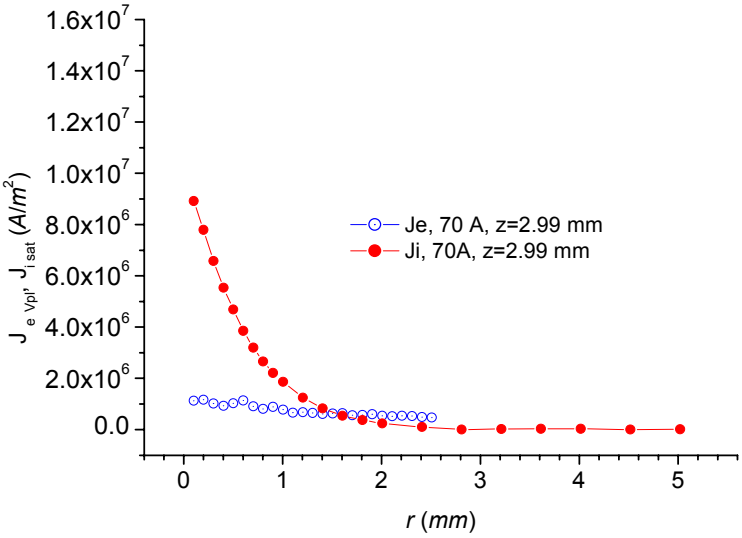

Figure 13.5 b, Arc current 70 A, same as before, z=2.99 mm from anode

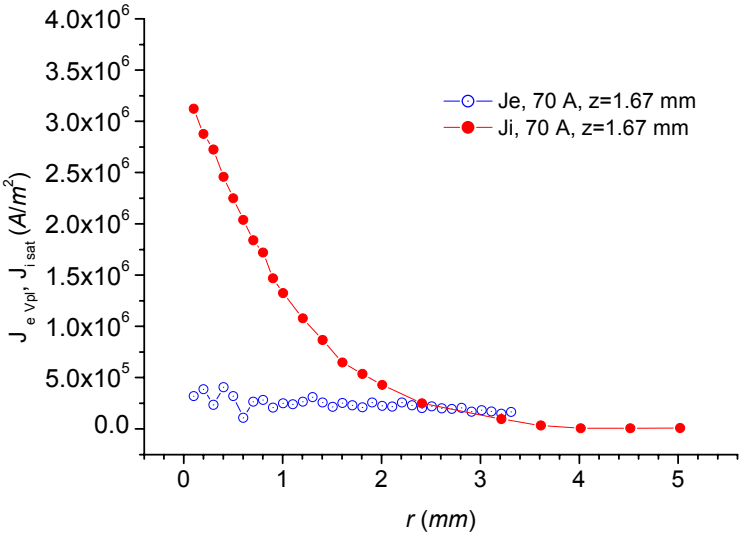

Figure 13.5 c, Arc current 70 A, same as before, z=1.67 mm from anode

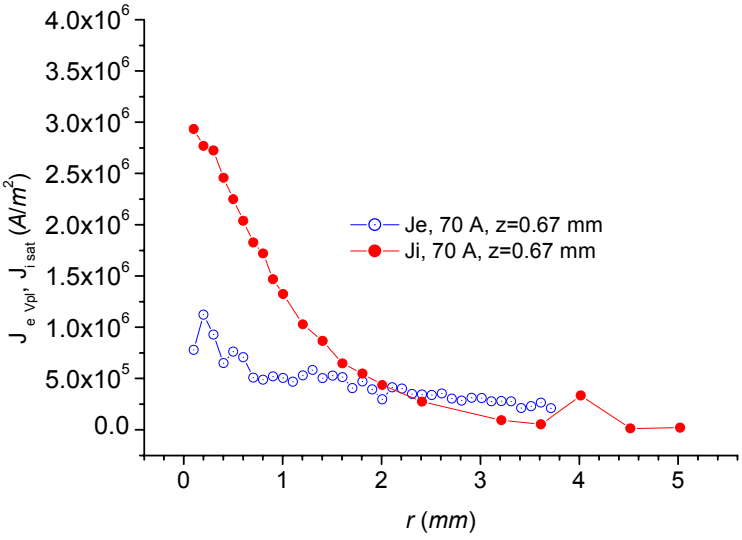

Figure 13.5 d, Arc current 70 A, same as before, z=0.67 mm from anode

From the examination of figure 13.4 and 13.5 the following observations are possible:

- The central values of the electron current densities are lower than the ions

- For both the 50 A and 70 A cases, a decrease in the probe height is accompanied by a decrease in the difference $j_i - j_e$, e.g. the two tend to equalize at lower arc heights.

The first observation suggests several possible causes

a. *The ion current density is too high*. It is difficult to assess this because (*i*) it has been shown that the number of collected ions is non-perturbing *with respect to the LTE number density*. An independent correction to include this effect is not possible, because this involves the number density computed at LTE; (*ii*) the integrated values of table 13.1 show that when the comparison is made with this kind of correction, it is the *electron* current density that leads to far too high total arc currents (*cf* the 50 *A* case).

b. *The electron current density is too low because it does not correspond to plasma potential, e.g. the latter is incorrect.* However, the *axial* determinations shown in Chapter 11 are consistent with what is available in the literature. It may well be that the *locality* of the plasma potential is put into question: (*i*) while the central region of the probe is at the plasma potential, other regions may be not and (*ii*) while a probe is at plasma potential in one dataset (e.g. for given bias conditions) other probes might be not. Both are contrary to results obtained on sub sets of the entire data base, which suggested these working hypotheses were correct.

c. *The hypothesis of constancy of the ion current density upon different probe bias is incorrect.* However, this assumption, which is at the base of the interpretation of the V-I curve seems qualitatively well founded because of the high ion to electron mobility ratio (e.g. mass ratio).

d. *Cooling affects the two species differently*. This can only occur if the cooling mechanism is different than recombination, contrary to the conclusions reached in Chapter 11 (section 11.10.1).

A possibility is to dismiss this determination of the electron current densities altogether on the basis that because the j_{isat} 'is' representative, the equality with the electrons' at plasma potential 'must' hold. However, the second observation made above about the current density difference also indicates that, irrespective of which of the preceding causes (*a* to *d*) occurs, this ceases to be effective at 'low' z and beyond a 'critical' radius $r_{cr.}$ In other words, it would suggest the existence of a region where the electron current density is greater or equal than that of the ions, $j_e \geq j_i$ (*cf* figure 13.4 and 13.5).

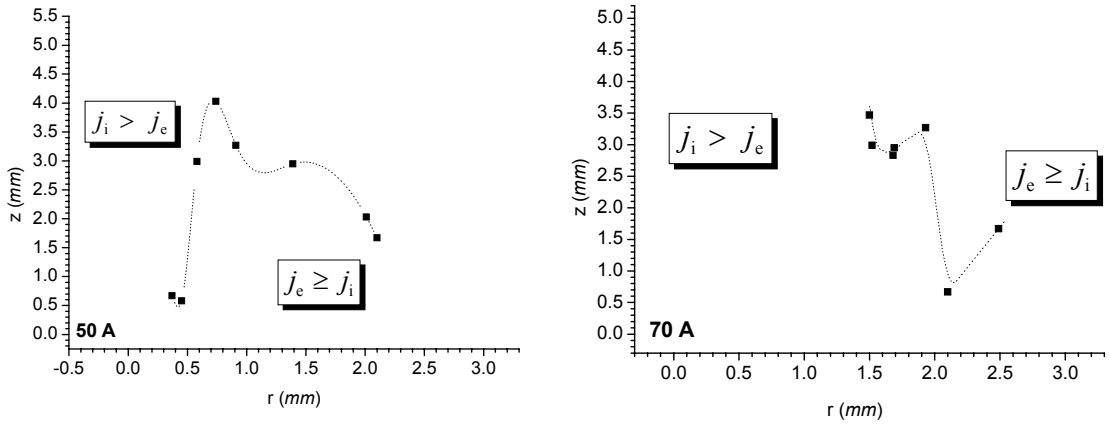

Figure 13.6 Qualitative representation of the arc region where current density consistency can be ascertained from data and a central region where further analysis is required. Left, arc current 50 *A*, right 70 *A*

Despite the very qualitative nature of this evaluation, the situation could be represented by figure 13.6 where the *loci* (*r,z*) of the coordinates where $j_{isat}=j_{e\,|Vpl}$ have been drawn. In each case, these curves separate the (*r,z*) plane into a region where the experimental data allows the conclusion that the *j's could be consistent*, by fulfillment of the requirement $j_e \geq j_i$, to the right of the curve, and an inner region where further analysis is required because of the opposite inequality.

13.6. Electrical Conductivity

1. The electrical conductivity can be determined from the knowledge of the temperature if a conductivity-temperature relationship is available (*cf* Chapter 1). The conductivity can be also be used to infer the electric current density from Ohm's law once the electric field is known, or, conversely, it can be determined from the field once the current density is known. However, there are methods to determine the conductivity directly and this would permit an independent determination of the temperature.

2. The radially averaged electrical conductivity can be determined from the formula

$$\sigma = \frac{I_p}{V_p}\frac{\ln(l_p / r_p)}{4\pi R_{arc}} \qquad (13.4)$$

reported in Chapter 4 and presented by Benilov [33]. The probe length l_p in (13.4) is computed at the instant of time *t* when the corresponding (*I, V*) couple was recorded, therefore it varies with *x*, the spatial coordinate of the given instant on the time axis. The corresponding local value can be obtained using the elementary step '*a*' in place of l_p.

3. The continuity model (formulae (4.4) and (4.5) in Chapter 4) gives

$$\frac{dI}{dV_\mathrm{p}} = \frac{3L\,\pi\,\sigma}{\ln\dfrac{\pi L}{4r_\mathrm{p}}\ln\dfrac{r_\mathrm{p}}{\lambda_\mathrm{D}}},\ \sigma = n_\infty e^2\left(\frac{ZD_\mathrm{i}}{kT_\mathrm{i}}+\frac{D_\mathrm{e}}{kT_\mathrm{e}}\right)$$

4. Use can also be made of the relationship

$$\sigma = \frac{\Delta I_\mathrm{p}}{\Delta V_\mathrm{p}} l_\mathrm{p}(x)/S,\ \ \Delta I_\mathrm{p} = \left|I_\mathrm{sat} - I_\mathrm{Vpl}\right|,\quad \Delta V_\mathrm{p} = \left|V_\mathrm{sat} - V_\mathrm{pl}\right|,\quad S = 2\pi r_\mathrm{p} l_\mathrm{p} \qquad (13.5)$$

where the current and voltage variations are taken between points located at the 'beginning' of the ion saturation V_sat, I_sat and the location of the plasma potential V_pl, I_pl, if known,. Also (13.4) is made local by using the elementary step '*a*' in place of the probe length l_p.

5. A different attempt has been made, by using the information gained in unbiased conditions in order to compute

$$\sigma = \frac{\Delta I_\mathrm{p}}{\Delta V_\mathrm{p}} l_\mathrm{p}(x)/S,\ \ \Delta I_\mathrm{p} = \left|I_\mathrm{p,R1} - I_\mathrm{p,R2}\right|,\quad \Delta V_\mathrm{p} = \left|V_\mathrm{p,R1} - V_\mathrm{p,R2}\right|,\quad S = 2\pi r_\mathrm{p} l_\mathrm{p} \qquad (13.6)$$

The method involves comparing two datasets obtained in unbiased (but not floating) conditions upon variation of the read-out resistors, R_1 and R_2 (*cf.* Chapter 7). In (13.5) $l_\mathrm{p}(x)$ is the probe active length at the position x with respect to the centre of the peak, and S the corresponding probe surface. The present method, should it provide reliable values has the advantage that it does not depend on assumptions about the shape of the V-I curve, like a rectilinear steep part, which implies Maxwellian distribution of electrons, nor the existence of the latter.

The choice of the resistors from the biased configuration with no bias applied, $R_1 = 4\ \Omega$, to the smallest among the unbiased configuration, R_2=149.5 Ω. The choice to operate in *unbiased* conditions is due to the need to perturb the plasma the least possible. However, the difference of these two resistors is too big, implying that the current drawn through the higher of the two resistors is 1% of the current drawn when the other resistor is applied, thus making the current variation substantially equal to the current pertaining to the smaller resistor. Operating in *floating* conditions would only worsen the situation as the chosen high floating resistor (67.72 kΩ), makes this mismatch even greater.

Also the choice of the biased configuration file is not straightforward. The dataset corresponding to zero bias brings us back to the steep part of the V-I curve, which is the one whose information is destroyed by collisions, so by the same argument used to

dismiss the other relationships discussed above, this determination should be discarded. By the same token, the least negative among the datasets, e.g. the one corresponding to a (nominal) positive bias, is also on the steep portion of the curve; in addition 1) it cannot be considered the least perturbative and 2) it provides higher values than the preceding choice but this is due to the higher current drawn, which, in turn, is very different than (and in fact dominates) the current collected in floating conditions.
The local values of the conductivity obtained ~10^{-2} $(\Omega m)^{-1}$, are too low to even access the temperature-conductivity tables. As anticipated above, this is due to the very small current difference between the two chosen datasets.

From each of these methods, because a conductivity-temperature relationship is available (Murphy's $\sigma = \sigma(T)$ curves [34], see figure 1.12 Chapter 1), the electron temperature can be determined. However, these formulae hold in the 'linear' part of the *V-I* curve, and looking at the results of Chapter 10 it is not obvious where the borders of this region should be placed. Some attempts were made to use the first three methods despite the limited applicability due to lower degree of ionization. These methods showed that the temperature determined by inversion of the $\sigma(T)$ given by Murphy, is of the order of 7,000 *K* in cases 1, 2 and 3. The values obtainable using the Frost's mixing rule conductivity for the intermediate ionization (*cf* section 2.8) were often below the lower limit for the $\sigma(T)$ relationship, see figure 13.7 left. Spitzer's full ionization formula gave higher temperatures, but still 'low' also considering the cooling discussed in Chapter 11) which points towards 9,000 to 11,000 *K* in comparable positions (*cf* section 11.2). The three electron temperatures obtained by use of the three $\sigma(T)$ relationships of section 2.8 are shown together in figure 13.7 for the 50 and 70 *A* cases.

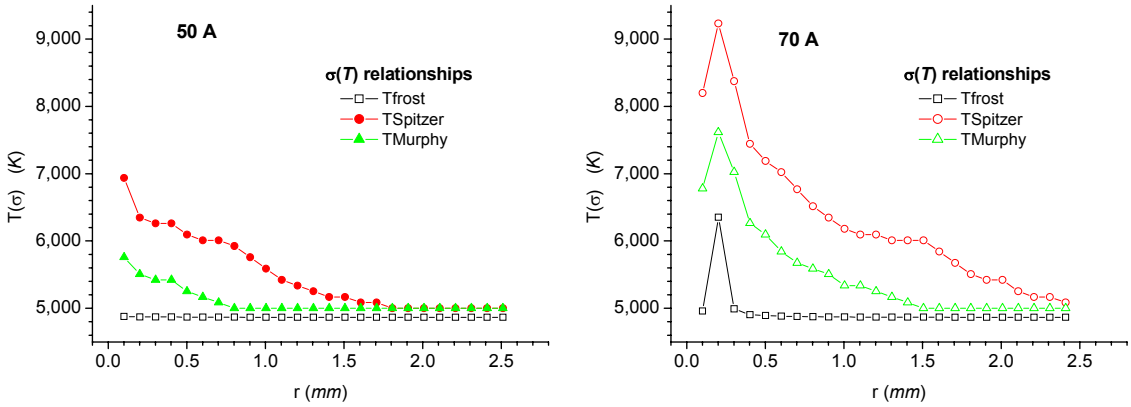

Figure 13.7 Temperatures from the directly measured electrical conductivity. Curves obtained using the relationships presented in Chapter 1. Left, 50 A, right, 70 A

These results show that direct determinations of the electrical conductivity which are consistent with the temperatures obtained din Chapter 11 cannot be obtained.
Conversely, using the temperatures obtained in Chapter 11 and the $\sigma(T)$ relationship (after Murphy [34]) the conductivity values obtained are higher. This result is only representative of the specific relationship shown in Chapter 2, therefore no examples are shown (*cf* figure 2.8).

13.7. Electric field

13.7.1 Axial electric field

1. The voltage as read by the probe in floating conditions is made of the contribution of the 'true' floating potential and of the local plasma potential. The central value of each peak can be plotted as a function of probe height to give the general behaviour of the potential in the plasma. The *assumption* of constant variations of the floating potential along the arc axis could make it possible to map the central electric field as a function of the height in the arc (measured from the anode). More precisely, it is often assumed that the variation of the measured probe potential as a function of height at *adjacent* points is entirely due to variations in the plasma potential [12]. Therefore, floating potential variations between adjacent points are considered to be negligible. In Chapter 12, it has been shown that this is not the case. Due to the dependency of the floating potential upon temperature, this also implies that the temperature differences between adjacent points must be small. 'Small', means less or comparable to the error on the read potential (~ 2%) and this is the allowed variability of the temperature along the arc height for the assumption to be founded. This implies that the choice of the distance (step size) between adjacent points is crucial in the procedure. Since the distance between neighbouring probes can be as much as 1 *mm*, with corresponding temperature variations of 1,000 *K* or more, the step has to be much smaller. It has been chosen here as the spatial resolution obtainable from the time resolution at the operating speed (0.02 *ms* at 5.02 *m/s* for this run, thus 100.4 μm).
The values of the electric field obtained by this method are shown in figure 13.8 left. Before differentiation, the probe potential was fitted to a second degree polynomial.

2. An alternative determination based on the axial derivative of the plasma potential (obtained from the floating potential as described in Chapter 12), is shown in figure 13.8 right. Because the absolute value of the potential is not relevant in the derivative and because the corrected version of figure 12.11 exists only for the case where an optical temperature is available, the uncorrected value is used for the derivative. This also means that both the electric field determinations refer to the cooled boundary layer region around the probes.

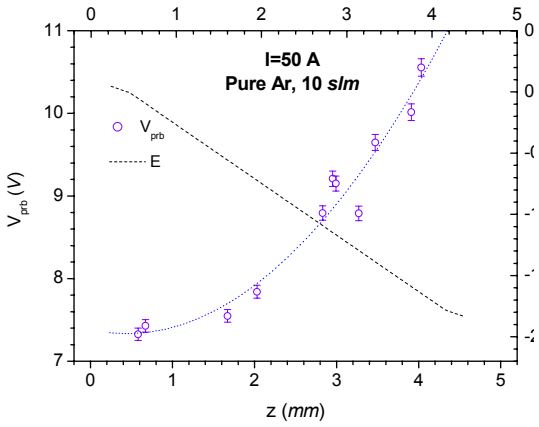
I=50 A
Pure Ar, 10 slm
V_prb
E
V_prb (V)
z (mm)

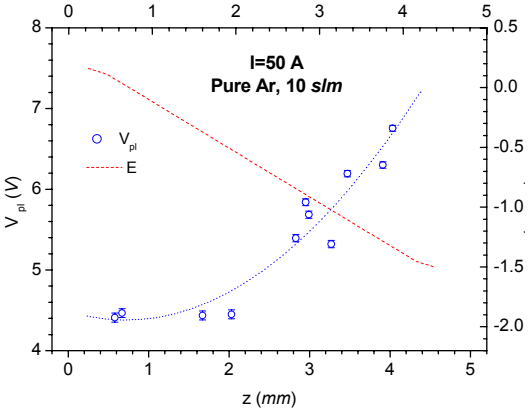
I=50 A
Pure Ar, 10 slm
V_pl
E
V_pl (V)
z (mm)

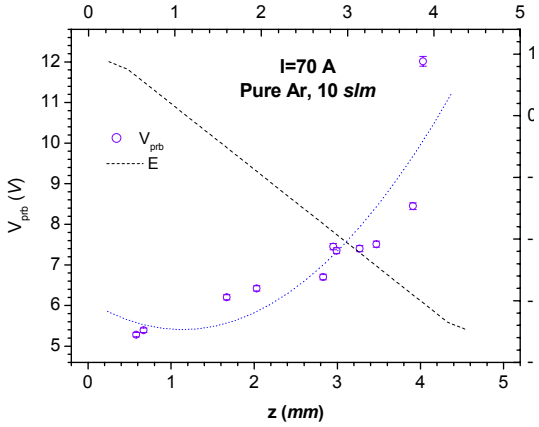
I=70 A
Pure Ar, 10 slm
V_prb
E
V_prb (V)
z (mm)

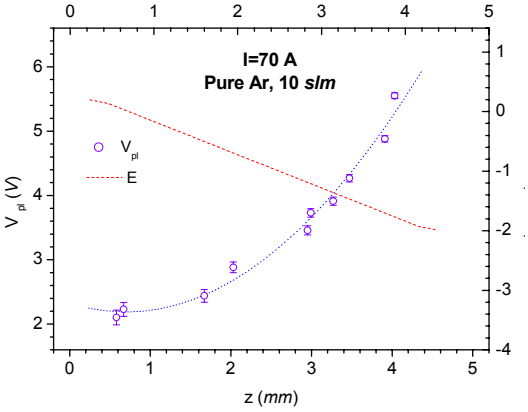
I=70 A
Pure Ar, 10 slm
V_pl
E
V_pl (V)
z (mm)

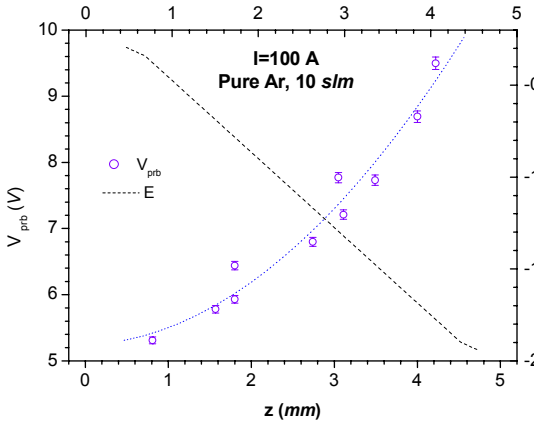
I=100 A
Pure Ar, 10 slm
V_prb
E
V_prb (V)
z (mm)

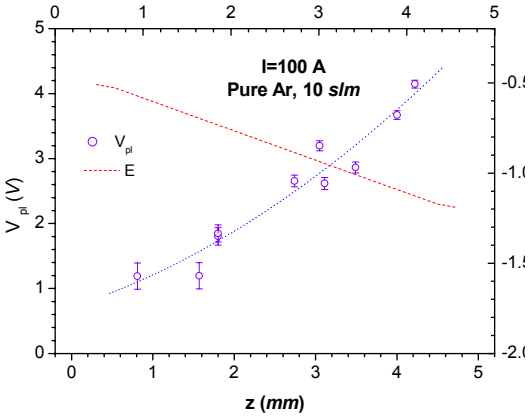
I=100 A
Pure Ar, 10 slm
V_pl
E
V_pl (V)
z (mm)

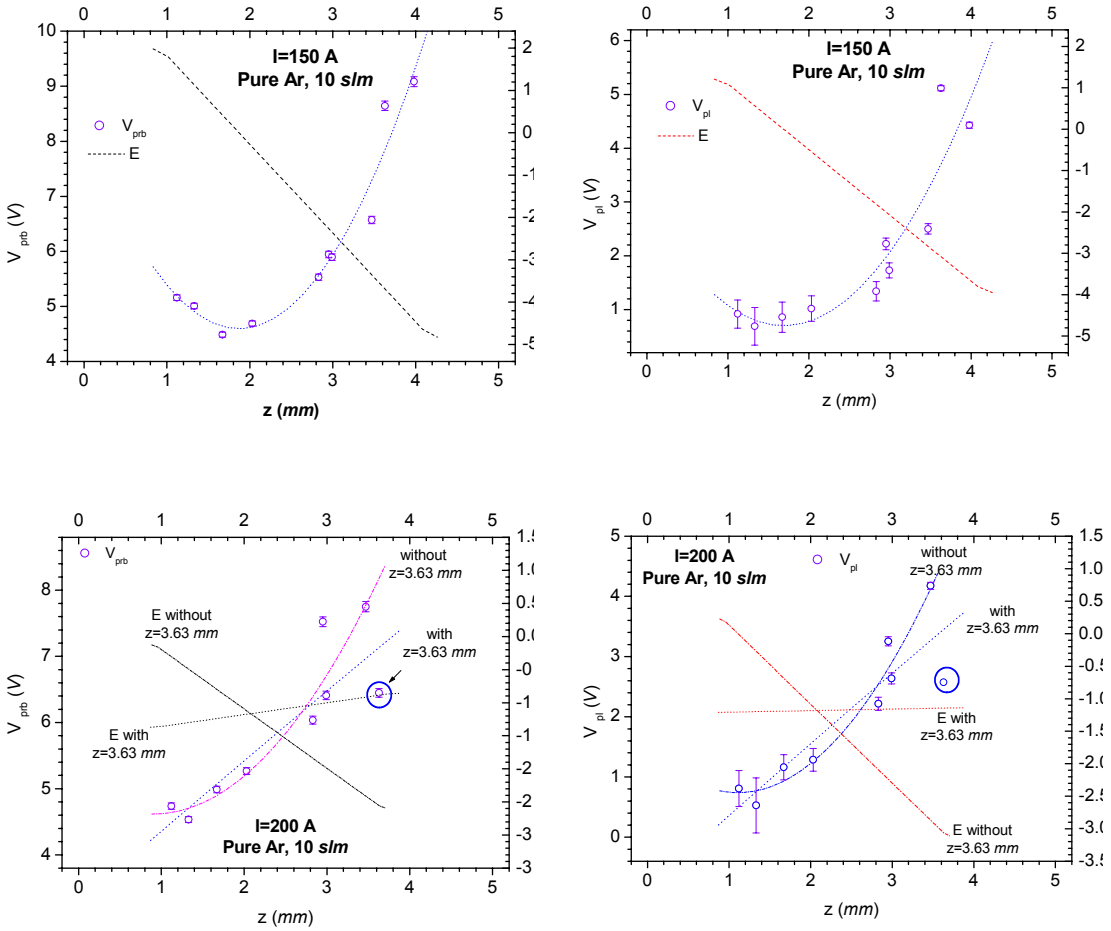

Figure 13.8 Axial probe potential (empty circles with error bar, left axes) and electric field (dot-dashed curve, right axes) for arc currents I=50, 70, 100, 150 and 200 *A*. Left column plots represent electric field based on the derivative of the probe *measured* potential. Plots on the right contain fields determined from the derivative of the *plasma* potential. The potentials are plotted positively for commodity, whereas the fields are represented with the correct sign. I=200 A shows different fields (see text).

From the examination of figure 13.8, the following observations can be made:

1. The electric field determined from the directly measured probe potential (left plot column, dashed curves on right axis) is always steeper than the one determined from the derivative of the plasma potential (plot column on the right, dashed curves on right axis). Correspondingly, the absolute value of the field is always higher for the probe voltage determinations. The exception is the higher arc current case, I=200 *A*.

2. The uncertainty on the electric fields obtained from the plasma potential (~6%, *cf* Appendix E) are higher than the ones obtained from the directly measured voltage, because they suffer from the inaccuracy on the temperature

3. The sign of the field for the three lowest currents, 50, 70 and 100 *A* is negative and increasing in absolute value from anode to cathode in the region accessible to probes. In these cases, the field corresponding to the probe closest to the anode is practically zero. At 150 *A* it changes sign at about mid-arc and at 200 *A* it is close to zero again

In the I=200 *A* case (*cf* in figure 13.8) high uncertainty on the filed exist because of the inclusion or exclusion of the point located at z=3.63 *mm*, a circumstance which changes the voltage structure and the corresponding electric field dramatically as seen by the two curves for the potential and the field ('with/without z=3.63 *mm*').

An assessment of the validity of the presented results has been performed

a. by extrapolating the electric field distribution along the total arc length; its integration gives a total arc voltage which can be compared with the one known by measurement. Because the electrode sheath voltages are not taken into account, this value is a lower limit. The comparison is shown in Table 13.2 for the voltages of figure 13.8

b. If the arc current density were known, use of Ohm's law $E = j/\sigma$ could be made. However, the high uncertainty on the current densities makes this evaluation very problematic.

The primary purpose of the comparison between the two presented methods is to establish whether the use of the directly measured probe voltage to determine the axial field is justified for those cases where a direct determination of the plasma potential cannot be obtained. This hypothesis is sometimes made on the basis that the floating potential is independent of arc height [12]. It is worth recalling that the plasma potential was obtained in Chapter 12 using the probe determined temperature of Chapter 11 and the corresponding floating potential.
It is apparent that in both methods the determinations provide electric fields which depend on the axial coordinate. This means that, as anticipated at the beginning of the section, *the assumption of negligibly variable floating potential with arc height is not justified at any of the arc currents*. The electric field can be computed only once the plasma potential is known.

Moreover, a comparison of the integrated extrapolated electric field obtained according to point *a* above, reported in table 13.2, shows that the two methods give a voltage within the correct order of magnitude which are always lower than the total arc voltage at every current. The exception is the *I*=150 *A* case which approaches more closely the value of the *total* arc voltage. However, considering the extrapolation performed without accounting for the electrodes sheaths the 150 A case appears too high: only 3.8 or 2.1 V would be ascribed to the column voltage in this case.

Arc current (*A*)	***E* from probe potential** $\left\|V\right\| = \int_{z=0}^{z=5} Edz$ **(*V*)**	**Measured total arc voltage (*V*)**	***E* from plasma potential** $\left\|V\right\| = \int_{z=0}^{z=5} Edz$ **(*V*)**
50	4.92	15.0	3.89
70	8.74	14.6	5.16
100	5.57	14.3	4.24
150	12.95	14.0	10.23
200	3.35	15.2	5.86

Table 13.2 comparison between the measured total arc voltage and the potential obtained integrating the fields obtained from probe voltage or plasma potential shown in figure 13.8

These result show that, within the limited accuracy, the majority of the voltage fall pertains to the electrode zones. Unfortunately, there is no way to attribute a fraction of this fall to either of the two electrode zones.

14. ARC STRUCTURE

14.1. Introduction

The structure of the arc as seen from electrostatic probes is both electrical and thermal. The major electrical characteristics were determined and shown in the preceding chapters, namely, the potential, the electric field, the electrical conductivity, and the current densities. Unfortunately, no local structure for the plasma potential or the electric field could be obtained and one has to be content with their axial structure (shown in Chapter 12 and 13 respectively).

Electrostatic probes can measure and define arc boundaries. When the probe is swept across the arc, the width of the peak indicates whether the probes are within or out of the arc. The cylindrical symmetry hypothesis allows the definition of an 'electrical radius'. Operation of probes in floating conditions shows electrical radii of the order of 20-25 *mm* or more for the highest currents. In contrast, when the probes are biased, the width of the peak shrinks considerably.
In section 14.2 the electrical boundaries are identified, whereas hints of a possible current structure are shown with the aid of the ion current densities presented in Chapter 13.

The thermal structure, defined by the temperature maps, is presented in section 14.3. Radial maps from optical spectroscopy measurements (*cf* figure 11.5) are limited by the requirement of a Partial Local Thermodynamical Equilibrium (PLTE) in order for the optical method to work. This sets a lower limit of the arc thermal edge at about 10,000 *K*. Probe determined temperatures can be constructed within the limitations of (*i*) the accuracy of the electrical current measurements and of (*ii*) the limited spatial region accessible to probes, which does not include the electrode region. This is discussed in section 14.4.
Some remarks about the electrical structure of the arc close to the electrodes are made in section 14.5 based on the axial values of the potentials shown in Chapter 12. In particular it is shown that the anode fall, sometimes ‘determined’ by means of extrapolated probe voltages cannot be computed correctly from probe measurements performed in the column.

In all cases, what is presented here as ‘arc structure’ refers to the cooled boundary layer around the probes.
Methods to correct for both the temperatures and the potentials have been shown in Chapter 11 and 12 respectively.

14.2. Electrical radius and current carrying region

The notion of a core 'current carrying region' is not new and was employed in the frame of the so-called 'Channel Model' [12]. A few experimental indications about its existence were given by Allum [35].
The peak structure obtained with probes operating in biased conditions leads to the definition of a 'current carrying region', fully contained and generally a fraction (up to 30%) of the arc width obtained in floating conditions. A visual inspection of a typical copper anode disk after arcing shows a series of concentric rings corresponding to the thermal transfer at the different currents. Their edges, although not sharply marked, are of the order of the current carrying region.

In [35] a single peak obtained in floating conditions was shown for conditions very similar to those used in this study (and $I = 100\ A$); it was stated that when biasing the probes the floating double peak reduced to a signal as wide as the central part of the floating peak. It was suggested that the latter peak width could be identified with a current carrying region. However, despite the broad agreement with the present case (5 *mm* total width at 100 *A* mid-arc in [35]) the biased peak was not shown, nor was it indicated to what bias it corresponded or whether this width could vary upon bias changes. In the following it is shown that:

- peaks are quite wide in floating conditions
- peak widths change in biased condition, decreasing by increasing (in modulus) the bias voltage until *ion saturation* is reached
- once saturation is reached the width does not appreciably change although a certain degree of scatter exists in the observed data

Figure 14.1 left reports *all the peaks* belonging to a *single applied bias* (-21.1 *V*). The peak width varies with probe height. The right part of figure 14.1 shows the biased peaks of the *same* probe (e.g. same height in the arc) subject to *different bias* voltages; the peak widths vary because of the applied bias voltage.

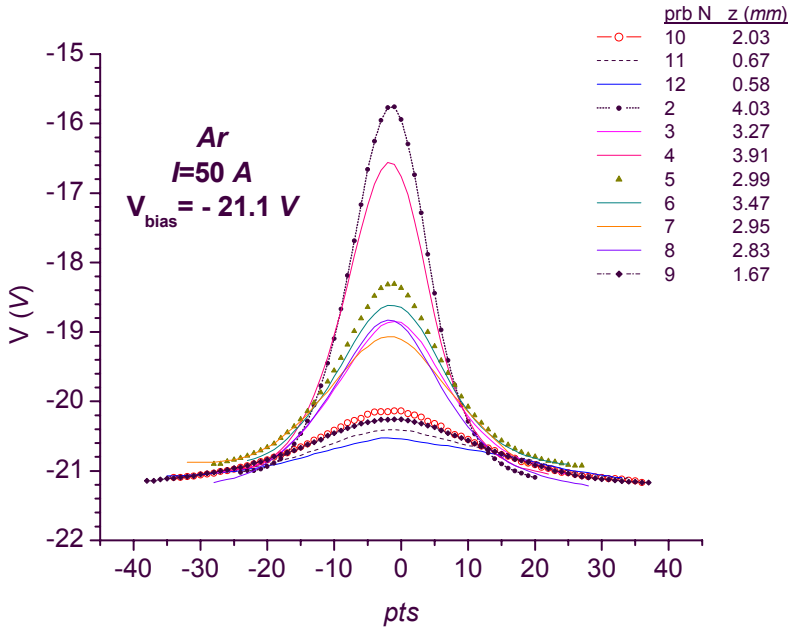

Figure 14.1 a Peak widths. Voltage peaks for all probes under specific bias voltage

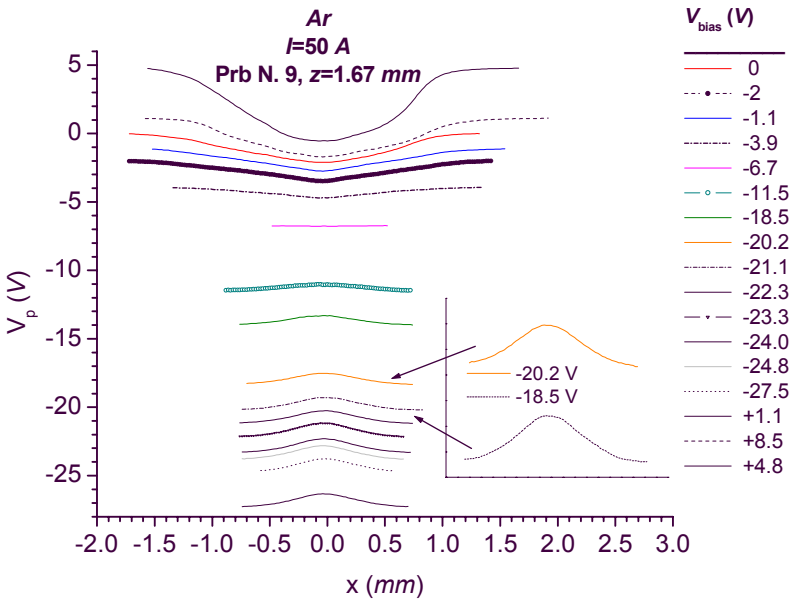

Figure 14.1 b, Peak widths. Peaks belonging to a single probe for different bias. Inset: two specific biases.

The width variation under different bias conditions make it possible to define a ‘radius’ describing the current carrying region under specific conditions. As an example, the

variation of the inverted peak width for a probe at about mid arc at 50 *A* is shown in figure 14.2.

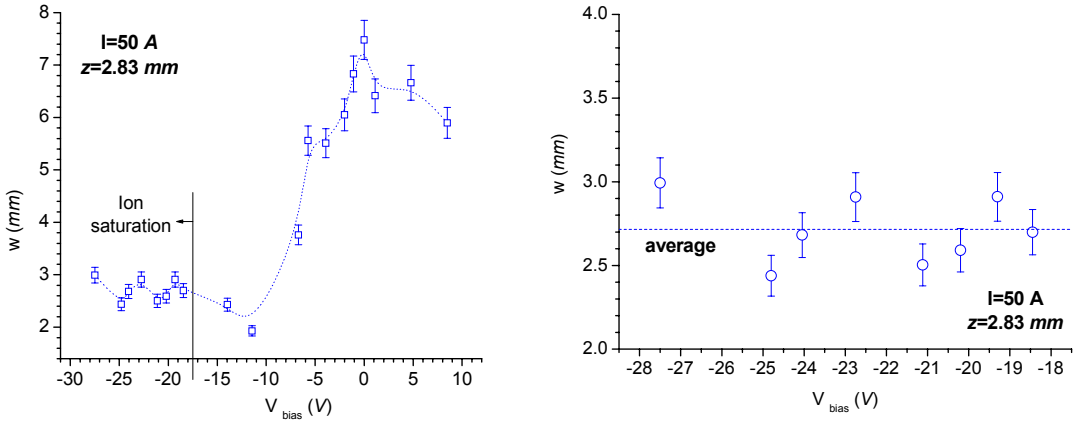

Figure 14.2 I=50 A, Probe height z=2.83 *mm*. Left, comparison between current peak widths for different biases. Right, particular of peak widths at ion saturation

On the right, a particular of this variation is visible in the region where this probe V-I saturates, showing a certain degree of scatter. Because in Chapter 13 it has been concluded that the ion current taken in saturation condition is representative of the true arc conduction current, it is proposed here to identify the ion saturation (inverted) peak width with the radius of the current carrying region.

In floating condition, charge is detectable at radii up to 25 *mm*, whereas in biased conditions this reduces to about 6 *mm* at maximum depending on the arc current. This is shown in figure 14.2 where the locations of the zero-current (peak edges) are shown on a (*z,r*) map for arc currents varying from 50 to 200 *A*. The values, which correspond to ion saturation (inner curve, empty squares) and floating conditions (outer curve, full squares), are the extremes among the possible radii: as shown in figure 14.1, every different probe bias results in a measured radius between these two extremes (even for nominal positive nominal biases, where the radii are smaller than the floating radius) .

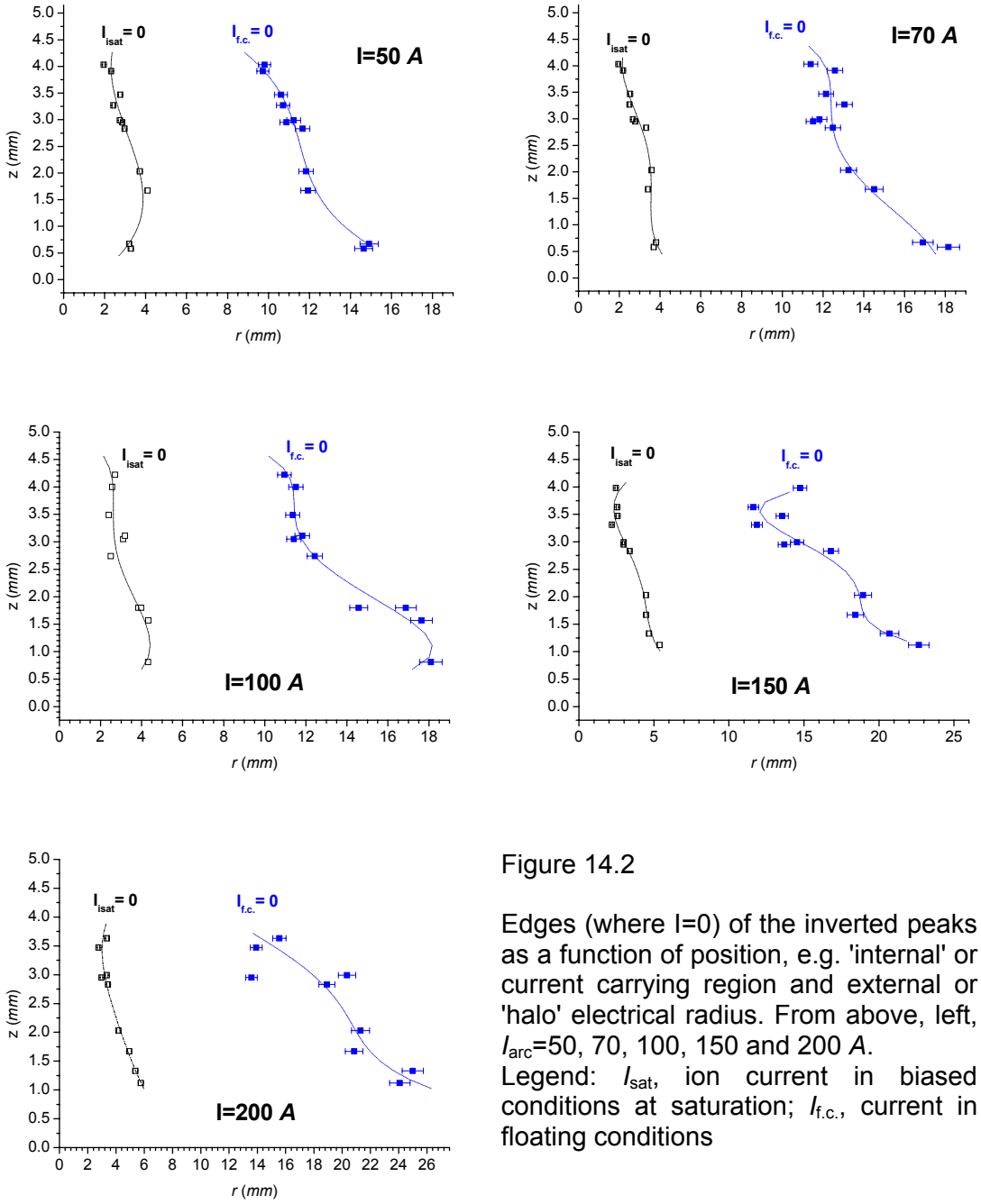

Figure 14.2

Edges (where I=0) of the inverted peaks as a function of position, e.g. 'internal' or current carrying region and external or 'halo' electrical radius. From above, left, I_{arc}=50, 70, 100, 150 and 200 *A*.
Legend: I_{sat}, ion current in biased conditions at saturation; $I_{f.c.}$, current in floating conditions

From figure 14.2 it can be observed that the 'halo', defined by the outer electrical radius (floating conditions) and the current carrying radius, defined by the ion saturation current density, both increase with total arc current. The choice of these two extremes is not without uncertainty. Having chosen the temperature, the number of collected ions (measured current) has been compared with the number of ions present at the same location and temperature based on the hypothesis of LTE. This latter comparison has been made in Chapter 11 where it was shown that the collected absolute number of

particles (within the probe elemental volume) is up to two orders of magnitude lower than the number of particles contained within the same volume in LTE conditions. Bearing in mind the degree of uncertainty in both the directly measured and in the temperature-computed number of particles, still it appears that the hypothesis of a substantially undisturbed 'charge draw' takes place. Therefore, the idea of a probe collecting broadly the ‘right’ number of charges locally available seems not unrealistic. As suggested in Chapter 13 this implies that the ion current density at ion saturation *is representative* of the plasma ion current density and as a consequence, the inner electrical radius could truly represent the extent of the current carrying region.

The shape of the radial distribution seems to qualitatively confirm this indication. By collecting all the (*j, r*) maps discussed in Chapter 13, the ion current density can be represented by the two-dimensional plots shown in figure 14.3 for arc currents from 50 to 200 *A*. These figures show that by increasing the arc current from 50 to 100 *A*, an increase in the inner (most luminous) region occurs towards the anode. From 150 *A* onwards, the current carrying region seems to expand toward the anode and distribute more uniformly along the arc length.
This is qualitatively in agreement with visual observation of a luminous core extending from the cathode down to perhaps mid-arc at the lowest current, 50 *A*, all enveloped in a less luminous halo, and of the wider and almost entirely Gaussian shaped core at 200 A, now enveloped along the whole cathode to anode distance in a Gaussian less luminous halo (although the region closer to the anode shows constriction in contrast with a purely Gaussian profile).

An examination of the *electron* current density is necessary to complete the notion of current carrying region. The electron current density, if correct, corresponds to the least disturbed probe in plasma configuration because the sheath is absent and the probe collects a purely random electron current. However, as indicated in Chapter 13, a thorough comparison between ion and electron current densities cannot be performed as long as the accuracies of the measured current densities are of the order of 100% or worse.
What is more, as indicated in Chapter 12, in all case except at *I* =50 and 70 *A*, the plasma potential was not attained by the probes. As a consequence, only the *I* =50 and 70 *A* cases are shown in figure 14.4. Also, as mentioned in Chapter 13, for the latter some doubts remain about the correct attainment of the plasma potential along the *radial* distance.

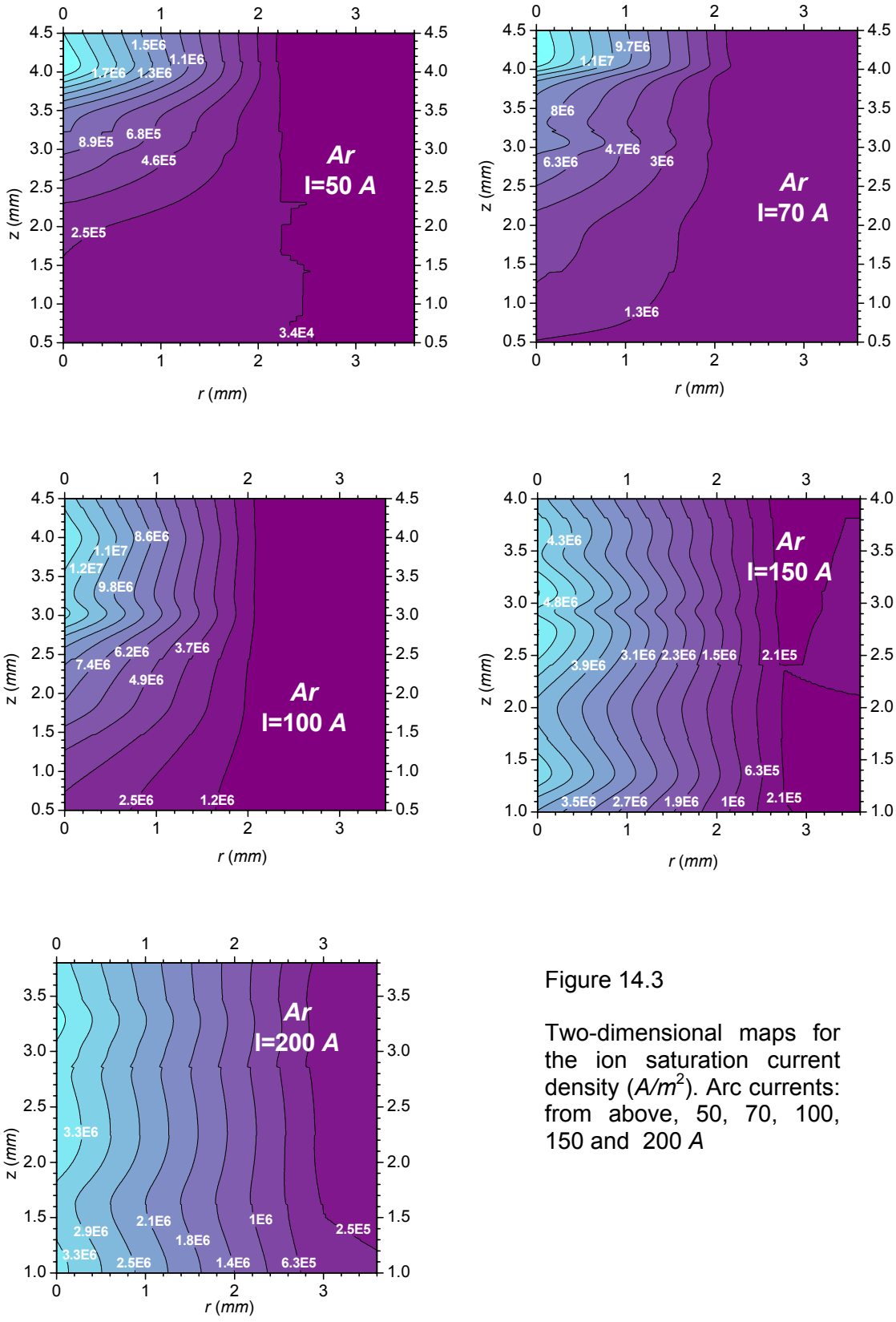

Figure 14.3

Two-dimensional maps for the ion saturation current density (A/m^2). Arc currents: from above, 50, 70, 100, 150 and 200 *A*

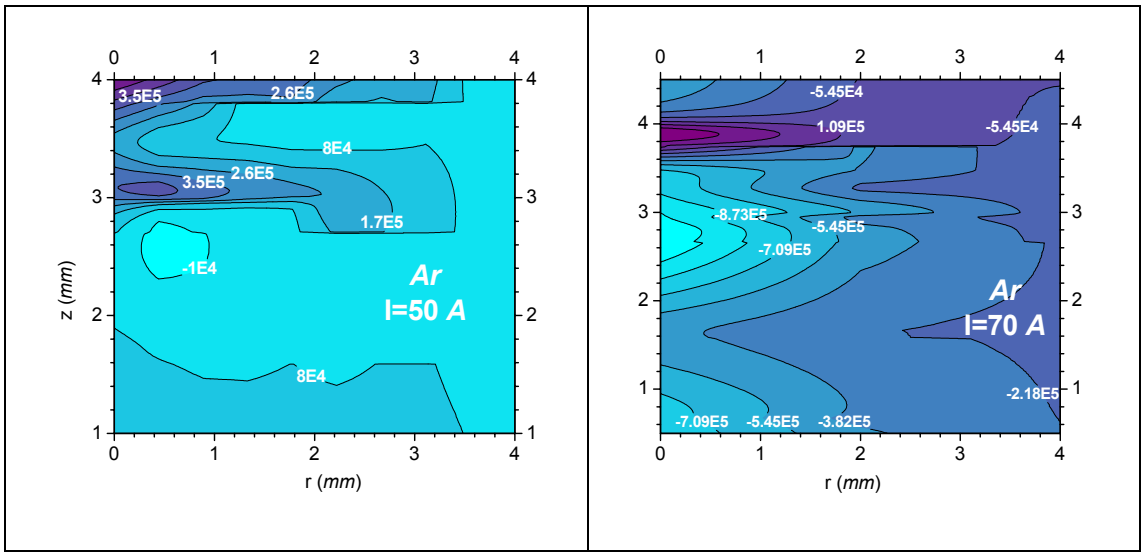

Figure 14.4 Two-dimensional maps for the electron current densities obtained from the currents measured at the plasma potential. I_{arc}=50 and 70 *A*

The 50 *A* case of the electron current density does not show a clear structure (figure 14.4 left), whereas the 70 *A* seems to have an inner contracted Gaussian-like shape, internal to the region defined by the curve ~$7.6 \cdot 10^5$ A/m^2 and a height of about 1 *mm* from the cathode, down to about mid arc (figure 14.4 right). In contrast, the ion case of figure 14.3 shows a luminous core from the cathode down to a height of about 4 *mm*. The intensity in the electron case, seems more distributed than in the ion cases at 70 *A*. For the electrons, the decaying factor is close to the unity along the axis; for the ion case the factor is about 7. This would suggest a conducting structure, made of different spatial electron and ion contributions. However, as mentioned in Chapter 13 the electron density values are lower than ion current density in the core (by a factor ~ 5.5 at mid arc, r~0.5 *mm*, down to ~3 approaching the arc outer edge). Even if this electron current density did correspond to the plasma potential, it is not the value that would be attainable at a hypothetical electron saturation region (which does not exist), e.g. it is possible that a higher value for j_e is more realistic, especially considering the rapid increase of the electron current upon relatively modest increase in the (positive) probe voltage. In this sense the value shown can be considered a lower limit.

It is interesting to compare the widths of the peaks taken in floating conditions with the peak widths taken under different biasing conditions. The right hand side of a floating peak is shown in figure 14.5 left, whereas its Abel inverted function is shown in the same figure on the right for two different probes at 50 A, z=0,58 *mm* and z=4.03 *mm*.

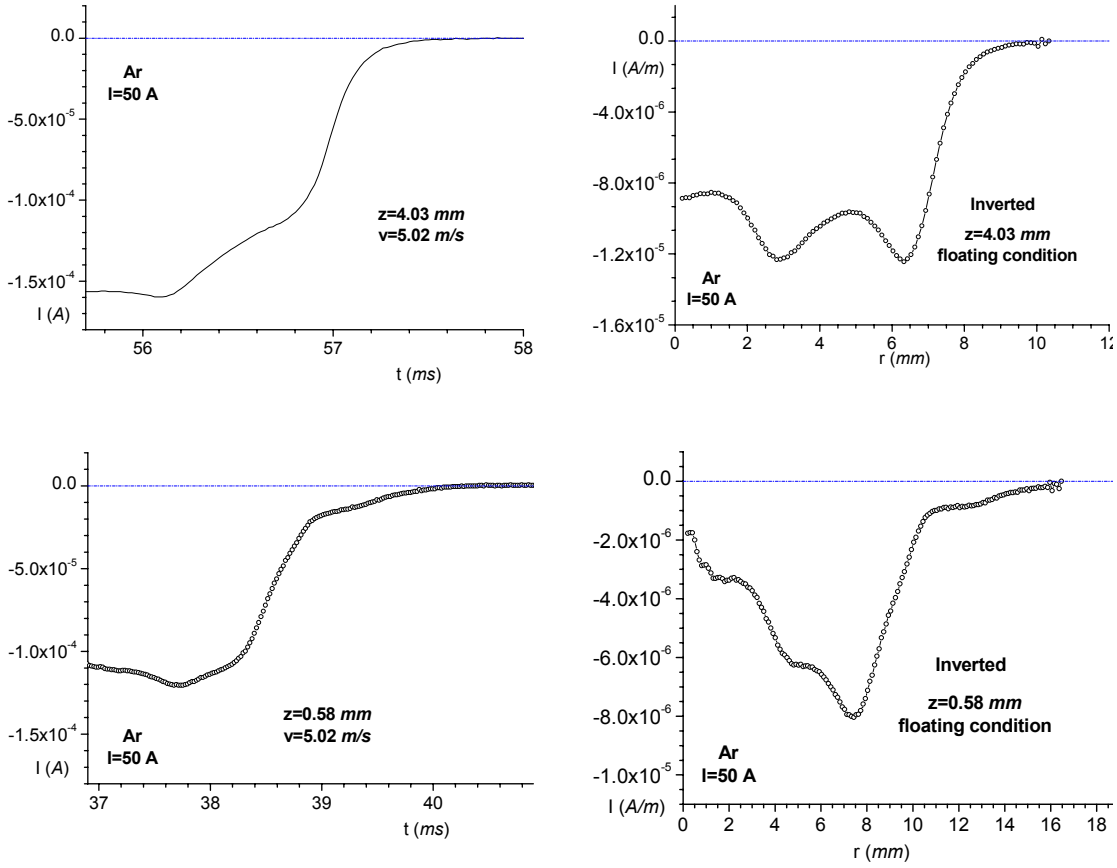

Figure 14.5 I=50 *A*, Examples of original and Abel inverted current peaks taken in floating conditions. *z*=4.03 *mm* and *z*=0.58 *mm*

Furthermore, a comparison of the Abel inverted current peaks taken under floating conditions, biased conditions with zero bias applied (thus electron currents) with the ion saturation current could help to reveal possible underlying conducting structures. This is done in figure 14.6a and b.

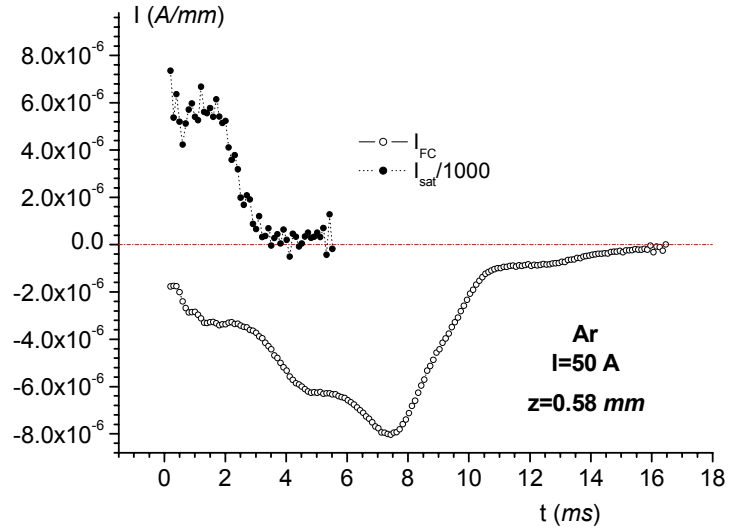

Figure 14.6 a I=50 *A*, probe height z=0.58 *mm*. Comparison between floating conditions current (empty circles) and ion saturation current distribution (full circles). Ion saturation current divided by a factor 1,000

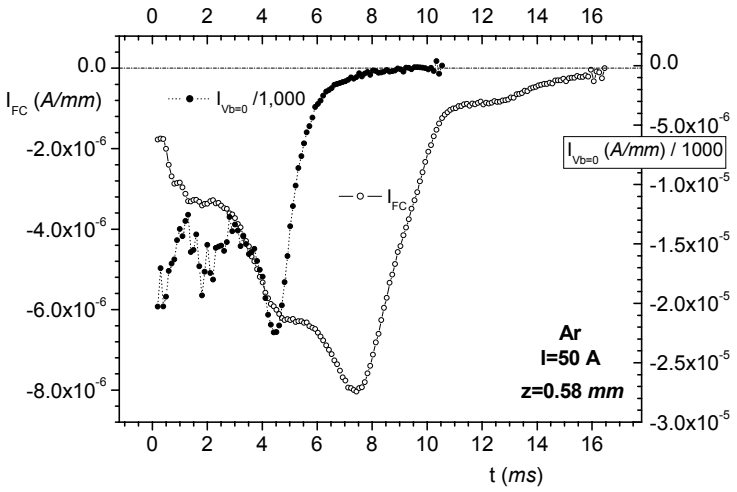

Figure 14.6 b I=50 *A*, probe height z=0.58 *mm*. Comparison between floating conditions current (empty circles) and electron current under zero bias conditions (full circles). Electron current at zero bias divided by a factor 1,000

The structures of the inverted signals present similarities. Figure 14.6 left shows that when the ion saturation current (full circles) is maximum, the electron current (empty circles) presents a minimum and vice versa.

The curves on the right (now two electron currents) under no bias (full circles) or in floating conditions (empty circles), show a structure which is *geometrically* similar. In other words, this plot could be interpreted (*i*) by comparing the currents at the same

radial coordinates, revealing the same behaviour shown in figure 14.5; or (*ii*) a numerical scaling factor seems to separate the two curves on both the scales so that specific features are shifted from one curve to the other.

A similar comparison performed for a different probe height is shown in figure 14.7 a-b.

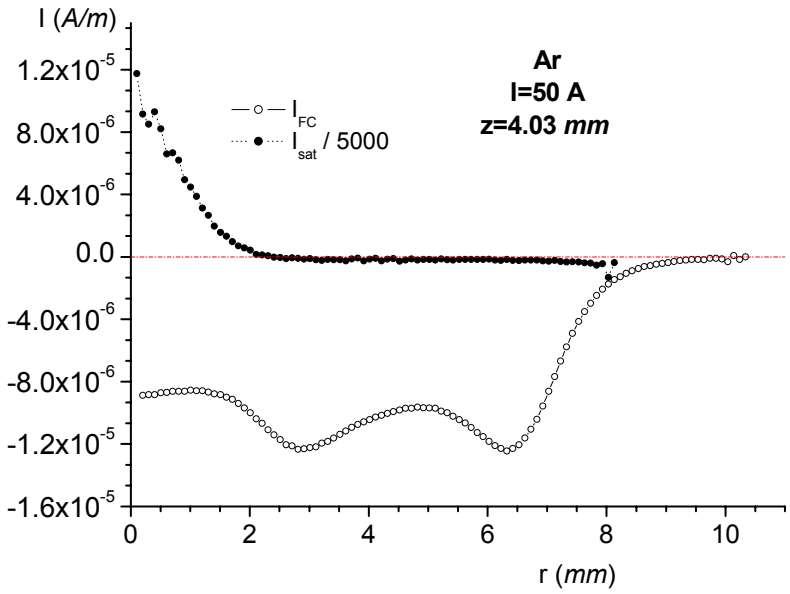

Figure 14.7 a, I=50 *A*, probe height z=4.03 *mm*. Comparison between floating conditions current (empty circles) and ion saturation current distribution (full circles). Ion current in saturation conditions divided by a factor 5,000

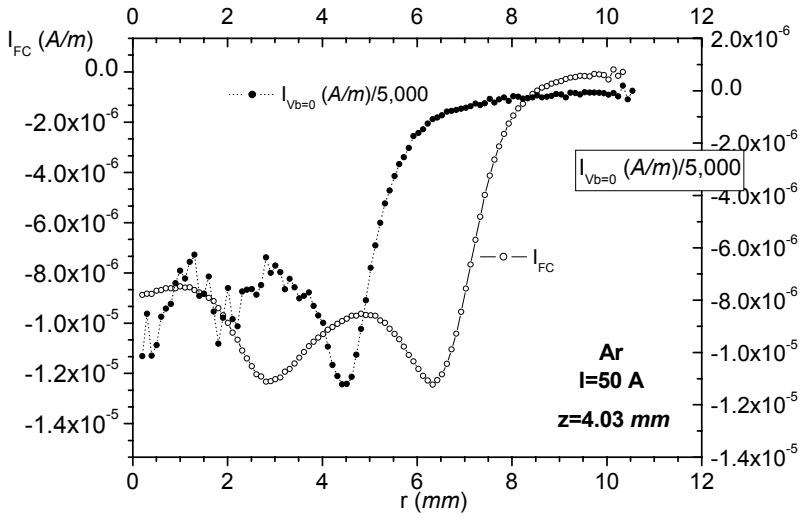

Figure 14.7 I=50 *A*, probe height z=4.03 *mm*. Comparison between floating conditions current (empty circles) and electron current under zero bias conditions (full circles). Electron current under no bias condition divided by a factor 5,000

The inverted signal structure for the higher z=4.03 *mm* probe is similar with respect to the comparison between the electron currents. In both cases an ion current region of ~2 *mm* (full circles) is 'seen' also by the floating condition signal (empty circles) with consistent radial dimension. For the ion current, the current carrying region seems limited to the first two millimetres thus to the first of the 'bumps' shown by the floating current.

Despite some intriguing structural similarities between the currents obtained under different conditions, no systematic study on this issue was performed. In fact, given the difficulties to compare the current densities it is not possible to pursue further analysis on the structure of the current conducting region in arcs as some hypotheses presented in section 13.5 would suggest (*cf* figure 13.5). It is hoped that direct measurement of local quantities by means of coated probes will help solving this issue (*cf* section 15.3 in the conclusions).

14.3. Thermometric maps

The comparison of the various temperatures examined in Chapter 11 showed that, irrespective of the method used (with the exception of the optical temperatures), the location of the isotherms is determined by the location and shape of the ion current density. Accordingly, the lowest temperature values in the radial direction, correspond to the intercept of the ion current with the axis, e.g. the thermal maps coincide in radial extension, with the ion current density maps. The thermal maps which refer to probe determined temperatures (substantially lower than the optical ones) are shown in figure 14.8 for the different arc currents.
As shown in Chapter 11, it is only possible to correct appropriately for the 'low' temperatures in all the arc current cases, once a precise determination of the flow velocity distribution (thus axial and radial) is available for variable arc current. As briefly mentioned in the conclusions, some indications about the boundary layer extension are experimentally available. From those, a preliminary estimation of the Reynolds number can be determined. However, as the latter depends on the viscosity, thus an additional parameter depending on temperature, it is felt that for the purpose of temperature determinations, the combined use of probe and optical techniques seems unavoidable.

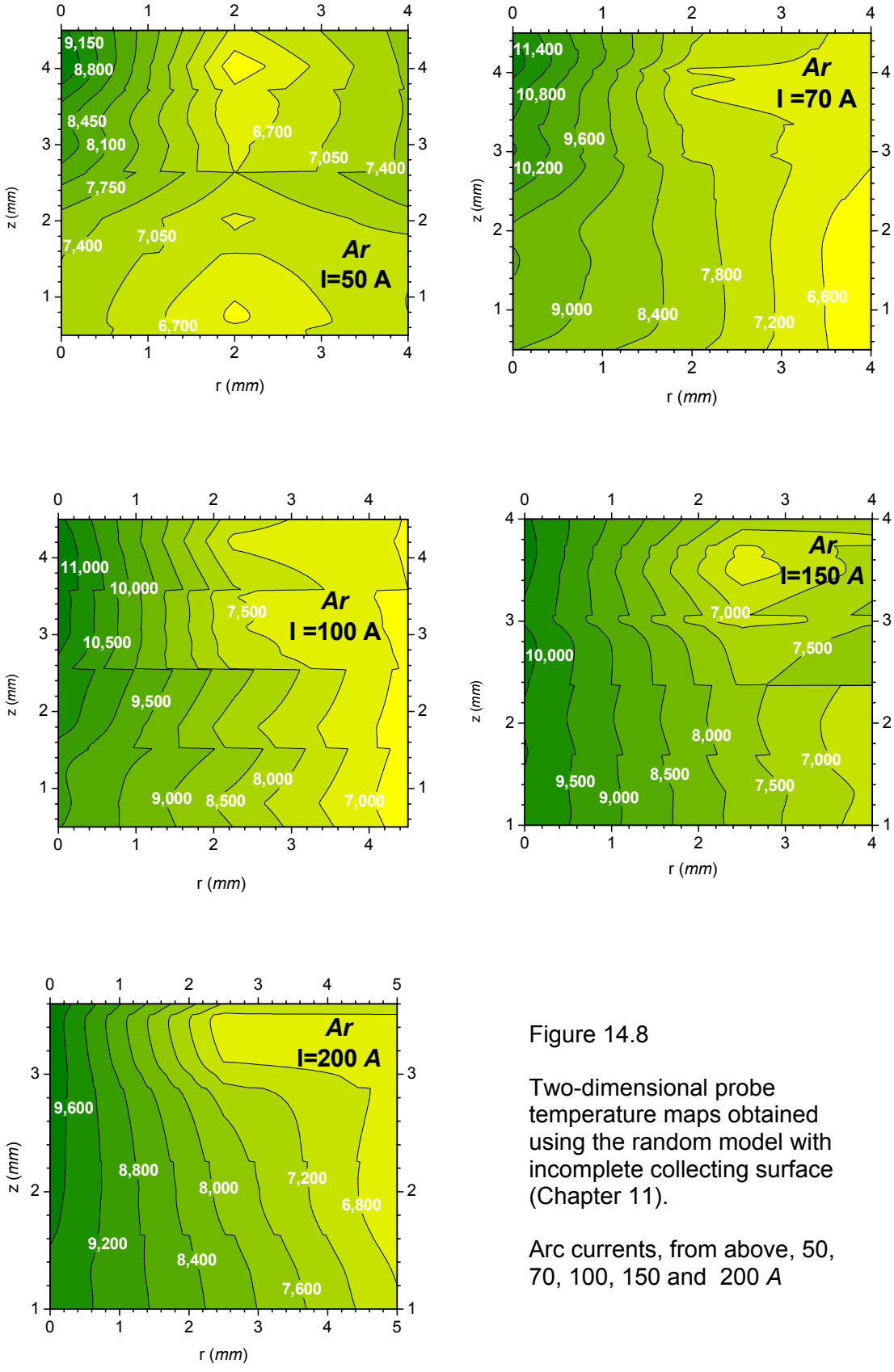

Figure 14.8

Two-dimensional probe temperature maps obtained using the random model with incomplete collecting surface (Chapter 11).

Arc currents, from above, 50, 70, 100, 150 and 200 *A*

However, with respect to the optical determinations, temperatures of the outer regions of the arcs seem attainable by probes, as values down to 6,500 *K* were shown. In optical emission spectroscopy the lower limit, corresponding to radial distances up to 4 *mm* at 200 *A*, is determined by the assumption of LTE. In the case of probes, the two-dimensional maps were obtained in the hypothesis of random motion under the equivalent thermal plasma assumption. Therefore, the question is why the probe determinations would be correct beyond this radial limits while the optical would not.

14.4 Thermodynamical Equilibrium

If a system isolated from the outside remains unperturbed for a time longer than the mean collision time, then it may be regarded as in equilibrium [36]. If the number of molecules per unit volume is large enough for the statistical fluctuations to be neglected, no gradient of any macroscopic property will exist either in space or in time and the velocity distribution will be constant and isotropic. When possible gradients that are forming are 'small' and the collision rates 'high' enough the velocity distribution of each macroscopically small element of the fluid will attain values that are appropriate to the local macroscopic properties of the element under consideration as this element moves through the gas. From the microscopic point of view, a status of Local Thermodynamic Equilibrium (LTE) is attained. At the macroscopic or continuum level, this corresponds to the 'isentropic' flow.
The question is then: are there sufficiently extended regions where the system can be found in local thermodynamic equilibrium? i.e. are there regions in which this equilibrium is at least partial (PLTE)?

Laboratory plasma cannot be considered in equilibrium because these are neither closed nor isolated systems. Energy exchanges take place both by radiation and by particle exchanges between the plasma and the surroundings (the anode is the material surface that will mostly affect the TIG arc). The sustainment of the plasma is achieved by external energy sources (and by a continuous mass flow in the cathode region for the TIG arc). When the input and output energy fluxes equalize, the system reaches a steady state, which is not in thermal equilibrium because these energy fluxes follow different channels. In the absence of thermodynamic equilibrium the mean atom, ion and electron energies may be different and the respective particle distribution functions may well depart from the Maxwellian. However, a partial equilibrium with respect to individual processes could take place (PLTE). In a plasma where the density of particles is not too high there exists a state where ions and electrons distributions are such that $T_i \approx T_a$ but $T_i \neq T_e$. Such a plasma is called non thermal. The reason why the density should not be too high is that if electrons interact with each other through the electrical field, then their

distribution *could* be Maxwellian (*cf* [37]). The distribution function of each single species can be close to Maxwellian if the rate of energy exchange from species to species and with the external environment is small with respect to the rates of exchange within the same species. Since the mass difference between ions and electrons is high, the energy transfer between those species is slow. Therefore a partial equilibrium is possible separately for the electron and the ion components. In these conditions all the processes in which only one components participates, must occur as if the plasma were in thermodynamic equilibrium. More precisely, according to [1] a PLTE state is characterized by the equality

$$T_{\mathrm{k}} = T_{\mathrm{s}} = T_{\mathrm{ex}} \tag{14.1}$$

where T_{k} is the kinetic temperature for all the particle species except the ground state, T_{s} is the temperature of ionization equilibrium as given by the Saha equation, and T_{ex} is the excitation temperature of the various states (the ground state excluded).

14.4.1 Conditions for LTE / PLTE

1. A widely used condition for the verification of the occurrence of LTE (for example, see [38, 39] is expressed in terms of a "minimum limiting electron density" [40].
This involves the consideration of optically thin versus optically thick plasmas. An optically thin plasma is a medium where radiation produced at a location is able to escape the plasma, without interactions; whereas in the optically thick plasma, the radiation emitted at a location is almost entirely adsorbed in the immediate surroundings. Experimentally, in the first case a discrete spectrum characteristic of the species is seen; in the second case, the radiation emitted as a function of frequency appears as a "continuum". In atmospheric pressure plasmas, an admixture of the two is observed.
Rigorously, a thin medium, where photons are able to escape bringing energy away from the plasma, cannot be in equilibrium. However, a necessary condition for LTE for optically thin plasma can be based on the requirement that the electron-ion collision rate must exceed the radiative rate by at least one order of magnitude (thus reducing the amount of 'energy escape' to a quantity negligible in first approximation). The condition

$$n_e = \frac{5}{8\sqrt{\pi}}\left(\frac{\alpha}{a_o}\right)^3 z^7 \left(\frac{E_2}{z^2 E_H}\right)^3 \left(\frac{kT}{z^2 E_H}\right)^{1/2} \approx 3.9\cdot 10^{17} z^7 \left(\frac{kT}{z^2 E_H}\right)^{1/2} \quad cm^{-3} \tag{14.2}$$

can be reduced by an order of magnitude for media that do not reach states sufficiently close to LTE. This has to be intended in the sense that the preceding relationship implies full LTE; however, in the words of Griem [40]: "*Partial Local Thermodynamical Equilibrium (PLTE) may occur as populations of high excited levels*

are related to the next ion's ground population by Saha-Boltzmann relations... or to the total population in all fine-structure levels of the ground state configuration". A reduction of about one order of magnitude with respect to (14.2) arises in the 'optically thicker' situation where the principal resonance lines are self-adsorbed and the decay rate of the first excited state is balanced by the excitation of the ground state [41]; while the only radiative mechanism which is not balanced by any inverse process (as required in an equilibrium process) is the radiative population for the ground state. Therefore, the values obtained with (14.2) should be reduced by a factor of 9.
In relationship (14.2) α=1/137 is the fine-structure constant, a_o=0.5*Å* is the Bohr radius, z is the ionic charge, E_H = 11.6 *eV* is the ionization energy for hydrogen, E_2 is the (single) ionization potential, E_2 =15.8 *eV* in argon, E_2 =24.6 *eV* in helium. The (minimum) limiting electron density for kT=1 *eV* (T=11,605 *K*) or 2 *eV* (T=23,210 *K*) in SI units is $n_e \approx 8.14 \cdot 10^{23}$ m^{-3} or $n_e \approx 1.15 \cdot 10^{24}$ m^{-3} for argon; $n_e \approx 3.07 \cdot 10^{24}$ m^{-3} or $n_e \approx 4.34 \cdot 10^{24}$ m^{-3} for helium. These values indicate that even the core, i.e. the region of the arc with highest charge density, is not in LTE conditions (*cf* figure 11.5). This is true also if one considers the mentioned reduction of a factor 9 (the 'one order of magnitude' mentioned above).
Moreover, spectroscopic measurements [1], see figure 11.5) indicate sharp temperature gradients along the arc radius that hardly fulfil the requirement of 'small' temperature variations mentioned above (and also reported in [41]. Figure 11.5 shows isotherms for the temperature obtained with different emission lines that are located at different radial position; therefore the description of the system in terms of different kinetic temperatures seems the most appropriate: once again the system cannot be in LTE, perhaps only in PLTE. But, comparing the two graphs in figure 11.5, temperature gradients of the order of 1,500 *K/mm* at arc mid-height (2.5 *mm*) for the 696.5 *nm* line or 2,000 *K/mm* for the 706.7 *nm* line are found. This means that gradients of 11 to 15% are found, which hardly fulfil the $\nabla T/T << 1$ condition even on a local basis.

2. It is generally believed that an increase in arc current reduces the causes for the departure from LTE so that for currents above 50 *A*, the arc is in LTE [19]. However, as reported in [42], earlier studies [43] showed departure from LTE, even in 400 *A* arcs with pressures up to 3 *atm*. In those cases, the departure is localized in the fringes of the arc. This might be due to the radially increasing optical thickness. According to [19] the equilibrium departures affect both equilibrium ionization and electron-ion temperature differences. The first, ionization equilibrium, is believed to hold in the central region (within 2.5 *mm* from the centre of the 100 *A* arc studied in [19]), whereas temperature equilibrium departures occur further from the axis (at 3.5 *mm* from the axis T_e=8,000 *K* while T_i=5,000 *K* [19]).

In view of the question posed at the end of section 14.3, the position assumed here is that the probe temperatures are accepted within the same geometrical limits in which

optical temperatures characterize arc regions in PLTE. The fact that these probe temperatures are lower has been attributed to recombination. In view of maintaining the quasi-neutrality, $n_i=n_e$, this implies that $T_i=T_e$ is still valid within the disturbed region ('boundary layer') even if there the optical temperatures are higher. In other words, it is the *practical* difficulty of obtaining emission intensities below the ones corresponding to temperatures of 9,000 to 10,000 *K* that limits the optical temperatures, rather than the intrinsic lack of LTE. In this sense, whether a true state of LTE is attained or not, probes can access temperatures that are not attainable by emission spectroscopy.

14.5 Arc electrode zone

It is sometimes stated [35, 44] that an extrapolation of the directly measured probe voltage to the anode should give an order of magnitude for the anode sheath fall. It is shown that this assumption is unjustified.

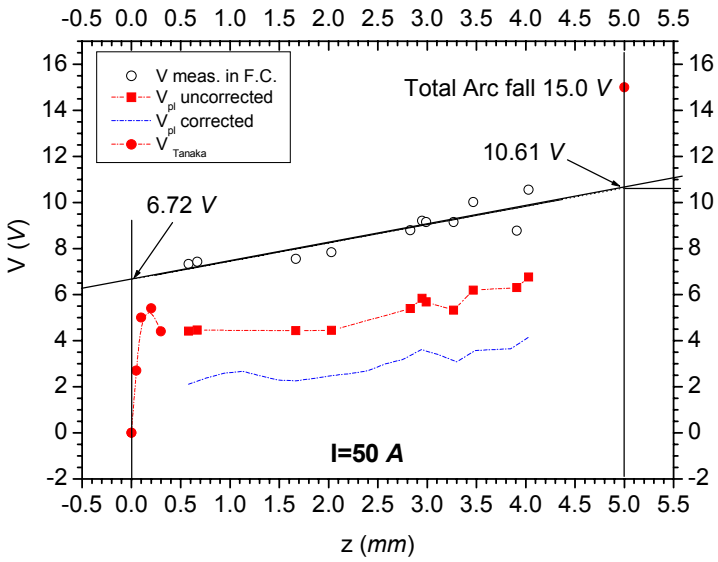

Figure 14.9 I=50 *A*. Plot of the axial measured potential (empty circle), plasma potential (uncorrected, full squares or corrected, broken line) as a function of height in arc. The values obtained by Tanaka *et al* [31] in the anode region (full circles) and the total arc voltage indicated at the cathode (15.0 *V*) are also shown (positive values are shown for convenience).

Observing the curves shown in figure 14.9, it can be seen that there are several reasons why the mentioned extrapolation is incorrect under the present circumstances:

1. The measured probe potential differs from the plasma potential by the floating potential shown in figure 12.8. Thus it is the plasma potential that should be (possibly) extrapolated.

2. The extrapolation performed towards both the electrodes depends crucially on the assumption of a linear dependency of the potentials on the arc height and on the choice of the 'limiting' points (e.g. *where* do the sheaths start). For the cathode region, given the measured total arc voltage of 15.0 *V*, the probe voltage extrapolation would give a cathode fall ~4.4 *V*, *lower* than the anode fall, ~ 6,72 *V*, perhaps contrary to the expectations of *lower* fields in the *larger* anode region (*cf* section 2.2)

3. The plasma potential shown in this work was obtained form the temperature determined in Chapter 12 and it refers to a cooled 'boundary layer' plasma around the probe. The latter circumstance is not considered in these extrapolations: the flow velocity has an axial as well as a radial dependency and the values closer to the anode should suffer the least inaccuracy, the ones closer to the cathode the greatest one. This circumstance could be immaterial if one were able to prove that the correction of the plasma potential at the lowest arc currents, here 50 *A*, is not necessary or of limited use because of 'low' flow velocity (*cf* section 11.6 and 11.7), as the matching with the values of Tanaka *et al* [31] would suggest. Alternatively, one could argue that the latter suffer form the same limitations due to the neglect of the flow when approaching the anode surface ('stagnation point').

4. The determination of Tanaka *et al* [31] shows a structure which is inconsistent with the idea of a smooth transition from the arc column towards the anode as the proposed extrapolation would suggest.

The determination of the total sheath fall needs to be accomplished by a dedicated experiment, capable of delivering direct measurement of the electric current distribution and values of the probe voltage close to the anode.

15. SUMMARY, CONCLUSIONS AND FURTHER WORK

15.1 Summary

The aim this work was twofold: to establish the degree of applicability of Langmuir probes to high ionization high pressure flowing (arc) plasmas and to explore the information obtainable concerning the arc structure.

For this purpose, an extensive critical assessment of the existing literature was performed in order to establish whether available probe theories could be employed for the interpretation of the data. Each of the presented theories, pre-selected from the much wider literature on Langmuir probes, showed some useful features, but none of these were found to be suitable to fully account for the major features which differentiate the arc plasma from the more usual low pressure plasmas, where probe devices have proven so successful in the past. High ionization, flow and consequent perturbation by cooling appear to be the major difficulties for the successful operation at high pressures. For this reason, the amount of numerical estimates on the key plasma and plasma-probe parameters has been quite extensive (Chapter 2). In order to prepare the background for the experiment, after an introduction to probe methods (Chapter 3), some questions concerning the onset of the sheath were addressed (Chapter 4). It was found that the Bohm criterion, widely evoked for many problems of plasma-wall interactions is of limited use under atmospheric pressures. Whether it can be generalized to collisional plasmas is still an open question in plasma physics (and in mathematical physics).
The probe regimes were compared in Chapter 5 and the most important findings made it possible to conclude that:
1. Continuum and Continuum plus Free Fall theories (CFF) are the most appealing candidates although it was recognized that experimental discrimination between these was very difficult if not impossible due to accuracy limitations of the technique.
2. The consideration of flow effects lead to the inclusion of diffusion-like theories which however, have only been proven over a quite narrow range of experimental conditions, including high temperature flames, which are not valid for collision dominated media where ionisation is high.

Estimations of non-ideality effects in the form of cooling of electrons and recombination were attempted in Chapter 6 and it was shown that according to a few existing criteria, electron cooling did not appear to be a critical issue. The evaluation of the Damkohler number revealed instead that within the limited knowledge of data on recombination, the latter could be important outside the sheath thus, under the present experimental conditions, within the boundary layer.

In the experiment, the selection of the methods to analyze the data has been guided with an eye to published results on *arcs rather than on probes*.
Some procedural details were given in Chapter 9 with the aim of illustrating both the numerous possible interrelations between plasma parameters and the complexity of the data structure provided by the experiment. The construction of the characteristic curves, a key tool in Langmuir probe theory has been possible in a *local* sense, e.g. allowing in principle the evaluation of all physical parameters through the Abel inversion but at the price of establishing, by means of simplified considerations on 'available particles', that the probe is equipotential (Chapter 10). As a consequence, the problem of the interpretation to give to Abel inverted probe voltages (e.g. 'voltage per unit length') has not been solved. The V-I curves obtained are of limited application under the present circumstances. That collisionality or high ionization could impede their full use was predicted in Chapter 6 and in effect the only exploitable part was found to be the ion saturation region, from which temperature determinations with the direct method of Gick were performed (Chapter 11).
The determination of the key parameters which characterize the arc, namely temperatures (Chapter 11) and potentials (Chapter 12) has been particularly difficult. It was realized that due to the complex fluid and heat interactions, the probe method alone was not sufficient to characterize the arc (thus providing 'new' information). It was therefore decided to use an independent experimental technique to assess the results. The author is well aware that very often the comparison of data obtained by different techniques complicates rather than simplifies the matter, but in this specific case, the advantage has been that the spectroscopic method based on the Fowler-Milne technique (even if far from settled with respect to some questions concerning LTE) is relatively well established and gave results in agreement with published data [4]. For this reason very little detailed information has been given about this method here, the reader being referred to the relevant literature on the subject. A review was in fact performed at Cranfield a few years ago [1] and was extensively used for the determination of the optical results.

Of the several possible temperature candidates, broadly divided in a 'CFF' and in a random family (modified by multiplicative factors related to geometry or thermal plasma assumption) the latter has been chosen, although the level of accuracy did not lead to selection with certainty within each family. The appealing proximity of the CFF

temperatures to the optical values has been discarded in favour of the random model. The choice of (1) the random model with (2) partial collecting surface has been motivated by the apparent [17, 18, 30, 33, 45, 46] existence of a sheath and pre-sheath. As a consequence the choice of the ion velocity to be the most probable rather than the thermal, appeared natural even considering that the opposite choice would have implied absence of pre-sheath. [Also, because with this choice the Bohm criterion would be satisfied in any case, its usefulness in the present circumstances appears doubtful].
The comparison of the probe temperature with the optical values made it possible to introduce the notion of 'cooling' intended in a broad sense to describe temperature lowering induced by probes. Despite the fact that this feature could have been foreseen as the major source of error from the very beginning, some considerations about the structure of the non monotonic, non-factorizable function used in the modified method of Gick have been made, with the purpose to exclude the notion that lower temperatures could be caused by an inappropriately high or low ion current drawn at saturation. Even if it has been found to be impossible to completely rule out this source of perturbation, an order of magnitude has been established in the first instance by the requirement that the number density computable from the measured current and the subsequent temperature must be lower than the density fixed by the optical temperature. This criterion has been made more strict by the observation that recombination should be inserted in the criterion, via a reduction of the electron density in the boundary layer estimated as a factor 50 to 70 (Chapter 11). Moreover, recombination has been established as the most likely cause of 'cooling' rather than momentum loss by collision within the boundary layer.
The direct determination of the plasma potential and of the electrical conductivity has been shown to be unattainable with any degree of reliability in the present conditions, mainly because of the incompleteness of the characteristic curve lacking a clearly defined steep part and the location of the plasma potential. This circumstance also impeded the usual procedure for the determination of the electron temperature (Chapter 3). However, the use of the temperature obtained in Chapter 11 allowed the computation of the (axial) floating potential and, by using the measured probe voltage, made it possible to determine the plasma potential. Because the electron temperature was depressed with respect to the optical value, a correction was performed using the latter and plasma potentials were obtainable which show agreement with published data when a comparison was possible. Despite the several steps involved in this construction, which may cause incidental agreements, it is felt that this is not the case, because of the broad agreement between the axial values of the floating potential.

The sheath potential was obtained using a wholly different approach described at the end of Chapter 10. By measuring the total power to the probe and assigning an average energy per particle to each ion under the assumption that the final kinetic energy is related to the difference between the bias and the probe potential, it was possible to

assign values to the sheath potential and, as a consequence, to the sheath thickness. These turned out to be close to the estimates of Chapter 4 although a clear-cut selection criterion for the choice has not been found. The thickness varying from just below to a few Debye lengths, confirmed the essentially collisionless nature of the sheath. However, serious doubts exist about the mentioned identification as demonstrated by (*i*) the disagreement between the sheath voltage computed in floating condition and the floating potential determined from the temperature and (*ii*) the only partial fulfilment of the condition for the sheath formation (Bohm criterion).

The question as to whether ion and electron current densities are representative of the true current flowing in the arc has been partly answered only in terms of reasonable assumptions. For the former, some degree of directionality towards the upstream region of the probe seems intrinsic in the arc structure; this is at variance with respect to the expected motion of charged particles under the action of an electric field alone (e.g. in absence of flows). However, the assumption of an ion current density substantially independent on probe bias, justified by the high ion to electron mass and thus mobility ratio, makes it possible to conclude that the ion current seen by the probe is of the correct order of magnitude of the current distribution within the arc.
For the electron current densities a range of variability has been set in that the lower limit would be guaranteed by the attainment of the plasma potential, which, even if not coinciding with the higher and unattainable electron saturation, guarantees purely electron current in absence of probe sheath, and as such can be thought of as the least disturbing condition for the arc. The upper limit would be the value obtainable from calculation in the random motion hypothesis with dynamics determined by the optical temperature. The latter value appears too high by an order of magnitude or so with respect to the limited data available in literature. Also, in this case, no attempts were made to the reconstruct a detailed current density structure which would include flowing, drift and thermal contributions, very likely of opposite orientation. It is for this reason that the optically determined values appear as an upper limit.

The axial electric field was estimated according to two different methods; the first, by differentiation of the directly measured *probe voltage*, which requires the assumption of negligible variations of the floating potential with arc height. As shown and discussed in Chapter 12 and 13 this assumption appears justified only at the highest arc current (200 *A*). In fact, the comparison with the results from the second method, e.g. the differentiation of the *plasma potential*, shows broad at these higher arc current values, whereas the lower 50, 70 and (perhaps) 100 *A* are in disagreement.

The structure of the arc described in Chapter 14 aims at collecting the data presented in the preceding chapter in a unified manner in order to extract further information and in particular to see whether a 'zone' approach was possible.

It has been shown that different operating conditions lead to different arc radii. This is attributed to the much lower current collected in floating conditions (to a factor ~ 10^{-4} lower). The notion of current conducting zone follows and the observed width increases with total arc current are expected. The outer 'floating' radius is somewhat larger than the typical heat wave rings observed on the anode disks after arcing. This is qualitatively in agreement with the slight constriction of the arc column close to the anode. It is thought that due to the much lower charge collected, this radius corresponds to the less luminous region of the arc, the 'halo' where ionization is still high enough to give rise to luminous phenomena, but where the current is substantially zero.

Both the ion and the electron current densities (when possible) were plotted in two-dimensional maps and a core region, expanding and elongating in z upon increase of the total arc current, is now visible also on paper. The absolute values of the electron densities are lower than expected and lower than the ion density but this is thought to be connected with the poor location of the *local* plasma potential.
It is difficult to draw conclusions about the possible onset of regions where steady conduction of charges of different sign might take place. A detailed study of the shape of the peaks produced in floating conditions, has been limited to the observation of some structural similarities between the Abel inverted ion and electron currents obtained under biased and floating conditions. In particular the occurrence of a central depressed region suggests that more research in that direction is required.
The temperature maps shown at the end of Chapter 14 complement the graphs either along the *z* or the *r* direction shown in Chapter 11, giving a clearer picture about the implied variability of the temperature as a function of position. The important issue of full attainment of LTE has not been explicitly addressed. Extensive use has been made of the ‘thermal’ assumption and of the equilibrium data of Olsen and Murphy, which have been the framework for every quantitative evaluation. This limitation has been dictated by *practical necessity* in absence of corresponding non-equilibrium data. Whilst the discussion of LTE in section 14.4 concluded that rigorously speaking a status of LTE *cannot* be attained in TIG arcs, the very few literature sources point to ion to electron temperature ratios very close to unity. This indicates considerable quantitative uncertainties about LTE (or PLTE) attainment in terms of location in the (*r,z*) plane, limiting value of the arc current, ionization level and pressure. Extensive work is still required in this direction.

15.2 Conclusions

To the best of the author’s knowledge, the present work represents the first extensive investigation of electrostatic probes in arcs that has been performed exhaustively addressing the most likely difficulties. The following quantities are obtained: temperature, potentials (floating and plasma) and, indirectly, conductivity and electric

field. Moreover, experimental estimations of the main sheath features were presented for the first time.

In the first part an in-depth analysis has been carried out to set the 'framework' made of evaluations of the key arc parameters. In the absence of clearly defined theoretical models a 'what if' approach to probe physics made it possible to identify and test the different regimes. Also, real world non-idealities (probe emissions, cooling, non-frozen chemistry) were considered together for the first time.
Previous works attempted to tackle different problems separately. For instance in [5, 26] a temperature determination was attempted which gave results similar to the ones obtained here; however, no description of what is truly observed was ever presented and no real justification of the model chosen was made. Also, it was previously believed [47, 48] that probes cannot be used in atmospheric pressure arcs because of the disruption of the V-I curve induced by collisions. It is shown here that this is only partly true in that no electron portion of the curve seems attainable in arcs, at least at the arc currents of interest in this work. Despite these drawbacks, the ion portion of the V-I curve can still be used to obtain the temperatures. Certainly, this requires the *appropriate interpretation* of the mechanisms taking place at the probe surface, but once the choice of the latter has been made, the accuracy of the reconstructed temperatures, 5%, seems quite respectable (*cf* Appendix E). In other words, it is only the choice of the operating model that limits the accuracy on the reconstructed temperature.

The major difficulty in operating probes in flowing plasma is the onset of a perturbation region which manifests itself in 'cooling' of the plasma. It has been shown here that this is mainly due to recombination. Thus, the onset of a fluid-flow induced perturbation region, called for simplicity the 'boundary layer' (*cf* Chapter 2), is the major source of complication towards the V-I curve interpretation. Therefore, one could argue that probes in arcs measure the features of this boundary layer rather than the bulk of the plasma. This seems true for the highest arc currents whereas the small influence of the inclusion of flow velocity effects at the lowest arc current (50 A) seem to suggest that a further lowering of the current (and thus of the flow velocity) could lead to a 'boundary layer' vanishing and, ultimately merging with the bulk of the plasma.
For the highest arc currents, even if the results shown here confirm the characterization of a cooled region rather than the bulk of the plasma, this is the first time that a conscious characterization of such a region has been performed. It is felt that the order of magnitude of its influence has been unveiled thanks to comparison with optical data, although experimental evidence on flows in arcs and results from numeric models are needed in order to predict the full range of influences of probes in arcs.
An alternative approach based on the direct determination on particle dynamic parameters has been attempted which made it possible to estimate the order of

magnitude of the sheath voltage and thickness. Once again it is the choice of the model that determines the accuracy of these estimations. The experiment shows that it is not only the thickness but also its *distribution* along the probe length that is accessible.

From this work, a further major difficulty emerges about the use of probes in arcs. This is related to the asymmetric way currents and voltages are treated. Whilst the Abel inverted current has a clear interpretation, the requirement of an equipotential probe causes disruption of information about the true *local* plasma potential. In fact, at the plasma potential, the non-existence of a sheath implies that the probe attains a voltage uniform along its length which equals the plasma potential. Because it is believed that the latter should have a radial distribution, the consequence is that the plasma is shorted by the probe under this circumstance, e.g. that *local* values of the plasma potential are not attainable by probes in arcs. Hence, the determination of the electron current density is also at risk. The uncertainty about the correct location of the local plasma potential makes it difficult to assess the imbalance between the ion and electron current distributions within the arc.
Finally, irrespective of the attainment of LTE, and within the limitations on the onset of cooling, it is believed that probes can access temperatures regions which are not attainable by emission spectroscopy.

15.3 Future work

From the foregoing discussion it is evident that several issues were left out of this work and in particular more elaborate treatments about heat transfer and effects related to the flow, both from the theoretical and the experimental point of view.
The completion of the study on the arc structure moving from the column towards one or both the electrodes is part of an ongoing project [49] in which the author of this work is involved. The purpose is to investigate the anode region by means of a dedicated ‘detector’ which is an enhanced version of the ‘split-anode’ technique [50]. The electrical current to the anode will be measured in the same fashion as the probe, but additional information about the voltage structure can be gained by matching the results from probe runs closer to the surface than in this work, perhaps down to 0.3 to 0.4 *mm* with the data obtained from the anode detector, which is set at the zero of the potential.
A detailed study of the charge capture mechanism is ongoing by using partially coated probes. The purpose is twofold. On the one hand the reduction of the collecting surface to a spot of the size of few microns can eliminate the need for the Abel inversion about which some doubts persist concerning its applicability in probe conditions. The comparison between ‘true’ (directly measured) local parameters, with previously Abel inverted quantities will clarify potential discrepancies connected to the application of the method to probes.
On the other hand, by direct comparison between currents measured at different locations on the probe, it will be possible to enhance the understanding of the

directional charge capture mechanism with the ultimate aim to unveil the different electric current contributions within the arc.

Finally, recent preliminary measurements performed with probes and optical spectrometer simultaneously, indicate the extension of the boundary layer surrounding the probe to be about three probe diameters but the experimental errors are still large (~ 1 probe diameter). Even if the latter figure seems discouragingly high in view of the application of the probe method, at least to short (5 *mm*) point-plane geometry arcs, this information can be used to obtain an indication of the flow velocity, which of considerable importance for the correct interpretation of the experimental results. Moreover, because of these results, (*i*) an up-scaling of the plasma linear dimensions (arc length) and (*ii*) a down-scaling of the plasma current (thus flow velocity) would make the probe method progressively immune to the problems illustrated and extend its use for the characterization of other kind of atmospheric plasmas where the effects of the flow are relatively minor.

APPENDICES

APPENDIX A - Current density distribution and magnetic field

It is supposed that current density and pressure have only radial dependence. This implies the only non zero component of the induction field is the azimuthal B_φ (isotropy). Assuming a time independent electrical field, the Ampere law for the total current density is satisfied (i.e. the displacement current is zero) and the corresponding Maxwell equation in cylindrical geometry is then:

$$\nabla \times \mathbf{B} = \frac{1}{r}\left[\frac{\partial}{\partial r}\left(rB_\varphi\right)\right] \tag{A.1}$$

The total current is obtained integrating this density from origin to the border R of the column:

$$I = 2\pi \int_o^R jrdr \tag{A.2}$$

1. Uniform current density

$$I = 2\pi \int_o^R jrdr = \frac{2\pi}{\mu_o}\int_o^R \frac{d}{dr}\left(rB\right)dr = \frac{2\pi}{\mu_o}RB \tag{A.3}$$

Inverting for B:

$$B(r) = \mu_o I/2\pi r \tag{A.4}$$

Evidently the magnetic induction decreases as $1/r$ out of the column considered as linear conductor. The maximum field is at $r=R$ in (A.3).

2. Parabolic current density

In the works by [29] the current density is assumed to be:

$$j_z(z,r) = j_o(z)\left[1-\left(\frac{r}{R(z)}\right)^2\right] \equiv j_o\left[1-\left(\frac{r}{R}\right)^2\right] \tag{A.5}$$

where j_o is the axial current density. The suffix z indicating the z component of j is omitted. Also, expression (A.5) refers to the height z (i.e. a different expression is needed for each z value).

The normalization requirement (current conservation)

$$I = \int j dS = 2\pi \int_0^R r j(r) dr \tag{A.6}$$

gives the non arbitrary axial current density related to the arc radius:

$$j_0 = \frac{2I}{\pi R^2} \tag{A.7}$$

The field is obtained as in the uniform case by inverting the integral of the Maxwell equation in cylindrical coordinates as in the previous section (*cf* A.2)

$$B_\theta = \frac{\mu j_o R^2}{4r} \tag{A.8}$$

It can be observed that any power law of the form

$$j = j_o \left[1 - \left(\frac{r}{R} \right)^n \right] \tag{A.9}$$

always gives rise to $B_\theta \sim 1/r$ whose expressions differ by a multiplicative factor containing n.

3. Gaussian current density

Allum in his model [16] assumes a gaussian current density distribution as based on the results of Gvozdetskii (referred to in [16]):

$$j_z(r,z) = j_o(0,z)\, e^{-br^2} \tag{A.10}$$

where j_o is the current density in the axial position and b is a "constant" to be determined by the normalization condition (current conservation) which can be written substituting the upper integration limit, R, with infinity provided $j(r,z) \to 0$ for $R \to \infty$ (in practice

satisfied after few 'standard deviations' $r \geq 3\sigma = 3\mathrm{w}$, where $w = FWHM$ (Full Width Half Maximum) of the curve). Integration yields

$$I = 2\pi j_o \int_o^\infty r e^{-br^2} dr = \left[br^2 = x,\ rdr = dx/2b \right] = \\ = \frac{\pi j_o}{b}\left(1 - e^{-\infty}\right) = \frac{\pi j_o}{b} \tag{A.11}$$

Integration of (A.2) and inversion for the induction gives the formula used in the text (where $\mu_o = 4\pi \cdot 10^{-7}$ *H/m*)

$$B(r) = \frac{\mu_0 I\left(1 - e^{-br^2}\right)}{2\pi r} = \frac{\mu_0 I\left(1 - e^{-\pi j_0 r^2 / I}\right)}{2\pi r} \tag{A.12}$$

APPENDIX B – The Bohm criterion

The following treatment is due to Riemann [100, 101] re-derives the Bohm criterion for cold ions and sets the mentioned two-scale mechanism for the description of the sheath and pre-sheath and thereafter treats the plasma –sheath transition for the case where $\varepsilon=\lambda_D/\lambda_i$ is small but finite. The hypotheses on which the model is based are (I) monoenergetic cold ions (II) a Boltzmann distribution for the electrons and (III) the existence of a perfect adsorbing wall.

Moreover, the limit $\varepsilon=\lambda_D/\lambda_i\to 0$ is assumed (actually in the original paper a generic characteristic length L is assumed whereas here the latter is identified with the ion mean free path). The negative wall repels all the electrons whose distribution is therefore not disturbed from the Boltzmann and the electron decrease is thought to build up a positive space charge that shields the potential distortion within some Debye lengths. Taking the latter as the smallest characteristic distance, the sheath can be considered planar, thin and collisionless. However, the shielding is questionable to some extent because the ion distribution is distorted due to the wall losses (the ion impinges the negative wall where it is neutralized). The following quantities are used:

$$y=\frac{m_i \mathrm{v}_z^2}{2kT_\mathrm{e}} \qquad \chi=-\frac{eU}{kT_\mathrm{e}}$$
$$n_{\mathrm{e,i}}=\frac{N_{\mathrm{e,i}}}{N_\mathrm{o}} \qquad \xi=\frac{z}{\lambda_\mathrm{D}} \tag{B.1}$$

thus normalizing the kinetic and potential energies to the electron thermal energy (it is customary to attribute a minus sign to the reduced potential; also note that '‘potential'’ means here “potential energy”). The electron and ion densities with the charged particle density N_o (in contrast to the rest of this work, where lowercase n's are dimensioned quantities). The space coordinate z, oriented normally to the surface is normalized with the Debye length. In these units, the ion continuity equation is

$$n_\mathrm{i} y^{1/2}=y_\mathrm{o}^{1/2} \tag{B.2}$$

the ion energy conservation is

$$y=y_\mathrm{o}/\chi \tag{B.3}$$

the electron Boltzmann factor is

$$n_e = e^{-\chi} \tag{B.4}$$

and Poisson's equation is

$$\frac{d^2\chi}{d\xi^2} = n_i - n_e \tag{B.5}$$

with the zero subscript referring to the sheath edge (defined below) where the sheath merges into the neutral plasma region. Using (B.3) and (B.4) the ion density

$$n_i = \left(1 + \frac{\chi}{y_o}\right)^{-1/2} \tag{B.6}$$

can be inserted in Poisson's equation that, after multiplication by $d\chi/d\xi$ can be integrated with the boundary condition

$$\chi, \frac{d\chi}{d\xi} \xrightarrow[\xi \to -\infty]{} 0 \tag{B.7}$$

implying a potential distortion that tends to zero at the sheath edge. The first integration gives

$$\left(\frac{d\chi}{d\xi}\right)^2 = 4y_o\left[\left(1 + \frac{\chi}{y_o}\right)^{1/2} - 1\right] + 2(e^{-x} - 1) \tag{B.8}$$

The second integration has to be made numerically. The boundary condition (the wall potential $\chi(0)$ is not essential because involves only a shift of the potential curves because the equation is spatially homogeneous). The plot in Riemann's paper for the solution with $\chi(0)=10$ for different ion energies y_o shows that the boundary condition (B.7) is fulfilled only if $y_o > 0.5$. Smaller ion energies do not allow any shielding. This can be seen expanding (B.8) in Taylor's series for $\chi \to 0$,

$$\left(\frac{d\chi}{d\xi}\right)^2 = \left(1 - \frac{1}{2y_o}\right)\chi^2 + O(\chi^3) \tag{B.9}$$

Which contradicts equation (B.8) if $y_o < 0.5$. The condition $y_o \geq 0.5$, or explicitly

$$v_{oz}^2 \geq v_B^2 = \frac{kT_e}{m_i} \tag{B.10}$$

is the Bohm criterion (Bohm 1949). The physical picture follows ([46], pp292-4) from a plot of the electron ion densities. The electron density decreases exponentially with χ according to (B.4). The ion density also falls because ions are accelerated by the wall potential (ion acceleration at constant current density). The only way to maintain a positive charge sheath (i.e. $n_i > n_e$, see eq. (B.5)) is that the ion density decreases slower than the electrons when $\chi \to 0$. This occurs only for sufficiently fast ions fulfilling condition (B.10). This facet can be illustrated further by using equations (B.4) and (B.6) to write

$$\rho_o = \left(\frac{dn_i}{d\chi} - \frac{dn_e}{d\chi} \right)_{\chi=0} \geq 0 \tag{B.11}$$

From the linearization of Poisson's equation (B.5) at the sheath edge

$$\frac{d^2\chi}{d\xi^2} = \rho_o \chi, \quad \chi \to 0^+ \tag{B.12}$$

one observes that when $\rho_o > 0$ (Bohm's criterion fulfilled) the previously assumed exponential damped distortions of the potential which correspond to the Debye shielding are obtained. On the contrary, when $\rho_o < 0$ (Bohm's criterion not fulfilled) equation (B.12) provides only oscillatory solutions which contradict the boundary condition (B.7)

APPENDIX C - Abel inversion

1. The measured value at any point along the x=vt axis is the sum of the contributions arising from all the portions of the probe which are in the arc at the instant of time t=x/v. Each contribution is weighted with an unknown source function, which has to be determined. The assumption is that each of the individual contributions is uncorrelated to the neighboring.

$$f(x) = \int_{y_1}^{y_2} g(x,y)dy, \quad x \in [-x_R, x_R] \tag{C.1}$$

As such, the problem of inverting (C.1) is an integral problem.

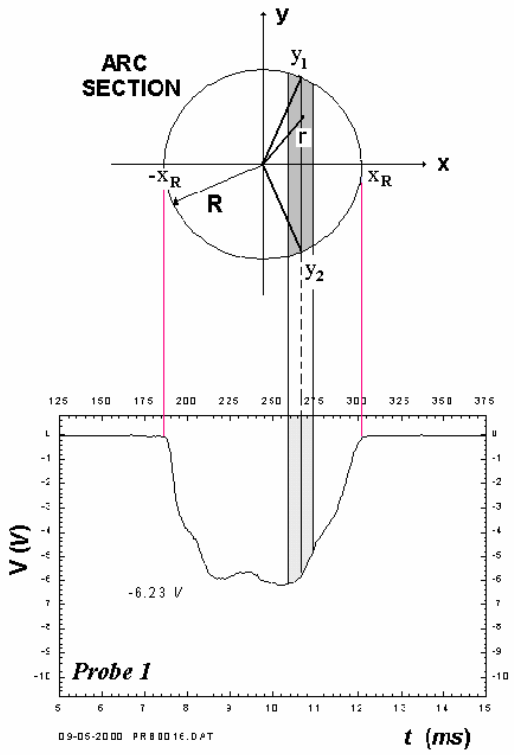

Figure C.1 Geometry of the Abel inversion. Upper, arc section, lower, generation of the of the signal value at time t = x/v.

Every point on the segment $[y_1, y_2]$ can be expressed in terms of the radius $r(x,y)$ at the point using

$$r^2 = x^2 + y^2, \quad y = \pm\sqrt{r^2 - x^2}, \quad dy = \pm\frac{rdr}{\sqrt{r^2 - x^2}} \tag{C.2}$$

where the plus sign is chosen for the upper quadrants. Upon conditions of cylindrical symmetry, using (C.2) in (C.1) gives

$$f(x) = 2\int_x^R \frac{rg(r)dr}{\sqrt{r^2 - x^2}} \tag{C.3}$$

and the problem involves the determination of the radial function $g(r)$ on the interval $[x,R]$.

Different formulae exist for the inversion of equation (C.3). The one employed by Nestor and Olsen is

$$g(r) = -\frac{1}{\pi}\int_r^R \frac{1}{\sqrt{x^2 - r^2}}\frac{df(x)}{dx}dx \tag{C.4}$$

2. Method of Nestor and Olsen [5]

The interval $[-x_R, x_R]$ is divided into N zones of length a with

$$x_k \le x \le x_{k+1}, \quad x_k = ka, \quad k = 1, 2, ...N \tag{C.5}$$

Upon the transformation $\begin{cases} u = x^2 \\ \mathrm{v} = r^2 \end{cases}$ equation (C.4), changes into

$$g(v) = -\frac{1}{\pi}\int_{\mathrm{v}}^{R^2} \frac{1}{\sqrt{u - \mathrm{v}}}\frac{dI(u)}{d\mathrm{v}}du \tag{C.6}$$

Dividing the integral in sub-integrals over each zone and assuming $I(u) = A + Bu$

$$g_k = -\frac{1}{\pi}\sum_{n=k}^{N-1}\frac{dI(u)}{du}\int_{(an)^2}^{[a(n+1)^2]}\frac{du}{\left[u-(ak)^2\right]^{1/2}},\quad \frac{dI(u)}{du}=\frac{f_{n+1}(u)-f_n(u)}{\left[a(n+1)^2\right]-(an)^2} \tag{C.7}$$

The discrete values of the inverted function are

$$g_k = -\frac{2}{\pi a}\sum_{n=k}^{N-1}A_{k,n}\left[f_{n+1}(x)-f_n(x)\right] \tag{C.8}$$

With

$$A_{k,n}=\frac{\left[(n+1)^2-k^2\right]^{1/2}-(n^2-k^2)^{1/2}}{2n+1} \tag{C.9}$$

The subtraction between adjacent points implied in (C.7) can be avoided by using the matrices B defined as

$$B_{k,n}=\begin{cases}-A_{k,k}, & n=k\\ A_{k,n-1}-A_{k,n}, & n\neq k\end{cases} \tag{C.10}$$

and the inverted function is

$$g_k(r) = -\frac{2}{\pi a}\sum_{k}^{N}B_{k,n}f_n(x) \tag{C.11}$$

This is the version ("Nestor-Olsen B") used in this work. The step *a* has been chosen equal to the spatial distance corresponding to the time interval between *subsequent* experimental points, $\delta\tau$=0.02 *ms*, *a*=v·$\delta\tau$=100.4 μ*m* where v=5.02 *m/s* is the probe velocity considered throughout the experimental data presented.

APPENDIX D - Equipotential probes

Each instantaneous value of the current $I(t)$ forming the peak is made of the contributions of charges propagating on the conductor surface along the probe direction (y) when the latter is at a given position within the arc.

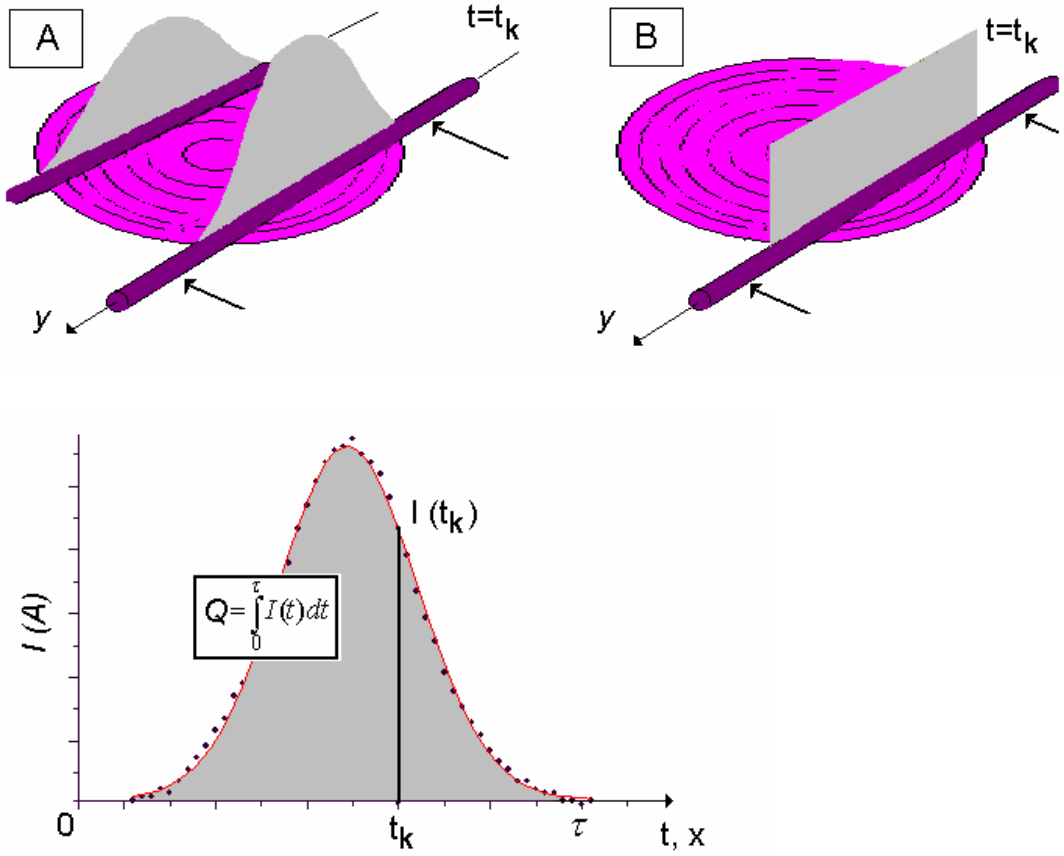

Figure D.1, up, formation of individual current values $I(t_k)$ along the probe length (coordinate y). A represents the hypothesis of structured potential, V=V(y). B, corresponds to the hypothesis of uniform (equipotential) probe. Lower part, the complete peak, with its total area equal to the charge collected by the probe after the arc crossing

By definition if v_d is the surface carrier drift velocity (assumed constant around its mean value, $v_d \equiv \langle v_d \rangle$), the current is $I(t) = nev_d$. Its instantaneous (and measured) value at the time $t_k \in [0, \tau]$ is determined by the distribution of charge carriers on the conductor surface [n in this paragraph]

$$I(t_k) = ev_d \int_0^u n(y)dy, \quad y \in [0,u] \qquad \text{(D.1)}$$

Neither of the two cases labelled A or B in figure D.1 is distinguishable by using the measured current or from the total charge collected. Case 'A' corresponds to the hypothesis of structured voltage along the probe, 'B' corresponds to the hypothesis of uniform potential (equipotential probe). Because of Ohm's law, $\rho = RS/l$ and $J = I/S$, assuming for simplicity constant resistance, we have $i = El/R$ so that the elementary current along the probe is

$\delta i = e\mathrm{v}_\mathrm{d} n(y)dy = E(y)\delta y / R$

and the field is

$$E(y) = e\mathrm{v}_\mathrm{d} R n(y) \qquad \text{(D.2)}$$

Because v_d, R and $n \neq 0$ then also $E \neq 0$ (as required by the existence of a current). Therefore, assuming a conservative field, $E = -\nabla V$ and

$$V = -\int_0^u \nabla V dy = -e\mathrm{v}_\mathrm{d} R \int_0^u n(y)dy \qquad \text{(D.3)}$$

which can be uniform along the probe, $V(y)$=const, only if n is uniform, in which case the probe is equipotential. Otherwise one must have $V=V(\mathrm{y})$. This means that the distribution of the potential along the probe is determined by the distribution of charge carriers on the probe surface. The question posed in the main text can be restated asking whether/how the charge carrier distribution on the probe surface is influenced by the distribution of the impinging particles from the plasma.

APPENDIX E – Error Analysis

When possible, the errors were propagated by the use of the exact theory of error (section E.2). However, when analytical relationships were not available or the degree of accuracy was difficult to evaluate, the more conservative approximate theory has been employed (section E.1).

E.1. Approximate error estimation

A quantity $c = a \pm b$ with δa and δb as absolute errors, is subject to an absolute error (upper limit)

$$\delta c \approx \delta a + \delta b \tag{E.1}$$

For $c = a\,b$ or $c = a / b$ an upper estimation for the relative error on c is

$$\delta c / c = \delta a / a + \delta b / b \tag{E.2}$$

The current density

$$j = I / S(z) \tag{E.3}$$

where $S(z)$ is the arc sectional area at height z given by

$$S(z) = \pi R_{arc}^2 (z) \tag{E.4}$$

and $R(z)$ is the arc *electrical radius* (defined in the text) given by the product of probe (central) velocity and the peak duration τ

$$R(z) = \mathrm{v}\tau \tag{E.5}$$

The probe (central) velocity is computed as

$$\mathrm{v} = 2\pi R_{\mathrm{path}} / T \tag{E.6}$$

in which R_{path} is the path radius, i.e. the distance from the centre of the probe disk to the centre of the arc (cathode tip position). T is the time period of the set of peaks.

The maximum (axial) electric field was considered in text

$$E_{\max} = -\nabla V_{\max} \tag{E.7}$$

where the uncertainty on V_{max} has been established from the standard deviation of the mean of a population of voltages belonging to each peak at the 4% level. This is higher than the average uncertainty on the single measurement as given by the instrumental

resolution at 12 bit (4.88 *mV*) and of the same order of magnitude (or slightly bigger) than the circuitry contact resistances that sum up to few *m*Ω.
The error on the field can be obtained by a discretization of the field variability (along the height points z_k) and the use of the elementary theory of errors, yield the absolute error for the field E_i at height z_i

$$\delta E_i \sim 2E_i\left(\frac{\delta V}{V_i - V_{i-1}} + \frac{\delta z}{z_i - z_{i-1}}\right) \qquad \text{(E.8)}$$

In Table E.1 the uncertainties for the 'primary' (i.e. measured) quantities are reported, some of which deserve comment. The peak duration uncertainty reflects the degree of arbitrariness in the edge-cut criterion (typical peak durations vary from 3 to 6 *ms* depending on conditions. Each peak is made of about 200 experimental points).
The time period (interval between homonymous peaks in a data-set) is the arithmetic average of 5 to 10 data-set values obtained under the same experimental conditions.
The probe height has been measured with a micrometric device with a 0.01 *mm* uncertainty. The positioning of each individual probe and its 'degree of straightness' were evaluated using the same instrument and are of the same order of magnitude; contributing to an overall uncertainty in z of ±0.02 *mm*.

Quantity - symbol	Experimental uncertainty
Peak time duration τ (*ms*)	$\delta\tau = \pm 0.1$ *ms*
Time period *T* (*ms*)	$\delta T = \pm 1$ *ms*
probe (central path) R_{path}(*mm*)	$\delta R_{path} = \pm 0.1$ *mm*
probe heights *z* (*mm*)	$\delta z = \pm 0.02$ *mm*
Total arc current I_t (*A*)	$\delta I_t = \pm 1$ *A*
Probe radius	$2r_p$=0.25 *mm* (±5% ∅) $\delta r_p / r_p$=2.5%

Table E.1.1. Uncertainties for primary quantities (as measured)

E.2 Constants and truncation used

Several physical constants are used throughout this work. These are assumed free of error in the sense that the accuracy given in the updated sources of references are beyond the accuracy attainable within the present work. This also means that the multiplication/division of these constants by very small/very big numbers is assumed negligible on the final result. This is obviously incorrect, but the following example clarifies the problem and the choices made here. An evaluation of the floating potential by means of formula

$$V_f = -\frac{kT_e}{e}\ln\left(\sqrt{\frac{m_i}{m_e}}\right) = -\frac{1.38\cdot10^{23}T_e}{1.60\cdot10^{-19}}\ln\left(\sqrt{\frac{6.64\cdot10^{-26}}{9.11\cdot10^{-31}}}\right) = -4.828562\cdot10^{-4}T_e$$

implies the comparison of mi with m_e; so the m_i used should retain as many digits as the minimum digit in m_e in order to compare the two numbers down to the same least significant digit. So, would the constants used have indicated with more significative digits, for example as in the following (where also k and T have been increased by 1 digit)

$$V_f = -\frac{kT_e}{e}\ln\left(\sqrt{\frac{m_i}{m_e}}\right) = -\frac{1.380\cdot10^{23}T_e}{1.602\cdot10^{-19}}\ln\left(\sqrt{\frac{6.63478\cdot10^{-26}}{9.1\cdot10^{-31}}}\right) = -4.822668\cdot10^{-4}T_e$$

The difference between the two is about $2\cdot10^{-5}$, corresponding to an uncertainty of
But the temperature may be determined at best with a 5% uncertainty, so for a T=15,600 K, the first formula would give V_f = -7.52336208 V whereas the second gives V_f =- 7.5296208 V with a difference of 6 mV corresponding to the 0.08%, which is well within this limit. Therefore, truncating the two at the second digit after the point, gives 7.52 V in the first and 7.53 V in the second, a mere 0.1%. A comparison with the typical uncertainty of the experimental probe voltages used jointly with V_f , about 1 to 2% (see next paragraph) reveals that it would be meaningless to search for a higher accuracy by including more significant digits. With this respect, the two versions of the above formula are considered equivalent. Consequently, the practical choice has been to 1) use the constants in a 'sensible manner', as done above when comparing the masses (and in general greatly different numbers) truncating the bigger quantity at the least significant digit used for the smaller (as in the second case shown) but 2) for the rest of the cases, by taking usually not more than three digits after the point.

Name	Symbol Value
Electric charge	e=1.602·10^{-19} C
Electron mass	m_e=9.11·10^{-31} kg
Boltzmann constant	k=1.38·10^{-23} J/K
Argon Ion mass	m_i=6.63478·10^{-26} kg

Table E.1.2 Constants used (see text for discussion of choice of digits)

2. Some transport properties are determined via the use of Olsen's thermal equilibrium $n(T)$ data presented in Chapter 1. Since no explicit formulation for the latter is possible, we assume the values of n ‘exact’ within the limitation of Olsen's determination. However, the following relationship is used for the determination of the ion mobility in CFF's model (Chapter 5)

$$\mu_i = \frac{eD}{kT} = \frac{e\lambda v}{3kT} = \frac{e\lambda}{3}\sqrt{\frac{2}{m_i kT}} \qquad \text{(E.9)}$$

So that since the temperature must be evaluated with its error. The current CFF's formula may be inverted for the temperature

$$\sqrt{T_e} = \frac{1}{n\lambda}\left(\frac{I}{a}\right)K,$$

where K includes the numerical constants. In other words, while an error on the mobility or on the mean free path (*cf* 1.18) is not evaluated explicitly, the error induced on the temperature via the current formula is propagated on the final temperature.

E.3 Exact formulation

The relationships used in the following assume gaussian distribution for the uncertainties of all the parameters involved. The formulae for the error propagation of the observable $f = f(x_1, x_2, ...x_n)$ are based on the total derivative formulae

$$\delta f = \sqrt{\sum_{k=1}^{n}\left(\frac{\partial f}{\partial x_k}\right)^2 (\delta x_k)^2}, \quad k = 1, 2, 3, ..., n \qquad \text{(E.10)}$$

This is applied to the formulae for the temperatures determined by inversion of the ion saturation current formulae. As mentioned in the previous section, the fundamental physical constants are assumed 'exact' within the choice made for the digits. The parameters are evaluated using the table containing the uncertainty on the primary measured quantities.

Measured voltage

The measured probe voltage is subject to an uncertainty of 1%.

Measured current

The probe current is measured by reading the voltage across the load resistor R_L which has a 1% tolerance (*cf* chapter 7), therefore a 1.4% error is found on the read current arising from the equal 1% contribution of voltage and read-out resistance.

Inverted current

There are no simple relationships between measured and inverted quantities for all the data points. A possible evaluation would be based on the formula obtained by propagating the errors on relationship (13) reported in appendix B and then evaluating the

error for some typical *k*'s. Alternatively, one can think of the determination of the inverted current as a counting problem (where each bin is determined by the spatial resolution) and take the corresponding error on the bin as the square root of the number of counts, e.g. assuming a Poisson model. This is not strictly correct, because this inverted current is then treated as a primarily measured quantity, but the magnitude of the error obtained this way is within a unit of the previous (and more complicated) method so that this simpler technique can be used for checking purposes. Using the former method, an error of 3.2 to 4.8% is obtained for some sampled values, whereas the latter simpler method gives 5% which can be considered as upper limit.

Temperatures by inversion of current formulae

Two kinds of current formulae were used for the determination of the temperature; the first is the random group, of the form

$$I = C\sqrt{T} \Rightarrow T = \left(\frac{I}{C}\right)^2$$

The second is the CFF group, of the form

$$I = CT \Rightarrow T = \frac{I}{C}$$

In the first case, the knowledge of the relative error on I and use of relationship (E.9) allows to write

$$\frac{\delta T}{T} = 2\frac{\delta I}{I}$$

Whereas in the second case

$$\frac{\delta T}{T} = \frac{\delta I}{I}$$

This obviously implies that the temperatures of the first group are less accurate than the ones obtained for the CFF family. However, as discussed in the text, in the latter determination (e.g. the electric current for the table) a further dependency on the mobility is present. An initial estimate purely based on the accuracy of the non inverted current would lead to an error of 2%. This is an upper limit because of the use of (E.2) instead of the exact (E.10). However, the discussion of the error on the inversion procedure mentioned above shows that 5% should be taken as the *lower* limit for the error on the temperatures from probes. Obviously, this does not include any quantitative judgment about the accuracy of the formula in describing the ‘correct’ physical picture.

Electric field

Differentiation of the probe potential or of the plasma potential with somewhat scattered data makes the evaluation of the quantity and of its error uncertain. The first method, based on the measured probe potential, uncertain to 1%, is more accurate than the second (when correct) whereas the second requires introduction of the floating potential, in turn determined through the temperature. Because the uncertainty on the latter largely dominates, the error for the second determination is much higher; using pure statistics a 5% standard deviation of the mean occurs. This is in broad agreement with, the correlation coefficient for the fit from which the quantity was determined, typically around 95%.

The determination of the electric field uncertainty based on the plasma potential (*cf* chapter 12) of chapter 11 from the measured probe potential and the temperature obtained in chapter 11

$$V_{\mathrm{pl}} = V_{\mathrm{prb}} - V_{\mathrm{f}} = V_{\mathrm{prb}} - \frac{kT_{\mathrm{e}}}{e}\ln\sqrt{\frac{m_{\mathrm{i}}}{m_{\mathrm{e}}}}$$

suffers from an uncertainty on the latter

$$\delta V_{\mathrm{pl}} = \sqrt{\left(\delta V_{\mathrm{prb}}\right)^2 + \left(\frac{k}{e}\ln\sqrt{m_{\mathrm{i}}/m_{\mathrm{e}}}\right)^2 \left(\delta T\right)^2} = \sqrt{\left(\delta V_{\mathrm{prb}}\right)^2 + 2.32\cdot 10^{-7}\left(\delta T\right)^2}$$

composed of the 1% on the measured potential and the 5% on the temperature

$$\delta V_{\mathrm{pl}} = \sqrt{\left(0.01 V_{\mathrm{prb}}\right)^2 + 2.32\cdot 10^{-7}\left(0.05 T\right)^2} = \sqrt{10^{-4} V_{\mathrm{prb}}^2 + 5.8\cdot 10^{-10} T^2}$$

and for, say, $V_{\mathrm{prb}} = 5\ V$ and T=10,000 K,

$$\delta V_{\mathrm{pl}} = 0.25\ V \Rightarrow \delta V_{\mathrm{pl}}/V_{\mathrm{pl}} = \frac{0.25}{5} = 4.9\%$$

Therefore for the field (E.2) gives

$$\frac{\delta E_i}{E_i} \approx \left(\frac{\delta V_{\mathrm{pl}}}{V_{\mathrm{pl}}} + \frac{\delta \mathrm{z}}{\mathrm{z}}\right) = 5.6\%$$

for the same plasma potential value and a probe height of 3 *mm* (typical location for this measured probe voltage at 50 *A*). This is the order of magnitude of the error for fields determined from the derivative of the plasma potential. (The approximate (E.2) form has been used since no direct functional dependency of E on the height has been used in the text, unless one uses the fits shown in section 12.6).

Current density

Both the ion and electron current densities suffer from the error on the measured ion current (relative error ~ 5%) and on the uncertainty on the geometrical factors, namely the probe radius:

$$j = \left(\frac{I}{a}\right)\frac{a}{2\pi r_p a} \tag{E.11}$$

Therefore, propagating according to (E.10)

$$\delta j = \sqrt{\left(\frac{\partial j}{\partial (I/a)}\right)^2 \left(\delta (I/a)\right)^2 + \left(\frac{\partial j}{\partial r_p}\right)^2 \left(\delta r_p\right)^2} =$$

$$= \sqrt{\left(\frac{1}{2\pi r_p}\right)^2 \left(\delta (I/a)\right)^2 + \left(\frac{I}{a}\frac{1}{2\pi r_p^2}\right)^2 \left(\delta r_p\right)^2} \approx$$

$$\approx \sqrt{1.6\cdot 10^6 (0.05)^2 + \left(\frac{I}{a}\right)^2 10^{14} (0.025 r_p)^2} \approx$$

$$\approx \sqrt{4\cdot 10^3 + 1\cdot 10^3 \left(\frac{I}{a}\right)^2}$$

where an uncertainty of 2.5% for the probe radius has been taken (Table E.1) and of 5% for the read current per unit length. It is clear that the dominant factor is the uncertainty on the probe radius Assuming a current per unit length between 10 *A/m*, typical for the arc fringes or low z probes at 50 *A*, and 380 *A/m*, at axial positions for the 200 *A* case, the magnitude of the uncertainty on the measured ion and electron current density is 452 A/m^2 and ~$1.2\cdot 10^4$ A/m^2 respectively.

E.4 Non-parallelism error

In the text it was stated that probe lengths of up to 70 *mm* were used. This length adds to the probe disk radius bringing the probe centre to 90 or 100 *mm* from the disk centre. This might still be an appreciably short distance when compared to arc radii which extend up to 15 *mm* (see figure E.1).

The probe path at the distance R from the disk centre is $l=R\alpha$, while the assumed rectilinear path is $l_r=2R_{arE.}$ The relationship between path radius R and arc radius R_{arc} is (see fig. E.1)

$$\tan\frac{\alpha}{2} = \frac{R_{arc}}{R} \tag{E.12}$$

Therefore, l_r=2R tan (α/2) and the ratio of the two paths is $\rho = 2(\tan(\alpha/2)/\alpha$, which varies from 1 at distances R - R_{arc} , reaches its maximum at R and decreases back to 1 at distances R + R_{arc} (see figure E.1). The assumption made in the text corresponds instead to the approximation 2 $R_{arc} \approx \alpha R$.
Referring only to the *central* path (where the discrepancy is maximum), with the values reported in the text (R_{arc} from 5 to 15 *mm* and R up to 100 *mm*) this ratio varies from ρ= 1.002 when R_{arc} = 5 *mm* to ρ=1.01 when R_{arc} =15 *mm*. This factor should be applied to correct each radius measurement.

The problem becomes more complex when dealing with *local* quantities, in which case every point along the time axis is the sum of contributions from a virtually infinite number of different paths.

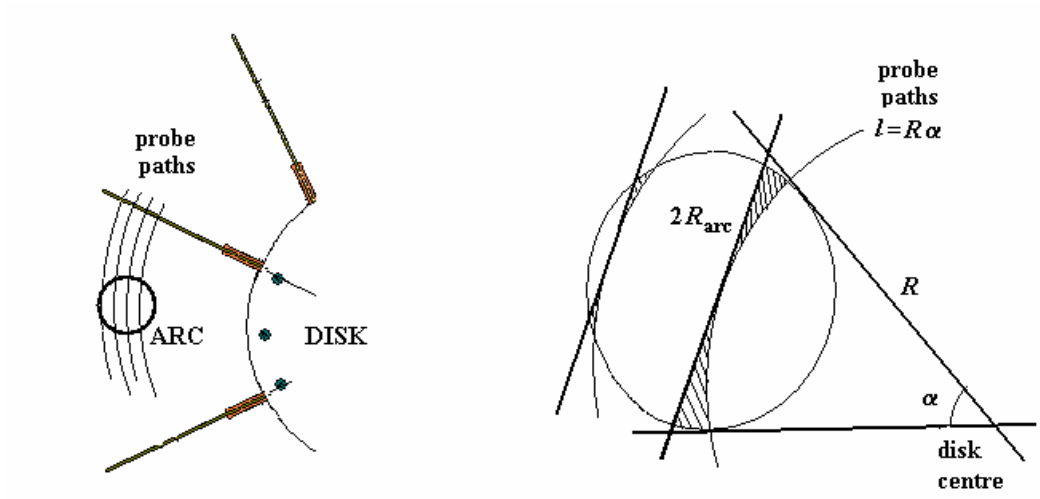

Figure E.1 Illustrating the non-parallelism error

APPENDIX F – UNITS

SI units are used throughout this work. However as customary in atomic and plasma physics, it is useful to express the temperature T in electron-volt (eV) through the relationship

$$1\ eV = 1.602 \cdot 10^{-19} J \qquad \text{(F.1)}$$

The Boltzmann constant is

$$k\ = 1.3807 \cdot 10^{23}\ J/K = 8.6142 \cdot 10^{-5}\ eV/K$$

From kinetic energy of a particle, $E = kT$, the temperature in atomic units reads

$$T = \frac{1\ eV}{8.6142 \cdot 10^{-5}\ eV/K} = 11,608.74 \approx 11,609\ K \qquad \text{(F.2)}$$

Therefore the energy of $1eV$ averaged over an ensemble of particles, *corresponds* to a temperature T=11,609 K.

REFERENCES

1. Lancaster, J.F., *The physics of welding*. 1983, Oxford: Pergamon Press.
2. Fauchais, P., Vardelle A., *Thermal plasmas.* IEEE Transactions on Plasma Science, 1997. **25**(6): p. 1258.
3. Schmidt, G., *Physics of high temperature plasmas*. 1966, New York: Academic Press.
4. Boyd, T.J.M., Sanderson, J.J., *Plasma dynamics*. 1969, London: Nelson.
5. Roberts, P.H., *An introduction to magnetohydrodynamics*. 1967, London: Longmans.
6. Shercliff, J.A., *A textbook of magnetohydrodynamics*. 1965, London: Pergamon press.
7. Alfven, H., Fälthammar, C.G., *Cosmical electrodynamics*. 1963, London, New York: Oxford University Press.
8. Clayton, D.D., *Principles of stellar evolution and nucleosynthesis*. 1983, N.Y. - London: The University of Chicago press.
9. Raizer, Y.P., *Gas discharge physics*. 1997, Berlin, Heidelberg: Springer.
10. Franklin, R.N., *Plasma phenomena in gas discharges*. 1976, Oxford: Clarendon Press.
11. Heimann, H.B., *Plasma spray coatings*. 1996, Weinheim: VCH.
12. Manos, D.M., Dylla, H.F., ed. Plasma etching, an introduction, ed. D.M. Manos, D.L.Flamm. 1989, Academic Press.
13. Liebermann, M.A., Lichtenberg, A. J., *Principles of plasma discharges and material processing*. 1994: John Wiley, N. Y.
14. Allum, C.J., *Power dissipation in the column of a TIG arc.* Journal of Physics D: Applied Physics, 1983. **16**: p. 2149-2165
15. Zhu, P., Lowke, J.J., Morrow, R., *A unified theory of free burning arc, cathode sheaths and cathodes.* Journal of Physics D: Applied Physics, 1992. **25**: p. 1221-1230.
16. Sansonnes, L., Haidar, J., Lowke JJ., *Prediction of properties of free burning arcs including effects of ambipolar diffusion.* Journal of Physics D: Applied Physics, 2000.
17. Wiese, W.L., ed. *Electric arcs*. Methods of experimental physics, atomic and electron physics, ed. L. Marton. Vol. 7, Part B. 1968, London, N.Y.: Academic press.
18. Roth, J.R., *Industrial plasma engineering, vol.1: Principles*. 1995, Bristol-Philadelphia: IOP Publishing.
19. Rethfeld, J., Wendelsdorf, T., Simon, G., *A self-consistent model for the cathode fall region of an electric arc.* Journal of Physics D: Applied Physics, 1996. **29**: p. 121-128.
20. Lowke, J.J., Kovyta, P., Schmidt, H.P., *Theory of free-burning arc columns including the influence of the cathode,.* Journal of Physics D: Applied Physics, 1985. **18**: p. 53.
21. Hemmi, R., Yokomizu, Y., Matsumura, T, *Anode-fall and cathode-fall voltages of air arc in atmosphere between silver electrodes,* Journal of Physics D: Applied Physics, 2003. **36**: p. 1097-1106
22. Thornton, M.F., *Spectroscopic determination of temperature distributions for a TIG arc*. 1993, Cranfield University.
23. Goodarzi, M., Choo R., Takasu T., Toguri, James M., *The effect of the cathode tip angle on the gas tungsten arc welding and welding pool I: Mathematical model of the arc.* Journal of Physics D: Applied Physics, 1997. **30**: p. 2744-2756.

24. Casado, E., Colomer, V., *The numerical modelling of joule heating effects in thoriated tungsten cathodes of high current arcs.* Journal of Physics D: Applied Physics, 2000. **33**: p. 1342-1347.

25. Nestor, O., *Heat intensity and current density distributions at the anode of high current inert gas arcs.* Journal of Applied Physics, 1962. **33**(5): p. 1638-1648.

26. Schoeck, P.A., *An investigation of the anode energy balance of high intensity arcs in argon.* In Modern Developments in heat transfer, W. Ibele (ed.), Academic Press 1963. p. 353-400.

27. Quigley, M.B.C., Richards, P.H., Swift-Hook, D.T., Gick, A.E.F., *Heat flow to the workpiece from a TIG welding arc.* Journal of Physics D: Applied Physics,, 1973. **6**: p. 2250-2258.

28. Richardson, I.M., *Charge capture and anode fall structure in high pressure arc discharge*. 1999, EPSRC Grant N. GR/RB 2648/01.

29. Golant, V.E., Zilinskij, A.P., Sacharov, S.E., *Fondamenti di fisica dei plasmi*. 1983: MIR Moscow-ER Rome (Italian translation).

30. Cambel, A.B., Duclos, D. P., Anderson, T.P., *Real gases*. 1963, London New York: Academic press.

31. Goldbach, C., Nollez, G., Popovic, S., Popovic, M., *Electrical conductivity of high pressure ionized argon.* Z. Naturforsch, 1978. **33a**: p. 11-17.

32. Devoto, R.S., *Transport coefficients of ionized argon.* Physics of Fluids, 1973. **16**(5): p. 616-623.

33. Phelps, A.V., *Momentum-transfer cross sections for slow electrons in he, ar, kr, and xe from transport coefficients.* Physical Review, 1964. **136**(6A): p. A-1538-45.

34. Brown, S.C., *Basic data for plasma physics*. 1959, New York: J.Wiley.

35. Frost, L.S., Phelps, A.V., *Momentum transfer cross sections for slow electrons in He, Ar, Kr, and Xe from transport coefficients.* Physical Review, 1964. **136**(6A): p. A1538-1545.

36. Cambel, A.B., Duclos, D. P., Anderson, T.P., *Plasma physics and magnetofluidmechanics*. 1963, New York: McGraw-Hill.

37. Chung, P.M., Talbot, L., Touryan, K.J., *Electric probes in stationary and flowing plasmas: Theory and application*. 1975, N.Y.: Springer.

38. Spitzer, L., *Physics of fully ionized gases*. 1956, New York: Interscience.

39. Olsen, H.N., *Thermal and electrical properties of an argon plasma.* The Physics of Fluids, 1959. **2**(6): p. 614-623.

40. Drellishack, K.S., Knopp, C.F., Cambel, Ali Bulent, *Partition functions and thermodynamic properties of argon plasma.* The Physics of Fluids, 1963. **6**(9): p. 1280-1288.

41. Pateyron, M., Elchinger, F., Delluc, G. Fauchais P., *Thermodynamic and transport properties of Ar-H_2 and Ar-He plasma gases used for spraying at atmospheric pressure. I: Properties of the mixtures.* Plasma Chemistry and Plasma Processing, 1992. **12**(4): p. 421-448.

42. Günther, K., Popovic, M.M., Popovic, S.S., Radtke, R., *Electrical conductivity of highly ionized dense hydrogen plasma: Ii. Comparison of experiment and theory.* Journal of Physics D: Applied Physics, 1976. **9**: p. 1139-1147.

43. Günther, K., Lang, S., Radtke, R., *Electrical conductivity and charge carrier screening in weakly non-ideal argon plasmas.* Journal of Physics D: Applied Physics, 1983. **16**: p. 1235-1243.

44. Murphy, A.B., *Transport coefficients of helium and argon-helium plasmas.* IEEE Transactions on Plasma Science, 1997. **25**(5): p. 809-814.

45. Chen, F.F., *Introduction to plasma physics and controlled fusion, vol. 1: Plasma physics*. 1984, New York, London: Plenum Press.

46. Fanara, C., *Langmuir probe in atmospheric arc plasmas: A review, technical report N.2, June*. 2001, Cranfield University.

47. Frost, L.S., *Conductivity of seeded atmospheric pressure plasmas.* Journal of Applied Physics, 1961. **33**(10): p. 2029-2036.

48. Murphy, A.B., Arundell, C.J., *Transport coefficients of argon, nitrogen, oxygen, argon-nitrogen, and argon-oxygen plasmas*, Plasma Chemistry and Plasma Processing, 1994. **14**: p. 451-490.

49. Murphy, A.B., *Private communication.* 2000.

50. Von Engel, A., *Ionized gases*. 1965, Oxford: Clarendon Press.

51. Loeb, J., *Fundamental processes of electric discharges in gases*. 1947: J. Wiley & sons, New York, London.

52. Davydov, A., *Über die Geschwindigkeitsverteilung der sich im elektrischen Felde bewegenden Elektronen.* A.Physik. Zeitschrift der Sovjetunion, 1935. **8**: p. 59-70.

53. Fanara, C., *Atmospheric plasma physics for material processing, part I.* 2000, Cranfield University: Cranfield.

54. Kovyta, P., Lowke J.J., *Two-dimensional analysis of free burning arcs in argon.* Journal of Physics D: Applied Physics, 1985. **18**: p. 53-70.

55. Kovyta, P., Cram, Journal of Physics D: Applied Physics, 2000. **33**.

56. Fuhs, A.E., *Instrumentation for high speed plasma flow*. 1965, New York, London, Paris: Gordon and Breach Science Publisher.

57. Allum, C.J., *Gas flow in the column of a TIG welding arc.* Journal of Physics D: Applied Physics, 1981. **Vol.14**: p. 1041-1059.

58. Tritton, D.J., *Physical fluid dynamics*. 1988, Oxford: Clarendon Press.

59. Burm, K.T.A.L., Goedheer, W.J., Schram, D.C., *Mach numbers for gases and plasmas in a convergent-divergent cascaded arc.* Physics of Plasmas, 1999. **6**(6): p. 2628-35.

60. Massey, B.S., *Mechanics of fluids*. 1979, New York: Van Nostrand Reinhold.

61. Bird, G.A., *Molecular gas dynamics and the direct simulation of gas flows*. 1994, Oxford: Clarendon Press.

62. Gick, A.E.F., Quigley, M.B.C., Richards, P.H., *The use of electrostatic probes to measure the temperature profiles of welding arcs.* Journal of Physics D: Applied Physics, 1973. **6**: p. 1941.

63. Allum, C.J., Metcalfe, J.C., Quigley, M.B.C, *A modified low pressure probe theory applied to measurement of temperature profiles in plasma welding*. 1977: CEGB Rep. N. R/MN925.

64. Dowden, J., Kapadia, Phiroze, Fenn, Bob, *Space charge in plasma arc welding and cutting.* Journal of Physics D: Applied Physics, 1993. **26**: p. 1215-1223.

65. Swift, J.D., Schwar, S., *Electrical probes for plasma diagnostics*. 1970, London: Iliffe.

66. Boulos, M.I., *Thermal plasma processing.* IEEE Transactions on Plasma Science, 1991. **19**(N.6).

67. Fournier, K.B., Cohen, M., May, M.J.,Goldstein, W. H., Atomic Data and Nuclear Data Tables, Table I, 1998. **70**(2): p. 231-54.

68. Blum, W., Rolandi, L., *Particle detection with drift chambers*. 1994, Berlin: Springer, p.56.

69. Ellis, H.W., Thackston, M.G., McDaniel, E.W., Mason, E. A., *Transport properties of gaseos ions over a wide energy range, part iii.* Atomic and Nuclear Data Tables, 1984. **31**: p. 113-151.

70. Takeda, S., *Swarm and plasma parameters.* Journal of the Physical society of Japan, 1990. **59**(10): p. 3435-3438.

71. Mott-Smith, H.M., Langmuir, I., *The theory of collectors in gaseous discharge.* Physical Review, 1926. **28**: p. 727.

72. Su, C.H., Kiel, R.E., *Continuum theory of electrostatic probes.* Journal of Applied Physics,, 1966. **37**(13): p. 4907.

73. Su, C.H., Lam, S.H., *Continuum theory of spherical electrostatic probes.* The Physics of Fluids, 1963. **6**(10): p. 1479.

74. Su, C.H., Sonin, A.A., *Theory of the electrostatic probe in a moderately ionized gas.* The Physics of Fluids, 1967. **10**(1): p. 124a.

75. Kiel, R.E., *Continuum electrostatic probe theory for large sheaths on spheres and cylinders.* Journal of Applied Physics, 1969. **40**(9): p. 3668.

76. Thomas, D.L., *Electrostatic probe in a flowing continuum plasma.* Electronics Letters, 1969. **5**(15): p. 341.

77. Thomas, D.L., *Continuum theory of cooled spherical electrostatic probes.* The Physics of Fluids, 1969. **12**(2).

78. Clements, R.M., Rizvi, S.A.H., Smy, P.R., *Langmuir probe characteristic in a high pressure plasma in the presence of convection and ionization,*IEEE Transaction on Plasma Science, 1994. **22**(4): p. 435.

79. Clements, R.M., Smy, P.R., *Langmuir probe measurement of electron temperature in high-pressure plasmas.* ournal of Applied Physics, 1973. **44**(8): p. 3550-6.

80. McLatchy, C.S., Smith, H.C.L., *The electron current to a Langmuir probe in a flowing high-pressure plasma.* IEEE Transactions on Plasma Science, 1991. **19**(6): p.1254-1258.

81. Dawe, J., Rizvi, Syed A.H., Smy, *Electron current to a cylindrical probe in a moving high pressure plasma.* IEEE Transactions on Plasma Science, 1993. **21**(1): p.202-207..

82. Clements, R.M., Oliver, B.M., Smy, P.R., *Pulsed spherical probe measurements of plasma conductivity in a flowing continuum plasma.* Journal of Physics D: Applied Physics, 1977. **10**: p. 2213-2224.

83. Carrer, G.F., Fendell, F.E., *Electrostatic probe in reacting gas.* The Physics of Fluids, 1970. **Vol. 13**(N. 12): p. 2966-2982.

84. Smy, P.R., *The use of Langmuir probes in the study of high pressure plasmas,* Advances in Physics, 1976. **25**: p. 517-553.

85. Cobine, J.B., *Gaseous conductors*. 1958, New York: Dover.

86. Schott, L., ed. *Electric probes*. Plasma diagnostics, Chapter 11, W.Hochte-Holtgreven (Eds.) 1968, Amsterdam: North-Holland.

87. Godyak, V.A., Sternberg, N., *Smooth plasma-sheath transition in a hydrodynamic model.* IEEE Transaction on Plasma Science, 1990. **18**(1): p. 159.

88. Kagan, Y.M., Perel, V.I., *Probe methods in plasma research.* Soviet Physics Uspekhi, 1964: p. 767-793.

89. Langmuir, I., Blodgett, K. B., *Currents limited by space charge between coaxial cylinders.* Physical Review, 1923. **22**: p. 347.

90. Das, G.C., Bornali Singha, Joyanti Cuhtia, *Characteristic behaviour of sheath formation in thermal plasma.* Physics of Plasmas, 1999. **6**(9): p. 3685.

91. Clements, R.M., Smy, P.R., *Langmuir probe measurement of electron temperature in a flowing high-density plasma.* Electronics Letters, 1970. **6**(17): p. 538.

92. Riemann, K.U., *The Bohm criterion and sheath formation.* Journal of Physics D: Applied Physics, 1991. **24**: p. 493-518.

93. Riemann, K.U., *The Bohm criterion and boundary conditions for a multicomponent system.* IEEE Transactions on Plasma Science, 1995. **23**(4): p. 709-716.

94. Franklin, R.N., Snell, J., *The transition from collisionless to collisional active plasma in the fluid model and the relevance of the Bohm criterion to sheath formation.* Physics of Plasmas, 2000. **7**(7): p. 3077-3083.

95. Brown, S.C., *Introduction to electric discharges in gases*. 1966, New York: J. Wiley.

96. Valentini, H.B., Glauche, E., *Boundary layers in collisional plasmas with local plasma generation and recombination in the volume and at the wall.* Plasma Sources science and Technology, 1996. **5**: p. 696-703.

97. Sheridan, T.E., Goree, J., *Collisional plasma sheath model.* The Physics of Fluids B, 1991. **3**(10): p. 2796-2804.

98. Mukherjee, S., John, P., *Equilibrium characteristics of strong ion sheaths in a partially ionized plasma.* IEEE Transactions on Plasma Science, 1995. **23**(2): p. 133-137.

99. Mukherjee, S., *Effect of charge exchange collisions on the static properties of a fully collisional ion sheath.* IEEE Transactions on Plasma Science, 1995. **23**(5): p. 816-821.

100. Klemperer, O., *Electron physics*. 1972, London: Butterworths.

101. Sheridan, T.E., Goree, J.A., *Analytic expansion for the electric potential in the plasma sheath.* IEEE Transactions on Plasma Science,, 1989. **17**(6): p. 884-888.

102. Wang, S.-B., Wendt, Amy E., *Sheath thickness evaluation for collisionless or weakly collisional bounded plasmas.* IEEE Transactions on Plasma Science,, 1999. **27**(5): p. 1358-1365.

103. Riemann, K.U., *The influence of collisions on the plasma sheath transition.* Physics of Plasmas, 1997. **4**(11): p. 4158-4166.

104. Lieberman, M.A., Lichtenberg, A. J., *Principles of plasma discharges and material processing*. 1994: John Wiley, N. Y.

105. Holmes, R., Freeston, I.L., *Comparison of probe and spectroscopic measurements in an argon plasma jet.* Journal of Physics D: Applied Physics, 1971. **4**: p. 452.

106. Gick, A.E.F., Quigley, M.B.C., Richards, P.H., *The use of electrostatic probes to measure the temperature profiles of welding arcs*. 1973, CEGB.

107. Freeston, I.L., Kelk, J.E., *Ion current to a plane probe in a flowing plasma.* Electronics Letters, 1970. **6**(25): p. 809.

108. Freeston, I.L., Kelk, J.E., *Measurement of ion density in a plasma torch using a plane probe.* Electronics Letters, 1970. **6**(25): p. 811.

109. Lam, S.H., *A general theory for the flow of weakly ionized gases.* AIAA Journal, 1964. **2**(2): p. 256.

110. Cohen, I.M., *Asymptotic theory of spherical electrostatic probes in a slightly ionized, collision-dominated gas.* The Physics of Fluids, 1963. **6**(10): p. 1492.

111. Clements, R.M., Smy, P.R., *Ion current from a collision-dominated flowing plasma to a cylindrical electrode surrounded by a thin sheath.* Journal of Applied Physics, 1970. **41**(9): p. 3745.

112. Clements, R.M., Smy, P.R., *Sheath convection effects with flush-mounted electrostatic probes.* Canadian Journal of Physics, 1971. **49**: p. 2540.

113. Clements, R.M., Kerr, R.D., Offenberger, A.A., Smy, P.R., *Transition from sheath-convection to saturation-current behaviour of a Langmuir probe in a flowing plasma.* Electronics Letters, 1972. **8**: p. 361-362.

114. Clements, R.M., Smy, P.R., *Ion saturation currents to planar Langmuir probes in a collision-dominated flowing plasma.* Journal of Physics D: Applied Physics, 1973. **6:** p.184-195..

115. Clements, R.M., Smy, P.R., *Comments on 'the use of electrostatic probes to measure the temperature profiles of welding arcs.* Journal of Physics D: Applied Physics, 1974. **7**(L133): p. Author's reply, L135.

116. Clements, R.M., Smy, P.R, *Transition from diffusion-convection to sheath-convection of a cold Langmuir probe in a moving compressible plasma to.* Journal of Physics D: Applied Physics, 1981. **14**: p. 1001-1008.

117. Clements, R.M., Dawe, J.R., Rizvi, S.A.H., Smy, P.R, *Measurement of sheath characteristics in the presence of convection and ionisation.* Canadian Journal of Physics, 1996. **74**: p. 671.

118. Smy, P.R., Noor, A.Ibn, *High-pressure Langmuir probe in a weak flowing plasma or a plasma sheath.* Journal of Applied Physics, 1976. **47**(4): p. 1327-1331.

119. Chung, P.M., Talbot, L., Touryan, K.J., *Electrostatic probes in stationary and flowing plasmas, part1 and 2.* AIAA Journal, 1974. **12**(2): p.133-154.

120. Tichy, M., Šicha, M., David, P., David, T., *A collisional model of the positive ion collection by a cylindrical Langmuir probe.* Contribution to Plasma Physics, 1994. **34**: p. 59-68.

121. Tichy, M., Kurdna, P., Behnke, J.F., Csambal, C., Klagge, S., *Langmuir probe diagnostics for medium pressure and magnetized low-temperature plasma.* Journal de Physique De France IV, 1997. **Colloque C4**(Supplement au Journal de Physique III): p. C4-397.

122. Tichy, M., Pfau, S., Špatenka, P., *Langmuir probe diagnostic of low temperature plasmas (review lecture)*, in *Workshop on Plasma diagnostics, 26-28 Aug. 1999*. 1999. Gent, Belgium.

123. Benilov, M.S., *Theory of electrical probes in flows of high-pressure weakly ionized plasma.* High Temperature, 1989. **26**(5): p. 780-793.

124. Carrer and Fendell, T.P.o.F.V., N. 12, 1970, pp. 2966.

125. Chang, W., Bienkowki, G.K., *Effects of electron emission on electrostatic probes at arbitrary pressures.* The Physics of Fluids, 1970. **13**(4): p.902-920.

126. Wasserstrom, E., Su, C.H., Probstein, R.F., *Kinetic theory approach to electrostatic probes.* The Physics of Fluids, 1965. **8**(1): p. 56-72.

127. Waymouth, J.F., *Perturbation of a plasma by a probe.* The Physics of Fluids, 1964. **7**: p. 1843.

128. Little, R.G., Waymouth, J.F., *Experimentally determined plasma perturbation by a probe.* The Physics of Fluids, 1966. **9**(4): p. 801.

129. Bohm, D., ed. *The characteristics of electrical discharges in magnetic fields*. ed. A. Guthrie, Wakerling, R.K. 1949, Mc Graw-Hill: New York. 77-86.

130. Sheridan, T.E., *How big is a small Langmuir probe?* Physics of Plasmas,, 2000. **7**(7): p. 3084-3088.

131. Huang, K.J., *Statistical mechanics*. 1987: Wiley, New York.

132. Allen, J.E., Boyd, R.L.F., Reynolds, P. in *Proceedings of the Physical Society*. 1957.

133. Laframboise, J.F., *Utias rept. 106*. 1966, University of Toronto.

134. Chen, F.F., *Saturation ion currents to Langmuir probes.* Journal of Applied Physics, 1965. **36**(3 (Part 1)): p. 675.

135. Fernandez Palop, J.I., Ballestreros, J., Colomer, V., Hernandez, M.A., *Theoretical ion current to cylindrical Langmuir probes for finite ion temperature values.* Journal of Physics D: Applied Physics, 1996. **29**: p. 2832.

136. Chou, Y., S., Talbot, L., Willis, D.R., *Kinetic theory for a spherical electrostatic probes in a stationary plasma.* The Physics of Fluids, 1966. **9**(11): p. 2150-2167.

137. Petrie, T.W., Pfender, E., ed. *A sweeping wire probe for the study of local heat transfer in plasmas*. Progress in heat and mass transfer, ed. T.F. Irvine, Ibele, W.E., Hartnett, J.P., Goldstein, R.J. Vol. 2, Eckert presentation volume. 1969, Pergamon Press: Oxford.

138. Holman, J.P., *Heat transfer*. 1990, New York: Mc Graw-Hill.

139. Zel'dovich, Y.B., Raizer, Yu. P., *Physics of shock waves and high-temperature hydrodynamic phenomena*, ed. R.F.P. W.D.Hayes. 1966: Academic Press, New York, London.

140. Menart J., M.S., Lin L., *Coupled radiative, flow and temperature-field analysis of a free-burning arc.* Journal of Physics D: Applied Physics,, 2000. **33**: p. 257.

141. Rosenberg, H.M., *The solid state*. 1989, Oxford: Oxford University Press.

142. Kittel, C., *Introduction to solid state physics*. 1996 N.Y., Brisbane, Toronto: J. Wiley & sons.

143. Beck, A.H.W., Ahmed, H., *An introduction to physical electronics*. 1968, London: Arnold.

144. CRC press, *CRC handbook of physics and chemistry, 1993-94.* 74th ed. 1993.

145. Testé, P., Chabreire, J. P., *Some improvements concerning the modeling of the cathodic zone of an electric arc (ion incidence of electron emission and the 'cooling effect').* Journal of Physics D: Applied Physics, 1996. **29**: p. 697-705.

146. Vilarinho, L.O., Fanara, C., t*o be published.* 2003.

147. Minerbo, G.N., Levy, M.E., SIAM Journal of Numerical Analysis, 1969. **6**: p. 598-616.

148. Anderssen, R.S., *Stable procedures for the inversion of Abel's equation.* J. Inst. Mathematics Applications, 1976. **17**: p. 329-342.

149. Nestor, O., Olsen H.N., *Numerical methods for reducing line and surface probe data.* SIAM Review, 1960. **2**(3): p. 200.

150. Purcell, E.M., *Elettricita' e magnetismo, la fisica di Berkeley Vol. 2*. 1985, Bologna, Zanichelli.

151. Lowke, J.J., Kovyta, P., Schmidt, H.P., *Theory of free-burning arc columns including the influence of the cathode.* Journal of Physics D: Applied Physics, 1992. **25**: p. 1600-1606.

152. Artsimovic, L., *Fisica elementare del plasma*. 1966, Moscow: Atomizdat., Roma 1975 (italian translation).

153. Hutchinson, I.H., *Principles of plasma diagnostics*. 1987, Cambridge: Cambridge University Press.

154. Benilov, M.S., *Ion saturation currents to spherical and cylindrical electrostatic probes in collisional plasmas.* Journal of Applied Physics, 1991. **70**(11): p. 6726-6731.

155. Tsuij, H., Toshisuke, H., *Ion current distribution around an electrically conductive body in ionized gas flow.* AIAA J., 1973. **11**(1): p. 100-102.

156. Benilov, M.S., *Modeling of a non-equilibrium cylindrical column of a low-current arc discharge.* IEEE Transactions on Plasma Science, 1999. **Vol 27**(N. 5): p. 1458.

157. Vilarinho, L.O., *Optical emission spectroscopy*. 2002, Internal Report Cranfield University: Cranfield.

158. Haddad, G.N., Farmer, A.J.D., Kovyta, P., Cram, L.E., *Physical processes in gas-tungsten arcs.* IEEE Transactions on Plasma Science, 1986. **PS-14**: p. 333.

159. Chang, C.W., Eagar T. W.,Szekely J. *The modelling of gas velocity fields in welding arcs,* in *Arc physics and weld pool behaviour,* London 8-10 May.1979. The Welding Institute, Abington, Cambridge 1980, Paper 13, p. 381-388.

160. Fang, M.T.C., Zhang, JinLing, Private communication, 2002.

161. Clements, R.M., Smy, P.R, *The floating potential of a Langmuir probe in a high-pressure plasma.* Journal of Physics D: Applied Physics, 1974. **7**: p. 551-562.

162. Tanaka, M., Ushio, M., *Observations of the anode boundary layer in free-burning argon arcs.* Journal of Physics D: Applied Physics, 1999. **32**: p. 906-912.

163. Bauder, U., Devoto, R.S., Mukherjee, D., *Measurement of electrical conductivity of argon at high pressure.* The Physics of Fluids, 1973. **16**(12): p. 2143-2148.

164. Poisel, H., Landers, F.J., Hoeβ, P., Bauder, U.H., *Electrical and optical properties of high-pressure argon plasma.* IEEE Transaction on Plasma Science, 1986. **PS-14**(4): p. 306-318.

165. Griem, H.R., *Principles of plasma spectroscopy*. 1997, Cambridge: Cambridge University Press.

166. Cram, L.E., Poladian, L., Roumeliotis, G., *Departures from equilibrium in a free-burning argon arc.* Journal of Physics D: Applied Physics, 1988. **21**: p. 418.

167. Bober, L., Tankin R. S., Journal of Quant. Spectrosc. Radiat. Transfer, 1970. **10**: p. 991-1000.

168. Allum, C.J., *Characteristics and structure of high pressure (1-42 bars) gas tungsten arcs, Ph.D. Thesis*. 1982, Cranfield University.